Calibration of the clumped-isotope thermometer in foraminifera and its application to paleoclimatic reconstructions of the mid-Pleistocene in the Gulf of Taranto

Marion Peral

université PARIS-SACLAY

LSCE

cea

UNIVERSITÉ PARIS SUD

NNT : 2018SACLS382

Thèse de doctorat

Calibration of the clumped-isotope thermometer in foraminifera and its application to paleoclimatic reconstructions of the mid-Pleistocene in the Gulf of Taranto

Thèse de doctorat de l'Université Paris-Saclay
préparée à l'Université Paris-Sud

École doctorale n°579 Sciences Mécaniques et Energétiques, Matériaux et Géosciences (SMEMAG)
Spécialité de doctorat : Terre solide : géodynamique des enveloppes supérieures, paléobiosphère

Thèse présentée et soutenue à Gif-sur-Yvette, le 19 octobre 2018, par

Marion Peral

Composition du Jury :

Giuseppe Siani *Professeur des Universités* *Laboratoire Géosciences Paris-Sud (GEOPS), UMR 8148*	Président
Cedric John *Directeur de Recherche* *Department of Earth Science and Engineering,* *Imperial College London, UK*	Rapporteur
Nele Meckler *Chargé de Recherche* *Department of Earth Science, University of Bergen,* *BJERKNES Center Norvège*	Rapporteur
Thibault De Garidel-Thoron *Chargé de Recherche (CNRS)* *CL-Climats – CEREGE, Aix-en-Provence, France*	Examinateur
Bruno Malaizé *Maitre de Conférences (HDR)* *UMR CNRS 5805 EPOC - OASU - Université de Bordeaux, France*	Examinateur
Dominique Blamart *Directeur de Recherche (CEA)* *LSCE, CNRS/CEA, IPSL, UVSQ, Paris-Saclay*	Directeur de thèse
Franck Bassinot *Directeur de Recherche (CEA)* *LSCE, CNRS/CEA, IPSL, UVSQ, Paris-Saclay*	Co-Directeur de thèse
Mathieu Daëron *Chargé de Recherche (CNRS)* *LSCE, CNRS/CEA, IPSL, UVSQ, Paris-Saclay*	Co-Encadrant de thèse

Remerciements

Bon ça y est, nous y sommes, la fin de ces trois ans d'aventure au LSCE. Il y a tant de personnes à remercier, mais commençons par le commencement, mes encadrants de thèse et mon jury :

Je souhaite commencer par mon directeur de thèse, Dr Blamart ou tonton Dominique, tant de surnoms, mais je ne les donnerai pas tous ! Dominique, ça a été un réel plaisir de travailler avec toi durant toutes ces années. Je te remercie pour ta gentillesse, ton soutien et ta présence, sans oublier ton humour, toujours plein de finesse ! J'espère que l'on restera en contact encore un bon moment.

Ensuite, je remercie vivement mon co-encadrant de thèse, Mathieu Daëron. J'ai beaucoup appris scientifiquement à tes côtés et particulièrement en statistiques... Je promets de m'inscrire à une formation python très prochainement ! Même si je sais que pour toi ça a été difficile que l'on ne partage pas cette passion pour le café, je serai toujours contente de te retrouver autour d'une Margarita !

Je remercie aussi mon co-directeur de thèse, Franck Bassinot, pour nos échanges scientifiques sur la partie « paléo » qui ont été instructifs et enrichissants. Nous partageons tous deux un trait de caractère bien spécifique, de vrai tête de mule, comme tu le dis si bien ! Mais c'est grâce à ça que nos échanges ont été prolifiques. Merci !

Un grand merci aussi aux membres du jury qui ont accepté de lire et d'évaluer ce travail : Cedric John, Nele Meckler qui ont été mes rapporteurs, Thibault de Garidel-Thoron, Bruno Malaizé, mes examinateurs et le président du jury, Giuseppe Siani. C'est toujours un plaisir de discuter avec vous. J'espère pouvoir vous revoir lors des prochaines conférences.

Voilà, et pourtant tellement d'autres personnes à remercier encore alors c'est parti :

D'abord, je souhaite remercie le CEA, qui a accepté ma candidature en thèse et m'a ainsi apporté un support financier durant ces 3 ans.

Cette thèse a été réalisée grâce à des collaborations. Je tiens donc également à remercier Catherine Kissel pour le temps que tu as pris dans ma recherche d'échantillons afin de réaliser au mieux cette calibration ; Franz Jorissen et son équipe pour votre chaleureux accueil à Angers ; les italiennes, Patrizia Maiorano, Angela Girone et Maria Marino, de l'Université de Bari pour votre investissement dans le projet de Montalbano Jonico et votre encadrement sur le terrain ; le laboratoire du CEREGE et particulièrement Thibault de Garidel-Thoron, Clara Bolton et Yannick Donnadieu pour votre gentillesse et votre intérêt scientifique ; et enfin le laboratoire EPOC, Thibault Caley, Bruno Malaizé, Linda Rossignol-Malaizé, Marie-Hélène Castéra et Jérôme Bonnin, qui m'ont vue grandir et m'ont toujours soutenue au cours de mes 9 ans d'études. J'espère pouvoir continuer à travailler avec vous tous dans le futur !

Un grand merci aussi à M. Jean-Claude Duplessy pour nos discussions toujours très enrichissantes.

Aline Govin et Natalia Vazquez Riveiros, comment vous dire merci… Vous deux, qui n'aviez rien à voir avec mon sujet de thèse, vous avez été très présentes pour m'aider à me lancer dans l'aventure. Je vous suis réellement reconnaissante et j'espère que l'on aura l'occasion de travailler ensemble et de se voir dans le futur. Je vous souhaite plein de bonheur pour la suite !

Je souhaite aussi remercier les géologues ou la partie obscure de la force…

Hervé Guillou, dit père castor, tu as été un vrai soutien pendant cette thèse, tu as su nous aider au mieux pour que tout se déroule de la meilleure façon possible, alors un énorme merci ! Merci aussi pour tes anecdotes d'antan, qui m'ont fait voyager au pays des jadis et t'a valu ce superbe surnom !

Merci aussi à Sébastien Nomade, pour ta joie de vivre, tes punchlines, et tes blagues ! Si, si, tes blagues ! Malgré tout, je suis forcée d'avouer que ça va me manquer… Au plaisir de te revoir et j'espère de travailler ensemble par la suite.

Et pour finir, Vincent Scao, merci pour ta zénitude et ces bons moments passés sur le terrain. Je suis sûre que la perruque de Dominique peut se recycler pour ton concert événement : le come-back de Claude François !

Je voudrais maintenant particulièrement remercier le reste de l'équipe paléocéan pour leur accueil et leur participation : Elisabeth Michel, Claire Waelbroeck et Bruno Lansard pour toutes nos discussions scientifiques qui ont permis d'avancer au mieux mes réflexions, merci aussi Claire de m'avoir donné l'opportunité d'embarquer sur le Marion-Dufresne, c'était une belle expérience ; Gulay Isguder pour ton aide dans la reconnaissance de certaines espèces de foraminifères ; Fabien Dewilde et Hélène Rebaubier pour votre soutien, votre gentillesse et votre investissement dans ma thèse… ça a été un réel plaisir de travailler avec vous ; et enfin, Anouk Villedieu, Laetitia Leroy et Nicolas Smialkowski, un grand merci pour votre aide sur le piquage et les mesures spectro, vous avez joué un rôle très important scientifiquement et personnellement durant ma thèse, mais j'y reviendrai plus tard…

Et plus largement, je voudrais remercier infiniment les nombreuses personnes avec qui j'ai eu la chance et le plaisir d'échanger au long de ma thèse, au détour des couloirs du LSCE, lors des missions, ou en conférences et à l'école d'été.

Les amis… Rien n'aurait été possible sans vous… Je pourrais écrire tant de chose pour vous remercier mais j'ai un nombre de pages limitées alors voilà :

D'abord mes deux co-bureaux… Qui aurait cru que partager un bureau permettrait de créer d'aussi bels amitiés. Alison tu as été un soutien énorme pendant 3 ans et je ne saurai trouver les mots pour te remercier. J'ai eu la chance de pouvoir suivre un peu ton parcours au LSCE et tu as été une réelle source d'inspiration et d'exemplarité pour moi. Et j'espère réellement que l'on pourra retravailler ensemble dans peu de temps, parce que nos commérages me manquent…! Et Dariouche… Ah Dariouche, un vrai boute-en-train ! On a toujours su trouver les mots pour se rassurer ou pour se faire rire ! Ou du moins les livres… D'ailleurs, voici un petit extrait du dernier que tu m'as offert (amis belges, je n'assume pas cette blague et m'en excuse par avance…) : « Un hélicoptère s'est écrasé dans un cimetière belge ; la police a déjà récupéré plus de 300 victimes. » (L'Humour pour les nuls). Alors ? Avoue, je suis beaucoup plus drôle que ça en vrai ! A vous deux, je promets d'installer votre

photo portrait sur mon futur bureau et d'utiliser uniquement mes super gommes Alpaga !

Ensuite, tous les copains ! Je dois dire que j'ai eu de la chance d'être tomber sur une aussi belle équipe avec qui partager le troisième étage du LSCE. Alors c'est parti, Laurine merci pour ta spontanéité, ta générosité, ta joie de vivre et ta présence... j'ai hâte de braver les cyclones pour venir te rendre visite à l'autre bout du monde ! Kristan, merci d'être toi, promet moi de continuer à être positif et à toujours dire « non mais… » ! Rana, tu es super, ne change rien ! J'ai hâte de commencer la petite chasse au trésor à Venise. Dr Claire, on s'appelle pour nos dispenses du prochain cours de maths… Laurie et Romain, merci d'avoir été ma bouffée d'air frais du sud-ouest ! Vive les poches et les chocolatines ! Laetitia, merci pour tout, tu es une fée de la cuisine ! Anouk et Naoufel, ou Maman et Papa, ça a été un véritable plaisir de passer ces 3 ans avec vous, j'ai hâte de refaire nos soirées jeux ! Nico, merci pour tout, je n'oublie pas que je te dois une bière pour ton prochain cours de jazz ! Juste mille mercis à vous tous ! Je vous souhaite que du bonheur pour la suite et j'ai hâte de vous revoir vite pour danser sur K-maro !

Et enfin les autres copains rencontrés bien avant cette aventure LSCE (Marion, Mickael, Marine, Clarisse, Alice, la team basket…) ou au cours de la thèse (les super cool USSP - included Ilja, Mirian…), un grand merci à vous d'avoir fait partie de ma vie pendant tout ce temps.

Je voudrais finir par ma famille et quelques personnes qui me sont proches. D'abord je souhaite remercie mon orthophoniste, Mme Guerrier, qui m'a suivie pendant plus de quinze ans et a su m'apprendre à me surpasser pour que j'arrive où j'en suis aujourd'hui. Ce sera toujours un plaisir de te revoir et d'aider d'autres enfants en difficulté scolaire à cause de la dyslexie. Ensuite, Jean-Charles, merci pour ta gentillesse et ta générosité, je suis contente de faire partie de ta vie. Ma mamie… une vraie force de la nature, j'espère avoir ta vivacité plus tard. Et, à mes oncles et tantes, mes cousins et cousines, merci à vous ! Pour finir, ma petite sœur, merci pour ton soutien qui dure déjà depuis ma première année de fac. Je ne peux que te souhaiter de vivre tes rêves et te promettre de t'accompagner à la hauteur de ton soutien pour moi. Et ma maman, ma petite maman, qui a toujours cru en moi, les mots me manquent pour te remercier… alors juste un énorme merci pour ton accompagnement depuis toutes ces années. Tu as été un pilier pendant ces 3 ans et a su supporter mes mauvaises humeurs, merci !

Voilà, mes dernières lignes… Pour finir, je souhaite citer un auteur qui m'est cher : « Rien ne développe l'intelligence comme les voyages » (Emile Zola), cette thèse fut un beau voyage. Merci à tous !

TABLE OF CONTENTS

Changes in Holocene Meridional circulation and poleward Atlantic flow: the bay of Biscay as a nodal point
Mary Y., Eynaud F., Colin C., Rossignol L., Brocheray S., Mojtahid M., Garcia J., Peral M., Howa H., Zaragosi S., Cremer M.
Climate of the Past. 2017

Most earth-surface calcites precipitate out of isotopic equilibrium
Daëron M., Drysdale R. N., Peral M., Huyghe D., Blamart D., Coplen T. B., Lartaud F., Zanchetta G.
Nature communication. In review

High-resolution foraminifer stable isotope record of MIS 19 at Montalbano Jonico, southern Italy: a window into Mediterranean climatic variability during a low-eccentricity interglacial
Nomade S., Bassinot F., Marino M., Simon Q., Dewilde F., Maiorano P., Isguder G., Blamart D., Girone A., Scao V., Pereira A., Toti F., Bertini A., Combourieu-Nebout N., Peral M., Bourlès D. L., Petrosino P., Gallicchio S., Ciaranfi N.
Quaternary Science Reviews. In review

Résumé en français / French summary

L'océan joue un rôle central dans la redistribution de la chaleur à l'échelle globale. La température des eaux océaniques est donc un élément clé de la variation climatique naturelle qui nous renseigne en particulier sur la sensibilité de celle-ci au forçage radiatif (insolation contrôlée par les paramètres orbitaux, teneur de l'atmosphère en gaz à effets de serre). Un des enjeux majeurs en paléoclimatologie est de reconstruire aussi précisément que possible l'amplitude des variations passées de température des masses d'eaux océaniques de surface et profondes. Le sujet de cette thèse s'inscrit dans cette problématique , il porte : (1) sur l'implémentation, l'amélioration et la calibration de la méthode de thermométrie appelée «clumping isotopique appliquée à l'analyse des coquilles calcaires ($CaCO_3$) de microfossiles marins unicellulaires, les foraminifères, et (2) sur l'application de cette méthode pour reconstruire les changements de température océanique lors de la transition du Pléistocène moyen, une période clé de l'histoire récente de la Terre qui voit la mise en place, il y a ~ 1 Million d'années (Ma), de cycles glaciaires-interglaciaires de grande amplitude et de période ~ 100 ka, typiques du climat moderne.

1. LE CONTEXTE CLIMATIQUE

Au cours du Quaternaire (2.588 Ma à aujourd'hui), le système climatique terrestre a subi des variations quasi-périodiques avec l'alternance de périodes froides (périodes glaciaires) et chaudes (périodes interglaciaires). Le timing de ces oscillations climatiques de grande ampleur est contrôlé par les variations des trois paramètres orbitaux de la terre que sont l'excentricité, l'obliquité et la précession. La combinaison des ces trois paramètres détermine la distribution saisonnière de l'insolation reçue par notre planète aux différentes latitudes. Le climat, aux échelles de 10^4-10^5 est donc sous la dépendance des variations naturelles et cycliques de ce forçage orbital, combinées à des rétroactions internes faisant intervenir la circulation océanique, la dynamique des calottes de glace et les variations des gaz à effet de serre. Si les variations orbitales constituent indéniablement le pacemaker des cycles glaciaires-interglaciaires, la réponse du climat est complexe et fortement non-linéaire comme le montre la transition

du Pléistocène moyen (MPT) caractérisée par un changement de la réponse climatique aux paramètres orbitaux qui se traduit par :

- Un changement de la période dominante des cycles glaciaires-interglaciaires (notés G-IG par la suite) qui passe de 41 000 ans (41 ka ; correspondant à l'obliquité) à ~100 000 ans (100 ka ; correspondant à l'excentricité),
- Une augmentation d'amplitude des cycles climatiques,
- Une augmentation de l'asymétrie entre les périodes glaciaires et les périodes interglaciaires (Figure 1; $\delta^{18}O$ stack des foraminifères benthiques de Lisiecki and Raymo, 2005).

Les limites temporelles et la définition même de cette transition climatique majeure font toujours débat au sein de la communauté scientifique (e.g. Ruddiman et al., 1986; Lisiecki and Raymo, 2005; Lang and Wolff, 2011; Head and Gibbard, 2015). Cependant, des études récentes (e.g. Head and Gibbard, 2015) fixent la MPT entre 1,4 et 0,4 Ma. Les principaux changements climatiques associés à la MPT sont résumés dans la Figure 1, découpée en 4 intervalles suivant la durée et l'intensité du signal de $\delta^{18}O$ des cycles G-IG :

- Intervalle A : Avant le Stade Isotopique Marin (MIS) 45 (1.4 Ma), Lisiecki and Raymo (2005) observent dans leur stack $\delta^{18}O$ sur les foraminifères benthiques (noté $\delta^{18}O_{stack}$ pour la suite) une symétrie entre les périodes glaciaires et interglaciaires. Cette cyclicité est associée à une période de 41 ka, correspondant à la prédominance de l'obliquité (Liu et al., 2008).
- Intervalle B : L'initiation de la MPT, au MIS 45, est associée à la diminution de la durée des interglaciaires et à l'allongement des glaciaires. Du MIS 45 au MIS 25, incluant le « super-interglaciaire » MIS 31 (DeConto et al., 2012), le contraste climatique entre les périodes glaciaires et interglaciaires augmente, et certains auteurs pensent que ce changement est associé à une diminution du taux de CO_2 atmosphérique et un refroidissement global des températures de surface des océans (Diekmann and Kuhn, 2002; Lisiecki and Raymo, 2005; Clark et al., 2006; McClymont et al., 2008, 2013; Sosdian and Rosenthal, 2009; Hönish et al., 2009; Chalk et al., 2017).
- Intervalle C : On note une intensification du signal de $\delta^{18}O_{stack}$ durant la période allant du MIS 24 au MIS 19. Cette période se caractérise par un allongement et une

intensification des périodes glaciaires, associée à un refroidissement global des températures océaniques de surface (Schefuß et al., 2003, 2005 ; Marino et al., 2008, 2011 ; Kim et al., 2013 ; McClymont et al., 2013) et d'importants changements climatiques comme l'intensification des moussons d'hiver en Asie du Sud-Est (Figure 1).

- Intervalle D : Le passage plus marqué des cycles glaciaire-interglaciaire à une période de 100 ka se réalise entre les stades MIS 19 et 12/11. Cette période est marquée par des grandes amplitudes climatiques et une forte asymétrie entre les cycles glaciaires-interglaciaires (Lisiecki and Raymo, 2005) : les entrées en glaciations sont plus lentes et les déglaciations plus rapides. La MPT se termine par le long et chaud interglaciaire MIS 11 (0,4 Ma) qui enregistre la plus grande amplitude climatique dans les données de $\delta^{18}O$ des foraminifères (Droxler et al., 2003 ; Lisiecki and Raymo, 2005 ; Weirauch et al., 2008 ; Candy et al., 2014).

Alors que le forçage orbital est la principale cause des oscillations glaciaire-interglaciaire au Quaternaire, le passage -durant la MPT- de cycles climatiques de 41 ka à des cycles de 100 ka, doit faire intervenir des mécanismes internes puisque le forçage orbital ne change pas à travers cette période. Plusieurs hypothèses ont été avancées, principalement associées à des mécanismes tels qu'un long refroidissement des eaux océaniques de surface entrainant l'expansion de la banquise Antarctique, l'érosion régolithique, la fertilisation des océans de l'hémisphère Sud (amélioration de la pompe biologique), ou bien encore, l'altération des silicates, ces trois derniers mécanismes agissant sur la teneur en CO2 atmosphérique (effet de serre)… Afin de comprendre les mécanismes qui agissent durant la MPT et tester les différentes hypothèses, il est primordial de bien documenter les changements d'amplitude des variations de températures des eaux océaniques de surface et de profondeur entre les périodes glaciaires et les périodes interglaciaires (évolution à long-terme, transfert de chaleur entre les basses et les hautes latitudes, sensibilité du climat...).

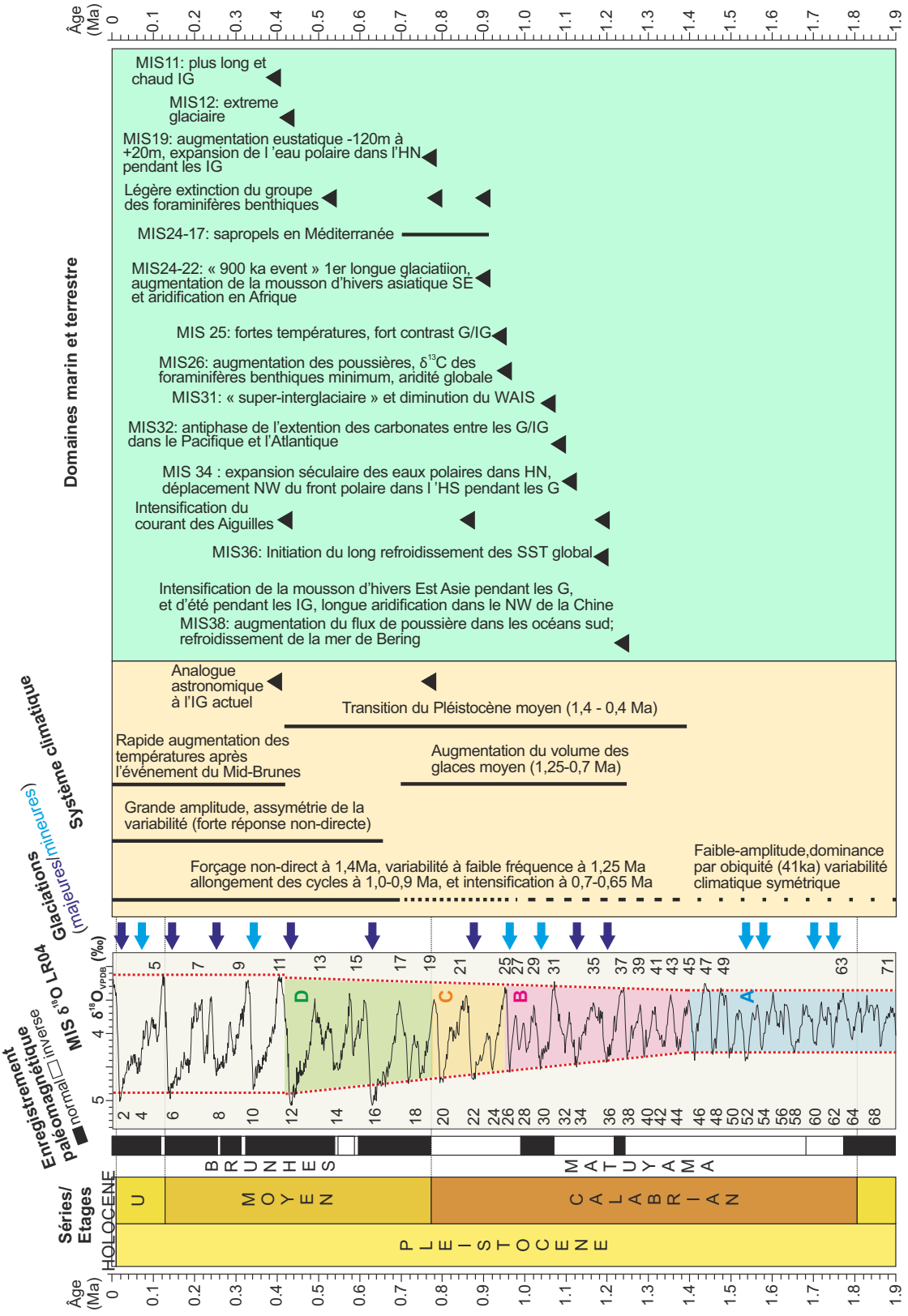

Figure 1 : Synthèse de l'évolution du système climatique lors de la MPT (1,4 Ma à 0,4 Ma) où sont distingués les principaux évènements terrestres et marins. Les données sont issues de Marra et al., 2014; Bellucci et al., 2015; Head et al., 2008; Lisiecki and Raymo, 2005, d'après Head and Gibbard, 2015, avec G: glaciaire et IG: Interglaciaire

Cette thèse s'intègre dans cette problématique. Elle a pour objectifs principaux (1) de développer le paléothermomètre dérivé du clumping isotopique au LSCE, (2) d'établir une **calibration robuste** pour son application à l'étude des foraminifères planctoniques et benthiques, et (3) d'appliquer cette méthode afin de documenter les **variations paléo-environnementales de la MPT** (évolution à long-terme, et focus sur deux périodes clés : le MIS 31 le MIS 19). Pour des raisons à la fois pratique et climatique, nous avons choisi de travailler sur une série marine récemment exondée, située sur le pourtour de la Méditerranée occidentale, à Montalbano Jonico. Cette série nous assure l'accès facile à un matériel d'étude abondant, un élément essentiel puisque la mesure du clumping-isotopique requière des échantillons de plusieurs milligrammes de $CaCO_3$, et plusieurs réplicats sont nécessaires sur chaque niveau étudié pour faire diminuer l'incertitude analytique à un niveau compatible avec les interprétations paléo-climatiques.

2. LA CALIBRATION Δ_{47} – TEMPERATURES DE CALCIFICATION DES FORAMINIFERES

L'estimation précise et fiable des températures océaniques du passé, reste aujourd'hui un enjeu scientifique majeur. De nombreuses méthodes ont été développées, basées sur des approches micropaléontologiques (technique des analogues modernes), biogéochimiques ($U^{k'}_{37}$, TEX_{86}) ou géochimiques (éléments traces, isotopie stable de l'oxygène…). Cependant, ces méthodes souffrent de nombreux biais et de problèmes encore mal contraints. Ainsi, les méthodes physico-chimiques les plus couramment employées ces dernières années (d18O, rapport Mg/Ca) souffrent-elles de biais telles que la dépendance à la composition isotopique de l'oxygène de l'eau de mer ($\delta^{18}O_{eau\ de\ mer}$), les variations de la salinité, ou l'impact de la biologie des organismes étudiés (effet vital).

Une méthode alternative prometteuse pour la reconstruction des températures du passé est le paléothermomètre basé sur le clumping isotopique dans les carbonates (Ghosh et al., 2006 ; Eiler, 2007, 2011). Noté Δ_{47}, ce clumping-isotopique décrit certaines propriétés statistiques caractérisant la répartition des isotopes du carbone (^{12}C, ^{13}C) et

de l'oxygène (^{16}O, ^{17}O, ^{18}O) dans le carbonate de calcium ($CaCO_3$). Pour des raisons thermodynamiques, ce paramètre varie uniquement avec la température de formation des carbonates (Schauble et al., 2006) et est peu sensible aux biais physico-chimiques. Malgré de nombreuses avancées méthodologiques, l'application de ce thermomètre aux foraminifères (un constituant majeur des sédiments océaniques) reste cependant très limitée avec seulement deux calibrations disponibles (Tripati et al., 2010 et Grauel et al., 2013). Ces travaux ont proposé de nouvelles procédures de nettoyage et fourni des observations importantes comme l'absence d'effets vitaux dans la relation entre Δ_{47} et la température. Cependant, il est important de noter que ces deux études ont été réalisées antérieurement à certaines avancées méthodologiques majeures comme la mise en place d'un référentiel pour définir les valeurs de Δ_{47} (Dennis et al., 2011), les recommandations de l'utilisation des paramètres isotopique de Brand et al. (2010) pour définir les données brutes (Daëron et al., 2016) ou encore la distribution systématique de standards internationaux (Meckler et al., 2014 ; Bernasconi et al., 2018). Par conséquent, l'utilisation de ces calibrations pour reconstituer des températures dans le passé reste problématique.

La première partie de ma thèse consiste donc à établir une calibration appliquée aux foraminifères pour utiliser le paléothermomètre clumping isotopique dans des études paléocéanographiques. Afin de proposer une calibration qui soit la plus complète et robuste possible, j'ai examiné certains problèmes méthodologiques tels que les potentiels biais qui peuvent influencer les mesures de Δ_{47}. Nous présentons dans cette thèse une nouvelle calibration basée sur l'analyse de 9 espèces de foraminifères planctoniques et 2 espèces benthiques, prélevées dans des sommets de carottes (< 4000 ans) provenant de diffèrent bassins océaniques (Figure 2). Cette calibration couvre une gamme de température allant de -2 à 25 °C, parfaitement pertinente pour une très grande majorité d'études paléocéanographiques.

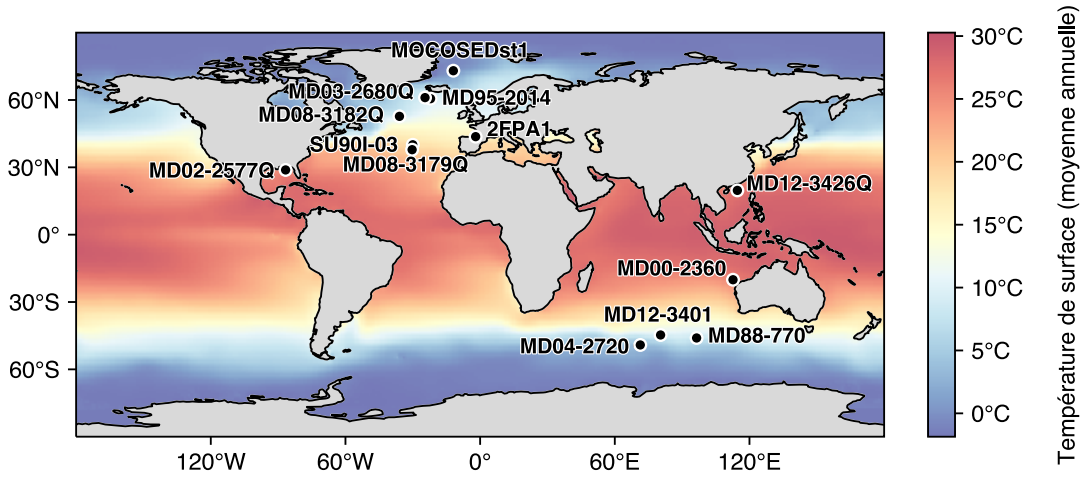

<u>Figure 2 :</u> Carte de localisation des sommets de carotte utilisée pour la calibration et les températures annuelles de surface de eaux issues du World Ocean Atlas (WOA13) en fond.

Pour établir une calibration, il faut tout d'abord déterminer quelles températures utiliser. Dans cette étude, 3 méthodes de détermination de températures ont été comparées (Figure 3) : (1) les températures issues de la base de données du World Ocean Atlas 2013 (WOA13), en estimant les profondeurs de vie et la saisonnalité des blooms de chaque espèce, (2) les températures de calcification des foraminifères calculées à partir des données de $\delta^{18}O$ en utilisant la calibration de Shackleton (1974), (3) les températures de calcification des foraminifères calculées à partir des données de $\delta^{18}O$ en utilisant la calibration de Kim et O'Neil (1997).

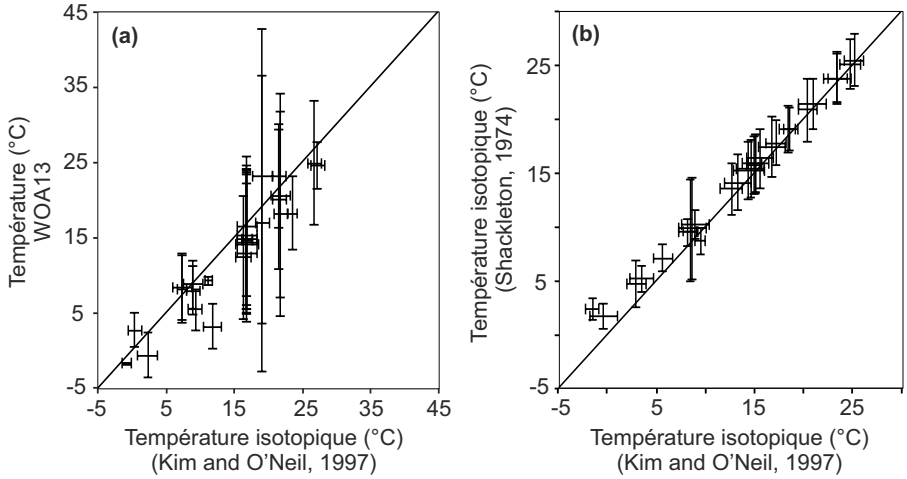

<u>Figure 3 :</u> Comparaison des températures (a) issues du WOA13 et dérivées des données isotopiques en utilisant la calibration de Kim et O'Neil (1997) et (b) dérivées des données isotopiques en utilisant la calibration de Shackleton (1974) et de Kim et O'Neil (1997)

Les températures (1) - (2) et (2) - (3) ont un relativement bon accord. Cependant, les températures (1) présentent de grandes incertitudes dues aux différentes hypothèses avancées sur la saisonnalité et la profondeur de vie des différentes espèces de foraminifères. La calibration de Kim et O'Neil (1997) couvre une gamme de température plus adaptée à cette étude que la calibration de Shackleton (1974), développée à partir des foraminifères benthiques uniquement. Pour ces raisons, les températures isotopiques (3) calculées avec l'équation de Kim et O'Neil (1997) ont été préférées pour établir cette calibration.

La méthode du clumping isotopique nécessite de piquer une grande quantité de matériel. Chaque mesure demande 2-3 mg de foraminifères (plusieurs centaines d'individus isolés sous loupe binoculaire). Pour obtenir une précision adaptée aux études paléocéanographiques, au minimum 4 réplicats doivent être analysés, soit 16 à 20 mg de foraminifères piqués (± 2000 individus) en incluant les pertes liées au protocole de nettoyage. Afin de réduire le temps de piquage, nous nous sommes intéressés aux effets liés à la taille des foraminifères. Pour combiner toutes les tailles de foraminifères ensemble en Δ_{47}, nous devons nous assurer qu'il n'y a pas de différence significative entre les différentes fractions. Pour cela, six espèces de foraminifères ont été piquées dans la plus large gamme de taille possible entre 200 et > 560 µm (par tranche de 50µm). La figure 4 présente les résultats de Δ_{47} et de $\delta^{18}O$ sur 6 espèces planctoniques et benthiques. Les valeurs Δ_{47} des différentes gammes de taille sont indiscernables les unes des autres. Les valeurs de $\delta^{18}O$ sont aussi indiscernables sauf pour une espèce (*G. inflata*). En effet, les effets liés à la taille des foraminifères sont très bien documentés aujourd'hui pour la méthode du $\delta^{18}O$. L'absence d'effet significatif en Δ_{47}, aux précisions obtenues, suggère que les différentes tailles de foraminifères peuvent être combinées les unes aux autres. Nous avons cependant considéré chaque mesure associée à une taille pour l'espèce *G. inflata* comme un échantillon individuel.

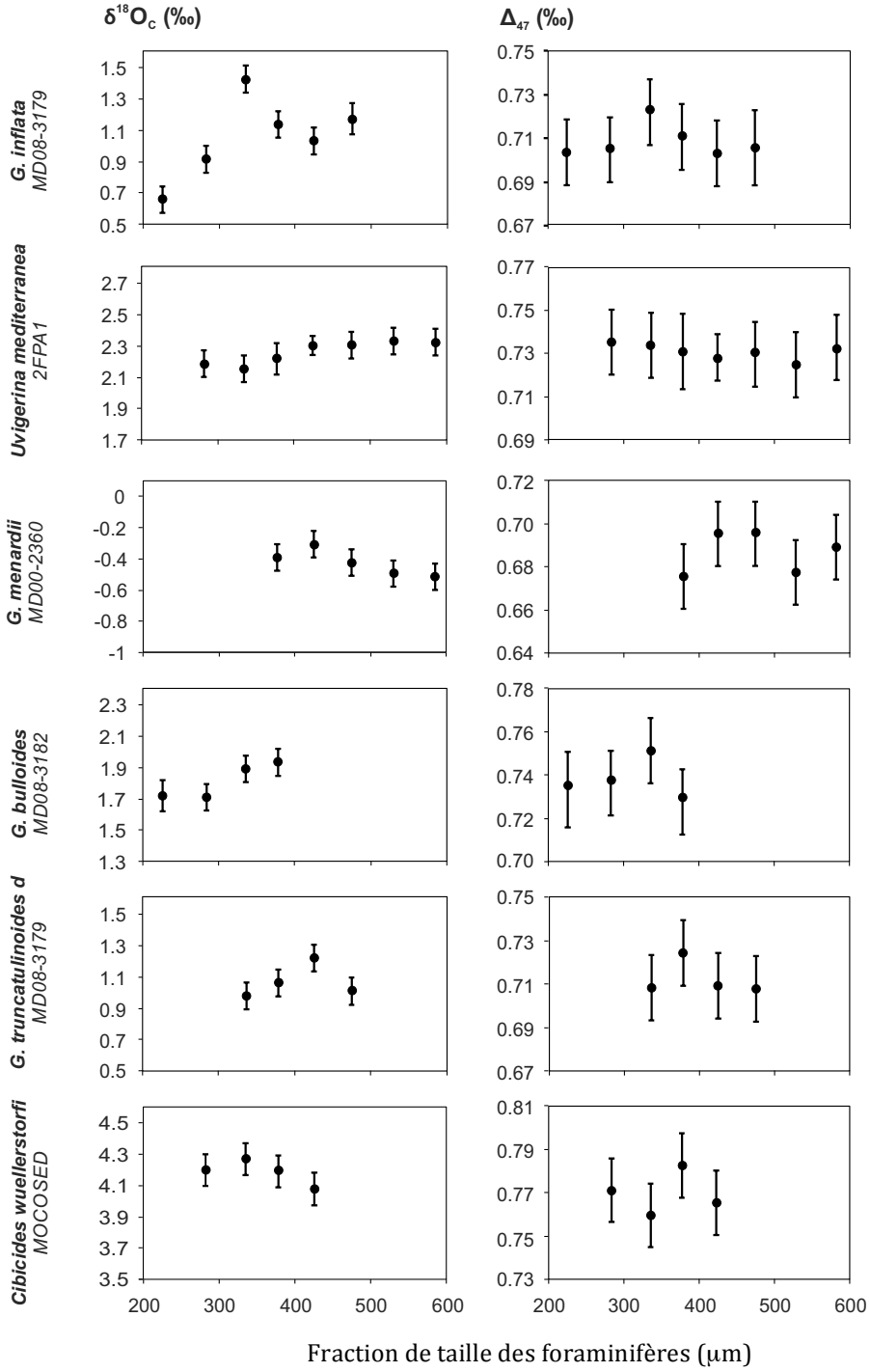

Figure 4 : Valeurs de $\delta^{18}O$ et Δ_{47} (2SE) pour six espèces de foraminifères à différentes fractions de taille.

Une relation robuste entre la température de calcification des foraminifères et les données Δ_{47} combinées par taille a donc été établie (Figure 5). Nous avons identifié un seul point de mesure anormale (« outlier ») à l'aide de tests statistiques. Cette régression présente une précision de l'ordre de ± 1 °C (95% Confidence Level).

Pour déterminer les potentiels biais associés à la biologie des espèces, nous avons calculé les résiduels pour chaque espèce utilisée dans la calibration. Les résiduels pour les espèces de surface, celles vivant à des plus grandes profondeurs dans la colonne d'eau et les foraminifères benthiques ne présentent pas de différence significative (Figure 6). Ce jeu de données permet de confirmer l'absence d'effets vitaux, comme les études précédentes l'avaient suggéré (Tripati et al., 2010 ; Grauel et al., 2013).

Ces données de calibration couvrent une gamme de salinité pertinente pour les études océanographiques (de 34 à 36). La Figure 7 présente le résiduel Δ_{47} de la calibration en fonction de la salinité. Aucune corrélation n'est observable entre ces deux grandeurs, ce qui signifie que la salinité n'a, à priori, pas d'effet sur la relation de Δ_{47} et la température.

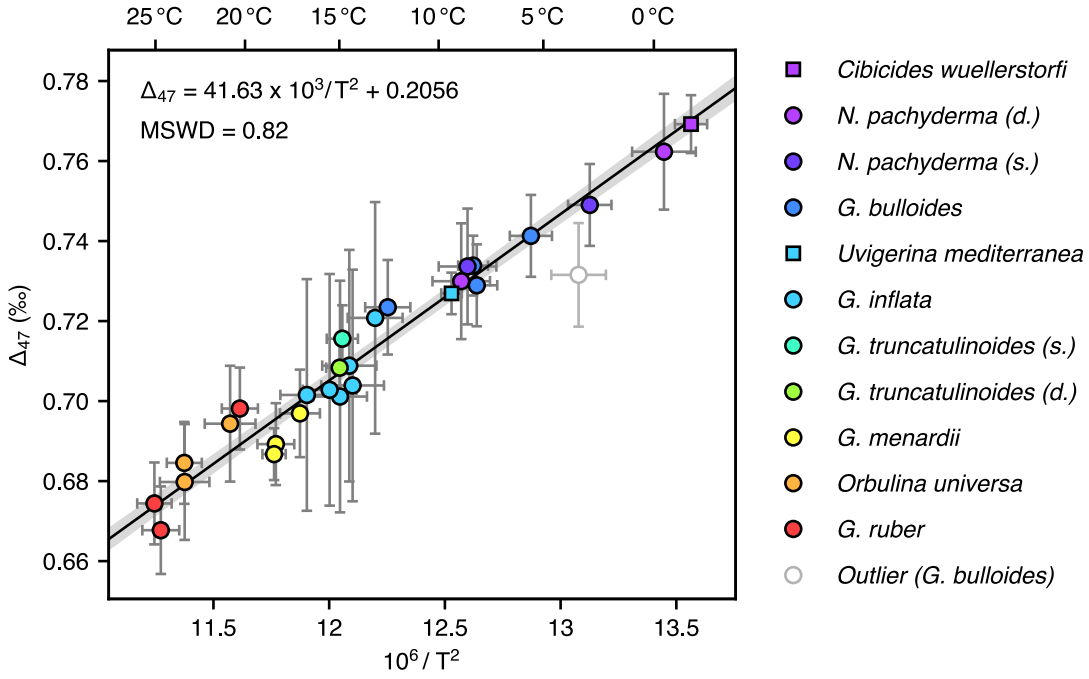

Figure 5 : Relation Δ_{47} vs T°C. les valeurs de Δ_{47} (moyennées et à 2SE) comparées aux températures dérivées des mesures isotopiques de l'oxygène (Kim et O'Neil, 1997) pour les foraminifères planctoniques (cercles) et benthiques (carrés) en combinant toutes les tailles de foraminifères. La droite de régression (noire) est calculée en suivant York et al. (2004) avec une incertitude à 95 % CL (bande grise).

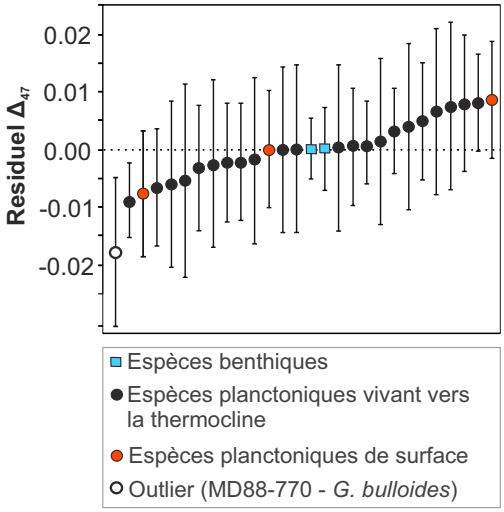

Figure 6 : Résiduel des valeurs de Δ_{47} pour les foraminifères benthiques (bleu), planctonique vivant à la surface (rouge) et les planctoniques vivant plus en profondeurs dans la colonne d'eau, l'« outlier » est en blanc.

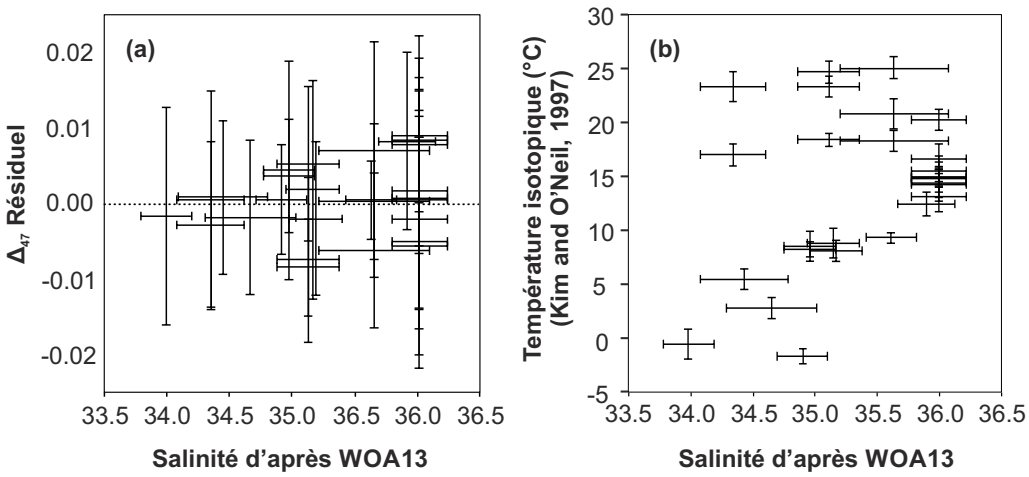

Figure 7 : Comparaison des résiduels Δ_{47} et de la salinité pour chaque espèce et sommet de carottes étudiés.

Très récemment, deux calibrations ont été publiées en utilisant les dernières avancées méthodologiques aussi utilisées pour cette étude, ce qui permet de comparer directement la relation Δ_{47}-température. Ces calibrations sont :

- La calibration de Breitenbach et al. (2018), basée sur des données de pisolithes (perle des cavernes ; « cave pearl ») et de foraminifères planctoniques
- La calibration de Kele et al. (2015, recalculée dans Bernasconi et al., 2018), basée

sur les analyses effectuées sur des travertins et des tufs.

Les données de foraminifères de Breitenbach et al. (2018) sont généralement en bon accord (aux incertitudes à 2SE) avec notre calibration (Figure 8). Cependant une partie de leurs données Δ_{47} sont 20 à 35 ppm plus bas que ce qui est attendu avec notre calibration. De plus, une partie de leurs échantillons est comprise entre 10-20 °C avec un regroupement autour de la valeur de Δ_{47} de ~ 0,68 ‰. La différence observée entre les deux jeux de données pourrait être due au choix des températures ou au protocole de nettoyage choisi.

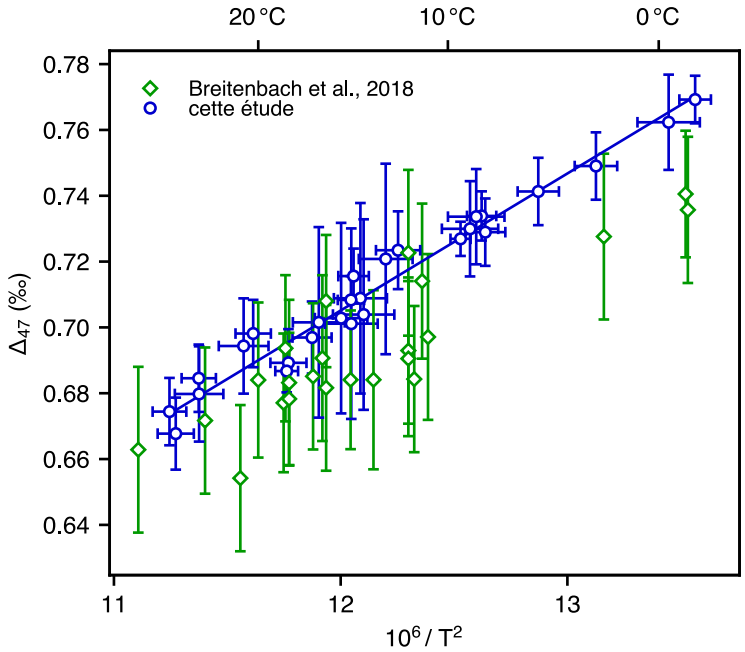

Figure 8 : Comparaison de la courbe de calibration Δ_{47} de Peral et al. (2018 ; ligne et données en bleu, à 2SE) et des données de foraminifères planctoniques de Breitenbach et al. (2018 ; en vert à 2SE).

Nous pouvons aussi comparer notre calibration avec les calibrations inorganiques présentées ci-dessus. Notre jeu de données sur les foraminifères est en très bon accord avec la droite de calibration de Kele et al. (2015 ; recalculée par Bernasconi et al., 2018), comme observé dans la figure 9. Cependant, la droite de régression basée sur la mesure Δ_{47} des « pisolithes » de Breitenbach et al. (2018) est légèrement en dessous de notre droite de calibration (Figure 9), correspondant à une estimation des températures plus froides de 2 à 4.5 °C entre 0 et 25 °C. Des études

futures sur les foraminifères et autres biocarbonates et carbonates inorganiques utilisant les mêmes standards carbonatés que nous, permettront d'améliorer les comparaisons inter-laboratoires.

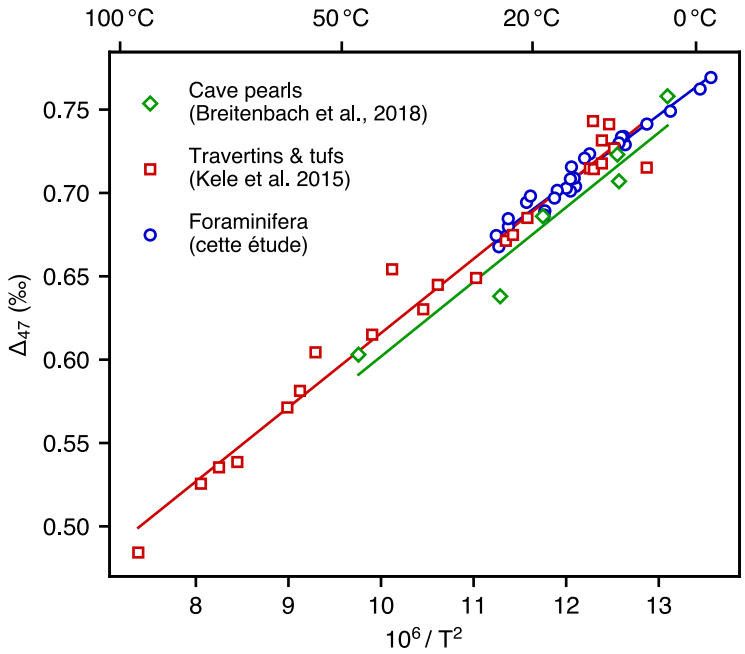

Figure 9 : Comparaison de nos valeurs de Δ_{47} sur les foraminifères (points bleus) avec les perles de cavernes («cave pearl ») de Breitenbach et al., 2018 (losanges verts) et les travertins et tufs de Kele et al., 2015 (carrés rouges).

Nous avons donc déterminé une relation robuste entre les valeurs de Δ_{47} et les températures de calcification des foraminifères planctoniques et benthiques, entre -2 et 25 °C et déterminé que les effets physico-chimiques, souvent impactant les autres méthodes de paléothermomètrie, n'influencent pas les valeurs de Δ_{47}. Le second objectif de ma thèse est donc d'appliquer cette nouvelle calibration à une étude paléocéanographique en Méditerranée couvrant la MPT.

3. APPLICATION DE LA CALIBRATION Δ_{47} - T DANS LES FORAMINIFERES A DES RECONSTITUTIONS PALEOCEANOGRAPHIQUES

Pour appliquer la méthode du clumping isotopique sur les foraminifères pour des reconstitutions paléo-environnementales au cours de la MPT, nous avons sélectionné la section de Montalbano Jonico (MJS), qui est une série marine exondée localisée dans le Sud de l'Italie. Cette série sédimentaire a été sélectionnée pour les raisons suivantes :

- Le bassin Méditerranée est une zone clé en paléoclimatologie du fait de sa sensibilité aux variations climatiques et de sa situation exceptionnelle, qui lui permet de subir à la fois l'influence de processus de hautes latitudes (eg. influence de l'Atlantique sur la circulation atmosphérique, entrée par le détroit de Gibraltar d'eaux polaires-subpolaires provenant de l'Atlantique nord et permettant le transfert de signaux associés aux instabilités de la calotte polaire), et de processus « tropicaux » (influence des variations de la mousson Africaine). Ces mécanismes jouent un rôle important dans la circulation océanique et le climat global.
- La section de Montalbano Jonico couvre du MIS 37 au MIS 16 avec un fort taux de sédimentation, donc recouvre la MPT.
- Cette série a fait l'objet de nombreuses études depuis une dizaine d'années, permettant ainsi d'insérer les données issues du paléo-thermomètre clumping-isotopique dans une approche multi-proxys.
- Enfin - élément crucial pour l'analyse du clumping isotopique dans les carbonates - la série exondée de Montalbano Jonico est très riche en foraminifères benthiques et est facile d'accès, permettant ainsi un échantillonnage aisé et la récupération de grandes quantités de matériel (pour effectuer des réplicats).

La MPT est une transition climatique majeure qui est toujours mal comprise avec de nombreuses questions non résolues sur les mécanismes internes qui agissent sur les changements de l'asymétrie, l'amplitude et la durée des cycles glaciaires-interglaciaires. Dans ce travail de thèse, je documente les changements paleoenvironnementaux au cours de la MPT en mer Méditerranée centrale en me focalisant sur l'analyse (1) de **plusieurs périodes glaciaires**, parce qu'une des caractéristiques importantes de la

MPT est l'intensification des conditions glaciaires en terme d'amplitude et de durée (une attention particulière est portée au MIS 22 qui correspond, dans de nombreux sites, au premier glaciaire présentant des valeurs de d18O élevées, typiques du Pleistocène supérieur) et (2) de **trois interglaciaires** : le MIS 31 et 19 parce que ce sont de potentiels analogues de l'Holocène du point de vue de leur configuration astronomique, et le MIS 21 qui est un interglaciaire intermédiaire qui suit le MIS22 (stade charnière de la MPT).

3.1. Les Périodes Glaciaires au Cours de la MPT a MJS

La série de Montalbano Jonico est divisée en deux intervalles (A : MIS 37 au MIS 22 ; B : MIS 22 au MIS 16) qui sont séparés par une courte lacune stratigraphique de ~ 10 ka dont l'origine est encore mal comprise. Au cours de l'Intervalle A, l'étude des stades glaciaires MIS 36, 34 et 30 montre que les conditions océanographiques sont relativement constantes, caractérisée par des valeurs ~ 0,7 ‰ de $\delta^{18}O$ de l'eau de mer (obtenus en couplant nos données de Δ_{47} et de $\delta^{18}O$), des températures froides en surface (~ 19 °C ; données issues des mesures de Mg/Ca) et en sub-surface (~ 9 °C ; données issues de la mesure du Δ_{47}), et une forte convection verticale des eaux (révélée par la faible différence entre le $\delta^{18}O$ des foraminifères planctoniques et des benthiques ; Figure 10). Durant l'Intervalle B, les périodes glaciaires sont légèrement plus variables. Le MIS 20 présente des conditions climatiques relativement similaires à celles de l'Intervalle A, alors que le MIS 22 est légèrement plus chaud en sub-surface (~ 12,1 °C ; Figure 10). Les deux intervalles glaciaires, le MIS 20 et 22, enregistrent des changements importants dans la colonne d'eau avant le démarrage de la déglaciation avec des épisodes de stratification qui pourraient être associés à de l'advection latérale d'eau plus chaude (~ 12,1 °C) pour le MIS 20 et plus froide (~ 9,4 °C) pour le MIS 22 (Figure 10). Nos interprétations paléoenvironnementales suggèrent que les changements majeurs dans les conditions glaciaires ne se produisent pas durant le MIS 22 à MJS.

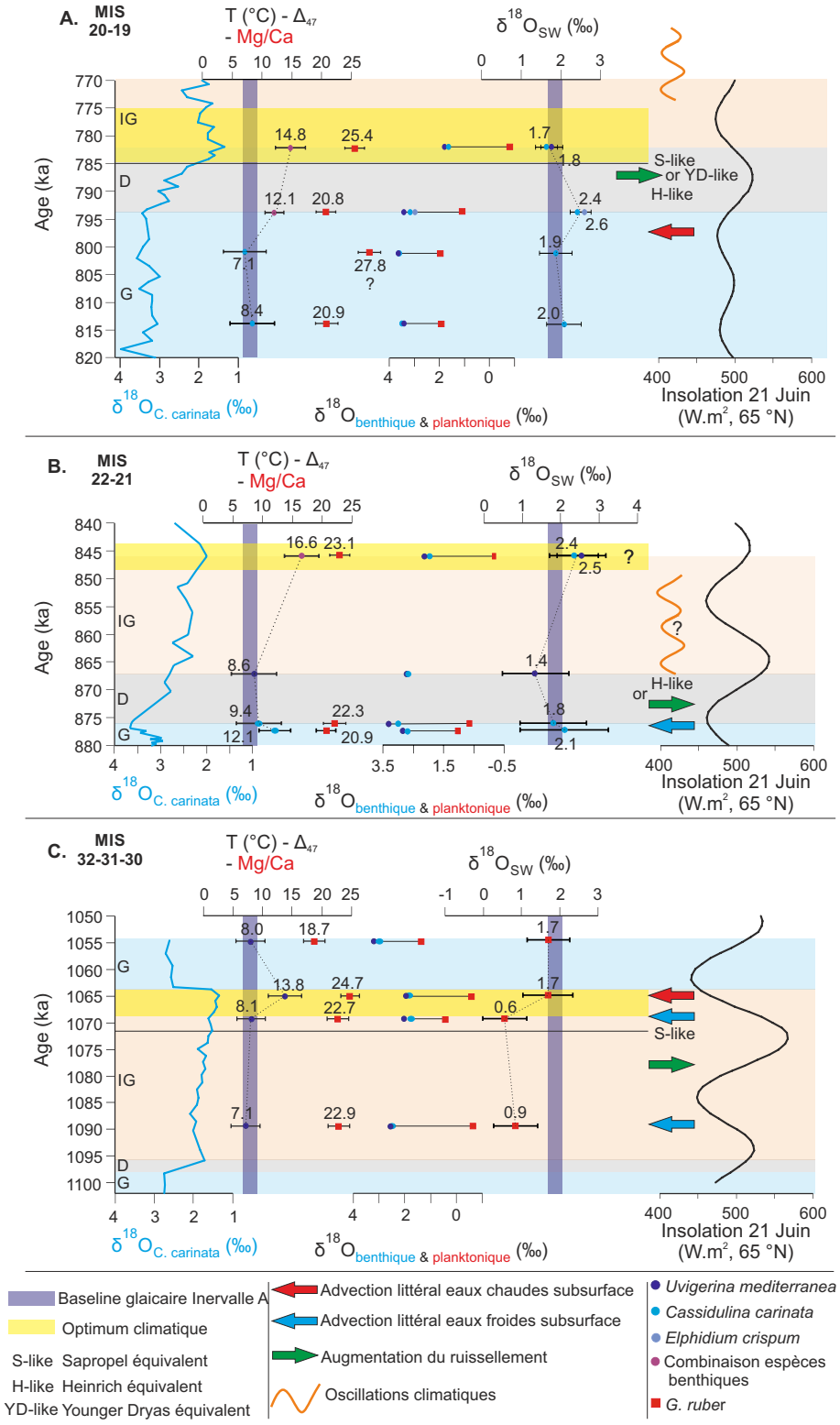

Figure 10 : Graphiques résumant les données et interprétations paléocéanographiques au cours des principaux cycles glaciaire-interglaciaires étudiés dans cette thèse à MJS : A. MIS 20-19 ; B. MIS 22-21 ; C. MIS 32-31-30 ; G : glaciaire, D : déglaciation, IG : interglaciaire.

3.2. Les Déglaciations au Cours de la MPT a MJS

Les trois déglaciations étudiées présentent de grandes différences. La Terminaison XV (MIS 32-31) est caractérisée par une diminution abrupte de $\delta^{18}O$, alors que les Terminaisons X (MIS 22-21) et IX (MIS 20-19) sont plus graduelles (Figure 10). De plus, la transition entre le MIS 22 et MIS 21 est caractérisée par des eaux froides en sub-surface (~ 8,6 °C) alors que la transition MIS 22-21 montre des eaux plus chaudes (~ 14,8 °C ; Figure 10). Ces deux transitions enregistrent une diminution du $\delta^{18}O$ de l'eau de mer, associée à une combinaison entre le signal global (lié à la diminution du volume des calottes glaciaires) et des processus locaux (liés à l'augmentation des précipitations et du ruissellement; Figure 10).

Si l'on regarde plus en détail la déglaciation MIS 20-19, en se basant sur les données à haute résolution disponibles (Bertini et al., 2015 ; Maiorano et al., 2016 ; Nomade et al., en révision ; Figure 11) nous observons que :

- Les températures de surface (issues de données d'alkénones et de Mg/Ca) au début de la déglaciation sont modérément froides (~ 18 °C), en raison probablement de l'entrée d'une masse d'eau froide provenant de l'Atlantique nord et associée à un épisode interprété comme un analogue aux événements de Heinrich du Pleistocène récent (Maiorano et al., 2016 ; Figures 10 et 11),

- Les températures de surface indiquent ensuite un épisode rapide très froid (~ 14 °C) qui peut être associé soit à l'équivalent de l'événement du Younger Dryas (Maiorano et al., 2016), soit à une augmentation du ruissellement et,

- Les proxies biologiques et le $\delta^{13}C$ benthiques ont été interprétés comme reflétant le dépôt d'un niveau « équivalent » à un sapropèle à la fin de la déglaciation et au démarrage du MIS19 (Maiorano et al., 2016 ; Nomade et al., en révision). Cette interprétation est supportée par nos données de $\delta^{18}O$ sur les foraminifères planctonique et benthique qui indiquent une forte stratification de la colonne d'eau (Figure 10).

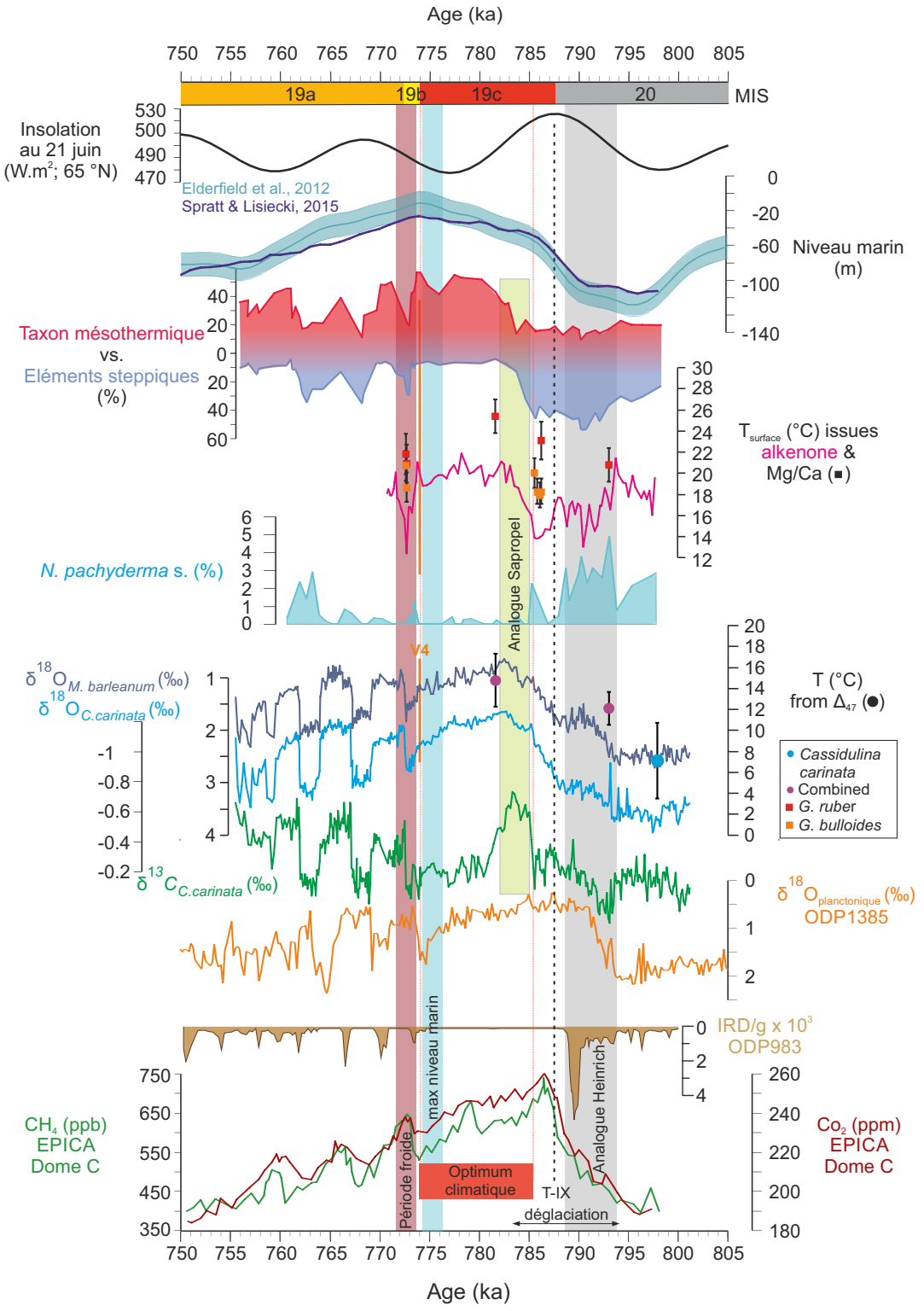

<u>Figure 11 :</u> Données paléoenvironnementales à haute résolution depuis la fin du MIS 20 au la fin du MIS 19 avec les données de $\delta^{18}O$ sur les foraminifères benthiques (Nomade et al., en révision), températures de surface issues des données alkénones (réalisées par T. Herbert, données non publiées) et polliniques (Bertini et al., 2015).

3.3. Les Périodes Interglaciaires au Cours de la MPT a MJS

Le conditions paléocéanographiques au début de l'interglaciaire MIS 31 (forte stratification, forte précipitation et ruissellement, eaux de surface et sub-surface froides ; Figure 10) sont interprétées comme (1) reflétant un phénomène d'advection latérale pour les eaux froides de sub-surface et (2) comme pouvant refléter des conditions paléo-environnementales favorables au dépôt d'un équivalent à un événement de sapropèle. L'hypothèse de conditions favorables au dépôt d'un sapropèle avait été formulée également par un fort ruissellement et une stratification de la colonne d'eau sur la base de données minéralogiques et micropaléontologiques. Cependant, un tel sapropèle – pouvant être synchrone du i-100 en Méditerranée (Lourens, 2004) - n'est pas observé dans la séquence de MJS au MIS 31 (contrairement au MIS 19 ou l'existence d'un « équivalent sapropèle » est avérée au début du MIS 19).

Autour de l'optimum climatique, les trois interglaciaires (MIS 31, 21 et 19) enregistrent des températures chaudes en surface (respectivement ~ 24,7; ~ 23,1 ; ~ 25,4 °C) et sub-surface (respectivement ~ 13,8 ; ~ 16,6 ; ~ 14,8 °C), et une colonne d'eau très stratifiée (Figure 10). Il est intéressant de noter que les optima climatiques du MIS 31 et MIS 21 se produisent vers la fin de ces interglaciaires (au moment du second pic d'insolation associé à un minimum de précession) alors que celui du MIS 19 se produit au début (lors du premier pic d'insolation), ce qui est aussi le cas pour les autres interglaciaires observés au Pléistocène supérieur.

L'optimum climatique du MIS 19 est suivi par des oscillations climatiques millénaires avec des phases froides et sèches alternant avec des phases chaudes et humides (Figure 11), conduisant au glaciaire MIS 18. Il est intéressant de noter que de potentiels oscillations sont aussi observées dans les données polliniques (Bertini et al., 2015) au MIS 21 à MJS et dans des données polliniques à hautes résolutions au MIS 31 sur la marge ibérique (Site U1385 ; Oliveira et al., 2017).

4. CONCLUSIONS

Dans cette thèse, nous avons tout d'abord établi une calibration de la méthode de thermométrie appelée « clumping isotopique » en testant différent paramètres comme l'influence des protocoles de nettoyage, de la taille des foraminifères, de la salinité et des effets spécifiques aux espèces benthiques, planctoniques vivant strictement à la surface et planctoniques vivant jusque dans la thermocline. Cette calibration apporte des informations primordiales pour reconstituer les variations de températures et de $\delta^{18}O$ de l'eau de mer. J'ai appliqué cette calibration pour des études paléo-environnementales au cours de périodes clés de la MPT dans la série de Montalbano Jonico avec un focus autour de certaines périodes glaciaires (dont le MIS 22), et les interglaciaires MIS 31 et MIS 19.

Nos données de Δ_{47}, $\delta^{18}O$ et Mg/Ca ont permis de montrer que les périodes glaciaires n'ont pas significativement varié au cours de la MPT en Méditerranée occidentale. Les interglaciaires MIS 31, MIS 21 et MIS 19, en revanche, montrent des différences sensibles.

Le thermomètre du clumping isotopique est une méthode prometteuse pour les reconstitutions paléo-environnementales, apportant des informations sur les variations des températures et du $\delta^{18}O$ de l'eau de mer. Même si les limites principales actuelles de cette technique restent la quantité de matériel requise et le temps d'analyse des échantillons, le Δ_{47} apporte une nouvelle perspective pour étudier les variations paléoclimatiques.

Part 1

THE STUDY OF ANCIENT CLIMATES:

MOTIVATION AND METHODS

Chapter 1

THE QUATERNARY CLIMATE SYSTEM AND ITS EVOLUTION

1. ORBITAL CLIMATE FORCING

During the Quaternary, the global climate repeatedly changed between cold glacial and warm interglacial periods. Gradual variations in insolation influence the climate on time scales of 10^4-10^5 years. (e.g. Milankovitch, 1920; Shackleton and Opdyke, 1973; Berger, 1978; Hays et al., 1976; Imbrie et al., 1992; Berger and Loutre, 1994; Ruddiman, 2006). Changes in the amount of incident solar energy, its seasonality and its latitudinal distribution are controlled by oscillations in Earth's orbital geometry, which is defined by three orbital parameters: obliquity, eccentricity and precession (Figure 1.1 A. B. C.; Milankovitch, 1920, 1941).

A. Obliquity is the angle of the earth's rotation axis relative to the orbital plane. It varies from 22 to 24.5 ° and changes with a main periodicity of ~ 41 ka (Figure 1.2.A.). Obliquity changes the latitudinal distribution of insolation during summer and winter seasons, with symmetric effects on both hemispheres (Berger and Loutre, 1992; Berger et al., 2010). The variation of energy received by the earth through obliquity changes is ~ 15 W/m^2.

B. Eccentricity reflects the departure of earth's orbit from quasi-circular to slightly elliptical shape (i.e. degree of flattening of the elliptical orbit), and varies with main periodicities of about ~ 100 ka and ~ 413 ka (Figure 1.2.B.). Eccentricity affects the mean annual insolation received by the Earth and modulates the amplitude of the precession parameter. The more eccentric the orbit, the stronger the magnitude of seasonal insolation changes at a given latitude (Berger, 1978; Berger and Loutre, 1992; Berger and Loutre, 2004). The variation of mean incident energy related to change is eccentricity is low (only ~ 2 W/m^2).

C. The precession of the equinoxes corresponds to the change in direction of the earth's rotation axis relative to a fixed point in space. The combination of precession and

rotation of the Earth's orbit leads to the climatic precession, which varies with periodicities of ~ 23 ka and ~ 19 ka (Figure 1.2.C.). It influences the total seasonal solar energy budget received at a given latitude. When a hemisphere experiences a warmer summer and a cooler winter, the opposite hemisphere has a warmer winter and a cooler summer. The variation of energy received by the earth in relation to changes in precession is ~ 50 W/m². Precession therefore plays a major role in the thermic contrast between seasons.

Changes in orbital forcing drove the growth and decay of ice-sheet that together with other feedback processes allowed the establishment of glacial-interglacial cycles.

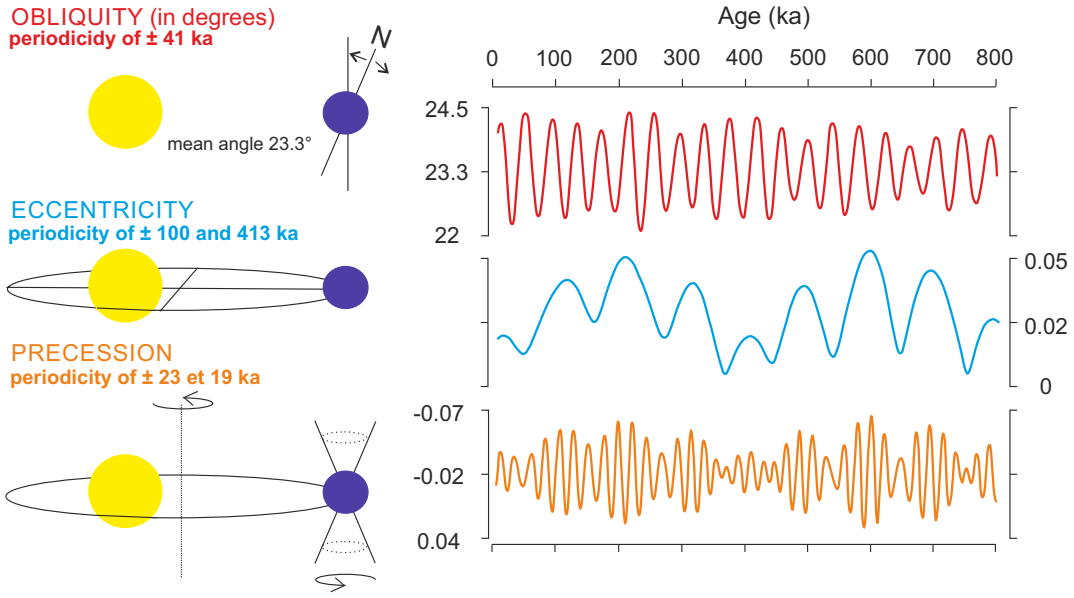

Figure 1.1: The Milankovitch theory - Orbital parameters and their periodic oscillations

2. CLIMATE RESPONSES TO ORBITAL FORCING

According to the astronomical theory of climate, the mean climatic state should respond directly to the orbital parameters, whose variations drive the glacial-interglacial cycles.

Milutin Milankovitch was the first to develop a structured and fully quantified hypothesis accounting for glacial/interglacial oscillations. He suggested that, at 65°N, when the insolation decreases, the winter snow persists throughout summer, leading to

ice-sheet growth and initiating a glaciation (Milankovitch, 1941). This cold summer is followed by a mild winter associated to high humidity transfers from low to high latitudes to poles (Kallen et al., 1979) that will favour the ice accumulation until the ice sheet becomes unstable, triggering a deglaciation. There is still some debate about the exact mechanisms driving deglaciation, involving the role of orbital variations and complex internal feedback mechanisms. Some authors propose, for instance, that the deglaciation phase must correspond to a high obliquity, which increases insolation at high latitudes (> 45°) in both hemispheres (Liu and Herbert, 2004), while others emphasize the role of rapid climatic variability associated to deglaciation (Barker et al., 2009).

Through the study of marine sedimentary archives, $\delta^{18}O$ recorded in benthic foraminifera or stratigraphy or SST allow to observe variations between glacials and interglacials (e.g. LR04 $\delta^{18}O$ of benthic foraminifera stack from Lisiecki and Raymo, 2005; Figure 1.3). The climatic response to orbital forcing is variable through the geological time and could also depend on internal factors (i.e. Zachos et al., 2001b; Ashkenazy and Tziperman, 2004; Huybers and Wunsch, 2004; Lisiecki and Raymo, 2005). The periodicity and amplitude modulation of climate variability can be extracted by spectral analysis methods applied on these continuous records. As an example (Figure 1.2) Kroon et al. (1998) applied this technic on the stratigraphic data obtained from sedimentary site ODP 967 in Mediterranean Sea over the last 3.2 Ma. The Figure 1.2 presents the age model (age versus depth) of the core at Site 967 and spectral analyses plots for three distinct periods.

According to this analysis (Figure 1.2), the late Pliocene (3.2 to ~ 2 Ma) was dominated by periodicities of ~ 41 ka and ~ 23 ka, which correspond to obliquity and precession forcing. By contrast, in the Pliocene and early Pleistocene (until about 1Ma), the obliquity-related periodicity (~ 41 ka) was the strongest signal, and this time interval is called therefore “obliquity world”.

The mean climatic response to the astronomical forcing can be explained by insolation changes driven by both precession and obliquity (Imbrie et al., 1992). In other words, obliquity alone has a moderated impact on ice volume variations (Maslin and Ridgwell, 2005) and models have difficulties to grow the north hemisphere ice-sheet with only obliquity forcing (e.g. Berger et., al 1999), because of the sensitivity to

precession (summer insolation in high latitudes). The insolation gradients at high and low latitudes correspond therefore to the coupling between obliquity and precession forcing. These dominant climatic forces between ~ 3 and ~ 1 Ma (Figure 1.2), allow the establishment of permanent ice sheets in North hemisphere (Imbrie et al., 1992; Berger et al., 1999; Raymo and Nisancioglu, 2003).

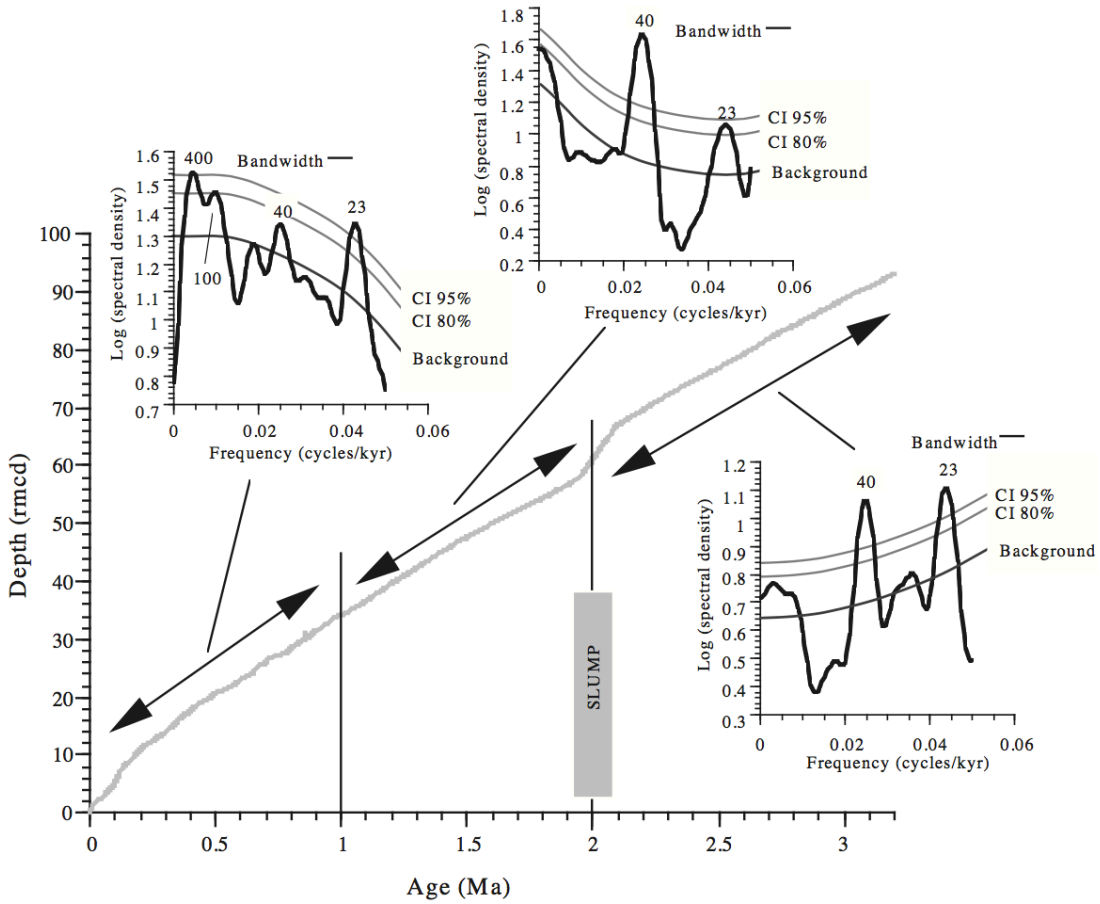

<u>Figure 1.2:</u> Stratigraphic data spectral analyse from sediments taken in Mediterranean Sea over the last 3.2 Ma (Kroon et al., 1998).

The late Pleistocene (the last 0.8 Ma) is dominated by ~ 400 ka, ~ 100 ka and ~ 23 ka cycles (Figure 1.2). The period dominated by ~ 400 - 100 ka cycles, related to the eccentricity of Earth's orbit, is called the "eccentricity world". During this period, eccentricity cannot produce the corresponding climatic (glacial-interglacial) oscillations by direct forcing because this only induces extremely small changes in insolation (~ 2 W/m^2). The glacial-interglacial climate responses change from dominant high-frequency (41 ka obliquity-driven) to low-frequency (100 ka eccentricity-driven), under no

detectable changes in orbital forcing (e.g. Pisias and Moore, 1981; Head and Gibbard, 2015). The eccentricity parameter alone cannot explain these changes of climatic response. Internal forcing/feedbacks may therefor cause instability of ice sheets and trigger the deglaciation phases under the eccentricity domination (Imbrie et al., 1993; Peltier and Marshall, 1995). This particular transition around 1 Ma during the Pleistocene, is named Mid-Pleistocene Transition (MPT).

3. MID-PLEISTOCENE TRANSITION PROBLEMATIC

The Mid-Pleistocene Transition (MPT) is also sometimes called "Early Middle Pleistocene Transition" or "Revolution" (Maasch, 1998; Berger and Jansen, 1994; Head and Gibbard, 2005). This period is characterized by a progressive increase of the climatic cycle amplitude, a shift from 41 ka to 100 ka of the climate response to orbital forcing and the apparition of a prominent asymmetry in large glacial-interglacial shifts, interglacial to glacial transitions being steep and glacial inceptions being more gradual. (Figure 1.3, LR04 $\delta^{18}O$ of benthic foraminifera stack from Lisiecki and Raymo, 2005). Many studies suggest that the transition was initiated at the Marine Isotopic Stage (MIS) 45, ~ 1.4 Ma ago, coinciding with a relative decrease in the duration of interglacials and an increase of glaciation amplitude. It was proposed that the end of the MPT corresponds to the MIS 12/11 transition (~ 0.4 Ma), which saw the onset of much higher amplitude interglacials in marine $\delta^{18}O$ records than earlier in the MPT (Ruddiman et al., 1986; Lisiecki and Raymo, 2005; Lang and Wolff, 2011; Head and Gibbard, 2015). However, changes during the MPT could be more pronounced around the MIS 24-22 (900 ka; Head and Gibbard, 2015b and reference inside). For this reason, the exact timing and the duration of the MPT are still under debate, as are its abruptness and the interpretation of the changes in $\delta^{18}O$ amplitude observed in marine carbonates between glacial and interglacial periods. Paleoclimatologists still discuss the role of orbital forcing and internal mechanisms involved. In this section, I describe the main characteristics of this major climatic transition and the internal processes that could potentially explain it.

3.1. Climate Evolution and Consequences Through the MPT

Figure 1.3 presents a summary of major climatic, marine and terrestrial events during the MPT (modified from Head and Gibbard, 2015).

The MPT is marked by two major stratigraphic events:

- The interval from MIS 31 to MIS 28 is defined by the Jaramillo Subchron, a short-term geomagnetic reversal whose chronology is still under debate, but could correspond to the period from 1.070 to 0.988 Ma (i.e. Shackleton et al., 1990; Horng et al., 2002; Lourens et al., 2005; Hilgen et al., 2012).
- MIS 19 coincides with the Matuyama-Brunhes reversal (Head and Gibbard, 2015), while the age of the limit is still debated, around 770 – 780 ka (i.e. Shackleton et al., 1990; Bassinot et al., 1994; Lourens et al., 2005; Ferretti et al., 2015).

In this section, I summarize the main climatic changes from MIS 45 (~ 1.4 Ma) to MIS 11 (~ 0.4 Ma). Before MIS 45 (a 41 ka world; Figure 1.3 - Interval A), in their $\delta^{18}O$ benthic stack (LR04), Lisiecki and Raymo (2005) observed a symmetric glacial/interglacial cycles with a periodicity of 41 ka, corresponding to obliquity parameter (Liu et al., 2008). After MIS 45, the MIS 36 - 25 (which include the "super-interglacial" MIS 31) are characterized by a progressive intensification of glacial/interglacial contrast. The period from MIS 26 to MIS 19 (including the "900 ka event") is marked by intense glaciations, with benthic $\delta^{18}O$ records reaching higher values than during previous glacials. Finally, the MIS19 to MIS 12/11 interval shows a strong increase in glacial-interglacial amplitude, with a clear asymmetry between cooling and warming trends (Figure 1.3).

3.1.1. From MIS 45 to MIS 25: Stronger Climatic Contrast Between Glacial/Interglacial Periods (Interval B in Figure 1.3)

The beginning of the MPT is marked by an increase of dust and iron fluxes in the Southern Ocean (1.25 Ma – MIS 38) during glacials, resulting in strengthened ocean fertilization and higher productivity (Martinez-Garcia et al., 2011). This fertilization

could have caused atmospheric CO_2 concentration to decrease (Hönish et al., 2009; Chalk et al., 2017).

In parallel, marine data imply global sea surface cooling consistent with the development of ice sheets (Diekmann and Kuhn, 2002; Lisiecki and Raymo, 2005; Clark et al., 2006; McClymont et al., 2008, 2013; Sosdian and Rosenthal, 2009; Head and Gibbard, 2015). The expansion of polar water in glacial/interglacial periods could also be a consequence of this cooling. It has been suggested that intensification of the East Asia winter monsoon (Heslop et al., 2002; Ding et al., 2005; Sun et al., 2010; Elderfield et al., 2012; Malaizé et al., 2012), favouring arid conditions during glacial periods in North-West China, may have resulted an increase the latitudinal contrast between glacial and interglacial periods (Wright and Flower, 2002; Schefuß et al., 2003, 2005; McClymont et al., 2008; Hernandez-Almeida et al., 2012, 2013) due to high northern latitude cooling (Han et al., 2014; Kin et al., 2014). This strong latitudinal contrast could facilitate moisture transport to high latitudes and therefore the growth of ice sheets (Hernandez-Almeida et al., 2012).

One noticeable period in the early MPT is MIS 31 (1.081 to 1.062 Ma; Lisiecki and Raymo, 2005), called "super-interglacial" event (DeConto et al., 2012). It is characterized by strong insolation at high latitudes, and an unusual orbital configuration (high obliquity and eccentricity and minimal precession). This MIS records the highest summer insolation levels of the Pleistocene, with two southern hemisphere maxima bracketed by a northern hemisphere maximum at 1.070 Ma (Laskar et al., 2004). Models predict an eustatic rise of 20 m compared to present-day sea levels, probably due to retreats of Greenland and Antarctica ice sheets (Raymo et al., 2006). Atmospheric reconstructions for MIS 31 suggest high concentrations of greenhouse gas (Hönisch et al., 2009; Charlk and Hain et al., 2012). The $\delta^{18}O$, bottom-water temperatures and SST records are all consistent with warmer conditions than today (McClymont et al., 2008; Scherer et al., 2008; Elderfield et al., 2012; Melles et al., 2012) accompanied by a decrease of sea ice around Antarctica (Teitler et al., 2015) and possibly a short-term dissipation of the Polar front (Flores and Sierro, 2007; Maiorano et al., 2009; Villa et al., 2012).

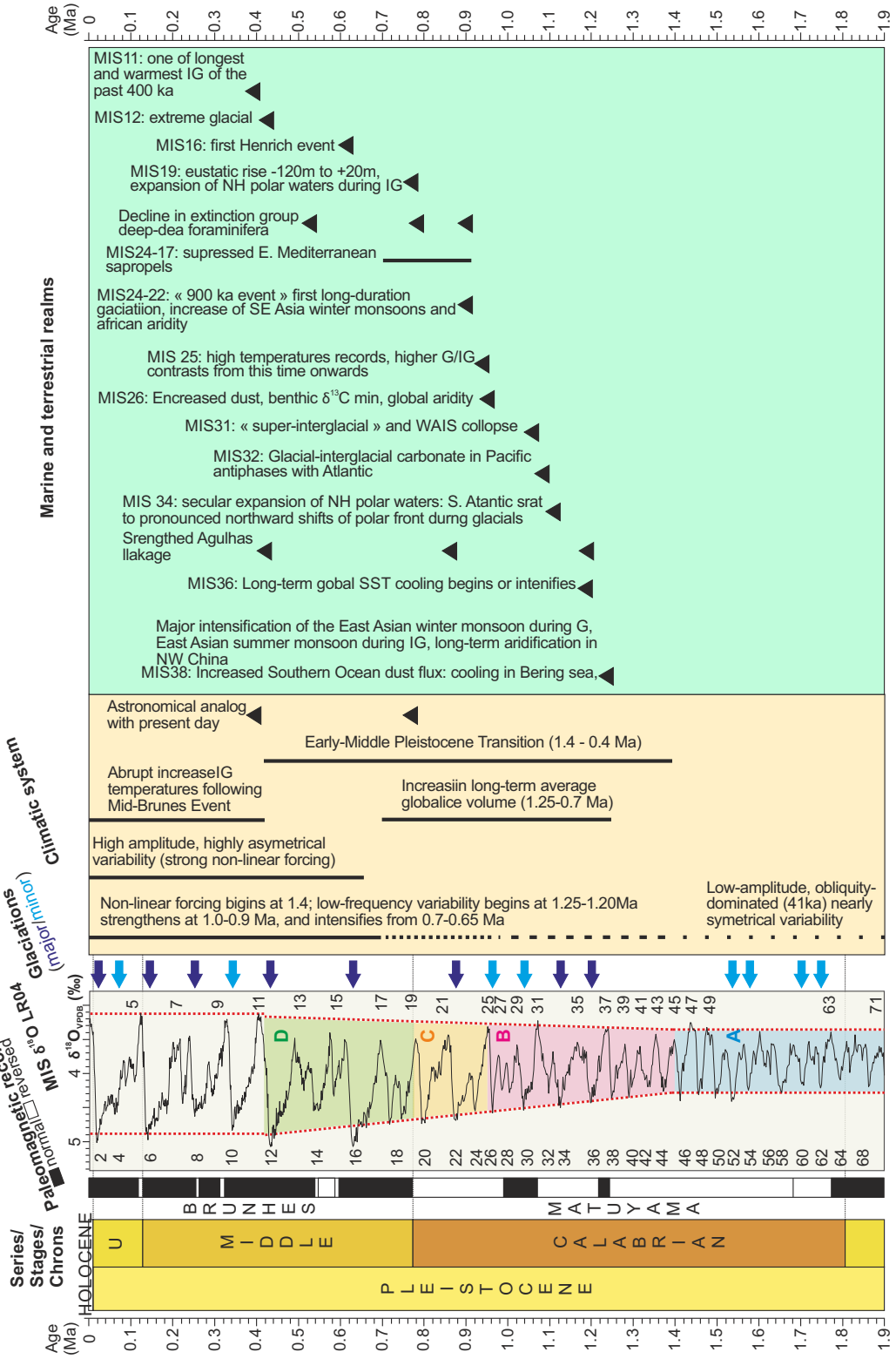

Figure 1.3: Characteristics of the climate system and major events based on marine and terrestrial records for the MPT (data: Marra et al., 2014; Bellucci et al., 2015; Head et al., 2008; Lisiecki and Raymo, 2005) from Head and Gibbard, 2015, with G: glacial and IG: Interglacial.

3.1.2. From MIS 24 to MIS 19: Lengthening and Intensification of Glaciations (Interval C in Figure 1.3)

MIS 24, often called the 900 ka event (Clark et al., 2006) is the first long-lasting glaciation of the Pleistocene (McClymont et al., 2013). From MIS 24 to 22, several studies found evidence for anomalously cool SST worldwide (e.g. Schefuß et al., 2003, 2005; Marino et al., 2009, 2011; Kim et al., 2014; McClymont et al., 2013). This cooler period is accompanied by an intensification of Asian winter monsoons (Heslop et al., 2002; Dodonov, 2005), a reduction of deep-sea circulation (Schmieder et al., 2000; Ferretti et al., 2005; Venuti et al., 2007; Marino et al., 2009; Elderfield et al., 2012; Pena and Goldstein, 2014) and the development of polar ice sheets (Weirauch et al., 2008; Elderfield et al., 2012). From MIS 22 to 12, the Antarctic polar front and westerlies may shift northward, even during interglacials, resulting in a high ventilation of the deep ocean (Schefuß et al., 2003, 2005; deMenocal, 2004; Toggweiler et al., 2006; Kemp et al., 2010). This postulated shift may be related to substantial changes in the African monsoon system implying with alternation of arid and moist climates in North Africa, ad deposition of sapropels events in eastern Mediterranean during MIS 24 to 17 (Larrasoana, 2003; Kemp et al., 2010).

Intense Ice-Rafted Debris (IRD hereafter) events are observed in North Atlantic marine records for the glacial terminations MIS 24/23, 22/21 and 20/19 (Henandez-Almeida et al., 2012). Compared to earlier cold periods, MIS 22 and 20 are marked by an intensification of glacial conditions (Henandez-Almeida et al., 2012) and by large drops in sea level (- 120 m relative to present sea level; Elderfield et al., 2012). However, $\delta^{18}O$ values in benthic foraminifera are higher for MIS 20 (0.814 Ma) than for MIS 22 (Lisiecki and Raymo, 2005; Elderfield et al., 2012; Henandez-Almeida et al., 2013). The increase of dust fluxes in the Eastern Mediterranean is evidence for weak African monsoons and extreme aridification in northeast Africa (Almogi-Labin, 2011). The MIS 20/19 termination is characterized by rapid eustatic rise (+ 20 m relative to present; Elderfield et al., 2012). MIS 19 is considered to be a good analogue of the current interglacial in terms of astronomical configuration and paleoclimatic records (Tzedakis et al., 2009, 2012; Tzedakis, 2010).

3.1.3. From MIS 18 to MIS 11: High Amplitude and Asymmetrical Variability (Interval D in Figure 1.3)

MIS 18 comprises two glacial phases separated by a weak interglacial (Railsback et al., 2015). This weak interglacial, MIS 17 and MIS 15 are all characterized by warm SST in southern oceans, and a southward displacement of the subtropical front (Marino et al., 2009).

MIS 16 is an unusually pronounced glacial period, marked by high concentration of IRD recorded in the North Atlantic (Lisiecki and Raymo, 2005; Hodell et al., 2008; Elderfield et al., 2012). The cooling phase supports the hypothesis that MIS 16 saw larger ice sheets than observed through the earlier MPT. These iceberg discharges could result from a weakening of thermohaline circulation in North Atlantic (Hodell et al., 2008).

MIS 13 is associated with exceptionally strong summer monsoon in the Northern Hemisphere (Schmieder et al., 2000). The high productivity observed during this stage in the Arabian Sea may be due to an intensification of the Atlantic meridional overturning circulation (Ziegler et al., 2010).

MIS 12 is one of the most extreme glacials across the MPT, with particularly high $\delta^{18}O$ values and frequency climate variability (Lisiecki and Raymo, 2005; Weirauch et al., 2008; Elderfield et al., 2012). This stage is also marked by perturbations in deep-water circulation and Antarctic Bottom Water production (Venuti et al., 2007).

MIS 11 (0.424 to 0.374 Ma) is one of the longest and warmest interglacials of the past 400 ka (Droxler et al., 2003; Weirauch et al., 2008; Candy et al., 2014). It is comparable to the Holocene in terms of orbital configuration (Berger and Loutre, 2003; Tzedakis et al., 2012), sea level (Bowen, 2010) and global marine temperatures (Candy et al., 2014).

3.2. Different Hypotheses for the Origin of the MPT

Although orbital variations constitute the first-order forcing on glacial-interglacial oscillations of the late Quaternary, they cannot explain alone the shifts in climatic periodicity and amplitude observed during the MPT. Various hypotheses have

been offered over the past decade regarding which internal mechanisms may explain this change in the global climatic response.

3.2.1. Global Temperatures Cooling

The MPT may have resulted from a global cooling trend (Zachos et al., 2001a). Numerous studies point to regional or global cooling over this period, which could allow larger ice sheets to persist in the late Pleistocene (Clark et al., 2006; Sosdian and Rossenthal, 2009, 2010; Herbert et al., 2010). Based on a world-wide SST stack, McClymont et al. (2013) documented a long-term cooling trend through the MPT (Figure 1.4), observable in both high and low latitudes, accompanied by a large increase in ice volume during glacials (Figure 1.4).

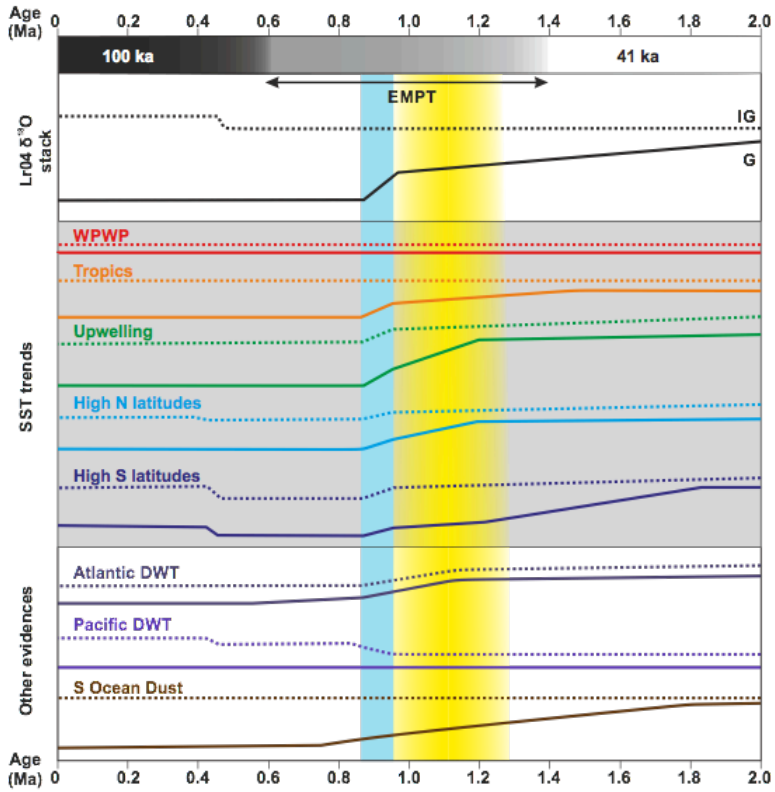

Figure 1.4: Schematic representation over the last 2 Ma, at different latitudes, of $\delta^{18}O$ *benthic foraminifera (Lisiecki and Raymo, 2005), together with SST, Deep-Water Temperatures (DWT) and dust particles for the same period of time (McClymont et al., 2013). IG stands for Interglacial (dashed line), and G for glacial (G) (solid lines). WPWP = West Pacific Warm Pool.*

The expansion of east Antarctic Ice Sheet (AIS) may have been caused by this long-term cooling. Models have shown that this hypothesis is supported if both hemispheres have dynamic ice sheets (Raymo et al., 2006). It also rests on the assumption that a small east AIS existed at the beginning of the MPT, and expanded enough over extensive marine ice shelves (Raymo et al., 2006; Scherer et al., 2008). The expansion of the west AIS could be caused by increasing the export of Antarctic bottom water into the North Atlantic (Lawrence et al., 2010).

This global temperature change could be caused by (1) fertilization of oceans - the "iron hypothesis"; (2) the dissociation of gas hydrates; or (3) an acceleration of silicate weathering (3).

(1) The Iron Hypothesis:

The long-term decline in greenhouse gases (particularly CO_2) was proposed by Raymo et al. (1997), Berger et al. (1999) and Clark et al. (2006) as a driving mechanism for the MPT. This decline in CO_2 could be due to several processes. However, the most widely referred explanation is the iron hypothesis (Watson et al., 2000; Ridgwell and Watson, 2002), according to which an increase in dust fluxes could fertilize the oceans, resulting in a net decrease of CO_2 due to the intensification of the biological pump, thus providing a cooling negative feedback. This hypothesis is supported by the recent study from Chalk and Hain et al. (2017) presenting atmospheric CO_2 reconstructions based on boron isotopes (^{11}B) in planktonic foraminifera. The authors propose that the CO_2 climate forcing could be a positive feedback that amplified the MPT climate change originally initiated by a change in ice sheet dynamics. They associated the significant change in atmospheric concentration observed with the increase of dust flux levels (Martinez-Garcia et al., 2011). However, other studies observed that atmospheric CO_2 levels did not change after 1 Ma (Hönish et al., 2009) or changed only very slowly (Tripati et al., 2011; van de Wal et al., 2011).

(2) Dissociation of Gas Hydrates:

Dissociation of gas hydrates (releasing methane, in particular), possibly due to poorly constrained changes in intermediate water circulation during the MPT, could explain the abrupt nature of Late Quaternary deglaciations ("clathrate gun hypothesis", Kennett et al., 2003). This hypothesis is supported by the strong correlation in ice cores between atmospheric methane concentrations and atmospheric temperature variations (Bock et al., 2010).

(3) Acceleration of Silicate Weathering:

The acceleration of silicate weathering, possibly reflecting changes in tectonic uplift and/or intensification of glaciation is expected to exert a strong influence on carbon sequestration rates (Berner and Raiswell., 1983), leading to a reduction in atmospheric CO_2 concentration and ultimately to global cooling (negative feedback). The uplifts could be correlated to increased silicate weathering and erosion of basement rocks by monsoonal precipitation or by repeated glaciations (Raymo, 1994; Vance et al., 2009; Tripati et al., 2011).

3.2.2. Changes in Heat Distribution

Tectonic processes may have an impact on the atmospheric and oceanic currents that could influence the global heat distribution. Atmospheric currents facilitate the transport of moisture from low to high latitudes and therefore the growth of ice sheets. In parallel, marine currents largely control the heat distribution in the world's ocean.

Continued progressive uplift of the Sierra Nevada, the Himalayas, and/or Tibetan plateau could have created a more Meridional atmospheric flow, favouring cooler summers in the high northern latitudes, reducing summer ablation of ice and inhibiting the northern ocean circulation (Ruddiman et al., 1986; Maslin et al., 2001). Furthermore, a hypothetical rapid uplift of the Tibetan Plateau has been proposed as a cause for modification of westerly jets trajectory with Meridional Asian monsoonal winds (Kutzbach et al., 1989; Han et al., 2012). This complex mechanism processes might have resulted in the dominant 100 ka cyclicity (Kutzbach et al., 1989; Han et al., 2012).

Another hypothesis is that the uplift of the Greenland-Scotland submarine ridge could have resulted in a southward shift of deep-water production in Nordic seas, with consequences on the global thermohaline circulation (Denton, 2000).

However, it should be noted that there is no consensus on the age and duration for several of these tectonic uplifts, and that their potential influence on global climates is still a matter of debate.

3.2.3. Progressive Regolith Erosion

This hypothesis is based on the size and thickness increase of the Laurentide ice sheet (Clark and Pollard, 1998; Clark et al., 2006; Sosdian and Rosenthal, 2009). The increased resistance to melting in the context of an "eccentricity world" could result from erosion, which caused the ice to rest directly on the bedrock, leading to higher frictional resistance. Thus stabilized, the Laurentide ice sheet could grow further before abruptly becoming unstable after reaching a certain size, which would be consistent with the first occurrence of IRD events in north Hemisphere Ocean and surrounding seas before and after the MIS 25 (Hernandez-Almeida et al., 2012, 2013).

3.2.4. Stochastic Processes

This hypothesis is based on the control of stochastic events that represent abrupt climate reorganizations (Meyers and Hinnov, 2010). The Pleistocene climate is largely orbitally-controlled, however, stochastic events near the beginning and the end of the MPT (~ 1.2 and ~ 0.7 Ma) could reorganized the climatic response to the 100 ka cyclicity (Meyers and Hinnov, 2010).

To summarize, almost all these potential causes, related to multiple feedbacks, are related to ice sheet growth, atmospheric and oceanographic circulations and inter-hemispheric relationships. Testing the validity of those potential mechanisms requires reconstructing such parameters as SST, bottom water temperatures or atmospheric CO_2 concentration. Absolute paleo-temperature records are particularly useful for

quantifying long-term cooling trends, and could provide improved reconstructions of ice sheet fluctuations by constraining oxygen isotopes ($\delta^{18}O_{SW}$) in past seawater.

In the next section, I present different methods to constrain past ocean temperatures.

Chapter 2

THE RECONSTRUCTION OF PAST OCEANIC TEMPERATURES

Over most of the geologic record, the study of sedimentary rocks has revealed alternations of strata formed under various climatic conditions. This climatic variability is attested either by sedimentary features/facies, or by marine fauna. However, precisely quantifying physical parameters like seawater temperatures remains quite challenging. Increasing awareness that the ocean plays an important role in modulating the Earth's climate has motivated the development of numerous methods to reconstruct past ocean temperatures, based on various approaches: either micropaleontological (transfer functions, modern analog techniques), biogeochemical ($U^{k'}_{37}$, TEX_{86}) or geochemical (based for instance on trace element ratios such as Mg/Ca or Li/Mg, $^{18}O/^{16}O$ isotope ratios, or clumped isotopes, all of them measured in bio-carbonate materials such as foraminifer shells). The following section offers a short overview of the most widely used among these paleothermometers.

1. MICROPALEONTOLOGICAL THERMOMETERS

Since the 19th century, palaeontologists have attempted to estimate past temperature trends, through the study of marine fossil assemblages. The same concept was later refined to precisely quantify paleo-temperatures based on marine microfossil assemblages. For instance, this approach allows reconstructing Sea Surface Temperatures (SST) by quantifying the relative abundances of planktonic organisms (figure 1.6). There are strong relationships between relative species abundances in a population and the physico-chemical variables (particularly temperature) characterizing their living environment (Imbrie and Kipp, 1971; Kucera et al., 2005a).

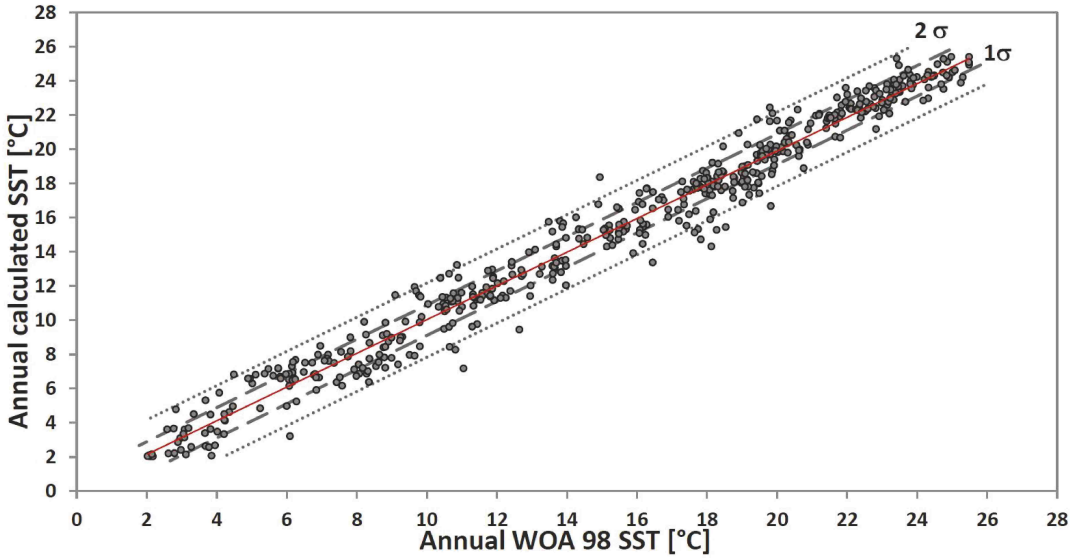

Figure 1.6: Comparison of annual SST calculated from foraminiferal Modern Analog Technique (MAT) database with Annual temperatures from World Ocean Atlas (WOA 98), from Haddam et al., 2017 (SD of fit residuals is 0.9 °C)

The three main groups of marine planktonic micro-organisms used for such reconstructions are (1) planktonic **foraminifera**, which are unicellular eukaryotic protists living in the upper hundred meters of the water column (Figure 1.7.A.; e.g. Waelbroeck et al., 1998; Kucera et al., 2005b; Caley et al., 2012; Werner et al., 2015; Haddam et al., 2016; Mary et al., 2016 - appendix); (2) **coccolithophorids**, unicellular eukaryotic phytoplankton living in the upper meters to hundred meters of the water column (Figure 1.7.B.; e.g. Giraudeau, 1992; Giraudeau and Rogers, 1994; Flores et al., 1999; Guerreiro et al., 2013, 2014; Ausin et al., 2015; Weiser et al., 2016) and (3) **dinoflagellate cysts**, which are calcareous or siliceous remains of dinoflagellates (flagellate eukaryotic protists, living at the surface of ocean and fresh waters; Figure 1.7.C.; e.g. de Vernal et al., 2001, 2006, 2013; Bringué and Rochon, 2014; Zonneveld and Sicha, 2016).

One of the first methods developed to estimate paleotemperatures from planktonic microfossils is transfer function. This technique is based on the assemblage of the most abundant fossils species, grouped according to climatic zones, such as tropics, sub-tropics, equatorial areas (Imbrie and Kipp, 1971).

More recently, the Modern Analog Technique (MAT) has mostly replaced the use of transfer functions. The MAT was developed to give the same statistical weigh to rare

species and abundant ones (Hutson, 1980; Prell, 1985), because the rare species can be as important as more abundant species in terms of sensitivity to environmental conditions such as temperature (Hecht, 1973; Hutson, 1980; Overpeck et al., 1985; Prell, 1985).

The reconstruction of SST is possible by comparison of the fossil species assemblages with database constituted by modern species assemblages retrieved from core-tops and associated to recent SST (e.g. Waelbrock et al., 1998; Haddam et al., 2016). The reconstructed temperature is based on the closest modern analogs, corresponding to the core-tops with the faunistic assemblages most similar to paleo-samples, defined by a mean of 300 individual.

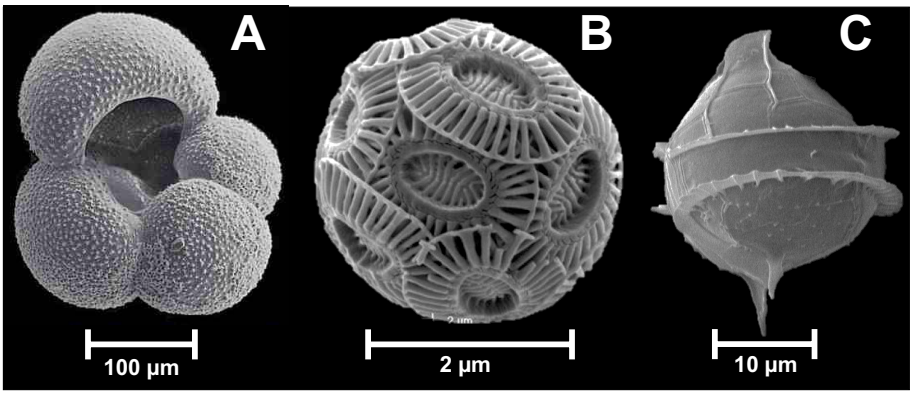

Figure 1.7: SEM pictures of a) planktonic foraminifera, b) coccolithophorid, c) dinoflagellate cysts.

The MAT method rests on two main assumptions: (1) that SST is the primary driver of microfaunal variation; and (2) that similar environmental conditions (SST) produce similar faunal assemblages over geologic time scales.

Furthermore, the MAT rests upon the actualism theory and the assumption that the relation between SST and species assemblages does not change through time. This technique is thus inherently limited by genetic changes and extinction/apparition of species over geologic time scales. It may also be limited by gaps in the available databases (e.g., lack of modern equivalents, insufficient geographic coverage and/or core-top age constraints), or influenced by parameters other that SST (bioturbation, salinity, diagenesis, near-shore waters…).

2. OXYGEN-18 THERMOMETER

One of the first quantitative geochemical paleothermometers is based on the oxygen-18 composition ($\delta^{18}O$) of oxygen-bearing minerals such as carbonates. In a landmark study, Urey (1947) calculated the temperature sensitivity of $^{18}O/^{16}O$ equilibrium fractionation between calcium carbonate and water, and described how the isotopic composition of marine carbonates could be used to reconstruct past temperatures of the ocean.

The first experimental calibration of this technique focussed on the fractionation between biogenic carbonates (Abalone: *Haliotididae*) and seawater (Epstein et al., 1951, 1953). Numerous calibrations based on marine biocarbonates (corals, foraminifera, molluscs, fish otoliths, bivalves, coccoliths) were subsequently published (e.g. Devereux, 1967; Shackleton, 1974; Wellington et al., 1996; Bemis et al., 1998; Goodwin et al., 2001; Juillet-Leclerc and Schmidt, 2001; Candelier et al., 2013; Marchitto et al., 2014). These studies established that there are substantial differences between the expected values and those observed, possibly due to kinetic isotope fractionation effects and/or apparent isotopic disequilibria associated with the biology of the calcifying organisms.

A well-known feature/limitation of oxygen-18 thermometry is its sensitivity to the isotopic composition of the parent waters. In many cases, it is challenging to precisely constrain past or present seawater $\delta^{18}O$ values ($\delta^{18}O_{sw}$). For instance, the conspicuous $\delta^{18}O$ record of glacial/interglacial cycles observed in bethic carbonates (e.g. Zachos et al., 2001a; Lisiecki and Raymo, 2005) reflects both temperature variations and the changing oxygen-18 composition of the ocean due to variations in the size of the continental ice caps, deconvolving these two signals is far from straightforward (Shackleton, 1967).

3. ORGANIC THERMOMETERS

3.1. Alkenones ($U^{k'}_{37}$ index)

The alkenone paleothermometer is based on the analysis of lipid biomarkers (alkenones) produced by marine planktonic organisms. Coccolithophorid *Emiliania huxleyi* is the most important alkenone producer today (de Leeuw et al., 1980; Marlowe et al., 1984a,b; Volkman et al., 1980). Alkenones are long-chained (C_{36}-C_{39}) *di-*, *tri-* and *tetra*-unsaturated ethyl- and methyl-ketones (Figure 1.8.A.). The $U^{k'}_{37}$ index quantifies the relative abundances of C_{37} alkenones with a double bond ($C_{37:2}$), relative to double and triple bound ($C_{37:3}$) molecules: $U^{k'}_{37}$ = [37 :2]/([37 :2]+[37 :3]). $U^{k'}_{37}$ has been found to be strongly correlated with temperature of the water where producer organisms grew (Figure 1.8.B; Brassell et al., 1986 ; Prahl and Wakeham, 1987). Alkenones are extracted from bulk sediments using a series of chromatographic purification steps (Volkman et al., 1980).

Calibrations based on core-top material (Prahl and Wakeham, 1987; Prahl et al., 1988; Sikes et al., 1991) are generally in good agreement with those based on coccolithophorid specimens grown under controlled laboratory conditions (Prahl et al., 1988), excepted by up to 5 °C (Prahl et al., 1988). Furthermore, some studies found a "linear" relationship between Uk'_{37} and temperature (Figure 1.8.C.; e.g. Muller et al., 1998), while others propose that the relationship is "nonlinear" (Figure 1.8.D.; e.g. Pelejero and Grimalt, 1997; Bentaleb et al., 2002; Conte et al., 2006). One explanation for the "nonlinear" relationship is potential saturation of the alkenone proxy at cold ($C_{37:3}$) and warm ($C_{37:2}$) temperature end-members, which could limit the applicability of this paleothermometer to extreme oceanic environments (Sikes and Volkman, 1993; Conte et al., 2006). These calibration discrepancies still remain an unresolved issue.

Arguably, the main potential biases associated with $U^{k'}_{37}$ thermometry are linked to "biology" (including ecology, physiology, and genetic effects). The living depth of alkenone-producing species may vary throughout the ocean basin, and their abundance and/or growth rate can also vary seasonally, impacting the reconstructed temperatures (Epstein et al., 1998; Popp et al., 2006). The genetic composition of natural populations may also influence alkenone production (Herbert et al., 2014). Furthermore, Weaver et

al. (1999) and Benthien and Muller (2000) have documented the temperature bias introduced on local SST records by lateral advection of alkenones coming from other areas.

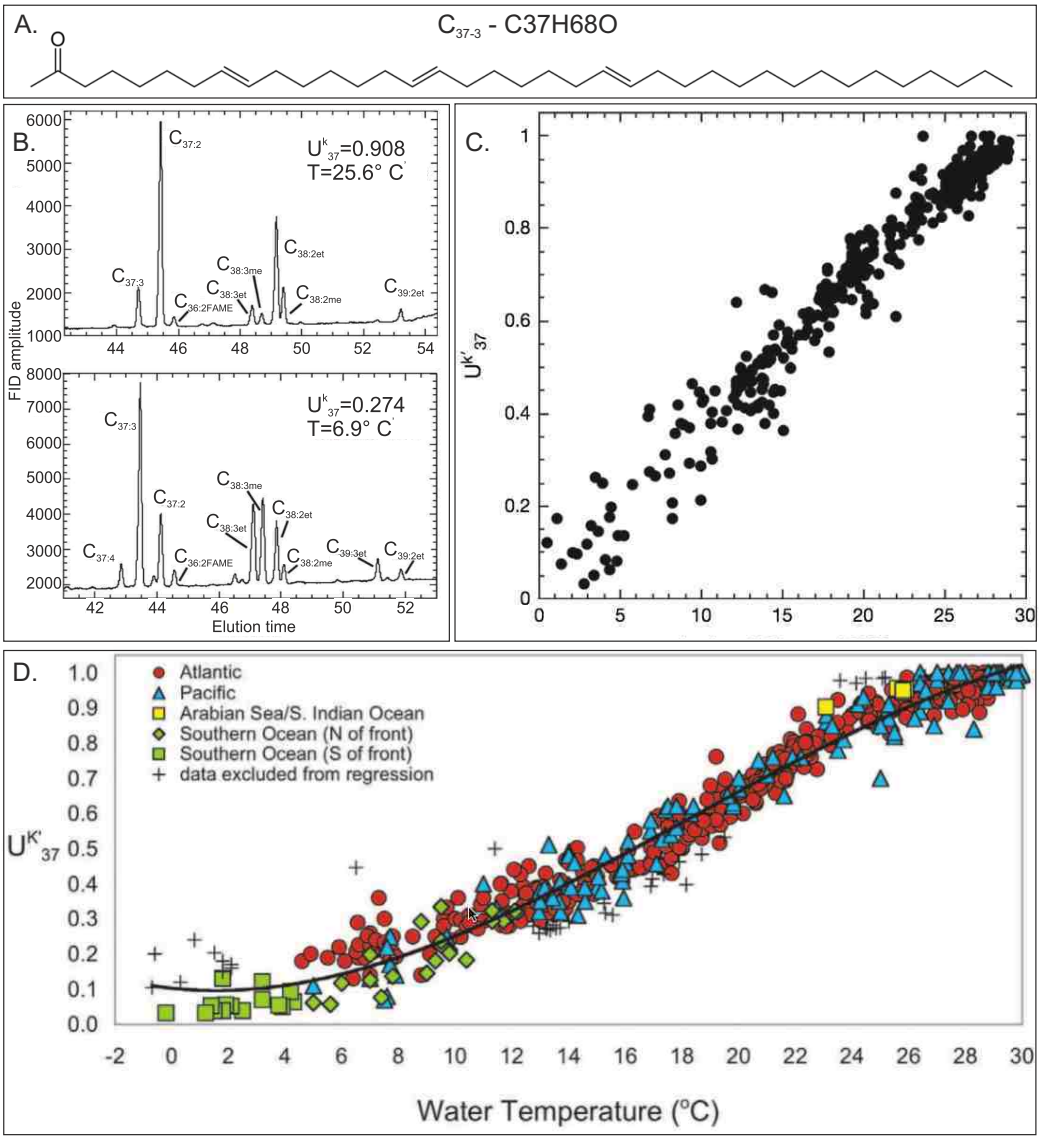

Figure 1.8: A. long-chained of unsaturated ethyl and methyl ketones with triple bond, *B. example of chromatograms of alkenone-containing in sediment where the intensities 3 peaks corresponding to $C_{37:4}$, $C_{37:3}$ and $C_{37:2}$ as a function of elution time, from Herbert, 2014, C. "linear" relationship between $U^{k'}_{37}$ and SST (1SE = 1.2-1.8 °C), from Muller et al., 1998, D. "non-linear" calibration (1SE = 1.2 °C), from Conte et al., 2006.*

3.2. Glycerol Dibiphytanyl Glycerol Tetraethers - GDGTs (TEX_{86} index)

This method is based on the analysis of archaeal tetraether lipids with 86 carbon atoms (TEX_{86}; Schouten et al., 2002), which are synthesized by marine prokaryotes Crenarchaeota (Karner et al., 2001), which produce different types of glycerol dibiphytanyl glycerol tetraethers (GDGTs, Figure 1.10a). GDGTs can comprise up to 3 cyclopentanyl group (Figure 1.9.A.: GDGT-I, GDGT-II, GDGT-III, GDGT-IV) or 4 cyclopentane moieties in addition to a cyclohexane ring (Figure 1.9.A.: Crenarchaeol; Schouten et al., 2000; Damsté et al., 2002). The relative abundance of cyclopentane groups increases with growth temperature (Gliozzi et al., 1983; Uda et al., 2001). Sea-surface temperatures can therefore be estimated by measuring the TEX_{86} index, defined as the relative amount of GDGTs (GDGTs-I-II-III-IV and Crenarchaeol) present in the sediment (Schouten et al., 2002). Numerous calibrations have been performed on modern sediments from different regions, such as the one shown in Figure 1.9.B. (e.g. Kim et al., 2008, 2010; Tierney and Tingley, 2014).

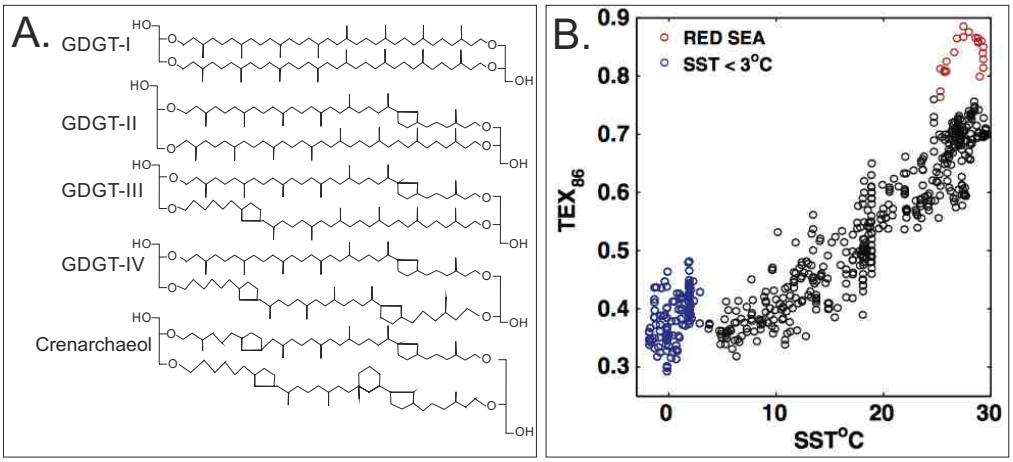

Figure 1.9: A. Molecular structure of GDGTs that comprise the TEX_{86} proxy (from Kim et al., 2008); B. regional calibration relationship between SST and TEX_{86}, from Tierney and Tingley, 2014.

This thermometer presents several advantages such as the resistance of GDGTs to diagenesis (Huguet et al., 2009; Jenkyns et al., 2012; Kim et al., 2009), the independence to changes in salinity and nutrient (Wuchter et al., 2004; Schouten et al

2007a) and the potential to reveal much higher growth temperature than $U^{k'}_{37}$ (Schouten et al., 2007b).

However, the radiogenic and stable carbon isotopes of these sediments provide contradicting information on the origin of GDGTs, particularly with respect to seasonality and depth of GDGTs production (Pearson et al., 2001; Wakeham et al., 2003; Shah et al., 2008; Hollis et al., 2012; Schouten et al., 2013; Taylor et al., 2013; Kim et al., 2015). Attempts to solve these uncertainties regarding depth/seasonality and transportation, have been based on regional calibrations (Tierney and Tingley, 2014 - Figure 1.9.B.; Kim et al., 2015), but to this date the fact that it is not possible to assign easily a depth or a season of production constitutes important drawbacks when using TEX_{86} for paleo-temperature reconstructions. In addition, other biases could be linked to non-thermal factors such as the GDGTs contaminant from terrestrial soils in shallow environment (Hopmans et al., 2004), *in situ* sedimentary production (Liu, 2011), and the response of GDGT synthesis to growth phase and dissolved [O_2] (Elling, 2015).

4. TRACE ELEMENT THERMOMETERS

4.1. Mg/Ca Thermometer

Most marine biocarbonates are low-magnesium calcium carbonates ($CaCO_3$). A small amount of Mg is substituted to Ca during calcification. The partition coefficient between Mg in seawater and Mg in the crystal matrix is temperature-dependant (Figure 1.10) and likely reflects both thermodynamic and physiological processes (Rosenthal et al., 1997; Lea et al., 1999; Erez, 2003; Bentov and Erez, 2006, Rollion-Bard et Blamart, 2015). This thermometer is primarily applied to foraminifera (Elderfield et al., 2006; Hintz et al., 2006; Allen et al., 2016 and references in), but has also been used in sea surface corals (Mitsuguchi et al., 1996; Hetzinger et al., 2009), bivalves (Celine et al., 2015) and coccoliths (Muller et al., 2011).

Most paleoclimatic applications of Mg/Ca thermometry are based on foraminifera. Interspecies differences in Mg/Ca signal were observed in numerous calibration studies on planktonic and benthic foraminifer shells (Lea et al., 1999;

Rosenthal et al., 1997; Lear et al., 2002; Anand et al., 2003; Elderfield et al., 2006; Marchitto et al., 2007), suggesting a strong influence of physiological processes, (so called "*vital" effects)*. As a result, many studies are limited to a small number of species and must rely on regional calibrations. What's more, inter-laboratory discrepancies appear to arise from the use of different cleaning protocols (Rosenthal et al., 2004). Mg/Ca ratios may also be influenced by physico-chemical variables other than temperature such as carbonate ion concentration (Elderfield et al., 2006; Rosenthal et al., 2006) or salinity (Nürnberg et al., 1996; Kisakürek et al., 2008; Mathien-Blard and Bassinot, 2009). These various methodological issues are the focus of an ongoing scientific debate.

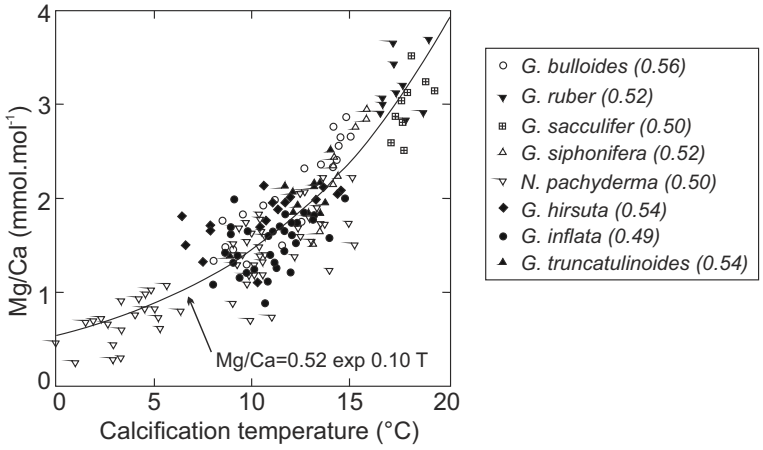

Figure 1.10: Relationship between Mg/Ca from foraminiferal shells and calcification temperature (1SE = 0.7 °C) (Elderfield and Ganssen, 2000).

4.2. Other Trace Element Thermometers

4.2.1. Li/Mg Thermometer

Vital effects similar to those affecting Mg/Ca in foraminifera are also observed in coral skeletons (Rollion-Bard et Blamart 2015; Meibom et al., 2008; Allison et al., 2010), possibly reflecting mixing between different carrier phases, influence of specific ion pumps, precipitation rate effects, Rayleigh fractionation, and/or pH change in the calcifying fluid. Of these possibilities, the most likely proposal seems to be kinetic effects that have influence on the number of defects (i.e. modification of the crystallographic structure), which are linked to the precipitation rate of the skeleton, and the partition

coefficients are the cause of the positive correlation between Li, Na, and Mg in the coral skeleton. Temperature has an indirect influence on the skeletal concentration of these elements through its effect on the skeletal growth rate (Sinclair et al., 2006; Gagnon et al., 2007, 2012; Holcomb et al., 2009; Rollion-Bard and Blamart, 2015).
To address the physiological control in coral skeletons, another paleothermometer was developed, based on the ratio between Li and Mg (Case et al., 2010; Hathorne, et al., 2013; Raddatz et al., 2013; Montagna et al., 2014) and seems to be less sensitive to vital effects. Recently, it has been shown that the Li/Mg ratio shows a strong correlation with temperature exclusively in aragonite foraminiferal shells (Marchitto et al., 2018), however the mechanisms of Li incorporation are still in debate.

4.2.2. Sr/Ca and Sr/U Thermometers

Another thermometer commonly used is the Sr/Ca ratio, applied to aragonite skeletons of corals, bivalves, sclerosponges and calcitic bivalves (Kinsman and Holland, 1969; Weber, 1973; Smith et al., 1979; Rosenheim et al., 2004; Lorrain et al., 2010; DeCarlo et al., 2015). In addition to its temperature dependence, the Sr/Ca ratio is also influenced by biomineralization processes (e.g. precipitation rates) and potentially by kinetic effects (Lorens, 1981; Morse and Bender, 1990; de Villiers et al., 1995; Tesoriero and Pankow, 1996; Cohen et al., 2001; Cohen et al., 2002; Gaetani et al., 2011; DeCarlo et al., 2015). U/Ca ratios have the potential to track changes in calcifying fluid (DeCarlo et al., 2015) and therefore to account for vital effects that influence Sr/Ca ratios (DeCarlo et al., 2016). In theory, combined measurements of Sr/Ca and U/Ca could be used to accurately reconstruct past temperature ("Sr/U thermometer"; DeCarlo et al., 2016).

5. CARBONATE CLUMPED ISOTOPE THERMOMETER

In a thermodynamically equilibrated carbonate mineral, the heavy isotopes of carbon (^{13}C) and oxygen (^{18}O) preferentially bond ("clump") together to form $^{13}C^{18}O^{16}O^{16}O^{2-}$ carbonate groups. This preferential clumping of heavy isotopes fundamentally results from the relationships between zero point energies of the

carbonate ion isotopologues (e.g., $[^{13}C^{18}O^{16}O_2]^{2-}$ vs $[^{13}C^{16}O_3]^{2-}$, $[^{12}C^{18}O^{16}O_2]^{2-}$, and $[^{12}C^{16}O_3]^{2-}$). This can be expressed through the equilibrium constant for the exchange reaction following (Ghosh et al., 2006; Schauble et al., 2006; Eiler, 2007, 2011)

$$(^{13}C^{16}O^{16}O^{16}O)^{2-} + (^{12}C^{18}O^{16}O^{16}O)^{2-} \Leftrightarrow (^{13}C^{18}O^{16}O^{16}O)^{2-} + (^{12}C^{16}O^{16}O^{16}O)^{2-}$$

The corresponding equilibrium constant varies as a function of the temperature (Schauble et al., 2006), and may be estimated by measuring the abundance of mass-47 in CO_2 (corresponding mainly to $^{13}C^{18}O^{16}O$) obtained by reaction with phosphoric acid (McCrea, 1950; Ghosh et al., 2006). For well-preserved carbonates precipitated in isotopic equilibrium, the mass-47 CO_2 abundance is slightly higher than expected for a random ("stochastic") distribution of isotopes. This mass 47 anomaly, noted Δ_{47}, can thus be used as a direct tracer of crystallization temperature.

Carbonate clumped isotope thermometry is still under development. Over the past few years it has benefitted from many methodological advances such as the implementation of an “absolute” reference frame anchored to theoretical equilibrium Δ_{47} values in CO_2 (Dennis et al., 2011); improved procedures to measure ion current background values (He et al., 2012); the distribution of international carbonate standards (Meckler et al., 2014; Bernasconi et al., 2018); and the use of updated ^{17}O correction parameters (Daëron et al., 2016, see in supplementary material). Concurrent with these methodological improvements, numerous calibration studies have been based on inorganic and biogenic carbonates (e.g. Ghosh et al., 2006; Tripati et al., 2010; Zaarur et al., 2011, 2013; Grauel et al., 2013; Came et al., 2014; Bonifacie et al., 2017; Katz et al., 2017; Kelson et al., 2017). In terms of paleoclimatic applications, the primary challenge of clumped isotope thermometer is arguably to achieve sufficiently precise inter-laboratory standardization of measurements, without which we cannot rely on published calibration studies. Yet, the early calibrations have led to important observations. In particular, the three foraminiferal core-top datasets (Tripati et al., 2010; Grauel et al., 2013; Breitenbach et al., 2018) concluded on the absence of vital effects that constitute a very promising method for reconstructions of paleo-temperatures. The second limitation is the amount of carbonate material required to estimate a temperature with acceptable uncertainties for paleoceanographic reconstructions.

Chapter 3

THE POTENTIAL OF CARBONATE CLUMPED ISOTOPE THERMOMETRY

The reconstruction of oceanic temperatures is critical to understand the processes driving climate variations. As discussed above, this may in theory be achieved using several existing methods, but all of them present substantial limitations. Carbonate clumped-isotope thermometry, based on precise Δ_{47} measurements, is a promising method for paleo-thermometry presenting two major advantages: (1) in many natural carbonates, Δ_{47} only depends on crystallization temperature, and (2) carbonate clumped-isotope thermometry may be applied to many different kinds of carbonates (corals, foraminifera, coccoliths, bivalves, otoliths, soils…). Importantly, this therefor opens up the possibility to directly reconstruct past seawater $\delta^{18}O$ values, providing insights into past global ice volumes and oceanic circulation patterns.

Foraminifera are widely used to decipher past oceanographic and climatic changes. Foraminifera are planktonic (living in the first hundred meters in the column water) or benthic organisms (living at the interface between water and sediment or in the first centimetres in the sediment), found in all kinds of marine environments. Most foraminifer shells are made of calcium carbonate ($CaCO_3$), mostly calcite although a few species are aragonitic. The isotopic composition of these shells may thus potentially be used to reconstruct sea surface and bottom water temperatures. So far, only three published studies have described the relationship between Δ_{47} and the calcification temperature of foraminifera (Tripati et al., 2010; Grauel et al., 2013). These early studies yielded important observations, particularly the absence of detectable Δ_{47} differences between various planktonic species (Figure 1.11 from Tripati et al., 2010).

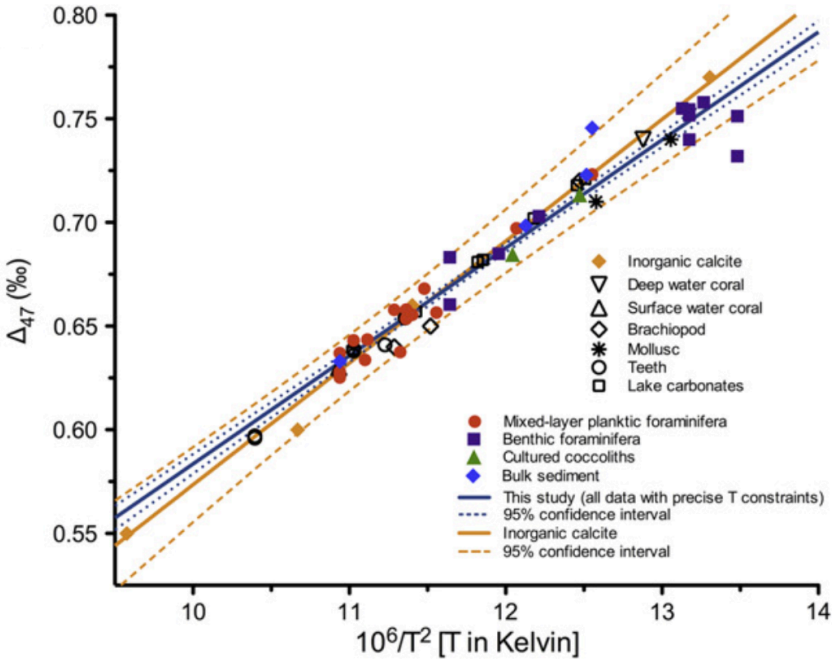

Figure 1.11: Δ_{47} – temperature relationship for various types of carbonates including foraminifera, coccoliths and bulk sediment suggesting the absence of species bias (taken from Tripati et al., 2010).

However, the empirical Δ_{47}-temperature relationships documented by these early studies cannot be directly used to reconstruct past oceanic temperatures, because (1) these observations predate important methodological advances in Δ_{47} thermometry (e.g., the CO_2 equilibrium reference frame of Dennis et al., 2011), (2) both studies used independent standardization, (3) the ^{17}O correction parameters used to process these data have since then been shown to introduce significant systematic errors which are difficult to correct *a posteriori*. Today, the systematic use of inter-laboratory standards makes possible the development of a common standardization procedure (e.g. ETH carbonate standards; Meckler et al., 2014; Bernasconi et al., 2018) and the direct comparison of Δ_{47} data obtained by different laboratories, such as we did with the planktonic foraminifera data set of Breitenbach et al. (2018).

In this context, the first goal of my PhD work was **to establish a robust relationship between Δ_{47} and the calcification temperature of planktonic and benthic foraminifer shells**, anchored to inter-laboratory carbonate standards using state-of-the-art analytical procedures. By performing a large number of inter-laboratory standard measurements, we aim facilitate the use of this new calibration by the whole

clumped-isotope community, as well as direct comparisons with other types of carbonates, such as slow-growing natural calcite and bivalves (Daëron et al., in prep, Huyghe et al., in prep). Furthermore, I picked as many species as possible from carefully selected core tops in order to explore in detail **potential species-related "vital" effect**s on foraminifer Δ_{47}.

In the context of paleoceanographic studies, the primary limiting factor of clumped isotope thermometry is the amount of material required to reach useful precision levels (e.g. ± 1.5 °C at 95 % confidence limits) on temperatures reconstructions. At LSCE, Δ_{47} measurements now require only 2 mg of $CaCO_3$, but this still entails picking (under binocular) excessively large amounts of foraminifera. As a consequence, the ability to use large foraminifer shells whenever possible, or to combine different size fractions is of key interest. Thus, I also investigated **potential foraminifer size effects** on clumped isotope values.

Beyond those concerns regarding foraminifer picking strategy, I also explored potential biases related to **cleaning protocols,** in order to define an optimal cleaning strategy. Different cleaning protocols found in the literature were compared based on SEM imagery (to observe potential dissolution effects) and on Δ_{47}, $\delta^{18}O$ and $\delta^{13}C$ values.

The new Δ_{47} foraminifer calibration is provided as a published article in Part 2. It includes discussion of all the results of our investigations on potential Δ_{47} biases associated with cleaning protocols, foraminifer size/species, and salinity.

My second objective was to take advantage of this revised calibration to reconstruct past oceanic temperatures in key climatic periods. Because of its particular scientific interest, as discussed above, I focused on the Mid-Pleistocene Transition. My main goal was to reconstruct marine water temperatures from an exonded marine sedimentary record located at Montalbano Jonico, in the South of Italy.

The Mediterranean area is a complex and very sensitive domain showing both high-latitude and tropical influences. It reflects and sometimes amplifies global climate changes and, in turns, have an impact on global ocean circulation and climate, in particular through the exit of warm and saline waters pouring into the North Atlantic

through the Gibraltar strait. A better understanding of its natural climate variability is also mandatory to improve our capacity to better anticipate the future climatic evolution of this densely populated area. All these elements explain why the Mediterranean area is a particularly interesting area to look at the effects of a global and large amplitude climate evolution such as the MPT.

We have documented paleoceanographic changes across the MPT in the central Mediterranean Sea based on the exonded series located near Montalbano (South of Italy). The Montalbano Jonico outcrop is easily accessible, making it a perfect choice for the clumped-isotope method, which requires a rather large quantity of foraminifers. The section of Montalbano Jonico covers the time interval from 1.25 to 0.65 Ma. As Δ_{47} analyses are time consuming, we narrowed the studied intervals to a few key periods across the MPT:

- Because the MPT is characterized by the amplification (both in intensity and duration) of glacial periods compared to the "41 ka-world", we selected and compared a few glacial episodes for this study (including MIS 22, a pivotal glacial which in many open ocean benthic records shows the first severe glacial conditions typical of the late Pleistocene);
- We also selected three interglacial: MIS31, MIS21 and MIS 19. MIS 31 and MIS 19 are considered as potential analogues to the current interglacial, the Holocene, because of the astronomical configuration at their onsets (high in obliquity, low in precession). We also analysed MIS 21 because it is an intermediate interglacial located between the two potential Holocene analogues, and because it followed MIS 22.
- Finally, we combined our data with high-resolution data to compare glacial/interglacial evolution through the MPT and refine some hypotheses.

In Part 3, I therefor present a multi-proxy study to reconstruct past changes in temperatures and vertical oceanographic gradients in the Gulf of Taranto over key periods of the MPT, with a particular interest for the glacial periods and MIS 31, MIS 21 and MIS 19.

REFERENCES

Allen K. A., Eggins S. M. and Haynes L. L. (2016) ScienceDirect Trace element proxies for surface ocean conditions : A synthesis of culture calibrations with planktic foraminifera. **193**, 197–221.

Allison N. and Finch A. A. (2010) δ11B, Sr, Mg and B in a modern Porites coral: the relationship between calcification site pH and skeletal chemistry. *Geochim. Cosmochim. Acta* **74**, 1790–1800.

Almogi-Labin A. (2011) The paleoclimate of the Eastern Mediterranean during the transition from early to mid Pleistocene (900 to 700ka) based on marine and non-marine records: An integrated overview. *J. Hum. Evol.* **60**, 428–436. Available at: http://dx.doi.org/10.1016/j.jhevol.2010.03.007.

Anand P., Elderfield H. and Conte M. H. (2003) Calibration of Mg / Ca thermometry in planktonic foraminifera from a sediment trap time series. **18**.

Ashkenazy Y. and Tziperman E. (2004) Are the 41 kyr glacial oscillations a linear response to Milankovitch forcing? *Quat. Sci. Rev.* **23**, 1879–1890.

Ausín B., Flores J., Sierro F., Grosjean M., Francés G. and Alonso B. (2015) Development of coccolithophore-based transfer functions in the western Mediterranean sea : a sea surface salinity reconstruction for the last 15 . 5 kyr. , 1635–1651.

Barker S., Diz P., Vautravers M. J., Pike J., Knorr G., Hall I. R. and Broecker W. S. (2009) Interhemispheric Atlantic seesaw response during the last deglaciation. *Nature* **457**, 1097.

Bassinot F. C., Labeyrie L. D., Vincent E., Quidelleur X., Shackleton N. J. and Lancelot Y. (1994) of the Brunhes-Matuyama magnetic reversal. **126**, 91–108.

Bellucci L., Sardella R. and Rook L. (2015) Large mammal biochronology framework in Europe at Jaramillo: the Epivillafranchian as a formal biochron. *Quat. Int.* **389**, 84–89.

Bemis B. E., Spero H. J., Bijma J. and Lea D. W. (1998) Reevaluation of the oxygen isotopic composition of planktonic foraminifera: Experimental results and revised paleotemperature equations. *Paleoceanography* **13**, 150–160.

Bentaleb I., Fontugne M. and Beaufort L. (2002) Long-chain alkenones and U37k′ variability along a south-north transect in the Western Pacific Ocean. *Glob. Planet. Change* **34**, 173–183.

Benthien A. and Müller P. J. (2000) Anomalously low alkenone temperatures caused by lateral particle and sediment transport in the Malvinas Current region, western Argentine Basin. *Deep. Res. Part I Oceanogr. Res. Pap.* **47**, 2369–2393.

Bentov S. and Erez J. (2006) Impact of biomineralization processes on the Mg content of foraminiferal shells: A biological perspective. *Geochemistry, Geophys. Geosystems* **7**.

Berger A. L. (1978) Long-Term Variations of Caloric Insolation Resulting from the Earth's Orbital Elements 1. *Quat. Res.* **9**, 139–167.

Berger A., Li X. S. and Loutre M.-F. (1999) Modelling northern hemisphere ice volume over the last 3 Ma. *Quat. Sci. Rev.* **18**, 1–11.

Berger A. and Loutre M.-F. (1992) Astronomical solutions for paleoclimate studies over the last 3 million years. *Earth Planet. Sci. Lett.* **111**, 369–382.

Berger A., Loutre M.-F. and Yin Q. (2010) Total irradiation during any time interval of the year using elliptic integrals. *Quat. Sci. Rev.* **29**, 1968–1982.

Berger A. and Loutre M. F. (1994) Precession, eccentricity, obliquity, insolation and

paleoclimates. In *Long-Term Climatic Variations* Springer. pp. 107–151.
Berger A. and Loutre M. F. (2004) Théorie astronomique des paléoclimats. *Comptes Rendus Geosci.* **336**, 701–709.
Berger W. H. and Jansen E. (1994) Mid-pleistocene climate shift-the Nansen connection. *polar Ocean. their role Shap. Glob. Environ.* **85**, 295–311.
Bernasconi S. M., Müller I. A., Bergmann K. D. and Sebastian F. M. Reducing uncertainties in carbonate clumped isotope analysis through consistent carbonate - based standardization.
Berner R. A. and Raiswell R. (1983) Burial of organic carbon and pyrite sulfur in sediments over Phanerozoic time: a new theory. *Geochim. Cosmochim. Acta* **47**, 855–862.
Bock M., Schmitt J., Möller L., Spahni R., Blunier T. and Fischer H. (2010) Hydrogen isotopes preclude marine hydrate CH4 emissions at the onset of dansgaard-oeschger events. *Science (80-.).* **328**, 1686–1689.
Bonifacie M., Calmels D., Eiler J. M., Horita J., Chaduteau C., Vasconcelos C., Agrinier P., Katz A., Passey B. H., Ferry J. M. and Bourrand J. (2017) ScienceDirect Calibration of the dolomite clumped isotope thermometer from 25 to 350 ° C , and implications for a universal calibration for all (Ca , Mg , Fe) CO 3 carbonates. *Geochim. Cosmochim. Acta* **200**, 255–279. Available at: http://dx.doi.org/10.1016/j.gca.2016.11.028.
Bowen D. Q. (2011) of the Past Corrigendum to " Sea level ~ 400 000 years ago (MIS 11): analogue for present and. , 5194.
Brassell S.C, Eglinton G, Marlowe I.T, Pflaumann U S. M. (1986) Molecular stratigraphy: a new tool for climatic assessment. *Nature* **320**, 129–133.
Breitenbach S. F. M., Mleneck-Vautravers M. J., Grauel A.-L., Lo L., Bernasconi S. M., Müller I. A., Rolfe J., Greaves M. and Hodell D. A. (2018) Coupled Mg/Ca and clumped isotope analyses of foraminifera provide consis- tent water temperatures Sebastian. *Geochim. Cosmochim. Acta*.
Bringué M., Pospelova V. and Field D. B. (2014) High resolution sedimentary record of dinoflagellate cysts reflects decadal variability and 20th century warming in the Santa Barbara Basin. *Quat. Sci. Rev.* **105**, 86–101.
Caley T., Giraudeau J., Malaize B., Rossignol L. and Pierre C. (2012) Agulhas leakage as a key process in the modes of Quaternary climate changes. *Proc. Natl. Acad. Sci.* **109**, 6835–6839. Available at: http://www.pnas.org/cgi/doi/10.1073/pnas.1115545109.
Came R. E., Brand U. and Affek H. P. (2014) Clumped isotope signatures in modern brachiopod carbonate. *Chem. Geol.* **377**, 20–30. Available at: http://dx.doi.org/10.1016/j.chemgeo.2014.04.004.
Candelier Y., Minoletti F., Probert I. and Hermoso M. (2013) Temperature dependence of oxygen isotope fractionation in coccolith calcite: A culture and core top calibration of the genus Calcidiscus. *Geochim. Cosmochim. Acta* **100**, 264–281.
Candy I., Schreve D. C., Sherriff J. and Tye G. J. (2014) Marine Isotope Stage 11: Palaeoclimates, palaeoenvironments and its role as an analogue for the current interglacial. *Earth-Science Rev.* **128**, 18–51.
Case D. H., Robinson L. F., Auro M. E. and Gagnon A. C. (2010) Environmental and biological controls on Mg and Li in deep-sea scleractinian corals. *Earth Planet. Sci. Lett.* Available at: http://dx.doi.org/10.1016/j.epsl.2010.09.029.
Celine P., P G. D., Julien T., Jean-marie M., Marcel B., Rene R., Yves-marie P. and Anne L.

(2015) Achimer An evaluation of Mg / Ca , Sr / Ca , and Ba / Ca ratios as environmental proxies in aragonite bivalve shells. **396**, 42–50.

Clark P. U., Archer D., Pollard D., Blum J. D., Rial J. A., Brovkin V., Mix A. C., Pisias N. G. and Roy M. (2006) The middle Pleistocene transition: characteristics, mechanisms, and implications for long-term changes in atmospheric pCO2. *Quat. Sci. Rev.* **25**, 3150–3184.

Clark P. U. and Pollard D. (1998) Origin of the middle Pleistocene transition by ice sheet erosion of regolith. *Paleoceanography* **13**, 1–9.

Cohen A. L., Layne G. D., Hart S. R. and Lobel P. S. (2001) Implications for the paleotemperature proxy a. *Paleoceanography* **16**, 20–26.

Cohen A. L., Owens K. E., Layne G. D. and Shimizu N. (2002) The effect of algal symbionts on the accuracy of Sr/Ca paleotemperatures from coral. *Science (80-.).* **296**, 331–333.

Conte M. H., Weber J. C., Schulte S. and Blanz T. (2006) sediments.

Daëron M., Blamart D., Peral M. and Affek H. P. (2016) Absolute isotopic abundance ratios and the accuracy of Δ47 measurements. *Chem. Geol.* **442**, 83–96. Available at: http://dx.doi.org/10.1016/j.chemgeo.2016.08.014.

Damsté J. S. S., Schouten S., Hopmans E. C., van Duin A. C. T. and Geenevasen J. A. J. (2002) Crenarchaeol. *J. Lipid Res.* **43**, 1641–1651. Available at: http://www.jlr.org/lookup/doi/10.1194/jlr.M200148-JLR200.

DeCarlo T. M., Gaetani G. A., Holcomb M. and Cohen A. L. (2015) Experimental determination of factors controlling U/Ca of aragonite precipitated from seawater: Implications for interpreting coral skeleton. *Geochim. Cosmochim. Acta* **162**, 151–165. Available at: http://dx.doi.org/10.1016/j.gca.2015.04.016.

Deconto R. M., Galeotti S., Pagani M., Tracy D., Schaefer K., Zhang T., Pollard D. and Beerling D. J. (2012) carbon release from thawing permafrost. , 6–11.

deMenocal P. B. (2004) African climate change and faunal evolution during the Pliocene-Pleistocene. *Earth Planet. Sci. Lett.* **220**, 3–24.

Dennis K. J., Affek H. P., Passey B. H., Schrag D. P. and Eiler J. M. (2011) Defining an absolute reference frame for "clumped" isotope studies of CO 2. *Geochim. Cosmochim. Acta* **75**, 7117–7131. Available at: http://dx.doi.org/10.1016/j.gca.2011.09.025.

Denton G. H. (2000) Does an asymmetric thermohaline–ice-sheet oscillator drive 100 000-yr glacial cycles? *J. Quat. Sci. Publ. Quat. Res. Assoc.* **15**, 301–318.

Devereux I. (1967) Temperature measurements from oxygen isotope ratios of fish otoliths. *Science (80-.).* **155**, 1684–1685.

Diekmann B. and Kuhn G. (2002) Sedimentary record of the mid-Pleistocene climate transition in the southeastern South Atlantic (ODP Site 1090). *Palaeogeogr. Palaeoclimatol. Palaeoecol.* **182**, 241–258.

Ding Z. L., Derbyshire E., Yang S. L., Sun J. M. and Liu T. S. (2005) Stepwise expansion of desert environment across northern China in the past 3.5 Ma and implications for monsoon evolution. *Earth Planet. Sci. Lett.* **237**, 45–55.

Dodonov A. E. (2005) The stratigraphic transition and suggested boundary between the Early and Middle Pleistocene in the loess record of northern Eurasia. *Geol. Soc. London, Spec. Publ.* **247**, 209–219.

Droxler A. W., Alley R. B., Howard W. R., Poore R. Z. and Burckle L. H. (2003) Unique and exceptionally long interglacial marine isotope stage 11: Window into earth warm future climate. *Geophys. Monogr. Ser.* **137**, 1–14.

Eiler J. M. (2007) “Clumped-isotope” geochemistry-The study of naturally-occurring, multiply-substituted isotopologues. *Earth Planet. Sci. Lett.* **262**, 309–327.

Eiler J. M. (2011) Paleoclimate reconstruction using carbonate clumped isotope thermometry. *Quat. Sci. Rev.* **30**, 3575–3588.

Elderfield H., Ferretti P., Crowhurst S., Mccave I. N., Hodell D. and Piotrowski A. M. (2012) Evolution of Ocean Temperature and Ice Volume Through the. *Science (80-.).* **337**, 704–710.

Elderfield H. and Ganssen G. (2000) Past temperature and δ18O of surface ocean waters inferred from foraminiferal Mg/Ca ratios. *Nature* **405**, 442–445.

Elderfield H., Yu J., Anand P., Kiefer T. and Nyland B. (2006) Calibrations for benthic foraminiferal Mg/Ca paleothermometry and the carbonate ion hypothesis. *Earth Planet. Sci. Lett.* **250**, 633–649.

Elling F. J. (2015) Factors controlling the lipid composition of marine planktonic Thaumarchaeota. .

Epstein L., Hondt D., Quinn G. and Hargraves P. E. (1998) An effect of dissolved nutrient concentrations based temperature estimates with Erniliania huxleyi clone values rate . These results provide a reasonable explanation for large isothermal variation in uK ’ 37 values of single coccolithophorid. *Currents*, 122–126.

Epstein S., Buchsbaum R., Lowenstam H. A. and Urey H. C. (1953) Revised Carbonate-Water Isotopic Temeprature Scale. *Geol. Soc. Am. Bull.* **64**, 1315–1325. Available at: http://www.geosociety.org/pubs/copyrt.htm#gsa.

Epstein S., Buchsbaum R., Lowenstam H. and Urey H. (1951) Geologic History of Sea Water. *Geol. Soc. Am. Bull.* **62**, 417–426.

Erez J. (2003) The Source of Ions for Biomineralization in Foraminifera and Their Implications for Paleoceanographic Proxies. *Rev. Mineral. Geochemistry* **54**, 115–149. Available at: http://rimg.geoscienceworld.org/cgi/doi/10.2113/0540115.

Ferretti P., Crowhurst S. J., Naafs B. D. A. and Barbante C. (2015) The Marine Isotope Stage 19 in the mid-latitude North Atlantic Ocean: Astronomical signature and intra-interglacial variability. *Quat. Sci. Rev.* **108**, 95–110. Available at: http://dx.doi.org/10.1016/j.quascirev.2014.10.024.

Flores J.-A., Gersonde R. and Sierro F. J. (1999) Pleistocene fluctuations in the Agulhas Current Retroflection based on the calcareous plankton record. *Mar. Micropaleontol.* **37**, 1–22.

Flores J.-A. and Sierro F. J. (2007) Pronounced mid-Pleistocene southward shift of the Polar Front in the Atlantic sector of the Southern Ocean. *Deep Sea Res. Part II Top. Stud. Oceanogr.* **54**, 2432–2442.

Freitas P. S., Clarke L. J., Kennedy H. and Richardson C. A. (2006) Environmental and biological controls on elemental (Mg / Ca , Sr / Ca and Mn / Ca) ratios in shells of the king scallop Pecten maximus. **70**, 5119–5133.

Gaetani G. A., Cohen A. L., Wang Z. and Crusius J. (2011) Rayleigh-based, multi-element coral thermometry: A biomineralization approach to developing climate proxies. *Geochim. Cosmochim. Acta* **75**, 1920–1932.

Gagnon A. C., Adkins J. F. and Erez J. (2012) Seawater transport during coral biomineralization. *Earth Planet. Sci. Lett.* **329**, 150–161.

Gagnon A. C., Adkins J. F., Fernandez D. P. and Robinson L. F. (2007) Sr/Ca and Mg/Ca vital effects correlated with skeletal architecture in a scleractinian deep-sea coral and the role of Rayleigh fractionation. *Earth Planet. Sci. Lett.* **261**, 280–295.

Ghosh P., Adkins J., Affek H., Balta B., Guo W., Schauble E. A., Schrag D. and Eiler J. M.

(2006) 13C-18O bonds in carbonate minerals: A new kind of paleothermometer. *Geochim. Cosmochim. Acta* **70**, 1439–1456.

Giraudeau J. (1992) Distribution of recent nannofossils beneath the Benguela system: southwest African continental margin. *Mar. Geol.* **108**, 219–237.

Giraudeau J. and Rogers J. (1994) Phytoplankton biomass and sea-surface temperature estimates from sea-bed distribution of nannofossils and planktonic foraminifera in the Benguela upwelling system. *Micropaleontology*, 275–285.

Gliozzi A., Paoli G., De Rosa M. and Gambacorta A. (1983) Effect of isoprenoid cyclization on the transition temperature of lipids in thermophilic archaebacteria. *Biochim. Biophys. Acta (BBA)-Biomembranes* **735**, 234–242.

Goodwin D. H., Flessa K. W., Schöne B. R. and Dettman D. L. (2001) Cross-Calibration of Daily Growth Increments, Stable Isotope Variation, and Temperature in the Gulf of California Bivalve Mollusk *Chione cortezi*: Implications for Paleoenvironmental Analysis. *Palaios* **16**, 387–398.

Grauel A., Goudeau M. S., Lange G. J. De and Bernasconi S. M. (2013) Climate of the past 2500 years in the Gulf of Taranto , central Mediterranean Sea : A high-resolution climate reconstruction based on δ 18 O and δ 13 C of Globigerinoides ruber (white).

Grauel A. L., Schmid T. W., Hu B., Bergami C., Capotondi L., Zhou L. and Bernasconi S. M. (2013) Calibration and application of the "clumped isotope" thermometer to foraminifera for high-resolution climate reconstructions. *Geochim. Cosmochim. Acta* **108**, 125–140. Available at: http://dx.doi.org/10.1016/j.gca.2012.12.049.

Guerreiro C., Oliveira A., De Stigter H., Cachão M., Sá C., Borges C., Cros L., Santos A., Fortuño J. M. and Rodrigues A. (2013) Late winter coccolithophore bloom off central Portugal in response to river discharge and upwelling. *Cont. Shelf Res.* **59**, 65–83.

Guerreiro C., Sá C., de Stigter H., Oliveira A., Cachão M., Cros L., Borges C., Quaresma L., Santos A. I., Fortuño J. M. and Rodrigues A. (2014) Influence of the Nazaré Canyon, central Portuguese margin, on late winter coccolithophore assemblages. *Deep. Res. Part II Top. Stud. Oceanogr.* **104**, 335–358.

Haddam N. A., Siani G., Michel E., Kaiser J., Lamy F., Duchamp-Alphonse S., Hefter J., Braconnot P., Dewilde F., Isgüder G., Tisnerat-Laborde N., Thil F., Durand N. and Kissel C. (2018) Changes in latitudinal sea surface temperature gradients along the Southern Chilean margin since the last glacial. *Quat. Sci. Rev.* **194**, 62–76.

Han W., Fang X. and Berger A. (2012) Tibet forcing of mid-Pleistocene synchronous enhancement of East Asian winter and summer monsoons revealed by Chinese loess record. *Quat. Res. (United States)* **78**, 174–184. Available at: http://dx.doi.org/10.1016/j.yqres.2012.05.001.

Hathorne E. C., Felis T., Suzuki A., Kawahata H. and Cabioch G. (2013) Lithium in the aragonite skeletons of massive Porites corals : A new tool to reconstruct tropical sea surface temperatures. *Paleoceanography* **28**, 143–152.

Hays J. D., Imbrie J. and Shackleton N. J. (1976) Variations in the Earth's orbit: pacemaker of the ice ages. In American Association for the Advancement of Science Washington, DC.

He J., Balzano L. and Szlam A. (2012) Incremental gradient on the Grassmannian for online foreground and background separation in subsampled video. *Proc. IEEE Comput. Soc. Conf. Comput. Vis. Pattern Recognit.*, 1568–1575.

Head M. J. and Gibbard P. L. (2015) Formal subdivision of the Quaternary

System/Period: Past, present, and future. *Quat. Int.* **383**, 4–35. Available at: http://dx.doi.org/10.1016/j.quaint.2015.06.039.

Head M. J., Pillans B. and Farquhar S. A. (2008) The Early-Middle Pleistocene transition: characterization and proposed guide for the defining boundary. *Episodes* **31**, 255.

Hecht A. D. (1973) A model for determining Pleistocene paleotemperatures from planktonic foraminiferal assemblages. *Micropaleontology*, 68–77.

Herbert T. D. (2013) *Alkenone Paleotemperature Determinations*. 2nd ed., Elsevier Ltd. Available at: http://dx.doi.org/10.1016/B978-0-08-095975-7.00615-X.

Herbert T. D., Peterson L. C., Lawrence K. T. and Liu Z. (2010) Tropical ocean temperatures over the past 3.5 million years. *Science (80-.).* **328**, 1530–1534.

Hernández-Almeida I., Sierro F. J., Flores J. A., Cacho I. and Filippelli G. M. (2013) Palaeoceanographic changes in the North Atlantic during the Mid-Pleistocene Transition (MIS 31-19) as inferred from planktonic foraminiferal and calcium carbonate records. *Boreas* **42**, 140–159.

Hernández-Molina F. J., Stow D. A. V, Alvarez-Zarikian C. A., Acton G., Bahr A., Balestra B., Ducassou E., Flood R., Flores J.-A. and Furota S. (2014) Onset of Mediterranean outflow into the North Atlantic. *Science (80-.).* **344**, 1244–1250.

Heslop D., Dekkers M. J. and Langereis C. G. (2002) Timing and structure of the mid-Pleistocene transition: Records from the loess deposits of northern China. *Palaeogeogr. Palaeoclimatol. Palaeoecol.* **185**, 133–143.

Hetzinger S., Halfar J., Kronz A., Steneck R. S., Adey W., Lebednik P. A. and Scho B. R. (2009) HIGH-RESOLUTION MG / CA RATIOS IN A CORALLINE RED ALGA AS A PROXY FOR BERING SEA TEMPERATURE VARIATIONS FROM 1902 TO 1967. , 2110.

Hilgen F. J., Lourens L. J., Van Dam J. A., Beu A. G., Boyes A. F., Cooper R. A., Krijgsman W., Ogg J. G., Piller W. E. and Wilson D. S. (2012) The neogene period. In *The geologic time scale* Elsevier. pp. 923–978.

Hintz C. J., Shaw T. J., Bernhard J. M., Chandler G. T., McCorkle D. C. and Blanks J. K. (2006) Trace/minor element: calcium ratios in cultured benthic foraminifera. Part II: Ontogenetic variation. *Geochim. Cosmochim. Acta* **70**, 1964–1976.

Hodell D. A., Channeil J. E. T., Curtis J. H., Romero O. E. and Röhl U. (2008) Onset of "Hudson Strait" Heinrich events in the eastern North Atlantic at the end of the middle Pleistocene transition (~640 ka)? *Paleoceanography* **23**, 1–16.

Holcomb M., Cohen A. L., Gabitov R. I. and Hutter J. L. (2009) Compositional and morphological features of aragonite precipitated experimentally from seawater and biogenically by corals. *Geochim. Cosmochim. Acta* **73**, 4166–4179. Available at: http://dx.doi.org/10.1016/j.gca.2009.04.015.

Hollis C. J., Taylor K. W. R., Handley L., Pancost R. D., Huber M., Creech J. B., Hines B. R., Crouch E. M., Morgans H. E. G., Crampton J. S., Gibbs S., Pearson P. N. and Zachos J. C. (2012) Early Paleogene temperature history of the Southwest Pacific Ocean: Reconciling proxies and models. *Earth Planet. Sci. Lett.* **349–350**, 53–66. Available at: http://dx.doi.org/10.1016/j.epsl.2012.06.024.

Hönisch B., Hemming N. G., Archer D., Siddall M. and McManus J. F. (2009) Atmospheric carbon dioxide concentration across the mid-Pleistocene transition. *Science* **324**, 1551–4. Available at: http://www.sciencemag.org/cgi/doi/10.1126/science.1171477%5Cnhttp://www.ncbi.nlm.nih.gov/pubmed/19541994.

Hopmans E. C., Weijers J. W. H., Schefuß E., Herfort L., Damsté J. S. S. and Schouten S.

(2004) A novel proxy for terrestrial organic matter in sediments based on branched and isoprenoid tetraether lipids. *Earth Planet. Sci. Lett.* **224**, 107–116.

Horng C. S., Lee M. Y., Pälike H., Wei K. Y., Liang W. T., Iizuka Y. and Torii M. (2002) Astronomically calibrated ages for geomagnetic reversals within the Matuyama chron. *Earth, Planets Sp.* **54**, 679–690.

Huguet C., Kim J.-H., de Lange G. J., Damsté J. S. S. and Schouten S. (2009) Effects of long term oxic degradation on the, TEX 86 and BIT organic proxies. *Org. Geochem.* **40**, 1188–1194.

Hutson W. H. (1980) The Agulhas Current during the Late Pleistocene: Analysis of modern faunal analogs. *Science (80-.).* **207**, 64–66.

Huybers P. and Wunsch C. (2004) A depth-derived Pleistocene age model: Uncertainty estimates, sedimentation variability, and nonlinear climate change. *Paleoceanogr. Paleoclimatology* **19**.

Imbrie J., Berger A., Boyle E. A., Clemens S. C., Duffy A., Howard W. R., Kukla G., Kutzbach J., Martinson D. G., Mcintyre A., Mix A. C., Morley J. J., Peterson L. C., Pisias N. G., Prell W. L., Raymo M. E., Shackleton N. J. and Lemaitre G. (1993) Milankovitch theory , the two shorter cycles can be explained radiation cycle (arising from of Geological Sciences , Brown 2 Institut d ' Astronomie et de G6ophysique of Earth , Atmospheric , and Planetary Earth Observatory , Columbia for Climatic and Sp. **8**, 699–735.

Imbrie J. and Kipp N. G. 1971. A new micropaleontologial method for quantitative paleoclimatology: Application to a Late Pleistocene Caribbean core. *Late Cenozoic Glacial Ages. Yale Univ. Press. New Haven* **3**, 71–181.

Iván H., Javier S. F., José-Abel F., Isabel C. and Michael F. G. (2012) Palaeoceanographic changes in the North Atlantic during the Mid-Pleistocene Transition (MIS 31–19) as inferred from planktonic foraminiferal and calcium carbonate records. *Boreas* **42**, 140–159. Available at: https://doi.org/10.1111/j.1502-3885.2012.00283.x.

Jenkyns H. C., Schouten-Huibers L., Schouten S. and Sinninghe Damsté J. S. (2012) Warm Middle Jurassic-Early Cretaceous high-latitude sea-surface temperatures from the Southern Ocean. *Clim. Past* **8**, 215–225.

Juillet-Leclerc A. and Schmidt G. (2001) A calibration of the oxygen isotope paleothermometer of coral aragonite from Porites. *Geophys. Res. Lett.* **28**, 4135–4138.

Källén E., Crafoord C. and Ghil M. (1979) Free oscillations in a climate model with ice-sheet dynamics. *J. Atmos. Sci.* **36**, 2292–2303.

Karner M. B., Delong E. F. and Karl D. M. (2001) Archaeal dominance in the mesopelagiczone of thePacific Ocean. *Nature* **409**, 507–510.

Katz A., Bonifacie M., Cartigny P. and Calmels D. (2017) ScienceDirect Laboratory-grown coccoliths exhibit no vital effect in clumped isotope (D 47) composition on a range of geologically relevant temperatures. **208**, 335–353.

Kelson J. R., Huntington K. W., Schauer A. J., Saenger C. and Lechler A. R. (2017) Toward a universal carbonate clumped isotope calibration: Diverse synthesis and preparatory methods suggest a single temperature relationship. *Geochim. Cosmochim. Acta* **197**, 104–131. Available at: http://dx.doi.org/10.1016/j.gca.2016.10.010.

Kemp A. E. S., Grigorov I., Pearce R. B. and Naveira Garabato A. C. (2010) Migration of the Antarctic Polar Front through the mid-Pleistocene transition: Evidence and climatic implications. *Quat. Sci. Rev.* **29**, 1993–2009. Available at: http://dx.doi.org/10.1016/j.quascirev.2010.04.027.

Kennett J. P., Cannariato K. G., Hendy I. L. and Behl R. J. (2003) *Methane hydrates in quaternary climate change: the clathrate gun hypothesi.*, Wiley Online Library.

Kim J.-H., Huguet C., Zonneveld K. A. F., Versteegh G. J. M., Roeder W., Damsté J. S. S. and Schouten S. (2009) An experimental field study to test the stability of lipids used for the TEX86 and U37K′ palaeothermometers. *Geochim. Cosmochim. Acta* **73**, 2888–2898.

Kim J.-H., Van der Meer J., Schouten S., Helmke P., Willmott V., Sangiorgi F., Koç N., Hopmans E. C. and Damsté J. S. S. (2010) New indices and calibrations derived from the distribution of crenarchaeal isoprenoid tetraether lipids: Implications for past sea surface temperature reconstructions. *Geochim. Cosmochim. Acta* **74**, 4639–4654.

Kim J.-H., Schouten S., Rodrigo-Gámiz M., Rampen S., Marino G., Huguet C., Helmke P., Buscail R., Hopmans E. C. and Pross J. (2015) Influence of deep-water derived isoprenoid tetraether lipids on the TEX86H paleothermometer in the Mediterranean Sea. *Geochim. Cosmochim. Acta* **150**, 125–141.

Kim J., Schouten S., Hopmans E. C., Donner B. and Damste J. S. S. (2008) Global sediment core-top calibration of the TEX 86 paleothermometer in the ocean. **72**, 1154–1173.

Kim S., Takahashi K., Khim B. K., Kanematsu Y., Asahi H. and Ravelo A. C. (2014) Biogenic opal production changes during the Mid-Pleistocene Transition in the Bering Sea (IODP Expedition 323 Site U1343). *Quat. Res. (United States)* **81**, 151–157. Available at: http://dx.doi.org/10.1016/j.yqres.2013.10.001.

Kinsman D. J. J. and Holland H. D. (1969) The co-precipitation of cations with CaCO3—IV. The co-precipitation of Sr2+ with aragonite between 16° and 96° C. *Geochim. Cosmochim. Acta* **33**, 1–17.

Kisakürek B., Eisenhauer A., Böhm F., Garbe-Schönberg D. and Erez J. (2008) Controls on shell Mg/Ca and Sr/Ca in cultured planktonic foraminiferan, Globigerinoides ruber (white). *Earth Planet. Sci. Lett.* **273**, 260–269.

Kroon D., Alexander I., Little M., Lourens L. J., Matthewson A., Robertson A. H. F. and Sakamoto T. (1998) 14 . OXYGEN ISOTOPE AND SAPROPEL STRATIGRAPHY IN THE EASTERN MEDITERRANEAN DURING THE LAST 3 . 2 MILLION YEARS 1. **160**, 181–189.

Kucera M., Rosell-Melé A., Schneider R., Waelbroeck C. and Weinelt M. (2005a) Multiproxy approach for the reconstruction of the glacial ocean surface (MARGO). *Quat. Sci. Rev.* **24**, 813–819.

Kucera M., Weinelt M., Kiefer T., Pflaumann U., Hayes A., Weinelt M., Chen M., Mix A. C., Barrows T. T., Cortijo E., Duprat J., Juggins S. and Waelbroeck C. (2005b) Reconstruction of sea-surface temperatures from assemblages of planktonic foraminifera : multi-technique approach based on geographically constrained calibration data sets and its application to glacial Atlantic and Pacific Oceans. **24**, 951–998.

Kutzbach J. E., Guetter P. J., Ruddiman W. F. and Prell W. L. (1989) Sensitivity of climate to late Cenozoic uplift in Southern Asia and the American West: Numerical experiments. *J. Geophys. Res. Atmos.* **94**, 18393–18407.

Lang N. and Wolff E. W. (2011) of the Past Interglacial and glacial variability from the last 800 ka in marine , ice and terrestrial archives. , 361–380.

Larrasoan J. C. (2003) Three million years of monsoon variability over the northern Sahara. , 689–698.

Lawrence K. T., Sosdian S., White H. E. and Rosenthal Y. (2010) North Atlantic climate

evolution through the Plio-Pleistocene climate transitions. *Earth Planet. Sci. Lett.* **300**, 329–342.

Lea D. W., Mashiotta T. A. and Spero H. J. (1999) Controls on magnesium and strontium uptake in planktonic foraminifera determined by live culturing. *Geochim. Cosmochim. Acta* **63**, 2369–2379.

Lear C. H., Rosenthal Y. and Slowey N. (2002) Benthic foraminiferal Mg / Ca-paleothermometry : A revised core-top calibration. *Geochim. Cosmochim. Acta* **66**, 3375–3387.

De Leeuw J. W., vd Meer F. W., Rijpstra W. I. C. and Schenck P. A. (1980) On the occurrence and structural identification of long chain unsaturated ketones and hydrocarbons in sediments. *Phys. Chem. Earth* **12**, 211–217.

Lisiecki L. E. and Raymo M. E. (2005) A Pliocene-Pleistocene stack of 57 globally distributed benthic D 18 O records. **20**, 1–17.

Liu X. L. (2011) Glycerol ether lipids in sediments : sources , diversity and implications Dissertation Xiao-Lei Liu. .

Liu Z., Cleaveland L. C. and Herbert T. D. (2008) Early onset and origin of 100-kyr cycles in Pleistocene tropical SST records. *Earth Planet. Sci. Lett.* **265**, 703–715.

Liu Z. and Herbert T. D. (2004) High-latitude influence on the eastern equatorial Pacific climate in the early Pleistocene epoch. *Nature* **427**, 720.

Lorens R. B. (1981) Sr, Cd, Mn and Co distribution coefficients in calcite as a function of calcite precipitation rate. *Geochim. Cosmochim. Acta* **45**, 553–561.

Lorrain A., Gillikin D. P., Paulet Y., Chauvaud L., Le A., Navez J., André L., Lorrain A., Gillikin D. P., Paulet Y., Chauvaud L., Mercier A. Le and Mercier A. Le (2010) Strong kinetic effects on Sr / Ca ratios in the calcitic bivalve To cite this version : HAL Id : hal-00452403 Strong kinetic effects on Sr / Ca ratios in the calcitic bivalve Pecten maximus.

Lourens L. J., Sluijs A., Kroon D., Zachos J. C., Thomas E., Bowles J. and Raffi I. (2005) Astronomical pacing of late Palaeocene to early Eocene global warming events. **435**, 1083–1087.

Loutre M.-F. and Berger A. (2003) Marine Isotope Stage 11 as an analogue for the present interglacial. *Glob. Planet. Change* **36**, 209–217.

Maasch K. A. (1988) Statistical detection of the mid-Pleistocene transition. *Clim. Dyn.* **2**, 133–143.

Maiorano P., Marino M., Balestra B., Flores J. A., Hodell D. A. and Rodrigues T. (2015) Coccolithophore variability from the Shackleton Site (IODP Site U1385) through MIS 16-10. *Glob. Planet. Change* **133**, 35–48. Available at: http://dx.doi.org/10.1016/j.gloplacha.2015.07.009.

Maiorano P., Marino M. and Flores J. A. (2009) The warm interglacial Marine Isotope Stage 31: Evidences from the calcareous nannofossil assemblages at Site 1090 (Southern Ocean). *Mar. Micropaleontol.* **71**, 166–175. Available at: http://dx.doi.org/10.1016/j.marmicro.2009.03.002.

Malaiz?? B., Jullien E., Tisserand A., Skonieczny C., Grousset E. F., Eynaud F., Kissel C., Bonnin J. ??me, Karstens S., Martinez P., Bory A., Bout-Roumazeilles V., Caley T., Crosta X., Charlier K., Rossignol L., Flores J. A. and Schneider R. (2012) The impact of African aridity on the isotopic signature of Atlantic deep waters across the Middle Pleistocene Transition. *Quat. Res.* **77**, 182–191. Available at: http://dx.doi.org/10.1016/j.yqres.2011.09.010.

Marchitto T. M., Bryan S. P., Curry W. B. and McCorkle D. C. (2007) Mg/Ca temperature

calibration for the benthic foraminifer Cibicidoides pachyderma. *Paleoceanography* **22**, 1–9.

Marchitto T. M., Bryan S. P., Doss W., McCulloch M. T. and Montagna P. (2018) A simple biomineralization model to explain Li, Mg, and Sr incorporation into aragonitic foraminifera and corals. *Earth Planet. Sci. Lett.* **481**, 20–29.

Marchitto T. M., Curry W. B., Lynch-Stieglitz J., Bryan S. P., Cobb K. M. and Lund D. C. (2014) Improved oxygen isotope temperature calibrations for cosmopolitan benthic foraminifera. *Geochim. Cosmochim. Acta* **130**, 1–11. Available at: http://dx.doi.org/10.1016/j.gca.2013.12.034.

Marino M., Maiorano P. and Flower B. P. (2011) Calcareous nannofossil changes during the Mid-Pleistocene Revolution: Paleoecologic and paleoceanographic evidence from North Atlantic Site 980/981. *Palaeogeogr. Palaeoclimatol. Palaeoecol.* **306**, 58–69. Available at: http://dx.doi.org/10.1016/j.palaeo.2011.03.028.

Marino M., Maiorano P., Lirer F. and Pelosi N. (2009) Response of calcareous nannofossil assemblages to paleoenvironmental changes through the mid-Pleistocene revolution at Site 1090 (Southern Ocean). *Palaeogeogr. Palaeoclimatol. Palaeoecol.* **280**, 333–349. Available at: http://dx.doi.org/10.1016/j.palaeo.2009.06.019.

Marlowe I. T., Brassell S. C., Eglinton G. and Green J. C. (1984) Long chain unsaturated ketones and esters in living algae and marine sediments. *Org. Geochem.* **6**, 135–141.

Marlowe I. T., Green J. C., Neal A. C., Brassell S. C., Eglinton G. and Course P. A. (1984) Long chain (n-c37-c39) alkenones in the prymnesiophyceae. distribution of alkenones and other lipids and their taxonomic significance. *Br. Phycol. J.* **19**, 203–216.

Marra F., Pandolfi L., Petronio C., Di Stefano G., Gaeta M. and Salari L. (2014) Reassessing the sedimentary deposits and vertebrate assemblages from Ponte Galeria area (Rome, central Italy): An archive for the Middle Pleistocene faunas of Europe. *Earth-Science Rev.* **139**, 104–122.

Martinez-Garcia A., Rosell-mele A., Geibert W. and Gersonde R. (2009) Links between iron supply , marine productivity , sea surface temperature , and CO 2 over the last 1 . 1 Ma. **24**, 1–14.

Martinez-Garcia A., Rosell-mele A., Jaccard S. L., Geibert W., Sigman D. M. and Haug G. H. (2011) Southern Ocean dust–climate coupling over the past four million years. *Lett. to Nat.* **0**, 1–5.

Mary Y., Eynaud F., Colin C., Rossignol L., Brocheray S., Mojtahid M., Garcia J., Peral M., Howa H., Zaragosi S. and Cremer M. (2017) Changes in Holocene meridional circulation and poleward Atlantic flow: The Bay of Biscay as a nodal point. *Clim. Past* **13**.

Maslin M. A. and Ridgwell A. J. (2005) Mid-Pleistocene revolution and the 'eccentricity myth.' *Geol. Soc. London, Spec. Publ.* **247**, 19–34.

Maslin M., Seidov D. and Lowe J. (2001) Synthesis of the nature and causes of rapid climate transitions during the Quaternary. *Ocean. Rapid Clim. Chang.*, 9–52.

Mathien-Blard E. and Bassinot F. (2009) Salinity bias on the foraminifera Mg/Ca thermometry: Correction procedure and implications for past ocean hydrographic reconstructions. *Geochemistry, Geophys. Geosystems* **10**.

Mcclymont E. L., Rosell-mele A., Haug G. H. and Lloyd J. M. (2008) Expansion of subarctic water masses in the North Atlantic and Pacific oceans and implications for mid-Pleistocene ice sheet growth. **23**, 1–12.

McClymont E. L., Sosdian S. M., Rosell-Melé A. and Rosenthal Y. (2013) Pleistocene sea-

surface temperature evolution: Early cooling, delayed glacial intensification, and implications for the mid-Pleistocene climate transition. *Earth-Science Rev.* **123**, 173–193.

McCrea J. M. (1950) On the isotopic chemistry of carbonates and a paleotemperature scale. *J. Chem. Phys.* **18**, 849–857.

Meckler A. N., Ziegler M., Mill??n M. I., Breitenbach S. F. M. and Bernasconi S. M. (2014) Long-term performance of the Kiel carbonate device with a new correction scheme for clumped isotope measurements. *Rapid Commun. Mass Spectrom.* **28**, 1705–1715.

Meibom A., Cuif J. P., Houlbreque F., Mostefaoui S., Dauphin Y., Meibom K. L. and Dunbar R. (2008) Compositional variations at ultra-structure length scales in coral skeleton. *Geochim. Cosmochim. Acta* **72**, 1555–1569.

Melles M., Melles M., Brigham-grette J., Minyuk P. S., Nowaczyk N. R., Wennrich V., Deconto R. M., Anderson P. M., Andreev A. A., Coletti A., Cook T. L., Haltia-hovi E., Kukkonen M., Lozhkin A. V, Rosén P., Tarasov P., Vogel H. and Wagner B. (2014) 2 . 8 Million Years of Arctic Climate. *Science (80-.).* **315**.

Meyers S. R. and Hinnov L. A. (2010) Northern Hemisphere glaciation and the evolution of Plio - Pleistocene climate noise. **25**, 1–11.

Milankovitch M. (1941) Kanon der Erdbestrahlung und seine Anwendung auf das Eiszeitenproblem: Royal Serbian Academy, Section of Mathematical and Natural Sciences, Belgrade, 633 p.(and 1998 reissue in English: Canon of Insolation and the Ice-Age Problem. *Belgrade, Serbian Acad. Sci. Arts, Sect. Math. Nat. Sci.*, 634.

Milankovitch M. (1920) Théorie mathématique des phénomènes thermiques produits par la radiation solaire.

Mitsuguchi T., Matsumoto E., Abe O., Uchida T. and Isdale P. (1996) Mg/Ca Thermometry in Coral Skeletons. *Science (80-.).* **274**, 961–963.

Montagna P., McCulloch M., Douville E., López Correa M., Trotter J., Rodolfo-Metalpa R., Dissard D., Ferrier-Pagès C., Frank N., Freiwald A., Goldstein S., Mazzoli C., Reynaud S., Rüggeberg A., Russo S. and Taviani M. (2014) Li/Mg systematics in scleractinian corals: Calibration of the thermometer. *Geochim. Cosmochim. Acta* **132**, 288–310.

Morse J. W. and Bender M. L. (1990) Partition coefficients in calcite: Examination of factors influencing the validity of experimental results and their application to natural systems. *Chem. Geol.* **82**, 265–277.

Müller M. N., Kısakürek B., Buhl D., Gutperlet R., Kolevica A., Riebesell U., Stoll H. and Eisenhauer A. (2011) Response of the coccolithophores Emiliania huxleyi and Coccolithus braarudii to changing seawater Mg2+ and Ca2+ concentrations: Mg/Ca, Sr/Ca ratios and δ44/40Ca, δ26/24Mg of coccolith calcite. *Geochim. Cosmochim. Acta* **75**, 2088–2102.

Müller P. J., Kirst G., Ruhland G., Von Storch I. and Rosell-Melé A. (1998) Calibration of the alkenone paleotemperature index U 37 K′ based on core-tops from the eastern South Atlantic and the global ocean (60 N-60 S). *Geochim. Cosmochim. Acta* **62**, 1757–1772.

Nürnberg D., Buma J. and Hemleben C. (1996) Assessing the reliability of magnesium in foraminiferal calcite as a proxy for water mass temperatures. *Geochim. Cosmochim. Acta* **60**, 803–814.

Overpeck J. T., Webb T. and Prentice I. C. (1985) Quantitative interpretation of fossil pollen spectra: dissimilarity coefficients and the method of modern analogs. *Quat. Res.* **23**, 87–108.

Pearson A., McNichol A. P., Benitez-Nelson B. C., Hayes J. M. and Eglinton T. I. (2001)

Origins of lipid biomarkers in Santa Monica Basin surface sediment: A case study using compound-specific Δ14C analysis. *Geochim. Cosmochim. Acta* **65**, 3123–3137.

Pelejero C. and Grimalt J. O. (1997) Pelejero_and_Grimalt97GCA.pdf. *Geochim. Cosmochim. Acta* **61**, 4789_4797.

Peltier W. R. and Marshall S. (1995) Coupled energy-balance/ice-sheet model simulations of the glacial cycle: A possible connection between terminations and terrigenous dust. *J. Geophys. Res. Atmos.* **100**, 14269–14289.

Pena L. D., Cacho I., Calvo E., Pelejero C., Eggins S. and Sadekov A. (2008) Characterization of contaminant phases in foraminifera carbonates by electron microprobe mapping. *Geochemistry, Geophys. Geosystems* **9**, 1–12.

Pena L. D. and Goldstein S. L. (2014) Thermohaline circulation crisis and impacts during the mid-Pleistocene transition. *Science (80-.).* **345**, 318–322. Available at: http://www.ncbi.nlm.nih.gov/pubmed/24968939.

Pisias N. G. and Moore Jr T. C. (1981) The evolution of Pleistocene climate: a time series approach. *Earth Planet. Sci. Lett.* **52**, 450–458.

Popp B. N., Bidigare R. R., Deschenes B., Laws E. A., Prahl F. G. and Tanimoto J. K. (2006) OCEANOGRAPHY : METHODS A new method for estimating growth rates of alkenone-producing haptophytes. *Cultures*, 114–129.

Prahl F. G., Muehlhausen L. A. and Zahnle D. L. (1988) Further evaluation of long-chain alkenones as indicators of paleoceanographic conditions. *Geochim. Cosmochim. Acta* **52**, 2303–2310.

Prahl F. G. and Wakeham S. G. (1987) Calibration of unsaturation patterns in long-chain ketone compositions for palaeotemperature assessment. *Nature* **330**, 367.

Prell W. L. (1985) *Stability of low-latitude sea-surface temperatures: an evaluation of the CLIMAP reconstruction with emphasis on the positive SST anomalies. Final report.*, Brown Univ., Providence, RI (USA). Dept. of Geological Sciences.

Raddatz J., Liebetrau V., Rüggeberg A., Hathorne E., Krabbenhöft A., Eisenhauer A., Böhm F., Vollstaedt H., Fietzke J., Correa M. L., Freiwald A. and Dullo W. (2013) Stable Sr-isotope , Sr / Ca , Mg / Ca , Li / Ca and Mg / Li ratios in the scleractinian cold-water coral Lophelia pertusa. *Chem. Geol.* **352**, 143–152. Available at: http://dx.doi.org/10.1016/j.chemgeo.2013.06.013.

Railsback L. B., Gibbard P. L., Head M. J., Voarintsoa N. R. G. and Toucanne S. (2015) An optimized scheme of lettered marine isotope substages for the last 1.0 million years, and the climatostratigraphic nature of isotope stages and substages. *Quat. Sci. Rev.* **111**, 94–106.

Raymo M. E. 1994 (1994) The Himalayas, organic carbon burial, and climate in the Miocene. *Paleoceanogr. Paleoclimatology* **9**, 399–404.

Raymo M. E., Lisiecki L. E. and Nisancioglu K. H. (2006) Plio-Pleistocene ice volume, Antarctic climate, and the global δ18O record. *Science (80-.).* **313**, 492–495.

Raymo M. E., Oppo D. W. and Curry W. (1997) The mid-Pleistocene climate transition : A deep sea carbon isotopic perspective records from the deep ocean , extending back examined in order to constrain decrease in mean. **12**, 546–559.

Ridgwell A. J. and Watson A. J. (2002) Feedback between aeolian dust, climate, and atmospheric CO_2 in glacial time. *Paleoceanography* **17**, 11-1-11–11. Available at: http://doi.wiley.com/10.1029/2001PA000729.

Rogerson E. J. R. (2012) Paleoceanography of the Atlantic-Mediterranean exchange: Overview and first quantitative assessment of climatic forcing. *Rev. Geophys.* **50**.

Rollion-bard C. and Blamart D. (2015) Possible controls on Li , Na , and Mg incorporation

into aragonite coral skeletons. *Chem. Geol.* **396**, 98–111. Available at: http://dx.doi.org/10.1016/j.chemgeo.2014.12.011.

Rosenheim B. E., Swart P. K., Thorrold S. R., Willenz P., Berry L. and Latkoczy C. (2004) High-resolution Sr/Ca records in sclerosponges calibrated to temperature in situ. *Geol. Soc. Am.* **32**, 145–148.

Rosenthal Y., Boyle E. A. and Labeyrie L. (1997) Last glacial maximum palechemistry and deepwater circulation in the Southern Ocean: Evidence from foraminiferal cadmium. *Paleoceanography* **12**, 787–796.

Rosenthal Y., Lear C. H., Oppo D. W. and Linsley B. K. (2006) Temperature and carbonate ion effects on Mg/Ca and Sr/Ca ratios in benthic foraminifera: Aragonitic species Hoeglundina elegans. *Paleoceanography* **21**, 1–14.

Rosenthal Y., Perron-Cashman S., Lear C. H., Bard E., Barker S., Billups K., Bryan M., Delaney M. L., DeMenocal P. B., Dwyer G. S., Elderfield H., German C. R., Greaves M., Lea D. W., Marchitto T. M., Pak D. K., Paradis G. L., Russell A. D., Schneider R. R., Scheiderich K., Stott L., Tachikawa K., Tappa E., Thunell R., Wara M., Weldeab S. and Wilson P. A. (2004) Interlaboratory comparison study of Mg/Ca and Sr/Ca measurements in planktonic foraminifera for paleoceanographic research. *Geochemistry, Geophys. Geosystems* **5**, 1–29.

Ruddiman W. F., Raymo M. and McIntyre A. (1986) Matuyama 41,000-year cycles: North Atlantic Ocean and northern hemisphere ice sheets. *Earth Planet. Sci. Lett.* **80**, 117–129.

Ruddiman W. F., Sarnthein M., Backman J., Baldauf J. G., Curry W., Dupont L. M., Janecek T., Pokras E. M., Raymo M. E., Stabell B., Stein R. and Tiedemann R. (1989) Late Miocene to Pleistocene Evolution of Climate in Africa and the Low-Latitude Atlantic: Overview of Leg 108 Results. *Proc. Ocean Drill. Program, 108 Sci. Results* **108**, 463–484. Available at: http://www-odp.tamu.edu/publications/108_SR/VOLUME/CHAPTERS/sr108_29.pdf.

Schauble E. A., Ghosh P. and Eiler J. M. (2006) Preferential formation of 13C-18O bonds in carbonate minerals, estimated using first-principles lattice dynamics. *Geochim. Cosmochim. Acta* **70**, 2510–2529.

Schefuß E., Schouten S., Jansen J. H. F. and Sinninghe Damsté J. S. (2003) African vegetation controlled by tropical sea surface temperatures in the mid-Pleistocene period. *Nature* **422**, 418. Available at: http://dx.doi.org/10.1038/nature01500.

Scherer R. P., Bohaty S. M., Dunbar R. B., Esper O., Flores J. A., Gersonde R., Harwood D. M., Roberts A. P. and Taviani M. (2008) Antarctic records of precession-paced insolation-driven warming during early Pleistocene Marine Isotope Stage 31. *Geophys. Res. Lett.* **35**, 1–5.

Schmieder F., von Dobeneck T. and Bleil U. (2000) The Mid-Pleistocene climate transition as documented in the deep South Atlantic Ocean: initiation, interim state and terminal event. *Earth Planet. Sci. Lett.* **179**, 539–549.

Schouten J. W., McAlexander J. H. and Koenig H. F. (2007) Transcendent customer experience and brand community. *J. Acad. Mark. Sci.* **35**, 357–368. Available at: http://link.springer.com/10.1007/s11747-007-0034-4.

Schouten S., Hopmans E. C., Pancost R. D. and Damste J. S. S. (2000) Widespread occurrence of structurally diverse tetraether membrane lipids: Evidence for the ubiquitous presence of low-temperature relatives of hyperthermophiles. *Proc. Natl. Acad. Sci.* **97**, 14421–14426. Available at: http://www.pnas.org/cgi/doi/10.1073/pnas.97.26.14421.

Schouten S., Hopmans E. C., Schefuß E. and Sinninghe Damsté J. S. (2002) Distributional veriations in marine crenarchaeol membrane lipids: a new tool for reconstructing ancient sea water temperatures? *Earth Planet. Sci. Lett.* **204**, 265–274. Available at: http://www.sciencedirect.com/science/article/pii/S0012821X02009792.

Schouten S., Hopmans E. C. and Sinninghe Damsté J. S. (2013) The organic geochemistry of glycerol dialkyl glycerol tetraether lipids: A review. *Org. Geochem.* **54**, 19–61. Available at: http://dx.doi.org/10.1016/j.orggeochem.2012.09.006.

Schouten S., Huguet C., Hopmans E. C., Kienhuis M. V. M. and Sinninghe Damsté J. S. (2007) Analytical methodology for TEX86 paleothermometry by high-performance liquid chromatography/atmospheric pressure chemical ionization-mass spectrometry. *Anal. Chem.* **79**, 2940–2944.

Shackleton N. (1967) Oxygen isotope analyses and Pleistocene temperatures re-assessed. *Nature* **215**, 15–17.

Shackleton N. J. (1974) Attainment of isotopic equilibrium between ocean water and the benthonic foraminifera geuns *Uvigerina*: Isotopic changes in the ocean during the last glacial. *Colloq. Int. du C.N.R.S.* **219**, 203–210.

Shackleton N. J., Berger A. and Peltier W. R. (1990) Shackletonetal_1990.pdf. *Trans. R. Soc. Edinburgh* **81**, 251–261.

Shackleton N. J. and Opdyke N. D. (1973) Oxygen isotope and palaeomagnetic stratigraphy of equatorial Pacific core V28-238: Oxygen isotope temperatures and ice volumes on a 10 5 year and 10 6 year scale. *Quat. Res.* **3**, 39–55.

Shah S. R., Mollenhauer G., Ohkouchi N., Eglinton T. I. and Pearson A. (2008) Origins of archaeal tetraether lipids in sediments: Insights from radiocarbon analysis. *Geochim. Cosmochim. Acta* **72**, 4577–4594.

Sikes E. L., Farrington J. W. t and Keigwin L. D. (1991) Use of the alkenone unsaturation ratio U37K to determine past sea surface temperatures: core-top SST calibrations and methodology considerations. *Earth Planet. Sci. Lett.* **104**, 36–47.

Sikes E. L. and Volkman J. K. (1993) Calibration of alkenone unsaturation ratios (Uk'37) for paleotemperature estimation in cold polar waters. *Geochim. Cosmochim. Acta* **57**, 1883–1889.

Sinclair D. J., Williams B. and Risk M. (2006) A biological origin for climate signals in corals - Trace element "vital effects" are ubiquitous in Scleractinian coral skeletons. *Geophys. Res. Lett.* **33**, 1–5.

Smith S. V, Buddemeier R. W., Redalje R. C. and Houck J. E. (1979) Strontium-calcium thermometry in coral skeletons. *Science (80-.).* **204**, 404–407.

Sosdian S. M. and Rosenthal Y. (2009) Deep-sea temperature and ice volume changes across the Pliocene-Pleistocene climate transitions. *Science (80-.).* **325**, 306–10. Available at: http://www.ncbi.nlm.nih.gov/pubmed/19608915.

Sosdian S. and Rosenthal Y. (2010) Response to Comment on "Deep-Sea Temperature and Ice Volume Changes Across the Pliocene-Pleistocene Climate Transitions." *Science (80-.).* **328**, 1480–1480. Available at: http://www.sciencemag.org/cgi/doi/10.1126/science.1186768.

Sr-u C., Decarlo T. M., Gaetani G. A., Cohen A. L., Foster G. L., Alpert A. E. and Stewart J. A. (2016) Coral Sr-U thermometry. , 626–638.

Sun Y., Wang X., Liu Q. and Clemens S. C. (2010) Impacts of post-depositional processes on rapid monsoon signals recorded by the last glacial loess deposits of northern China. *Earth Planet. Sci. Lett.* **289**, 171–179. Available at: http://dx.doi.org/10.1016/j.epsl.2009.10.038.

Taylor K. W. R., Huber M., Hollis C. J., Hernandez-Sanchez M. T. and Pancost R. D. (2013) Re-evaluating modern and Palaeogene GDGT distributions: Implications for SST reconstructions. *Glob. Planet. Change* **108**, 158–174. Available at: http://dx.doi.org/10.1016/j.gloplacha.2013.06.011.

Teitler L., Florindo F., Warnke D. A., Filippelli G. M., Kupp G. and Taylor B. (2015) Antarctic Ice Sheet response to a long warm interval across Marine Isotope Stage 31: A cross-latitudinal study of iceberg-rafted debris. *Earth Planet. Sci. Lett.* **409**, 109–119. Available at: http://dx.doi.org/10.1016/j.epsl.2014.10.037.

Tesoriero A. J. and Pankow J. F. (1996) Solid solution partitioning of Sr2+, Ba2+, and Cd2+ to calcite. *Geochim. Cosmochim. Acta* **60**, 1053–1063.

Tierney J. E. and Tingley M. P. (2014) ScienceDirect A Bayesian , spatially-varying calibration model for the TEX 86 proxy. *Geochim. Cosmochim. Acta* **127**, 83–106. Available at: http://dx.doi.org/10.1016/j.gca.2013.11.026.

Toggweiler J. R., Russell J. L. and Carson S. R. (2006) Midlatitude westerlies, atmospheric CO2, and climate change during the ice ages. *Paleoceanography* **21**, 1–15.

Transition M., Chalk T. B., Hain M. P., Foster G. L., Rohling E. J., Sexton P. F. and Badger M. P. S. (2017) Causes of ice age intensification across the.

Tripati A. K., Eagle R. A., Thiagarajan N., Gagnon A. C., Bauch H., Halloran P. R. and Eiler J. M. (2010) 13C-18O isotope signatures and "clumped isotope" thermometry in foraminifera and coccoliths. *Geochim. Cosmochim. Acta* **74**, 5697–5717. Available at: http://dx.doi.org/10.1016/j.gca.2010.07.006.

Tripati A. K., Roberts C. D., Eagle R. A. and Li G. (2011) A 20 million year record of planktic foraminiferal B/Ca ratios: Systematics and uncertainties in pCO2 reconstructions. *Geochim. Cosmochim. Acta* **75**, 2582–2610. Available at: http://dx.doi.org/10.1016/j.gca.2011.01.018.

Tzedakis P. C. (2010) The MIS 11 - MIS 1 analogy, southern European vegetation, atmospheric methane and the "early anthropogenic hypothesis. *Clim. Past* **6**, 131–144.

Tzedakis P. C., Raynaud D., McManus J. F., Berger A., Brovkin V. and Kiefer T. (2009) Interglacial diversity. *Nat. Geosci.* **2**, 751.

Uda I., Sugai A., Itoh Y. H. and Itoh T. (2001) Variation in molecular species of polar lipids from Thermoplasma acidophilum depends on growth temperature. *Lipids* **36**, 103–105.

Urey H. C. (1947) The thermodynamic properties of isotopic substances. *J. Chem. Soc.*, 562–581. Available at: http://dx.doi.org/10.1039/JR9470000562.

Vance D., Teagle D. A. H. and Foster G. L. (2009) Variable Quaternary chemical weathering fluxes and imbalances in marine geochemical budgets. *Nature* **458**, 493.

Venuti A., Florindo F., Michel E. and Hall I. R. (2007) Magnetic proxy for the deep (Pacific) western boundary current variability across the mid-Pleistocene climate transition. *Earth Planet. Sci. Lett.* **259**, 107–118.

Vernal A. de, Henry M., Matthiessen J., Mudie P. J., Rochon A., Boessenkool K. P., Eynaud F., Grøsfjeld K., Guiot J., Hamel D., Harland R., Head M. J., Kunz-Pirrung M., Levac E., Loucheur V., Peyron O., Pospelova V., Radi T., Turon J. L. and Voronina E. (2001) Dinoflagellate cyst assemblages as tracers of sea-surface conditions in the Northern North Atlantic, Arctic and sub-Arctic seas: The new "n = 677" data base and its application for quantitative palaeoceanographic reconstruction. *J. Quat. Sci.* **16**, 681–698.

De Vernal A., Hillaire-Marcel C., Rochon A., Fréchette B., Henry M., Solignac S. and Bonnet

S. (2013) Dinocyst-based reconstructions of sea ice cover concentration during the Holocene in the Arctic Ocean, the northern North Atlantic Ocean and its adjacent seas. *Quat. Sci. Rev.* **79**, 111–121. Available at: http://dx.doi.org/10.1016/j.quascirev.2013.07.006.

de Vernal A., Rosell-Melé A., Kucera M., Hillaire-Marcel C., Eynaud F., Weinelt M., Dokken T. and Kageyama M. (2006) Comparing proxies for the reconstruction of LGM sea-surface conditions in the northern North Atlantic. *Quat. Sci. Rev.* **25**, 2820–2834.

Villa G., Fioroni C., Persico D., Roberts A. and Florindo F. (2013) Middle Eocene to Late Oligocene Antarctic glaciation/deglaciation and Southern Ocean productivity. *Paleoceanography*, 223–237.

de Villiers S., Nelson B. K. and Chivas A. R. (1995) Biological controls on coral Sr/Ca and δ18O reconstructions of sea surface temperatures. *Science (80-.).* **269**, 1247–1249.

Volkman J. K., Johns R. B., Gillan F. T., Perry G. J. and Bavor Jr H. J. (1980) Microbial lipids of an intertidal sediment—I. Fatty acids and hydrocarbons. *Geochim. Cosmochim. Acta* **44**, 1133–1143.

Waelbroeck C., Labeyrie L., Duplessy J., Guiot J., Labracherie M., Leclaire H. and Duprat J. (1998) Improving past sea surface temperature estimates based on planktonic fossil faunas Abstract . A new method of past sea surface temperature reconstruction based on the modem analog technique on the indirect approach has been developed : the revised analog . **13**, 272–283.

Wakeham S. G., Lewis C. M., Hopmans E. C., Schouten S. and Sinninghe Damsté J. S. (2003) Archaea mediate anaerobic oxidation of methane in deep euxinic waters of the Black Sea. *Geochim. Cosmochim. Acta* **67**, 1359–1374.

van de Wal R. S. W., de Boer B., Lourens L. J., Köhler P. and Bintanja R. (2011) Reconstruction of a continuous high-resolution CO₂ record over the past 20 million years. *Clim. Past* **7**, 1459–1469. Available at: https://www.clim-past.net/7/1459/2011/.

Watson a J., Bakker D. C., Ridgwell a J., Boyd P. W. and Law C. S. (2000) Effect of iron supply on Southern Ocean CO2 uptake and implications for glacial atmospheric CO2. *Nature* **407**, 730–733.

Weaver P. P. E., Chapman M. R., Eglinton G., Zhao M., Rutledge D. and Read G. (1999) Combined coccolith, foraminiferal, and biomarker reconstruction of paleoceanographic conditions over the past 120 kyr in the northern North Atlantic (59°N, 23°W). *Paleoceanography* **14**, 336–349.

Weber J. N. (1973) Incorporation of strontium into reef coral skeletal carbonate. *Geochim. Cosmochim. Acta* **37**, 2173–2190.

Weijers J. W. H., Schouten S. and Spaargaren O. C. (2006) Occurrence and distribution of tetraether membrane lipids in soils : Implications for the use of the TEX 86 proxy and the BIT index. **37**, 1680–1693.

Weirauch D., Billups K. and Martin P. (2008) Evolution of millennial-scale climate variability during the mid-Pleistocene. *Paleoceanography* **23**, 1–16.

Weiser J., Hahn A. and Zabel M. (2016) Late Holocene paleoceanographic changes off south-western Africa as inferred from coccolithophore assembl .... Africa as inferred from coccolithophore assemblages.

Wellington G. M., Dunbar R. B. and Merlen G. (1996) Calibration of stable oxygen isotope signatures in Galapagos corals. *Paleoceanogr. Paleoclimatology* **11**, 467–480.

Werner K., Müller J., Husum K., Spielhagen R. F., Kandiano E. S. and Polyak L. (2015)

Holocene sea subsurface and surface water masses in the Fram Strait e Comparisons of temperature and sea-ice reconstructions. *Quat. Sci. Rev.* Available at: http://dx.doi.org/10.1016/j.quascirev.2015.09.007.

Wuchter C., Schouten S., Coolen M. J. L. and Sinninghe Damst?? J. S. (2004) Temperature-dependent variation in the distribution of tetraether membrane lipids of marine Crenarchaeota: Implications for TEX86 paleothermometry. *Paleoceanography* **19**, 1–10.

Zaarur S., Affek H. P. and Brandon M. T. (2013) A revised calibration of the clumped isotope thermometer. *Earth Planet. Sci. Lett.* **382**, 47–57. Available at: http://dx.doi.org/10.1016/j.epsl.2013.07.026.

Zaarur S., Olack G. and Affek H. P. (2011) Paleo-environmental implication of clumped isotopes in land snail shells. *Geochim. Cosmochim. Acta* **75**, 6859–6869.

Zachos J. C., Shackleton N. J., Revenaugh J. S., Pa H. and Flower B. P. (2001) Climate Response to Orbital Forcing Across the Oligocene-Miocene Boundary. **292**, 274–278.

Zachos J., Pagani M., Sloan L., Thomas E. and Billups K. (2001) Trends , Rhythms , and Aberrations in Global Climate 65 Ma to Present. **292**, 686–693.

Ziegler M., Tuenter E. and Lourens L. J. (2010) The precession phase of the boreal summer monsoon as viewed from the eastern Mediterranean (ODP Site 968). *Quat. Sci. Rev.* **29**, 1481–1490. Available at: http://dx.doi.org/10.1016/j.quascirev.2010.03.011.

Zonneveld K. A. F. and Siccha M. (2016) Dino fl agellate cyst based modern analogue technique at test — A 300 year record from the Gulf of Taranto (Eastern Mediterranean). *Palaeogeogr. Palaeoclimatol. Palaeoecol.* **450**, 17–37. Available at: http://dx.doi.org/10.1016/j.palaeo.2016.02.045.

Part 2

METHODOLOGICAL DEVELOPMENTS

In the context of the first thesis on clumped isotopes at LSCE, my first objective was to establish the precise relationship between Δ_{47} and calcification temperature in foraminifera. With that goal in mind, I aimed to address the methodological issues presented in the following section. The results of this work were recently published in *Geochimica et Cosmochimica Acta.*

Owing to the collection of sedimentary cores of the LSCE, which span large range of latitude areas of the Earth's oceans, I was able to select core tops covering a wide range of sea surface temperatures for this calibration exercise. In addition, to combine both planktonic and benthic foraminifera in this study, I collaborated with specialists of benthic foraminifera. This set of calibration samples had to fulfil the following criteria:

- To cover the widest possible range of temperature (-2 to 25 °C) and achieve a relatively even temperature distribution across this range.

- Core tops were dated through AMS ^{14}C dating when their had not been dated in previous studies, and only the youngest samples (terminal Holocene: < 4 000 years) were kept in the final database in order to be confidently compared to modern ocean conditions.

- Foraminifer abundance had to be sufficient for collecting ~20 mg of material, in order to minimize final analytical errors on Δ_{47} (minimum of 4 analytical replicates). Following the method described by Patterson and Fishbein (1989), I first performed a basic count of all potentially interesting core tops to determine the abundance of each species of foraminifera. This allowed me to select the most abundant species in order to perform Δ_{47} measurements on mono-specific foraminifera samples. The total amount of foraminifera picked for this study (including methodological tests) exceeds 1.7 grams (about 130 000 individuals).

Chapter 1

UPDATED CALIBRATION OF THE CLUMPED ISOTOPE THERMOMETER IN PLANKTONIC AND BENTHIC FORAMINIFERA

Marion Peral[1], Mathieu Daëron[1], Dominique Blamart[1], Franck Bassinot[1], Fabien Dewilde[1], Nicolas Smialkowski[1], Gulay Isguder[1], Jérôme Bonnin[2], Frans Jorissen[3], Catherine Kissel[1], Elisabeth Michel[1], Natalia Vázquez Riveiros[1,4], Claire Waelbroeck[1]

[1] Laboratoire des Sciences du Climat et de l'Environnement, LSCE/IPSL, CEA-CNRS UVSQ, Université Paris-Saclay, F-91191 Gif-sur-Yvette, France
[2] Université de Bordeaux, CNRS, Environnements et Paléoenvironnements Océaniques et Continentaux (EPOC), UMR 5805, Allée Geoffroy St Hilaire, 33615 Pessac Cedex, France
[3] UMR CNRS 6112 LPG-BIAF Bio-Indicateurs Actuels et Fossiles, Université d'Angers, 2, Boulevard Lavoisier, 49045 Angers Cedex, France
[4] Now at: IFREMER, Laboratoire Géodynamique et enregistrement Sédimentaire, 29280, Plouzané, France

Published in: *Geochimica et Cosmochimica Acta* (2018)

ABSTRACT

Accurate reconstruction of past ocean temperatures is of critical importance to paleoclimatology. Carbonate clumped isotope thermometry ("Δ_{47}") is a relatively recent technique based on the strong relationship between calcification temperature and the statistical excess of ^{13}C-^{18}O bonds in carbonates. Its application to foraminifera holds great scientific potential, particularly because Δ_{47} paleotemperature reconstructions do not require assumptions regarding the ^{18}O composition of seawater. However there are still relatively few published observations investigating the potential influence of parameters such as salinity or foraminiferal size and species. We present a new calibration data set based on 234 replicate analyses of 9 planktonic and 2 benthic species of foraminifera collected from recent core-top sediments, with calcification temperatures ranging from -2 to 25 °C. We observe a strong relationship between Δ_{47} values and independent, oxygen-18 estimates of calcification temperatures:

$$\Delta_{47} = 41.63 \times 10^3 / T^2 + 0.2056$$

The formal precision of this regression (±0.7-1.0 °C at 95 % confidence level) is much smaller than typical analytical errors. Our observations confirm the absence of significant species-specific biases or salinity effects. We also investigate potential foraminifer size effects between 200 and > 560 µm in 6 species, and conclude that all size fractions from a given core-top location and species display statistically undistinguishable Δ^{47} values. These findings provide a robust foundation for future inter-laboratories comparisons and paleoceanographic applications.

Keywords: Carbonate clumped isotopes / foraminifera / paleothermometry

INTRODUCTION

The global ocean is a major component of the Earth's climate system because of its role in the redistribution of heat from low to high latitudes. Precisely constraining the physical and chemical characteristics of water masses (temperature and salinity, in particular) is essential to the study of past and present ocean dynamics and climate. For over sixty years, biogenic carbonates such as planktonic and benthic foraminifer shells have provided estimates of sea surface and bottom ocean temperatures based on oxygen isotope carbonate thermometry (Urey, 1947; Epstein et al., 1951; Emiliani, 1966; Shackleton, 1967). A well-known limitation of this classical technique is its sensitivity to the oxygen isotope composition of seawater ($\delta^{18}O_{sw}$), which in many cases complicates the interpretation of marine $\delta^{18}O$ records (Shackleton, 1967). Several alternative paleothermometers have been developed over the years to address this issue, either based on organics such as $U^{k'}_{37}$ (Brassell et al., 1986; Müller et al., 1998; Herbert, 2013) and TEX_{86} (Schouten et al., 2002; Kim et al., 2008, 2010) or based on trace elements in biogenic calcite (e.g., Mg/Ca in foraminifera; Elderfield and Ganssen, 2000; Lea, 2013). However, these alternative proxies have their own limitations, such as the effect of water column recycling, carbonate and sediment diagenesis, sensitivity to the presence of methane, salinity and/or species effect (Mathien-Blard and Bassinot, 2009; Herbert, 2013; Zhang et al., 2016).

Carbonate clumped isotope thermometry is an alternative isotopic technique developed over the past decade (Ghosh et al., 2006; Eiler, 2007; Eiler, 2011). It is based on the quantification of subtle statistical anomalies in the abundance of doubly substituted carbonate isotopologues ($^{13}C^{18}O^{16}O^{16}O^{2-}$) relative to a random distribution of isotopes. These anomalies may be considered to reflect equilibrium reactions taking place in the aqueous and/or mineral phases, such as:

$$^{13}C^{16}O^{16}O^{16}O^{2-} + {}^{12}C^{18}O^{16}O^{16}O^{2-} \Leftrightarrow {}^{13}C^{18}O^{16}O^{16}O^{2-} + {}^{12}C^{16}O^{16}O^{16}O^{2-}$$

For fundamental physical reasons, the right-hand side of this reaction is thermodynamically favoured, and the corresponding equilibrium constant varies with temperature (Schauble et al., 2006). As a result, carbonate minerals precipitated under conditions close to isotopic equilibrium are expected to contain a slightly higher

abundance of ^{13}C-^{18}O bonds than that predicted for a stochastic distribution of isotopes. This statistical anomaly should decrease systematically with crystallization temperature, and may be preserved over geologic time scales in the absence of diagenesis and solid-state redistribution of isotopes (Eiler 2011; Passey and Henkes, 2012; Stolper and Eiler, 2016). The conversion of carbonate to CO_2 by phosphoric acid reaction (McCrea, 1950) also preserves this signal, so that the calcification temperature can be estimated by precisely measuring Δ_{47}, defined as the statistical overabundance of mass-47 CO_2 (Ghosh et al., 2006). An important difference between the oxygen-18 and clumped-isotope thermometers is that the latter does not require any assumption to be made about the oxygen isotope composition of the aqueous phase.

Over the past decade, a number of calibration studies have investigated the relationship between Δ_{47} and temperature in inorganic carbonates (Ghosh et al., 2006; Dennis and Schrag, 2010; Zaarur et al., 2013; Tang et al., 2014; Defliese et al., 2015; Kele et al., 2015; Kluge et al., 2015; Tripati et al., 2015; Bonifacie et al., 2017; Kelson et al., 2017; Breitenbach et al., 2018; Levitt et al., 2018) and biogenic carbonates such as corals, otoliths, brachiopods, molluscs, foraminifera and coccoliths (Ghosh et al., 2006; Tripati et al., 2010; Thiagarajan et al., 2011; Zaarur et al., 2011; Eagle et al., 2013; Grauel et al., 2013; Came et al., 2014; Douglas et al., 2014; Wacker et al., 2014; Katz et al., 2017). Only two of these calibrations specifically focus on foraminifera: the finding by Tripati et al. (2010) that different foraminiferal species appear to follow a single relationship between temperature and Δ_{47} was subsequently confirmed by Grauel et al. (2013). These early calibration studies produced a significant body of observations whose importance should not be understated. However, both of them predate substantial methodological advances in the field of clumped isotope measurements, namely the definition by Dennis et al. (2011) of an "absolute" reference frame anchored to theoretical equilibrium Δ_{47} values in CO_2 (although Grauel et al. published their observations in 2013, their analyses were performed earlier and the results are reported in the older Δ_{47} reference frame), and the systematic distribution of inter-laboratory carbonate standards. As a result, using these early observations to precisely reconstruct past seawater temperatures is not straightforward.

Here, we present new calibration data for Δ_{47} in foraminifera covering a wide range of temperatures (-2 °C to 25 °C) that are relevant to paleoceanographic studies.

We first compare the potential chemical and isotopic impact of the sample cleaning protocols used in previous studies. We then investigate different strategies for obtaining Δ_{47}-independent constraints on calcification temperatures. Finally, we focus on the possible influence of salinity, and potential biases associated with foraminifer size and species.

2. MATERIALS AND METHODS

2.1. Samples

Twelve sedimentary core-tops from the North Atlantic, Austral and Pacific basins (Figure 2.1 and Table 1) were selected based on their abundance of foraminifera. We targeted 9 planktonic and 2 benthic species, covering a wide temperature range, from -2 °C to 25 °C. Individual foraminifera were hand-picked in different size fractions from 200 to 560 µm. We hereafter define each sample as a unique combination of core-top, species and size fraction. From each of these 58 samples, we used between 16 and 20 mg of foraminifera for stable isotope analyses (Δ_{47}, $\delta^{18}O$, $\delta^{13}C$).

All core-tops were chronologically constrained following the MARGO recommendations (Kucera et al., 2005) and correspond to Late Holocene ages (0-4 ka, Table 1). Age intervals were determined by AMS (Accelerator Mass Spectrometry) radiocarbon dating, by the presence of Rose Bengal stained foraminifera (alive at the time of collection or shortly before it; Walker et al., 1974) implying recent sediments, or by external stratigraphic controls (e.g., $\delta^{18}O$ stratigraphy). New ^{14}C dating supporting the present study was performed on monospecific foraminiferal shells at the UMS-ARTEMIS facility (CNRS-CEA, Saclay, France), using a Pelletron 3 MV AMS. Radiocarbon analyses were performed following the standard procedure described by Tisnérat-Laborde et al. (2001). Uncalibrated radiocarbon ages were converted to calendar ages using the calib-7.1 software (Stuiver et al., 2017) and the marine-13 calibration dataset (Reimer et al., 2013), with reservoir age corrections depending on core-top locations (Table 1).

Table 2.1: Core top locations and water depths with species considered in our calibration and chronological constraints listing from cooler to warmer temperatures defined using Kim and O'Neil (1997).

Core	Latitude (°N)	Longitude (°E)	Water depth (m)	Species	Core-top cal. yrs BP (95% CL)	Reservoir ^{14}C age (yr. ±1σ)	References
MOCOSEDst1	73.04	-11.93	1839	*Cibicides wuellerstorfi*; *N. pachyderma* s	6317 (+150/-94)	451 ± 35 [(a)]	(1)
MD04-2720	-49.13	71.36	750	*N. pachyderma* d	n.a.		
MD88-770	-46.02	96.45	3290	*G. bulloides*	6158 * (±120)		(2-3)
MD12-3401	-44.69	80.4	3445	*G. bulloides*	< 4000 **		(4)
MD95-2014	60.59	-22.08	2397	*G. bulloides*	715 (+94/-149)	502 ± 52 [(b)]	(1)
MD08-3182Q	52.71	-35.94	1355	*N. pachyderma* s; *G. bulloides*	500 (+40/–53)		(5)
MD03-2680Q	61.06	-24.55	1812	*N. pachyderma* d	402		(6)
2FPA1	43.67	-2.00	664	*Uvigerina mediterranea*	< 4000 ***		(1)
SU90I-03	40.05	-30	2475	*G. bulloides*	2013 (+125/-120)	401 ± 34 [(c)]	(1)
MD08-3179Q	37.86	-30.3	2036	*G. ruber*; *G. inflata*; *G. truncatulinoides* s; *G. truncatulinoides* d	4403 (+153/-121)	401 ± 34 [(c)]	(1)
MD12-3426Q	19.73	114.61	3630	*G. menardii*; *O. universa*	1755 (+159/-139)	341 ± 50 [(d)]	(1)
MD00-2360	-20.08	112.67	980	*G. menardii*; *O. universa*; *G. ruber*	3622 (+135/-137)	466 ± 31 [(e)]	(1)
MD02-2577Q	28.84	-86.67	4076	*G. menardii*; *O. universa*; *G. ruber*	1107 (+110/-105)	318 ± 21 [(f)]	(1)

* Age determined at 21 cm in the core
** Age determined by stratigraphic control
*** Age determined by presence of Rose Bengal
(1) This study; (2) Hatte et al. 2008; (3) Rogers and De Deckker 2011; (4) Vazquez Riveiros et al. 2016; (5) Kissel et al. 2013 and (6) Kissel et al. 2009
[(a)] Mangerud and Gulliksen 1975; [(b)] Broecke and Olson 1961; [(c)] Abrantes et al. 2005; [(d)] Southon et al. 2002; [(e)] Squire et al. 2013 and [(f)] Hadden and Cherkinsky 2015.
Species used for AMS radiocarbon dating

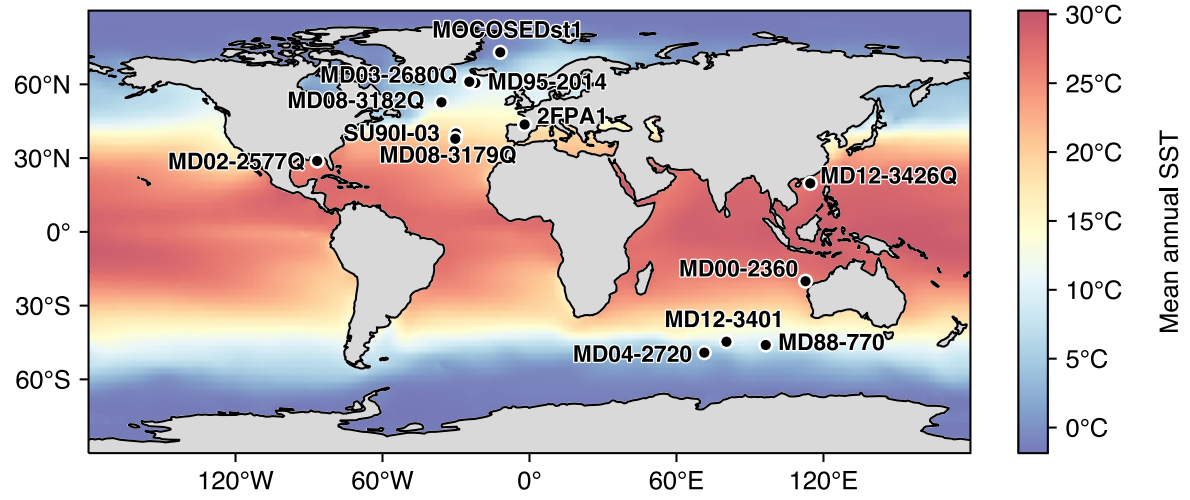

Figure 2.1: Map of core-top location used to establish this calibration, with the mean annual SST from WOA13.

2.2. Sample Pre-Treatment

The top 10 mm of sediment from each core-top were collected and dried overnight at 50 °C. The samples were wet sieved to collect the size fraction larger than 150 µm. The foraminifera were then hand-picked from different size fractions between 200 and > 560 µm (Table 2). Foraminifer shells were cleaned to eliminate organic and detrital contaminants. Following the approach of Grauel et al. (2013), we tested two cleaning procedures based on earlier foraminifer Δ_{47} calibration studies (Tripati et al., 2010; Grauel et al., 2013, respectively protocol #1 and protocol #2 hereafter). Both cleaning procedures require the following initial steps:

- Gently crush foraminifera between two glass slides to open all chambers;
- Rinse the foraminifer fragments at least twice with ultrapure water in an ultrasonic bath for one minute (repeat if necessary, until the water remains clear and colourless);
- Rinse twice with reagent-grade methanol in an ultrasonic bath for 30 seconds.

In the original protocol (#1) of Tripati et al. (2010), a final step required adding a cold dilute solution of 1% H_2O_2, to remove possible organic contaminants. Grauel et al. (2013) used instead a 10% H_2O_2 buffered at pH 8 with a phosphate solution. In the present study we used 1% H_2O_2 with a sodium hydroxide buffer in an attempt to minimize potential alteration of the original bio-carbonate. Scanning Electron Microscopy (SEM) images acquired at the GEOPS laboratory (Figure 2.2) and stable and clumped isotope analyses (Figure 2.3) were used to compare the effects of both protocols and to test their ability to remove all traces of ethanol and Rose Bengal. SEM images of uncleaned shells reveal the presence of numerous coccoliths and detrital grains adhering to the shell surface (Figure 2.2-a). Protocol #2 (Figure 2.2-b) successfully removes such incrusted contaminants, exposing well-preserved foraminiferal calcite. Conversely, protocol #1 (Figure 2.2-c) produces visible dissolution and recrystallization features to the shell fragments. Based on these optical observations, protocol #2 seems to yield optimal preservation of the initial state of the foraminiferal tests.

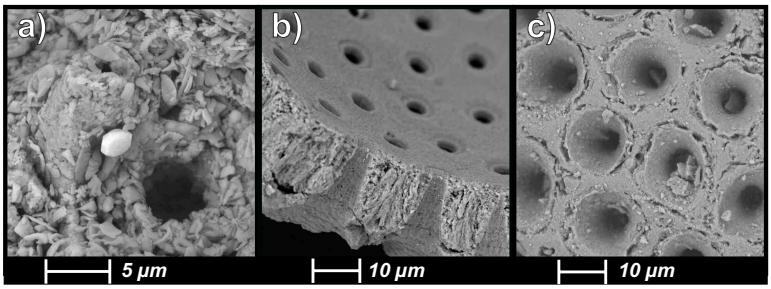

Figure 2.2: Scanning Electron Microscopy (SEM) pictures of G. ruber shells: a) before cleaning, b) after cleaning using the protocol of Grauel et al., 2013; and c) after cleaning using the protocol of Tripati et al., 2010.

Carbon-13, oxygen-18 and clumped isotope measurements were also performed on the cleaned samples to assess potential isotopic effects (Figure 2.3). No significant differences in $\delta^{18}O$, $\delta^{13}C$ and Δ_{47} values were observed between foraminifera treated with the two protocols (Figure 2.3a.b). Additionally, the same test was performed on foraminifera that had been soaked beforehand for 15 days in ethanol (Figure 2.3c.d) and in a mixture of ethanol and Rose Bengal (Figure 2.3e.f). Again, all stable isotope analyses

were found to yield statistically undistinguishable values after cleaning with either protocol. Based on the observations summarized above, and because none of our calibration samples comes from environments with high organic productivity such as upwelling regions, we decided to avoid the potentially destructive oxidative step of protocol #1 and cleaned all of our calibration samples by following protocol #2.

Table 2.2: $\delta^{18}O_{VPDB}$ and Δ_{47} values for different size ranges within each species.

Cores and Species	Size fraction (µm)	N*	$\delta^{18}O_{VPDB}$ (‰)	SE**	Δ_{47} (‰)	SE**
2FPA1	250-315	4	2.18	0.04	0.732	0.007
Uvigerina	315-355	4	2.14	0.04	0.730	0.007
mediterranea	355-400	3	2.21	0.05	0.727	0.009
	400-450	8	2.29	0.03	0.725	0.005
	450-500	4	2.29	0.04	0.726	0.007
	500-560	4	2.32	0.04	0.721	0.007
	> 560	4	2.31	0.04	0.729	0.007
MD00-2360	355-400	4	-0.41	0.04	0.675	0.007
G. menardii	400-450	4	-0.32	0.04	0.696	0.007
	450-500	4	-0.44	0.04	0.696	0.007
	500-560	4	-0.51	0.04	0.677	0.007
	> 560	4	-0.53	0.04	0.689	0.007
MD08-3179	200-250	4	0.65	0.04	0.702	0.007
G. inflata	250-315	4	0.90	0.04	0.703	0.007
	315-355	4	1.41	0.04	0.721	0.007
	355-400	4	1.12	0.04	0.709	0.007
	400-450	4	1.02	0.04	0.701	0.007
	450-500	3	1.16	0.05	0.704	0.009
MD08-3179	315-355	4	0.98	0.04	0.704	0.007
G. truncatulinoides	355-400	4	0.99	0.04	0.721	0.007
(d.)	400-450	4	1.07	0.04	0.705	0.007
	450-500	4	1.03	0.04	0.703	0.007
MD08-3182	200-250	3	1.77	0.05	0.730	0.009
G. bulloides	250-315	4	1.71	0.04	0.733	0.007
	315-355	4	1.79	0.04	0.748	0.007
	355-400	4	1.77	0.04	0.724	0.007
MOCOSED	250-315	4	4.07	0.04	0.771	0.007
Cibicides	315-355	4	4.13	0.04	0.759	0.007
wuellerstorfi	355-400	4	4.06	0.04	0.783	0.007
	400-450	4	3.97	0.04	0.765	0.007

* N: number of replicates
** SE = standard error

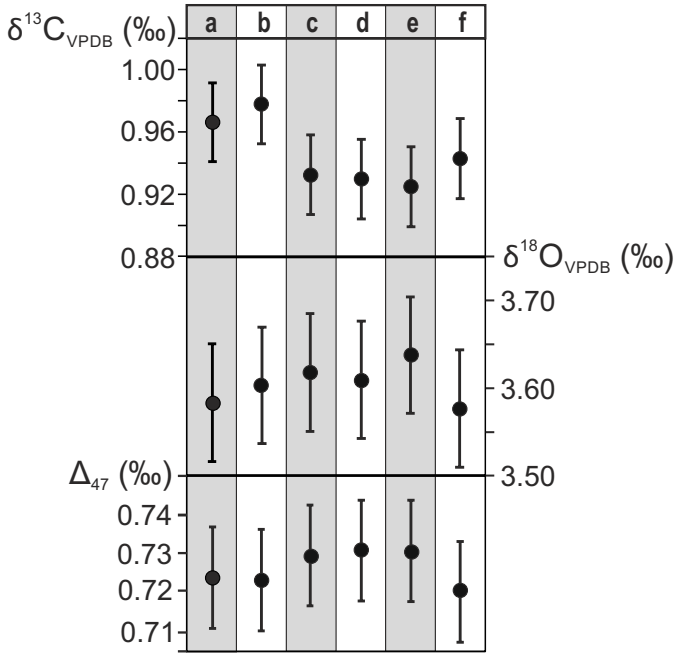

Figure 2.3: $\delta^{13}C$, $\delta^{18}O$ and Δ_{47} values (2SE) of Elphidium crispium obtained after: (a) cleaning protocol of Grauel et al., 2013 in grey bands; (b) cleaning protocol of Tripati et al., 2010 in white bands; (c) 15 days in ethanol followed by (a); (d) 15 days in ethanol followed by (b); (e) 15 days in ethanol and Rose Bengal followed by (a); and (f) 15 days in ethanol and Rose Bengal followed by (b).

2.3. Analytical Methods

2.3.1. Δ_{47} Measurements

A total of 361 clumped-isotope analyses were performed at the Laboratoire des Sciences du Climat et de l'Environnement (LSCE) using the same equipment and procedures as those described by Daëron et al. (2016). Carbonate samples weighing between 2 and 3 mg were dissolved in a common phosphoric acid bath at 90°C for 15 minutes. After cryogenic removal of water, the evolved CO_2 passed through a Porapak Q column (50/80 mesh, 1 m length, 2.1 mm ID) held at −20°C under helium 6.0 flow (25 mL/min). CO_2 was then quantitatively recollected by cryogenic trapping, and transferred by gas expansion into an Isoprime 100 dual-inlet mass spectrometer equipped with six Faraday collectors (m/z 44 to 49). Each analysis took about 3 hours,

during which sample gas and working reference gas were allowed to flow from matching, 10 mL reservoirs into the source, through a pair of fused silica capillaries (65 cm length, 110 µm ID). Every 20 minutes, gas pressures were adjusted to achieve a mass 44 current of 40 nA, with differences between sample and reference gas generally below 0.1 nA. Background currents were measured in all high-gain collectors (m/z 45 to 49) before and after each pressure adjustment, with gas flowing into the source, and are found to strongly correlate with mass 44 current.

Background-corrected ion current values were processed using the IUPAC isotopic parameters (Brand et al., 2010) to compute $\delta^{13}C_{VPDB}$, $\delta^{18}O_{VPDB}$ and Δ_{47}^{raw} values for each analysis. The isotopic composition ($\delta^{13}C$, $\delta^{18}O$) of our working reference CO_2 was computed based on nominal $\delta^{13}C_{VPDB}$, $\delta^{18}O_{VPDB}$ values for carbonate standard ETH-3 ($\delta^{13}C_{VPDB}$ = 1.71 ‰, $\delta^{18}O_{VPDB}$ = -1.77 ‰, recomputed by Bernasconi et al., in review) and an oxygen-18 acid fractionation factor of 1.008176 (Das Sharma et al., 2002).

Four carbonate standards, ETH-1 to ETH-4 (Meckler et al., 2014; Bernasconi et al., in review), were then used to convert Δ_{47}^{raw} to absolute Δ_{47} values, following the procedure described by Daëron et al. (2016). The nominal Δ_{47} values for these standards are those recomputed by Bernasconi et al. (in review) using IUPAC parameters, respectively 0.258 ‰ for ETH-1, 0.256 ‰ for ETH-2, 0.691 ‰ for ETH-3 and 0.507 ‰ for ETH-4.

2.3.2. Traditional Stable Isotope Measurements

Traditional oxygen and carbon stable isotope analyses were also performed for each sample (defined above as a unique combination of core-top species and size fraction). An average of 20-30 planktonic and 5 benthic foraminifer tests were hand-picked for each replicate analysis, with at least 4 replicates per sample. Foraminifera were then cleaned in an ultrasonic bath of reagent-grade methanol for a few seconds to eliminate impurities (Duplessy, 1978 without the roasting step). $\delta^{18}O_{VPDB}$ and $\delta^{13}C_{VPDB}$ values were measured at LSCE using three inter-calibrated mass spectrometers (a GV-Isoprime, an Isoprime 100 and a VG-Optima) and standardized to VPDB using NBS-19 and NBS-18 carbonate standards (Coplen, 1996). For NBS-19, assigned values are: $\delta^{18}O_{VPDB}$ = -2.20 ‰ and $\delta^{13}C_{VPDB}$ = 1.95 ‰ and for NBS-18, designated values are:

$\delta^{18}O_{VPDB}$ = -23.01 ± 0.10 ‰ and $\delta^{13}C_{VPDB}$ = -5.01 ± 0.03 ‰. The uncertainties reported here for traditional stable isotope measurements are based on the external reproducibility of in-laboratory carbonate standards, with 1SD = 0.05 ‰ for $\delta^{18}O_{VPDB}$ and 1SD = 0.03 ‰ for $\delta^{13}C_{VPDB}$.

2.4. Independent Constraints on Calcification Temperatures

Two alternative approaches to estimate the calcification temperatures of foraminifera were considered. The first one relies on the World Ocean Atlas temperature database (WOA13, Locarnini et al., 2013, https://www.nodc.noaa.gov/OC5/woa13), and the second one is based on "isotopic" temperatures estimated by combining foraminifer $\delta^{18}O$ measurements with the local oxygen-isotope composition of seawater ($\delta^{18}O_{SW}$) derived from the Global Seawater Oxygen-18 Database (LeGrande and Schmidt, 2006, https://data.giss.nasa.gov/o18data).

2.4.1. WOA13 Temperatures

For benthic foraminifera, we extracted the mean annual bottom temperature at each core location (field "t_an" in the WOA13-V2 dataset), with uncertainties corresponding to the standard deviation values given by the interpolation in the WOA13 dataset.

For planktonic foraminifera, we calculated the average water column temperature over a range of calcification depths depending on species and core-top location. According to Tolderlund and Bé (1971) and Durazzi (1981), calcification depths in the North Atlantic Ocean correspond to 0-10 m for *G. ruber*. For *G. bulloides, O. universa, G. truncatulinoides, G. inflata, G. menardii,* and *N. pachyderma*, the depths associated are comprised between 0 and 300 m. In the Indian Ocean, Duplessy et al. (1981) placed the depth of calcification for all these species within and below the mixed layer, except for *G. ruber* and *G. menardii* which are believed to remain respectively at the surface and within the mixed layer (0-200 m). In the South China Sea, *G. ruber* and *G. menardii* are described as living near the surface and in the top 200 m, respectively

(Pflaumann and Jian, 1999). Finally, the living depth of *O. universa* being very poorly constrained to the best of our knowledge, we assume that it lives at the same depth as *G. menardii,* by analogy with the North Atlantic Ocean. Furthermore, the seasonality of phytoplankton blooms remains poorly constrained in the literature. We thus followed a conservative approach by averaging the monthly mean temperatures of summer, spring and fall (excluded December, January and February) for each core, with assigned uncertainties reflecting both seasonal and vertical variability, quantified as the standard deviation of all temperature data for a given site, with a monthly temporal resolution and a uniform depth resolution of one meter over the range of (species-dependent) living depths.

2.4.2. Isotopic Temperatures

In an attempt to reduce the uncertainties related to our assumptions on the calcification depth and seasonality of each species, we compared the WOA13 temperatures to oxygen isotope temperature estimates, derived from either one of two equations: Shackleton (1974) modified by 0.27 ‰ (Hut, 1987) to express seawater and carbonate $\delta^{18}O$ values relative to VSMOW and VPDB, respectively (equation 1), and Kim and O'Neil (1997) modified for consistency with the use of an acid fractionation factor of 1.01025 (equation 2)

$$T = 16.9 - 4{,}38 \times (\delta^{18}O_{C/VPDB} - \delta^{18}O_{SW/VSMOW} + 0.27) + 0.10 \times (\delta^{18}O_{C/VPDB} - \delta^{18}O_{SW/\,VSMOW} + 0.27)^2$$

(equation 1)

Where T is the isotopic temperature in °C and $\delta^{18}O_{C/VPDB}$ and $\delta^{18}O_{SW/\,VSMOW}$ are the $\delta^{18}O$ of the foraminiferal calcite relative to VPDB and of the seawater relative to VSMOW, respectively. Following Marchitto et al. (2014), *Cibicides* $\delta^{18}O$ were adjusted to the *Uvigerina* scale by 0.47 ‰.

$$1000 \ln(\alpha_{cc/w}) = 18.03 \times 1000 / T - 32.17$$

(equation 2)

Where T is temperature in K and $\alpha_{cc/w}$ is the oxygen-18 fractionation factor between calcite and water: $\alpha_{cc/w} = (1 + \delta^{18}O_{C/SMOW} / 1000) / (1 + \delta^{18}O_{SW/SMOW} /1000)$ with $\delta^{18}O_{C/SMOW}$ and $\delta^{18}O_{SW/SMOW}$ corresponding to foraminiferal calcite and seawater, respectively, both relative to VSMOW. Again, following the recommendation of Marchitto et al. (2014), $\delta^{18}O_c$ values for *Uvigerina* were adjusted by subtracting 0.47 ‰.
It is well know that different planktonic foraminifer species from the same core may yield different $\delta^{18}O_C$ values due to differences in depth and seasonality calcification (e.g. Mix, 1987; Ortiz et al., 1995; Schiebel, 2002; Mortyn and Charles, 2003; Jonkers and Kurcera, 2015). Precise characterization of these species-specific effects is still very much an open issue. However, the FAME (Foraminifera As Modeled Entities) model recently developed by Roche et al. (2017) implies that, assuming that planktonic foraminifera follow the oxygen-18 fractionation law of Kim & O'Neil (1997), variations in calcification depth and seasonality provide a good first-order prediction for $\delta^{18}O_c$ values, with root mean square residuals on the order of 0.2 ‰ for *G. ruber, G. bulloides*, and *N. pachyderma*. These residuals are similar to the errors we assigned to our $\delta^{18}O_{SW}$ values (see below), which dominate the uncertainties in our isotopic temperature estimates. For this reason, no species-specific adjustments were applied to our planktonic samples.

Seawater $\delta^{18}O$ values at each core site were extracted from the gridded data set of LeGrande and Schmidt (2006). For benthic foraminifera, we only considered bottom $\delta^{18}O_{sw}$ values. Because of the poor constraints on calcification depths for planktonic species (see above), we compared mean $\delta^{18}O_{sw}$ values averaged over 0-50 m and 0-500 m. The differences in mean δ^{18}Osw between these two depth ranges are on the order of 0.03 ± 0.08 ‰, indicating that the choice of water depth is not critical for our core sites. We have thus considered averaged $\delta^{18}O_{sw}$ between 0 and 500 m. The uncertainties in $\delta^{18}O_{sw}$ for each core site were defined as the quadratic sum of the site-specific standard deviation of $\delta^{18}O_{sw}$ within the top 500 m of the water column and a constant error of 0.20 ‰ assigned to the GISS grid interpolation. To the best of our knowledge, the true uncertainties in the gridded values of LeGrande and Schmidt have not been quantified, but we believe that our arbitrary choice of 0.20 ‰ is conservative. Final uncertainties

on the isotopic temperatures are propagated based on the $\delta^{18}O_{sw}$ uncertainties assigned above and the (external) analytical error on $\delta^{18}O_c$ values.

3. RESULTS

The complete results for each foraminifer and standard carbonate analysis are provided in Table S4. The measurements were performed over the course of five independent analytical sessions from May 2015 to September 2017.

Table 2 summarizes Δ_{47} and $\delta^{18}O_c$ values of all samples for which at least 4 different size fractions were analysed. The mean results for all samples grouped by species and core-top are reported in Table 3, together with the estimated foraminifera calcification depth and $\delta^{18}O_{sw}$, and the three different estimates of calcification temperatures defined in section 2.4. Mean Δ_{47} values range from 0.669 to 0.769 ‰. The lowest Δ_{47} values were observed in *G. ruber* (MD02-2577) at an estimated temperature from Equation 2 of 25.1 ± 1.1 °C and the highest in *C. wuellerstorfi* (MOCOSED) at -1.6 (± 0.8 °C).

3.1. External Reproducibility of $\delta^{13}C$, $\delta^{18}O$ and Δ_{47} Measurements

Clumped isotope analyses require measuring the $\delta^{13}C$ and $\delta^{18}O$ values of each sample. We compared these values to those obtained from traditional IRMS methods. The two methods yield statistically indistinguishable results. All $\delta^{13}C$ and $\delta^{18}O$ values considered hereafter are those obtained as part of the clumped isotope analyses.

We can assess the long-term analytical reproducibility of our isotopic measurements based on repeated analyses of the ETH standards:

$$\sigma^2 = \frac{\sum(x_r - \bar{x_s})^2}{N_r - N_s}$$

where σ is an aggregate estimate of long-term reproducibility, x_r are the values from each replicate measurement of all standards, $\overline{x_s}$ is the average value for the corresponding standard, N_r is the total number of standard replicate analyses (N_r = 127) and N_s is the number of standards considered (N_s = 4). The σ statistic is computed in the same way for $\delta^{13}C_{VPDB}$, $\delta^{18}O_{VPDB}$ and Δ_{47}, yielding external reproducibilities of 0.032 ‰, 0.084 ‰ and 0.0166 ‰, respectively.

We may also compute σ for all of our calibration samples instead of the ETH standards, which yields a slightly improved Δ_{47} reproducibility of 0.0135 ‰ and comparable reproducibilities for $\delta^{13}C$ and $\delta^{18}O$. Computing combined σ values taking into account all standards and calibration samples, the final external error assigned to each of our Δ_{47} replicate measurements is 0.0148 ‰.

4. DISCUSSION

4.1. Foraminifera Δ_{47} versus Size Effect

In order to investigate potential size effects on measured Δ_{47} values, we considered six foraminiferal species for which we have at least 4 different size fractions (Figure 2.4, Table S4). The corresponding Δ_{47} and $\delta^{18}O_C$ values are listed in Table 2. All measurements within each species are statistically indistinguishable, with the single exception of $\delta^{18}O_C$ values for *Globorotalia inflata*, which vary over a range of 0.8 ‰ (Figure 2.4). Although the corresponding Δ_{47} values remain statistically indistinguishable from each other, they nevertheless appear to be positively correlated with $\delta^{18}O_C$ (Pearson correlation coefficient = 0.79), consistent with the hypothesis that the observed isotopic differences between different size fractions of *G. inflata* reflect different calcification temperatures that may be due to seasonality or depth habitats. For this species, we thus decided to treat each size fraction as an individual sample with its own calcification temperature constrained by its $\delta^{18}O_C$.

Table 2.3: $\delta^{18}O$ and Δ_{47} compositions of each samples with corresponding average $\delta^{18}O$ of seawater and three different estimates of calcification temperature respectively based on WOA13. Shackleton (1974) and Kim and O'Neil (1997).

Core	Species	FCD (m) *	N*	$\delta^{18}O$sw (‰ VSMOW)	SE**	$\delta^{18}O$c (‰ VPDB)	SE**	T WOA13 (°C)	SD**	T S74 (°C)	SE**	T K97 (°C)	SE**	Δ_{47} (‰)	SE*
MOCOSED	*Cibicides wuellerstorfi*	1839	16	0.27	0.20	4.06	0.02	-0.9	0.1	2.5	0.5	-1.6	0.4	0.7692	0.00
MD04-2720	*N. pachyderma (d.)*	0-300	4	-0.34	0.21	3.16	0.04	2.0	1.6	1.8	0.6	-0.4	0.7	0.7623	0.00
MOCOSED	*N. pachyderma (s.)*	0-300	8	0.10	0.28	2.80	0.03	0.2	1.2	4.8	1.1	2.9	0.5	0.7490	0.00
MD88-770	*G. bulloides*	0-300	5	-0.24	0.20	2.34	0.04	11.1	1.5	5.2	0.6	3.4	0.6	0.7316	0.00
MD12-3401	*G. bulloides*	0-300	8	-0.15	0.21	1.91	0.03	8.7	1.4	7.2	0.7	5.6	0.5	0.7413	0.00
MD95-2014	*G. bulloides*	0-300	8	0.39	0.20	1.86	0.03	8.3	1.6	9.6	0.7	8.1	0.5	0.7289	0.00
MD08-3182	*G. bulloides*	0-300	15	0.33	0.38	1.76	0.02	6.8	2.3	9.7	2.4	8.3	0.4	0.7339	0.00
MD08-3182	*N. pachyderma (s.)*	0-300	4	0.33	0.38	1.70	0.04	6.8	2.3	10.0	2.4	8.6	0.7	0.7336	0.00
MD03-2680	*N. pachyderma (d.)*	0-300	4	0.36	0.20	1.66	0.04	8.3	1.6	10.3	0.7	8.9	0.7	0.7300	0.00
2FPA1	*Uvigerina mediterranea*	664	31	0.59	0.20	2.26	0.02	10.6	0.3	8.8	0.6	9.4	0.3	0.7269	0.00
SU90-03	*G. bulloides*	0-300	6	1.07	0.26	1.56	0.04	15.4	4.2	13.6	1.2	12.5	0.6	0.7234	0.00
MD08-3179	*G. inflata* 315-355 µm	0-300	4	1.07	0.27	1.41	0.04	15.9	4.8	14.2	1.3	13.2	0.7	0.7208	0.00
MD08-3179	*G. inflata* 450-500 µm	0-300	3	1.07	0.27	1.16	0.05	15.9	4.8	15.3	1.4	14.3	0.8	0.7039	0.00
MD08-3179	*G. inflata* 355-400	0-300	4	1.07	0.27	1.12	0.04	15.9	4.8	15.5	1.4	14.5	0.7	0.7088	0.00
MD08-3179	*G. truncatulinoides (s.)*	0-300	12	1.07	0.27	1.05	0.03	15.9	4.8	15.8	1.4	14.8	0.4	0.7156	0.00
MD08-3179	*G. inflata* 400-450 µm	0-300	4	1.07	0.27	1.02	0.04	15.9	4.8	15.9	1.4	15.0	0.7	0.7011	0.00
MD08-3179	*G. truncatulinoides (d.)*	0-300	16	1.07	0.27	1.02	0.02	15.9	4.8	15.9	1.4	15.0	0.4	0.7083	0.00
MD08-3179	*G. inflata* 250-315 µm	0-300	4	1.07	0.27	0.90	0.04	15.9	4.8	16.4	1.4	15.5	0.7	0.7028	0.00
MD08-3179	*G. inflata* 200-250 µm	0-300	4	1.07	0.27	0.65	0.04	15.9	4.8	17.6	1.4	16.7	0.7	0.7015	0.00
MD12-3426	*G. menardii menardi*	0-200	7	0.10	0.23	-0.40	0.03	18.1	10.1	17.9	1.1	17.1	0.5	0.6969	0.00
MD02-2577	*G. menardii menardi*	0-300	8	0.76	0.23	-0.01	0.03	20.6	7.0	19.1	1.1	18.3	0.5	0.6892	0.00
MD00-2360	*G. menardii menardi*	0-200	20	0.35	0.23	-0.44	0.02	22.4	2.5	19.2	1.0	18.4	0.3	0.6867	0.00
MD08-3179	*G. ruber*	0-10	8	1.07	0.27	-0.11	0.03	20.4	4.8	21.0	1.5	20.3	0.5	0.6981	0.00
MD02-2577	*Orbulina universa*	0-200	4	0.76	0.23	-0.53	0.04	20.6	7.0	21.5	1.2	20.8	0.7	0.6944	0.00
MD12-3426	*Orbulina universa*	0-200	4	0.10	0.23	-1.71	0.04	18.1	10.1	23.9	1.2	23.3	0.7	0.6798	0.00
MD00-2360	*Orbulina universa*	0-300	8	0.35	0.23	-1.47	0.03	20.4	3.5	23.9	1.1	23.4	0.5	0.6846	0.00
MD00-2360	*G. ruber*	0-10	7	0.35	0.23	-1.74	0.03	25.8	1.6	25.2	1.2	24.7	0.5	0.6677	0.00
MD02-2577	*G. ruber*	0-10	8	0.76	0.23	-1.40	0.03	25.4	4.2	25.5	1.3	25.1	0.5	0.6744	0.00

* FCD: Foraminiferal Calcification Depth, N: number of replicates ** SD = standard deviation – SE = standard error

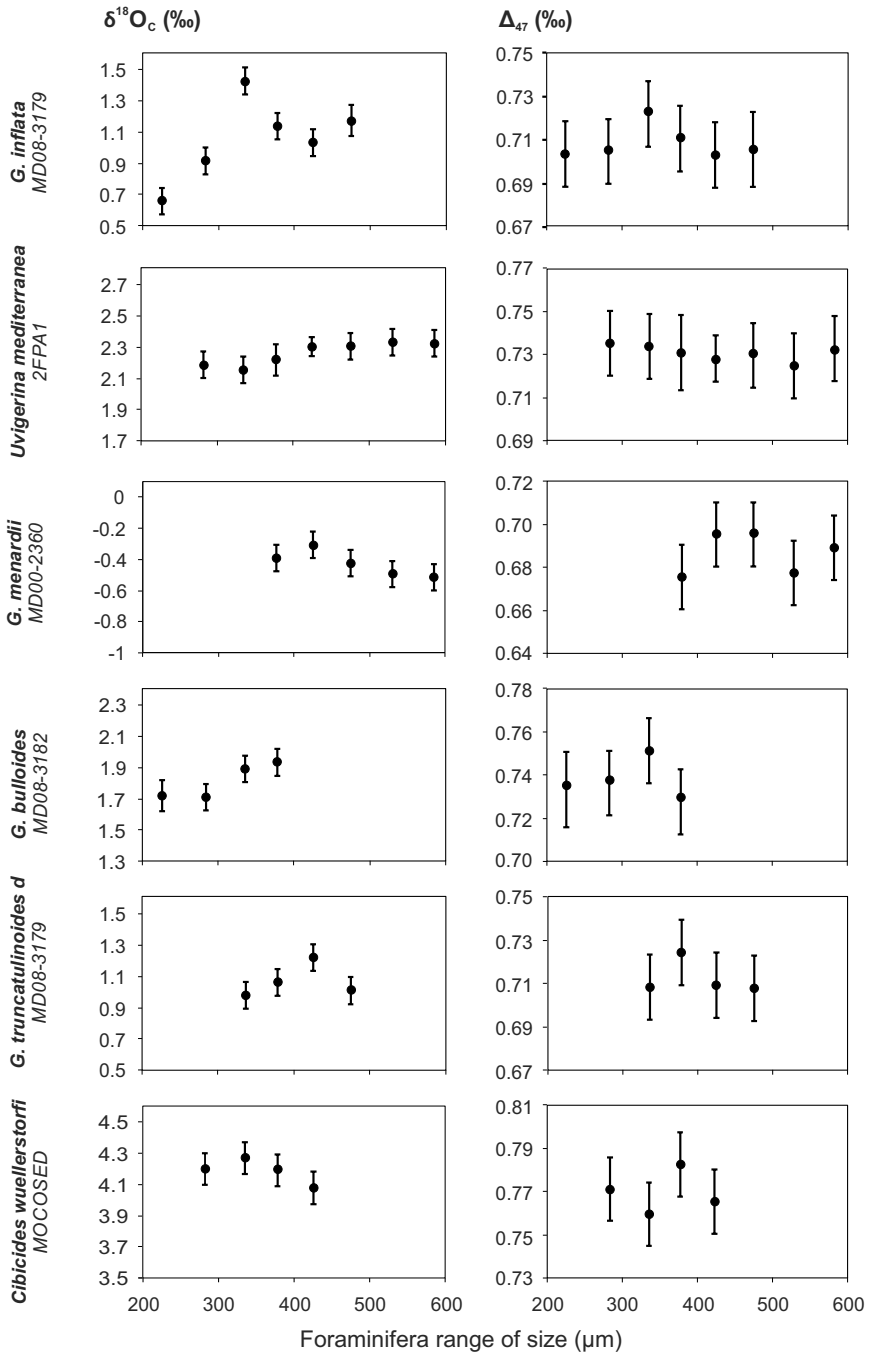

Figure 2.4: $\delta^{18}O$ and Δ_{47} values (2SE) of six foraminifera species for different size fractions.

Our observations do not strictly rule out potential foraminifer size biases, but they imply that such biases must be smaller than what can be resolved with the typical Δ_{47} precision we obtain from 4 analytical replicates (SE = 7-8 ppm). The absence of detectable size effect implies that we may combine the isotopic results from all size

fractions (excluding *G. inflata*). From a practical point of view, this greatly facilitates picking enough material for a large number of replicates.

4.2. Assignment of Independent Temperature Constraints

Figure 2.5a shows a comparison between temperatures estimated from WOA13, and the isotopic temperatures derived from equation 2 (Kim and O'Neil, 1997). The two methods are generally in poor agreement, with discrepancies from 0.2 °C to 6 °C affecting many of our samples. These discrepancies are most likely related to the assumptions that had to be made regarding the calcification depth of each species. This would be consistent with past studies which argued that foraminifera species may occupy water depth ranges more variable than traditionally assumed, and that habitat depth may vary significantly from one location to another (Mortyn and Charles, 2003; Simstich et al., 2003). Because local $\delta^{18}O_{sw}$ values vary much less with depth and seasonality than water temperature does, it is reasonable to expect that isotopic estimates of calcification temperatures are less sensitive to assumptions of calcification depth and seasonality. It should be noted that the uniformity of $\delta^{18}O_{sw}$ values from the gridded interpolation does not result from a paucity of observations but from the uniformity in WOA salinity values (LeGrande and Schmidt, 2006).

In Figure 2.5b, we compare the isotopic temperatures obtained using equation 1 (Shackleton, 1974) and equation 2 (Kim and O'Neil, 1997). Unsurprisingly, the two equations yield different but highly correlated temperature estimates, with differences gradually decreasing from low to high temperatures. These differences range from 2 °C to 1.5 °C for the lowest temperatures (< 9 °C) and remain below 1 °C to 0.5 °C for temperatures above 25 °C. Whereas the calibration of Shackleton (1974) covers a restricted temperature range corresponding to benthic foraminifera (< 7 °C), that of Kim and O'Neil (1997) covers a larger temperature range, potentially applicable to benthic and planktonic foraminifera. We thus decided to use the oxygen isotopic temperatures from Equation 2.

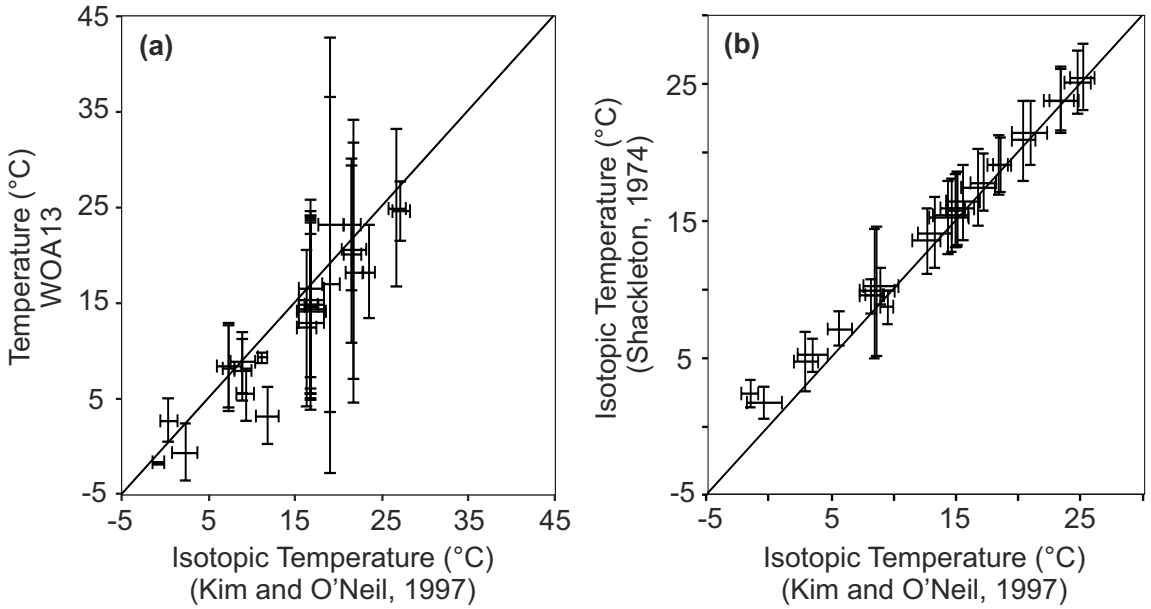

Figure 2.5: Independent temperature comparison from (a) WOA13 and oxygen isotopic data using the Kim and O'Neil (1997) equation and (b) oxygen isotopic temperatures computed with Shackleton (1974) and Kim and O'Neil (1997) equations.

4.3. Relationship Between Temperature and Δ_{47}

Based on the absence of detectable foraminifer size effect demonstrated in section 4.1, we may average the replicates measurements of Δ_{47} obtained for samples differing only in size fraction, and all replicate measurements of $\delta^{18}O_C$ (excluding *G. inflata*) to compute the estimates of calcification temperatures, from equation 2. This results in 28 calibration data points corresponding to different species and core-top location (Figure 2.6 and Table 3).

Mean Δ_{47} values for these 28 samples strongly correlate with ^{18}O-derived estimates of calcification temperature. The standard errors associated with these 28 data points range from 2.7 to 8.5 ppm for Δ_{47} and from 0.4 to 0.7 °C for temperature, implying that both variables significantly contribute to the uncertainties of the regression. We thus compute the total least squares regression of Δ_{47} on $1/T^2$ (with T in K) using the formulation of York et al. (2004).

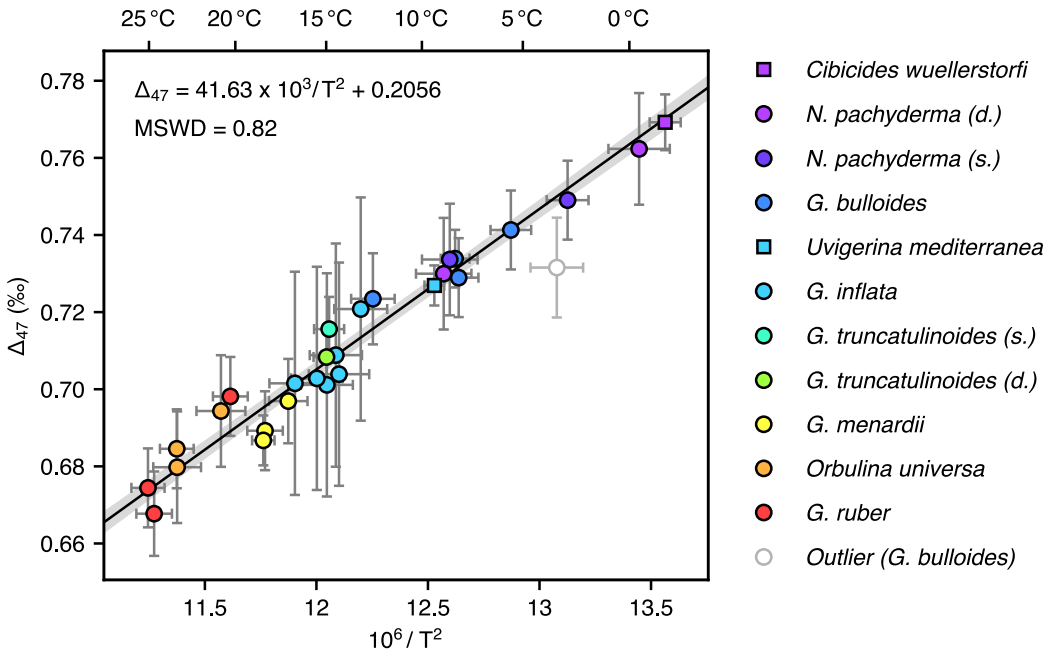

Figure 2.6: Δ_{47} values (mean and 2SE) compared to isotopic temperatures (mean and 2SE) obtained with Kim and O'Neil, 1997 for planktonic (circle) and benthic (square) foraminifera samples, combining all size fraction. The calibration regression (black line) is calculated following York et al. (2004) with 95% confidence level (grey band).

An examination of the fit residuals (Figure 2.6) suggests that the data point associated with sample MD88-770-*G. bulloides* might be a statistical outlier, defined as an anomalous observation very unlikely to result from statistical error alone. Grubbs' test for a single outlier (Grubbs, 1969; Stefansky, 1972) rejects the null hypothesis of no outliers at a 95% significance level (p = 0.026). This anomaly is unlikely to result from an isotopic effect specific to *G. bulloides*, because the four other samples of the same species have all statistically null residuals. However, core MD88-770 is located near the boundary between two of the salinity/oxygen-18 regions used to produce the gridded $\delta^{18}O_{sw}$ values of LeGrande and Schmidt (2006), implying that the seawater oxygen isotope values which we assigned to this particular sample are poorly constrained. Furthermore, variations in the position of the polar front between the Indian and Austral Oceans cause $\delta^{18}O_{SW}$ values to vary seasonally. We thus conclude *a posteriori* that we cannot reliably assign an isotopic temperature to this data point, and hereafter exclude it from the calibration data set. However, we note that the WOA13 temperature

for MD88-770-*G. bulloides* is 11.1 ± 1.5 °C, which would place this sample only 0.011 ± 0.007 (1SE) ‰ above the new regression line (Figure 2.6).

Recomputing the total least squares regression (Figure 2.6) yields the following relationship:

$$\Delta_{47} = 41.63 \times 10^3 / T^2 + 0.2056$$

(Equation 3)

In order to assess goodness of fit, we may compute the reduced chi-squared statistic, also known as mean square weighted deviation (MSWD):

$$MSWD = \frac{1}{N_s - 2} \sum_i \frac{(Y_i - AX_i - B)^2}{\sigma_{Yi}^2 + A^2 \sigma_{Xi}^2}$$

where X_i and Y_i are the observations (respectively $1/T^2$ and Δ_{47}), with corresponding standard errors σ_{Xi} and σ_{Yi}, and $N_s = 27$ is the number of observations. Note that our (X_i, Y_i) observations are not fully independent from each other, because Δ_{47} values are anchored to a shared set of carbonate standard measurements, and because estimated $\delta^{18}O_{sw}$ values for samples from the same core-top should be highly correlated. We thus only use the MSWD as a qualitative indicator of goodness-of-fit. Our regression model yields a MSWD of 0.82, suggesting that our assigned uncertainties may be slightly overestimated compared to the scatter observed in our results.

Computing the formal standard errors for this regression is not straightforward because the slope and intercept values of equation 3 are strongly anti-correlated, and calculations taking their covariance into account are sensitive to rounding errors. We may, however, reformulate Equation 3 in terms of the barycentre of our ($1/T_0^2$) values:

$$\Delta_{47} = A \times 10^3 (1/T^2 - 1/T_0^2) + B$$

$$A = 41.63 \pm 0.84 \text{ (1SE)}$$

$$B = 0.7154 \pm 0.0011 \text{ (1SE)}$$

$$T_0 = 12.61 \text{ °C}$$

Using this new formulation, parameters A and B are now independent, and the standard error of our regression model is simply expressed as:

$$\sigma^2(\Delta_{47}) = \sigma^2(A)\ (1/T^2 - 1/T_0^2)^2 + \sigma^2(B)$$

Based on this formulation, the 95 % confidence limits of our regression model range from ± 0.7 °C to ± 1 °C between -2 °C and 25 °C. As a result, the precision of absolute temperature reconstructions based on equation 3 will generally be limited by errors in Δ_{47} measurements (including any inter-laboratory biases) rather than by our regression errors. For instance, in the hypothetical case of repeated Δ_{47} measurements of a single sample with an external reproducibility of 0.015 ‰, between 50 and 90 replicate analyses would be required to reach 95 % confidence limits of ± 1 °C.

4.4. Species-Specific Effects on Foraminiferal Δ_{47}

Figure 2.7 shows the Δ_{47} regression residuals for our calibration samples labelled by habitat depth (benthic, surface or thermocline). Excluding the single outlier discussed above, the surface-dwelling species (*G. ruber*) is statistically indistinguishable from the thermocline- and deep-dwelling species (*N. pachyderma*, *G. menardii*, *O. universa, G. inflata* and *G. truncatulinoides, G. bulloides*). The two benthic species, *U. mediterranea* and *C. wuellerstorfi*, are in excellent agreement with the overall regression model, despite the well-established observation that they appear to follow different oxygen-18 fractionation laws.

The absence of species effect on Δ_{47} among the planktonic and benthic foraminifera investigated here, is consistent with the findings of Tripati et al. (2010) and Grauel et al. (2013), and suggests that the above calibration relationship may be applicable to most foraminifera.

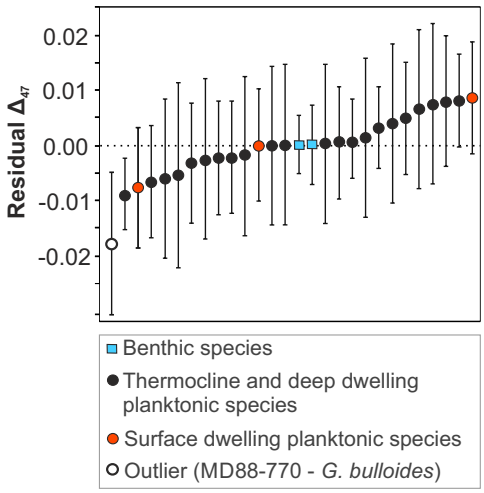

Figure 2.7: Δ_{47} residuals (2SE) for benthic foraminifera (blue square), surface dwelling planktonic foraminifera (red circles) and thermocline and deep dwelling planktonic species (black circles) ranged by growing residual. Outlier sample (white circle) is included for comparison.

4.5. Foraminiferal Δ_{47} versus Salinity Effect

Seawater salinity values at each core-top location were extracted from the gridded data set of WOA13 (Zweng et al., 2013). As we did with the GISS $\delta^{18}O_{sw}$ values, (section 2.4.2) we compared the average salinity over 0-50 m and 0-500 m depths. As for $\delta^{18}O_{sw}$ values, average salinities at our core-top locations are not sensitive to the choice of the depth interval, so we compute average salinity values over the top 500 m of the water column. Uncertainties were estimated at each core-top site as the quadratic sum of a nominal error of 0.20 psu arbitrarily assigned to the WOA13 data set and the site-specific standard deviation of salinity over the top 500 m of the water column.

Our samples cover a salinity range from 34 to 36 psu, which corresponds to the typical salinity values of the world ocean. As shown in Figure 2.8-a, no correlation is detectable between Δ_{47} residuals and salinity. Mathematically, this could conceivably result from a strong covariation of temperature and salinity at our core-top sites, but this is not the case (Figure 2.8-b). We thus conclude, as did Grauel et al. (2013), that salinity has no detectable influence on the clumped isotope composition of foraminifera growing at a given temperature.

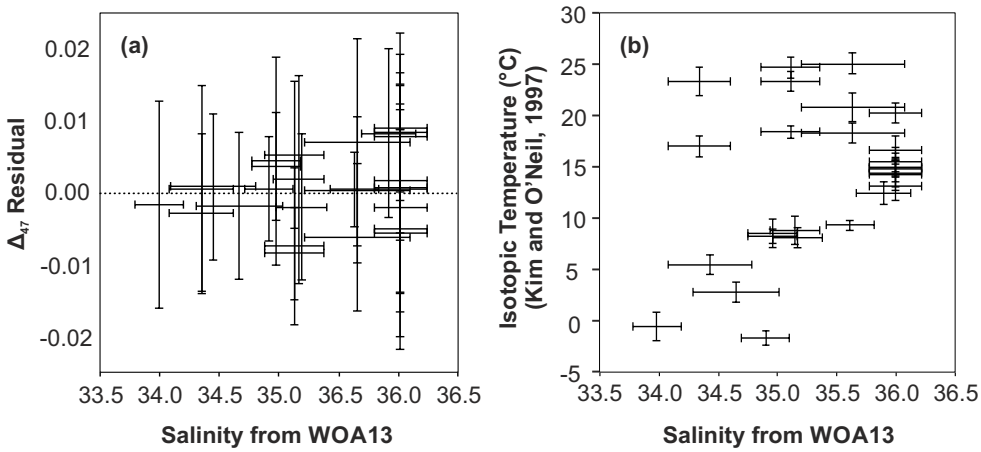

Figure 2.8: (a) Δ_{47} residuals (2SE) and (b) temperature derived from Kim and O'Neil, (1997), both compared to salinity, for each species and core-top location.

4.6. Comparison with Previous Calibrations

The only two calibrations directly relevant to foraminifera (Tripati et al., 2010; Grauel et al., 2013) belong to an early period of clumped isotope measurements, where major methodological advances such as the introduction of the "absolute" reference frame of Dennis et al. (2011) were not taken into account. Nevertheless, several of their conclusions (e.g., the lack of detectable species or salinity biases) are fully consistent with our findings, reinforcing the notion that Δ_{47} values in foraminifera from very different environments appear to be determined exclusively by calcification temperature.

In many cases, the lack of common carbonate standards shared between calibrations studies, as well as the uncertainties associated with acid temperature corrections, preclude precise comparisons between calibration equations from different laboratories. Nevertheless, we note that the slope of Equation 3 is indistinguishable from those obtained in several recent studies based on large numbers of observations on synthetic and natural carbonates covering wide temperature ranges (Bonifacie et al., 2017; Kelson et al., 2017).

We may, however, precisely compare our results to those from other studies provided (i) that they are anchored to the ETH standards (or to internal laboratory standards referenced to the ETH standards), and (ii) that raw data are processed using

the IUPAC isotopic parameters of Brand et al. (2010). Here we consider the recently published dataset of Breitenbach et al. (2018) and the tufa/travertine calibration of Kele et al. (2015), which was recently reprocessed by Bernasconi et al. (in review).

Breitenbach et al. (2018) reported Δ_{47} values of core-top foraminifera, and compared them with a clumped-isotope calibration based on inorganic cave pearls. Their foraminifera data (Figure 2.9) are generally within error bars of our calibration line, but a large fraction of their samples display Δ_{47} values 20–35 ppm lower than expected from our Equation 3. Most of their observations lie between 10 and 20 °C, with many Δ_{47} values clustered around 0.68 ‰. The reason for these slightly lower Δ_{47} values and weaker correlation with temperature remains unclear. Although Breitenbach et al. assigned calcification temperatures based on the WOA database, reprocessing their observations using our oxygen-18 temperature approach does not eliminate the discrepancies between the two studies. Alternatively, the observed differences could result from the use of different cleaning protocols. Breitenbach et al. (2018) included an oxidative step using 5% H_2O_2. Although our cleaning tests (Figure 2.3) imply that the use of 1% H_2O_2 has no detectable isotopic effects, it is conceivable that higher H_2O_2 concentrations would slightly bias Δ_{47} values through cryptic recrystallization at room temperature. More generally, these observations called for future foraminifera intercomparison exercises.

We are also able to compare our results to inorganic calibrations based on tufa and travertines (Kele et al., 2015, reprocessed by Bernasconi et al., in review) and cave pearls (Breitenbach et al., 2018), both of which have been applied to foraminifera (Rodriguez-Sanz et al., 2017; Breitenbach et al., 2018). The three calibrations display virtually identical slopes (Figure 2.10). Moreover, our results are in full agreement with the Kele et al. (2015) data over the temperature range where they overlap (6–5 °C). The cave pearl calibration predicts slightly lower Δ_{47} values, possibly consistent with the similar offset seen in Figure 2.9, resulting in slightly colder temperature estimates (by 2–4.5 °C between 0 °C and 25 °C), which would be problematic for most paleoceanographic reconstructions.

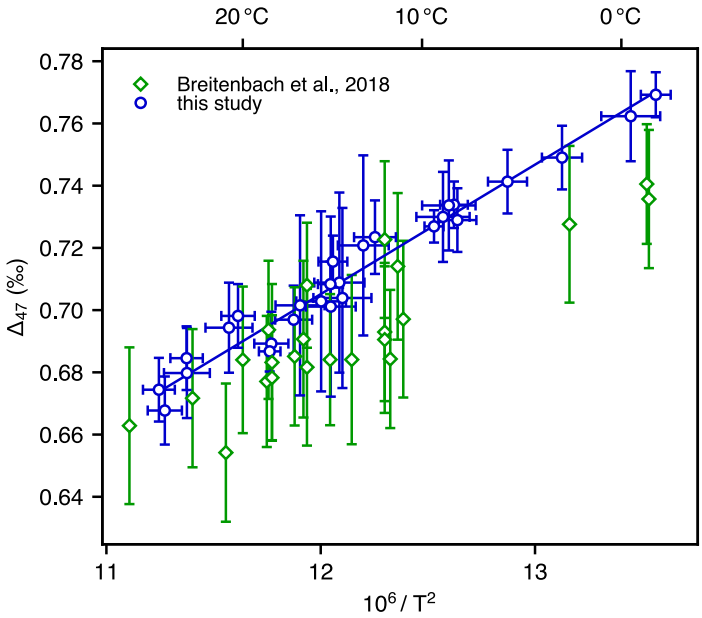

Figure 2.9: Comparison of our foraminifer Δ_{47}-temperature calibration in blue dots (95 % confidence) with the foraminifer dataset from Breitenbach et al. (2018) in green diamonds (uncertainties at 2SE).

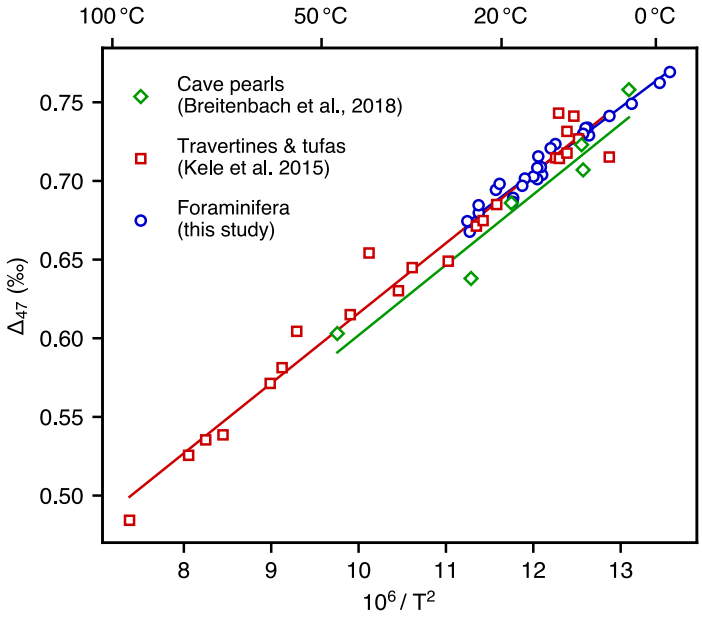

Figure 2.10: Comparison of our foraminifer Δ_{47} – temperature calibration in blue dots with the cave pearl calibration of Breitenbach et al. (2018) in green diamonds and the travertines and tufas calibration of Kele et al. (2015), recalculated by Bernasconi et al. (in review) using the parameters recommended by Daëron et al. (2016) in red squares.

Although our regression errors are small enough to meet the requirements of most paleoclimate studies, inter-laboratory comparisons of Δ_{47} measurements generally remain significantly less precise. In our view, this is primarily due to the lack of common carbonate standards. Because the observations reported here are tightly anchored to the widely distributed carbonate standards ETH-1/2/3, it should be possible to precisely compare our findings to independent Δ_{47} measurements standardized in the same way, and we anticipate that future studies can fully benefit from our calibration.

5. CONCLUSION

We have investigated the relationship between the Δ_{47} values of foraminifera and calcification temperatures using samples collected in core-tops from different oceanic basins, yielding a robust calibration for temperatures ranging from -2 °C to 25 °C. Based on the study of 9 planktonic and 2 benthic foraminiferal species chosen among the most commonly used in paleoclimatology, we conclude that our results confirm the absence of statistically significant species and salinity effects at our precision level, so that Δ_{47} values in planktonic and benthic foraminifera seem to be exclusively determined by temperature. We found no evidence for detectable size effects on Δ_{47} over a wide range of sizes in 6 species of planktonic and benthic foraminifera, suggesting that it is possible to combine foraminifera of different size fractions, which should result in notable gains in picking time, total number of analytical replicates and, ultimately, final paleotemperature precision.

Our dataset is indistinguishable from the tufas and travertines calibration of Kele et al. (2015, reprocessed) and generally very close to the cave pearl calibration of Breitenbach et al. (2018), both using common carbonate standards and analytical process. Defining optimal standardization procedures to minimize systematic inter-laboratory discrepancies in clumped isotope measurements is a matter of ongoing debate, and so we took care to include a large number of international carbonate standard analyses in the results reported here. Future foraminifer studies using the

same carbonate standards should provide an excellent opportunity to test whether this strategy yields a significant improvement in inter-laboratory reproducibility.

REFERENCES

Abrantes F., Lebreiro S., Rodrigues T., Gil I., Bartels-Jónsdóttir H., Oliveira P., Kissel C. and Grimalt J. O. (2005) Shallow-marine sediment cores record climate variability and earthquake activity off Lisbon (Portugal) for the last 2000 years. *Quat. Sci. Rev.* **24**, 2477–2494.

Bonifacie M., Calmels D., Eiler J. M., Horita J., Chaduteau C., Vasconcelos C., Agrinier P., Katz A., Passey B. H., Ferry J. M. and Bourrand J. J. (2017) Calibration of the dolomite clumped isotope thermometer from 25 to 350 °C, and implications for a universal calibration for all (Ca, Mg, Fe)CO3carbonates. *Geochim. Cosmochim. Acta* **200**, 255–279. Available at: http://dx.doi.org/10.1016/j.gca.2016.11.028.

Brand W. A., Assonov S. S. and Coplen T. B. (2010) Correction for the 17O interference in δ(13C) measurements when analyzing CO2 with stable isotope mass spectrometry (IUPAC Technical Report). *Pure Appl. Chem.* **82**, 1719–1733. Available at: https://www.degruyter.com/view/j/pac.2010.82.issue-8/pac-rep-09-01-05/pac-rep-09-01-05.xml.

Brassell S.C, Eglinton G, Marlowe I.T, Pflaumann U S. M. (1986) Molecular stratigraphy: a new tool for climatic assessment. *Nature* **320**, 129–133.

Breitenbach S. F. M., Mleneck-Vautravers M. J., Grauel A.-L., Lo L., Bernasconi S. M., Müller I. A., Rolfe J., Greaves M. and Hodell D. A. (2018) Coupled Mg/Ca and clumped isotope analyses of foraminifera provide consis- tent water temperatures Sebastian. *Geochim. Cosmochim. Acta*.

Broecker W. S. and Olson E. A. (1961) Lamont radiocarbon measurements VIII. *Radiocarbon* **3**, 176–204.

Came R. E., Brand U. and Affek H. P. (2014) Clumped isotope signatures in modern brachiopod carbonate. *Chem. Geol.* **377**, 20–30. Available at: http://dx.doi.org/10.1016/j.chemgeo.2014.04.004.

Coplen T. B. (1996) Editorial : More uncertainty than necessary. **11**, 369–370.

Daëron M., Blamart D., Peral M. and Affek H. P. (2016) Absolute isotopic abundance ratios and the accuracy of Δ47 measurements. *Chem. Geol.* **442**, 83–96. Available at: http://dx.doi.org/10.1016/j.chemgeo.2016.08.014.

Defliese W. F., Hren M. T. and Lohmann K. C. (2015) Compositional and temperature

effects of phosphoric acid fractionation on Δ47 analysis and implications for discrepant calibrations. *Chem. Geol.* **396**, 51–60.

Dennis K. J., Affek H. P., Passey B. H., Schrag D. P. and Eiler J. M. (2011) Defining an absolute reference frame for "clumped" isotope studies of CO 2. *Geochim. Cosmochim. Acta* **75**, 7117–7131. Available at: http://dx.doi.org/10.1016/j.gca.2011.09.025.

Dennis K. J. and Schrag D. P. (2010) Clumped isotope thermometry of carbonatites as an indicator of diagenetic alteration. *Geochim. Cosmochim. Acta* **74**, 4110–4122. Available at: http://dx.doi.org/10.1016/j.gca.2010.04.005.

Douglas P. M. J., Affek H. P., Ivany L. C., Houben A. J. P., Sijp W. P., Sluijs A., Schouten S. and Pagani M. (2014) Pronounced zonal heterogeneity in Eocene southern high-latitude sea surface temperatures. *Proc. Natl. Acad. Sci. U. S. A.* **111**, 1–6. Available at: http://www.ncbi.nlm.nih.gov/pubmed/24753570%5Cnhttp://www.pnas.org/content/111/18/6582.

Duplessy J.-C. (1978) Isotope studies. *Clim. Change* **3**, 47–67.

Duplessy J. C., Bé A. W. H. and Blanc P. L. (1981) Oxygen and carbon isotopic composition and biogeographic distribution of planktonic foraminifera in the Indian Ocean. *Palaeogeogr. Palaeoclimatol. Palaeoecol.* **33**, 9–46.

Durazzi J. T. (1981) Stable-isotope studies of planktonic foraminifera in North Atlantic core tops. *Palaeogeogr. Palaeoclimatol. Palaeoecol.* **33**, 157–172.

Eagle R. A., Eiler J. M., Tripati A. K., Ries J. B., Freitas P. S., Hiebenthal C., Wanamaker A. D., Taviani M., Elliot M., Marenssi S., Nakamura K., Ramirez P. and Roy K. (2013) The influence of temperature and seawater carbonate saturation state on 13C-18O bond ordering in bivalve mollusks. *Biogeosciences* **10**, 4591–4606.

Eiler J. M. (2007) "Clumped-isotope" geochemistry-The study of naturally-occurring, multiply-substituted isotopologues. *Earth Planet. Sci. Lett.* **262**, 309–327.

Eiler J. M. (2011) Paleoclimate reconstruction using carbonate clumped isotope thermometry. *Quat. Sci. Rev.* **30**, 3575–3588.

Emiliani C. (1966) Isotopic Paleotemperatures. *Science (80-.).* **154**, 851–857. Available at: http://www.jstor.org/stable/1719432.

Epstein S., Buchsbaum R., Lowenstam H. and Urey H. (1951) Geologic History of Sea Water. *Geol. Soc. Am. Bull.* **62**, 417–426.

Fontanier C., MacKensen A., Jorissen F. J., Anschutz P., Licari L. and Griveaud C. (2006) Stable oxygen and carbon isotopes of live benthic foraminifera from the Bay of Biscay: Microhabitat impact and seasonal variability. *Mar. Micropaleontol.* **58**, 159–183.

Ghosh P., Adkins J., Affek H., Balta B., Guo W., Schauble E. A., Schrag D. and Eiler J. M. (2006) 13C-18O bonds in carbonate minerals: A new kind of paleothermometer. *Geochim. Cosmochim. Acta* **70**, 1439–1456.

Gonfiantini R., Stichler W. and Rozanski K. (1995) STANDARDS AND INTERCOMPARISON MATERIALS DISTRIBUTED BY THE INTERNATIONAL ATOMIC ENERGY AGENCY FOR STABLE ISOTOPE MEASUREMENTS. *IAEA-TECDOC*.

Grauel A. L., Schmid T. W., Hu B., Bergami C., Capotondi L., Zhou L. and Bernasconi S. M. (2013) Calibration and application of the "clumped isotope" thermometer to foraminifera for high-resolution climate reconstructions. *Geochim. Cosmochim. Acta* **108**, 125–140. Available at: http://dx.doi.org/10.1016/j.gca.2012.12.049.

Grubbs F. E. (1969) Procedures for detecting outlying observations in samples. *Technometrics* **11**, 1–21.

H. Elderfield and G. Ganssen (2000) Past temperature and d18O of surface ocean waters inferred from foraminiferal Mg/Ca ratios. *Lett. to Nat.* **705**, 442–445.

Hadden C. S. and Cherkinsky A. (2015) 14 C Variations in Pre-Bomb Nearshore Habitats of the Florida Panhandle, USA. *Radiocarbon* **57**, 469–479.

Hatté C., Hodgins G., Jull A. J. T., Bishop B. and Tesson B. (2008) Marine chronology based on 14C dating on diatoms proteins. *Mar. Chem.* **109**, 143–151.

Herbert T. D. (2013) *Alkenone Paleotemperature Determinations*. 2nd ed., Elsevier Ltd. Available at: http://dx.doi.org/10.1016/B978-0-08-095975-7.00615-X.

Hut G. (1987) Consultants' group meeting on stable isotope reference samples for geochemical and hydrological investigations.

Jonkers L. and Kuˇ M. (2015) Global analysis of seasonality in the shell flux of extant planktonic Foraminifera. *Biogeosciences*, 2207–2226.

Katz A., Bonifacie M., Hermoso M., Cartigny P. and Calmels D. (2017) Laboratory-grown coccoliths exhibit no vital effect in clumped isotope (Δ47) composition on a range of geologically relevant temperatures. *Geochim. Cosmochim. Acta* **208**, 335–353.

Kele S., Breitenbach S. F. M., Capezzuoli E., Meckler A. N., Ziegler M., Millan I. M., Kluge T.,

Deák J., Hanselmann K., John C. M., Yan H., Liu Z. and Bernasconi S. M. (2015) Temperature dependence of oxygen- and clumped isotope fractionation in carbonates: A study of travertines and tufas in the 6–95°C temperature range. *Geochim. Cosmochim. Acta* **168**, 172–192.

Kelson J. R., Huntington K. W., Schauer A. J., Saenger C. and Lechler A. R. (2017) Toward a universal carbonate clumped isotope calibration: Diverse synthesis and preparatory methods suggest a single temperature relationship. *Geochim. Cosmochim. Acta* **197**, 104–131. Available at: http://dx.doi.org/10.1016/j.gca.2016.10.010.

Kim J.-H., Van der Meer J., Schouten S., Helmke P., Willmott V., Sangiorgi F., Koç N., Hopmans E. C. and Damsté J. S. S. (2010) New indices and calibrations derived from the distribution of crenarchaeal isoprenoid tetraether lipids: Implications for past sea surface temperature reconstructions. *Geochim. Cosmochim. Acta* **74**, 4639–4654.

Kim J., Schouten S., Hopmans E. C., Donner B. and Damste J. S. S. (2008) Global sediment core-top calibration of the TEX 86 paleothermometer in the ocean. **72**, 1154–1173.

Kim S.-T. and O'Neil J. R. (1997) Equilibrium and nonequilibrium oxygen isotope effects in synthetic carbonates. *Geochim. Cosmochim. Acta* **61**, 3461–3475. Available at: http://linkinghub.elsevier.com/retrieve/pii/S0016703797001695.

Kissel C., Laj C., Mulder T., Wandres C. and Cremer M. (2009) The magnetic fraction: A tracer of deep water circulation in the North Atlantic. *Earth Planet. Sci. Lett.* **288**, 444–454. Available at: http://dx.doi.org/10.1016/j.epsl.2009.10.005.

Kissel C., Van Toer A., Laj C., Cortijo E. and Michel E. (2013) Variations in the strength of the North Atlantic bottom water during Holocene. *Earth Planet. Sci. Lett.* **369**, 248–259.

Kluge T., John C. M., Jourdan A.-L., Davis S. and Crawshaw J. (2015) Laboratory calibration of the calcium carbonate clumped isotope thermometer in the 25–250°C temperature range. *Geochim. Cosmochim. Acta* **157**, 213–227.

Kucera M., Rosell-Melé A., Schneider R., Waelbroeck C. and Weinelt M. (2005) Multiproxy approach for the reconstruction of the glacial ocean surface (MARGO). *Quat. Sci. Rev.* **24**, 813–819.

Lea D. W. (2013) *Elemental and Isotopic Proxies of Past Ocean Temperatures*. 2nd ed.,

Elsevier Ltd. Available at: http://dx.doi.org/10.1016/B978-0-08-095975-7.00614-8.

LeGrande A. N. and Schmidt G. A. (2006) Global gridded data set of the oxygen isotopic composition in seawater. *Geophys. Res. Lett.* **33**, 1–5.

Levitt N. P., Eiler J. M., Romanek C. S., Beard B. L. and Johnson C. M. (2018) Near Equilibrium 13 C - 18 O Bonding During Inorganic Calcite Precipitation under Chemo - Stat Conditions. *Geochemistry, Geophys. Geosystems*.

Locarnini R. A., Mishonov A. V., Antonov J. I., Boyer T. P., Garcia H. E., Baranova O. K., Zweng M. M., Paver C. R., Reagan J. ., Johnson D. R., Hamilton M. and Seidov D. (2013) NOAA Atlas NESDIS 73 WORLD OCEAN ATLAS 2013 Volume 1: Temperature. **1**. Available at: http://www.researchgate.net/publication/260389845_NOAA_Atlas_NESDIS_73_WORLD_OCEAN_ATLAS_2013_Volume_1_Temperature.

Mangerud J. and Gulliksen S. (1975) Apparent radiocarbon ages of recent marine shells from Norway, Spitsbergen, and Arctic Canada. *Quat. Res.* **5**, 263–273.

Marchitto T. M., Curry W. B., Lynch-Stieglitz J., Bryan S. P., Cobb K. M. and Lund D. C. (2014) Improved oxygen isotope temperature calibrations for cosmopolitan benthic foraminifera. *Geochim. Cosmochim. Acta* **130**, 1–11. Available at: http://dx.doi.org/10.1016/j.gca.2013.12.034.

Mathien-Blard E. and Bassinot F. (2009) Salinity bias on the foraminifera Mg/Ca thermometry: Correction procedure and implications for past ocean hydrographic reconstructions. *Geochemistry, Geophys. Geosystems* **10**.

McCrea J. M. (1950) On the isotopic chemistry of carbonates and a paleotemperature scale. *J. Chem. Phys.* **18**, 849–857.

Meckler A. N., Ziegler M., Mill??n M. I., Breitenbach S. F. M. and Bernasconi S. M. (2014) Long-term performance of the Kiel carbonate device with a new correction scheme for clumped isotope measurements. *Rapid Commun. Mass Spectrom.* **28**, 1705–1715.

Mix A. C. (1987) *Chapter 6 - The oxygen-isotope record of glaciation*. v. K-3. eds. W. F. Ruddiman and H. E. Wright, North America and adjacent oceans during the last deglaciation: Boulde, Colorado, Geological Society of America, The Geology of North America.

Mortyn P. G. and Charles C. D. (2003) Planktonic foraminiferal depth habitat and δ18O

calibrations: Plankton tow results from the Atlantic sector of the Southern Ocean. *Paleoceanography* **18**, n/a-n/a. Available at: http://doi.wiley.com/10.1029/2001PA000637.

Müller I. A., Violay M. E. S., Storck J. C., Fernandez A., van Dijk J., Madonna C. and Bernasconi S. M. (2017) Clumped isotope fractionation during phosphoric acid digestion of carbonates at 70 °C. *Chem. Geol.* **449**, 1–14.

Müller P. J., Kirst G., Ruhland G., Von Storch I. and Rosell-Melé A. (1998) Calibration of the alkenone paleotemperature index U 37 K′ based on core-tops from the eastern South Atlantic and the global ocean (60 N-60 S). *Geochim. Cosmochim. Acta* **62**, 1757–1772.

Murray S. T., Arienzo M. M. and Swart P. K. (2016) Determining the Δ47 acid fractionation in dolomites. *Geochim. Cosmochim. Acta* **174**, 42–53. Available at: http://dx.doi.org/10.1016/j.gca.2015.10.029.

Ortiz D., Mix A. C. and Collier R. W. (1995) Environmental control of living symbiotic and asymbiotic Environmental control of living symbiotic and asymbiotic foraminifera of the California Current. *Paleoceanography* **10**, 987–1009.

Passey B. H. and Henkes G. A. (2012) Carbonate clumped isotope bond reordering and geospeedometry. *Earth Planet. Sci. Lett.* **351–352**, 223–236. Available at: http://dx.doi.org/10.1016/j.epsl.2012.07.021.

Patterson R. T. and Fishbein E. (1989) Determine the Number of Point Counts Needed for. *J. Paleontol.* **63**, 245–248.

Pflaumann U. and Jian Z. (1999) Modern distribution patterns of planktonic foraminifera in the South China Sea and western Pacific : a new transfer technique to estimate regional sea-surface temperatures. *Mar. Geol.* **156**, 41–83.

Reimer P. J., Bard E., Bayliss A., Beck J. W., Blackwell P. G., Ramsey C. B., Buck C. E., Cheng H., Edwards R. L., Friedrich M., Grootes P. M., Guilderson T. P., Haflidason H., Hajdas I., Hatté C., Heaton T. J., Hoffmann D. L., Hogg A. G., Hughen K. A., Kaiser K. F., Kromer B., Manning S. W., Niu M., Reimer R. W., Richards D. A., Scott E. M., Southon J. R., Staff R. A., Turney C. S. M. and van der Plicht J. (2013) IntCal13 and Marine13 Radiocarbon Age Calibration Curves 0–50,000 Years cal BP. *Radiocarbon* **55**, 1869–1887. Available at: https://www.cambridge.org/core/product/identifier/S0033822200048864/type/

journal_article.

Roche D. M., Waelbroeck C., Metcalfe B. and Caley T. (2017) FAME (v1 . 0): a simple module to simulate the effect of planktonic foraminifer species-specific habitat on their oxygen isotopic content. *Geosci. Model Dev.* **18**, 1–22.

Rodriguez-Sanz L., Bernasconi S. M., Marino G., Heslop D., Müller I. A., Fernandez A., Grant K. M. and Rohling E. J. (2017) Penultimate deglacial warming across the Mediterranean Sea revealed by clumped isotopes in foraminifera. *Sci. Rep.*, 1–11.

Rogers J. and De Deckker P. (2011) Environmental reconstructions of the upper 500 m of the southern Indian Ocean over the last 40 ka using Radiolarian (Protista) proxies. *Quat. Sci. Rev.* **30**, 876–886. Available at: http://dx.doi.org/10.1016/j.quascirev.2011.01.006.

Schauble E. A., Ghosh P. and Eiler J. M. (2006) Preferential formation of 13C-18O bonds in carbonate minerals, estimated using first-principles lattice dynamics. *Geochim. Cosmochim. Acta* **70**, 2510–2529.

Schauer A. J., Kelson J., Saenger C. and Huntington K. W. (2016) Choice of 17 O correction affects clumped isotope (Δ 47) values of CO 2 measured with mass spectrometry. , 2607–2616.

Schiebel R. (2002) Planktic foraminiferal sedimentation and the marine calcite budget. *Global Biogeochem. Cycles* **16**.

Schmiedl G., Pfeilsticker M., Hemleben C. and Mackensen A. (2004) Environmental and biological effects on the stable isotope composition of recent deep-sea benthic foraminifera from the western Mediterranean Sea. *Mar. Micropaleontol.* **51**, 129–152.

Schouten S., Hopmans E. C., Schefuß E. and Sinninghe Damsté J. S. (2002) Distributional veriations in marine crenarchaeol membrane lipids: a new tool for reconstructing ancient sea water temperatures? *Earth Planet. Sci. Lett.* **204**, 265–274. Available at: http://www.sciencedirect.com/science/article/pii/S0012821X02009792.

Shackleton N. (1967) Oxygen isotope analyses and Pleistocene temperatures re-assessed. *Nature* **215**, 15–17.

Shackleton N. J. (1974) Attainment of isotopic equilibrium between ocean water and the benthonic foraminifera geuns *Uvigerina*: Isotopic changes in the ocean during the last glacial. *Colloq. Int. du C.N.R.S.* **219**, 203–210.

Sharma S. Das, Patil D. J. and Gopalan K. (2002) Temperature dependence of oxygen isotope fractionation of CO 2 from magnesite-phosphoric acid reaction. *Geochim. Cosmochim. Acta* **66**, 589–593.

Simstich J., Sarnthein M. and Erlenkeuser H. (2003) Paired δ 18 O signals of Neogloboquadrina pachyderma (s) and Turborotalita quinqueloba show thermal stratification structure in Nordic Seas. *Mar. Micropaleontol.* **48**, 107–125.

Southon J., Kashgarian M., Fontugne M., Metivier B. and Yim W. W. S. (2002) Marine reservoir corrections for the Indian Ocean and Southeast Asia. *Radiocarbon* **44**, 167–180.

Squire P., Joannes-Boyau R., Scheffers A. M., Nothdurft L. D., Hua Q., Collins L. B., Scheffers S. R. and Zhao J. (2013) A marine reservoir correction for the Houtman-Abrolhos archipelago, east Indian Ocean, Western Australia. *Radiocarbon* **55**, 103–114.

Stefansky W. (1972) Rejecting outliers in factorial designs. *Technometrics* **14**, 469–479.

Stolper D. A. and Eiler J. M. (2016) Constraints on the formation and diagenesis of phosphorites using carbonate clumped isotopes. *Geochim. Cosmochim. Acta* **181**, 238–259.

Stuiver M., Reimer P. J. and Reimer R. W. (2017) CALIB 7.1 [WWW program] at http://calib. org. *Last accessed*, 8–24.

Tang J., Dietzel M., Fernandez A., Tripati A. K. and Rosenheim B. E. (2014) Evaluation of kinetic effects on clumped isotope fractionation (δ47) during inorganic calcite precipitation. *Geochim. Cosmochim. Acta* **134**, 120–136. Available at: http://dx.doi.org/10.1016/j.gca.2014.03.005.

Thiagarajan N., Adkins J. and Eiler J. (2011) Carbonate clumped isotope thermometry of deep-sea corals and implications for vital effects. *Geochim. Cosmochim. Acta* **75**, 4416–4425. Available at: http://dx.doi.org/10.1016/j.gca.2011.05.004.

Tisnérat-Laborde N., Poupeau J. J., Tanau J. F. and Paterne M. (2001) DEVELOPMENT OF A SEMI-AUTOMATED SYSTEM FOR ROUTINE PREPARATION OF CARBONATE SAMPLES. *17th Int. 14C Conf.* **43**, 299–304.

Tolderlund D. S. and Bé A. W. H. (1971) Seasonal distribution of planktonic foraminifera in the western North Atlantic. *Micropaleontology*, 297–329.

Tripati A. K., Eagle R. A., Thiagarajan N., Gagnon A. C., Bauch H., Halloran P. R. and Eiler J.

M. (2010) 13C-18O isotope signatures and "clumped isotope" thermometry in foraminifera and coccoliths. *Geochim. Cosmochim. Acta* **74**, 5697–5717. Available at: http://dx.doi.org/10.1016/j.gca.2010.07.006.

Tripati A. K., Hill P. S., Eagle R. A., Mosenfelder J. L., Tang J., Schauble E. A., Eiler J. M., Zeebe R. E., Uchikawa J., Coplen T. B., Ries J. B. and Henry D. (2015) Beyond temperature: Clumped isotope signatures in dissolved inorganic carbon species and the influence of solution chemistry on carbonate mineral composition. *Geochim. Cosmochim. Acta* **166**, 344–371. Available at: http://dx.doi.org/10.1016/j.gca.2015.06.021.

Urey H. C. (1947) The thermodynamic properties of isotopic substances. *J. Chem. Soc.*, 562–581. Available at: http://dx.doi.org/10.1039/JR9470000562.

Vázquez Riveiros N., Govin A., Waelbroeck C., Mackensen A., Michel E., Moreira S., Bouinot T., Caillon N., Orgun A. and Brandon M. (2016) Mg/Ca thermometry in planktic foraminifera: Improving paleotemperature estimations for G. bulloides and N. pachyderma left. *Geochemistry, Geophys. Geosystems* **17**, 1249–1264. Available at: http://dx.doi.org/10.1002/2015GC006234.

Wacker U., Fiebig J., Tödter J., Schöne B. R., Bahr A., Friedrich O., Tötken T., Gischler E. and Joachimski M. M. (2014) Empirical calibration of the clumped isotope paleothermometer using calcites of various origins. *Geochim. Cosmochim. Acta* **141**, 127–144.

Walker D. A., Linton A. E. and Schafer C. T. (1974) Sudan Black B; a superior stain to Rose Bengal for distinguishing living from non-living foraminifera. *J. Foraminifer. Res.* **4**, 205–215.

York D., Evensen N. M., Martínez M. L. and De Basabe Delgado J. (2004) Unified equations for the slope, intercept, and standard errors of the best straight line. *Am. J. Phys.* **72**, 367–375. Available at: http://aapt.scitation.org/doi/10.1119/1.1632486.

Zaarur S., Affek H. P. and Brandon M. T. (2013) A revised calibration of the clumped isotope thermometer. *Earth Planet. Sci. Lett.* **382**, 47–57. Available at: http://dx.doi.org/10.1016/j.epsl.2013.07.026.

Zaarur S., Olack G. and Affek H. P. (2011) Paleo-environmental implication of clumped isotopes in land snail shells. *Geochim. Cosmochim. Acta* **75**, 6859–6869.

Zhang Y. G., Pagani M. and Wang Z. (2016) Ring Index: A new strategy to evaluate the integrity of TEX86paleothermometry. *Paleoceanography* **31**, 220–232.

Zweng M. M., Reagan J. R., Antonov J. I., Locarnini R. A., Mishonov A. V, Boyer T. P., Garcia H. E., Baranova O. K., Johnson D. R. and Seidov D. (2013) World ocean atlas 2013. Volume 2, Salinity.

Part 3

APPLICATION OF CLUMPED ISOTOPES TO RECONSTRUCTION OF PALEOENVIRONMENTAL CHANGES DURING KEY INTERVALS ACROSS THE MID-PLEISTOCENE TRANSITION IN THE MEDITERRANEAN SEA

In order to apply the clumped-isotope approach to foraminifera for paleo-environmental reconstructions across the MPT, and to provide robust paleo-temperature reconstructions, we looked for marine series, meeting the following criteria:

- The series should be located in an area marked by clear paleoclimatic and/or paleoceanographic changes across the MPT,
- The series should cover a wide time interval, making it possible to assess both long-term changes and orbital to sub-orbital environmental variations within the MPT;
- The series should provide large amounts of foraminifera making it possible to target key intervals with enough analytical replicates to significantly reduce analytical uncertainties in estimated temperatures.

We selected the marine section of Montalbano Jonico (MJS hereafter). This marine series is well known, having been one of the nominees for the recent selection of the *Global Stratotype Section and Point of the Middle Pleistocene Stage* ("Golden Spike"). Numerous past geological studies have established that the MJS records Mediterranean climate changes over the MPT. The section covers the stratigraphic interval from MIS 37 to MIS 16 (~ 1.2 – 0.6 Ma) with very high sedimentation rates (see below). Because of late Pleistocene tectonic uplift, this marine section is now exposed on land. The outcrop being located a few hour drive away from Bari or Naples, making it easy to organize field trips to collect large amounts of sedimentary material. Finally, due to the marginal deposition environment, benthic foraminifera are abundant in the MJS sediments, allowing to perform stable-isotope ($\delta^{18}O$, $\delta^{13}C$ and clumped-isotope) and Mg/Ca ratio measurements without limitation of material.

For this project, we worked in collaboration with:

- Patrizia Maiorano, Maria Marino and Angela Girone from the University of Bari who lead the Montalbano project, helped for sampling during the field trip and performed the previous works on the section.
- Tim Herbert from Brown University who performed all the alkenone measurements (unpublished data).

In this Part, I will present the Montalbano Jonico section and quickly summarize the current knowledge on changes occurring across the MPT in the central Mediterranean area. I then describe and discuss the results of my analyses performed on 15 samples (Figure 3.1) from Interval A and Interval B, covering from MIS 36 to MIS 19, with a special emphasis on two key periods: MIS 31/30 in Interval A (see Part1 - Chapter 1; MIS 31 – "super-interglacial") and MIS 20/19 in Interval B (see Part1 - Chapter 1; MIS 19 – analogue to the present interglacial). These new data help to better understand paleo-environmental changes in the Gulf of Taranto across the MPT, and offer an opportunity to discuss the strengths and limitations of the clumped-isotope method applied to foraminifer paleo-reconstructions.

The Chapter 2 about the paleoceanographic study over Interval A of MJS and Chapter 3 about the Interval B are presented as articles. For a practical point of view, the study area and the methods are presented in part 1 to limit the repetitions.

Chapter 1

THE MONTALBANO JONICO SECTION AND THE MPT IN THE CENTRAL MEDITERREANEAN AREA

1. LOCATION AND CHRONOSTRATIGRAPHIC FRAMEWORK OF THE MONTALBANO JONICO SECTION

The Montalbano Jonico Section (MJS), in southern Italy, is located in the Lucania Basin of Bradano Trough (Balduzzi et al., 1982; Casnedi, 1988), between the Apennines Mountains and the Apulian Platform (Figure 3.1). The base of the MJS is of Early Pliocene age and displays deformation associated with polyphasic active thrusts, as a result of interactions between Apulian foreland and Brandano foredeep dated of Plio-Pleistocene. As a consequence, a series of small-scale marine/lacustrine basins were formed (Patacca and Scandone, 2007), accompanied by the deposition, over the Meso-Cenozoïc units, of Apulian foreland sedimentary series (Cassedi et al., 1982).

The MJS comprises ~ 450-m-thick, upward-coarsening deposits ranging from hemipelagic silty clays to silty sands (Figure 3.1 – Montalbano Jonico composite section). It is interspersed by nine volcanoclastic layers (labelled V1-V9) and five sapropel layers identifiable by benthic foraminiferal assemblages (D'Alessandro et al., 2003; Stefanelli, 2003; Stefanelli et al., 2005; Maiorano et al., 2008). The MJS is divided into two parts: Interval A (lower part of the section – 168 m thick, from MIS 37 to MIS 23) and Interval B (upper part of the section – 280 m thick; from MIS22 to MIS17/16 transition), separated by a stratigraphic gap whose estimated duration is ~ 9.4 ka and whose origin is not fully understood.

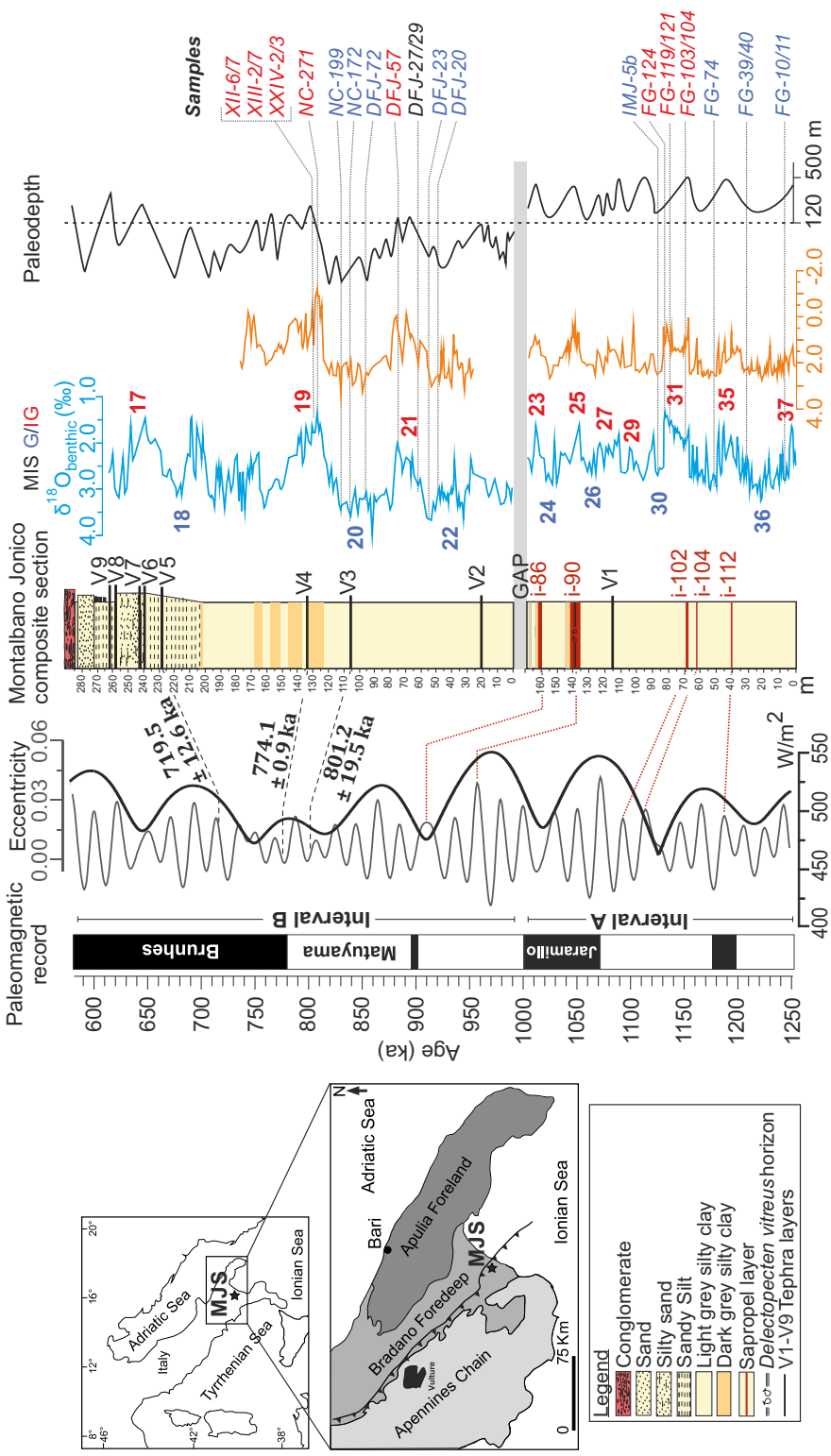

Figure 3.1: Geological context of Montalbano Jonico section (MJS), with paleoenvironmental and biostratigraphical details from Ciaranfi et al. (2001, 2010), Stefanelli (2003, 2004), D'Alessandro et al (2003), Maiorano et al. (2004, 2010), Girone et al. (2013); δ18Op and δ18Ob (Brilli, 1998; Brilli et al., 2000 and Ciaranfi et al., 2010); correlation to sapropel stratigraphy according to Lourens (2004) and Konijnendijk et al. (2014); summer insolation from Laskar et al. (2004) and $^{40}Ar/^{39}Ar$ ages of V3-V5 (Ciaranfi et al., 2010; Maiorano et al., 2010; Petrosino et al., 2015; Simon et al., 2017 and Nomade et al., in review). G = glacials; IG = interglacials.

The chrono-stratigraphical framework of MJS is based on stable oxygen isotope measurements on benthic ($\delta^{18}O_b$; *Cassidulina carinata*) and planktonic ($\delta^{18}O_p$; *Globigerina bulloides*) foraminifera (Figure 3.1), combined with calcareous plankton biostratigraphy, radiometric dating ($^{40}Ar/^{39}Ar$) and identification of sapropel layers. The whole series covers the interval from MIS 37 to MIS 17/16. In the lower part of the section, astronomical age-model was developed by tuning the sapropel layers to precession minima (applying a 3 ka time lag), while in the upper part of the section, astronomical tuning was achieved by visual comparison of $\delta^{18}O$ to ODP Site 975 $\delta^{18}O_{planktonic}$ (Lourens, 2004). Additional tie-points were provided by the $^{40}Ar/^{39}Ar$ age of tephra V3 and V5 (Ciaranfi et al., 2010; Maiorano et al., 2010; Petrosino et al., 2015). The chrono-stratigraphic frame indicates that the MJS covers the time interval from 1.240 to 0.645 Ma (Ciaranfi et al., 2010). The estimated sedimentation rate ranges from 0.28 to 0.9 m/ka for Interval A and from 0.5 to 2 m/ka for Interval B (Ciaranfi et al., 2010; Maiorano et al., 2010). Recent studies have re-assessed the age model for MIS 20 and MIS 19 (belonging to Interval B, hereafter referred to as Ideal Section or IS) based on a new high-resolution benthic foraminifera $\delta^{18}O$ records and revised, more accurate $^{40}Ar/^{39}Ar$ age of tephra V4 (Simon et al., 2017; Nomade et al., in review – see appendix).

2. STATE OF THE ART OF PALEOENVIRONMENTAL CHANGES RECORDED OVER THE MPT IN MJS

Over the whole period considered here, the MJS water depth, estimated from benthic foraminifer assemblages, never exceeded 500 m. Paleodepth reconstructions indicate a clear evolution from lower circalittoral - upper bathyal for Interval A to upper circalittoral – shelf environments for Interval B (Figure 3.1 – Paleodepth; Stefanelli, 2003; D'Alessandro et al., 2003). This evolution of water depths is an important factor to take into account for paleoenvironmental reconstructions as the evolution from deeper interval A to shallower interval B has been likely associated with changes in water masses as well as a stronger influence of continental runoffs. In other words, the bottom temperatures recorded into Interval A might not be directly comparable to bottom temperatures recorded into Interval B because they potentially record the temperature

of different water masses. However, the paleoceanographic interpretation could be done for each Interval independently.

2.1. Interval A

The major paleoenvironmental changes that occurred during the Interval A of MJS spanning from 1.24 to 0.9 Ma (MIS 37 to 23), are the results of orbitally-controlled global climate (Girone et al., 2013). Micropaleontological assemblages, oxygen isotope data and the occurrence of sapropel-like events highlight the orbital forcing on paleoclimatologic changes (Girone et al., 2013). The formation of those sapropel-like events could be driven by two mechanisms: (i) the stratification of upper water column and preservation of organic material and/or (ii) the enhancement of sea surface water productivity (Girone et al., 2013). The glacial interglacial cycles through Interval A are the result of complex interactions of both global climate change and also regional settings. This is particularly noteworthy with the long MIS 31 interglacial (from 1082 to 1062 ka), whose mineralogical and micropaleontological data suggest a particularly warm period, probably affected also by changes in local precipitation regime (Stefanelli, 2004; Joannin et al., 2008; Girone et al., 2013).

The MIS 31 began to be well studied in MPT records because of its unusual orbital configuration, which can make this interglacial one of the precursor to high-amplitude eccentricity-dominated cycles and a potential analogue to Holocene (Scherer et al., 2008). This MIS 31 is characterized by its long duration under warm environment especially in North Atlantic (e.g. Helmke et al., 2003; Bintanja et al., 2005; Bintanja and Van de Wal, 2008; Naafs et al., 2013). However, on the Iberian margin, reconstructed-SST and atmospheric temperatures form pollen data show a moderated warming during the MIS 31 associated with low seasonal distribution of precipitation (Oliveira et al., 2017). The Mediterranean basin is therefor a key area to study the potential influence of tropical processes.

2.2. Interval B

Interval B (MIS22-MIS17/16) had initially been studied at low resolution with a particular focus on time interval from MIS 20 to MIS 18 (Stefanelli, 2003, 2004; Aiello et al., 2015; Bertini et al., 2015; Toti, 2015; Maiorano et al., 2016), while a recent study has investigated high-resolution data on MIS 20-19 (Nomade et al., in review). The complex deglaciation leading to MIS 19 seems to have been likely affected by ice-sheet dynamic and regional changes linked to periodical intensification of moisture associated either to tropical mechanisms and/or enhanced transports from the Atlantic. The data from previous studies conclude about the incursion of polar-subpolar North Atlantic water, concomitant with IRD discharges that could suggest potential Heinrich-like events (Maiorano et al., 2016). These cold conditions could be followed by another cold event, potentially analogue to Younger-Dryas-like event as suggested by specific-species abundance (e.g. *N. labyrinthus*; Maiorano et al., 2016). Just after this potential second cold event, data suggested deposition sapropel-like event, with peculiar strong stratification of the column water (e.g. attested by $\delta^{13}C$; Nomade et al., in review). This sapropel-like event marks the lower limit of the MIS19 climate optimum – MIS 19c. High-resolution $\delta^{18}O$ records display millennial scale oscillations through the MIS19b and MIS 19a that have been associated to periodical northward shifts of ITCZ and/or enhanced eastward transport of water from the Atlantic Ocean (Nomade et al., in review).

All these interpretations are based on the hypothesis that recorded data reflect global signal rather than regional processes. To support this hypothesis, we have decoupled the $\delta^{18}O$ signal via clumped isotope, comparing the processes that occur during deglaciations between MIS 22-21 and MIS 20-19. I performed clumped isotope analyses on benthic foraminifera and Mg/Ca on planktonic foraminifera, and reconstructed oxygen isotope of seawater ($\delta^{18}O_{SW}$) from paired Δ_{47}-$\delta^{18}O$ data. Furthermore, the high-resolution interpretations of MIS 20-19 are sustained by indirect proxy evidence, such as planktonic calcareous fossil assemblages and $\delta^{18}O$ records to interpret hydrological changes in water temperatures and oxygen isotope of seawater.

In order to get a more precise understanding of these changes, I compared Mg/Ca-temperatures on planktonic foraminifera with high-resolution alkenone-temperatures.

3. METHODS

3.1. Traditional Stable Isotope Analyses

Planktonic and benthic foraminifera were hand-picked for traditional stable isotope analyses. Around 20-30 individuals of *Globigerinoides ruber* and *Cassidulina carinata* and 7-15 individuals for *Uvigerina mediterranea* and *Elphidium crispum*, were picked from the 200-355 µm fraction. From 1 to 5 replicate analyses of $\delta^{18}O$ and $\delta^{13}C$ were performed. Foraminifera were cleaned in an ultrasonic bath with reagent-grade methanol for few seconds to eliminate impurities. $\delta^{18}O_{VPDB}$ and $\delta^{13}C_{VPDB}$ values were measured at LSCE using a MultiCarb system coupled to a dual-inlet Isoprime (Elementar). Standardization to VPDB was based on repeated measurements of international reference materials NBS 19 and NBS 18, with respective nominal values for $\delta^{18}O_{VPDB}$ of - 2.20 ‰ and - 23.01 ‰, and for $\delta^{13}C_{VPDB}$ of 1.95 ‰ and - 5.01 ‰. The uncertainties reported here for traditional stable isotope measurements are based on the external reproducibility of in-laboratory carbonate standards (MARGO) with 1SD = 0.05 ‰ for $\delta^{18}O_{VPDB}$ and 1SD = 0.03 ‰ for $\delta^{13}C_{VPDB}$.

2.2. Clumped-isotope Analyses

A total of 257 clumped-isotope analyses were performed at LSCE, including 143 measurements on benthic foraminifera, through the Interval A and B, and 114 measurements of carbonate standards. We used the equipment and procedures described by Peral et al. (2018; c.f. Chapter 2). Based on our earlier findings, we combined foraminifer size fraction and cleaned them following the Grauel et al. (2013) protocol. Conversion of Δ_{47}^{raw} to absolute Δ_{47} values was done using carbonate standards (ETH-1/2/3; Meckler et al., 2014; Bernasconi et al., 2018), following the procedure described by Daëron et al. (2016). "Absolute" Δ_{47} values were then converted to

temperatures using the calibration of Peral et al. (2018; Chapter 2).

A total of about 1 g of benthic foraminifera (about 81 000 individuals) was picked to perform the clumped-isotope measurements for both Interval A and B. Where possible, three species of benthic foraminifera were picked from each samples (i.e. stratigraphic depth), *Uvigerina mediterranea* (200-355 μm), *Cassidulina carinata* (200-315 μm) and *Elphidium crispum* (200-450 μm; only for one sample). From 2 to 27 replicates for each sample/species pair were done in 4 sessions of measurements between July 2016 and June 2018. The first session (2016-07) and the last one (2018-05) were corrected for a slow trend observed in the measured Δ_{47} values of ETH-3, probably resulting from subtle changes in the ion collector backgrounds. Each analytical session (defined as continuous period of Δ_{47} measurements) was assigned independent external Δ_{47} reproducibility based on repeated analyses of standards and samples, respectively 15.9 ppm, 13.9 ppm, 20.9 ppm and 18.1 ppm (1SD).

2.3. Analyses of Mg/Ca Ratio

Mg/Ca measurements were performed at LSCE on planktonic and benthic foraminifera. A minimum of 30 foraminifera (~ 250 μg) were hand-picked in the size range of 250 and 355 μm, and cleaned following the Barker et al. (2003) protocol. Each sample was analysed by inductively coupled plasma mass spectrometry (ICP-MS), using a PlasmaQuant ELITE system from Analytik Jena. After a preliminary run to estimate the Ca concentration, samples were then diluted to a uniform Ca concentration of around 100 ppm. Mg/Ca ratios were determined by intensity ratio method described in Villiers et al. (2002). The calibration standards were prepared from single element standards in solution for all the elements (e.g. Ca, Sr, Mg), bought from Fisher chemical. Instrumental precision for Mg/Ca ratios is in average ± 1.1 %, with daily variations from 0.9 to 1.6% determined by several replicates of a standard solution of known Mg/Ca composition.

The Mg/Ca ratios from planktonic foraminifer were performed on two species *G. ruber* and *G. bulloides* and for benthic foraminifera on *U. mediterranea*. The ratios were converted to temperature using species-specific calibrations:

- For *G. ruber*: we used the calibration of Anand et al., 2003

$$Mg/Ca = 0{,}449\ (\pm\ 0{,}06)\ \exp(0{,}09 \times T)$$

- For *G. bulloides*: we used the calibration of Mashiotta et al., 1999

$$Mg/Ca = 0{,}47\ (\pm\ 0{,}03)\ \exp(0{,}107\ (\pm\ 0{,}003) \times T)$$

- For *U. mediterranea*: we used the calibration of Elderfield et al., 2010

$$Mg/Ca = 0.86\ (\pm\ 0.05) + 0.07\ (\pm\ 0.005) \times T$$

where T (in °C) is the temperature.

The uncertainties were calculated by propagating the analytical errors and uncertainties associated with calibrations.

Chapter 2

INTERVAL A – SEA WATER TEMPERATURE AND OXYGEN-ISOTOPE COMPOSITION CHANGES IN THE MEDITERRANEAN SEA DURING THE "SUPER-INTERGLACIAL" MIS 31 INFERRED FROM CLUMPED ISOTOPE THERMOMETRY

1. INTRODUCTION

During the Early Middle Pleistocene transition (EMPT; 1.4 to 0.4 Ma; e.g. Head and Gibbard, 2015) the Earth's climate experienced a gradual change in the frequency and amplitude of glacial-interglacial cycles. The earlier period of the transition was dominated by obliquity-driven, 41 ka cycles, which were replaced in the later period of the MPT by higher amplitude, ~ 100-ka G-I cycles (Ruddiman et al., 1986; Lisiecki and Raymo, 2005; Lang and Wolff, 2011; Head and Gibbard, 2015). This climatic transition is recorded in the marine and terrestrial realms as changes in intensity and duration of both glacials and interglacials. The Marine Isotopic Stage (MIS) 31, also called "super interglacial" (Pollard and DeConto, 2009; DeConto et al., 2012; Melles et al., 2014; Coletti et al., 2015) from 1082 to 1062 ka (Lisiecki and Raymo, 2005), is a peculiar interglacial. Some authors suggested that it could be a precursor to high-amplitude ~ 100 ka cycles because of its duration (Scherer et al., 2008). Its onset is characterized by an unusual orbital configuration (high obliquity, high eccentricity and minimum precession) resulting in the highest summer insolation levels of the Pleistocene (Laskar et al., 2004). This strong orbital forcing combined with relatively high atmospheric CO_2 concentrations (Hönisch et al., 2009; Tripati et al., 2011) likely contributed to the length and warmth of MIS 31, which lasted ~ 35 ka. In high latitudes and particularly in the north Atlantic, most of MIS 31 records point to warm oceanic temperatures, consistent with milder conditions than during the Holocene (e.g. Helmke et al., 2003; Bintanja et al., 2005; Bintanja and Van de Wal, 2008; Naafs et al., 2013). However, a few records provide evidence of variability in the magnitude of its warming (e.g. Ruddiman et al.,

1989; McClymont et al., 2008; Hillaire-Marcel et al., 2011; Oliveira et al., 2017). In South West (SW) Iberian margin (Site U1385), sea surface temperature (SST) and atmospheric temperature (reconstructed from pollen data) were not exceptionally high (Oliveira et al., 2017). This high-resolution vegetation reconstruction shows millennial-scale climate oscillations throughout MIS 31 with several colder and drier episodes. This variability, however, is not observed in SST reconstructions suggesting a decoupling between atmospheric and marine processes. These millennial-scale oscillations could be driven by low-latitude insolation forcing, leading to a episodic southern shift of the temperate westerlies (Oliveira et al., 2017).

Studying MIS 31 could bring interesting pieces of information about natural climate evolution of an interglacial period, which was triggered by similar orbital forcing than MIS19 or the Holocene (high obliquity and low precession), but took place during the early part of the MPT. In this work, I applied the clumped isotope approach to better constrain MIS 31 evolution in the marine section of Montalbano Jonico (in the southern part of Italy).

The Mediterranean Sea is a complex area, under both tropical and high-latitude influences. The African monsoon shifts periodically northward and impacts the hydrology of the Mediterranean basin as well as global circulation patterns, through an intensification of precipitation and changes in the transfer of latent heat to the atmosphere. Ice-sheet dynamics can also play an important role in the Mediterranean area due to potential entrance of polar-subpolar North Atlantic waters. Understanding future climate evolution of the densely populated Mediterranean area is a key scientific objective, which requires a thorough understanding of natural variability under different forcing and different mean climate states. Yet, past oceanographic and climatologic changes in the Mediterranean area remain poorly documented beyond the most recent climatic cycles. The exposed section of Montalbano Jonico (MJS) represents a valuable marine sedimentary record for studying changes on land and in the marine realm under different glacial-interglacial cycles across the MPT. The continuous MIS 31 is defined in $\delta^{18}O$ of benthic foraminifera between the mid-slope of MIS 32/31 and of MIS 31/30, therefore from about 1095 to 1064 ka based on the age model of Maiorano et al. (2010), tuned to the $\delta^{18}O_{planktonic}$ of ODP Site 975 (Lourens, 2004). The MIS 31 is characterized by a climatic optimum lasting about 10 ka, from 1075 to 1065 ka (based

on planktonic foraminifera assemblages; Girone et al., 2013). Micropaleontological and mineralogical data suggest warm and wet conditions associated with changes in the local precipitation regime with potential effects on sea surface temperature and salinity through enhanced freshwater input into the basin (Stefanelli, 2003; Joannin et al., 2008; Girone et al., 2013). The wet climate could result from the strong northern summer insolation during precession minima with high obliquity and eccentricity. This warm climate phase probably coincided with regional tectonic instability that may have influenced local patterns of erosion and sediment transport (Girone et al., 2013). The paleoenvironmental changes over MIS 31 at MJS could be therefore the result of interaction between global climate change and regional factors such as landscape evolution.

In order to reconstruct the amplitude of the warming and understand the relative contribution of those global and local factors, quantitative water temperatures estimates have to be reconstructed as well as oxygen isotope of the seawater ($\delta^{18}O_{SW}$). We have defined a "climatic baseline" of the adjacent glacial periods (MIS 36, MIS 34 and MIS 30) and obtained temperature quantification of this apparently very warm interglacial. To exploit the full potential of this Mediterranean sequence, we took advantage of recent developments on clumped-isotopes and applied our new foraminifer calibration (Peral et al., 2018; Part 2).

The main advantages of the Δ_{47} thermometer are the absence of detectable vital and salinity effects in planktonic and benthic foraminifera (Tripati et al., 2010; Grauel et al., 2013; Peral et al., 2018) and the fact that it does not require any knowledge of seawater $\delta^{18}O$ (noted $\delta^{18}O_{SW}$ hereafter) in which the carbonate calcified. Combining Δ_{47} and $\delta^{18}O_C$ measurements in foraminifera thus allows reconstructing both past seawater temperatures and $\delta^{18}O_{SW}$. Due to the low quantity of planktonic foraminifera, we have also performed Mg/Ca measurements to provide complementary SST estimates to be compared with Δ_{47}-derived temperatures in benthic foraminifera in the same samples. In this part, I provide new constraints on seawater changes during MIS 31 and nearby glacials periods (MIS 36, 34 and 30) in the Ionian Sea. I also discuss the potential of the clumped-isotope thermometer as a paleoclimatologic proxy to reconstruct past changes in $\delta^{18}O_{SW}$.

2. RESULTS

2.1. $\delta^{18}O_{vpdb}$ Measurements

$\delta^{18}O$ measurements were performed on 2 species of benthic foraminifera (*Cassidulina carinata* and *Uvigerina mediterranea*) and one species of planktonic foraminifera (*Globigerinoides ruber*), except for the older two samples (FG-39/40 and FG-10/11) because *G. ruber* were not present in large enough quantity (Figure 3.2). All the results are summarized in Table 3.1. We calculated the absolute difference ($\Delta^{18}O_c$, hereafter) between the two benthic species and between each of these benthic species and the planktonic species, *G. ruber* (Table 3.2).

Table 3.1: $\delta^{18}O_{VPDB}$ and $\delta^{13}C_{VPDB}$ values for each sample within each species.

Sample	Species	MIS	N	$\delta^{13}C_{VPDB}$	SE	$\delta^{18}O_{VPDB}$	SE
IMJ-5b	*C. carinata*	30	1	-0,36	0,03	2,98	0,05
FG-124		31	1	-0,65	0,03	1,87	0,05
FG-119/121		31	1	-0,08	0,03	1,76	0,05
FG-103/104		31	1	-1,17	0,03	2,49	0,05
FG-74		34	5	-0,60	0,01	3,08	0,02
FG-38/42		36	1	-0,93	0,03	3,21	0,05
FG-8/13		36	1	-0,46	0,03	3,05	0,05
IMJ-5b	*G. ruber*	30	2	1,42	0,02	1,36	0,04
FG-124		31	4	1,12	0,02	-0,58	0,03
FG-119/121		31	1	0,90	0,03	0,44	0,05
FG-103/104		31	1	0,23	0,03	-0,64	0,05
FG-74		34	5	0,90	0,01	1,71	0,02
IMJ-5b	*U. mediterranea*	30	2	-0,37	0,02	3,22	0,04
FG-124		31	4	-0,53	0,02	1,91	0,03
FG-119/121		31	2	-0,47	0,02	2,05	0,04
FG-103/104		31	4	-0,70	0,02	2,55	0,03
FG-74		34	1	-0,31	0,03	3,22	0,05
FG-39/40		36	4	-0,48	0,02	3,52	0,03
FG-10/11		36	2	-0,63	0,02	2,97	0,04

The $\Delta^{18}O_c$ between benthic shells from the same stratigraphic level varies between 0.05 and 0.30 ‰. This variability, which is larger than the internal analytical uncertainty (± 0.05 ‰), could result to some extent from the potential effect of bioturbation, which had mixed vertically foraminifers that had grown under slightly

different conditions. This observed differences could also result from so-called "vital" effects. However, according to Grossman (1984), *Uvigerina spp.* and *Cassidulina ssp.* are believed to precipitate following the equation of Kim and O'Neil (1997). The large observed variability and the small number of intervals studied here do not allow us to reach our own conclusion about potential systematic differences between *Cassidulina carinata* and *Uvigerina mediterranea* that could be associated to vital effects on $\delta^{18}O_c$.

Variations in the difference between benthic species and the planktonic species *G. ruber* ($\Delta^{18}O_{c\ (p\ VS\ b)}$, hereafter) are larger than the inter-benthic variability, and are, as expected, primarily driven by changes in the planktonic $\delta^{18}O$ values. $\Delta^{18}O_{c\ (p\ VS\ b)}$ values remain relatively constant for glacial periods (MIS 36, 34 and 30), hovering between 1.37 and 1.86 ‰. By contrast, a much larger variability is observed for the interglacial period (MIS 31), with benthic-planktonic differences ($\Delta^{18}O_{c\ (p\ VS\ b)}$) varying between 1.32 and 3.19 ‰ (Figure 3.5).

Table 3.2: Difference (absolute values in ‰, PDB) of $\delta^{18}O$ between each species, in red the interglacial period and in blue the glacial periods

Samples	MIS	$\Delta^{18}O$ (‰) *C. carinata – U. mediterranea*	$\Delta^{18}O$ (‰) *U. mediterranea - G. ruber*	$\Delta^{18}O$ (‰) *C. carinata – G. ruber*
IMJ-5b	30	0,24	1,86	1,62
FG-124	31	0,05	2,50	2,45
FG-119/121	31	0,29	1,61	1,32
FG-103/104	31	0,07	3,19	3,13
FG-74	34	0,14	1,50	1,37
FG-39/40	36	0,30	-	-
FG-10/11	36	0,08	-	-

2.2. Temperatures Estimated from Clumped-isotope Measurements

Our clumped-isotope analyses on benthic foraminifera provide valuable pieces of information about past "bottom water" temperature. Paleodepth reconstructions have shown that the water depth was only a few hundred meters at the time of deposition (D'Alessandro et al., 2003; Stefanelli, 2003). It shall never been forgotten that, in the Montalbano Jonico section, those benthic data actually represent sub-surface conditions as we are dealing with margin deposits. In the rest of this manuscript, we may use

sometime the term, "subsurface water", for data (i.e. Δ_{47}-derived temperature, reconstructed $\delta^{18}O_{SW}$) using benthic foraminifers.

Final Δ_{47} values and the corresponding temperature reconstructions are given in Table 3.3 and presented in Figure 3.2. During MIS 36, Δ_{47}-derived temperatures for *U. mediterranea* and *C. carinata* are statistically indistinguishable from each other. These two species have been described as shallow infaunal and epifaunal, respectively, and living in organic rich sediments (Altenbach et al., 1999; Fontanier et al., 2002; Murray, 2006). Taking advantage of the absence of species-related effect in clumped isotopes (Tripati et al., 2010; Grauel et al., 2013; Peral et al., 2018), and assuming that temperature differences between the water-sediment interface and the first few centimetres within sediment remain negligible, we may combine these two benthic species to compute average Δ_{47}-derived temperatures with a reduced analytical error. Furthermore, the potential sediment mixing effect due to bioturbation is largely reduced because of the large quantity of material required for Δ_{47} measurements.

Δ_{47}-derived temperature values during the glacial periods remain relatively constant within errors, ranging between 8 ± 1.2 °C and 11.2 ± 1.6 °C (samples FG-10/11, FG-39/40, FG-74 and IMJ-5b). At the beginning of MIS 31, Δ_{47}-derived temperature values are initially similar to the glacial period estimates (samples FG-103/104 and FG-119/121) and then increase to 13.8 ± 1.5 °C at the end of the interglacial (sample FG-124).

Table 3.3: $\delta^{18}O_{VPDB}$, $\delta^{13}C_{VPDB}$, Δ_{47} values and temperatures derived from Δ_{47} values for each sample within each species

Sample	Species	MIS	N	$\delta^{13}C_{VPDB}$	SE	$\delta^{18}O_{VPDB}$	SE	Δ_{47}	SE	T (°C)	SE
IMJ-5b	*U. mediterranea*	30	15	-0,44	0,01	3,45	0,02	0,732	0,005	8,0	1,2
FG-124	*U. mediterranea*	31	11	-0,58	0,01	2,19	0,03	0,711	0,005	13,8	1,5
FG-119/121	*U. mediterranea*	31	12	-0,43	0,01	2,21	0,03	0,732	0,005	8,1	1,3
FG-103/104	*U. mediterranea*	31	12	-0,83	0,01	2,75	0,03	0,735	0,005	7,1	1,2
FG-74	*U. mediterranea*	34	2	-0,52	0,04	3,61	0,09	0,728	0,011	9,2	3,0
FG-39/40	*C. carrinata*	36	4	-0,82	0,03	3,51	0,06	0,716	0,010	12,6	2,9
	U. mediterranea	36	4	-0,71	0,01	3,77	0,04	0,737	0,007	6,7	1,8
	Combined	36	27	-0,72	0,01	3,68	0,03	0,731	0,006	8,4	1,5
FG-10/11	*C. carrinata*	36	4	-0,59	0,03	3,17	0,06	0,712	0,010	13,5	2,9
	U. mediterranea	36	4	-0,57	0,01	3,34	0,04	0,724	0,007	10,3	1,9
	Combined	36	5	-0,57	0,01	3,28	0,03	0,720	0,006	11,2	1,6

* Combined: mix of *C. carinata* and *U. mediterranea*

2.3. Temperatures Estimated from Mg/Ca Ratio Measurements

The Mg/Ca results are provided in Table 3.4 and in Figure 3.2. Reconstructions of SST were based on planktonic species *G. ruber*, while those sub-surface water temperatures, which may be compared with the clumped-isotope results, were based on Mg/Ca analyses performed on *U. mediterranea*.

As expected, Mg/Ca-derived SSTs (noted Mg/Ca-SST hereafter) indicate colder temperatures during the glacials MIS 36 (FG-10/11 and FG-39/40), MIS 34 (FG-74) and MIS 30 (IMJ-5b) than during interglacial MIS 31 (FG-103/104, FG-119/121 and FG-124). Within the interglacial period, SSTs increase from 22.5 to 24.7 °C in the upper part of MIS 31.

Mg/Ca-derived sub-surface water temperatures for glacial periods are in good agreement with our Δ_{47}-derived temperature estimates. By contrast, for the interglacial MIS 31, Mg/Ca-derived temperatures obtained from *U. mediterranea* are higher than Δ_{47}-derived temperatures and increase from 12.6 to 17.1 °C (samples FG-103/104 and FG-124). Two replicates of sub-surface water temperatures estimates for sample FG-119/121 yield unrealistic warm values of 28.7 °C and 21.5 °C, higher than or comparable to SST estimates for the same samples.

Table 3.4: Mg/Ca values and temperatures derived from Mg/Ca values for each samples and species

Samples	MIS	N	Mg/Ca	Species	T (°C)	SE
IMJ-5b	30	1	2,41	*G. ruber*	18,7	0,9
FG-124	31	1	4,14		24,7	0,8
FG-119/121		1	3,45		22,7	0,9
FG-103/104		1	3,51		22,9	0,9
FG-74	34	1	2,70		19,9	0,8
IMJ-5b	30	1	1,54	*U. mediterranea*	6,9	0,8
FG-124	31	1	2,26		17,1	0,9
FG-119/121		**1**	**3,06**		**28,6**	**1,7**
FG-119/121		**1**	**2,52**		**20,9**	**1,5**
FG-103/104		1	1,94		12,6	1,0
FG-74	34	1	1,73		9,6	0,7
FG-39/40	36	1	1,63		8,1	0,8
FG-10/11		1	1,60		7,8	0,8

2.4. Seawater $\delta^{18}O$ Records Resulting of Paired Δ_{47}- $\delta^{18}O_c$ Data

Seawater $\delta^{18}O$ ($\delta^{18}O_{SW}$) reconstructions derived from paired Δ_{47}-$\delta^{18}O_C$ data are presented in Table 3.5 and Figure 3.2. We combined our Δ_{47}-derived temperature estimates with the corresponding $\delta^{18}O_C$ values of *U. mediterranea*, using the $^{18}O/^{16}O$ fractionation relationship of Kim and O'Neil (1997):

$$1000 \ln(\alpha_{cc/w}) = 18.03 \times 1000 / T - 32.17 \qquad (1)$$

Where T is temperature in ° Kelvin (K) and $\alpha_{cc/w}$ is the oxygen-18 fractionation factor between calcite and water: $\alpha_{cc/w} = (1 + \delta^{18}O_{C/VSMOW} / 1000) / (1 + \delta^{18}O_{SW/VSMOW} /1000)$ with $\delta^{18}O_{C/VSMOW}$ and $\delta^{18}O_{SW/VSMOW}$ corresponding to foraminiferal calcite and seawater, respectively, both relative to VSMOW.

Reconstructed bottom water (benthic) $\delta^{18}O_{SW}$ values range from 0.6 to 2.0‰ (VSMOW) with higher values during glacial periods than during interglacials. Within MIS 31 these values are relatively low (0.6 ± 0.6 ‰ (2SE) for FG-103/104 and 0.8 ± 0.6 ‰ (2SE) for FG-119/121), excepted at the end of MIS 31 (FG-124), with a $\delta^{18}O_{SW}$ increasing to 1.7 (± 0.6 ‰ 2SE).

Table 3.5: $\delta^{18}O_{SW}$ records derived from paired Δ_{47}-$\delta^{18}O_C$ in Uvigerina mediterranea, using the O-isotopic fractionation factor at equilibrium of Kim and O'Neil (1997), in red the interglacial period and in blue the glacial periods.

Samples	MIS	Species	T (°C)	SE	δ^{18}Oc (‰)	SE	δ^{18}Osw (‰)	SE
IMJ-5b	30	*U. mediterranea*	8,0	1,2	3,2	0,04	1,7	0,3
FG-124	31	*U. mediterranea*	13,8	1,5	1,9	0,03	1,7	0,3
FG-119/121	31	*U. mediterranea*	8,1	1,3	2,1	0,04	0,6	0,3
FG-104	31	*U. mediterranea*	7,1	1,2	2,6	0,03	0,8	0,3
FG-74	34	*U. mediterranea*	9,2	3,0	3,2	0,05	2,0	0,7
FG-39/40	36	*U. mediterranea*	6,7	1,8	3,5	0,03	1,7	0,4
FG-10/11	36	*U. mediterranea*	10,3	1,9	3,0	0,04	2,0	0,4

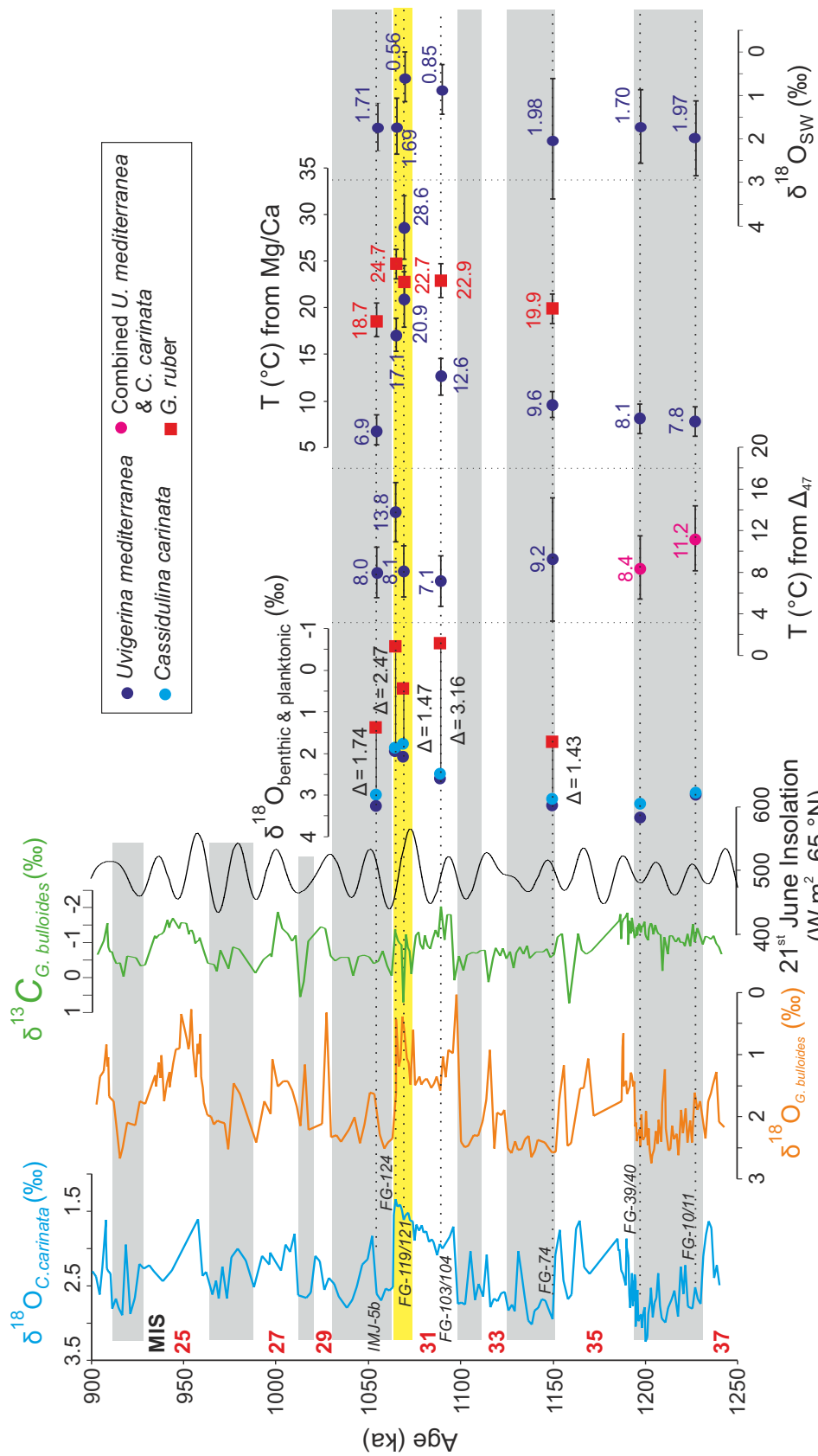

Figure 3.2: Synthesis of the main results for Interval A of MIS, with a comparison between benthic and planktonic $\delta^{18}O$, temperatures derived from Δ_{47} and Mg/Ca ratio and reconstituted $\delta^{18}O$ of the seawater (VSMOW) (all uncertainties are 2SE). The results are compared to $\delta^{18}O$ curve of benthic and planktonic foraminifera (from Brilli, 1998; Brilli et al., 2000; Ciaranfi et al., 2010), $\delta^{13}C$ obtained on G. bulloides (Brilli, 1998) and 21 June insolation at 65 °N.

3. DISCUSSION

3.1 Comparison of Clumped Isotope and Mg/Ca-derived Temperatures

Two different paleothermometers, Mg/Ca and Δ_{47}, were used to quantify reconstruct changes in sub-surface temperatures recorded by benthic foraminifera. Throughout the three glacials within Interval A of MJS, both thermometers yield very similar estimates (Figure 3.3). By contrast, during the interglacial MIS 31, Mg/Ca-derived temperatures are significantly higher than those derived from Δ_{47}. Sample FG-119/121 (MIS 31) offers the most extreme example, with unrealistic benthic Mg/Ca temperatures (28.6 ± 1.7 °C), which are warmer than the coeval SST values obtained on G. ruber (22.7 ± 0.9 °C; Figure 3.2).

Sample FG-119/121, was analysed twice because our initial measurement yielded a high concentration of iron. The concentrations of other elements (Al, K…) appear to be normal, which apparently ruled the possibility that this high iron concentration could be associated with insufficient removal of fine detrital material. Despite the low content of Mn, we re-analysed sample FG-119/121 with an additional leaching step to remove more efficiently potential Fe-oxides. In this second batch, the iron concentration is lower than the first run as are the other elements, such as Mn, Al, K..., usually associated with oxide and clay contaminants. Thus, we find it unlikely that the erroneously high Mg/Ca values observed for MIS 31 would be primarily due to Fe-oxide coating.

An alternative explanation would be the existence of diagenetic calcite overgrowth, which is known to be Mg-enriched relative to primary foraminiferal calcite (Boussetta et al., 2011; Sabbatini et al., 2011). If true, an early diagenetic process should affect both benthic and planktonic foraminifera, while our Mg/Ca-derived SST estimates do not seem to provide unrealistic values for MIS 31. Thus, the challenge is to identify a process preferably affecting benthic foraminifera by increasing their Mg content, and which would not strongly bias the clumped-isotope thermometer, nor the Mg/Ca content of planktonic foraminifers. For now, we remain unable to offer a satisfying explanation for this apparent Mg/Ca bias. To solve the problem, it is necessary to

conduct a specific study in order to understand the possible mechanisms of biomineralization and early diagenesis process, which is beyond the scope of this study.

Both thermometers yield similar values for sub-surface water temperature throughout Interval A, with the exception of this for sample FG-103/104 (Figure 3.3). As noted above, we found abnormal values of Mg/Ca-derived temperatures in sample FG-119/121. The same diagenetic process may also be at play in samples FG-124 and FG-103/104 (although with a smaller amplitude), explaining the slightly higher Mg/Ca-derived temperatures compared to clumped-derived temperatures. Thus we based the following paleoenvironmental interpretations on Δ_{47}-derived temperatures and consider Mg/Ca-derived temperatures only obtained on *G. ruber* for surface conditions.

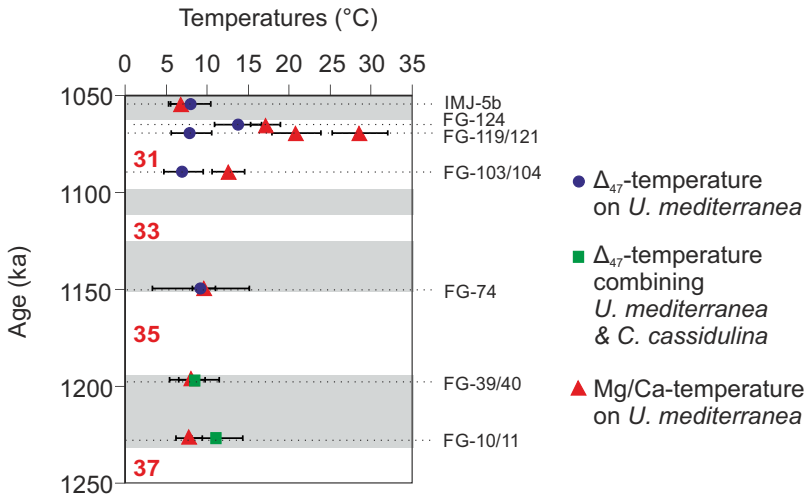

Figure 3.3: Comparison of Δ_{47} and Mg/Ca-derived temperatures on benthic foraminifera (uncertainties at 2 SE). Grey bands are the glacial periods, red numbers are the interglacial MIS.

3.2. Paleoenvironmental Changes During Glacial Periods

Paired Δ_{47}-$\delta^{18}O$ data obtained on *U. mediterranea* were used to reconstruct past $\delta^{18}O$ of sub-surface seawater. As expected, the glacial waters are oxygen-18-enriched relative to MIS 31 water, probably most likely reflecting larger continental ice sheets. The difference of $\delta^{18}O_c$ between the surface (planktonic foraminifera) and sub-surface (benthic foraminifera; $\Delta^{18}O_{c\,(p\,vs\,b)}$) can be used to address the vertical stratification (e.g. Zahn et al., 1991). Lower $\Delta^{18}O_{c\,(p\,vs\,b)}$ values are observed for glacial periods (MIS 34 and 30) compared to those for MIS 31, which argues for a more efficient vertical mixing

during glacials (Figure 3.2). This is related to higher values of glacial $\delta^{13}C_{planktonic}$ that could reflect an increase in surface productivity resulting from a more efficient upwelling of nutrient-enriched sub-surface waters (Figure 3.2; Brilli, 1998).

To the best of our knowledge, our results provide the first sub-surface temperature reconstruction for the three glacial periods (MIS36, 34 and 30) in the central Mediterranean Sea. Our Δ_{47}-derived temperature estimates are rather low ranging between 8 and 11.2 °C (Figure 3.2 and 3.3) in the three glacial periods. By contrast, modern temperature at ~ 100 m (thermocline) water-depth in the Gulf of Taranto is ~ 13 °C (Pinardi et al., 2016). The Mg/Ca-derived SSTs are ~ 19 °C for MIS 34 and MIS 30 (Figure 3.2), which is colder than the current, annually averaged temperature in the Gulf of Taranto is ~ 23 °C (Pinardi et al., 2016).

The MJS offers an excellent opportunity to compare sea and land environmental evolutions because of its proximity to the coast (Ciaranfi et al., 2001; D'Alessandro et al., 2003; Stefanelli, 2003). The reconstructions of land conditions are based on pollen assemblages and can be summarized by the use of the ratio between two groups of taxa: mesothermic and steppic taxa. This ratio reflects the climatic sensitivity of the continent, allowing to discriminate between warm-temperate (mesothermic dominance) and cold episodes (steppic dominance; Figure 3.4; Joannin et al., 2008). One of the most abundant local taxa is the mesophilous deciduous tree *Quercus*, which is also the most representative taxon of the mesothermic plants recorded through the Interval A (Joannin et al., 2008). This taxon suggests that warm-temperate periods are also characterized by a significant humidity (Rossignol-Strick and Paterne, 1999). Several warm/temperate and wet phases characterized by mesothermic element dominance are recorded during the interglacial periods through the Interval A, while the glacial periods are characterized by cold and dry climate with the dominance of steppic elements (Figure 3.4; Joannin et al., 2008). The Mg/Ca SST reconstructions from the beginning of MIS 34 record relatively warm conditions, coeval with warm land conditions drifting slowly to cooler conditions through the glacial period (Joannin et al., 2008). The high abundance of tropical-subtropical marine species (Figure 3.4) from previous study (Girone et al., 2013) also suggests warm conditions in surface waters (*G. ruber* and *G. tennellus*). Based on based on our Mg/Ca-derived SST, MIS 30 is marked by cooling SST compared to the previous warm MIS 31, which combined with abrupt decrease of

tropical-subtropical planktonic species indicates colder conditions (Figure 3.4; Girone et al., 2013). The mesothermic vs. steppic elements ratio also suggests cold and dry climate. Such cold/dry conditions on land may significantly reduce the river runoff, which is clearly evidenced by colder Mg/Ca-derived SST and saltier surface waters (as evidence by our high $\delta^{18}O_{SW}$ reconstruction), thus making the upper water column more prone to vertical mixing.

3.2 Paleoenvironmental Changes During the Super-Interglacial MIS 31

MIS 31 presents distinctive paleoenvironmental conditions compared to other interglacial periods of the Interval A as it seems to be particularly long with warm and wet conditions (Joannin et al., 2008; Girone et al., 2013; summarized in Figure 3.4). The age model used for Interval A (Maiorano et al., 2010) has set this MIS 31 bounding ages of about 1095 and 1064 ka, spanning two peaks of summer insolation. This interglacial climate is a combination of regional and global influences (Girone et al., 2013). Continental paleo-environmental data indicate warm and wet conditions (Joannin et al., 2008; Figure 3.4), consistent with warm surface waters as suggested by planktonic foraminifer assemblages (Girone et al., 2013; Figure 3.4). Our reconstructed Mg/Ca-SSTs imply warmer surface water than during glacial periods with the strongest warming episode taking place in the last part of MIS 31, during the low peak of $\delta^{18}O$. By contrast, our benthic Δ_{47}-derived temperatures suggest that, in most of MIS 31, sub-surface temperatures do not differ significantly from those reconstructed during glacial periods, except at the very end of MIS 31 where both estimated-SST and subsurface-derived temperature increase significantly. Based on multi-proxy data, we may divide MIS 31 into four main climatic intervals (Figure 3.5) that are described below.

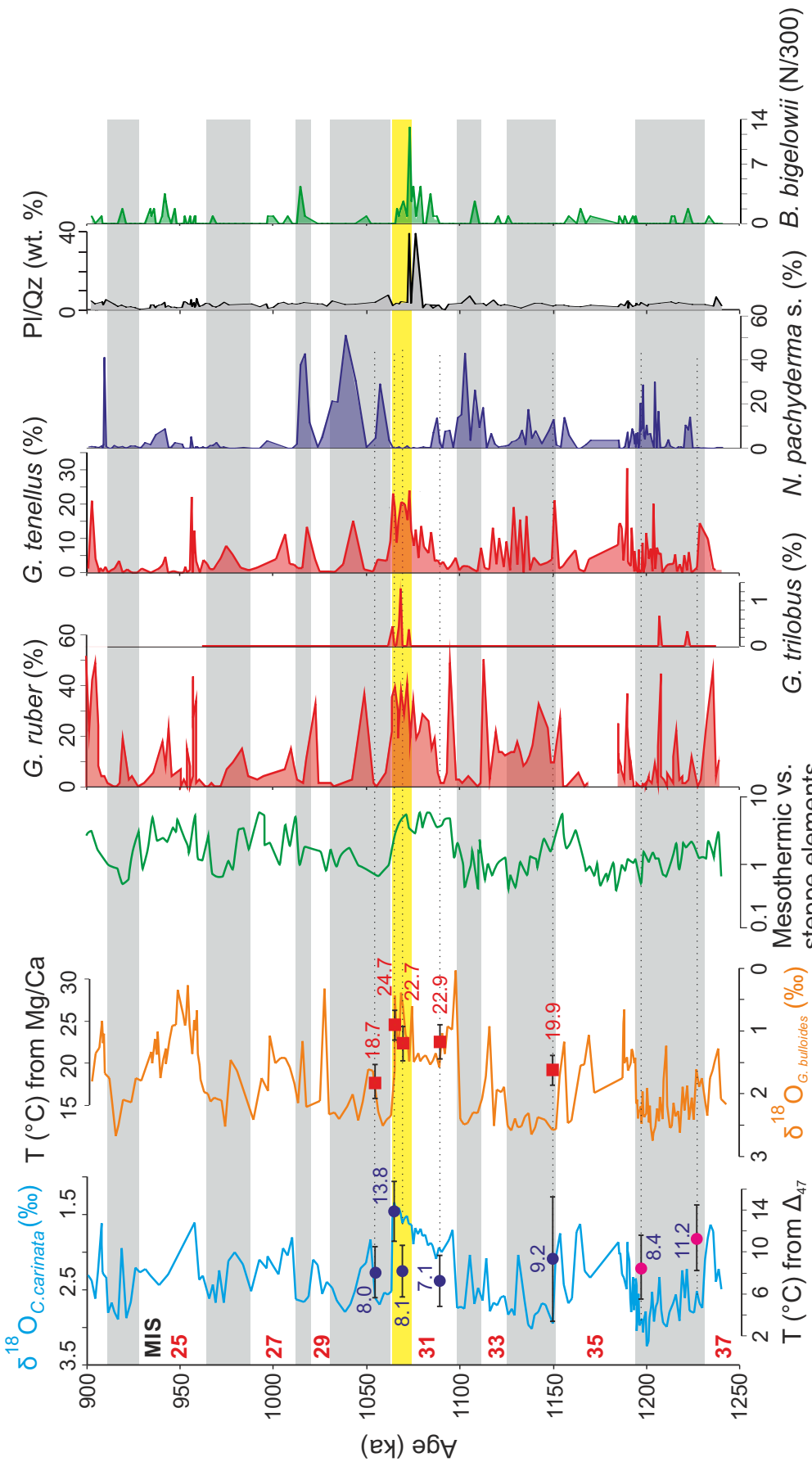

Figure 3.4: $\delta^{18}O$ curves of benthic and planktonic foraminifera through the Interval A of MJS (from Brilli et al., 1998; Brilli et al., 2000; Ciaranfi et al., 2010) with benthic temperature from Δ_{47} measurements and SST from Mg/Ca ratio, the ratio Mesothermic vs steppe elements (Joannin et al., 2008), calcareous planktonic abundance and plagioclase/quartz ratio (Girone et al., 2013). The grey bands correspond to glacials periods and the yellow to climatic optimum for MIS 31.

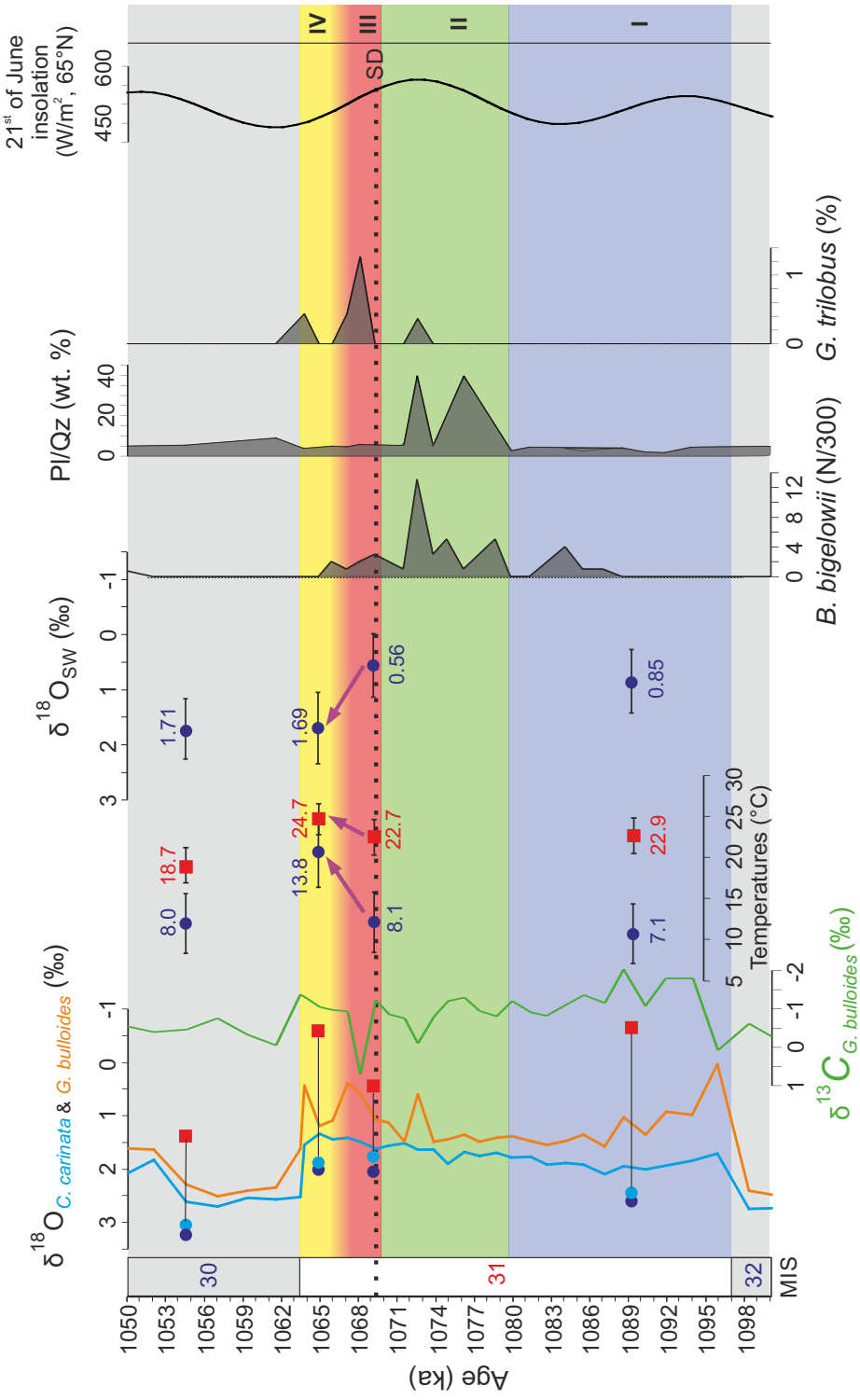

Figure 3.5: Zoom on MIS 31 with $\delta^{18}O$ curve of benthic and planktonic foraminifera (from Brilli, 1998; Brilli et al., 2000; Ciaranfi et al., 2010), our $\delta^{18}Oc$ between benthic and planktonic foraminifera, sub-surface and surface temperature, from Δ_{47} measurements and Mg/Ca ratio, abundance of B. bigelowii and ratios of plagioclase vs quartz (Girone et al., 2013) and summer and 21 June insolation at 65 °N. These data allow to define 4 intervals (I, II, III, IV). SD = sapropel i-100 (Lourens, 2004).

3.2.1. Interval I (from 1096 to 1080 ka)

The sub-surface reconstructed $\delta^{18}O_{SW}$ record yields a ~ 1 ‰ (± 0.3 ‰ 1SE) decrease relative to earlier glacials MIS 34 and 36 (Figures 3.2 and 3.5). On the other hand, the dominance of mesothermic taxa (Figure 3.2; Joannin et al., 2008) suggests that the beginning of MIS 31 is characterized by warm and wet climate on land. Furthermore, our large $\Delta^{18}O_{c\ (p\ VS\ b)}$ suggest a strong vertical stratification, which is likely associated with a weak surface productivity, as evidence by the low planktonic $\delta^{13}C$ (Figure 3.5). Our oxygen-18-depleted sub-surface $\delta^{18}O_{SW}$ reconstructions thus potentially reflect a combination of a global signal associated to the decay of continental ice sheets and the impact of increased precipitation on the salinity of sub-surface water in the central Mediterranean area. Yet, the strong stratification revealed by the high, vertical $\delta^{18}O$ gradient suggests that the impact of increased precipitation on sub-surface $\delta^{18}O_{SW}$ in MJS is not local, and is most probably laterally advected through thermocline circulation.

Planktonic foraminiferal assemblages (Figure 3.4) indicate a progressive increase of tropical-subtropical species (*Globigerinoides ruber* and *G. tenellus*) with a concomitant significant decrease of abundance of subpolar species *Neogloboquadrina pachyderma* s. (s. = left coiling; Girone et al., 2013). This previous observations together with our new SST reconstruction from Mg/Ca, imply warming surface water conditions during the onset of MIS 31 (Tolderlund, and Bé, 1971; Kucera and Kennett, 2002). Otherwise, cold sub-surface water Δ_{47}-derived temperature are recorded which remain indistinguishable from the glacial baseline defined above (Figure 3.2). The near glacial temperature of sub-surface waters might be explained by the relative temperature invariance of water masses advected to the Gulf of Taranto and the strong stratification of the water column, which prevents vertical mixing and the downward influence of warmer surface waters.

3.2.2. Interval II (from 1080 to 1069 ka)

Due to the time constraints inherent to a 3-year PhD and the time-consuming demands of foraminifer picking and cleaning and clumped-isotope analyses, for now we do not provide have any measurements to report for Interval II. Below, we briefly

summarize the data available from previous studies to depict the evolution of this interval.

One of the main features of this interval is the occurrence of the marine nannofossil *Braarudosphaera bigelowii* indicative of low-salinity environments in coastal waters (Siesser, 1992). This species presents a relatively low abundance through Interval A (Figure 3.4), except during MIS 31, which shows a peak at ~ 1072 ka (Figure 3.5). This abundance peak implies hyposaline surface-water conditions. The coeval increase of plagioclase/quartz ratio (Pl/Qz; Figure 3.5) suggests an enhanced erosion and transport of siliciclastic material from the Gorgoglione Formation (Dell'Anna et al., 1988; Cavalcante et al., 2007). This provides an independent argument in favour of the increased runoff scenario to explain the low surface water salinity. Furthermore, the low values of planktonic $\delta^{13}C$ (Brilli, 1998) suggest low surface productivity probably due to a strong vertical stratification, which is evidenced by the high relative abundance of the deep leaving coccolith species *Florisphaera profunda* (Girone et al., 2013). The prolonged warm and wet climate phase (e.g. mesothermic taxa dominance, Figure 3.2) during MIS 31 may have strengthened regional precipitation, near MJS, resulting in the deposition of poorly evolved detrital material (high plagioclase/quartz ratio) and increasing freshwater runoffs fluxes, favouring the stratification of the upper surface water. This paleoenvironmental conditions might thus constitute an environmental setting favourable to the deposition of a sapropel-like that could be synchronous to the sapropel event in insolation cycle 100 (i-100), dated at 1069 ka (Lourens, 2004).

However, the peak of freshwater input is dated at 1072 ka according to age model of Maiorano et al. (2010), while the sapropel is dated at 1070 ka by Lourens (2004). If we are correct in assuming that these two episodes are synchronous, than the small difference in age could be simply explained by the limitation of the astronomically-derived age model. The age model of MJS is based on astronomical tuning using a 3 ka time lag between each identified *sapropel-like* layer and minima of precession (following recommendations of Lourens, 2004). As the sapropel-like event i-100 was not highlighted in MJS in previous studies (e.g. Girone et al., 2013), the 3 ka time lag were not applied in building the age-model of MIS 31 (Ciaranfi et al., 2010; Maiorano et al., 2010; Petrosino et al., 2015). Furthermore, the typical uncertainty associated with astronomical tuning is ± 6 ka between 3 and 1 Ma (Lisiecki and Raymo, 2005). Within

the limits of astronomical age-model, we can hypothesize that the observed sapropel-like event in MJS may be analogue to the i-100 sapropel.

The absence of visual evidence of this sapropel-like event on field is puzzling, but is might be explained by inadequate sampling resolution, by post-depositional oxidation of organic matter or by regional settings. In the context of shallow environment, the mechanisms allowing the deposition of sapropel may be different than those associated to classical sapropel identified in deeper Mediterranean waters

3.2.3. Interval III (from 1069 to ? ka)

Approximately 3 ka after the increase of detrital sediment input and freshwater runoff (as suggested by the increase in % of *B. bigelowii*), our results hint at a phase of efficient vertical convection in the water column, as evidenced by low $\Delta^{18}O_{c\,(p\,VS\,b)}$ and increase of $\delta^{13}C$ values, which is likely associated to a reduction of freshwater input (drop in *B. bigelowii*; Figure 3.5). However, the reconstructed benthic Δ_{47}-derived temperature remains cold sub-surface waters, similar to the glacial temperatures, as well as our reconstituted subsurface $\delta^{18}O_{SW}$. Girone et al. (2013), based on planktonic foraminifer assemblages (i.e. the abundance of *G. trilobus*; Fig. 3.5), suggested that this interval should correspond to the beginning of the climatic optimum, which starts around 1075 ka. However, our reconstructed Mg/Ca-SST does not show any significant increase compared to estimated Mg/Ca-SST from Interval I. Because vertical mixing affects rapidly the upper water column, we do not expect to observe a conservation of glacial-like, cold subsurface conditions after the onset of Interval II (see above). However, we can hypothesize a combination of vertical mixing and a control to a large extent by lateral advection of water masses as part of thermocline circulation in the central Mediterranean basin.

3.2.4. Interval IV (from ? to 1064 ka)

The chronological boundary between Interval III and Interval IV is poorly constrained due to the low resolution of our dataset. However, both Intervals present different paleoenvironmental conditions.

Interval IV appears to have seen more stratified upper surface waters than Interval III, as evidenced by the higher $\Delta^{18}O_{c\ (p\ VS\ b)}$. As already seen above, this stronger stratification seems to be associated with a drop in surface productivity, as suggested by low planktonic $\delta^{13}C$ values (Figure 3.5). In spite of this, benthic Δ_{47}-derived temperatures increase significantly compared to Interval III (Figure 3.5). Similarly, our reconstructed subsurface $\delta^{18}O_{SW}$ reconstructions increase compared to the previous intervals becoming similar to the values recorded for glacial periods. If our suggestion of a strong vertical stratification is correct, such an increase of benthic temperatures and $\delta^{18}O_{SW}$ cannot be directly related to vertical advection of surface waters and, again, suggests that bottom water conditions are chiefly controlled by lateral advection of sub-surface waters (warmer and enriched $\delta^{18}O_{SW}$ during this interval IV). Further work will be necessary to test this hypothesis.

In the previous study of Girone et al. (2013), the climatic optimum was estimated to have occurred between 1075 and 1065 ka, based on the SST maximum deduced from planktonic foraminifer abundance (Figure 3.4) and the sharp peak of *G. trilobus* percentage associated with light $\delta^{18}O$ values (Figure 3.5). This climatic optimum was also described by a prolonged humid phase, responsible for intensified river freshwater runoff and hyposaline surface waters (Girone et al., 2013). Here, we find evidence for seawater temperature maximum at ~ 1065, with warm Mg/Ca-derived SST recorded during Interval IV (Figure 3.4). Due to the low resolution of our dataset, however, we are not able to refine precisely the chronological limits of such a climatic optimum. Yet, as stated above, sample FG119-121 (at about ~ 1069 ka) shows a similar SST than what we reconstructed for interval III. This suggests that the climatic optimum was probably shorter than suggested by Girone et al. (2013), starting only after 1069 ka instead of 1075 ka.

4. Conclusions

The first-order environmental changes throughout MJS-Interval A reflect the interaction between global processes controlled by orbital parameters and regional climatic processes. Using clumped isotopes, we constrain a "baseline glacial temperature" around 9 °C for local sub-surface waters and high subsurface $\delta^{18}O_{SW}$.

The geochemical data through MIS 31, which have been be divided into four intervals, make possible to show importance of sub-surface lateral advections and runoff, and quantify the climatic optimum warming that occurs at the end of this interglacial.

The figure 3.6 offers a schematic representation of main oceanographic and climatic features corresponding to the four intervals of MIS 31. Interval I is characterized by strong vertical stratification potentially due to lateral advection of cold sub-surface water. The sub-surface temperatures (Δ_{47}-derived temperatures) are cold, similar to those we reconstructed from several glacial periods of interval A, while the SST (Mg/Ca-SST) increases compared to glacial periods. This surface temperature increase is associated with the increase of tropical-subtropical species (Figure 3.6-I). Our reconstructed sub-surface $\delta^{18}O_{SW}$ are low compared to the glacial periods.

The following Interval II is characterized also by a strong stratification of the water column (as suggested by the high relative of *F. profunda*), accompanied by the deposition of more poorly altered detrital material (stronger plagioclase/quartz ratio) suggesting increased precipitation and more active runoff from land (Figure 3.6-II; Girone et al., 2013). This paleoenvironmental conditions might favour deposition of a sapropel-like that could be synchronous to the sapropel event i-100 (Lourens, 2004).

The hypothetical deposition of a sapropel-like event would be followed by an episode of vertical mixing (in Interval III), which is characterized, however, by cold sub-surface temperatures and low $\delta^{18}O_{SW}$, potentially resulting to lateral advection (Figure 3.6-III). We are not able to provide hypothesis about processes occurring during this Interval. This last Interval could be associated to the climatic optimum with high-reconstructed SST and possible lateral advection of warm sub-surface water (Figure 3.6-IV).

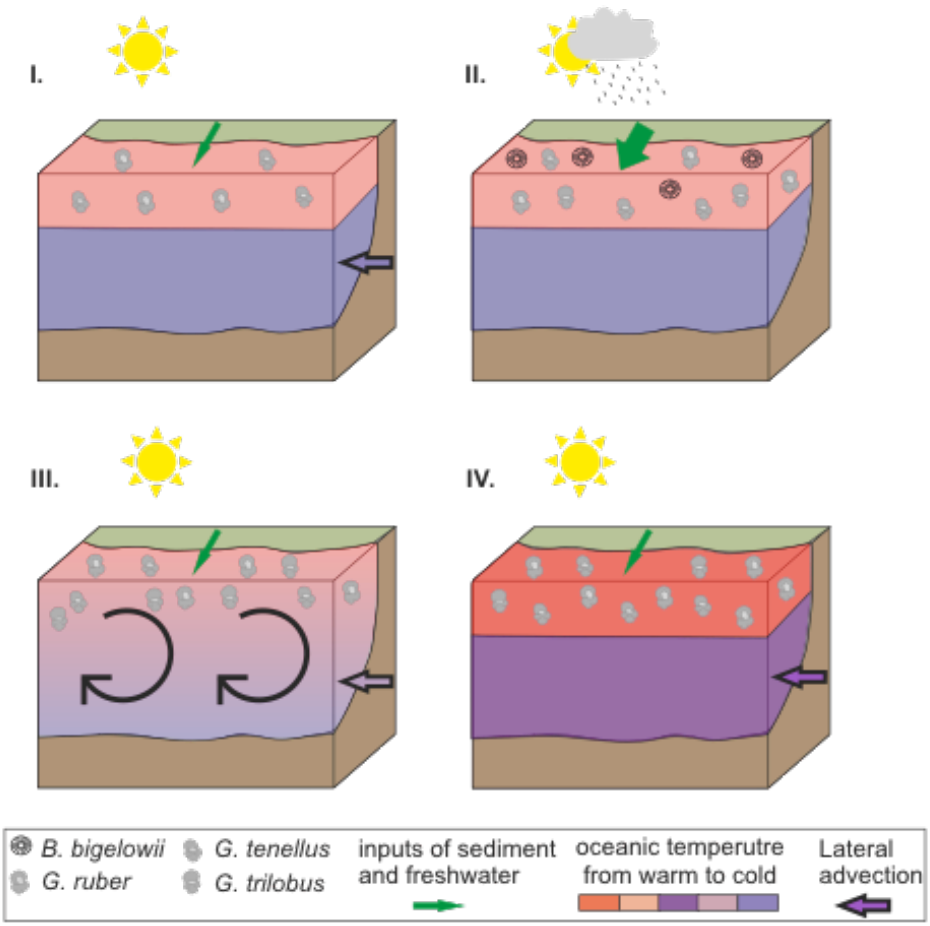

Figure 3.6: Schematic paleoceanographic changes over the 4 intervals of MIS 31 at MJS

Although study is still in progress, the work done so far offers a good illustration that clumped isotope analyses are particularly valuable when paired with higher-resolution but less quantitative proxies, allowing us to test qualitatively different hypotheses. Our results should be complemented by additional analyses, particularly during MIS 32 and high resolution of SST reconstructions to test the hypotheses of depositional sapropel-like event and improve the chronological constraints on the climatic optimum.

We also observe good agreement between Mg/Ca and Δ_{47}-derived temperatures on benthic foraminifera during the glacial periods, but here the Mg/Ca proxy seems to suffer from bias during the interglacials periods; this issue is still under question.

Chapter 3

INTERVAL B: DEGLACIATION PROCESSES AND HYDROLOGICAL CHANGES IN THE MEDITERRANEAN SEA FROM MIS 22 TO MIS 19 AS REVEALED BY CLUMPED-ISOTOPE, Mg/Ca, AND $\delta^{18}O$ DATA FROM FORAMINIFERA

1. INTRODUCTION

Quantitative paleoenvironmental records are of major importance for understanding and modelling past climates, and anticipating future global changes. Understanding the present "interglacial" period comes in large part from the study of past interglacials, each of which corresponds to a different combination of orbital configuration and greenhouse gas concentrations (e.g. Tzedakis et al. 2012; Yin and Berger, 2012). Over the last 1 Ma, MIS 5e (e.g. Kukla et al., 1997, 2002; Rioual et al., 2001), MIS 11 (e.g. Berger and Loutre, 2002; Tzedakis et al., 2010; Candy et al., 2014) and MIS 19 (e.g. Pol et al., 2010; Tzedakis et al. 2012; Giaccio et al., 2015) are generally considered as the best analogues for the Holocene. Several studies have focused on MIS 19 because its onset coincided with a maximum of obliquity in phase with a minimum of precession, as is the case for the Holocene (e.g. Pol et al., 2010; Tzedakis et al. 2012; Giaccio et al., 2015).

Changes in the terrestrial and marine realms across the Early Mid-Pleistocene Transition (EMPT; 1.4 to 0.4 Ma; Head and Gibbard, 2015) have been documented with continuous and high resolution records for MIS 19 and especially for the MIS 19 *sensu stricto* (i.e. MIS 19c hereafter; e.g. Tzedakis et al., 2012; Giaccio et al., 2015; Sánchez-Goñi et al., 2016) in Antarctic (EPICA Dome C; e.g. Pol et al., 2010), in North Atlantic (e.g. Ferretti et al., 2015) or on the Iberian margin (e.g. Hodell et al., 2015; Sánchez-Goñi et al., 2016). These records depict a climatic optimum (within MIS 19c) followed by a progressive degradation and the occurrence of millennial-scale climatic oscillations (MIS 19b and MIS 19a) leading to the glacial MIS 18 (e.g. Tzedakis et al., 2012; Giaccio et al.,

2015; Sánchez-Goñi et al., 2016). This climatic degradation coincides with an increase of continental ice cover explaining the progressive drop of sea level (Elderfield et al., 2012) and was amplified by decreasing insolation and global atmospheric CO_2 levels (Lüthi et al., 2008). The rapid millennial oscillations could reflect the influence of ice-sheet dynamics on North Atlantic oceanic circulation and atmospheric processes (Tzedakis et al., 2012; Giaccio et al., 2015), and/or periodic intensification of tropical moisture transport toward the Mediterranean region (Sánchez-Goñi et al., 2016).

Studying the climate evolution of the Mediterranean basin across MIS19 (an analogue of Holocene in terms of orbital forcing) is likely to provide useful insights into past climate evolution of a particularly sensitive area which is under a complex interplay of tropical and polar influences, and help decipher what could have been its future climatic evolution without man-induced perturbation. For such a study, a particularly interesting archive is the emerged marine sedimentary series of the Montalbano Jonico Section (MJS hereafter; Maiorano et al., 2016; Simon et al., 2017; Nomade et al., in review). MJS studies of MIS 19 benefit from strong chronological constraints based on $^{40}Ar/^{40}Ar$ ages of the tephra layer V4 and $^{10}Be/^{9}Be$ data at the Brunhes-Matuyama transition. Furthermore, we may take advantage of marine-terrestrial interaction reconstructions, based on paired marine microfossils and pollen assemblages (Aiello et al., 2015; Bertini et al., 2015; Marino et al., 2015; Maiorano et al., 2016), and on recent high-resolution $\delta^{18}O$, $\delta^{13}C$ and alkenone records from benthic foraminifera (Nomade et al., in review; Tim Herbert, Brown University, unpublished data), both of which provide information on the climatic variability throughout MIS 19. The MJS also offers detailed records of marine microfossils, pollen assemblages, and foraminifer stable isotopes covering the interval from MIS 20 to MIS 18. Also available are relative paleodepth reconstructions based on ostracod assemblages (Aiello et al., 2015), which suggest that water depths varied from 100 to 200 m, consistent with the regression of high latitude ice caps during the MIS 20-19 deglaciation, as recorded by decreasing $\delta^{18}O$ on benthic foraminifera ($\delta^{18}O_b$ hereafter; Nomade et al., in review).

The deglaciation between MIS 20 and MIS 19, corresponding to the Termination IX, is characterized by the advection of cold surface waters that may come from North Atlantic, which occur during a "Heinrich-like event" followed by a potential "Bølling-Allerød-like event" and a "Younger Dryas-like event" (Maiorano et al., 2016). During MIS

19c, continental and marine records point to the existence of a shallow-water analogue to a sapropel event (also known as "red interval", Maiorano et al., 2016; "ghost sapropel", Emeis et al., 2000; or "i-cycle 74", Lourens, 2004). This hypothesis is supported by enhanced stratification of the upper water column and/or increased productivity as suggested by a negative excursion in benthic foraminifera $\delta^{13}C$ (Nomade et al., in review), and low oxygen content at the sediment-water interface (Stefanelli, 2003). The continental (Bertini et al., 2015) and marine records also hint at an increase in sea surface temperatures (SST) and climate amelioration on land coeval with a rapid increase in annual precipitation, both of which are favourable conditions for sapropel formation (Maiorano et al., 2016; Nomade et al., in review). The MIS 19c is associated with warm and wet conditions, probably combined with warm surface waters (Bertini et al., 2015; Maiorano et al., 2016 and Nomade et al., in review).

A large part of the above interpretations rests, however, upon an incomplete dataset and, in particular, we lack carefully absolute estimates of seawater temperatures and $\delta^{18}O$ (noted $\delta^{18}O_{SW}$ hereafter), which would allow to document changes of regional precipitation. The only available marine paleotemperatures when I started this PhD work were those derived from planktonic foraminifer assemblages. However, due to the local context during MIS19 (i.e. shallow marginal environment, near the coastline), it is likely that changes in planktonic assemblages were strongly affected by other factors than temperature (e.g. productivity, salinity). In order to better understand the climatic variations through the mid-Pleistocene in MJS, I reconstructed SSTs using Mg/Ca ratio in planktonic foraminifer and will compare them with a high-resolution SST record from alkenone measurements performed by T. Herbert (Brown University, unpublished data). I reconstructed bottom water temperatures with clumped isotope measurements (Δ_{47} hereafter) on benthic foraminifera. I also estimate past $\delta^{18}O_{SW}$ values based on paired Δ_{47}-$\delta^{18}O$ results. Furthermore, I reconstructed bottom water temperatures from benthic foraminifer Mg/Ca analyses, which makes it possible to compare clumped isotope measurements in benthic foraminifera.

In this study, I investigate changes in the marine realm across two couple of glacial-interglacial periods in MJS: MIS 22 - MIS 21 and MIS 20 – MIS 19, corresponding respectively to Termination X and IX.

2. RESULTS

2.1. $\delta^{18}O$ Measurements

$\delta^{18}O_{VPDB}$ and $\delta^{13}C_{VPDB}$ measurements were performed on 3 species of benthic (*Cassidulina carinata, Elphidium crispum* and *Uvigerina mediterranea*) and one species of planktonic foraminifera (*Globigerinoides ruber*), except for sample DFJ-27/29 (transition between MIS 22 and MIS 21) because *G. ruber* specimens were not present in sufficient quantity (Figure 3.7). All the results are summarized in Table 3.6. We calculated the absolute $\delta^{18}O$ difference ($\Delta^{18}O_c$) between each species (Table 3.7).

Table 3.6: $\delta^{18}O_{VPDB}$ and $\delta^{13}C_{VPDB}$ values for each sample within each species.

Sample	Species	MIS	N	$\delta^{13}C_{VPDB}$	SE	$\delta^{18}O_{VPDB}$	SE
NC-271	*C. carinata*	19	4	-0,78	0,02	1,64	0,03
NC-199		20	4	-0,37	0,02	3,18	0,03
NC-172		20	1	-0,47	0,03	3,59	0,05
DFJ-72		20	1	-0,45	0,03	3,50	0,05
DFJ-57		21	4	-0,69	0,02	1,95	0,03
DFJ-27/29		22/21	1	-0,41	0,03	2,72	0,05
DFJ-23		22	2	-0,52	0,02	3,00	0,04
DFJ-20		22	4	-0,64	0,02	2,68	0,03
NC-199	*E. crispum*	20	4	0,91	0,02	3,00	0,03
NC-271	*G. ruber*	19	4	0,82	0,02	-0,80	0,03
NC-199		20	4	0,71	0,02	1,10	0,03
NC-172		20	1	0,76	0,03	1,97	0,05
DFJ-72		20	1	0,96	0,03	1,94	0,05
DFJ-57		21	4	0,77	0,02	-0,16	0,03
DFJ-23		22	1	0,54	0,03	0,65	0,05
DFJ-20		22	2	0,65	0,02	1,00	0,04
NC-271	*U. mediterranea*	19	4	-0,44	0,02	1,77	0,03
NC-199		20	2	-0,17	0,02	3,43	0,04
NC-172		20	2	-0,23	0,02	3,61	0,04
DFJ-72		20	2	-0,18	0,02	3,43	0,04
DFJ-57		21	4	-0,33	0,02	2,14	0,03
DFJ-27/29		22/21	2	-0,33	0,02	2,72	0,04
DFJ-23		22	2	-0,30	0,02	3,32	0,04
DFJ-20		22	2	-0,52	0,02	2,83	0,04

The variability of $\Delta^{18}O_c$ between the three species of benthic foraminifera ranges between 0 and 0.43 ‰ (Table 3.6), which is larger than the internal analytical uncertainty (± 0.05 ‰). The discrepancy could result to some extent from the potential effect of bioturbation, which may have mixed vertically foraminifers that had grown under slightly different conditions. Yet, the good replication of measurements suggests homogeneous samples. This observed differences could also result from so-called "vital" effects. However, *Uvigerina spp.* and *Cassidulina ssp.* are believed to precipitate following the equation of Kim and O'Neil (1997), according to Grossman (1987), and the ecology of *E. crispum* is poorly documented. The important variability and the low number of intervals studied here do not allow us to quantify potential systematic species-specific oxygen-18 biases between *C. carinata*, *U. mediterranea* and *E. crispum*.

The difference of $\delta^{18}O_c$ ($\Delta^{18}O_{c\ (p\ VS\ b)}$ hereafter) values between planktonic and benthic species for glacial periods (MIS 22 and 20) varies between a minimum of ~ 1.49 and maximum of ~ 1.83 ‰, except for sample DFJ-23 (MIS 22), which yields ~ 2.5 ‰, a value comparable to those for interglacial periods. The two interglacials (MIS 21 and 19) show much higher differences between planktonic and benthic species, ranging from 2.08 to 2.57 ‰.

Table 3.7: Difference (absolute values in ‰, PDB) of $\delta^{18}O$ between each species, in red interglacial periods, in blue the glacial periods and in black the transitional samples between two MIS.

Samples	MIS	$\Delta^{18}O$ (‰) *C. carinata – U. mediterranea*	$\Delta^{18}O$ (‰) *E. crispum – C. carinata*	$\Delta^{18}O$ (‰) *E. crispum – U. mediterranea*	$\Delta^{18}O$ (‰) *E. crispum – G. ruber*	$\Delta^{18}O$ (‰) *U. mediterranea - G. ruber*	$\Delta^{18}O$ (‰) *C. carinata – G. ruber*
NC-271	19	0.13				2.57	2.44
NC-199	20/19	0.25	0.18	0.43	1.9	2.33	2.08
NC-172	20	0.02				1.64	1.62
DFJ-72	20	0.07				1.49	1.56
DFJ-57	21	0.19				2.30	2.11
DFJ-27/29	22/21	0.00					
DFJ-23	22	0.32				2.67	2.35
DFJ-20	22	0.15				1.83	1.68

2.2. Temperatures Estimated from Clumped-isotope Measurements

Δ_{47} results and the corresponding reconstructed temperatures for Interval B are shown in Table 3.8 and Figure 3.7. The three benthic species (*U. mediterranea*, *C. carinata* and *E. crispum*) are shallow infaunal or epifaunal species (Altenbach et al., 1999; Fontanier et al., 2002; Murray, 2006), which can live on different substrates, such as sand or algae (Murray, 1963). Taking advantage of the absence of species-specific effect in clumped isotope (Tripati et al., 2010; Grauel et al., 2013; Peral et al., 2018), we may combine these three benthic species together, assuming that they is no significant temperature difference between the water-sediment interface (epifaunal species habitat) and the first centimetres of sediments were the infaunal species are found.

Table 3.8: $\delta^{18}O_{VPDB}$, $\delta^{13}C_{VPDB}$, Δ_{47} values and temperatures derived from Δ_{47} values for each sample within each species

Sample	Species	MIS	N	$\delta^{13}C_{VPDB}$ (‰)	SE	$\delta^{18}O_{VPDB}$ (‰)	SE	Δ_{47}	SE	T (°C)	SE
NC-271	*C. carrinata*	19	5	-0,68	0,03	1,96	0,06	0,713	0,007	13,3	2,0
	U. mediterranea	19	8	-0,48	0,02	2,00	0,05	0,705	0,006	15,7	1,6
	Combined	19	13	-0,55	0,02	1,98	0,04	0,708	0,004	14,8	1,3
NC-199	*C. carrinata*	20/19	6	-0,29	0,02	3,57	0,05	0,718	0,006	11,8	1,8
	Elphidium crispum	20/19	27	0,95	0,01	3,53	0,02	0,717	0,003	12,2	0,9
	Combined	20/19	33	0,78	0,01	3,54	0,02	0,717	0,003	12,1	0,8
NC-172	*C. carrinata*	20	4	-0,62	0,01	3,75	0,04	0,736	0,007	7,1	1,8
DFJ-72	*C. carrinata*	20	4	-0,59	0,01	3,50	0,04	0,731	0,007	8,4	1,9
DFJ-57	*C. carrinata*	21	3	-0,59	0,03	2,35	0,06	0,693	0,007	19,2	2,1
	U. mediterranea	21	5	-0,51	0,03	2,33	0,06	0,710	0,007	14,1	2,0
	Combined	21	10	-0,55	0,02	2,34	0,04	0,701	0,005	16,6	1,5
DFJ-27/29	*U. mediterranea*	22/21	4	-0,43	0,01	2,94	0,04	0,730	0,007	8,6	1,9
DFJ-23	*C. carrinata*	22	4	-0,63	0,01	3,21	0,04	0,727	0,007	9,4	1,9
DFJ-20	*C. carrinata*	22	5	-0,63	0,03	2,94	0,08	0,717	0,009	12,1	2,6

* Combined: mix of *C. carinata* and *U. mediterranea* or mix of *C. carinata* and *E. crispum*

The reconstructed glacial temperatures range from 7.1 °C (± 3.6 °C, 2SE) to 12.1 °C (± 4.2 °C, 2SE), while interglacial temperatures are warmer, with a lower variability (16.6 ± 3 °C 2SE for MIS 21 and 14.8 ± 2.6 °C 2SE for MIS 19). It is worth

noting that the two samples (DFJ-27-29 and NC-172) respectively corresponding to the transitions between MIS 22 – MIS 21 and between MIS 20 – MIS 19, yield significantly different temperatures, respectively 8.6 ± 3.8 °C and 12.1 ± 1.6 °C (2SE).

2.3. Temperatures from Mg/Ca Ratio

In addition to clumped-isotope-derived temperatures, we also performed Mg/Ca ratio measurements to estimate past temperatures and compare the two approaches on a single set of samples. All the analyses (Table 3.9) were performed on the benthic foraminifera *U. mediterranea* and the planktonic foraminifera - *G. ruber*, when there was enough material (Figure 3.7) and *G. ruber* and *G. bulloides* during the MIS 19c at a higher resolution (Figure 3.10).

Mg/Ca-reconstructed bottom water temperatures are in the range 9.7–18.2 °C. Surprisingly, the glacial periods yield warmer bottom temperatures than the interglacials: the glacial MIS 22 samples yield anomalously high bottom temperatures of 18.2 ± 2.6 °C (2SE) and 17.2 ± 2.4 °C (2SE), and MIS 20 bottom temperatures are 14.1 and 14.7 °C (± 2.2 °C, 2SE). The transitional, deglaciation samples record temperatures comparable to those derived from Δ_{47}, with 9.7 °C (± 1.8 °C, 2SE) for MIS22-21 and 14.7 °C (± 2.2 °C, 2SE) for MIS20-19. Bottom water temperatures for interglacial periods are indistinguishable, within analytical uncertainties, from Δ_{47}-derived reconstructions, with 11.9 °C (± 1.4 °C, 2SE) for MIS 21 and 12.9 °C (± 1.6 °C, 2SE) for MIS 19 (Table 3.9; Figure 3.7).

By contrast, Mg/Ca-SST throughout Interval B vary much less, ranging between 20.8 ± 1.8 °C (2SE) and 23.1 ± 1.6 °C (2SE), except for samples NC-199 (transition from MIS 20 and 19), with a SST of 27.8 °C (± 1.8 °C 2SE) and sample NC-271 (MIS 19) with a SST of 25.4 °C (± 1.6 °C 2SE; Table 3.9; Figure 3.7).

The high-resolution record of Mg/Ca-SST, covering MIS 19, displays warmer temperatures for *G. ruber* than for *G. bulloides* (Table 3.9; Figure 3.10).

Table 3.9: Mg/Ca values and temperatures derived from Mg/Ca values for each samples and species

Samples	MIS	N	Mg/Ca	Species	T (°C)	SE
XII-6	19	1	3,33	*G. bulloides*	18,3	0,6
XII-7		1	3,22		18,0	0,6
XIII-2		1	3,32		18,3	0,6
XIII-4		2	3,98		20,0	0,7
XII-6	19	1	3,59	G. ruber	23,1	0,9
NC-271		1	4,41		25,4	0,8
NC-199	20/19	1	2,93		20,8	0,8
NC-172	20	1	5,46		27,8	0,9
DFJ-72		1	2,94		20,9	0,9
DFJ-57	21	1	3,59		23,1	0,8
DFJ-23	22	1	3,35		22,3	0,9
DFJ-20		1	2,94		20,9	0,8
NC-271	19	1	1,96	*U. mediterranea*	12,9	0,8
NC-199	20/19	1	2,09		14,7	1,1
NC-172	20	1	2,09		14,7	1,1
DFJ-72		1	2,04		14,1	1,1
DFJ-57	21	1	1,89		11,9	0,7
DFJ-27/29	22/21	1	1,74		9,7	0,9
DFJ-23	22	1	2,26		17,2	1,2
DFJ-20		1	2,33		18,2	1,3

2.4. Temperatures from Alkenone Measurements

T. Herbert produced a high-resolution (40-cm intervals corresponding to 0.4-1.3 ka) record of alkenone temperature estimates using the $U^{K'}_{37}$ calibration of Müller et al. (1998). The alkenone-derived SSTs range from 12 °C to 22 °C (Figure 3.11), showing relatively warm temperatures (≥ 19 °C) during the end of MIS 20, followed by a rapid decrease to ~ 16 °C during the deglaciation. The end of the deglaciation is marked by a negative shift of SST to ~ 14 °C before an increase until ~ 20 °C.

2.5. Paired Δ_{47} - $\delta^{18}O_C$ Reconstructions of Seawater $\delta^{18}O$

The seawater $\delta^{18}O$ records ($\delta^{18}O_{SW}$, hereafter) derived from paired Δ_{47}-$\delta^{18}O_C$ data are presented in Table 3.7 and Figure 3.7. We paired the temperatures estimated from Δ_{47}

measurements and the respective $\delta^{18}O_C$ values of each benthic species, using the synthetic calcite calibration of Kim and O'Neil (1997) to constrain past $\delta^{18}O_{SW}$ values. When it was possible, we have used the species-combined Δ_{47}-temperatures (in bold; Table 3.7). Reconstructed $\delta^{18}O_{SW}$ ranges from 1.35 ‰ (± 0.8 ‰ 2SE) to 2.6 ‰ (± 0.4 ‰ 2SE). Considering the analytical uncertainties, there is no evidence of significant changes between glacial and interglacial periods.

Table 3.10: Reconstructed $\delta^{18}O_{SW}$ (1SE) from paired Δ_{47}-$\delta^{18}O_C$ in Uvigerina mediterranea, Cassidulina carinata and Elphidium crispum, using the calibration of Kim and O'Neil (1997). In red the interglacial periods, in blue the glacial periods and in black the transitional ones. The bold temperatures are combined Δ_{47}-temperatures.

Samples	Species	MIS	T (°C)	SE	δ^{18}Oc (‰)	SE	δ^{18}Osw (‰)	SE
NC-271	*C. carinata*	19	**14,8**	**1,3**	1,64	0,03	1,64	0,3
NC-271	*U. mediterranea*		**14,8**	**1,3**	1,77	0,03	1,77	0,3
NC-199	*C. carinata*	20/19	**12,1**	**0,8**	3,18	0,03	2,59	0,2
NC-199	*E. crispum*		**12,1**	**0,8**	3,00	0,03	2,41	0,2
DFJ-72	*C. carinata*	20	8,4	1,9	3,50	0,05	2,08	0,4
NC-172	*C. carinata*		7,1	1,8	3,59	0,05	1,87	0,4
DFJ-57	*C. carinata*	21	**16,6**	**1,5**	1,95	0,03	2,35	0,3
DFJ-57	*U. mediterranea*		**16,6**	**1,5**	2,14	0,03	2,54	0,3
DFJ-27/29	*U. mediterranea*	22/21	8,6	1,9	2,72	0,04	1,35	0,4
DFJ-20	*C. carinata*	22	12,1	2,6	2,68	0,03	2,09	0,6
DFJ-23	*C. carinata*		9,4	1,9	3,00	0,04	1,81	0,4

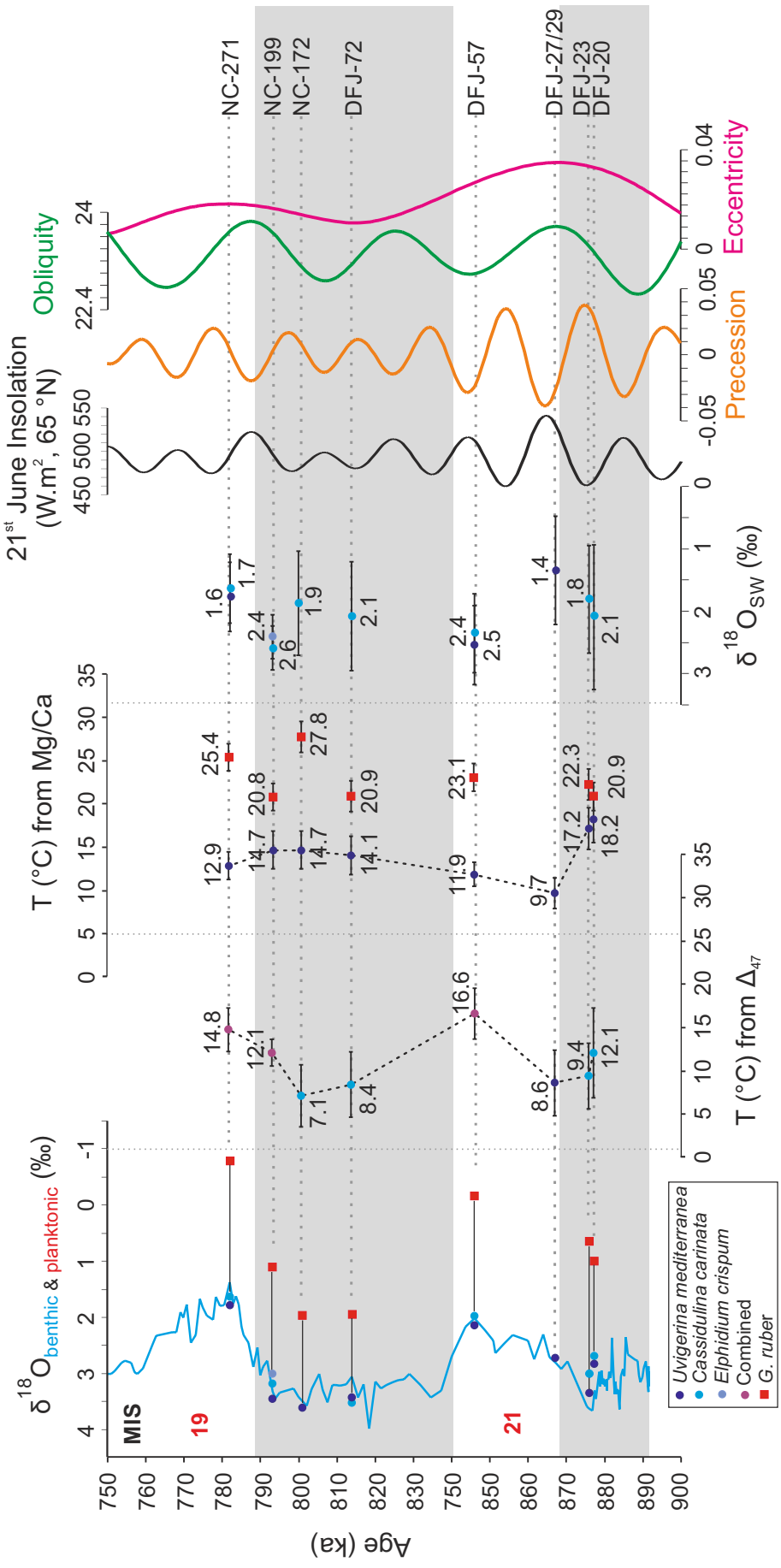

Figure 3.7: Main results of this study for Interval B of MJS, including comparison between benthic and planktonic δ18O, temperatures derived from Δ_{47} and Mg/Ca ratio and reconstituted $\delta^{18}O$ of the seawater (all uncertainties are 2SE). The results are compared to $\delta^{18}O$ curve of benthic foraminifera (from Brilli, 1998; Brilli et al., 2000 and Ciaranfi et al., 2010) and insolation (21st of June at 65 °N), precession, obliquity and eccentricity. The chronology was taken from Marino et al. (2015).

3. DISCUSSION

3.1. How Well do the Two Paleothermometers Agree With Each Other?

In this section, we compare sub-surface water temperature estimates derived from clumped isotopes and from Mg/Ca ratios (Figure 3.8) obtained on benthic foraminifers. The Mg/Ca temperatures do not show significant changes between glacial and interglacial periods. By contrast, Δ_{47} temperatures display larger variations seemingly correlated with benthic foraminifer $\delta^{18}O$ oscillations. The Mg/Ca temperatures are higher than the Δ_{47}-derived ones during glacial periods, and lower during interglacial periods. During the glacial MIS 22, the Mg/Ca-temperatures are 18.2 ± 1.2 °C and 17.2 ± 1.3 °C (2SE), whereas modern temperatures at 100 m depth in the Gulf of Taranto are about 13 °C (Pinardi et al., 2016). We thus suspect that Mg/Ca-temperatures are biased in some way. Factors, which may lead to abnormally high Mg/Ca ratio in foraminifera, are:

- High salinity: contrary to clumped isotope measurements (Grauel et al., 2013; Peral et al., 2018), Mg/Ca could be affected by salinity (Mathien-Blard and Bassinot, 2009). As far as surface waters are concerned, however, reconstructed Mg/Ca-SST performed on planktonic foraminifera in MJS show realistic temperatures, suggesting that there is no strong salinity bias. Regarding a potential salinity effect on benthic Mg/Ca-temperature, the uncertainties on our $\delta^{18}O_{SW}$ values reconstructed from paired Δ_{47}-$\delta^{18}O$ remain too large for us to test this hypothesis.

- Fe-oxides coating: our ICP-MS data show relatively high values of iron that could be due to detrital material or oxide contamination. However, the concentrations of other elements such as Mn, Al, K… appear to be low, ruling out a strong detrital or oxide contamination. As relatively high values of Fe are detected in our standards too, we cannot out rule out that we faced some contamination problem during the ICP-MS measurement procedure.

- Mg-rich calcite coating: because seawater is richer in Mg than Ca, the deposition of small amount of overgrowth calcite on foraminifer shells, during early diagenesis

(with Mg content reaching several %) can lead to erroneously Mg/Ca values. This effect explains anomalously high Mg/Ca values observed in the Mediterranean area on foraminifers retrieved from core tops (Boussetta et al., 2011; Sabbatini et al., 2011). However, these diagenetic processes should affect both benthic and planktonic species, while our Mg/Ca-derived temperature estimates do not seem to provide unrealistic SST values for the glacial periods.

- Seawater composition: The Mg/Ca-thermometer is based on the assumption that Mg/Ca in seawater is constant and invariant through time. This assumption is likely to be true at glacial/interglacial timescales over the Pleistocene in open oceans due to the long residence time of Mg and Ca. However, we cannot be certain that seawater Mg/Ca remained constant over the margins of the Gulf of Taranto due to potential Mg and Ca contribution from nearby river runoffs.
- Dissolved CO_2-carbonate system: It has been shown that Mg/Ca of benthic foraminifers may also be affected by bottom water pH or $[CO_3^{2-}]$ (Elderfield et al., 2006; Raitzsch et al., 2008). We cannot rule out the possibility that discrepancies observed between benthic Mg/Ca- temperatures and Δ_{47}-temperatures reflect changes in the chemistry of bottom waters.

In conclusion, as in the earlier Part 3 Chapter 2, we observe "anomalously high" Mg/Ca-temperatures but we are not able to confidently conclude about the mechanisms that could explain such high Mg/Ca values. Additional data such as MEB observations (coupled with electron microprobe) or XRD analyses will be necessary to conclude about potential diagenetic imprints and the presence of oxide coating or Mg-rich calcite. Past changes in $[CO_3^{2-}]$ and/or pH reconstructed from B/Ca ratios or $\delta^{11}B$ would be mandatory to reconstruct past changes in water saturation relative to calcite and confirm the possibility of calcite precipitation during early diagenesis and/or the impact of bottom water chemistry on benthic foraminifer Mg/Ca. Finally, it is notable that the Mg/Ca-temperatures in MJS appear anomalously high during the interglacial periods of interval A, while for Interval B, it is during glacial periods that anomalously high values are observed. In the rest of this study, we favour the use of subsurface Δ_{47}-temperatures for paleoceanographic interpretations.

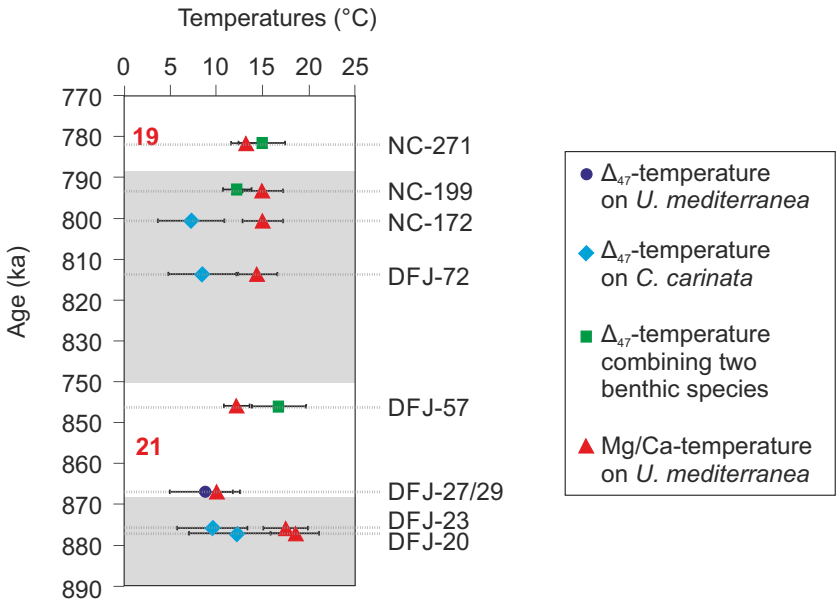

Figure 3.8: Comparison of Δ_{47} and Mg/Ca-temperatures (2SE) performed on benthic foraminifera through the Interval B of MJS

3.2. Paleoceanographic Changes for the Glacial-Interglacial Couple MIS 22 and MIS 21

While MIS 20 and MIS 19 are well documented and have been studied in detail recently (Maiorano et al., 2016, Nomade et al., in review), this is not the case for stages 21 and 22, for which we have much less data. Below, we document paleoenvironmental changes during glacial MIS 22 and interglacial MIS 21 and we attempt to gain some insight into the local deglaciation scenario by improving the interpretation of the $\delta^{18}O$ record. We thus reconstruct the variability of sub-surface water temperatures and $\delta^{18}O_{SW}$ based on benthic records using Δ_{47} thermometer, where, for surface waters, we used Mg/Ca-SST. Although our sampling resolution is low, the strategic choice of sample location in the sedimentary series of MJS provides strong constraints. Over the MIS 22-21 interval, we selected two samples during the glacial (high $\delta^{18}O_b$), one sample during the interglacial period (low $\delta^{18}O_b$) and one sample during the transition between MIS 22 and MIS 21 (noted MIS 22-21 hereafter).

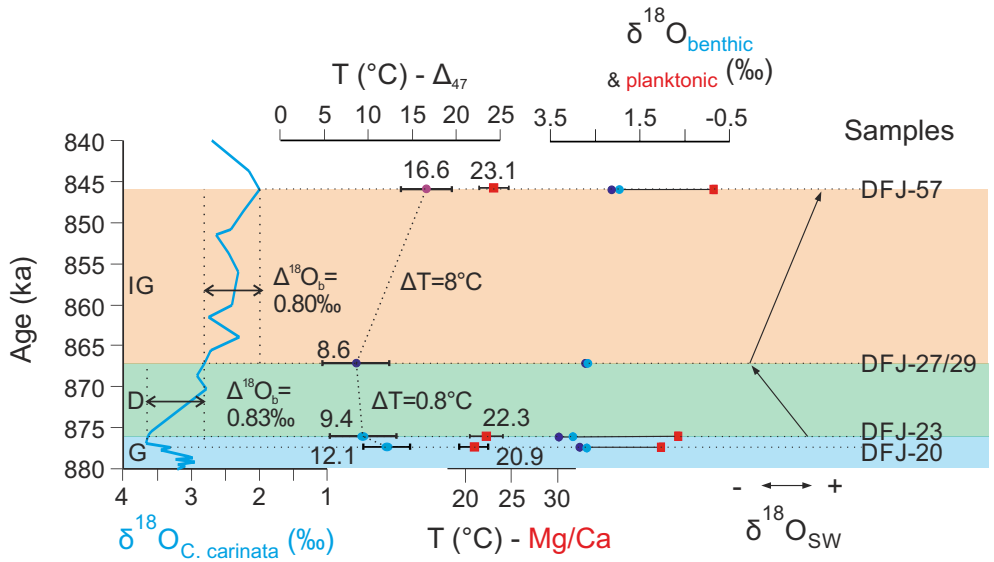

Figure 3.9: Zoom on the $\delta^{18}O_{benthic}$ data and temperatures from clumped isotope measurements for MIS 22 and MIS 21 couple, with $\Delta^{18}O_{benthic}$, ΔT of sub-surface temperatures, Mg/Ca-SST and $\Delta^{18}O_{c\,(p\ VS\ b)}$. The blue band refers to the glacial MIS 22 (G), green to the deglaciation (D) and orange to the interglacial MIS 21 (IG). Dots light bleu are C. carinata, drack bleu U. mediterranea and purple is combination of two benthic species. Square red are G. ruber.

3.2.1. Glacial MIS 22

The two samples from MIS 22 provide different pieces of information. Firstly, the older sample (DFJ-20) is characterized by a relatively warm sub-surface Δ_{47}-temperature comparable to today (~ 13 °C; Pinardi et al., 2016), by mild Mg/Ca-SST of 20.9 °C while the current surface temperature is ~ 24 °C (Pinardi et al., 2016; Figure 3.9). The $\Delta^{18}O_{c\,(p\ VS\ b)}$ can be used as vertical stratification proxy (Zahn et al., 1991), with high difference being associated to strong stratification of the water column. For this stratigraphic level, the $\Delta^{18}O_{c\,(p\ VS\ b)}$ is small, suggesting a mixing phase (Figure 3.9). Then, the second sample (DFJ-23) records a slightly colder sub-surface Δ_{47}-temperature (9.4 ± 1.9 °C) and higher Mg/Ca-SST (22.3 ± 0.9 °C; Figure 3.9). $\Delta^{18}O_{c\,(p\ VS\ b)}$ is high, implying upper surface water stratification (Figure 3.9).

Changes in sub-surface temperature reconstructed from benthic Δ_{47} appears coherent with vertical mixing history reconstructed from $\Delta^{18}O_{c\,(p\ VS\ b)}$, with lower bottom temperature when stratification is stronger and higher bottom temperature associated

to more active vertical mixing. Yet, one cannot rule out the possibility that sub-surface temperature history is also controlled to some extent by lateral thermocline water advection, with cold water of North Atlantic or Adriatic origins (Pinardi et al., 2016).

3.2.2. Deglaciation MIS 22/21

The deglaciation between MIS 22 and MIS 21 is marked by the last glacial sample (DFJ-23) and the "transitional" sample (DFJ-27/29). This deglaciation is characterized by a - 0.83 ‰ drop of $\delta^{18}O_{C.\ carinata}$ (Figure 3.9). Assuming no change of $\delta^{18}O_{SW}$, such a change in $\delta^{18}O_C$ of *C. carinata* would require a change of + 3.2 °C. However, clumped isotope sub-surface water temperatures indicate less than 1 °C variation (Figure 3.9) through this interval, leading to the conclusion of a significant decrease of sub-surface $\delta^{18}O_{SW}$. This could be the result of different mechanisms acting at a global scale, (changes in ice-sheet volume), and/or at a more local scale.

This $\delta^{18}O_{SW}$ decrease calls for an input of 0^{18}-depleted waters. Part of that signal could be related to the input of freshwater coming from land into the basin. However, this hypothesis would imply a strong vertical stratification of the water column, which would be coherent with the preservation of relatively cold, sub-surface temperatures but not with the change of sub-surface $\delta^{18}O_{SW}$ (Figure 3.7). Due to absence of *G. ruber* in the sample DFJ-27/29, we are not able to describe surface water changes during this interval.

Oxygen-18 depletion could also be due to lateral incursion of cold water from the North Atlantic. This hypothesis may be supported by high percentage of IRD recorded (Venz and Hodell, 1999) during Termination X in ODP 982 (North Atlantic). The cold Atlantic water resulting from the melting of continental ice-sheet could enter through the Gibraltar strait into the Mediterranean Sea. A second possible source of freshwater could be waters from Adriatic origin (Pinardi et al., 2016) that could gain their low $\delta^{18}O_{SW}$ signature from the melting of Alpine glaciers.

3.2.3. Interglacial MIS 21

The $\delta^{18}O_{benthic}$ for interglacial MIS 21 changes of 0.8 ‰ similar to the deglaciation, which is equivalent to a temperature change of ~ 3.3 °C if considering constant $\delta^{18}O_{SW}$ (Figure 3.9). However, the sub-surface temperature from clumped isotope measurements shows a more larger difference of about ~ 8 °C (Figure 3.9). This implies an increase of $\delta^{18}O_{SW}$, by about 1‰ (Figure 3.7). Because we expect a decrease of $\delta^{18}O_{SW}$ due to the decrease of ice-sheet volume during interglacial period, this recorded increase of $\delta^{18}O_{SW}$ may be associated to local processes rather than global signal.

The $\delta^{18}O_{SW}$ rise could be explained by important evaporation and/or a strongly reduced runoff. These hypotheses are supported by recorded warm Mg/Ca-SST concomitant to higher $\delta^{18}O_b$ (Figure 3.9). Furthermore, pollen assemblages suggest the alternation of warm/wet and cold/dry phases (Bertini et al., 2015) resulting from changes in the evaporation/precipitation budget. Because of our low-resolution data, we average the $\delta^{18}O_{SW}$ signal over the different periods of warm/wet and cold/dry conditions. Furthermore, our $\Delta^{18}O_{c\,(p\ VS\ b)}$ is recorded as high gradient at the optimum of MIS 21, suggesting vertical stratification. This stratification episode, which is concomitant to a warm and wet phase (Bertini et al., 2015), suggests that the stratification of the water column is likely due to input of freshwater coming from land.

3.3. Paleoceanographic Changes for the Glacial-Interglacial Couple MIS 20 and MIS 19

MIS 20 and MIS 19 in the MJS have already been the focus of several studies (Aiello et al., 2015; Bertini et al., 2015; Toti, 2015; Maiorano et al., 2016; Nomade et al., in review). The late MIS 20 is characterized by cold and dry climatic conditions on land associated with high abundance of polar-subpolar marine species (Bertini et al., 2015; Maiorano et al., 2016). We have selected 3 samples: two during the MIS 20 (DFJ-72 and NC-172) and one at the end of glacial MIS 20 (NC-199; Figure 3.10). We also selected two samples, which bracket the deglaciation (NC-271; Figure 3.10) associated with Termination IX. This deglaciation is characterized by two events, which could be

described respectively as (1) a Heinrich-like event possibly followed by a Bølling-Allerød-like event then by a Younger Dryas-like event (Maiorano et al., 2016), and (2) as a sapropel-like event marking the onset of the MIS 19c climate optimum (Maiorano et al., 2016; Nomade et al., in review). In the next section, I discuss these paleoenvironmental changes based on sub-surface Δ_{47}-derived temperatures, $\delta^{18}O_{SW}$ reconstructions, and SST reconstructions derived from alkenone and Mg/Ca measurements, in order to quantify temperature variations and to test the existing hypotheses regarding MIS 20 and MIS 19.

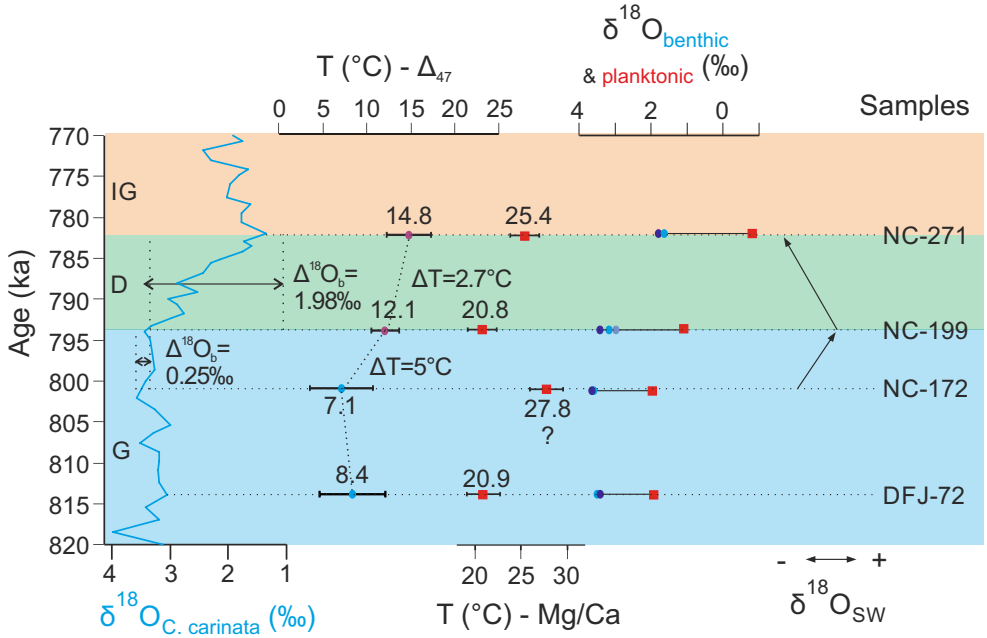

Figure 3.10: Zoom on the $\delta^{18}O_{benthic}$ data and temperatures from clumped isotope measurements for MIS 20 and MIS 19 couple, with $\Delta^{18}O_{benthic}$, ΔT of sub-surface temperatures, Mg/Ca-SST and $\Delta^{18}O_{c\ (p\ VS\ b)}$. The blue band refers to the glacial MIS 20 (G), green to the deglaciation (D) and orange to the interglacial MIS 19 (IG). Dots light bleu are C. carinata, blue-grey E. crispum, drack bleu U. mediterranea and purple is combination of two benthic species. Square red are G. ruber.

3.3.1. Glacial MIS 20

Glacial MIS 20 is characterized by cold sub-surface Δ_{47}-temperatures and Mg/Ca-SST (excepted for samples NC-172 which yields unrealistic reconstructed SST values

(see part 4.1 for potential explanation of Mg/Ca-biases) and good vertical mixing (as evidenced by our low gradient of $\Delta^{18}O_{c\,(p\,VS\,b)}$; Figure 3.10). These observations, combined to the constant high value of $\delta^{18}O_b$ (Figure 3.10) suggest that the climatic conditions over MIS 20 remained relatively cold and stable.

The late MIS 20 (between NC-172 and NC-199) is corresponds to a change in $\delta^{18}O_{benthic}$ value of -0.25 ‰ (Figure 3.10), equivalent to a temperature increase of ~ 1 °C, assuming constant $\delta^{18}O_{SW}$. However, bottom water temperatures derived from Δ_{47} increase by ~ 5 °C (Figure 3.10), implying that $\delta^{18}O_b$ reflects the combined effects of this temperature change and an increase of $\delta^{18}O_{SW}$ in the order of ~ 1 ‰. However, SSTs derived from our Mg/Ca and the alkenone imply cold and constant surface water (Figure 3.11), consistant with SST reconstructed from foraminiferal and nannofossils assemblages (PC1 nannofossil and foraminifera) and with high abundance of cold species *N. pachyderma* s. (Figure 3.11-A; Maiorano et al., 2016). The decrease of temperature gradient between subsurface (Δ_{47}-temperature) and surface (Mg/Ca-SST) is associated to a high $\Delta^{18}O_{c\,(p\,VS\,b)}$, which we have used so far to characterize a strong water stratification (Figure 3.10). Such a odd combination of warmer sub-surface temperatures and strong stratification, associated with the increase of $\delta^{18}O_{SW}$, may suggest that thermocline hydrography is, once again, chiefly dominated by lateral advection, which brings warmer sub-surface water at the end of MIS 20.

3.3.2. Deglaciation MIS 20/19

The deglaciation is marked by a $\Delta^{18}O_b$ value of 2 ‰, equivalent to 8 °C of temperature change while the Δ of temperatures derived from clumped isotope is only 2.7 °C (Figure 3.10). Here, the $\delta^{18}O_{benthic}$ signal therefore primarily reflects a decrease of $\delta^{18}O_{SW}$, likely corresponding to a combination of global climatic signal and regional processes. Our results confirm the hypothesis advanced by Nomade et al. (in review). This decrease of $\delta^{18}O_{SW}$ is likely due to a combination of change in ice volume and enhancement of runoff.

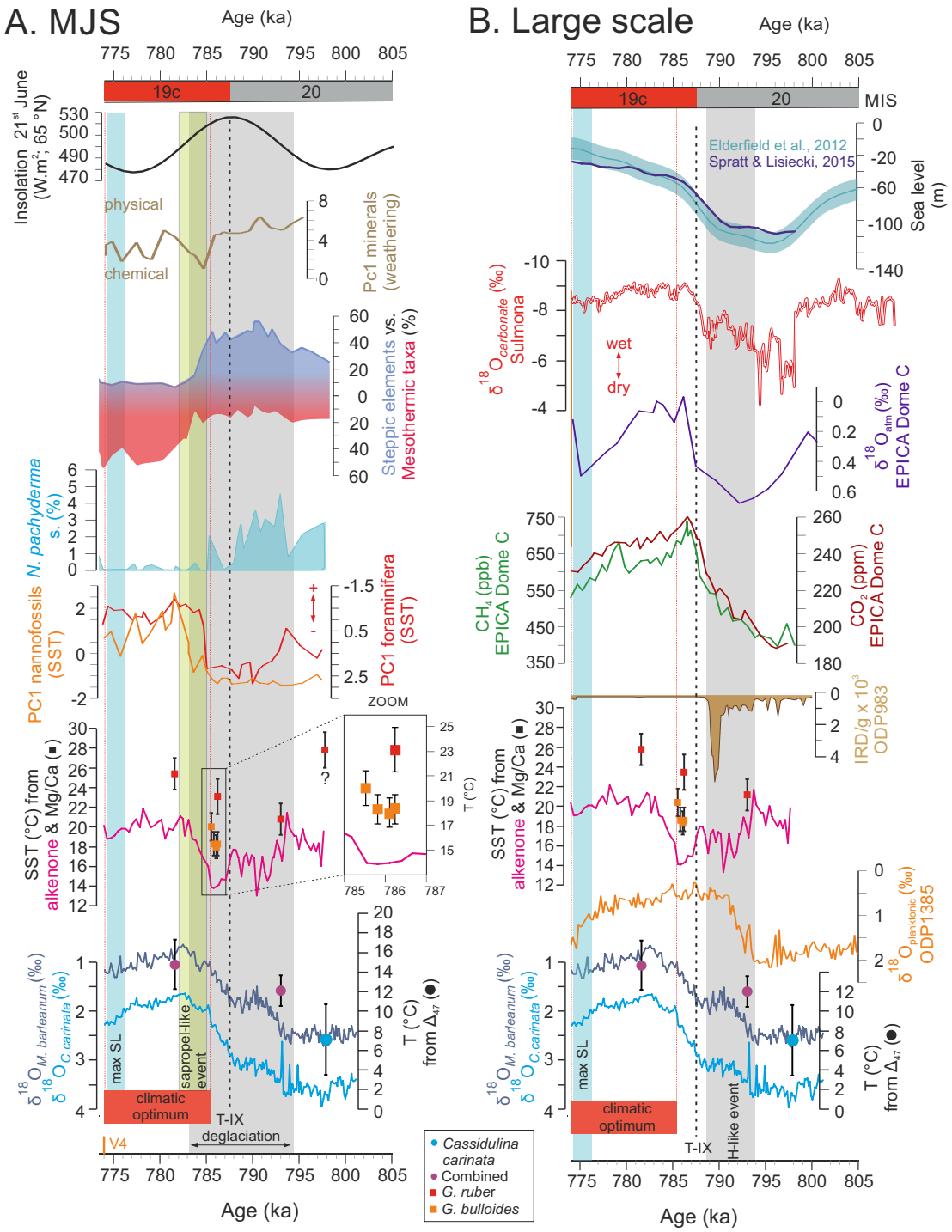

Figure 3.11: Paleoenvironmental data from late MIS 20 to MIS 19c with subsurface Δ_{47}-temperatures, SST from alkenones (T. Herbert) and Mg/Ca measurements, compared to A. MJS high-resolution $\delta^{13}C$ and $\delta^{18}O_{benthic}$ (Nomade et al., in review), PC1 curve of mineralogical data and of foraminifera and nannofossils, percentage of N. pachyderma s. (Maiorano et al., 2016), the mesothermic and steppic taxa (Bertini et al., 2015), and B. larger scale data EPICA Dome C data (CH_4 from Loulergue et al., 2008; CO2 from Lüthi et al., 2015 and $\delta^{18}O_{atm}$ from Extier et al., 2018), IRD data of ODP983 (Kleiven et al., 2011), $\delta^{18}O_{planktonic}$ and log(Ca/Ti) from ODP1385 (Hodell et al., 2015; Sánchez-Goñi et al., 2016), $\delta^{18}O_{carbonate}$ from Sulmona (Giaccio et al., 2015), sea level change (Elderfield et al., 2012; Spratt and Lisiecki, 2015) and insolation at 21st of June (65 °N).

3.3.2.1. Until Termination IX

The first part of this deglaciation (extending until Termination IX in Figure 3.11, according to Nomade et al., in review) appears to have seen a short-term decrease of SSTs (alkenones-SST; Figure 3.11). This observation is in agreement with principal component analysis (PC hereafter) on calcareous planktonic and nonnofossils assemblages and dynocyst assemblage studies (Maiorano et al., 2016; Figure 3.11-A). Such a short-duration drop in SST could be caused by cold polar-subpolar water incursion into the Mediterranean Sea coming from North Atlantic (Maiorano et al., 2016). The incursion of polar-subpolar water from North Atlantic into the Mediterranean Sea appears to be coeval (considering the uncertainties of respective age models) with IRD discharge in North Atlantic. High IRD discharges are recorded at the site ODP 983 (Figure 3.11; Kleiven et al., 2011), and ODP 980 (Venz and Hodell, 1999) and associated to a Heinrich-like event. Furthermore, on the Iberian margin (ODP U1385), a recent study presents SST reconstructions based on planktonic foraminiferal assemblages (Martin-Garcia et al., in review). During the deglaciation, the SST decrease while the percentage of North Atlantic Current species increases, was interpreted as resulting from an interruption of the warm Azore Current advection to site U1385 (Martin-Garcia et al., in review).

On-land climatic conditions during this deglaciation, pollen assemblages (Bertini et al., 2015; Toti, 2015), show the presence of steppic pollen elements (Figure 3.11-A) implying cold and dry conditions favourable to open landscapes and facilitating the physical erosion of carbonate bedrock, consistent with weathering indicator results from mineralogical PC (Figure 3.11-A; Maiorano et al., 2016). Moreover, at a larger scale, EPICA Dome C records low CO_2 implying relatively cold conditions (Lüthi et al., 2008), and low CH_4 and $\delta^{18}O_{atm}$ (Loulergue et al., 2008; Extier et al., 2018), consistent with dry conditions (Figure 3.11-B). These interpretations are also supported by findings frm the Sulmona paleolake located in Italy (Giaccio et al., 2015), which recorded dry conditions, as evidenced by low $\delta^{18}O_{carbonate}$ values of the bulk carbonate (Giaccio et al., 2015; Figure 3.11-B). This observation favours the hypothesis of lateral advection of cold and ^{18}O-

depleted surface waters coming from North Atlantic rather than enhancement of runoff to explain the decrease of $\delta^{18}O_{SW}$.

3.3.2.2. Until inception of MIS 19c

The second part of the deglaciation at MJS (until the inception of MIS 19c; associated with Termination IX) sees a reduction in polar-subpolar planktonic foraminifer species (e.g., *N. pachyderma* s.; Figure 3.11-A) and an increase in tropical species (*G. inflata*, *O. universa*, *S. murabilis/hyperacanthus*) with a rapid reoccurrence of "cold" species at ~ 785 ka (Maiorano et al., 2016). Surprinsingly, the SST reconstructions from foraminifer and nannofossils PC analyses (Maiorano et al., 2016; Figure 3.11-A) show an abrupt increase of SST, whereas alkenone record a rapid negative shift of SST (Figure 3.11). We thus performed Mg/Ca measurement on *G. bulloides* and *G. ruber* where enough material could be found. Our results show systematically higher *G. ruber* SSTs than using *G. bulloides*, which could be explained by a difference of living depth (*G. bulloides* is known to calcify at greater depths in the water column than *G. ruber*, which lives at the surface) and/or of seasonality. Moreover, Mg/Ca-SSTs from *G. ruber* are warmer alkenone-derived SST. Again, this could reflect a depth effect, as coccoliths usually bloom deeper in the water column (within the upper thermocline or the lower mixed-layer, enriched in nutrients) or a difference in seasonality of calcification. In spite of this systematic offset, the decrease in SST is consistent between the two proxies (Figure 3.11-Zoom).

During this cold episode at 785 ka, Maiorano et al. (2016) noticed the presence of the dynocyst *N. labyrinthus*, commonly used as a tracer of the Younger Dryas in the western Mediterranean Sea during the last deglaciation (e.g. Rouis-Zargouni et al., 2012). These authors interpret, therefore, the short-lived increase in tropical planktonic species as resulting from a Bølling-Allerød-like interstadial and the subsequent cooling of surface waters as a Younger Dryas-like event. However, the dynocyst *N. labyrinthus* has been also found in post- and pre-sapropelic assemblage during the last deglaciation in Eastern Mediterranean (Ionian and Levantine Basin; Zonneveld, 1995).

An alternative hypothesis could explain this cold episode, which is an input of freshwater coming from land. The wetter conditions implied by the Sulmona record of

$\delta^{18}O_{carbonate}$ is interpreted as weak evapotranspiration during this period (Giaccio et al., 2015; Figure 3.11-B) in the central Mediterranean region. High concentrations of atmospheric CH_4 (also from EPICA Dome C) are thought to result from high humidity in tropical areas, and suggest strong monsoons during this period (Figure 3.11-B). A local increase in precipitation would tend to strengthen chemical weathering (PC1 minerals; Figure 3.11-A) and result in a large input of freshwater into the sea, decreasing SST values (alkenone and Mg/Ca-SST; Figure 3.11). As this cold SST episode is followed by a sapropel-like event (analogue to the "red interval", Maiorano et al., 2016 or "ghost sapropel", Emeis et al., 2000 or i-cycle 74, Lourens, 2004), the hypothesis of freshwater input has therefore to be considered. However, the pollen assemblage recorded at MJS suggests cold and dry conditions on land, concomitant to this decrease of SST (Figure 3.11-A), which is in contradiction with potential higher precipitation. To better constrain the mechanisms that occur during this period, high-resolution pollen records are required.

3.3.3. Interglacial MIS 19

Due to the time constraints inherent to a 3-year PhD and the time consuming task of picking, cleaning and measuring benthic foraminifers for clumped-isotopes, we do not provide yet any results for MIS 19. Below, we briefly summarize the data available from previous studies.

MIS 19c is defined by a climatic optimum as the period spanning from the beginning of the sapropel-like event to the establishment of maximum of sea level (Figure 3.11; Nomade et al., in review). Marine (planktonic taxa) and terrestrial (pollen taxa) proxies from the MJS imply synchronous climatic amelioration on land and in the sea (Bertini et al., 2015; Maiorano et al., 2016; Figure 3.11-A), in agreement with alkenone-SST reconstructions which record a rapid warming followed by stable conditions throughout this period (Figure 3.11-A). A similar evolution is observed on the Iberian margin (ODP U1385, Hodell et al., 2015; Sánchez-Goñi et al., 2016; Figure 3.11-B).

However, initially low values of $\delta^{18}O_{benthic}$ progressively increase over the same period (Nomade et al., in review; Figure 3.11). Large-scale proxies also record this slow

climatic degradation (i.e. the decrease of CO_2 data from EPICA Dome C; Figure 3.11-B). Furthermore, the decrease of CH_4 and $\delta^{18}O_{atm}$ from EPICA Dome C and $\delta^{18}O_{carbonate}$ from Sulmona suggest the progressive establishment of drier conditions (Figure 3.11-B). This progressive climatic degradation could lead to millennial scale oscillations with warmer and wetter phases, interleaved by cold and dry episodes (MIS 19b and MIS 19a; Nomade et al., in review). These rapid millennial oscillations could reflect the influence of ice-sheet dynamics on North Atlantic oceanic circulation and atmospheric processes (Tzedakis et al., 2012; Giaccio et al., 2015), and/or periodic intensification of tropical moisture transport toward the Mediterranean region (Sánchez-Goñi et al., 2016). More detailed data over this period are required to infer the processes at play in the central Mediterranean basin.

4. CONCLUSION

By combining clumped-isotope thermometry with other, higher-resolution proxies, we document paleoenvironmental changes over two couples of glacial-interglacial cycles, from MIS 22 to MIS 19, and constrain local oceanographic variations occurring during the MIS 22/21 and MIS 20/19 deglaciations. The Δ_{47} data we obtain on benthic foraminifera yield realistic bottom temperatures. Based on these results we are able to propose different climatic scenarios. MIS 22 records relatively warm sub-surface Δ_{47}-temperature decreasing toward the end of this glacial. Potential lateral advection of cold sub-surface water can explain this decrease and the transition of more stratified water column. The deglaciation between MIS 22/21 is characterized by cold sub-surface Δ_{47}-temperatures and a decrease of $\delta^{18}O_{SW}$, potentially resulting from a combination of global and regional signals, with an input of cold water that could result from incursions of cold North Atlantic water or from increased runoff. The MIS 21 seems to reflect exclusively local processes leading to an increase in $\delta^{18}O_{SW}$. This regional signal could be linked to potential oscillations between cold/dry and warm/wet episodes, as documented by pollen data (Bertini et al., 2015). MIS 20 presents cold and relative stable climatic conditions with well-ventilated waters. However, the end of MIS 20 is marked by an increase of $\delta^{18}O_{SW}$ and sub-surface Δ_{47}-temperatures, suggesting lateral

advection of warm sub-surface water. The deglaciation MIS 20/19 is characterized by a combination of global signal and more regional processes, likely associated to the cold water from North Atlantic, coeval with a Heinrich-like event. This event is followed by a cold episode, which may potentially be explained by 1) a Younger-Dryas-like event preceded by a Bølling-Allerød-like event (Maiorano et al., 2016) or 2) input of freshwater coming from land and leading to the subsequent sapropel-like event.

Although our current dataset provides critical pieces of information, these observations do not allow us to unambiguously conclude about the processes that occurred during these periods. Detailed micropaleontological and mineralogical data are required over the MIS 22 and 21, to be able to reconstruct potential millennial-scale oscillations evidenced by pollen data (Bertini et al., 2015). Higher resolution records of pollen and SST reconstructions are needed at MJS, as well as studies of key regions such as the Western Mediterranean, the Iberian margin and the North Atlantic to improve the regional constraints on the climatic processes involved. From a methodological point of view, the difference in term of absolute values observed between Mg/Ca and alkenone-SST and sub-surface Mg/Ca- and Δ_{47}-temperature is likely due to biases, which still need to be elucidated. It would thus be interesting to extend these paired proxy analyses to a larger span of the section.

REFERENCES

Aiello G., Barra D. and Parisi R. (2015) Lower-Middle Pleistocene ostracod assemblages from the Montalbano Jonico section (Basilicata, Southern Italy). *Quat. Int.* **383**, 47–73. Available at: http://dx.doi.org/10.1016/j.quaint.2014.11.010.

Altenbach A. V., Pflaumann U., Schiebel R., Thies A., Timm S. and Trauth M. (1999) Scaling percentages and distributional patterns of benthic Foraminifera with flux rates of organic carbon. *J. Foraminifer. Res.* **29**, 173–185. Available at: http://jfr.geoscienceworld.org/content/29/3/173.abstract.

Anand P., Elderfield H. and Conte M. H. (2003) Calibration of Mg / Ca thermometry in planktonic foraminifera from a sediment trap time series. **18**.

Balduzzi A., Casnedi R., Crescenti U., Mostardini F. and Tonna M. (1982) Il Plio-Pleistocene del sottosuolo del bacino lucano (Avanfossa appenninica). *Geol. Rom.* **21**, 89–111.

Bernasconi S. M., Müller I. A., Bergmann K. D. and Sebastian F. M. Reducing uncertainties in carbonate clumped isotope analysis through consistent carbonate - based standardization.

Bertini A., Toti F., Marino M. and Ciaranfi N. (2015) Vegetation and climate across the Early-Middle Pleistocene transition at Montalbano Jonico, southern Italy. *Quat. Int.* **383**, 74–88.

Bintanja R. and Van De Wal R. S. W. (2008) North American ice-sheet dynamics and the onset of 100,000-year glacial cycles. *Nature* **454**, 869–872.

Bintanja R., Van De Wal R. S. W. and Oerlemans J. (2005) Modelled atmospheric temperatures and global sea levels over the past million years. *Nature* **437**, 125–128.

Boussetta S., Bassinot F., Sabbatini A., Caillon N., Nouet J., Kallel N., Rebaubier H., Klinkhammer G. and Labeyrie L. (2011) Diagenetic Mg-rich calcite in Mediterranean sediments: Quantification and impact on foraminiferal Mg/Ca thermometry. *Mar. Geol.* **280**, 195–204. Available at: http://dx.doi.org/10.1016/j.margeo.2010.12.011.

Brilli, M., 1998. Stratigrafia isotopica del carbonio e dell'ossigeno della successione infra e mesopliocenica di Montalbano Jonico (Basilicata, Italia meridionale). Tesi di Dottorato di Ricerca in Scienze della terra XI ciclo. Università degli Studi di Roma "La Sapienza"112 pp

Brilli M., Lerche L., Ciaranfi N. and Turi B. (2000) Evidences of precession and obliquity orbital forcing in oxygen-18 isotope composition of Montalbano Jonico Section (Basilicata, southern Italy). *Appl. Radiat. Isot.* **52**, 957–964.

Casnedi R. (1988) La Fossa bradanica: origine, sedimentazione e migrazione. *Mem. Soc. Geol. It* **41**, 439–448.

Casnedi R., Crescenti U. and Tonna M. (1982) Evoluzione dell'avanfossa adriatica meridionale nel Plio-Pleistocene, sulla base di dati di sottosuolo. *Mem. Soc. Geol. It* **24**, 243–260.

Cavalcante F., Fiore S., Lettino A., Piccarreta G. and Tateo F. (2007) Illite-Smectite mixed layer in Sicilide shales and piggy-back deposits of the Gorgoglione Formation (Southern Apennines): geological inferences. *Boll. della Soc. Geol. Ital.* **126**, 241–254.

Ciaranfi N., Lirer F., Lirer L., Lourens L. J., Maiorano P., Marino M., Petrosino P., Sprovieri M., Stefanelli S., Brilli M., Girone A., Joannin S., Pelosi N. and Vallefuoco M. (2010)

Integrated stratigraphy and astronomical tuning of lower-middle Pleistocene Montalbano Jonico section (southern Italy). *Quat. Int.* **219**, 109–120. Available at: http://dx.doi.org/10.1016/j.quaint.2009.10.027.

Coletti A. J., DeConto R. M., Brigham-Grette J. and Melles M. (2015) A GCM comparison of Pleistocene super-interglacial periods in relation to Lake El'gygytgyn, NE Arctic Russia. *Clim. Past* **11**, 979–989.

D'Alessandro A., La Perna R. and Ciaranfi N. (2003) Response of macrobenthos to changes in palaeoenvironments in the Lower–Middle Pleistocene (Lucania Basin, Southern Italy). *Quat.* **16**, 167–183.

Deconto R. M., Galeotti S., Pagani M., Tracy D., Schaefer K., Zhang T., Pollard D. and Beerling D. J. (2012) carbon release from thawing permafrost. , 6–11.

Dell'Anna L., Laviano R. and Loiacono F. (1988) Caratteri composizionali e granulometrici di alcune facies politiche del Flysh di Gorgoglione (Torrente Casale, alta valle del Fiume Agri). *Mem. della Soc. Geol. Ital.* **41**, 827–839.

Elderfield H., Ferretti P., Crowhurst S., Mccave I. N., Hodell D. and Piotrowski A. M. (2012) Evolution of Ocean Temperature and Ice Volume Through the. *Science (80-.).* **337**, 704–710.

Elderfield H., Greaves M., Barker S., Hall I. R., Tripati A., Ferretti P., Crowhurst S., Booth L. and Daunt C. (2010) A record of bottom water temperature and seawater d 18 O for the Southern Ocean over the past 440 kyr based on Mg / Ca of benthic foraminiferal Uvigerina spp . *Quat. Sci. Rev.* **29**, 160–169. Available at: http://dx.doi.org/10.1016/j.quascirev.2009.07.013.

Elderfield H., Yu J., Anand P., Kiefer T. and Nyland B. (2006) Calibrations for benthic foraminiferal Mg/Ca paleothermometry and the carbonate ion hypothesis. *Earth Planet. Sci. Lett.* **250**, 633–649.

Emeis K., Struck U., Schulz H., Rosenberg R., Bernasconi S., Erlenkeuser H., Sakamoto T. and Martinez-ruiz F. (2000) Temperature and salinity variations of Mediterranean Sea surface waters over the last 16 , 000 years from records of planktonic stable oxygen isotopes and alkenone unsaturation ratios. **158**, 259–280.

Extier T., Landais A., Bréant C., Prié F., Bazin L., Dreyfus G., Roche D. M. and Leuenberger M. (2018) On the use of δ18Oatm for ice core dating. *Quat. Sci. Rev.* **185**, 244–257.

Ferretti P., Crowhurst S. J., Naafs B. D. A. and Barbante C. (2015) The Marine Isotope Stage 19 in the mid-latitude North Atlantic Ocean: astronomical signature and intra-interglacial variability. *Quat. Sci. Rev.* **108**, 95–110.

Fontanier C., Jorissen F. J., Licari L., Alexandre A., Anschutz P. and Carbonel P. (2002) Live benthic foraminiferal faunas from the Bay of Biscay: Faunal density, composition, and microhabitats. *Deep. Res. Part I Oceanogr. Res. Pap.* **49**, 751–785.

Giaccio B., Regattieri E., Zanchetta G., Nomade S., Renne P. R., Sprain C. J., Drysdale R. N., Tzedakis P. C., Messina P., Scardia G., Sposato A. and Bassinot F. (2015) Duration and dynamics of the best orbital analogue to the present interglacial. *Geology* **43**, 603–606.

Girone A., Capotondi L., Ciaranfi N., Di Leo P., Lirer F., Maiorano P., Marino M., Pelosi N. and Pulice I. (2013) Paleoenvironmental changes at the lower Pleistocene Montalbano Jonico section (southern Italy): Global versus regional signals. *Palaeogeogr. Palaeoclimatol. Palaeoecol.* **371**, 62–79. Available at: http://dx.doi.org/10.1016/j.palaeo.2012.12.017.

Goñi M. F. S., Llave E., Oliveira D., Naughton F., Desprat S. and Ducassou E. (2016) Climate changes in south western Iberia and Mediterranean Out fl ow variations

during two contrasting cycles of the last 1 Myrs : MIS 31 – MIS. *Glob. Planet. Change* **136**, 18–29. Available at: http://dx.doi.org/10.1016/j.gloplacha.2015.11.006.

Grauel A., Goudeau M. S., Lange G. J. De and Bernasconi S. M. (2013) Climate of the past 2500 years in the Gulf of Taranto , central Mediterranean Sea : A high-resolution climate reconstruction based on δ 18 O and δ 13 C of Globigerinoides ruber (white).

Grauel A. L., Schmid T. W., Hu B., Bergami C., Capotondi L., Zhou L. and Bernasconi S. M. (2013) Calibration and application of the "clumped isotope" thermometer to foraminifera for high-resolution climate reconstructions. *Geochim. Cosmochim. Acta* **108**, 125–140. Available at: http://dx.doi.org/10.1016/j.gca.2012.12.049.

Grossman E. L. (1987) Stable isotopes in modern benthic foraminifera; a study of vital effect. *J. Foraminifer. Res.* **17**, 48–61.

Grossman E. L., Texas A., Station C. and Tx U. S. A. (1984) BORDERLAND among others). Several species of benthic foraminifera including Planulina wuellerstorfi have been shown to have constant magnitudes of 180 disequilib- (Belanger et al ., 1981 ; Graham et al ., 1981). Apparent carbon isotope dis-. **47**.

Head M. J. and Gibbard P. L. (2015) Early-Middle Pleistocene transitions: Linking terrestrial and marine realms. *Quat. Int.* **389**, 7–46. Available at: http://dx.doi.org/10.1016/j.quaint.2015.09.042.

Helmke J. P., Bauch H. A. and Erlenkeuser H. (2003) Development of glacial and interglacial conditions in the Nordic seas between 1.5 and 0.35 Ma. *Quat. Sci. Rev.* **22**, 1717–1728.

Hillaire-Marcel C., De Vernal A. and McKay J. (2011) Foraminifer isotope study of the Pleistocene Labrador Sea, northwest North Atlantic (IODP Sites 1302/03 and 1305), with emphasis on paleoceanographical differences between its "inner" and "outer" basins. *Mar. Geol.* **279**, 188–198.

Hodell D., Lourens L., Crowhurst S., Konijnendijk T., Tjallingii R., Jiménez-Espejo F., Skinner L., Tzedakis P. C., Abrantes F., Acton G. D., Zarikian C. A. A., Bahr A., Balestra B., Barranco E. L., Carrara G., Ducassou E., Flood R. D., José-Abel Flores, Furota S., Grimalt J., Grunert P., Hernández-Molina J., Kim J. K., Krissek L. A., Kuroda J., Li B., Lofi J., Margari V., Martrat B., Miller M. D., Nanayama F., Nishida N., Richter C., Rodrigues T., Rodríguez-Tovar F. J., Roque A. C. F., Goñi M. F. S., Sierro F. J., Singh A. D., Sloss C. R., Stow D. A. V., Takashimizu Y., Tzanova A., Voelker A., Xuan C. and Williams T. (2015) A reference time scale for Site U1385 (Shackleton Site) on the SW Iberian Margin. *Glob. Planet. Change* **133**, 49–64.

Hönisch B., Hemming N. G., Archer D., Siddall M. and McManus J. F. (2009) Atmospheric carbon dioxide concentration across the mid-Pleistocene transition. *Science* **324**, 1551–4. Available at: http://www.sciencemag.org/cgi/doi/10.1126/science.1171477%5Cnhttp://www.ncbi.nlm.nih.gov/pubmed/19541994.

Joannin S., Ciaranfi N. and Stefanelli S. (2008) Vegetation changes during the late Early Pleistocene at Montalbano Jonico (Province of Matera, southern Italy) based on pollen analysis. *Palaeogeogr. Palaeoclimatol. Palaeoecol.* **270**, 92–101.

Kim S.-T. and O'Neil J. R. (1997) Equilibrium and nonequilibrium oxygen isotope effects in synthetic carbonates. *Geochim. Cosmochim. Acta* **61**, 3461–3475. Available at: http://linkinghub.elsevier.com/retrieve/pii/S0016703797001695.

Kleiven H. K. F., Hall I. R., Mccave I. N., Knorr G. and Jansen E. (2011) Coupled deep-water fl ow and climate variability in the middle Pleistocene North Atlantic.

Konijnendijk T. Y. M., Ziegler M. and Lourens L. J. (2014) Chronological constraints on Pleistocene sapropel depositions from high-resolution geochemical records of ODP Sites 967 and 968. *Newsletters Stratigr.* **47**, 263–282. Available at: http://openurl.ingenta.com/content/xref?genre=article&issn=0078-0421&volume=47&issue=3&spage=263.

Kucera M. and Kennett J. P. (2002) Causes and consequences of a middle Pleistocene origin of the modern planktonic foraminifer Neogloboquadrina pachyderma sinistral. *Geology* **30**, 539–542.

Kukla G. J. (2000) The last interglacial. *Science (80-.).* **287**, 987–988.

Kukla G., McManus J. F., Rousseau D.-D. and Chuine I. (1997) How long and how stable was the last interglacial? *Quat. Sci. Rev.* **16**, 605–612.

Lang N. and Wolff E. W. (2011) of the Past Interglacial and glacial variability from the last 800 ka in marine , ice and terrestrial archives. , 361–380.

Laskar J., Robutel P., Joutel F., Gastineau M., Correia A. C. M. and Levrard B. (2004) Astrophysics A long-term numerical solution for the insolation. **285**, 261–285.

Lisiecki L. E. and Raymo M. E. (2005) A Pliocene-Pleistocene stack of 57 globally distributed benthic D 18 O records. **20**, 1–17.

Loulergue L., Schilt A., Spahni R., Masson-Delmotte V., Blunier T., Lemieux B., Barnola J. M., Raynaud D., Stocker T. F. and Chappellaz J. (2008) Orbital and millennial-scale features of atmospheric CH4over the past 800,000 years. *Nature* **453**, 383–386.

Lourens L. J. (2004) Revised tuning of Ocean Drilling Program Site 964 and KC01B (Mediterranean) and implications for the D 18 O , tephra , calcareous nannofossil , and geomagnetic reversal chronologies of the past 1 . 1 Myr. **19**, 1–20.

Maiorano P., Capotondi L., Ciaranfi N., Girone a, Lirer F., Marino M., Pelosi N., Petrosino P. and Piscitelli a (2010) Vrica-Crotone and Montalbano Jonico sections: A potential unit-stratotype of the Calabrian Stage. *Episodes* **33**, 218–233. Available at: http://www.scopus.com/inward/record.url?eid=2-s2.0-79957631816&partnerID=40&md5=9cd1dec5a710f096255da80208d8f766.

Maiorano P., Marino M., di Stefano E. and Ciaranfi N. (2004) Calcareous nannofossil events in the Lower-Mildle Pleistocene transition at the Montalbano Jonico section and ODP site 964: Calibration with isotope and sapropel stratigraphy. *Riv. Ital. di Paleontol. e Stratigr.* **110**, 547–557.

Marino M., Bertini A., Ciaranfi N., Aiello G., Barra D., Gallicchio S., Girone A., La Perna R., Lirer F., Maiorano P., Petrosino P. and Toti F. (2015) Paleoenvironmental and climatostratigraphic insights for Marine Isotope Stage 19 (Pleistocene) at the Montalbano Jonico succession, South Italy. *Quat. Int.* **383**, 104–115.

Mashiotta T. A., Lea D. W. and Spero H. J. (1999) Glacial–interglacial changes in Subantarctic sea surface temperature and δ18O-water using foraminiferal Mg. *Earth Planet. Sci. Lett.* **170**, 417–432.

Mathien-Blard E. and Bassinot F. (2009) Salinity bias on the foraminifera Mg/Ca thermometry: Correction procedure and implications for past ocean hydrographic reconstructions. *Geochemistry, Geophys. Geosystems* **10**.

Mcclymont E. L., Rosell-mele A., Haug G. H. and Lloyd J. M. (2008) Expansion of subarctic water masses in the North Atlantic and Pacific oceans and implications for mid-Pleistocene ice sheet growth. **23**, 1–12.

Meckler A. N., Ziegler M., Mill??n M. I., Breitenbach S. F. M. and Bernasconi S. M. (2014) Long-term performance of the Kiel carbonate device with a new correction scheme for clumped isotope measurements. *Rapid Commun. Mass Spectrom.* **28**, 1705–1715.

Melles M., Melles M., Brigham-grette J., Minyuk P. S., Nowaczyk N. R., Wennrich V., Deconto R. M., Anderson P. M., Andreev A. A., Coletti A., Cook T. L., Haltia-hovi E., Kukkonen M., Lozhkin A. V, Rosén P., Tarasov P., Vogel H. and Wagner B. (2014) 2 . 8 Million Years of Arctic Climate. *Science (80-.).* **315**.

Müller P. J., Kirst G., Ruhland G., Von Storch I. and Rosell-Melé A. (1998) Calibration of the alkenone paleotemperature index U 37 K′ based on core-tops from the eastern South Atlantic and the global ocean (60 N-60 S). *Geochim. Cosmochim. Acta* **62**, 1757–1772.

Murray J. (2006) *Ecology and Applications of Benthic Foraminifera*. ed. Cambridge university press, United States of America by Cambridge University Press, new York.

Naafs B. D. A., Hefter J. and Stein R. (2013) Millennial-scale ice rafting events and Hudson Strait Heinrich (-like) Events during the late Pliocene and Pleistocene: a review. *Quat. Sci. Rev.* **80**, 1–28.

Oliveira D., S M. F., Naughton F., Polanco-martínez J. M., Jimenez-espejo F. J., Grimalt J. O., Martrat B., Voelker A. H. L., Trigo R., Hodell D. A., Abrantes F. and Desprat S. (2017) Unexpected weak seasonal climate in the western Mediterranean region during MIS 31 , a high-insolation forced interglacial nchez Go n. *Quat. Sci. Rev.* **161**, 1–17.

Patacca, E., Scandone, P., 2004. The Plio-Pleistocene thrust belt-foredeep system in the southern Apennines and Sicily (Italy). In: *Crescenti, et al. (Ed.), Special Volume of the Italian Geological Society for the IGC 32 Florence 2004. Società Geologica Italiana, Roma*, pp. 93–129.

Peral M., Daëron M., Blamart D., Bassinot F., Dewilde F., Smialkowski N., Isguder G., Jorissen F., Kissel C., Michel E., Va N. and Waelbroeck C. (2018) ScienceDirect Updated calibration of the clumped isotope thermometer in planktonic and benthic foraminifera. **239**, 1–16.

Petrosino P., Jicha B. R., Mazzeo F. C., Ciaranfi N., Girone A., Maiorano P. and Marino M. (2015) The Montalbano Jonico marine succession: An archive for distal tephra layers at the Early-Middle Pleistocene boundary in southern Italy. *Quat. Int.* **383**, 89–103.

Pinardi N., Lyubartsev V., Cardellicchio N., Caporale C., Ciliberti S., Coppini G., Pascalis F. De, Dialti L., Federico I., Filippone M., Grandi A., Guideri M., Lecci R., Lamberti L., Lorenzetti G., Lusiani P., Macripo C. D., Maicu F., Mossa M., Tartarini D., Trotta F., Umgiesser G. and Zaggia L. (2016) Marine Rapid Environmental Assessment in the Gulf of Taranto : a multiscale approach. , 2623–2639.

Pol K., Masson-Delmotte V., Johnsen S., Bigler M., Cattani O., Durand G., Falourd S., Jouzel J., Minster B., Parrenin F., Ritz C., Steen-Larsen H. C. and Stenni B. (2010) New MIS 19 EPICA Dome C high resolution deuterium data: Hints for a problematic preservation of climate variability at sub-millennial scale in the “oldest ice.” *Earth Planet. Sci. Lett.* **298**, 95–103. Available at: http://dx.doi.org/10.1016/j.epsl.2010.07.030.

Pollard D. and DeConto R. M. (2009) Modelling West Antarctic ice sheet growth and collapse through the past five million years. *Nature* **458**, 329–332.

Rioual P., Andrieu-Ponel V., Rietti-Shati M., Battarbee R. W., De Beaulieu J. L., Cheddadi R., Reille M., Svobodova H. and Shemesh A. (2001) High-resolution record of climate stability in France during the last interglacial period. *Nature* **413**, 293–296.

Rossignol-Strick M. and Paterne M. (1999) A synthetic pollen record of the eastern Mediterranean sapropels of the last 1 Ma: implications for the time-scale and

formation of sapropels. *Mar. Geol.* **153**, 221–237.

Rouis-Zargouni I., Turon J. L., Londeix L., Kallel N. and Essallami L. (2012) The last glacial-interglacial transition and dinoflagellate cysts in the western Mediterranean Sea. *Comptes Rendus - Geosci.* **344**, 99–109.

Ruddiman W. F., Raymo M. and McIntyre A. (1986) Matuyama 41,000-year cycles: North Atlantic Ocean and northern hemisphere ice sheets. *Earth Planet. Sci. Lett.* **80**, 117–129.

Ruddiman W. F., Sarnthein M., Backman J., Baldauf J. G., Curry W., Dupont L. M., Janecek T., Pokras E. M., Raymo M. E., Stabell B., Stein R. and Tiedemann R. (1989) Late Miocene to Pleistocene Evolution of Climate in Africa and the Low-Latitude Atlantic: Overview of Leg 108 Results. *Proc. Ocean Drill. Program, 108 Sci. Results* **108**, 463–484. Available at: http://www-odp.tamu.edu/publications/108_SR/VOLUME/CHAPTERS/sr108_29.pdf.

Sabbatini A., Bassinot F., Boussetta S., Negri A., Rebaubier H., Dewilde F., Nouet J., Caillon N. and Morigi C. (2011) Further constraints on the diagenetic influences and salinity effect on Globigerinoides ruber (white) Mg/Ca thermometry: Implications in the Mediterranean Sea. *Geochemistry, Geophys. Geosystems* **12**.

Scherer R. P., Bohaty S. M., Dunbar R. B., Esper O., Flores J. A., Gersonde R., Harwood D. M., Roberts A. P. and Taviani M. (2008) Antarctic records of precession-paced insolation-driven warming during early Pleistocene Marine Isotope Stage 31. *Geophys. Res. Lett.* **35**, 1–5.

Siesser W. G., Bralower T. J. and De Carlo E. H. (1992) Mid-Tertiary Braarudosphaera-rich sediments on the Exmouth Plateau. *Unkn. J.*, 653–663.

Simon Q., Bourlès D. L., Bassinot F., Nomade S., Marino M., Ciaranfi N., Girone A., Maiorano P., Thouveny N., Choy S., Dewilde F., Scao V., Isguder G., Blamart D. and Team A. (2017) Authigenic 10 Be / 9 Be ratio signature of the Matuyama – Brunhes boundary in the Montalbano Jonico marine succession. *Earth Planet. Sci. Lett.* **460**, 255–267. Available at: http://dx.doi.org/10.1016/j.epsl.2016.11.052.

Stefanelli S. (2003) Benthic foraminiferal assemblages as tools for paleoenvironmental reconstruction of the early-middle Pleistocene Montalbano Jonico composite section. *BOLLETTINO-SOCIETA Paleontol. Ital.* **42**, 281–300.

Stefanelli S., Capotondi L. and Ciaranfi N. (2005) Foraminiferal record and environmental changes during the deposition of the Early-Middle Pleistocene sapropels in southern Italy. *Palaeogeogr. Palaeoclimatol. Palaeoecol.* **216**, 27–52.

Tolderlund D. S. and Bé A. W. H. (1971) Seasonal distribution of planktonic foraminifera in the western North Atlantic. *Micropaleontology*, 297–329.

Toti F. (2015) Interglacial vegetation patterns at the Early-Middle Pleistocene transition: a point of view from the Montalbano Jonico section (Southern Italy). *Alp. Mediterr. Quat.* **28**, 2015.

Tripati A. K., Eagle R. A., Thiagarajan N., Gagnon A. C., Bauch H., Halloran P. R. and Eiler J. M. (2010) 13C-18O isotope signatures and "clumped isotope" thermometry in foraminifera and coccoliths. *Geochim. Cosmochim. Acta* **74**, 5697–5717. Available at: http://dx.doi.org/10.1016/j.gca.2010.07.006.

Tripati A. K., Roberts C. D., Eagle R. A. and Li G. (2011) A 20 million year record of planktic foraminiferal B/Ca ratios: Systematics and uncertainties in pCO2 reconstructions. *Geochim. Cosmochim. Acta* **75**, 2582–2610. Available at: http://dx.doi.org/10.1016/j.gca.2011.01.018.

Tzedakis P. C., Channell J. E. T., Hodell D. A., Kleiven H. F. and Skinner L. C. (2012)

Determining the natural length of the current interglacial. *Nat. Geosci.* **5**, 138–142. Available at: http://dx.doi.org/10.1038/ngeo1358.

Venz K. A., Hodell D. A., Stanton C. and Wamke D. A. (2000) A 1 . 0 Myr record of Glacial North Atlantic Intermediate Water variability from ODP site 982 in the northeast Atlantic of the resumed under full interglacial The magnitude of benthic. **14**, 42–52.

de Villiers S., Greaves M. and Elderfield H. (2002) An intensity ratio calibration method for the accurate determination of Mg/Ca and Sr/Ca of marine carbonates by ICP-AES. *Geochemistry, Geophys. Geosystems* **3**, n/a-n/a. Available at: http://doi.wiley.com/10.1029/2001GC000169.

Yin Q. Z. and Berger A. (2012) Individual contribution of insolation and CO2to the interglacial climates of the past 800,000 years. *Clim. Dyn.* **38**, 709–724.

Zahn R., Pedersen F., Bornhold B. D. and Mix A. C. (1991) WATER MASS CONVERSION IN THE GLACIAL SUBARCTIC PACIFIC (54°N, 148°W): PHYSICAL CONSTRAINTS AND THE BENTHIC- PLANKTONIC STABLE ISOTOPE RECORD Rainer. *Paleoceanography* **6**, 543–560.

Zonneveld K. A. F. (1995) Palaeoclimatic and palaeo-ecological changes during the last deglaciation in the Eastern Mediterranean implications for dinoflagellate ecology. **84**, 221–253.

Part 4

SYNTHESIS & PERSPECTIVES

The PhD work presented here has been focused on two main objectives: (1) implementing, refining and testing the applicability of optimal analytical procedures for clumped-isotope thermometry on foraminifer shells, at LSCE; (2) applying clumped-isotope methods to the reconstruction of paleoceanographic changes in the Gulf of Taranto (Mediterranean Sea) during the mid-Pleistocene transition, particularly on several glacials and during two key interglacial periods, MIS 31 and MIS 19, potentially analogues to Holocene in terms of orbital forcing.

Below, we provide a concise overview of our key findings and of new insights regarding the methodology of clumped-isotope and Mg/Ca thermometry, and the usefulness of paired Δ_{47}-$\delta^{18}O$ analyses for paleoenvironmental studies. Finally, I offer some recommendations for future research.

1. METHODOLOGICAL DEVELOPMENTS

1.1. Clumped-isotope Thermometry in Foraminifera

In Part 2, I present a new calibration of the clumped-isotope thermometer in foraminifer shells. This work is based on a large set of recent to modern samples (< 4 ka) retrieved from core-tops with a worldwide distribution. My primary goal was to constrain the relationship between Δ_{47} values and calcification temperatures in seven planktonic and two benthic foraminifer species across a wide range of temperatures (-2 to 25 °C). Several cleaning approach were tested in the early stage of this work. In total, about 1.7 g of foraminifers, equivalent to ~ 130,000 individuals, were hand-picked under a binocular microscope. The shells were cracked opened, carefully cleaned, and their clumped-isotope composition (Δ_{47}) was analysed using state-of-the-art procedure. These measurements are precisely anchored to a set of inter-laboratory carbonate standards from ETH Zürich.

A strongly correlated relationship was observed between Δ_{47} values and calcification temperatures estimated from foraminifer oxygen-18 composition:

$$\Delta_{47} = 41.63 \times 10^3 / T^2 + 0.2056$$

Comparisons between various groups of species (surface-dwelling planktonic, thermocline-dwelling planktonic, or benthic foraminifera) over the full range of temperatures supports the absence of detectable species-specific effect. Our results also establish that Δ_{47} does not appear to vary significantly with shell size, by comparison of size fractions from 200 to > 560 μm for seven foraminifer species. It is thus possible to combine different fractions when picking foraminifera in core sections with limited material (which is the general case in paleoceanographic studies). This point is of particular interest because it may considerably reduce the time required to hand-pick foraminifera, and increase attainable temporal resolutions. Finally, we found no evidence for salinity effects over the typical salinity range (from 34 to 36) of the global ocean.

These findings confirm the usefulness of clumped-isotope thermometry in foraminifer studies, and provide a robust calibration framework to interpret future results. However, we still don't know enough about the diagenetic processes, which may alter the original Δ_{47} signal (dissolution/recrystallization and/or solid-state reorganization) of marine carbonates in sedimentary settings, especially at long geologic time scales (> 100 Ma). It will be interesting to quantify these potential effects, which significantly alter the original information on biomineralization processes in old sedimentary series.

Owing to the use of common inter-laboratory carbonate standards; we are able to precisely compare our foraminifer calibration relationship with two other carbonate calibration studies performed in different laboratories. Our results are perfectly consistent with the inorganic calcite data obtained by Kele et al. (2015) on travertines and tufa, and quite similar to those of Breitenbach et al. (2018) based on speleothems (cave pearls). It appears likely that the systematic use of common carbonate standards will significantly reduce inter-laboratory discrepancies, so that it should be possible to precisely compare the results obtained here to future calibration studies, most particularly to several ongoing foraminifer studies.

We are also able to compare the foraminifer calibration dataset to other types of biogenic and inorganic carbonates also analysed at LSCE, but still unpublished (e.g., Huyghe et al., in prep). The high precision of the foraminifer calibration line makes it possible to detect subtle but statistically significant differences between biogenic calcites (bivalves and foraminifera) on one hand and extremely slow-growing inorganic calcites from Devils Hole and Laghetto Basso believed to have achieved isotopic equilibrium (Daëron et al., in review, see appendix).

Recent Δ_{47} calibration studies on coccoliths suggest the existence of species-specific effect in natural modern settings (A. Katz, PhD thesis, 2017). An interesting future area of research would be to compare Δ_{47} in coccoliths and planktonic formainifera for various periods, to better understand the timing and mechanism of this potential "vital" effects in coccolithophorids. By the end of my PhD employment period, I plan to have performed a first series of analyses of this kind (APIC 2018 project – see below for details).

The application of clumped isotopes in paleoceanographic studies using foraminifera remains rare because of the large amounts of material required for precise measurements. Some of the results reported here, such as the absence of significant shell size and species-specific effects on Δ_{47} values, demonstrate that sampling strategies may be adjusted to mitigate this issue. Other important factors include the use of highly efficient IRMS techniques such as LIDI (Long Intergration Dual Inlet), or the recent development of a dedicated system for the 3D identification and automatic sorting of foraminifera (FIRST project, CEREGE Laboratory, France). It is thus very likely that the temporal resolution, analytical precision, and ease of implementation of clumped-isotope foraminifer studies will improve in the near future.

1.2. Comparison of Temperatures Reconstructed from Different Methods

Comparison between different techniques of paleothermometry may reveal discrepancies that must be understood and properly accounted for. We have thus compared clumped isotope and Mg/Ca measurements on benthic foraminifera from same stratigraphic layers in MJS (cf. Part 3). Our Mg/Ca-derived temperatures give what appear as unrealistic values in some intervals, suggesting possible biases during interglacial periods in Interval A and glacial periods in Interval B. For now, we are not able to conclude on a satisfying explanation for this potential Mg/Ca bias. However, the process seems to preferably affect benthic foraminifera by increasing their Mg content, and does not apparently bias the clumped-isotope thermometer nor the Mg/Ca content of planktonic foraminifers. To solve this issue, it is necessary to conduct specific studies on biomineralization and early diagenesis process to understand and quantify the possible mechanisms. Also in the MJS, we have compared Mg/Ca-temperatures in planktonic foraminifera with alkenone-temperatures over the MIS 19. We observe higher planktonic Mg/Ca-derived temperatures than alkenone-derived temperatures that could reflect potential difference living depth or seasonality of the organisms. We propose to perform additional Mg/Ca measurements to better constraint this issue.

In the near future, I am planning to compare clumped-isotope temperatures to results obtained with various other paleo-temperature methods, in a open ocean situation. I have started to work on a sediment core (MD96-2048) located underneath the Agulhas current, in the Mozambique Channel (Figure 4.1). Earlier works were performed using $U^{k'}_{37}$, TEX_{86}, Mg/Ca and MAT, (Caley et al., 2011, and Caley PhD thesis, 2011; Caley et al., 2018). Previous study revealed huge discrepancy-ies between those paleo-thermometers, reaching up to ~ 5 °C (Caley et al., 2011). I proposed to complement this dataset by a record of Δ_{47}-derived temperatures over the last 1.26 Ma (work in progress; in collaboration with EPOC laboratory, University of Bordeaux, France).

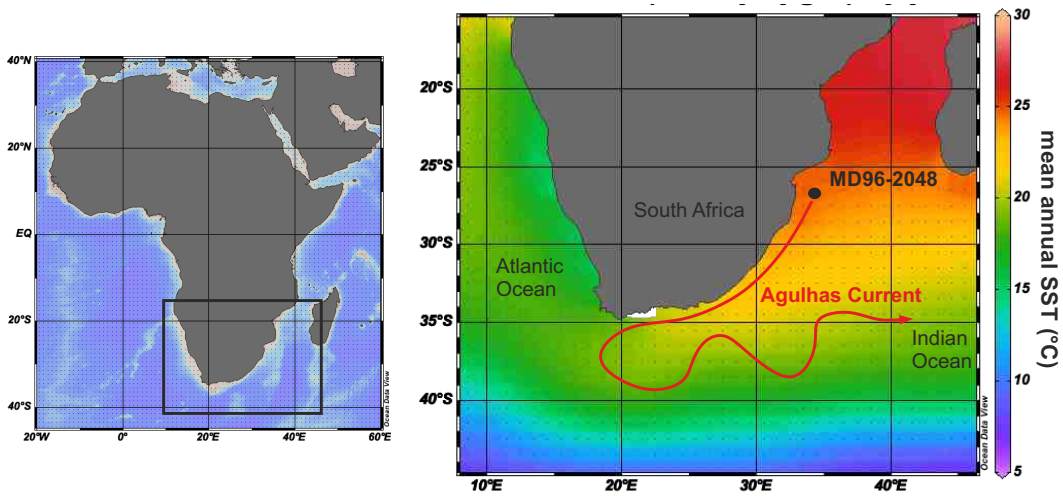

Figure 4.1: Map location of the core MD96-2048 in the Agulhas current, background is the modern mean annual SST.

2. APPLICATIONS OF CLUMPED-ISOTOPE CALIBRATION FOR PALEOCEANOGRAPHIC RECONSTRUCTIONS

2.1. MPT Issue

2.1.1. Synthesis of Paleoceanographic Changes Across the MPT at Montalbano Jonico

The MPT is a major climatic transition with still many unsolved questions regarding the internal mechanisms that were involved and could explain the drastic change in the shape, amplitude and duration of glaciation-interglacial cycles. We have documented paleoceanographic changes across the MPT in the central Mediterranean Sea. As Δ_{47} analyses are time consuming, we focused on a few intervals that (i) provided us with the necessary material for replicate analyses, (ii) and correspond to key periods of the MPT:

- We analysed several glacial periods, because changes in glacial/interglacial dynamics across the MPT correspond more particularly to the progressive degradation of

glacial conditions, both in amplitude and duration. Among these glacial periods, we have included MIS 22, which, in several deep-sea benthic records, is the first glacial showing a strong increase in benthic $\delta^{18}O$ relative to glacials from the "41 ka-world";

- We also focused on three interglacial: MIS31, MIS21 and MIS 19. Due to the astronomical configuration (high obliquity, low in precession), MIS 31 and MIS 19 are considered as potential analogues to the Holocene, making these two stages particularly interesting to study natural variations the MPT. We have used MIS 21 as an intermediate interglacial between these two potential Holocene analogues.

Over the whole period considered here, the MJS water depth, estimated from benthic foraminifer assemblages, indicate an evolution towards shallower depths (Figure 3.1 – Part 3 – Chapter 1). It is believed that the most important paleo-depth change occurred between Interval A and B. This explains why we split the MPT in two distinct parts. Despite this issue, we propose a summarized comparison of our key results, synthetized in Figure 3.12. We expected a potential increase of sub-surface water associated to tectonic movement, but we did not observed such an evolution, suggesting that the influence of climate dominate the potential tectonic effects.

2.1.1.1. Glacial periods over the MPT at MJS

Throughout MJS Interval A (including MIS 30), the glacial periods show relatively similar conditions (Chapter 2 – Part 3) characterized by high $\delta^{18}O_{SW}$ (~ 1.7 ‰), cold SST (~ 19 °C) and sub-surface (~ 9 °C) temperature and well-mixed water (Figure 4.2). During the Interval B of MJS, glacial periods are slightly more variable. The environmental conditions during MIS 20 are similar to those occurring during glacials of Interval A, while MIS 22 appears to be warmer than earlier glacials (Figure 4.2). Both MIS 22 and MIS 20 recorded significant change in the water column prior to the beginning of deglaciations, with stratification episodes potentially associated to lateral advection of cold water for MIS 22 and warm water for MIS 20 (Figure 4.2). Paleodepth reconstructions suggest a shallower environment during MIS 20 than during MIS 22, suggesting that variations of paleodepth is

not the main explanation for the difference observed between these two stages. Our paleoenvironmental reconstructions suggest that MIS 22 has not experienced severe climate conditions and is not, therefore, a pivotal glacial of the MPT in the Montalbano Jonico section.

As explained above, because Δ_{47} analyses are time-consuming, I could only study a few glacials. In further study on MPT in the Mediterranean Sea, it would be much valuable (1) to perform similar approaches used in this thesis to document the MIS 32 (Interval A) for a better understanding of the processes occurring at the end of the glacials, and analyse the MIS32/MIS31 transition (Interval A) and (2) to obtain pollen, micropaleontological and/or mineralogical data for MIS 22 to constraint the continental signals over this glacial.

2.1.1.2. Deglaciation periods over the MPT at MJS

The three deglaciations present strong difference. Termination XV (MIS 32-31) is characterised by an abrupt decrease of $\delta^{18}O_C$, while the two others (terminations X-MIS22/21 and IX – MIS20/19) are more gradual (Figure 4.2). Furthermore, MIS 22/21 transition is relatively cold in sub-surface at MJS, while the MIS 20/19 transition is warmer in sub-surface (Figure 4.2). Both transitions recorded decrease of subsurface $\delta^{18}O_{SW}$, likely associated to a combination of global signal (decrease of ice-sheet volume) and local processes (enhancement of runoff or incursion of North Atlantic water; Figure 4.2). If we focus on MIS 20/19, for which high-resolution data is available, the deglaciation showed several steps: (1) moderately cold SST (~ 18 °C), likely related to the incursion of cold waters from the North Atlantic and concomitant to an *Heinrich-like* event (Figure 4.2) and followed by a further episode of decrease in SST (~ 14 °C; Maiorano et al., 2016 and T. Herbert data; Chapter 3 – Part 3), followed by (2) the deposition of a sapropel-like event (Maiorano et al., 2016), corresponding to a strong stratification of the water column during the deglaciation (high $\Delta^{18}O_{c\ (p\ VS\ b)}$).

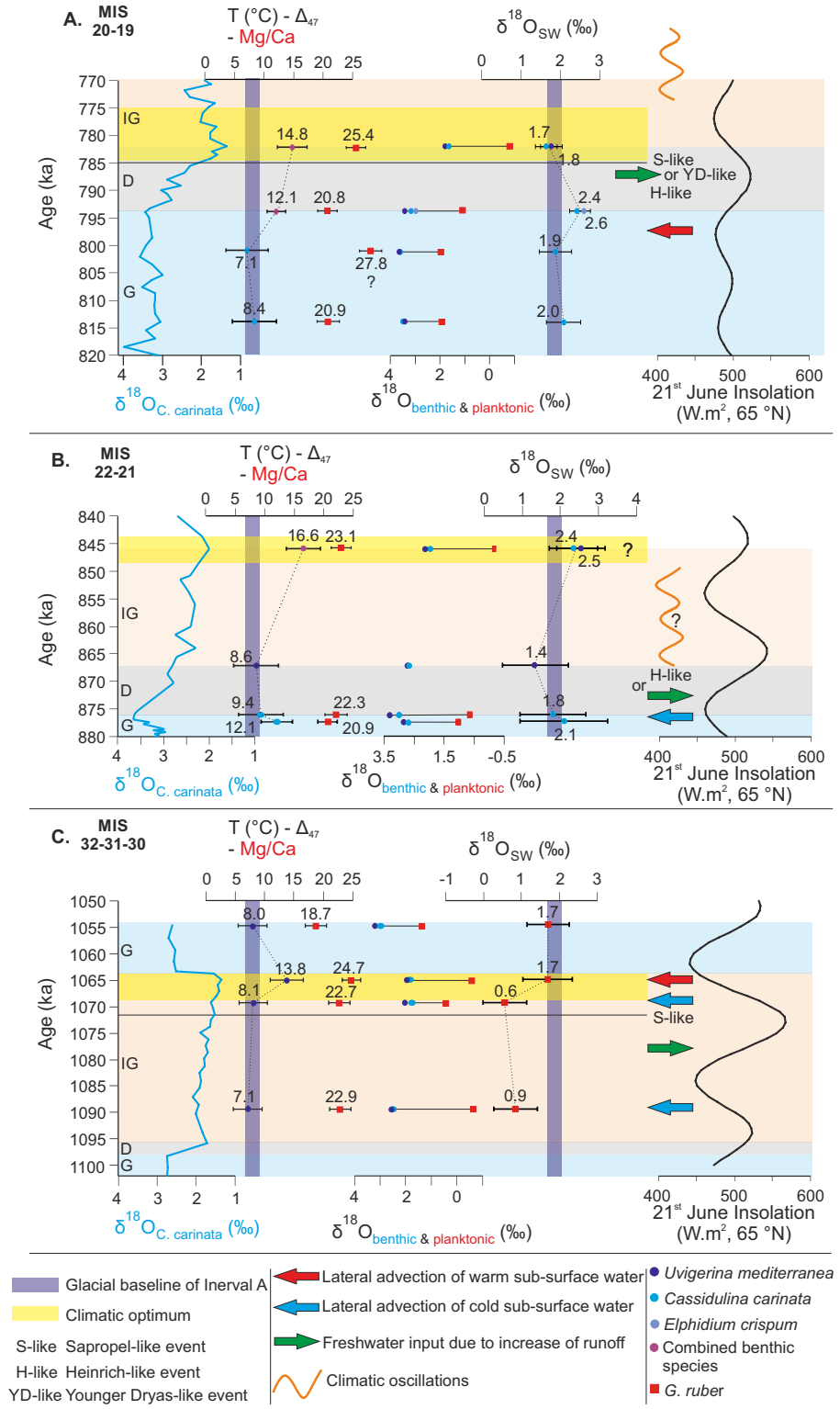

<u>Figure 4.2:</u> Graphic summarizing major paleoceanographic data and interpretations across three main glacial/interglacial cycles studied at MJS during my PhD: A. MIS 32-31-30, B. MIS 22-21 and C. MIS 20-19. G: Glacials, D: Deglaciations and IG: Interglacials.

To further address changes in MJS beyond what I could achieve in this PhD work, it would be interesting to (1) document paleoceanographic changes over MIS 32-31 and perform high-resolution $\delta^{18}O_C$ to refine chronological constraints of this deglaciation, (2) complete our dataset with other proxies over MIS 22-21 and (3) perform clumped isotope measurements during the cold SST shift of MIS 20-19 (observed by alkenones) to define it origin: runoff enhancement or Younger Dryas-like event by paired Δ_{47}-$\delta^{18}O$ (Chapter 3 – Part 3).

2.1.1.3. Interglacial periods over the MPT at MJS

Paleoceanographic conditions during the beginning of MIS 31 (strong stratification, cold subsurface and surface sea temperatures, Figure 4.2-A) are likely associated to strong precipitation and freshwater runoff together with the lateral advection of subsurface cold water. Such a strong vertical stratification has been found associated to the deposition of a sapropel-like event in MIS19. However, no sapropel-like layer has been found at MJS during MIS 31, whereas in the Mediterranean Sea, the sapropel i-100 deposited during this interval. Further studies will be necessary to decipher whether specific conditions blocked the deposition of a carbon-rich material in the Gulf of Taranto during MIS 31. The two others interglacials MIS 21 and MIS 19 do not recorded similar conditions.

All three studied interglacials (MIS 31, MIS 21 and MIS 19) record warm (surface and subsurface) waters and a well-stratified water column during their climatic optimum (high $\Delta^{18}O_{c\ (p\ VS\ b)}$; Figure 4.2). The climatic optimum occurs at the end of MIS 31, associated with the second peak of summer insolation (Figure 4.2-A). Interestingly, the optimum climatic of MIS 21 characterized by warm SST (~ 23.1 °C) and subsurface (~ 16.6 °C) temperature, and minimum of $\delta^{18}O_C$), also occurs at the end of the interglacial (Figure 4.2-B), while the climatic optimum of MIS 19 takes place at its beginning, associated to the first peak of summer boreal insolation (Figure 4.2-C), which is also the case for all interglacials after the MPT.

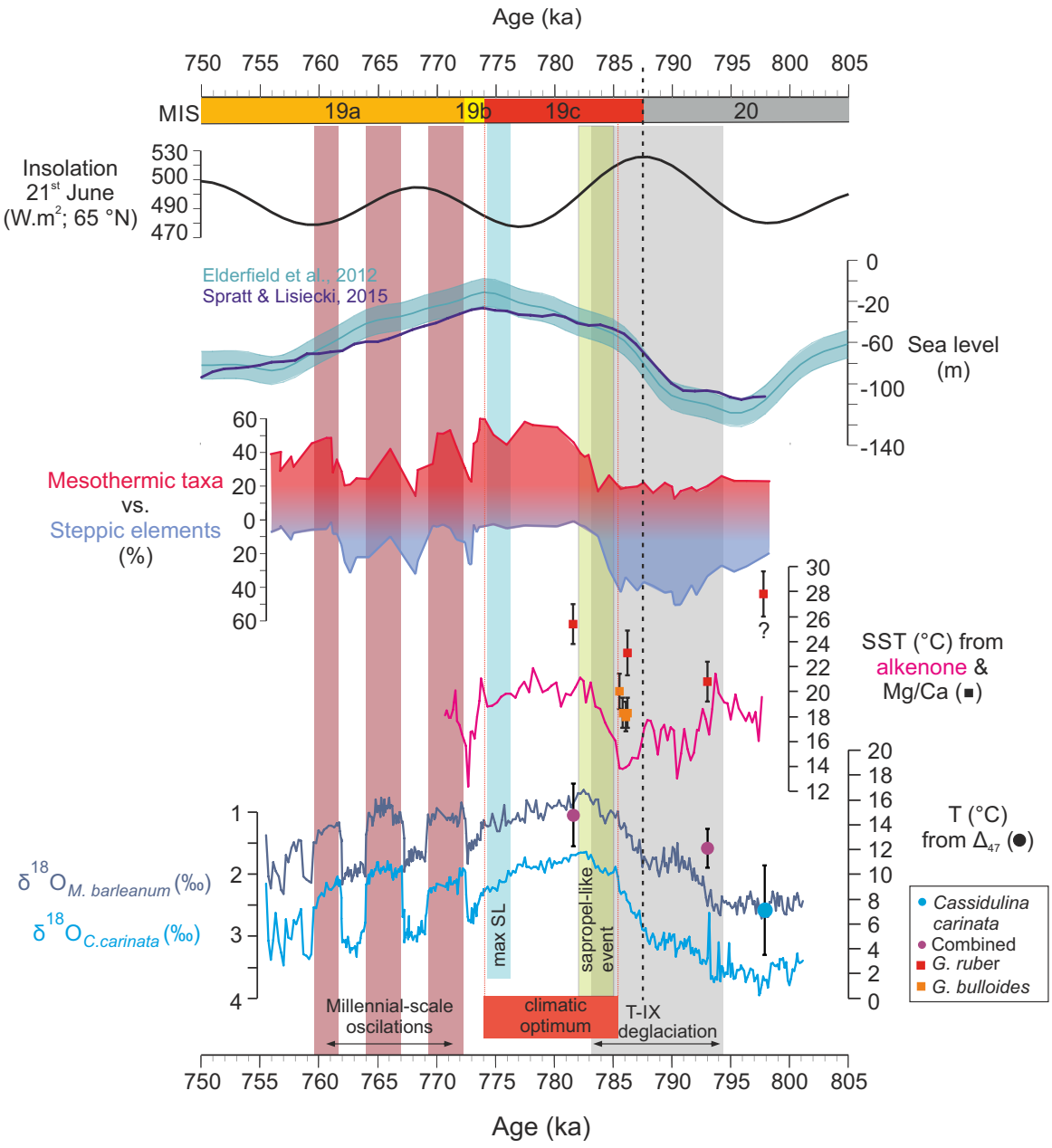

<u>Figure 4.3:</u> paleoenvironmental data from late MIS 20 to MIS 19 with millennial-scale oscillations (MIS 19b and MIS 19a) observed in $\delta^{18}O_b$ records (Nomade et al. in review), alkenones-derived SST (performed by T. Herbert) and pollen data (Bertini et al., 2015).

The MIS 19 climatic optimum is followed by millennial-scale oscillation between warm/wet and cold/dry phases (Figure 4.2-C; Figure 4.3), which take place during the progressive transition towards glacial MIS 18. It is interesting to note that potential warm/wet and cold/dry phases are observed in pollen data over MIS 21 at MJS (Bertini et al., 2015) and millennial-scale oscillations are recorded in high-resolution pollen data through the MIS 31 on the Iberian margin (Site U1385; Oliveira et al., 2017).

To better constraint the climatic optimum and better understand in which context and why do the potential millennial or sub-orbital scale oscillations take place (e.g. before climatic optimum in MIS31 and after the climatic optimum in MIS 19), it would be crucial to perform high-resolution isotopic data, sea temperature reconstructions and micropaleontological assemblages over MIS 31 and MIS 21 in MJS.

2.1.2. Future Research: Toward a Better Understanding of the Mediterranean Climate and Oceanographic Changes Through the MPT

Despite the complexity of the Mediterranean climate, MJS is a good candidate to develop application of clumped isotope through the MPT and explore the influence of high-latitude and tropical influences on the Mediterranean basin. In order to test the hypothesis proposed in this thesis, it will be necessary (1) to perform additional, higher resolution analyses on the MIS 31 and especially over the Interval II (cf. hypothetical deposition of sapropel-like event potentially analogue to i-100; Chapter 3 – Part 2) in order to better constrain freshwater inputs, (2) to extend the multi-proxy approach (mineralogical, micropaleontological, terrestrial and geochemical) over the MIS 21 and MIS 22 (Chapter 3 – Part 3), and (3) to reinforce the high resolution records for MIS 20 and MIS 19, particularly for the pollen assemblages (Chapter 3 – Part 3).

Furthermore, it would be particularly important to propose and/or test hypotheses involving the relationship between ice-sheet dynamic and tropical influences. Obtaining high-resolution, well quantified paleo-data over a transect from high latitudes in the North Atlantic ocean to MJS, with a focus on western Mediterranean Sea, particularly nearly

Gibraltar strait to track potential incursion of cold North Atlantic water, would be of great interest. Stage periods could be selected such as Holocene, MIS 11, MIS 19, MIS 31 and one MIS under 41-ka cycle (MIS 45 for example) with the objectives to (1) specifically focus on the deglaciation processes under 41-ka and 100-ka worlds and (2) understand the millennial scales observed in MJS during MIS 19 and on the Iberian margin, during the MIS 31.

2.1.3. MPT in Larger-geographical Scale

Understanding what drove the shift between a world dominated by 41 ka oscillations and the present world, dominated by asymmetric ~100 ka glacial-interglacial cycles, will bring some valuable pieces of information about complex feedback mechanisms involved in the Earth climate response to insolation forcing. To infer the processes that occur during this period, study of key region over the world would be necessary. For example, the southern oceans could also provide crucial information on the processes that took place during the MPT: the Agulhas current (Figure 4.1) is a key player for the global ocean circulation and climate changes (e.g. Beal et al., 2011). This current transports heat and salt from the Indian Ocean to the South Atlantic affecting the Atlantic Meridional Overturning Circulation (AMOC). In parallel to our multiproxy-SST comparison, we will look carefully at sea-surface salinity changes between glacial and interglacial periods over the last 1.26 Ma using $\delta^{18}O_{SW}$ derived from paired Δ_{47}-$\delta^{18}O$ (work in progress).

2.2. Applications of Clumped Isotopes Over the Cenozoic

Recently, Steffen et al. (2018) published a schematic illustration of possible future pathways of the climate (Figure 4.4). In this Figure, the authors represent the current Earth system in black circle (Figure 4.4). The blue line represents the glacial-interglacial cycles under 100 ka forcing, the green line the response of Earth system if the temperature stabilized after an increase of 2 °C compared to the preindustrial condition (orange star), as recommended in the IPCC report, and the red line the Earth system response if the

temperature increases more than 2 °C. In a stabilized context, the Earth system could revert back to glacial-interglacial cycles. However, in the context of hothouse earth, the retrograde step is still uncertain. To better understand and predict the Earth system response, it is important to document previous periods under warmer conditions such as the Mid-Holocene (A in Figure 4.4), the Eemian (B in Figure 4.4), the Mid-Pliocene (C in Figure 4.4) or the Mid-Miocene (D in Figure 4.4).

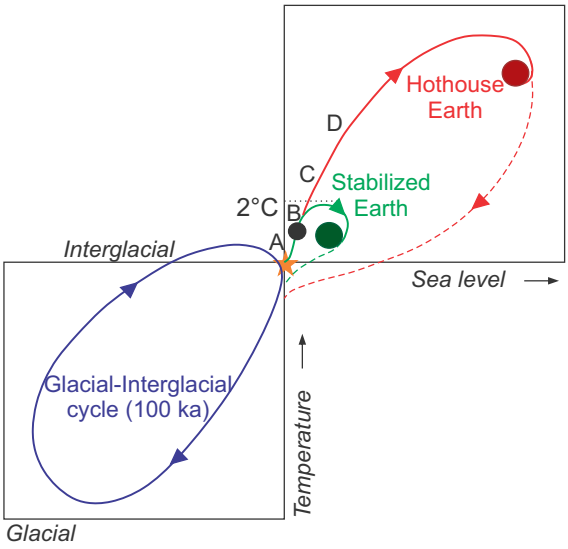

Figure 4.4: Illustration of possible future pathways of the climate, modified from Steffen et al., 2018. The black circle is the current Earth system, the orange star is the preindustrial conditions, A. condition during the Mid-Holocene, B. during the Eemien, C. during the Mid-Pliocene and D. during the Mid-Miocene.

The Cenozoic (last 65 Ma) is characterized by important climatic changes, summarized in Figure 4.5. The global climate varies from warm conditions with ice-free poles, to much colder conditions with massive continental ice sheets and polar ice caps. At shorter time-scale, the climate repeatedly changes between cold glacial and warm interglacial periods (Figure 4.5; Zachos et al., 2001). Some particular interesting warm periods are identified such as the Mid-Miocene climatic Optimum followed by a long gradual climate cooling. To better constrain the future prediction of the climate system, it is important to document past changes over this period (Steffen et al., 2018).

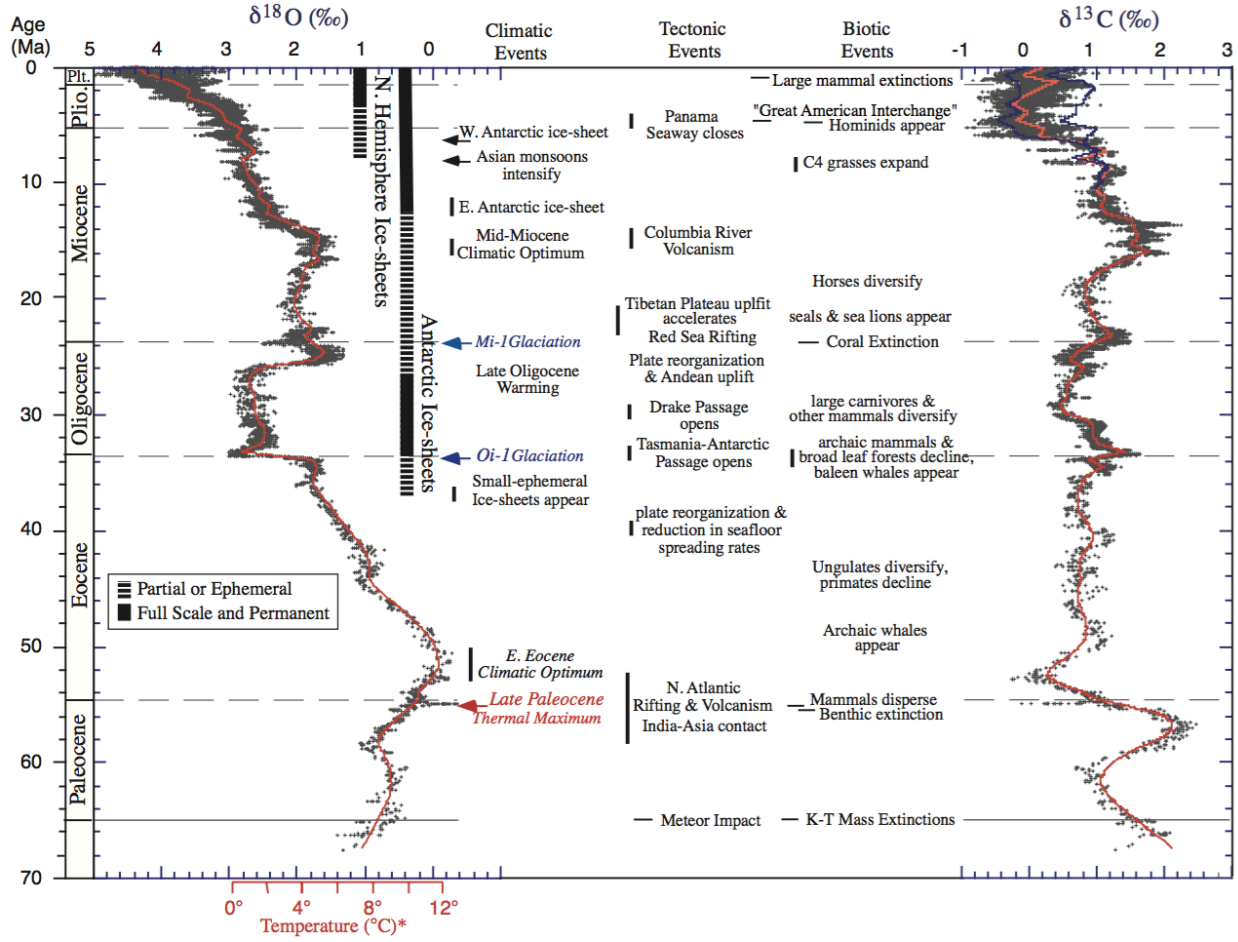

Figure 4.5: *Global climatic variation over the last 65 Ma, based on deep-sea oxygen and carbon records, compiled by Zachos et al., 2001*

By the end of my PhD, I'll be enrolled in APIC 2018 project in collaboration with the CEREGE laboratory (Aix-en-Provence) about the reconstruction of temperature from the Mid-Miocene toward the Pliocene in Indian Ocean. This project aims at (1) obtaining quantitative SST, (2) comparing Δ_{47} in foraminifera and coccoliths to determine potential "vital" effects, (3) using new methodological developments (e.g. automatic picking of foraminifera) and (4) integrating these results into numerical models, which required physical constraints. I will therefore perform measurements on planktonic foraminifera and coccolithes to compare the SST reconstructions from two different planktonic calcareous fossils, and document the large variations of temperatures over this period (in progress).

The clumped isotope thermometer is therefore a very promising tool for reconstructing paleoceanographic changes because it allows reconstructing quantitative temperatures and estimated $\delta^{18}O$ of seawater. Even if the sampling resolution is low because of the amount of material required, this valuable information derived from Δ_{47} brings a new perspective for studying past climate variations.

REFERENCES

Beal L. M., De Ruijter W. P. M., Biastoch A., Zahn R., Cronin M., Hermes J., Lutjeharms J., Quartly G., Tozuka T. and Baker-Yeboah S. (2011) On the role of the Agulhas system in ocean circulation and climate. *Nature* **472**, 429.

Bertini A., Toti F., Marino M. and Ciaranfi N. (2015) Vegetation and climate across the Early-Middle Pleistocene transition at Montalbano Jonico, southern Italy. *Quat. Int.* **383**, 74–88.

Breitenbach S. F. M., Mleneck-Vautravers M. J., Grauel A.-L., Lo L., Bernasconi S. M., Müller I. A., Rolfe J., Greaves M. and Hodell D. A. (2018) Coupled Mg/Ca and clumped isotope analyses of foraminifera provide consis- tent water temperatures Sebastian. *Geochim. Cosmochim. Acta*.

Caley T., Extier T., Collins J. A., Schefuß E., Dupont L., Malaizé B., Rossignol L., Souron A., McClymont E. L. and Jimenez-Espejo F. J. (2018) A two-million-year-long hydroclimatic context for hominin evolution in southeastern Africa. *Nature*, 1.

Caley T., Kim J. H., Malaizé B., Giraudeau J., Laepple T., Caillon N., Charlier K., Rebaubier H., Rossignol L., Castañeda I. S., Schouten S. and Sinninghe Damsté J. S. (2011) High-latitude obliquity as a dominant forcing in the Agulhas current system. *Clim. Past* **7**, 1285–1296.

Kele S., Breitenbach S. F. M., Capezzuoli E., Meckler A. N., Ziegler M., Millan I. M., Kluge T., Deák J., Hanselmann K., John C. M., Yan H., Liu Z. and Bernasconi S. M. (2015) Temperature dependence of oxygen- and clumped isotope fractionation in carbonates: A study of travertines and tufas in the 6–95°C temperature range. *Geochim. Cosmochim. Acta* **168**, 172–192.

Maiorano P., Bertini A., Capolongo D., Eramo G., Gallicchio S., Girone A., Pinto D., Toti F., Ventruti G. and Marino M. (2016) Climate signatures through Marine Isotope Stage 19 in the Montalbano Jonico section (Southern Italy): A land–sea perspective. *Palaeogeogr. Palaeoclimatol. Palaeoecol.* **461**, 341–361. Available at: http://linkinghub.elsevier.com/retrieve/pii/S0031018216303819.

Oliveira D., S M. F., Naughton F., Polanco-martínez J. M., Jimenez-espejo F. J., Grimalt J. O., Martrat B., Voelker A. H. L., Trigo R., Hodell D. A., Abrantes F. and Desprat S. (2017) Unexpected weak seasonal climate in the western Mediterranean region during MIS 31 , a high-insolation forced interglacial nchez Go n. *Quat. Sci. Rev.* **161**, 1–17.

Steffen W., Rockström J., Richardson K., Lenton T., Folke C., Liverman D., Summerhayes C., Barnosky A., Cornell S., Crucifix M., Donges J., Fetzer I., Lade S., Scheffer M., Winkelmann R. and Schellnhuber H. J. (2018) Trajectories of the Earth System in the Anthropocene. *Proc. Natl. Acad. Sci. U. S. A.* **in review**, 1–45.

Zachos J., Pagani M., Sloan L., Thomas E. and Billups K. (2001) Trends , Rhythms , and Aberrations in Global Climate 65 Ma to Present. **292**, 686–693.

Appendix

CO-AUTHORED PUBLICATIONS

Absolute isotopic abundance ratios and the accuracy of Δ_{47} measurements

M. Daëron[(1)], D. Blamart[(1)], **M. Peral**[(1)], H. Affek[(2)]

(1) Laboratoire des Sciences du Climat et de l'Environnement, LSCE / IPSL, CEA-CNRS-UVSQ, Université Paris-Saclay, France;
(2) Institute of Earth Sciences, Hebrew University of Jerusalem, Israel;
Corresponding author: daeron@lsce.ipsl.fr

Submitted to *Chemical Geology* on April 18, 2016
Revised on August 1
Accepted on August 8.
doi: 10.1016/j.chemgeo.2016.08.014

ABSTRACT

Clumped isotope measurements aim to quantify some statistical properties of the isotopologue population in a given sample, which requires prior knowledge of the absolute isotopic abundance ratios in reference materials such as VSMOW or VPDB. In the case of CO_2, matters are further complicated by the need to define a mass-dependent fractionation law linking the three stable isotopes of oxygen. Conversion from raw mass spectrometric data to mass-47 anomalies (Δ_{47}) thus relies on four external parameters: the ($^{13}C/^{12}C$) ratio of VPDB, the ($^{17}O/^{16}O$) and ($^{18}O/^{16}O$) ratios of VSMOW (or VPDB-CO_2), and the slope of the triple oxygen isotope line (λ). Here we investigate the influence that these isotopic parameters exert on measured Δ_{47} values, using: (a) real-world data corresponding to seven months of measurements; (b) simple simulations based on randomly generated data; (c) precise comparisons between water-equilibrated CO_2 samples and between carbonate standards believed to share quasi-identical Δ_{47} values; (d) reprocessing of two carbonate calibration data sets with different slopes of Δ_{47} versus T.

We demonstrate that the use of different sets of isotopic parameters generally produces systematic offsets as large as 0.04 ‰ in measured Δ_{47} values, even after following the established standardization procedures. What's more, even using a single set of isotopic parameters can produce intra- and inter-laboratory discrepancies in measured Δ_{47} values, if some of these parameters are inaccurate, and depending on the isotopic compositions of the standards used for conversion to the absolute scale of *Dennis et al. (2011),* these errors should correlate strongly with either $\delta^{13}C$ or $\delta^{18}O$, or more weakly with both. Based on measurements of samples expected to display quasi-identical Δ_{47} values, such as 25 °C water-equilibrated CO_2 with different carbon and oxygen isotope compositions, or high-temperature standards ETH-1 and ETH-2, we conclude that the traditional set of isotopic parameters used in all early clumped isotope studies produces large, systematic errors controlled by the relative bulk isotopic compositions of samples and standards. These errors are likely to be one of the key factors responsible for current inter-laboratory discrepancies, but cannot easily explain the conflicting carbonate calibration slopes obtained by different groups. By contrast, the isotopic parameters of *Brand et al. (2010)* appear to yield accurate Δ_{47} values regardless of bulk isotopic composition. Based on these findings, we offer recommendations aiming to minimize errors related to the choice of isotopic parameters.

1 INTRODUCTION

In natural molecular materials, to a first-order approximation, stable isotopes combine into isotopologues according to a stochastic distribution. As a result, if "bulk" isotopic abundance ratios such as $\left({}^{13}C/{}^{12}C\right)$ or $\left({}^{18}O/{}^{16}O\right)$ are known, the abundance of each isotopologue may be computed, using only statistical distribution rules, to a reasonably good level of accuracy. Conversely, bulk isotope ratios can be directly calculated from the abundances of singly-substituted isotopologues such as $^{16}O^{13}C^{16}O$ and $^{18}O^{12}C^{16}O$. Although this approximation remains valid for most measurements of bulk isotope ratios, many types of materials are nevertheless expected to display detectable deviations from stochastic distribution in multiply-substituted isotopologues (e.g., *Wang et al., 2004; Schauble et al., 2006*). Clumped isotope geochemistry is the study of such stochastic anomalies in natural materials, and has experienced rapid progress over the past decade (e.g., *Eiler and Schauble, 2004; Ghosh et al., 2006; Eiler, 2007, 2011; Yeung et al., 2012; Stolper et al., 2014*), along with significant methodological advances (e.g., *Huntington et al., 2009; Dennis et al., 2011; He et al., 2012*).

So far, a majority of clumped isotope studies have targeted carbonate minerals and CO_2, with a wide range of scientific applications including paleoclimatology, thermal and diagenetic histories of crustal rocks, biomineralization processes, and atmospheric CO_2 studies. Such applications rely on measurements of Δ_{47}, a statistical parameter closely related to the stochastic anomaly in $^{16}O^{13}C^{18}O$. Today, these measurements are routinely standardized either by comparison to CO_2 samples with a known Δ_{47} value ("thermodynamic gas standards"), as described by *Dennis et al. (2011),* or using a set of *ad hoc* international carbonate standards whose composition has been tied to that of thermodynamic gas standards (*Meckler et al., 2014*). In theory, this ensures that all modern clumped isotope measurements of CO_2 and carbonates are reported in the same metrological framework, allowing direct comparison of results from different laboratories. In practice, inter-laboratory differences remain larger than expected from instrumental precision alone (S. Bernasconi, panel discussion on interlaboratory comparisons, Fifth International Clumped Isotope Workshop, 2016). Strikingly, the calibration functions for low-temperature carbonate clumped isotope thermometry published by various groups suffer from large discrepancies (up to 0.08 ‰ for carbonates formed at 25 °C, which is equivalent to a difference of 20–30 °C), and the corresponding calibration slopes (i.e. temperature sensitivity of Δ_{47}) range from 2.6 to 4.4 ppm/K at 20 °C

(Figure 4 from *Spencer and Kim, 2015*). Even within a single laboratory, thermodynamic gas standards prepared from CO_2 of very different bulk isotope compositions can show large discrepancies, as reported by *Schauer et al. (2016b).* In the present study, we investigate one of the potential causes for these discrepancies, namely the effects that different data reduction procedures may have on reported, "absolute" Δ_{47} values.

Clumped isotope measurements in CO_2, and by extension in carbonate minerals, have so far relied on precise determination of relative isotopologue abundances using dual-inlet mass spectrometry (e.g., *Eiler and Schauble, 2004; Huntington et al., 2009*). One inherent limitation of this approach is that some independent assumptions are needed to constrain the relationship between the $\delta^{17}O$ and $\delta^{18}O$ values of any given sample. Traditionally, such ^{17}O "corrections" assume that triple oxygen isotope differences between a sample and a given reference material (e.g., VSMOW) follow a mass-dependent relationship of the form:

$$\Delta^{17}O = \ln\left(R^{17} / R^{17}_{ref}\right) - \lambda \ln\left(R^{18} / R^{18}_{ref}\right) = 0 \quad (1)$$

where R^{17}, R^{18}, R^{17}_{ref} and R^{18}_{ref} refer to the ($^{17}O/^{16}O$) and ($^{18}O/^{16}O$) abundance ratios in the sample and an international reference material, respectively (e.g., *Brand et al., 2010,* and references therein). In the above equation, λ can be described as a phenomenological constant linking the oxygen isotope compositions of materials related to each other through similar fractionation processes, such as for instance most carbonates precipitated from oceanic or meteoric waters (*Assonov and Brenninkmeijer, 2003a*). Although the use of such a mass-dependent law is almost universal, there is no consensus regarding the choice of a reference material, nor the numerical values of R^{17}_{ref} and λ. In some cases, this is a natural consequence of studying different types of samples, such as tropospheric CO_2 (e.g., *Hofmann et al., 2012*) versus surface carbonate minerals. In other cases, different laboratories analyzing similar types of samples nevertheless use different ^{17}O correction parameters (e.g., for historical reasons, or because of different default software values) and rely on established standardization procedures to correct for any resulting discrepancies.

With respect to clumped isotopes, the use of a mass-dependent ^{17}O correction may bring about two different kinds of problems. Firstly, some samples may deviate significantly from the assumed mass-dependent law, exhibiting large ^{17}O anomalies ($\Delta^{17}O$ in equation 1). If not taken into account in the

computation of isotopologue abundance ratios, such anomalies lead to small, systematic errors in estimates of Δ_{47} (*Olack and Colman, 2016*), but these effects are not the focus of the present study. A second issue concerns the comparison of measurements between laboratories using slightly different ^{17}O correction parameters (or, similarly, slightly different values for R^{13}_{VPDB}). Although these differences in data processing are known to have a non-negligible effect on "raw Δ_{47}" values (*Olack et al., 2013*), one might expect that they would cancel out after subsequent conversion to "absolute" Δ_{47} (*Affek and Eiler, 2006*). Our objective here is to assess the validity of this assumption, by processing a large set of raw mass spectrometric data using different numerical values of R^{13}_{VPDB}, R^{17}_{ref}, R^{18}_{ref} and λ (hereafter collectively referred to as "isotopic parameters"). In order to focus on this specific issue, within the scope of this work we make the conventional assumption that all carbonate samples conform strictly to some version of equation (1), i.e., that $\Delta^{17}O = 0$ for all carbonate measurements. Although this might not be strictly the case for some samples in our data set, it should have no bearing on our conclusions regarding the use of different isotopic parameters.

2 METHODS

2.1 Overview

Figure 1 presents a schematic overview of our methodology. The raw data set is composed of "working gas" delta values for various carbonate samples and thermodynamic gas standards. These raw numbers are processed using several independent sets of isotopic parameters (R^{13}_{VPDB}, R^{17}_{ref}, R^{18}_{ref} and λ), to compute corresponding, independent sets of $\delta^{13}C$, $\delta^{18}O$ and Δ^{raw}_{47} values for each analysis. Each data set is then converted to absolute Δ_{47} values based on the thermodynamic gas standards. The final computed values for each sample are compared in order to characterize potential bias introduced by the choice of isotopic parameters. Calculations are performed sequentially, using Python scripts provided as supplementary material, ensuring that all other aspects of data processing are strictly the same.

2.2 Real-world data set

The 327 measurements considered here were performed over a seven-month period from May to December 2015. All of them were analyzed at the Laboratoire des Sciences du Climat et de l'Environnement (LSCE) using the same equipment and procedures. Carbonate samples between 2.6 and 4.0 mg

were dissolved in a common acid bath held at 90 °C. After cryogenic removal of water, the evolved CO_2 passed through a Porapak Q column (50/80 mesh, 1 m length, 2.1 mm ID) held at –20 °C under helium 6.0 flow (25 mL/mn). CO_2 was then quantitatively recollected by cryogenic trapping, and transferred by gas expansion into an Isoprime 100 dual-inlet mass spectrometer equipped with six Faraday collectors (m/z 44 to 49). Each analysis lasted about 3 h, during which sample and working reference gas were allowed to flow from matching, 10 mL reservoirs into the source, through a pair of fused silica capillaries (65 cm length, 110 µm ID). Every 20 mn, gas pressures were adjusted to achieve a mass 44 current of 40 nA, with differences between sample and reference gas generally below 0.1 nA. Background currents were measured in all high-gain collectors (m/z 45 to 49) before and after each pressure adjustment, with gas flowing into the source, and are found to correlate strongly with mass 44 current.

High-temperature thermodynamic gas standards were prepared by sealing 30–35 µmol CO_2 into quartz tubes (12 cm length, 6 mm OD), heating them to 1000 °C for 2 h, followed by quenching in liquid nitrogen immediately before analysis. Low-temperature thermodynamic gas standards were prepared by sealing 30–35 µmol CO_2 into borosilicate tubes pre-loaded with 60 µL water, followed by equilibration in a water bath at 25 °C for a minimum of three full days. All thermodynamic gas standards were prepared from a single tank of CO_2, and thus had very similar $\delta^{13}C_{VPDB}$ values around -3.6 ‰. $\delta^{18}O_{VPDB\text{-}CO_2}$ values (including those of 1000 °C standards) varied from -28 ‰ to $+11$ ‰ as a result of equilibration with waters of different isotopic composition, either collected from high-latitude precipitation or prepared by evaporative enrichment of local deionized water. To the best of our knowledge, all published Δ_{47} studies have so far assumed that water-equilibrated and carbonate-evolved CO_2 conform to the same triple oxygen isotope law. Although this is unlikely to be strictly the case, this discrepancy is expected to manifest as a small, constant error (Figure 2) between water-equilibrated CO_2 and carbonate-derived samples, and initially we do not attempt to address this particular issue. We do, however, take into account ^{17}O anomalies (ranging from -88 to $+15$ ppm relative to VSMOW, with $\lambda = 0.528$) in all waters used to prepare the 1000 °C and 25 °C gas standards. These $\Delta^{17}O$ values were measured at LSCE by A. Landais using water fluorination *(Barkan and Luz, 2005; Landais et al., 2012),* and are explicitly accounted for in subsequent calculations.

Owing to the use of a fully automated preparation system, sample trapping and purification protocols did not significantly differ between gas standards and carbonates, nor between individual samples. Analyses are grouped into four distinct "sessions", each corresponding to several weeks of continuous measurements. For each of the 327 measurements, the following information is recorded: a unique identification number; a session identifier; for thermodynamic gas standards, the temperature of CO_2 equilibration (25 °C or 1000 °C); the carbon and oxygen isotopic composition of the working reference gas relative to VPDB-CO_2 (defined as CO_2 produced by reacting virtual VPDB calcite with phosphoric acid at 25 °C); and the differences in background-corrected ion beam intensity ratios between analyte and working reference gases, noted δ^{45} to δ^{49}.

2.3 Random data simulations

In addition to the raw data set described in the previous section, we can randomly generate raw data corresponding to an arbitrary number of simulated measurements. In order to do so, we start with random "true" values for $\delta^{13}C_{VPDB}$, $\delta^{18}O_{VPDB\text{-}CO_2}$, Δ_{47}, and, in some cases (see below), for bulk isotopic composition of the working reference gas. Thermodynamic gas standards can be generated in the same way, but with non-random Δ_{47} based on the theoretical values of *Wang et al. (2004).* Using an arbitrarily chosen set of isotopic parameters, these numbers are then converted to "working gas" delta values (δ^{45} to δ^{49}), and can be subsequently processed following the exact same procedures as for real-world measurements. In order to focus purely on data processing effects (as opposed to machine-specific analytical artifacts), we assume "perfect" mass spectrometric measurements with no compositional nonlinearities and no isotopic scrambling ($\Delta_{47}^{raw} = \Delta_{47}$).

2.4 Choice of isotopic parameters

Each set of isotopic parameters considered hereafter is defined by the numerical values of R_{VPDB}^{13}, R_{ref}^{18}, R_{ref}^{17}, and λ.

R_{PDB}^{13} was initially determined by *Craig (1957),* based on earlier measurements of isotope abundance ratios in air and limestone-derived CO_2 by *Nier (1950),* and assuming a mass-dependent oxygen fractionation exponent of $\lambda = 0.5$ between them. Subsequently, *Chang and Li (1990)* reported a slightly lower value based on comparisons between NBS carbonate standards and pre-

cisely calibrated mixtures of ^{13}C-depleted and ^{13}C-enriched $BaCO_3$. The latter was accepted as reference value by the International Union of Pure and Applied Chemistry (*Rosman and Taylor, 1998*).

Similarly, R^{18}_{VSMOW} was measured by *Baertschi (1976)* by comparison with calibrated mixtures of $D_2{}^{18}O$ and $H_2{}^{16}O$. Although VSMOW may be used to anchor the mass-dependent oxygen fractionation law defined by equation (1), a more natural reference for CO_2 and carbonate samples is VPDB-CO_2, whose R^{18} value can be computed from the oxygen isotope composition of VPDB relative to VSMOW ($\delta^{18}O = 30.92$ ‰, *Coplen et al., 1983*) and the 25 °C acid fractionation factor of 1.01025 from *Friedman and O'Neil (1977):*

$$R^{18}_{\text{VPDB-CO}_2} = R^{18}_{VSMOW} \times 1.03092 \times 1.01025 \quad (2)$$

Several values for R^{17}_{VSMOW} and $R^{17}_{\text{VPDB-CO}_2}$ have been reported over the years (cf Table 1 from *Assonov and Brenninkmeijer, 2003a*). For example, *Li et al. (1988)* were able to constrain the ratio (R^{17}/R^{13}) in VSMOW by comparing the abundance of mass-45 isotopologues in CO_2 prepared from isotopically normal and ^{17}O-depleted O_2. Another determination of this ratio was obtained by *Assonov and Brenninkmeijer (2003b)* using a similar method, updated to correct for known instrumental effects. It should be noted that both of these measurements provide estimates of R^{17}_{VSMOW} which scale linearly with the value of R^{13}_{VPDB}.

Finally, as noted above, the λ parameter should not be interpreted as reflecting a single fractionation process but rather as a phenomenological description of a population of samples. For example, *Gonfiantini et al. (1995)* recommended the use of $\lambda = 0.5164$ based on the oxygen isotope compositions of 35 terrestrial samples including waters and rocks (*Matsuhisa et al., 1978*). Alternatively, *Assonov and Brenninkmeijer (2003a)* argued that the oxygen isotope composition of most carbonates is ultimately derived from the global water pool, so that the corresponding value $\lambda = 0.528$ (*Meijer and Li, 1998; Barkan and Luz, 2005*) should be used instead, and they subsequently assumed a mass-dependent oxygen fractionation exponent of $\lambda = 0.528$ between VMOW and VPDB-CO_2 (*Assonov and Brenninkmeijer, 2003b*) :

$$R^{17}_{\text{VPDB-CO}_2} = R^{17}_{VSMOW} \times (1.03092 \times 1.01025)^{\lambda} \quad (3)$$

In the present study, we consider the following combinations of isotopic parameters. The [*Gonfiantini*] parameters are those originally used by the Caltech group (*Huntington et al., 2009,* online supporting information), and, to the best of our knowledge, by most clumped isotope laboratories today. It uses the R^{13}_{PDB} value of *Craig (1957),* and defines VSMOW as the reference material in the triple oxygen isotope equation, with the R^{17}_{VSMOW} value of *Li et al. (1988)* and $\lambda = 0.5164$ after *Matsuhisa et al. (1978).* The other combinations of parameters considered here use a value of $\lambda = 0.528$ and each of them is named according to their choice of values for R^{13}_{VPDB} and R^{17}_{VSMOW}. For instance, the [*Craig + Li*] combination uses the R^{13}_{PDB} value of *Craig (1957)* and the R^{17}_{VSMOW} value of *Li et al. (1988).* It should be noted that the [*Chang + Assonov*] parameters are identical to those proposed by *Brand et al. (2010),* and for the sake of brevity we may use [*Chang + Assonov*] and [*Brand*] as equivalent labels.

All numbers corresponding to these five sets of parameters are listed in Table 1, and the corresponding triple oxygen isotope lines are plotted in Figure 3.

2.5 Calculation of $\delta^{13}C$, $\delta^{18}O$ and Δ^{raw}_{47} values

Regardless of which isotopic parameters are selected, computing the carbon and oxygen isotope composition of a given analyte requires solving an equation of the form:

$$-3\,K^2\,(R^{18})^{2\lambda} + 2\,K\,R^{45}\,(R^{18})^{\lambda} + 2\,R^{18} - R^{46} = 0 \tag{4}$$

where R^{18} is the ($^{18}O/^{16}O$) ratio in the analyte; R^{45} and R^{46} the CO_2 mass ratios (45/44) and (46/44); and $K = R^{17}_{ref}\,(R^{18}_{ref})^{-\lambda}$ (*Santrock et al., 1985*). In the more general case of an independently known or assumed value for $\Delta^{17}O$, the K parameter becomes:

$$K = \exp(\Delta^{17}O)\,R^{17}_{ref}\,(R^{18}_{ref})^{-\lambda} \tag{5}$$

Although equation (4) generally has no analytical solution, it can be solved to a very good approximation by conversion to a second-order Taylor polynomial, allowing $\delta^{18}O$ and $\delta^{13}C$ values to be determined with an accuracy better than 0.02 ppm (computational details in Appendix A; Python and Excel implementations provided as supplementary material). Raw Δ_{47} values are then calculated in the usual way, as described by *Huntington et al. (2009):*

$$\Delta_{47}^{\text{raw}} = \left(\frac{R_{\text{measured}}^{47}}{R_{\text{stochastic}}^{47}} - 1\right) - \left(\frac{R_{\text{measured}}^{46}}{R_{\text{stochastic}}^{46}} - 1\right) - \left(\frac{R_{\text{measured}}^{45}}{R_{\text{stochastic}}^{45}} - 1\right) \quad (6)$$

It might be noted that the last two terms in this formula should both be equal to zero as a consequence of equation (4). Using the Taylor polynomial approximation mentioned above, they indeed never exceed 0.02 ppm, so that equation (6) can be simplified to:

$$\Delta_{47}^{\text{raw}} = \frac{R_{\text{measured}}^{47}}{R_{\text{stochastic}}^{47}} - 1 \quad (7)$$

Depending on the context, Δ_{47} values and their uncertainties (both dimensionless) may be expressed in permil or ppm units.

2.6 Computation of absolute Δ_{47} values

Conversion of Δ_{47}^{raw} to absolute Δ_{47} values constrained by thermodynamic gas standards can be described by the following relationship:

$$\Delta_{47}^{\text{raw}} = a\,\Delta_{47} + b\,\delta^{47} + c \quad (8)$$

Although the above equation uses a different formalism, the underlying corrections are strictly equivalent to those described by *Dennis et al. (2011),* with parameters a, b and c being respectively related to scrambling effects, compositional nonlinearity, and non-stochasticity of the working gas. Within each measurement session, numerical values for (a, b, c) can be determined by least-squares fitting of the gas standard results, for which equilibrium Δ_{47} values are derived from the theoretical model of *Wang et al. (2004).* An example implementation is included in the supplementary material.

The best-fit values for (a, b, c) are then used to calculate absolute Δ_{47} for all samples in the same session, by simple rearrangement of (8):

$$\Delta_{47} = (\Delta_{47}^{\text{raw}} - b\,\delta^{47} - c)/a \quad (9)$$

3 RESULTS AND DISCUSSION

3.1 Are Δ_{47} values sensitive to the choice of isotopic parameters?

In the context of this study, we define $\Delta(\Delta_{47})$ as the difference, for any single measurement, between the absolute Δ_{47} value computed using one set of parameters and that computed using the [*Gonfiantini*] parameters. It should be noted that this arbitrary choice does not imply that the [*Gonfiantini*] output is more accurate.

3.1.1 Relationship between $\Delta(\Delta_{47})$ and $\delta^{13}C$ in real-world measurements

Considering all of the real-world data described above, $\Delta(\Delta_{47})$ values for the [*Brand*] parameters vary from -27 to $+12$ ppm (Figure 4a). In this case, although $\Delta(\Delta_{47})$ is poorly correlated with Δ_{47}, there seems to be some structure to their relationship, as illustrated by the clustered distribution of markers in Figure 4a. The finding that $\Delta(\Delta_{47}) \approx 0$ for all of the thermodynamic gas standards (both at 25 °C and 1000 °C) can be understood simply as a consequence of the conversion to absolute Δ_{47} values, which necessarily assigns a single, temperature-dependent value to the standard gases. It should be noted, however, that the vertical spread of standard gas markers in Figure 4a is minuscule, which does not appear to be the case for other types of measurements shown here, suggesting that all equilibrated gases share some attribute which dictates the value of $\Delta(\Delta_{47})$.

By contrast, $\Delta(\Delta_{47})$ is strongly correlated with $\delta^{13}C$ values (Figure 4b). Because all of our thermodynamic gas standards are prepared from the same CO_2 tank with $\delta^{13}C_{VPDB} \approx -3.6$ ‰, the use of different isotopic parameters affects them all in the same manner, offsetting Δ_{47}^{raw} by a uniform amount which cancels out in the conversion to absolute Δ_{47} values.

This strong correlation with $\delta^{13}C$ is a systematic feature of our real-world data set, as can be verified by modifying the original [*Gonfiantini*] parameters in various ways (Figure 4b), such as changing R^{13}_{VPDB} to the value of *Chang and Li (1990)* and/or changing λ to the meteoric water value of 0.528. The respective effects of these various changes are additive, and, as expected, the intersection of all regression lines corresponds to the gas standards ($\delta^{13}C_{VPDB} = -3.6$ ‰ and $\Delta(\Delta_{47}) = 0$).

3.1.2 Random data simulation results

The random data simulations described in section 2.3 provide us with a more general view of the observations described above.

As a starting point, we computed Δ_{47}^{raw} values, using either the [*Gonfiantini*] or the [*Brand*] parameters, for 100 simulated measurements with $\delta^{13}C_{VPDB}$ and $\delta^{18}O_{VPDB\text{-}CO_2}$ values between -30 ‰ and $+30$ ‰, Δ_{47} between 0 ‰ and 1 ‰, and working reference gas $\delta^{13}C_{VPDB}$ and $\delta^{18}O_{VPDB\text{-}CO_2}$ between -30 ‰ and $+30$ ‰ (all of which were randomly generated from uniform distributions). By analogy with $\Delta(\Delta_{47})$, here we define $\Delta(\Delta_{47}^{raw})$ as the difference, for each measurement, between Δ_{47}^{raw} computed from the [*Brand*] parameters and Δ_{47}^{raw} computed from [*Gonfiantini*].

The exact analytical formulation of $\Delta(\Delta_{47}^{raw})$ is extremely cumbersome. Alternatively, as shown in Figure 5, $\Delta(\Delta_{47}^{raw})$ can be described to a very good approximation (with a root-mean-square error of 0.3 ppm), by the following relationship:

$$\Delta(\Delta_{47}^{raw}) = A\left(\delta^{13}C\,[s] - \delta^{13}C\,[wg]\right) + B\left(\delta^{18}O\,[s] - \delta^{18}O\,[wg]\right) \qquad (10)$$

where $\delta^{13}C[s]$ and $\delta^{13}C[wg]$ are the respective $\delta^{13}C_{VPDB}$ values of the sample and working gas, $\delta^{18}O[s]$ and $\delta^{18}O[wg]$ their respective $\delta^{18}O_{VPDB\text{-}CO_2}$ values. Coefficients A and B were computed by least-squares fitting of the 100 simulated measurements, yielding $A = -5.38 \times 10^{-4}$ and $B = +6.95 \times 10^{-4}$. Because this equation reflects a purely mathematical effect, the best-fit values for (A,B) would not change significantly for a different (sufficiently large) set of random data.

Although using different isotopic parameters thus affects Δ_{47}^{raw} in a simple, systematic manner, it should be noted that these effects have a dimensionality of 2, i.e. $\Delta(\Delta_{47}^{raw})$ varies as a function of two independent parameters. Subsequent conversion to the absolute scale also behaves as a function of two independent parameters (δ^{47} and Δ_{47}^{raw}), but only the former is directly linked to bulk isotope compositions ($\delta^{47} \approx \delta^{13}C + \delta^{18}O$). To illustrate this point, let us consider a situation where all thermodynamic gas standards share the same $\delta^{13}C$ value. In that case, δ^{47} only varies with $\delta^{18}O$, so that the conversion to absolute values will also cancel the effects of parameter B in equation (10). The $\delta^{13}C$ effects (parameter A), however, are left uncorrected, as displayed in Fig-

ure 4b. Conversely, if all thermodynamic gas standards share the same $\delta^{18}O$ value, conversion to the absolute scale will correct for parameter A but not for B.

In order to test this prediction, we generated a second set of 50 simulated measurements, with random, uniformly distributed $\delta^{13}C_{VPDB}$ and $\delta^{18}O_{VPDB\text{-}CO_2}$ values between -15 ‰ and $+15$ ‰ and random Δ_{47} values between 0.05 ‰ and 0.9 ‰. In this case, the working gas composition was assigned constant values ($\delta^{13}C_{VPDB} = 0$ ‰, $\delta^{18}O_{VPDB\text{-}CO_2} = 0$ ‰) to imitate real-world measurement conditions. We then arbitrarily assumed that the [*Brand*] parameters are the "true" ones and used these parameters to compute the working gas delta values (δ^{45} to δ^{49}) for each of the 50 simulated samples. We can then convert these samples to the absolute scale using the [*Gonfiantini*] parameters, based on three hypothetical sets of 16 thermodynamic gas standards. All gas standards in the first set have identical $\delta^{13}C_{VPDB} = 0$ ‰ and variable $\delta^{18}O_{VPDB\text{-}CO_2}$ values (Figure 6a); gases from the second one have random $\delta^{13}C_{VPDB}$ and $\delta^{18}O_{VPDB\text{-}CO_2}$ values (Figure 6b); and all gases in the third set have variable $\delta^{13}C_{VPDB}$ values and identical $\delta^{18}O_{VPDB\text{-}CO_2} = 0$ ‰ (Figure 6c).

As predicted, the resulting measurement errors (defined as the difference between the Δ_{47} value measured using [*Gonfiantini*] and the "true" starting value) are perfectly correlated with $\delta^{13}C$ in the first case, weakly correlated with both $\delta^{13}C$ and $\delta^{18}O$ in the second one, and perfectly correlated with $\delta^{18}O$ in the third one (Figure 6). In all three cases, the amplitude of Δ_{47} errors remains the same, on the order of 40 ppm. One important result of this simulation is that using a single set of isotopic parameters does not ensure that Δ_{47} measurements remain consistent through time or between laboratories: if these isotopic parameters are inaccurate, the resulting Δ_{47} errors are significant, and vary strongly with the bulk isotopic compositions of the standards used for conversion to the absolute scale.

3.1.3 Variability between sessions in real-world measurements

Going back to our real-world data, residuals for the regression of $\Delta(\Delta_{47})$ as a linear function of $\delta^{13}C_{VPDB}$ (Figure 4b, [*Brand*] versus [*Gonfiantini*]) are plotted in Figure 7. Due to strong correlation between the two variables, these residuals remain extremely small, within ±0.5 ppm. However, all residuals within a single analytical session (defined as a continuous period of stable instrumental/analytical conditions) are themselves well correlated with $\delta^{13}C$. In other

words, data from each session would yield slightly different regression slopes in Figure 4b, although differences from one session to another would remain within ±0.5 ppm.

These differences can be understood as a consequence of equations (9) and (10). Differences in isotopic parameters affect Δ_{47}^{raw} in a mathematically predictable way. As discussed in the previous section, conversion to the absolute scale partially corrects for these effects, but the remaining Δ_{47} offsets are scaled by a factor of $1/a$ in the conversion (equation 9). We would thus expect that session-to-session variability of the a parameter manifests as small differences in the regression slope of $\Delta(\Delta_{47})$ versus $\delta^{13}C$. This prediction is consistent with the observations from our real-world data set, where session-specific regression slopes are indeed proportional to $1/a$ (Figure 7).

3.1.4 Methodological implications

The findings described above have serious implications regarding modern analytical protocols. For one thing, it is clear that the use of different parameters in different research groups is likely to produce Δ_{47} discrepancies up to several tens of ppm (e.g., Figure 4). Furthermore, even if Δ_{47} measurements were universally processed using identical but inaccurate parameters, the random data simulations summarized in Figure 6 still predict significant errors which will strongly depend on the bulk isotopic compositions of the standards used for conversion to the absolute scale, again resulting in notable discrepancies between different research groups. Incidentally, the large, ^{13}C-dependent offsets in thermodynamic gas standard measurements recently reported by *Schauer et al. (2016b)* can be simply interpreted as a result of isotopic parameter effects such as those described above (see also *Olack and Colman, 2016* and *Schauer et al., 2016a,* in review).

In the strictest sense, theory predicts that equilibrium Δ_{47} values will vary slightly with $\delta^{13}C$ and $\delta^{18}O$, because mass-47 CO_2 includes three isotopologues with different stochastic anomalies at a given temperature *(Wang et al., 2004).* However, this effect remains out of reach of current precision limits (computation details and example values are provided in Appendix B). Therefore we expect, using accurate isotopic parameters, that samples with different bulk isotope compositions but known to have quasi-identical mass-47 anom-

alies will yield identical Δ_{47} values within analytical uncertainties, providing us with an empirical basis for testing the accuracy of various sets of isotopic parameters.

3.2 Optimal isotopic parameters for water-equilibrated CO_2

As discussed above, it is possible to search for isotopic parameters which would result in quasi-identical measured Δ_{47} values for CO_2 samples with different bulk isotope compositions and equilibrated at a known temperature. We thus prepared three sample groups with $\delta^{13}C_{VPDB}$ values of -37.8, -23.8 and -3.7 ‰, respectively, and equilibrated them at 25 °C with 60 µL aliquots of the same deionized water whose ^{17}O excess was independently measured by water fluorination ($\delta^{18}O_{VSMOW} = +10.5$ ‰, $\Delta^{17}O_{water} = +5$ ppm relative to VSMOW). Samples in the most ^{13}C-enriched ("eEG") and ^{13}C-depleted ("CdEG-B") groups were prepared from two different commercial tanks of CO_2, while those from the third group ("CdEG-A") were produced by acid digestion of commercial, reagent-grade calcium carbonate (Rhône-Poulenc Prolabo). Molar ratios of CO_2 to H_2O were on the order of 1:100, ensuring quasi-identical triple oxygen isotope compositions for all equilibrated samples. In the conversion to absolute Δ_{47} values, only the samples in the ^{13}C-enriched group ("eEG") were treated as thermodynamic gas standards.

Two other types of thermodynamic gas standards were prepared from the same ^{13}C-enriched CO_2, either equilibrated at 25 °C with a mixture of high-latitude meteoric waters ($\delta^{18}O_{VSMOW} = -20.6$ ‰, $\Delta^{17}O_{water} = -34$ ppm), or heated to 1000 °C after equilibration at room temperature with a different mixture of high-latitude meteoric waters ($\delta^{18}O_{VSMOW} = -28.7$ ‰, $\Delta^{17}O_{water} = -88$ ppm). Although δ^{47}-enriched heated gases were also analyzed over the course of the experiment, they were excluded from this particular dataset so that the "compositional slope" (parameter *b* in equation 8) is exclusively constrained by the 25 °C gas standards.

Table 2 lists the average isotopic compositions of these five different gases. All samples were analyzed within a single session in February 2016, following the same protocols as those described in section 2. For each measurement, the calculation of $\delta^{18}O$ from equation (4) was based on an assumed $\Delta^{17}O$ value (relative to VSMOW) inherited from its equilibration water, with an additional modifier of -205.1 ppm based on the oxygen isotope fractionation factors reported by *Barkan and Luz (2012)* for CO_2-H_2O equilibrium at 25 °C:

$$^{18}\alpha = 1.041036$$
$$\ln(^{17}\alpha)/\ln(^{18}\alpha) = 0.5229$$
$$\ln(^{17}\alpha) - 0.528 \times \ln(^{18}\alpha) = -0.0002051$$

Raw data for this water equilibration experiment were processed using the [*Chang + Assonov*], [*Chang + Li*], , [*Craig + Assonov*], and [*Craig + Li*] parameters, and for comparison purpose also using those of [Gonfiantini]. The results are summarized in Table 2 and Figure 8. By design, the samples treated as thermodynamic standards (eEG, dEG and dHG) retain their nominal Δ_{47} values for all sets of isotopic parameters. By contrast, Δ_{47} values for the ^{13}C-depleted samples CdEG-A and CdEG-B vary by up to 50 ppm, and, as predicted, these offsets are almost perfectly proportional to the difference in $\delta^{13}C$ relative to eEG. All three sets of parameters using the *Li et al. (1988)* value for R^{17}_{VSMOW} (including [*Gonfiantini*]), yield non-zero slopes of Δ_{47} versus $\delta^{13}C$. By contrast, both [*Assonov*] sets produce Δ_{47} values between 922.5 and 926.9 ppm, statistically indistinguishable from the equilibrium value of 925.0 ppm. As can be verified using the source code for Figure 8 (provided in the supplementary material), these results do not depend in any significant way on the $\Delta^{17}O$ modifier used to account for CO_2-H_2O equilibrium fractionation.

Based on the plots in Figure 8, it appears that Δ_{47} versus $\delta^{13}C$ slopes are not very sensitive to the numerical value of R^{13}_{VPDB}, but vary significantly with the ratio of R^{13}_{VPDB} / R^{17}_{VSMOW}. Assuming that our values for R^{18}_{VSMOW} and λ are correct, these results imply that the determination of R^{13}_{VPDB} / R^{17}_{VSMOW} by *Assonov and Brenninkmeijer (2003b)* is more accurate than the previous estimate by *Li et al. (1988).*

3.3 Optimal isotopic parameters for carbonate samples

A conceptually similar experiment can be made by comparing the Δ_{47} values computed for the ETH-1 and ETH-2 carbonate standards. To the best of our knowledge, these two standards, whose $\delta^{13}C_{VPDB}$ values differ by 12 ‰, were produced through identical heating experiments (10 h, 600 °C, 155 MPa, from Table 1 in *Meckler et al., 2014*). Assuming that their bond reordering kinetics are similar (which is probably not strictly true but remains a reasonable first-order assumption), one would thus expect their true Δ_{47} values to be very close. To test this prediction, we computed average Δ_{47} for ETH-1 (n = 18) and ETH-2 (n = 13) based on the real-world data set described in section 2.2.

As pointed out by *Assonov and Brenninkmeijer (2003a),* triple oxygen isotope parameters applicable to CO_2 produced by acid digestion of carbonates should be closely related to those applicable to natural surface waters. We might assume, for instance, as did *Brand et al. (2010),* that VPDB-CO_2 plots on the same triple oxygen isotope line as VSMOW ($\Delta^{17}O = 0$). Alternatively, one may assign carbonates a constant but non-zero value to $\Delta^{17}O$ (relative to VSMOW), based on analyses of CO_2 produced from NBS-19. Two such experiments were reported by *Passey et al. (2014)* and *Barkan et al. (2015),* with respective results of $\Delta^{17}O = -0.135$ ‰ and $\Delta^{17}O = -0.227$ ‰. These three options correspond to three different triple oxygen isotope lines, hereafter referred to as [*Brand*], [*Passey*] and [*Barkan*] (see Table 1).

In this round of calculations, we explicitly account for a $\Delta^{17}O$ difference between carbonates ($\Delta^{17}O = 0$, -135 or -227 ppm relative to [*Chang + Assonov*]) and water-equilibrated CO_2 ($\Delta^{17}O = -205.1$ ppm). As before, we also account for independently measured water ^{17}O anomalies in our thermodynamic gas standards.

Table 3 lists the average Δ_{47} values and the difference between ETH-1 and ETH-2, computed for each set of isotopic parameters (including [*Gonfiantini*] for comparison). The [*Gonfiantini*] parameters yield a statistically significant difference of 21 ± 9 ppm (1SE), which compares well with the 18 ppm (1SE) systematic error predicted for the [*Gonfiantini*] parameters, based on the slope from Figure 4b and the difference in $\delta^{13}C$.

Because [*Brand*], [*Passey*] and [*Barkan*] assume different ^{17}O anomalies between the carbonates and the thermodynamic gas standards, the resulting Δ_{47} values of ETH-1 and ETH-2 covary by up to 10 ppm, consistent with the small effects predicted in Figure 2. However, as shown in Figure 9, these three options yield much smaller Δ_{47} differences on the order of 4 ± 9 ppm, demonstrating that all three sets of parameters derived from [*Chang + Assonov*] produce quasi-identical Δ_{47} values for ETH-1 and ETH-2.

At face value, these findings appear to be at odds with those of *Meckler et al. (2014),* who reported quasi-identical values for ETH-1 and ETH-2 despite using the [*Gonfiantini*] parameters (A. Meckler, pers. comm.). It is difficult to offer anything but conjecture without reprocessing the corresponding raw data set, but we note that the *Meckler et al.* values could result from using thermodynamic gas standards with bulk isotopic compositions different from ours. For

example, in the purely hypothetical case where 1000 °C gas standards ("heated gases") were prepared from ETH-1 and ETH-2 themselves, the final Δ_{47} values for these standards are expected to be independent from the choice of isotopic parameters.

Our ETH results are consistent with those of the water equilibration experiment described in section 3.2. However, these ETH measurements suffer from one potential limitation: they are strongly constrained by the measured values of our 1000 °C gas standards ("heated gases"), whose ^{17}O anomalies are not as robustly constrained as those of water-equilibrated CO_2 standards. Although our heated gases are initially prepared from CO_2 equilibrated with waters with well-known $\Delta^{17}O$ values, there have been numerous observations (e.g. *Huntington et al., 2009*) that the subsequent heating protocol can cause $\delta^{18}O$ values to change by up to several permil, possibly due to oxygen exchange between CO_2 and the quartz tube. Such oxygen exchange reactions potentially modify ^{17}O anomalies, so that heated gas measurements may be slightly less accurate than those of water-equilibrated gas standards. However, to the best of our knowledge, this remains for now a purely hypothetical issue, and testing it will require high-precision, direct measurements of $\Delta^{17}O$ in CO_2.

3.4 Carbonate calibration discrepancies

In order to assess the influence of different isotopic parameters on carbonate calibration lines from different research groups, we reprocessed the raw data used by *Zaarur et al. (2013),* and compared the results with those obtained for unpublished synthetic carbonates precipitated at LSCE. Experimental details of the precipitation techniques are not directly relevant here, but the protocols used at Yale and LSCE were very similar, apart from the isotopic composition of the CO_2 used to prepare saturated solutions, resulting in carbonates with different $\delta^{13}C_{VPDB}$ values (-32.6 and $+9.9$ ‰ on average, respectively).

Although the Yale measurements predate the widespread adoption of the absolute scale of *Dennis et al. (2011),* we can still perform the corresponding corrections for each session, based on repeated analyses of heated gases (1000 °C) and of three internal laboratory standards (one CO_2 tank, one speleothem and one Carrara marble), whose absolute Δ_{47} values were determined for different isotopic parameters by comparison with thermodynamic gas standards at 1000 °C and 25 °C. Five out of the seven *Zaarur et al.* calibration samples, pre-

cipitated at temperatures ranging from 5 to 65 °C, were robustly constrained by these internal standards, and the two unconstrained samples were found to have very little influence on the best-fit calibration line itself.

Figure 10 illustrates the contrast between the Yale and LSCE calibration lines. In an effort to remain as close as possible to the raw data, here we report measured Δ_{47} values without any correction for acid reaction temperatures (25 °C at Yale versus 90 °C at LSCE), resulting in a large Δ_{47} difference at a given temperature (0.084 ‰ and 0.118 ‰ at 25 °C for [*Gonfiantini*] and [*Brand*], respectively). Strikingly, the distance between the Yale and LSCE calibrations increase by 36 ppm when switching from the [*Gonfiantini*] to the [*Brand*] parameters. These large shifts do not significantly affect the calibration slopes, however. The [*Brand*] slope for Yale (4.4 ppm/K at 20 °C, consistent with the findings of *Zaarur et al., 2013*) is 40 % steeper than the [*Brand*] slope for LSCE (3.1 ppm/K at 20 °C), and these values barely change when using the [*Gonfiantini*] parameters.

Generally speaking, each calibration data set for the carbonate clumped isotope thermometer will differ in terms of the relative bulk isotope compositions of samples and standards. Thus, as implied by the random data simulations described in section 3.1.2 and summarized in Figure 6, it is difficult to predict how each published calibration would change (or not) for a different set of parameters. Nevertheless, from the Yale/LSCE comparison reported here, we infer that some aspects of the current discrepancies between published carbonate calibrations (e.g., Figure 4 from *Spencer and Kim, 2015*) can be explained by such sample/standard compositional differences and/or by the use of different isotopic parameters. These effect, however, do not appear to provide an explanation for the large reported differences in carbonate calibration slopes.

4 RECOMMENDATIONS

Based on all the results presented above, it appears likely that data reduction procedures contribute significantly to current inter-laboratory discrepancies. This is not simply a matter of agreeing on a single set of isotopic parameters: the choice of certain values, including the [*Gonfiantini*] parameters originally used by the Caltech group, demonstrably leads to spurious effects such as those displayed in Figure 8a. To make matters worse, these effects will

manifest in very different ways depending on the relative bulk isotope compositions of samples and of the standards used for conversion to the absolute scale (Figure 6).

A natural way forward would be to establish consensus on a set of isotopic parameters known to make Δ_{47} measurements quasi-independent of bulk isotope compositions. Based on the observations reported here, and with the caveat that these results require independent confirmation, we offer the following recommendations:

(1) Raw data processing should use the [*Brand*] isotopic parameters listed below. Note that with these numbers, the choice of VSMOW or VPDB-CO_2 as a triple oxygen isotope reference material is of no consequence, because they are both assumed to belong to the [*Chang + Assonov*] water line.

$$\begin{aligned}
R^{13}_{\text{VPDB}} &= 0.01118 && \text{(\textit{Chang and Li, 1990})}\\
R^{18}_{\text{VSMOW}} &= 0.00200520 && \text{(\textit{Baertschi, 1976})}\\
R^{17}_{\text{VSMOW}} &= 0.00038475 && \text{(\textit{Assonov and Brenninkmeijer, 2003b,} re-scaled)}\\
R^{18}_{\text{VPDB-CO}_2} &= 0.00208839 && \text{(derived from \textit{Baertschi, 1976} using equation 2)}\\
R^{17}_{\text{VPDB-CO}_2} &= 0.00039310 && \text{(\textit{Assonov and Brenninkmeijer, 2003b,} re-scaled)}\\
\lambda &= 0.528 && \text{(\textit{Barkan and Luz, 2005})}
\end{aligned} \tag{11}$$

Using these parameters, the measurements reported here yield statistically indistinguishable Δ_{47} values for ETH-1 and ETH-2, with a combined average value of 218.3 ± 4.4 ppm (1SE, N = 31, 90 °C acid reaction, no acid temperature correction).

Technically, it would be possible to take into account the respective ^{17}O anomalies of water-equilibrated and carbonate-evolved CO_2. However, the discrepancy between the results of *Passey et al. (2014)* and *Barkan and Luz (2012)* implies that the ^{17}O composition of VPDB-CO_2 is not well constrained enough to do so with confidence. For now, we recommend that all types of measurements be processed using the unmodified parameters listed above, keeping in mind that doing so will produce a systematic, quasi-constant bias of a few ppm in carbonate samples relative to water-equilibrated gases.

(2) H_2O-equilibrated gas standards should be produced using water with small ^{17}O anomalies relative to VSMOW. In practice, pure meteoric waters and mixtures of meteoric waters should meet these requirements, with expected

$\Delta^{17}O$ values ranging from -0.1 ‰ (corresponding to a Δ_{47} offset of $+3.6$ ppm based on Figure 2) to $+0.05$ ‰ (Δ_{47} offset of -1.8 ppm). By contrast, isotopic enrichment by evaporation may potentially produce large negative ^{17}O anomalies (e.g., -0.4 ‰ was observed at LSCE under rapid evaporation conditions). Thus, if possible, $\Delta^{17}O$ in such evaporatively enriched waters should be measured independently.

(3) Raw data processing software should be able to solve equation (4) to a level of precision better than 0.1 ppm, which would allow two-way, lossless conversion between working gas delta values (δ^{45} to δ^{49}), bulk isotope compositions and clumped isotope anomalies, and ensure that the simpler definition of Δ_{47} (equation 7) is mathematically equivalent to the traditional one. Using the Taylor polynomial approximation described in Appendix A, such precision is easily achieved in virtually any software environment. By way of example, two reference implementations for Python and Excel are provided as supplementary material, which also allow taking into account potential ^{17}O anomalies for each analyte. We also provide an online application (*http://daeron.fr/clumpycrunch*), based on the algorithms described above, which makes it simple to process new raw data sets using any combination of isotopic parameters, and allows conversion to absolute Δ_{47} values.

(4) Conversion of past measurements from one set of isotopic parameters to a different one can be done in two ways. If working gas delta values (δ^{45} to δ^{49}) are available (including those of all related thermodynamic gases standards and/or carbonate standards), one may directly reprocess the raw data based on the new parameters. Alternatively, one could use a relationship between Δ_{47}^{raw}, $\delta^{13}C$ and $\delta^{18}O$ similar to that of equation (10), but a requirement of this approach is that the reported values for $\delta^{13}C$ and $\delta^{18}O$ must conform to equation (4) to a very good approximation, which is not necessarily the case for existing commercial software.

5 CONCLUSIONS

The mathematical treatment of raw data produced by IRMS analyses of CO_2 has evolved over time. Instrumental precision improvements and the increasing need for inter-laboratory consistency prompted a shift from the original *Craig (1957)* equations to the more accurate *Santrock et al. (1985)* correction procedure and its successors (e.g., *Brand et al., 2010*). Clumped isotopes require increased precision, at the level of a few ppm, and present new, specific

challenges in terms of linearity correction and standardization procedures. Because of these requirements, however, clumped isotopes also offer new opportunities to test the accuracy of absolute isotopic ratios in reference materials.

Based on the observations reported above, the isotopic parameters reported by *Brand et al. (2010)* appear to yield accurate Δ_{47} values regardless of bulk isotopic composition. The recommendations offered here rely critically on measurements of samples believed to share quasi-identical Δ_{47} values. Pending independent confirmation of these results, we expect that systematic use of the isotopic parameters listed above will help reduce inter-laboratory discrepancies, particularly for samples with "exotic" bulk isotopic compositions.

ACKNOWLEDGEMENTS

We are indebted to A. Schauer, whose presentation at the fifth international clumped isotope workshop (*Schauer et al., 2016b*) provided the original motivation for this work. This article was significantly improved thanks to the thoughtful comments of an anonymous reviewer. We also thank A. Landais for performing analyses of ^{17}O excess in water, and E. Michel for providing us with a tank of ^{13}C-depleted CO_2. The Yale data reprocessed here was originally measured by S. Zaarur and various members of the Affek group. The clumped isotope facility at LSCE was established with the help of many former members of the Eiler group at Caltech, most particularly B. Passey, and with financial support from the following institutions : Région Ile-de-France; Direction des Sciences de la Matière du Commissariat à l'Energie Atomique; Institut National des Sciences de l'Univers, Centre National de la Recherche Scientifique; Universtité de Versailles / Saint-Quentin-en-Yvelines. This is LSCE contribution #5802.

APPENDIX

A Taylor polynomial calculation of $\delta^{18}O$ and $\delta^{13}C$

Computing $\delta^{18}O$ requires solving the following equation (generalized from *Santrock et al., 1985*):

$$\begin{gathered} -3K^2(R^{18})^{2\lambda} + 2K(R^{45})(R^{18})^{\lambda} + 2R^{18} - R^{46} = 0 \\ \text{with :} \quad K = \exp(\Delta^{17}O)\, R^{17}_{ref}\, (R^{18}_{ref})^{-\lambda} \end{gathered} \tag{A.1}$$

We may define x as the dimensionless value of $\delta^{18}O_{VPDB\text{-}CO_2}$:

$$R^{18} = (1+x)R^{18}_{VPDB\text{-}CO_2} \tag{A.2}$$

Combining equations (A.1) and (A.2) yields:

$$A(1+x)^{2\lambda} + B(1+x)^{\lambda} + C(1+x) + D = 0 \tag{A.3}$$

with:

$$\begin{aligned} A &= -3K^2\, (R^{18}_{VPDB\text{-}CO_2})^{2\lambda} \\ B &= 2K\, R^{45}\, (R^{18}_{VPDB\text{-}CO_2})^{\lambda} \\ C &= 2\, R^{18}_{VPDB\text{-}CO_2} \\ D &= -R^{46} \end{aligned}$$

Because $x \ll 1$, we can use the following second-order Taylor polynomials:

$$\begin{aligned} (1+x)^{2\lambda} &\approx 1 + 2\lambda x + \lambda(2\lambda-1)x^2 \\ (1+x)^{\lambda} &\approx 1 + \lambda x + \tfrac{1}{2}\lambda(\lambda-1)x^2 \end{aligned} \tag{A.4}$$

Substitution of (A.4) into (A.3) yields :

$$ax^2 + bx + c \approx 0 \tag{A.5}$$

with:

$$\begin{aligned} a &= A\,\lambda(2\lambda-1) + B\,\lambda(\lambda-1)/2 \\ b &= 2A\,\lambda + B\,\lambda + C \\ c &= A + B + C + D \end{aligned}$$

which is solved trivially by:

$$x \approx \frac{-b + (b^2 - 4ac)^{1/2}}{2a} \approx \delta^{18}O_{VPDB\text{-}CO_2} \tag{A.6}$$

$\delta^{13}C$ may then be computed directly:

$$\begin{aligned} R^{17} &= K(R^{18})^{\lambda} \\ R^{13} &= R^{45} - 2R^{17} \\ \delta^{13}C_{VPDB} &= R^{13}/R^{13}_{VPDB} - 1 \end{aligned} \tag{A.7}$$

Using this method, the errors on computed values of $\delta^{13}C$, $\delta^{18}O$, and Δ_{47}^{raw} remain smaller than 2×10^{-5} ‰ for all $\delta^{13}C_{VPDB}$ and $\delta^{18}O_{VPDB\text{-}CO_2}$ values between -50 ‰ and $+50$ ‰.

B Influence of bulk isotopic composition on equilibrium values of Δ_{47} in CO_2

According to Table 4 in *Wang et al. (2004),* equilibrium values for mass-47 isotopologues of CO_2 at 300 K are:

$$\begin{aligned} \Delta_{^{16}O^{13}C^{18}O} &= \Delta_{638} = 0.9384 \text{ ‰} \\ \Delta_{^{17}O^{12}C^{18}O} &= \Delta_{728} = 0.1681 \text{ ‰} \\ \Delta_{^{17}O^{13}C^{17}O} &= \Delta_{737} = 1.0738 \text{ ‰} \end{aligned} \tag{B.1}$$

Let us consider the case of a CO_2 sample with known $\delta^{13}C_{VPDB}$ and $\delta^{18}O_{VPDB\text{-}CO_2}$. The following equations use the dimensionless expression of delta values, so that:

$$\begin{aligned} R^{13} &= R^{13}_{VPDB} \times (1 + \delta^{13}C) \\ R^{18} &= R^{18}_{VPDB\text{-}CO_2} \times (1 + \delta^{18}O) \\ R^{17} &= R^{17}_{VPDB\text{-}CO_2} \times (1 + \delta^{18}O)^{\lambda} \end{aligned} \tag{B.2}$$

Stochastic isotopologue abundance ratios are then:

$$\begin{aligned} R(^{16}O^{13}C^{18}O)_{stoch} &= 2R^{13}R^{18} \\ R(^{17}O^{12}C^{18}O)_{stoch} &= 2R^{17}R^{18} \\ R(^{17}O^{13}C^{17}O)_{stoch} &= R^{13}(R^{17})^2 \end{aligned} \tag{B.3}$$

so that:

$$\Delta_{47} = \frac{2R^{13}R^{18}(1+\Delta_{638}) + 2R^{17}R^{18}(1+\Delta_{728}) + R^{13}(R^{17})^2(1+\Delta_{737})}{2R^{13}R^{18} + 2R^{17}R^{18} + R^{13}(R^{17})^2} - 1 \tag{B.4}$$

By combining equations (B.1), (B.2) and (B.4), equilibrium Δ_{47} values may be computed for a given bulk isotopic composition ($\delta^{13}C_{VPDB}$, $\delta^{18}O_{VPDB\text{-}CO_2}$) at 300 K. For example, the compositional differences in equilibrium Δ_{47} values between samples in our ^{13}C-depleted CO_2 equilibration experiment (Table 2) and VPDB-CO_2 are listed in Table 4.

C Supplementary data

Supplementary material associated with this article (`http://dx.doi.org/10.1016/j.chemgeo.2016.08.014`) includes source code for generating all figures except Figure 1, and, by way of example, Python scripts and an Excel spreadsheet intended to facilitate the conversion of past and future measurements from one set of isotopic parameters to another.

REFERENCES

Affek, H. and Eiler, J. (2006). Abundance of mass 47 CO_2 in urban air, car exhaust, and human breath. *Geochimica et Cosmochimica Acta* 70, pp. 1–12. doi: 10.1016/j.gca.2005.08.021.

Assonov, S.S. and Brenninkmeijer, C.A.M. (2003a). On the ^{17}O correction for CO_2 mass spectrometric isotopic analysis. *Rapid Communications in Mass Spectrometry* 17, pp. 1007–1016. doi: 10.1002/rcm.1012.

Assonov, S.S. and Brenninkmeijer, C.A.M. (2003b). A redetermination of absolute values for $^{17}R_{VPDB\text{-}CO2}$ and $^{17}R_{VSMOW}$. *Rapid Communications in Mass Spectrometry* 17, pp. 1017–1029. doi: 10.1002/rcm.1011.

Baertschi, P. (1976). Absolute ^{18}O content of Standard Mean Ocean Water. *Earth and Planetary Science Letters* 31, pp. 341–344.

Barkan, E. and Luz, B. (2005). High-precision measurements of $^{17}O/^{16}O$ and $^{18}O/^{16}O$ ratios in H_2O. *Rapid Communications in Mass Spectrometry* 19, pp. 3737–3742.

Barkan, E. and Luz, B. (2012). High-precision measurements of $^{17}O/^{16}O$ and $^{18}O/^{16}O$ ratios in CO_2. *Rapid Communications in Mass Spectrometry* 26, pp. 2733–2738. doi: 10.1002/rcm.6400.

Barkan, E., Musan, I., and Luz, B. (2015). High-precision measurements of $\delta^{17}O$ and $^{17}O_{excess}$ of NBS19 and NBS18. *Rapid Communications in Mass Spectrometry* 29, pp. 2219–2224. doi: 10.1002/rcm.7378.

Brand, W.A., Assonov, S.S., and Coplen, T.B. (2010). Correction for the ^{17}O interference in $\delta(^{13}C)$ measurements when analyzing CO_2 with stable isotope mass spectrometry (IUPAC Technical Report). *Pure and Applied Chemistry* 82:8, pp. 1719–1733. doi: 10.1351/PAC–REP–09–01–05.

Chang, T.L. and Li, W. (1990). A calibrated measurement of the atomic weight of carbon. *Chinese Science Bulletin* 35:290.

Coplen, T.B., Kendall, C., and Hopple, J. (1983). Comparison of stable isotope reference samples. *Nature* 302:5905, pp. 236–238. doi: 10.1038/302236a0.

Craig, H (1957). Isotopic standards for carbon and oxygen and correction factors for mass spectrometric analysis of carbon dioxide. *Geochimica et Cosmochimica Acta* 12, pp. 133–149.

Dennis, K.J., Affek, H.P., Passey, B.H., Schrag, D.P., and Eiler, J.M. (2011). Defining an absolute reference frame for 'clumped' isotope studies of CO_2. *Geochimica et Cosmochimica Acta* 75, pp. 7117–7131. doi: 10.1016/j.gca.2011.09.025.

Eiler, J.M. (2007). "Clumped-isotope" geochemistry—The study of naturally-occurring, multiply-substituted isotopologues. *Earth and Planetary Science Letters* 262, pp. 309–327. doi: 10.1016/j.epsl.2007.08.020.

Eiler, J.M. (2011). Paleoclimate reconstruction using carbonate clumped isotope thermometry. *Quaternary Science Reviews* 30, pp. 3575–3588. doi: 10.1016/j.quascirev.2011.09.001.

Eiler, J.M. and Schauble, E. (2004). $^{18}O^{13}C^{16}O$ in Earth's atmosphere. *Geochimica et Cosmochimica Acta* 68:23, pp. 4767–4777. doi: 10.1016/j.gca.2004.05.035.

Friedman, I. and O'Neil, J.R. (1977). *Compilation of stable isotope fractionation factors of geochemical interest*. Tech. rep. U.S. Geological Survey Professional Paper 440-KK.

Ghosh, P., Adkins, J., Affek, H., Balta, B., Guo, W., Schauble, E.A., Schrag, D., and Eiler, J.M. (2006). ^{13}C–^{18}O bonds in carbonate minerals: a new kind of paleothermometer. *Geochimica et Cosmochimica Acta* 70, pp. 1439–1456. doi: 10.1016/j.gca.2005.11.014.

Gonfiantini, R., Stichler, W., and Rozanski, K. (1995). *Standards and intercomparison materials distributed by the International Atomic Energy Agency for stable isotope measurements*. IAEA-TECDOC-825.

He, B., Olack, G.A., and Colman, A.S. (2012). Pressure baseline correction and high-precision CO_2 clumped-isotope (Δ_{47}) measurements in bellows and micro-volume modes. *Rapid Communications in Mass Spectrometry* 26, pp. 2837–2853. doi: 10.1002/rcm.6436.

Hofmann, M.E.G., Horváth, B., and Pack, A. (2012). Triple oxygen isotope equilibrium fractionation between carbon dioxide and water. *Earth and Planetary Science Letters* 319–320, pp. 159–164. doi: 10.1016/j.epsl.2011.12.026.

Huntington, K.W., Eiler, J.M., Affek, H.P., Guo, W., Bonifacie, M., Yeung, L.Y., Thiagarajan, N., Passey, B., Tripati, A., Daëron, M., and Came, R. (2009). Methods and limitations of 'clumped' CO_2 isotope (Δ_{47}) analysis by gas-source isotope-ratio mass spectrometry. *Journal of Mass Spectrometry* 44, pp. 1318–1329. doi: 10.1002/jms.1614.

Landais, A., Steen-Larsen, H.C., Guillevic, M., Masson-Delmotte, V., Vinther, B., and Winkler, R (2012). Triple isotopic composition of oxygen in surface snow and water vapor at NEEM (Greenland). *Geochimica et Cosmochimica Acta* 77, pp. 304–316. doi: 10.1016/j.gca.2011.11.022.

Li, W., Ni, B., Jin, D., and Chang, T.L. (1988). Measurement of the absolute abundance of oxygen-17 in VSMOW. *Chinese Science Bulletin* 33, pp. 1610–1613.

Matsuhisa, Y., Goldsmith, J.R., and Clayton, R.N. (1978). Mechanisms of hydrothermal crystallization of quartz at 250 °C and 15 kbar. *Geochimica et Cosmochimica Acta* 42, pp. 173–182.

Meckler, A.N., Ziegler, M., Millán, M.I., Breitenbach, S.F.M., and Bernasconi, S.M. (2014). Long-term performance of the Kiel carbonate device with a new correction scheme for clumped isotope measurements. *Rapid Communications in Mass Spectrometry* 28, pp. 1705–1715. doi: 10.1002/rcm.6949.

Meijer, H.A.J. and Li, W.J. (1998). The use of electrolysis for accurate $\delta^{17}O$ and $\delta^{18}O$ isotope measurements in water. *Isotopes in Environmental and Health Studies* 34:4, pp. 349–369. doi: 10256019808234072.

Nier, A.O. (1950). A redetermination of the relative abundances of the isotopes of carbon, nitrogen, oxygen, argon, and potassium. *Physical Review* 77:6, pp. 789–793. doi: 10.1103/PhysRev.77.789.

Olack, G. and Colman, M. (2016). Influence of ^{17}O correction parameters on calculation and calibration of Δ_{47}. *Goldschmidt abstracts*, p. 2378.

Olack, G., He, B., and Colman, M. (2013). Corrections for ^{17}O interference, effects on Δ_{47} determination. *AGU Fall Meeting*, V53B–2772.

Passey, B.H., Hu, H., Ji, H., Montanari, S., Li, S., Henkes, G.A., and Levin, N.E. (2014). Triple oxygen isotopes in biogenic and sedimentary carbonates. *Geochimica et Cosmochimica Acta* 141, pp. 1–25. doi: 10.1016/j.gca.2014.06.006.

Rosman, K.J.R. and Taylor, P.D.P. (1998). Isotopic Compositions of the Elements 1997. *Journal of Physical and Chemical Reference Data* 27:6, pp. 1275–1287. doi: 10.1063/1.556031.

Santrock, J., Studley, S.A., and Hayes, J.M. (1985). Isotopic Analyses Based on the Mass Spectrum of Carbon Dioxide. *Analytical Chemistry* 57, pp. 7444–1448.

Schauble, E.A., Ghosh, P., and Eiler, J.M. (2006). Preferential formation of ^{13}C–^{18}O bonds in carbonate minerals, estimated using first-principles lattice dynamics. *Geochimica et Cosmochimica Acta* 70, pp. 2510–2529. doi: 10.1016/j.gca.2006.02.011.

Schauer, A.J., Kelson, J., Saenger, C., and Huntington, K.W. (2016a). Choice of ^{17}O correction affects clumped isotope (Δ_{47}) values of CO_2 measured with mass spectrometry. *Rapid Communications in Mass Spectrometry*. In review.

Schauer, A.J., Kelson, J., Saenger, C., and Huntington, K.W. (2016b). Is the absolute reference frame absolute? An apparent dependency of Δ_{47} on $\delta^{13}C$ in CO_2. *Fifth International Clumped Isotope Workshop*.

Spencer, C. and Kim, S.-T. (2015). Carbonate clumped isotope paleothermometry: a review of recent advances in CO_2 gas evolution, purification, measurement and standardization techniques. *Geosciences Journal* 19:2, pp. 357–374. doi: 10.1007/s12303–015–0018–1.

Stolper, D.A., Sessions, A.L., Ferreira, A.A., Santos Neto, E.V., Schimmelmann, A., Shusta, S.S., Valentine, D.L., and Eiler, J.M. (2014). Combined ^{13}C-D and D-D clumping in methane: Methods and preliminary results. *Geochimica et Cosmochimica Acta* 126, pp. 169–191. doi: 10.1016/j.gca.2013.10.045.

Wang, Z., Schauble, E.A., and Eiler, J.M. (2004). Equilibrium thermodynamics of multiply substituted isotopologues of molecular gases. *Geochimica et Cosmochimica Acta* 68:23, pp. 4779–4797. doi: 10.1016/j.gca.2004.05.039.

Yeung, L.Y., Young, E.D., and Schauble, E.A. (2012). Measurements of $^{18}O^{18}O$ and $^{17}O^{18}O$ in the atmosphere and the role of isotope-exchange reactions. *Journal of Geophysical Research - Atmospheres* 117, p. D18306. doi: 10.1029/2012JD017992.

Zaarur, S., Affek, H.P., and Brandon, M.T. (2013). A revised calibration of the clumped isotope thermometer. *Earth and Planetary Science Letters* 382, pp. 47–57. doi: 10.1016/j.epsl.2013.07.026.

Designation	Isotopic parameters	Sources
[*Gonfiantini*]	$R^{13}_{PDB} = 0.0112372$	*Craig (1957)*
	$R^{18}_{VSMOW} = 0.0020052$	*Baertschi (1976)*
	$R^{17}_{VSMOW} = 0.0003799$	*Li et al. (1988)*
	$\lambda = 0.5164$	*Matsuhisa et al. (1978)*
[*Brand*]	$R^{13}_{VPDB} = 0.01118$	*Chang and Li (1990)*
[*Chang + Assonov*]	$R^{18}_{VSMOW} = 0.0020052$	*Baertschi (1976)*
	$R^{17}_{VSMOW} = 0.00038475$	*Assonov and Brenninkmeijer (2003b)*, rescaled to R^{13}_{VPDB}
	$R^{18}_{VPDB\text{-}CO_2} = 0.00208839$	derived from R^{18}_{VSMOW} using eq. (2)
	$R^{17}_{VPDB\text{-}CO_2} = 0.00039310$	*Assonov and Brenninkmeijer (2003b)*, rescaled to R^{13}_{VPDB}
	$\lambda = 0.528$	*Barkan and Luz (2005)*
[*Craig + Assonov*]	$R^{13}_{PDB} = 0.0112372$	*Craig (1957)*
	$R^{18}_{VSMOW} = 0.0020052$	*Baertschi (1976)*
	$R^{17}_{VSMOW} = 0.00038672$	*Assonov and Brenninkmeijer (2003b)*
	$\lambda = 0.528$	*Barkan and Luz (2005)*
[*Chang + Li*]	$R^{13}_{VPDB} = 0.01118$	*Chang and Li (1990)*
	$R^{18}_{VSMOW} = 0.0020052$	*Baertschi (1976)*
	$R^{17}_{VSMOW} = 0.0003780$	*Li et al. (1988)*, rescaled to R^{13}_{VPDB}
	$\lambda = 0.528$	*Barkan and Luz (2005)*
[*Craig + Li*]	$R^{13}_{PDB} = 0.0112372$	*Craig (1957)*
	$R^{18}_{VSMOW} = 0.0020052$	*Baertschi (1976)*
	$R^{17}_{VSMOW} = 0.0003799$	*Li et al. (1988)*
	$\lambda = 0.528$	*Barkan and Luz (2005)*
[*Barkan*]	$R^{13}_{VPDB} = 0.01118$	*Chang and Li (1990)*
	$R^{18}_{VPDB\text{-}CO_2} = 0.00208839$	derived from R^{18}_{VSMOW} using eq. (2)
	$R^{17}_{VPDB\text{-}CO_2} = 0.00039301$	$\Delta^{17}O = -227$ ppm vs VSMOW (*Barkan et al., 2015*)
	$\lambda = 0.528$	*Barkan and Luz (2005)*
[*Passey*]	$R^{13}_{VPDB} = 0.01118$	*Chang and Li (1990)*
	$R^{18}_{VPDB\text{-}CO_2} = 0.00208839$	derived from R^{18}_{VSMOW} using eq. (2)
	$R^{17}_{VPDB\text{-}CO_2} = 0.00039305$	$\Delta^{17}O = -135$ ppm vs VSMOW (*Passey et al., 2014*)
	$\lambda = 0.528$	*Barkan and Luz (2005)*

Table 1: All sets of isotopic parameters considered in this study. [*Brand*] and [*Chang + Assonov*] are formulated relative to different oxygen reference materials but are nevertheless strictly equivalent. Note that for reasons of consistency, the *Brand et al. (2010)* value for $R^{18}_{VPDB\text{-}CO_2}$ listed here is slightly greater than that originally reported, but this difference is entirely negligible in the context of the present study.

Group	Eq. T (°C)	$\Delta^{17}O_{water}$ (ppm, VSMOW)	Parameters	$\delta^{13}C_{VPDB}$ (‰)	$\delta^{18}O_{VPDB\text{-}CO_2}$ (‰)	Δ_{47} (ppm, ±1SE)
eEG	25	+5	[*Gonfiantini*]	-3.60	10.81	925.0 ± 6.7
(n = 4)			[*Craig + Li*]	-3.62	10.81	925.0 ± 6.7
			[*Chang + Li*]	-3.62	10.81	925.0 ± 6.7
			[*Craig + Assonov*]	-3.64	10.81	925.0 ± 6.7
			[*Chang + Assonov*]	-3.64	10.81	925.0 ± 6.7
dEG	25	−34	[*Gonfiantini*]	-3.63	-20.22	925.0 ± 6.0
(n = 5)			[*Craig + Li*]	-3.62	-20.22	925.0 ± 6.0
			[*Chang + Li*]	-3.62	-20.22	925.0 ± 6.0
			[*Craig + Assonov*]	-3.62	-20.22	925.0 ± 6.0
			[*Chang + Assonov*]	-3.62	-20.22	925.0 ± 6.0
dHG	1000	−88	[*Gonfiantini*]	-3.61	-27.43	26.6 ± 7.8
(n = 3)			[*Craig + Li*]	-3.60	-27.43	26.6 ± 7.8
			[*Chang + Li*]	-3.60	-27.43	26.6 ± 7.8
			[*Craig + Assonov*]	-3.59	-27.43	26.6 ± 7.8
			[*Chang + Assonov*]	-3.59	-27.43	26.6 ± 7.8
CdEG-A	25	+5	[*Gonfiantini*]	-23.71	10.48	897.9 ± 4.8
(n = 8)			[*Craig + Li*]	-23.73	10.48	907.8 ± 4.8
			[*Chang + Li*]	-23.73	10.48	908.5 ± 4.8
			[*Craig + Assonov*]	-23.77	10.48	926.1 ± 4.8
			[*Chang + Assonov*]	-23.77	10.48	926.9 ± 4.8
CdEG-B	25	+5	[*Gonfiantini*]	-37.63	10.16	874.4 ± 6.7
(n = 4)			[*Craig + Li*]	-37.65	10.16	891.2 ± 6.7
			[*Chang + Li*]	-37.65	10.16	892.4 ± 6.7
			[*Craig + Assonov*]	-37.71	10.16	922.5 ± 6.7
			[*Chang + Assonov*]	-37.71	10.16	923.7 ± 6.7

Table 2: Results of the water equilibration experiment. Sample groups eEG, dEG and dHG are treated as thermodynamic gas standards (and thus have constant Δ_{47} values), while groups CdEG-A and CdEG-B are treated as unknown samples. Standard errors are based on the overall external reproducibility (SD = 13.5 ppm) of all replicate measurements in this data set.

Parameters	**ETH-1** (ppm, ±1SE) n = 18	**ETH-2** (ppm, ±1SE) n = 13	**ETH-1 – ETH-2** (ppm, ±1SE)
[*Gonfiantini*]	228.1 ± 5.6	207.4 ± 6.8	20.7 ± 8.8
[*Brand*]	229.0 ± 5.6	224.4 ± 6.8	4.5 ± 8.8
[*Passey*]	223.3 ± 5.6	219.0 ± 6.8	4.3 ± 8.8
[*Barkan*]	219.4 ± 5.6	215.3 ± 6.8	4.2 ± 8.8

All values are unmodified Δ_{47} for 90 °C acid reaction.

Table 3: Comparison of Δ_{47} values for ETH-1 and ETH-2 computed using different isotopic parameters. Except for the [*Gonfiantini*] parameters, which are included for comparison only, these values take into account ^{17}O differences between carbonate-derived CO_2 and water-equilibrated gases. Standard errors are based on the external reproducibility (SD = 24 ppm) of each standard over the course of seven months.

Sample	$\delta^{13}C_{VPDB}$ (‰)	$\delta^{18}O_{VPDB\text{-}CO_2}$ (‰)	Δ_{47} difference (ppm)
eEG	-3.64	10.81	-0.24
dEG	-3.62	-20.22	$+0.18$
CdEG-A	-23.77	10.48	-0.76
CdEG-B	-37.71	10.16	-1.13

Table 4: Δ_{47} difference between our water-equilibrated samples and VPDB-CO_2, for 300 K equilibrium. See Appendix B for computation details

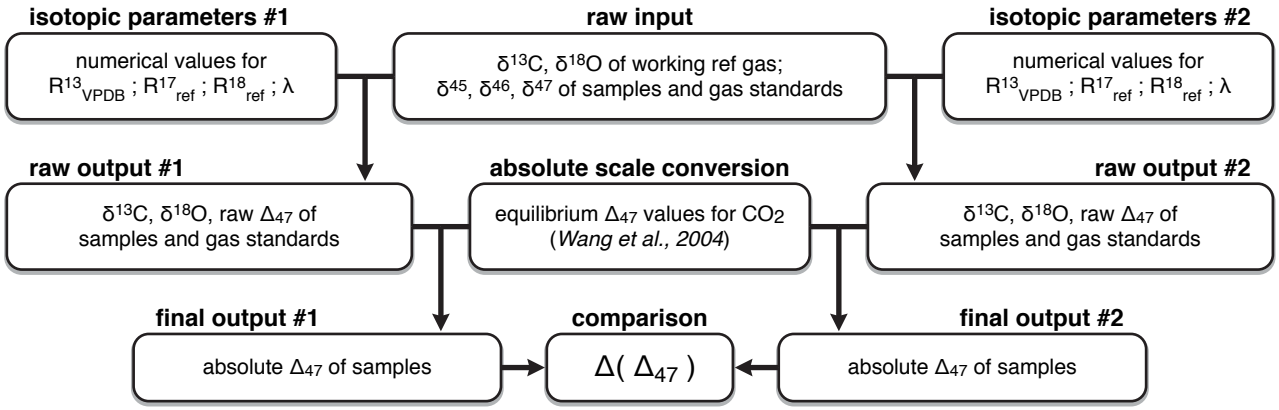

Figure 1: Schematic overview of our data processing methodology.

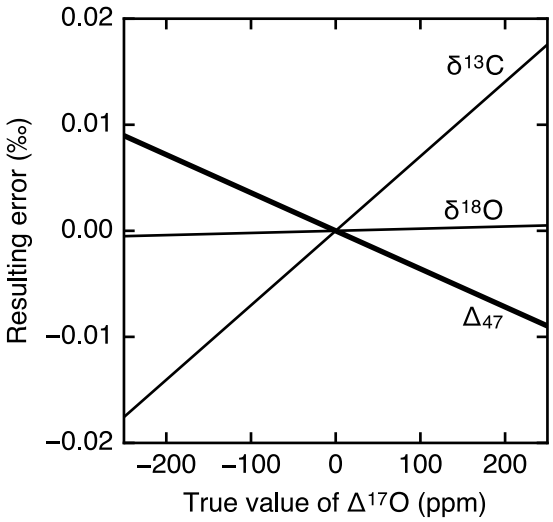

Figure 2: Errors resulting from wrongly assuming $\Delta^{17}O = 0$. An ^{17}O anomaly of +0.1 ‰, if not accounted for, causes computed $\delta^{13}C$, $\delta^{18}O$ and Δ_{47} values to be off by +0.0070 ‰, +0.0002 ‰ and – 0.0036 ‰ respectively. These errors are calculated for a stochastic sample with the same bulk isotopic composition as VPDB-CO_2, using the isotopic parameters of *Brand et al. (2010),* but would not change much for different values of $\delta^{13}C$, $\delta^{18}O$ and Δ_{47} nor for different sets of isotopic parameters. Source code provided as supplementary material.

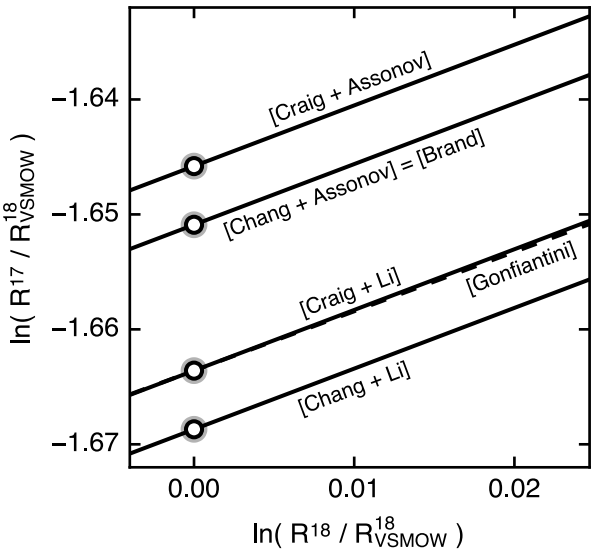

Figure 3: Triple oxygen isotope lines corresponding to the isotopic parameters listed in Table 1. Round markers correspond to the oxygen isotope composition of VSMOW. Source code provided as supplementary material.

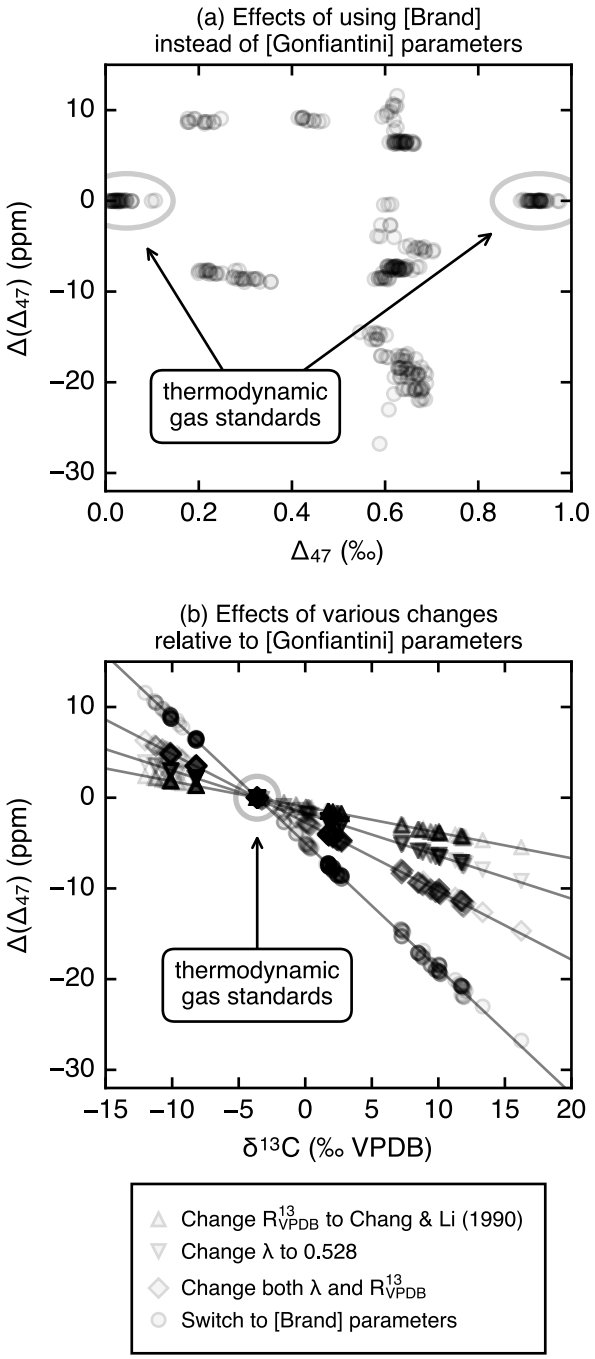

Figure 4: Effects of performing raw data reduction using different isotopic parameters. $\Delta(\Delta_{47})$ is the sample-to-sample difference in final, absolute Δ_{47} values, relative to the [*Gonfiantini*] parameters. Source code provided as supplementary material.

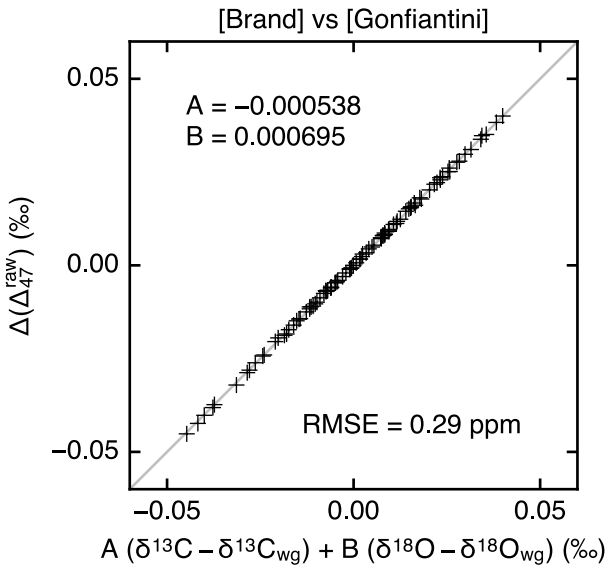

Figure 5: Relationship between $\Delta(\Delta_{47}^{raw})$, $\delta^{13}C$ and $\delta^{18}O$ based on random simulation data for 100 measurements. "RMSE": root mean square error. Source code provided as supplementary material.

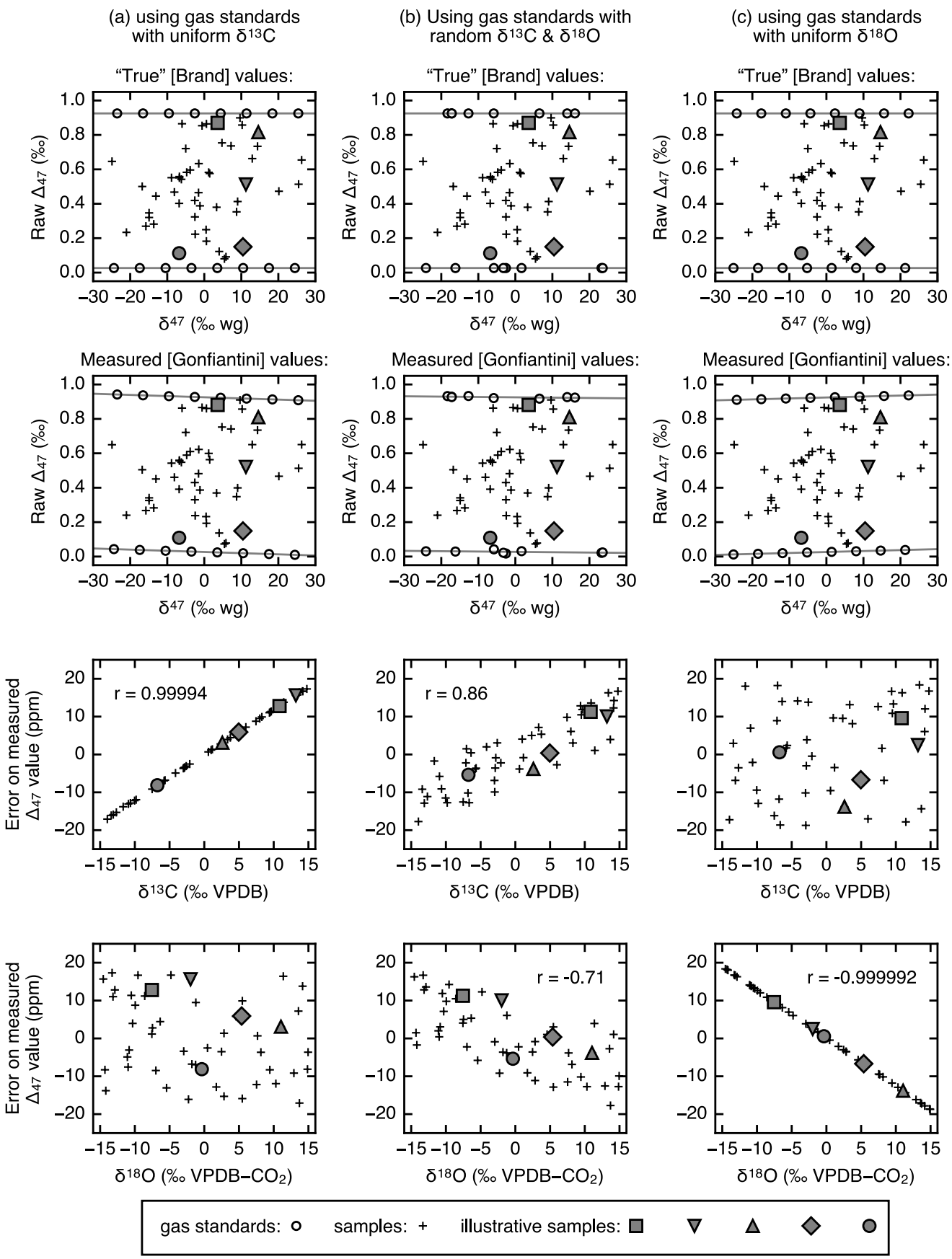

Figure 6 (caption on next page)

Figure 6: Computation of errors resulting from the use of inaccurate isotopic parameters, based on random simulation data for 50 samples. Raw measurement data are generated by arbitrarily assuming that the [*Brand*] parameters are accurate, then processed using the [*Gonfiantini*] parameters in three different hypothetical situations: (a) data corrected using 16 thermodynamic gas standards with identical values of $\delta^{13}C$; (b) data corrected using 16 gas standards with random $\delta^{13}C$ and $\delta^{18}O$ values; (c) data corrected using 16 gas standards with identical values of $\delta^{18}O$. "r": Pearson correlation coefficient. Source code provided as supplementary material.

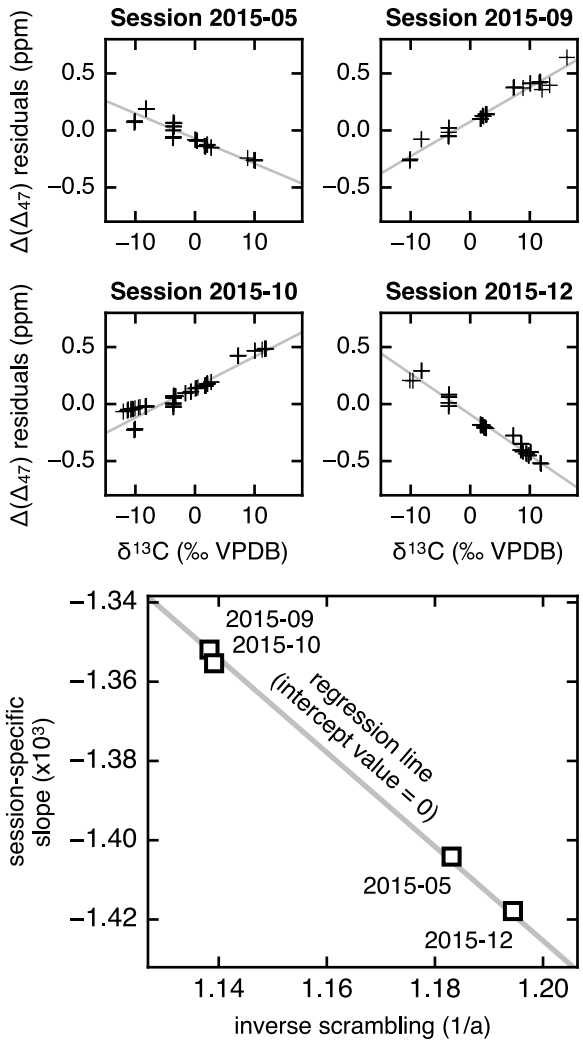

Figure 7: Residuals of $\Delta(\Delta_{47})$ for the [*Brand*] parameters relative to the corresponding trend line in Figure 4b. Although these residuals remain very small, they are not random. Instead, they appear tightly correlated to $\delta^{13}C$ within each analytical session (defined as a continuous period of instrumental stability), meaning that data from different sessions follow slightly different trends. As discussed in section 3.1.3, this behavior reflects session-to-session variability in the scrambling correction (parameter *a* in equation 9). Source code provided as supplementary material.

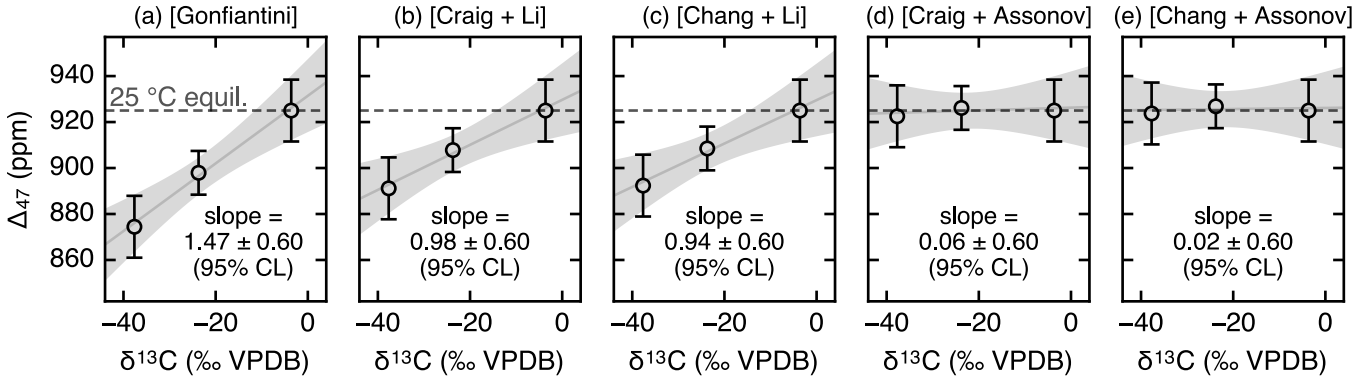

Figure 8: Results of our water equilibration experiment. Three CO_2 samples with quasi-identical $\delta^{18}O$ and $\Delta^{17}O$ values but very different $\delta^{13}C$ were all isotopically equilibrated at 25 °C. Although their true Δ_{47} values are expected to be undistinguishable, their measured values appear different unless raw data are processed using the [*Craig + Assonov*] or the [*Chang + Assonov*] parameters. Measurement error bars correspond to ± 2SE. "CL": confidence limits. Source code provided as supplementary material.

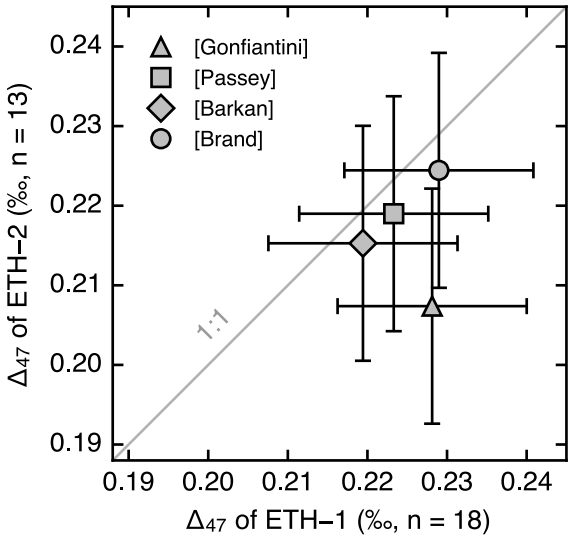

Figure 9: Comparison of absolute Δ_{47} values for ETH-1 and ETH-2 computed using different sets of isotopic parameters. These two standards have different bulk isotopic compositions but their clumped isotope signatures are expected to be very similar (see section 3.3). All parameters except those from the [*Gonfiantini*] set yield statistically indistinguishable Δ_{47} values for ETH-1 and ETH-2 (Table 3). Error bars correspond to 95 % confidence limits, based on 18 analyses of ETH-1 and 13 analyses of ETH-2. Source code provided as supplementary material.

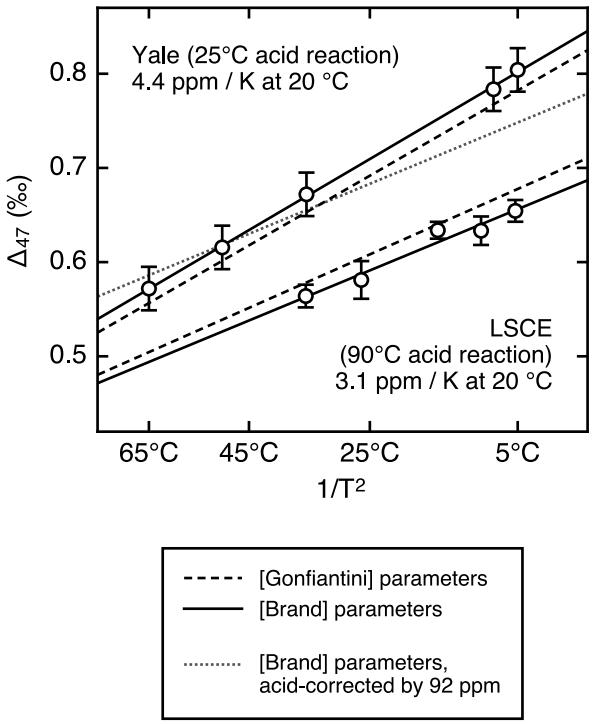

Figure 10: Comparison of two carbonate calibration lines processed using [*Gonfiantini*] (dashed lines) versus [*Brand*] (solid lines and round markers, error bars correspond to ± 2SE). Source code provided as supplementary material.

CHANGES IN HOLOCENE MERIDIONAL CIRCULATION AND POLEWARD ATLANTIC FLOW: THE BAY OF BISCAY AS A NODAL POINT

Yannick Mary[1], Frédérique Eynaud[1], Christophe Colin[2], Linda Rossignol[1], Sandra Brocheray[1,a], Meryem Mojtahid[3], Jennifer Garcia[3], **Marion Peral**[1,b], Hélène Howa[3], Sébastien Zaragosi[1], and Michel Cremer[1]

[1]Laboratoire Environnements et Paléoenvironnements Océaniques et Continentaux (EPOC), UMR 5805, Université de Bordeaux, 33615 Pessac, France

[2]Laboratoire Géosciences, Université de Paris-Sud, 91405 Orsay CEDEX, France

[3]UMR CNRS6112 LPG-BIAF, Recent and Fossil Bio-Indicators, Angers University, 2 Bd Lavoisier, 49045 Angers CEDEX 01, France

[a]now at: Institut Polytechnique LaSalle-Beauvais, Dpt Géosciences, 19 rue Pierre Waguet, BP 30313, 60026 Beauvais, France

[b]now at: Laboratoire des Sciences du Climat et de l'Environnement (LSCE-IPSL), Domaine du CNRS, bât.12, 91198 Gif-sur-Yvette, France

Correspondence to:

Yannick Mary (pelagos@hotmail.fr) and

Frédérique Eynaud (frederique.eynaud@u-bordeaux.fr)

Published in: *Climate of the Past* (2017)

ABSTRACT

This paper documents the evolution over the last 10 kyr of one of the key parameters of climate: sea-surface temperatures (SSTs) in the North Atlantic. We focus on the southern Bay of Biscay, a highly sensitive oceanographic area regarding the dynamics of the North Atlantic subpolar and subtropical gyres (SPG and STG respectively). This site furthermore offers unique sedimentary environments characterized by exceptional accumulation rates, enabling the study of Holocene archives at (infra) centennial scales. Our results mainly derive from planktonic foraminiferal association analysis on two cores from the southern Landes Plateau. These associations are used as the basis of modern analogue technique transfer functions to track past hydro- graphical changes. SST reconstructions were thus obtained at an exceptional resolution and compared to a compilation of Holocene records from the northeastern North Atlantic. From this regional perspective are shown fundamental timing differences between the gyre dynamics, nuancing classical views of a simple meridional overturning cell. Our study highlights that western Europe underwent significant oscillations of (annual) SST during the last 10 kyr. During well-known intervals of mild boreal climate, warm shifts of more than 3 °C per century are accurately concomitant with positive sea-surface temperature anomalies and rise of micropalaeontological indicators of gyre dynamics in the northern North Atlantic, pointing to periods of greater intensity of the North Atlantic Current (SPG cell especially). Conversely, the SST signal records short-term cold anomalies, which could be related to weaker SPG dynamics.

INTRODUCTION

The Atlantic Meridional Overturning Circulation (AMOC) and its dynamics are critical regarding the modulations of climate (amplitude and frequency) over Europe (westerlies, droughts and/or stormy periods, e.g. Clark et al., 2002; Bryden et al., 2005; Dawson et al., 2004; Magny et al., 2003; Sorrel et al., 2009; Trouet et al., 2012; Van Vliet-Lanoe et al., 2014a, b; Jackson et al., 2015). The two connected North Atlantic gyres, the subpolar gyre (SPG) and the subtropical gyre (STG) are fundamental for these processes as they transfer heat and salt toward the Nordic seas (e.g. McCartney and Mauritzen, 2001; Pérez-Brunius et al., 2004; Hatun et al., 2005; Morley et al., 2014) where convection occurs (e.g. Lozier and Stewart, 2008). Their expansions and con- tractions notably control the inflow from the North Atlantic Current (NAC) to higher latitudes, thus also affecting the heat budget of the Greenland–Iceland–Norwegian seas, which is critical in the meridional climatic balance (e.g. Hatun et al., 2005). During the late Holocene, changes in the STG and SPG dynamics contributed to well-known climatic anomalies in western Europe, such as the Little Ice Age or the Medieval Warm Period/Anomaly, and probably played a major role at longer timescales (Thornalley et al., 2009; Colin et al., 2010; Copard et al., 2012; Sorrel et al., 2012; Staines-Urías et al., 2013; Morley et al., 2014).

By providing the first Holocene inventory of (infra) centennial hydrographic changes in the inner Bay of Biscay, this paper aims at testing European temperate oceanic signals vs. those from a broader North Atlantic view with a focus on the SPG dynamics. Our study site (Fig. 1) is ideally located under the temperate eastern limb of the NAC, in the southern Bay of Biscay and not far from the STG/SPG divergence zone (e.g. Planque et al., 2003). This geographic configuration provides to this marine environment a high sensitivity regarding Northern Hemisphere climatic signals at present (e.g. Le Cann and Serpette, 2009; Esnaola et al., 2013; Garcia-Soto and Pingree, 2012), echoing pan-Atlantic hydrographical changes, somewhat with amplified responses. Actually, the southern Bay of Biscay records at present the warmest SST (especially in summer) of the mid-latitude temperate band of the North Atlantic with a significant warming trend over the last decades (e.g. Koutsikopoulos et al., 1998; Valencia et al., 2003; deCastro et al., 2009; see also maps at

http://www.nodc.noaa.gov/ cgi-bin/OC5/woa13fv2/woa13fv2.pl?parameter=t). Previous works done on sedimentary archives in the same area have furthermore evidenced a strong potential to track down the Holocene variability (Mojtahid et al., 2013; Garcia et al., 2013; Brocheray et al., 2014; Mary et al., 2015).

Today, the Bay of Biscay is characterized by a complex, variable sea-surface circulation with strong seasonal changes, marked by a September–October versus March–April SOMA pattern (e.g. Pingree and Le Cann, 1990; Pin- gree and Garcia-Soto, 2014). The main surface current in the Bay of Biscay is the European Slope Current (ESC), flowing northward along the Armorican Shelf (Fig. 1), with important spatial and seasonal variations (Garcia-Soto and Pin- gree, 2012; Charria et al., 2013). Circulation can reverse during summer along the shelf break, flowing weakly southwest- ward (Charria et al., 2013). In autumn–winter, the northward flow reaches a maximum, especially when combining with southern intrusions from the Iberian Poleward Current (IPC) which flows along the western Iberian margin (e.g. Peliz et al., 2005) before turning eastward at Cape Finisterre (NW Spain). The IPC northward extension into the Bay of Biscay is known as the Navidad Current (e.g. Garcia-Soto et al., 2002; Le Cann and Serpette, 2009). The winter mixing of the IPC and ESC is designated as the European Poleward Current (EPC, Garcia-Soto and Pingree, 2012), and drives relatively warm and saline water to the Nordic seas, contributing to their heat and salt budget. The Bay of Biscay is additionally strongly marked by surface water inflow coming from the North Atlantic Current (Fig. 1), which enters the Bay from its northwestern boundary (Pingree, 2005; Pingree and Garcia-Soto, 2014; Ollitrault and Colin de Verdière, 2014). In contrast with surface circulation of the inner Bay of Biscay, the NAC water inflow shows only limited seasonal variability. At inter-annual timescales however, NAC oscillations are mainly driven by westerly wind regime (Pingree, 2005), and consequently by the North Atlantic Oscillation (NAO), one of the key modes of climatic variability in the North Atlantic. So far, little is known about long-term oscillations of the NAC inflow into the Bay. Modern surveys of SST variability over the last 150 years in the Bay of Biscay report that temperature oscillations are mainly controlled by the Atlantic Multi-decadal Oscillation (AMO; Garcia-Soto and Pingree, 2012). The influence of the NAO on SST in the Bay of Biscay is more complex and contributes only little to the observed long-

term trend, although sharp, inter-annual changes of the NAO index impact annual SST variability (Garcia-Soto and Pingree, 2012, Fig. 1c). Moreover, NAO conditions influence large-scale oceanic circulation patterns indirectly responsible for surface temperature anomalies over the Bay (Pingree, 2005; Garcia-Soto and Pingree, 2012; see also the synthesis within Mary et al., 2015).

The present paper is based on analyses conducted on two high-resolution well-dated cores from the southern part of the inner Bay of Biscay (Fig. 1, Table 1): core KS10b (e.g. Mojtahid et al., 2013) and core PP10-07 (e.g. Brocheray et al., 2014). These cores show exceptionally high sedimentation rates for the Holocene, up to 200 cm kyr^{-1} for core PP10-07, and 86 cm kyr^{-1} for core KS10b (see detailed description of these archives and of their sedimentological context in the respective references). Here we present past Holocene SST data reconstructed after an ecological transfer function based on the modern analogue technique (see Sect. 2, Methods) applied to planktonic foraminiferal assemblages. These Bay of Biscay sea-surface reconstructions are compared to selected North Atlantic Holocene records using a data mining exercise (referencing sea-surface reconstructions of high time-resolution) done in the frame of the French ANR HAMOC (Holocene North Atlantic Gyres and Mediterranean Overturning dynamic through Climate Changes) project database (see http://hamoc-interne.epoc. u-bordeaux1.fr/doku.php?id=start).

2. METHODS

2.1 Age Models

Updated age models have been built for the Bay of Biscay cores. All raw ^{14}C ages were calibrated and converted to calendar ages using the Marine13 calibration curve and the recommended age reservoir of 405 years (Reimer et al., 2013), as no adequate and robust local age reservoir values exist in the area (see Mary et al., 2015, for a discussion). Smooth-spline regression based on the published ^{14}C dates (n = 12 for core Ks10b, Mojtahid et al., 2013) were applied (Fig. 2). For core PP10-07, two supplementary ^{14}C dates were obtained at the top of the sequence (Table 2) and the age model was built using a 5° polynomial regression (Fig. 2). The core MD03-2693 age model (also exploited in this paper) was built using linear interpolation based on pub- lished ^{14}C and ^{210}Pb (n = 3 and n = 8, respectively, Mary et al., 2015). Age–depth modelling and calibration were per- formed using the dedicated software Clam (Blaauw, 2010), written in the open-source statistical environment R (http: //www.r-project.org/).

Table 1: Location and references of the southern Bay of Biscay cores used in this study.

Cruise, Core label	Latitude (°N)	Longitude (°E)	Water depth (m)	Longitudinal distance (km) from the shore	Data sources and references
SARGASS, PP10-07	43.677	−2.228	1472	58	This work, Brocheray et al. (2014)
PROSECAN IV, KS10b	43.833	−2.050	550	50	This work, Mojtahid et al. (2013)
SEDICAR/PICABIA, MD03-2693	43.654	−1.663	431	15	This work, Gaudin et al. (2006), Mary et al. (2015)

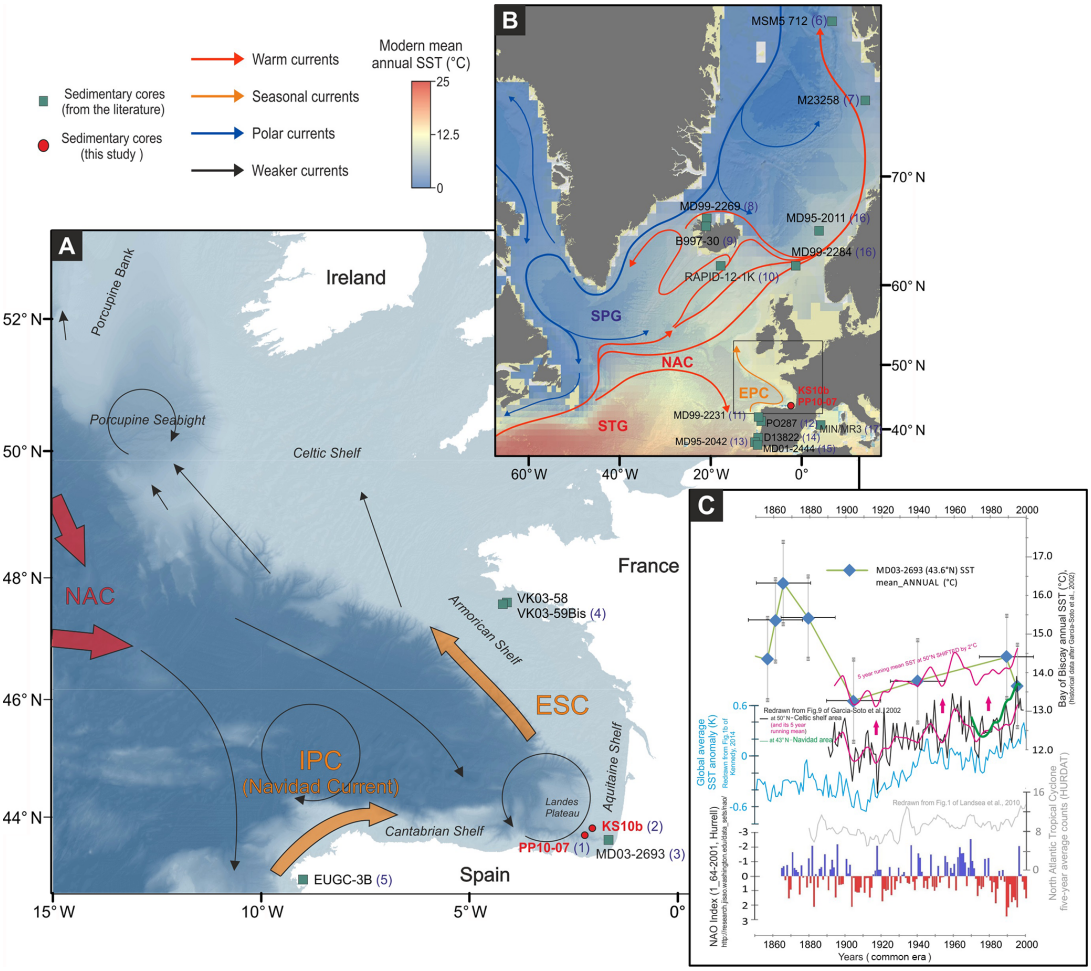

<u>Figure 1:</u> (a) Map showing the regional scheme of the main surface currents in the Bay of Biscay, drawn after the compilation of modern hydrological survey from Pingree and Garcia-Soto (2014). North Atlantic Current (NAC), Iberian Poleward Current (IPC), and European Slope Current (ESC) are respectively represented by the red and orange arrows. The studied sedimentary cores PP10-07 and KS10b from the inner Bay of Biscay are shown in red. Bathymetry from EMODNET. Additional Holocene records cited in the text are displayed by green squares. (b) North Atlantic general circulation pattern (SPG, subpolar gyre; STG, subtropical gyre; EPC, European Poleward Current; after Lherminier and Thierry, 2015) with the location of the northern and southern sedimentary records discussed in the text. Core references: (1) Brocheray et al. (2014); (2) Mojtahid et al. (2013); (3) – Gaudin et al. (2006), Mary et al. (2015); (4) Naughton et al. (2007a); (5) Pena et al. (2010); (6) Werner et al. (2013); (7) Sarnthein et al. (2003); (8) Giraudeau et al. (2004); (9) Andrews and Giraudeau (2003); (10) Thornalley et al. (2009); (11) Naughton et al. (2007b); (12) Abrantes et al. (2011); (13) Chabaud et al. (2014); (14) Rodrigues et al. (2009); (15) Martrat et al. (2007); (16) Risebrobakken et al. (2011); (17) Cisneros et al. (2016). (c) SST evolution over the last centuries in the Bay of Biscay (from the MD03-2693 sedimentological record and from the compilation of Garcia-Soto et al., 2002) and comparison, from top to bottom with the Global SST anomaly (after Kennedy, 2014), the Atlantic Tropical Cyclone Counts (after Landsea et al., 2010) and the NAO index of Hurell (http://research.jisao.washington.edu/data_sets/nao/).

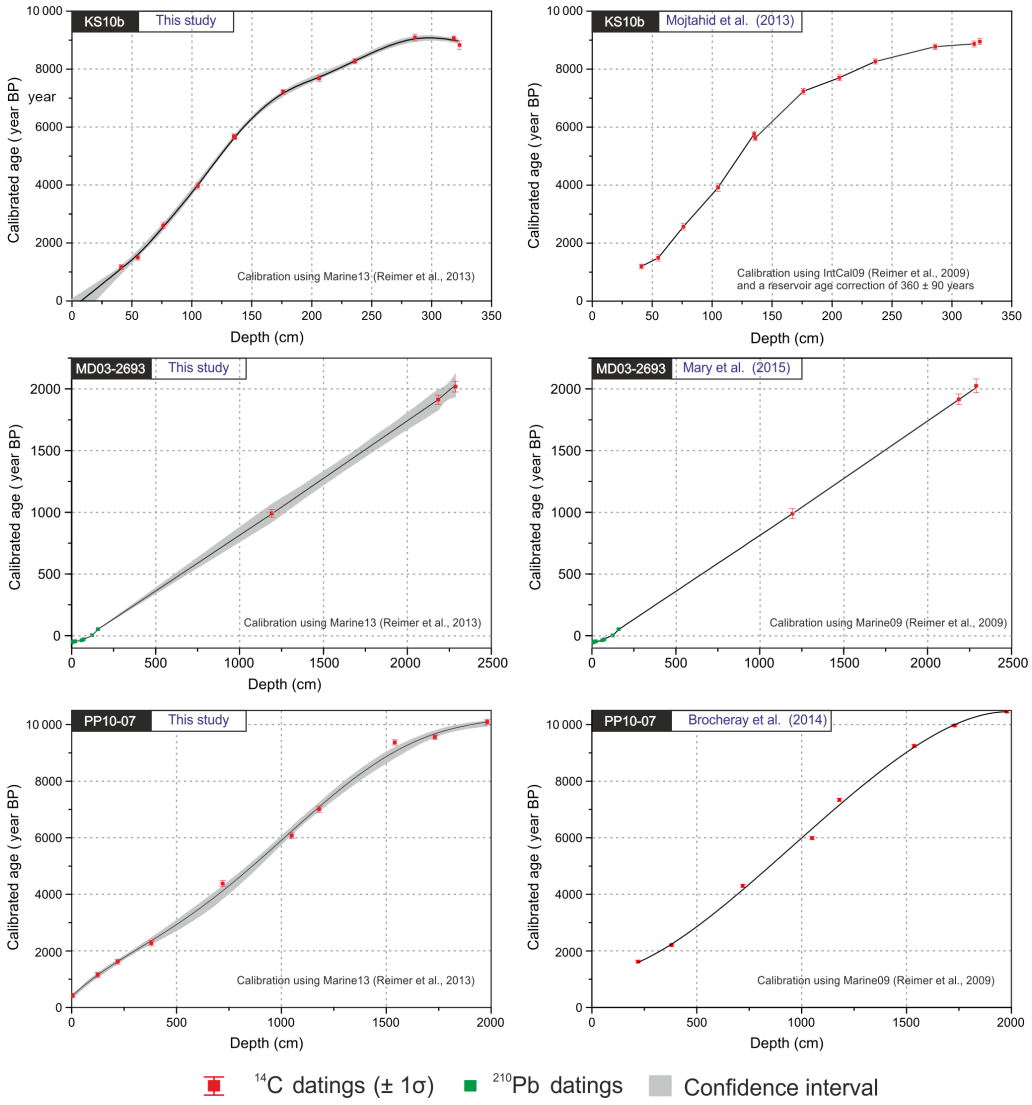

Figure 2: Revised age models for cores KS10b, MD03-2693 and PP10-07 (left panels) compared to previous published age models (right panels with original references).

2.2 Past Hydrographical Parameter Quantification

Planktonic foraminifera (PF) assemblages were used to quantify sea-surface parameters: species abundances were determined (counts of 300 specimens at least) on the > 150 µm fraction from sedimentary aliquots retrieved at maximum 10 cm intervals along the studied cores, thus giving a mean time resolution of 50 and

150 years for cores PP10-07 and KS10b respectively (see Supplement for de- tailed data). SST reconstructions were calculated using the Modern analogue technique (MAT) a method successfully developed on PF (e.g. Pflaummann et al., 1996; Kucera et al., 2005; Telford and Birks, 2011; Guiot and de Vernal, 2007, 2011). The calculations derive from modern spectra previously compiled and tested separately in the frame of the MARGO exercise for the North Atlantic Ocean and the Mediterranean Sea respectively (Kucera et al., 2005; Hayes et al., 2005). They are based on sediment surface samples analysed for their contents in PF (specific relative abundances) and thus offer the advantage of already having integrated regional taphonomic processes. At EPOC (Environnements et Paléoenvironnements Océaniques et Continentaux) laboratory, these two MARGO databases were summed to provide larger analogue choices and ambiguous data points were excluded (i.e. non-stratigraphically con- strained points showing anomalies in the biogeographical distribution), resulting in a final training set of n = 1007 modern analogues. Modern sea-surface parameters were extracted from the WOA ATLAS with the sample tool developed by Schäfer-Neth and Manschke (2002). The latter was developed for the MARGO programme and interpolates the 10 m World Ocean Atlas WOA-1998 mean seasonal and mean annual temperatures over the four existing data points surrounding the sample location (see http://www.geo. uni-bremen.de/geomod/staff/csn/woasample.html) thus providing spatio-temporal averaged values of SST (see Kucera et al., 2005, for MARGO analytical developments and Telford et al., 2013, for further considerations).

Table 2. Summary of AMS ^{14}C ages of core PP10-07 with calendar correspondences. Bold numbers underline raw age data, whereas italic numbers identify converted age values.

Depth in core PP10-07 (cm)	Sample	Material	Ref. number	mg C	$\delta^{13}C$	pMC corrected	RAW ^{14}C Age year BP	Corrected reservoir age/−400 year BP	Calibrated age (median age) CLAM year BP	-2σ year	$+2\sigma$ year	Error year	Confidence %
4.5	PP10-07 3–6 cm (TR1)	Bulk planktonic foraminifera	SacA39103	0.572	0.12	90.6 ± 0.24	**790** ± 30	*390*	***423***	*353*	*493*	*70*	*92.6*
124.5	PP10-07 124–125 cm (TR2)	Bulk planktonic foraminifera	SacA39104	0.455	−1.1	82.1 ± 0.24	**1590** ± 30	*1190*	***1149.5***	*1063*	*1236*	*86.5*	*95*
219.5	PP10-07 218–221	Bulk planktonic foraminifera	SacA 29590	0.7	0.2	77.5 ± 0.19	**2050** ± 30	*1650*	***1618***	*1533*	*1702*	*85*	*95*
380	PP10-07 380	Bulk planktonic foraminifera	SacA 26975	0.78	–4,6	72.2 ± 0.24	**2615** ± 30	*2215*	***2271***	*2175*	*2366*	*96*	*95*
720.5	PP10-07 720–721	Bulk planktonic foraminifera	SacA 26976	1	–0.9	58.8 ± 0.22	**4265** ± 30	*3865*	***4380***	*4272*	*4487*	*108*	*95*
1050	PP10-07 1050	Bulk planktonic foraminifera	SacA 26977	1.1	–5.2	49.4 ± 0.17	**5660** ± 30	*5260*	***6070***	*5970*	*6170*	*100*	*95*
1180	PP10-07 1180	Bulk planktonic foraminifera	SacA 29591	0.69	–0.3	44.6 ± 0.14	**6490** ± 30	*6090*	***7007***	*6897*	*7116*	*110*	*95*
1540	1537–1543 1537–1543	Bulk planktonic foraminifera	SacA 26978	1.17	−1.9	33,8 ± 0.17	**8705** ± 40	*8305*	***9371***	*9276*	*9466*	*95*	*95*
1731.5	PP10-07 1730–1733	Bulk planktonic foraminifera	SacA 29592	0.84	–0.8	33 ± 0.12	**8900** ± 30	*8500*	***9556***	*9477*	*9635*	*79*	*95*
1981.5	PP10-07 1980–1983	Bulk planktonic foraminifera	SacA 29593	1	−1.5	31.6 ± 0.12	**9270** ± 30	*8870*	***10 093***	*9992*	*10 193*	*101*	*92*

Calculations were run under the R software with the BIOINDIC package (ReconstMAT script) developed by J. Guiot (https://www.eccorev.fr/spip.php?article389) using relative abundances of PF with no mathematical transformation (no logarithmic or square root transformations which are frequently used to increase the equitability within assemblages for instance; see Guiot and de Vernal, 2007, for a re- view).

Past hydrological parameter values are derived from a weighted average of the SST values of the five best analogues. The maximum weight is given for the closest analogue in terms of statistical distance (i.e. dissimilarity minimum). The ReconstMAT script furthermore includes the calculation of a threshold regarding this statistical distance, which prevents calculation in the case of poor- or non-analogous situations. The degree of confidence of this method allows reconstruction of seasonal and annual SST with a maximum root mean square error of prediction (RM- SEP) of 1.3 °C (see Supplement). This method (named MATR_1007PF for modern analogue technique derived from 1007 modern spectra of PF assemblages) was extensively tested at EPOC including comparisons with similar MAT developed regionally on PF (e.g. Salgueiro et al., 2008, 2010) providing very coherent reconstructions along the western European margin (see Eynaud et al., 2013, for further details) and producing pertinent palaeoceanographical series (see Penaud et al., 2011; Sánchez-Goñi et al., 2012, 2013, for records also produced with MATR_1007PF). Additionally, our work benefited from modern calibrations conducted on PF from the same area of the Bay of Biscay (i.e. Retailleau et al., 2009, 2012).

3. HOLOCENE SST OSCILLATIONS IN THE BAY OF BISCAY

Despite the different bathymetric and physiographic positions of the studied cores (Fig. 1, Table 1), reconstructed annual SST in the Bay of Biscay shows coherent oscillations of remarkably similar timing (Fig. 3a). Small amplitude differences are observed between the two studied records, but synchronous warm periods are clearly identified between 8.2 and 7.4 and between 6.6 and 5.6 kyr BP, these intervals roughly corresponding to the upper and lower limits of the mid-Holocene hypsithermal in the North Atlantic region (e.g. Eynaud et al., 2004; Walker et al., 2012; Tanner et al., 2015).

On historical timescales, warm intervals are detected in both cores between 2.6 and 1.8 kyr BP (Roman Warm Period, RWP) and between 1.2 and 0.5 kyr BP (Medieval Warm Period, MWP), although less obvious in core KS10b because of the lower time resolution. An offset of up to 4°C above mean annual modern values is observed during a large temperature excursion around ca. 2 kyr BP in core PP10-07 only. The amplitude of the warmings detected between 8.2 and 7.4 and between 6.6 and 5.6 kyr BP reaches 2 to 3 °C in both records. Such amplitudes in the detected SST warm pulses are especially high in comparison to modern annual values. However, considering the strong modern seasonal SST variations in the Bay of Biscay (as shown on Fig. 3a), a 4 °C shift of mean annual SST is coherent with a deviation of annual mean temperature toward mean summer values.

Comparison of the southern Bay of Biscay SST reconstructions with other records from the western European margin (Figs. 3, 4 and 5) suggests that the observed millennial-scaled warm episodes are coherent features which reflect characteristic climatic patterns, at least expressed regionally, but also probably more broadly. Indeed, further along the Bay of Biscay margin, other high-resolution Holocene archives reveal similar and synchronous episodes (Fig. 3c). Concomitantly to the observed warm SST pulses also seen within the seasonal means (see Supplement), Holocene pollen assemblages from core VK03-58bis (pollen data not shown; Naughton et al., 2007a) indicate a decrease in mean annual precipitations; this drought being related, according to the authors, to a change in the seasonality with warmer summers especially. In the same way, the evolution of

coccolithophorid concentrations in the subpolar North Atlantic along the Irminger Current pathway, interpreted as indicating stronger contribution of NAC water toward the Nordic seas (Andrews and Giraudeau, 2003; Giraudeau et al., 2004; Mo- ros et al., 2012), showed strong similarities with the Bay of Biscay SST signals. Peaks in coccolithophorid abundances in cores B997-330 and MD99-2269 (Fig. 4e and f) (see location on Fig. 1) were recorded synchronously to the warm pulses in the Bay of Biscay, with especially positively marked anomalies detected around 2 and 8kyrBP. The Bay of Biscay SST oscillations further correspond with those reconstructed from marine records from the Barents Shelf (see location on Fig. 1) from core MSM5/5-712-2 (Werner et al., 2013, Fig. 3c) and core M23258 (Sarnthein et al., 2003; Fig. 3d). This coherency suggests teleconnections between the southern Bay of Biscay and the Nordic seas, probably due to a common driving mechanism linked to the NAC inflow vigour and its split between the SPG and the STG.

In between the observed warm intervals, SST reconstructions of core PP10-07 and KS10b reveal several low values slightly colder than today (Fig. 3a). The time interval between 5.6 and 2.6 kyr BP is characterized by temperatures around −1 °C cooler compared to the modern ones. This period roughly corresponds to the late Holocene Neoglacial Cooling (e.g. Eynaud et al., 2004; Wanner et al., 2008; Walker et al., 2012). In the same way, short-lived events of 2°C cooling are visible around ca. 8.2, 7, 5.5, 4, 2.9 and 1.7 kyr BP (Figs. 3 and 4). The three older anomalies are synchronous and well marked in both KS10b and PP10-07 cores.

The comparison of the timing of these cold spells to other existing Holocene reconstructions from the North Atlantic Ocean reveals that they represent coherent and reproducible features (Fig. 4). Interestingly, density anomalies thought to reflect millennial-scale variability in the SPG dynamics (Thornalley et al., 2009; Farmer et al., 2011) were recorded nearly synchronously (within the age model uncertainties) in the southern Iceland Basin (it is especially obvious be- fore 4 ka). These anomalies were interpreted (i.e. Thornalley et al., 2009) as reflecting a strong/*weak*, longitudinally ex- tended/*contracted* SPG thus driving more/*less* vigorous but fresher/*saltier* Atlantic inflow throughout the Faroe current branch and thus modulating the AMOC strength. The good temporal correspondence between the cold spells detected in core PP10-07 (even if shorter) and the

density anomalies (core RAPiD-12-1K, Fig. 4h) registered in the subpolar North Atlantic support, as seen for warm events, a direct teleconnection with the inner Bay of Biscay, probably throughout a STG/SPG seesaw which would influence tracks/intensities of the temperate westerlies. The short-lived cold anomalies of PP10-07 are furthermore concomitant with periods of increased storminess identified in various coastal sediments from the NW European margin (Holocene storm periods after Sorrel et al., 2012, Fig. 3g). These periods have been related to a weakened, westward contracted SPG, involving a rapid feedback in the atmospheric dynamics (e.g. westerlies intensity and/or latitudinal migrations).

In the subtropical North Atlantic, study of benthic foraminiferal stable isotopes in core EUGC-3B (located in the Galician Shelf; Pena et al., 2010; see Fig. 1) also showed similar cold anomalies which were interpreted by the authors as suggesting enhanced contribution of colder, eastern North Atlantic Central waters (ENACW) reaching the Iberian mar- gin during these events.

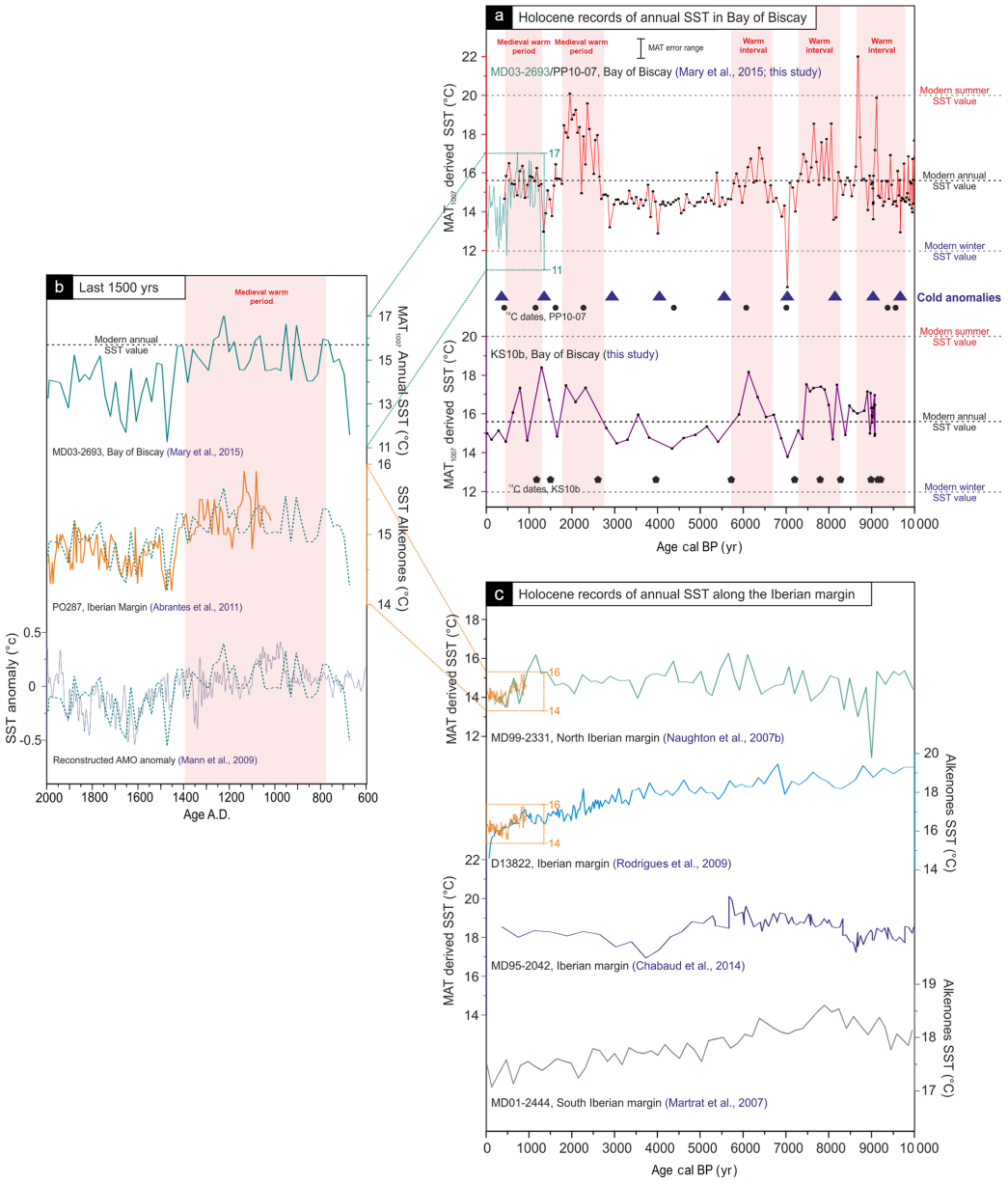

<u>Figure 3:</u> Mean annual sea surface temperature (SST) records from the western European margin. (a) Holocene SST signals from cores PP10-07 and KS10b (this study) reconstructed using the modern analogue technique (MAT) based on planktonic foraminifera (see Sect. 2, Methods), and compared to SST signal of the adjacent core MD03-2693 (Mary et al., 2015). Black dots identify ^{14}C age control points. (b) SST signals spanning the last 1500 years in the Bay of Biscay (core MD03-2693) based on MAT and from the Iberian margin (core PO287-06; Abrantes et al., 2011) using alkenones. Reconstructed signals are compared with the AMO reconstruction of Mann et al. (2009). The dotted curve represents core MD03-2693 signal transposed on top of the two other curves. (c) Holocene SST signals from the Iberian margin using MAT based on planktonic foraminifera for cores MD99-2331 (after Naughton et al., 2007b) and MD95-2042 (after Chabaud et al., 2014) and alkenones for cores D13882 (after Rodrigues et al., 2009) and MD01-2444 (after Martrat et al., 2007).

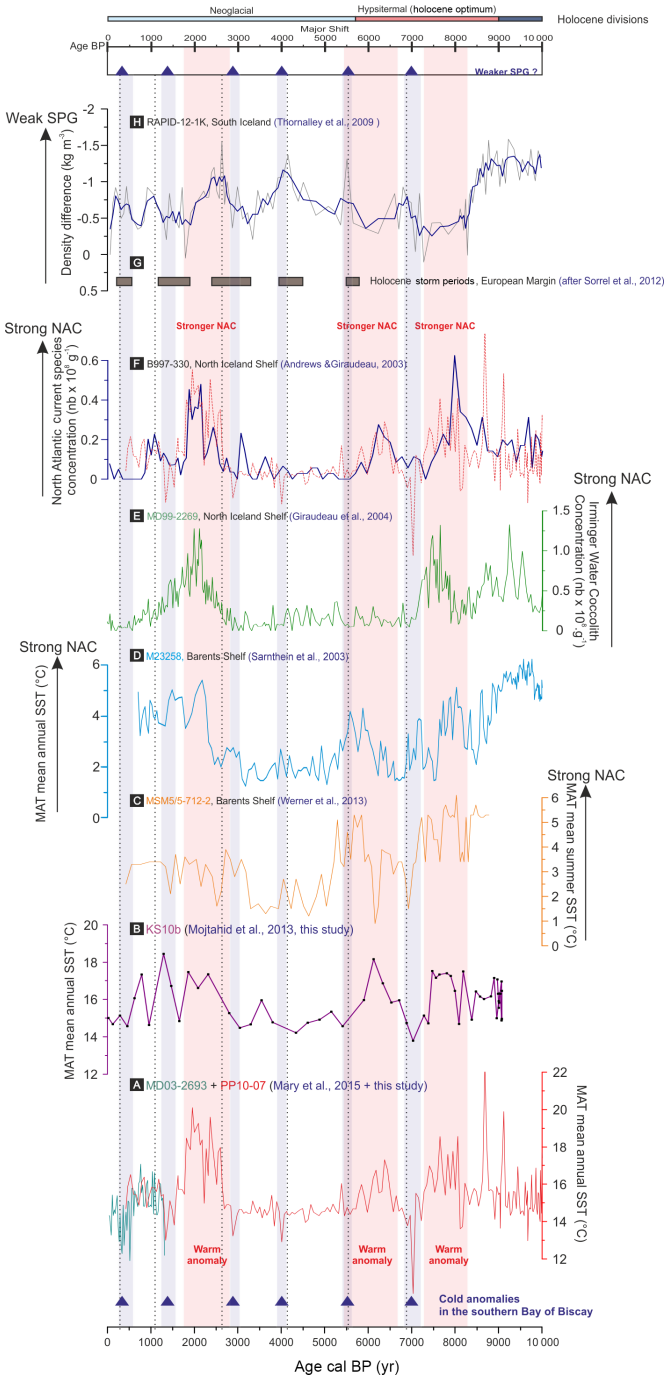

<u>Figure 4:</u> Comparison of annual SST Holocene signals from the Bay of Biscay (a, b) with records from the northern North Atlantic highlighting variations of the NAC intensity and SPG dynamics; (c) SST signal of core MSM5/5-712-2 (Fram Strait; Werner et al., 2013) and of (d) core M23258 (Barents Shelf, after Sarnthein et al., 2003), both reconstructed using the modern analogue technique (MAT) based on planktonic foraminifera; (e) concentration of NAC indicator coccolith species in core MD99-2269 (North Iceland Shelf, after Giraudeau et al., 2004) and in (f) core B997-330 (North Iceland Shelf, after Andrews and Giraudeau, 2003; the PP10-07 record here is also plotted by a thin dotted red line to underline the comparison); (g)

Holocene storm periods (after Sorrel et al., 2012) reconstructed from sedimentological evidence from a compilation of coastal cores in northwestern Europe; and (h) core Rapid-12-1K (Thornalley et al., 2009) proxy for upper-water-column stratification, calculated using derived Mg / Ca and $\delta^{18}O$ temperatures and salinities of G. bulloides and G. inflata. Dotted vertical lines point out events of density difference between the near-surface and base of the seasonal thermocline in the southern Iceland Basin. The topmost dark blue triangles and light blue vertical bands point to cold anomalies recorded in the southern Bay of Biscay (potentially corresponding to a weak SPG). Pink bands conversely highlight periods of warmth which also correspond to enhanced NAC activity north of Iceland. Changes in gyre circulation dynamics are compared with the Holocene division of Wanner et al. (2008).

4. THE EUROPEAN POLEWARD CURRENT AND THE INFLUENCE OF SUBTROPICAL SOURCED WATERS IN THE BAY OF BISCAY

Modern surveys (e.g. Garcia-Soto et al., 2002; Lozier and Stewart, 2008; Garcia-Soto and Pingree, 2012) and palaeoceanographic time series (e.g. Mojtahid et al., 2013) recently evidenced the influence of the IPC, and its extension in the Bay of Biscay (i.e. Navidad Current; Garcia-Soto et al., 2002), on surface circulation and hydrological conditions along the European margin. At present, these incursions of warm waters in the bay occur during winter under specific seasonal wind regimes (of southerly wind off Portugal and westerly wind off northern Spain, Charria et al., 2013) and negative anomalies of sea level pressure over the North Atlantic (Pingree and Garcia-Soto, 2014). While these conditions were previously related to a negative mode of the NAO (Garcia-Soto et al., 2002), recent analysis of instrumental time series showed that weather conditions responsible for the Navidad Current may not always correspond to a fixed value of the NAO index (Pingree and Garcia-Soto, 2014). The Navidad Current occasionally creates warm SST anomalies, and enhanced transport of warm water through the pole, and could thus be the vector of planktonic exotic (from sub- tropical origin) faunal invasions in the inner Bay of Biscay (see Mojtahid et al., 2013, and Garcia et al., 2013, for example in the fossil record; see Garcia-Soto and Pingree, 2012, and Pingree and Garcia-Soto, 2014, for example in instrumental time series) which could bias our SST reconstructions. In the following, we thus examine the hypothesis of a persistent poleward surface current during the Holocene that would have triggered the

observed SST warm anomalies in the PP10-07 and KS10b records.

In order to test the coherence of surface hydrographic features along the temperate and subtropical adjacent portions of the European margin, we compared Bay of Biscay SST reconstructions with existing SST (annual) records produced along the Iberian margin (Fig. 3b and c). We first test this link over historical times, compiling SST high-resolution data obtained on the proximal core MD03-2693 (after Mary et al., 2015), which accurately complete those from core PP10-07 (see Fig. 3a between 0.5 and 1.5 ka and Fig. 5a, even if the cores are not tuned on each other, i.e. keeping their independent age models; see also Mary et al., 2015, and its supplement), with additional high-resolution records (Fig. 3b). The combination of these records reveals a slight warming associated with the Medieval Warm Period and coherent low- amplitude multi-decadal SST oscillations, which echo those of AMO anomalies as reconstructed by Mann et al. (2009). Especially striking is the high degree of synchronicity detected between the Iberian margin (core PO287-06; Abrantes et al., 2011) and the Bay of Biscay at the scale of the last 1.5 kyr, despite differences in the proxies used to generate palaeo-SST (alkenones vs. MAT on PF respectively) and age–model uncertainties (which probably explain off- sets of a few hundred years around AD 1200). The good coherence with AMO reconstructions further supports modern oceanographic assumptions of AMO driving multi-decadal change of SST in the area (Garcia-Soto and Pingree, 2012) and shows that this modulation is at least valid for the late Holocene. Interestingly, modern winter incursions of Iberian water through the Bay of Biscay take place during periods of increasing AMO (Garcia-Soto and Pingree, 2012). During these episodes, warm winter anomalies of up to 1.1 $^{\circ}$ C are observed in the Bay of Biscay, which are consistent with the amplitude of the warmings detected in both MD03-2693 and PP10-07 past reconstructions.

However, over the longer Holocene perspective, existing SST records from the Iberian margin do not reveal any coherent patterns with those from the Bay of Biscay over the last 10 kyr (Fig. 3c). Regardless of the proxies involved in SST reconstructions (alkenones and MAT), there is no evidence of any earlier distinct SST excursions in the high time resolution data of the Iberian cores MD99-2331, D13882, MD95- 2042 and MD01-2444 (Fig. 3c; see also Fig. S4 in the Supplement) or elsewhere in other lower-resolution

Holocene records from the same area (Naughton et al., 2007b; Martrat et al., 2007; Rodrigues et al., 2009; Voelker and de Abreu, 2011; Chabaud et al., 2014). The early Holocene SST reconstructions in this area show a monotonic long-term decrease of SST correlated with the Holocene decline of summer insolation (e.g. Marchal et al., 2002; see also Fig. S4), which contrasts strongly with the warm episodes observed in core PP10-07 and KS10b at that time (see Fig. S4 in the Supplement). Taking into account the similarities between late Holocene records in the Iberian margin and in the Bay of Biscay, our data thus suggest a disconnection between these two regions during the first part of the Holocene, up to 1.5 kyr BP. We interpret this divergence as a distinct response of the Bay of Biscay to North Atlantic millennial changes in the NAC/SPF system dynamics (e.g. Pérez-Brunius et al., 2004) whereas southwestern Europe has probably undergone a mixed influence of diverse subtropical climatic trends. Sea- surface environments from the Bay of Biscay, located at the interface between the SPG and STG influences may have, as currently observed in frontal regions, recorded an amplified signature of NAC shifts, themselves driven by contraction/extension phases of the whole North Atlantic gyre sys- tem (STP, SPG and polar gyre also). To decipher the role of each of these gyres is at present not possible on the basis of our records only, and requires additional high-resolution comparable marine archives along a latitudinal gradient at least between 30 and 60° N. The analyses of the influence of Mediterranean hydrographic changes (via the Mediterranean outflow export especially) together with those linked to the eastern North Atlantic upwelling region would also be very important to tackle in such a context.

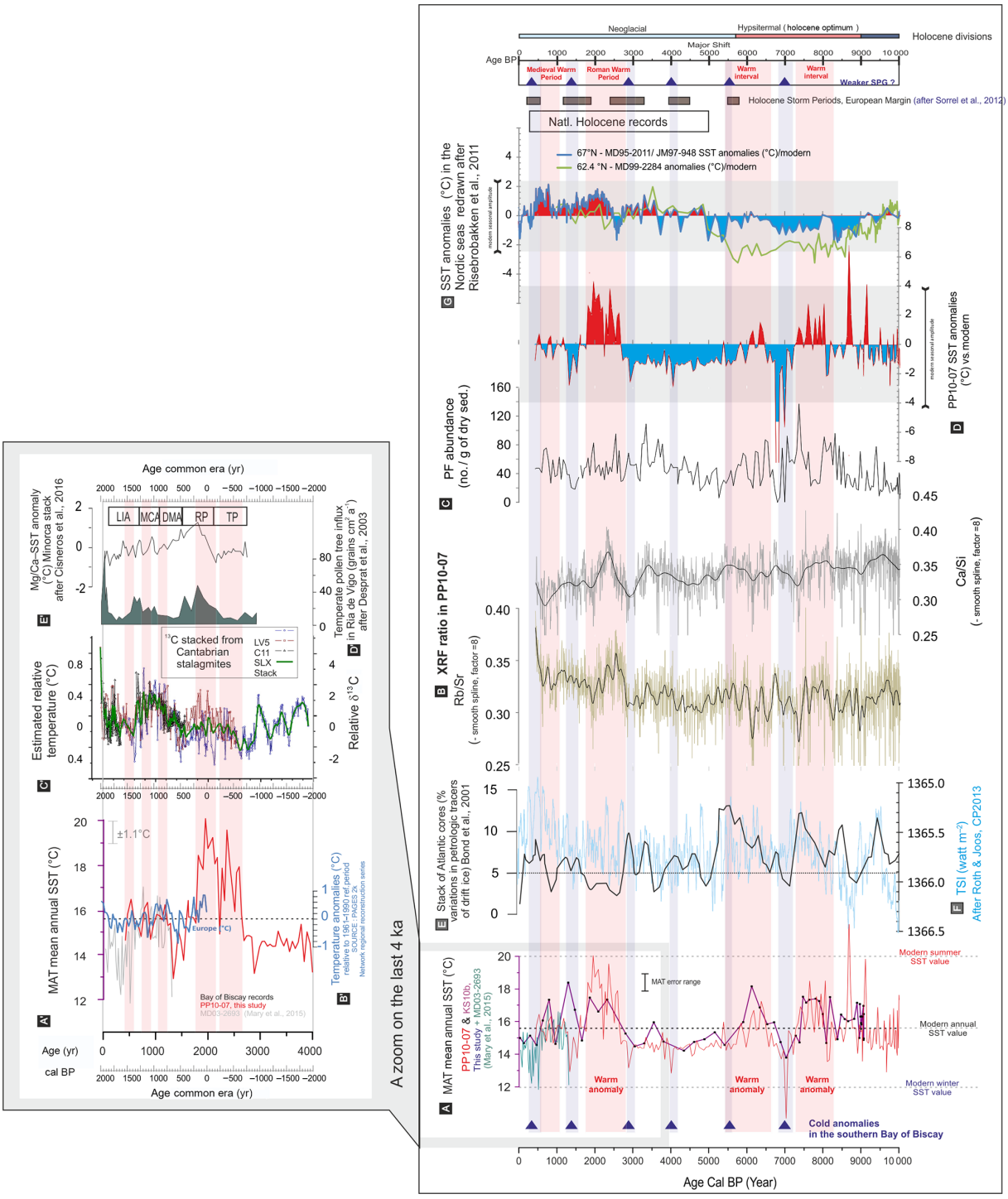

<u>Figure 5:</u> Gathering data and forcing: comparison of the Bay of Biscay (BB) signals (a annual SST, b XRF ratio in PP10-07, c planktonic foraminifera absolute abundances in PP10-07, d annual SST anomalies vs. modern mean in PP10-07), with key Holocene records, i.e. (e) Bond et al. (2001) record; (f) total solar irradiance reconstruction after Roth and Joos (2013); (g) annual SST anomalies in the Nordic seas (eastern) digitized from Risebrobakken et al. (2011, Fig. 3). The dark blue triangles and light blue vertical bands point to cold anomalies recorded

in the BB (potentially corresponding to a weak SPG). On the left are compiled data from the last 4 kyr with (a′) BB annual SST; (b′) reconstruction of the European temperature anomalies (from 30-year averages) of the PAGES 2k Network (2013); (c′) Cantabrian speleothem $\delta^{13}C$ stack reflecting 4 kyr land surface temperature changes, digitized after Martín-Chivelet et al. (2011); (d′) temperate pollen tree influx from the proximal Ria de Vigo, redrawn after Desprat et al. (2003), (e′) Mg / Ca SSt anomaly in Minorca and related historical events after Cisneros et al. (2016) (Talaiotic Period – TP; Roman Period – RP; "Dark Middle Ages" – DMA; Medieval Climate Anomaly – MCA; Little Ice Age – LIA).

5. IMPLICATION FOR HOLOCENE CLIMATE DYNAMICS

In agreement with modern climate observations (e.g. Ba et al., 2014), North Atlantic palaeoceanographic studies de- scribe a strong impact of the SPG dynamics on the NAC inflow toward high latitudes and global circulation during the Holocene (Bianchi and McCave, 1999; Oppo et al., 2003; Pérez-Brunius et al., 2004; Thornalley et al., 2009; Giraudeau et al., 2010; Moros et al., 2012; Staines-Urías, 2013; Morley et al., 2014). Freshwater fluxes in the Labrador Sea and wind stress over the North Atlantic are key drivers of eastern expansions/contractions of the SPG (Hatun et al., 2005), thus also controlling the salinity balance over the North Atlantic, boreal deep-water convection and Northern Hemisphere climate patterns. The compilation of proxy records from further south in the Bay of Biscay indicates that the Holocene relatively long-term periods of warming are interbedded/superposed to rapid, millennial cold anomalies of SPG origin (Fig. 4). In agreement with other North Atlantic records, strong NAC occurs preferentially during the Holocene optimum (Berner et al., 2008; Solignac et al., 2008), and during the Roman Warm Period (Werner et al., 2012). In contrast, the occurrences of cold anomalies in the North Atlantic follow a 1500-year periodicity during the Holocene (e.g. Thornalley et al., 2009; Debret et al., 2007; Sorrel et al., 2012), and are accurately reflected by the SST PP10-07 record (Fig. 4f).

As also suggested by recent studies of modern time series (Lozier et al., 2010; Lozier, 2012), Holocene SST records from the Bay of Biscay evidence a decoupling of gyre dynamics, and a potential gyre-specific expression of the AMOC. Model studies similarly

question the meridional coherence of the AMOC, revealing an inherent character of its mid-latitude variability at decadal timescales (Bingham et al., 2007), mainly driven by wind forcing and eddy variability. While our findings support coherent sea-surface hydrographical patterns between subtropical and temperate environments along the western European margin, suggesting a coupled SPG/STG gyre dynamics over the last 1.5 to 2kyr, earlier Holocene contexts seem to have been rather favourable to a gyre-specific expression, i.e. each gyre being related to intrinsic forcing mainly due to their latitudinal position and to proximal saline/fresh water intrusions.

To tentatively go further in the interpretations, we have compiled bibliographic sources dealing with the Holocene climatic variability. Many of the relevant records are considered in Figs. 4 and 5, with a close-up representation over the last 4 kyr in Fig. 5a to e, which gathers proximal European records. Related interpretations and elements regarding the SPG/STG (and other ocean and climate features when existing) were also compiled as a table (see Table S2 in the Supplement) to provide a comprehensive summary which is conceptualized in Fig. 6. With this exercise, it is confirmed that no definitive trend could be assessed over the whole Holocene. It seems rather that the delimitation of the mid-Holocene is of high relevance regarding the latitudinal coherence of climatic events. Probably in relation with the influence of relict ice-sheet melting (and thus fresh-water injection in the SPG) and the related sea-level rise stop, key connections and feedbacks may have taken place after 6/5 ka only, thus triggering modern oceanographic and climatic modes. Actually, when focusing on the early Holocene, warm anomalies in the Bay of Biscay coincide with signals of significant NAC inflow in the GIN seas (Figs. 4 and 6a), but are not clearly seen on records from close to European ice sheets (Fig. 5e). At a millennial scale, these events seem to be in phase with evidences of solar activity changes (Fig. 5f – reverted scale) and important pulses of ice-drifting in the North Atlantic (after Bond et al., 2001, Fig. 5g). The centennial evolution within each event is however more complex. Over the last 5 kyr, trends seem to be more clearly expressed with, especially during the last millennia, good coherency at the local and regional scales (Fig. 5a to e). Warm/cold shifts occur in a well-defined temporal frame, relevant at least over Europe, but hardly attributable on the basis of our work to a preferential radiative forcing (internal as external).

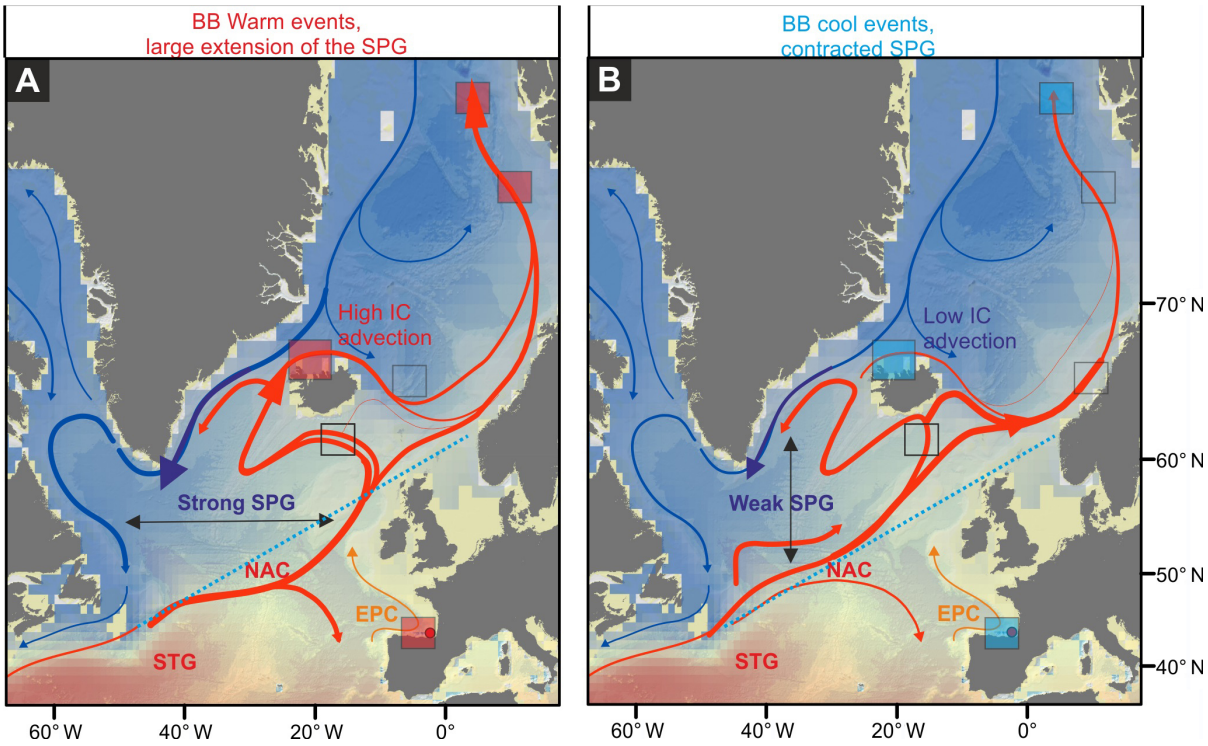

Figure 6: Tentative scheme of North Atlantic oceanic circulation changes associated to contrasted BB SST scenarios (a, BB warm anomalies; b, BB cool events). This figure, primarily based on Fig. 1b, was constructed compiling previous works of Staines-Urías et al. (2013) and of Morley et al. (2014) (see also Table S2). Squares identify the key records used in Figs. 4 and 5, with colours indicating warm/cool situation or empty when no clear trend is detectable.

To understand climatic processes behind these observations and test their coherency region per region, a pan- (North)-Atlantic view is however required, emphasizing the need for comprehensive data compilation efforts as those undertaken for instance in the work conducted for the Ocean2k SST synthesis (e.g. McGregor et al., 2015) or the PAGES 2K Network consortium (http://pastglobalchanges. org/ini/wg/2k-network/intro). SST records should however be supplemented by complementary parameters when possible, especially to document hydrographic processes at various depths, in order to better understand the 3-D articulation of the oceanic thermal and dynamic responses to various Holocene forcing (e.g. changes in insolation, sea-level–gateway connection, volcanism, or even anthropogenic related, which could have been cumulative or not).

6. CONCLUSION

Our study, which documents Holocene surface hydrographical changes at unprecedented timescales in the Bay of Biscay, reveals contrasted patterns (warm vs. cool SST), which correlate with other North Atlantic proxy records interpreted to be responding to North Atlantic gyre dynamics. Coherently with stronger NAC inflow in the Nordic seas as detected in other archives from the northern North Atlantic, our high-resolution sedimentary records identify specific warm periods during the early Holocene and at ca. 2 kyr BP and reveal that northward advection of subtropical waters may have influenced SST oscillations in the Bay of Biscay during the last 1.5 kyr BP. In addition, SST signals from the Bay of Biscay show the occurrence of short-term cold anomalies, interpreted here as the signature of changes in SPG dynamics. The influence of the two main North Atlantic gyres, i.e STP vs. SPG, observed asynchronously over most of the Holocene in the Bay of Biscay, indicate fundamental differences in the temporal variability of their dynamics, contrasting with the idea of a coherent, basin-wide-driven, overturning cell in the North Atlantic. Our results suggest a gyre-specific expression of the AMOC where intrinsic salinity valves, linked to the latitudinal and geographical contexts, are of major importance. That may contribute to strong regionalisms in the response of the North Atlantic hydrography to Holocene climatic changes and point to the need to be as precise as possible when modelling this key component in the Earth climate system. This also urges for a densification (and maybe diversification) in the coverage of past Holocene archives.

Data availability. Data will be set on
http://www.pangaea.de/(doi:10.1594/PANGAEA.872166).
The Supplement related to this article is available online at doi:10.5194/cp-13-201-2017-supplement.

Author contributions. Yannick Mary and Frédérique Eynaud designed the study and wrote the paper in the frame of the ANR HAMOC project coordinated by Christophe Colin. Frédérique Eynaud, Linda Rossignol, Meryem Mojtahid, Jennifer Garcia, Marion Peral, and Hélène Howa performed and/or supervised planktonic foraminifera assemblage analyses and picking for the datings. Frédérique Eynaud ran the transfer function. Yannick Mary performed age modelling with the help of Frédérique Eynaud and Meryem Mojtahid. Sandra Brocheray, Sébastien Zaragosi and Michel Cremer investigated the sedimentology of core PP10-07. All authors contributed to discussions and interpretation of the results.

Acknowledgements. Analyses documented in this study have been supported by the French ANR HAMOC. We are grateful to the captain and crew of the RV *Pourquoi Pas?* and to the scientific team of the 2010-SARGASS cruise. This work beneficiated from ^{14}C AMS measurement facilities thanks to the ARTEMIS French project. We thank Giovanni Sgubin, Didier Swingedouw and Eleanor Georgiadis for useful discussions and comments on the manuscript. This is an UMR EPOC contribution.
Edited by: T. Kiefer Reviewed by: J. Scourse and one anonymous referee

References

Abrantes, F., Rodrigues, T., Montanari, B., Santos, C., Witt, L., Lopes, C., and Voelker, A. H. L.: Climate of the last millennium at the southern pole of the North Atlantic Oscillation: An inner- shelf sediment record of flooding and upwelling, Clim. Res., 48, 261–280, 2011.

Andrews, J. T. and Giraudeau, J.: Multi-proxy records showing sig- nificant Holocene environmental variability: the inner N. Iceland shelf (Hunafloi), Quaternary Sci. Rev., 22, 175–193, 2003.

Ba, J., Keenlyside, N. S., Latif, M., Park, W., Ding, H., Lohmann, K., Mignot, J., Menary, M., Otterå, O. H., Wouters, B., Salas y Melia, D., Oka, A., Bellucci, A., and Volodin, E.: A multi-model comparison of Atlantic multidecadal variability, Clim. Dynam., 43, 2333–2348, 2014.

Berner, K. S., Koç, N., Divine, D., Godtliebsen, F., and Moros, M.: A decadal-scale Holo-cene sea surface temperature record from the subpolar North Atlantic constructed using diatoms and statis- tics and its relation to other climate parameters, Paleoceanography, 23, PA2210, doi:10.1029/2006PA001339, 2008.

Bianchi, G. G. and McCave, I. N.: Holocene periodicity in North Atlantic climate and deep-ocean flow south of Iceland, Nature, 397, 515–517, 1999.

Bingham, R. J., Hughes, C. W., Roussenov, V., and Williams R. G.: Meridional coherence of the North Atlantic merid- ional overturning circulation, Geophys. Res. Lett., 34, L23606, doi:10.1029/2007GL031731, 2007.

Blaauw, M.: Methods and code for "classical" age-modelling of ra- diocarbon sequences, Quat. Geochronol., 5, 512–518, 2010.

Bond, G., Kromer, B., Beer, J., Muscheler, R., Evans, M. N., Show- ers, W., Hoffmann, S., Lotti-Bond, R., Hajdas, I., and Bonani, G.: Persistent solar influence on North Atlantic climate during the Holocene, Science, 294, 2130–2136, 2001.

Brocheray, S., Cremer, M., Zaragosi, S., Schmidt, S., Eynaud, F., Rossignol L., and Gillet, H.: 2000 years of frequent turbidite ac- tivity in the Capbreton Canyon (Bay of Biscay), Mar. Geol., 347, 136–152, doi:10.1016/j.margeo.2013.11.009, 2014.

Bryden, H. L., Longworth, H. R., and Cunningham, S. A.: Slow- ing of the Atlantic meridional overturning circulation at 25° N, Nature, 438, 655–657, 2005.

Chabaud, L., Sanchez Goni, M. F., Desprat, S., and Rossignol, L.: Land-sea climatic variability in the eastern North Atlantic subtropical region over the last 14,200 years: Atmospheric and oceanic processes at different timescales, Holocene, 24, 787– 797, 2014.

Charria, G., Lazure, P., Le Cann, B., Serpette, A., Reverdin, G., Louazel, S., Batifoulier, F., Dumas, F., Pichon, A., and Morel, Y.: Surface layer circulation derived from Lagrangian drifters in the Bay of Biscay, J. Marine Syst., 109–110, S60–S76, doi:10.1016/j.jmarsys.2011.09.015, 2013.

Cisneros, M., Cacho, I., Frigola, J., Canals, M., Masqué, P., Mar- trat, B., Casado, M., Grimalt, J. O., Pena, L. D., Margaritelli, G., and Lirer, F.: Sea surface temperature variability in the central-western Mediterranean Sea during the last 2700 years: a multi-proxy and

multi-record approach, Clim. Past, 12, 849–869, doi:10.5194/cp-12-849-2016, 2016.
Clark, P. U., Pisias, N. G., Stocker, T. F., and Weaver, A. J.: The role of the thermohaline circulation in abrupt climate change, Nature, 415, 863–869, 2002.
Copard, K., Colin, C., Henderson, G. M., Scholten, J., Dou- ville, E., Sicre, M.-A., and Frank, N.: Late Holocene interme- diate water variability in the northeastern Atlantic as recorded by deep-sea corals, Earth Planet. Sc. Lett., 313–314, 34–44, doi:10.1016/j.epsl.2011.09.047, 2012.
Colin, C., Frank, N., Copard, K., and Douville, E.: Neodymium isotopic composition of deep-sea corals from the NE At- lantic: implications for past hydrological changes dur- ing the Holocene, Quaternary Sci. Rev., 29, 2509–2517, doi:10.1016/j.quascirev.2010.05.012, 2010.
Dawson, A., Elliott, L., Noone, S., Hickey, K., Holt, T., Wadhams, P., and Foster, I.: Historical storminess and climate "see-saws" in the North Atlantic region, Mar. Geol., 210, 247–259, 2004.
Debret, M., Bout-Roumazeilles, V., Grousset, F., Desmet, M., Mc- Manus, J. F., Massei, N., Sebag, D., Petit, J.-R., Copard, Y., and Trentesaux, A.: The origin of the 1500-year climate cy- cles in Holocene North-Atlantic records, Clim. Past, 3, 569–575, doi:10.5194/cp-3-569-2007, 2007.
deCastro, M., Gómez-Gesteira, M., Alvarez, I., and Gesteira, J. L. G.: Present warming within the context of cooling–warming cy- cles observed since 1854 in the Bay of Biscay, Cont. Shelf Res., 29, 1053–1059, doi:10.1016/j.csr.2008.11.016, 2009.
Desprat, S., Sánchez-Goñi, M. F., and Loutre, M.-F.: Revealing cli- matic variability of the last three millennia in northwestern Iberia using pollen influx data, Earth Planet. Sc. Lett., 213, 63–78, 2003.
Esnaola, G., Sáenz, J., Zorita, E., Fontán, A., Valencia, V., and Lazure, P.: Daily scale wintertime sea surface temperature and IPC-Navidad variability in the southern Bay of Biscay from 1981 to 2010, Ocean Sci., 9, 655–679, doi:10.5194/os-9-655-2013, 2013.
Eynaud, F., Turon, J. L., and Duprat, J.: Comparison of the Holocene and Eemian palaeoenvironments in the South Icelandic Basin: Dinoflagellate cysts as proxies for the North Atlantic sur- face circulation, Rev. Palaeobot. Palyno., 128, 55–79, 2004.
Eynaud, F., Rossignol, L., and Gasparotto, M.-C.: Planktic foraminifera throughout the Pleistocene: From cell to popula- tions to past marine hydrology, Chap. 8, in: Foraminifera: Clas- sification, Biology, and Evolutionary Significance, edited by: Georgescu, M. D., Nova Science Publishers, New York, NY, 2013.
Farmer, E. J., Chapman, M. R., and Andrews, J. E.: Holocene tem- perature evolution of the subpolar North Atlantic recorded in the Mg / Ca ratios of surface and thermocline dwelling planktonic foraminifers, Global Planet. Change, 79, 234–243, 2011.
Garcia, J., Mojtahid, M., Howa, H., Michel, E., Schiebel, R., Char- bonnier, C., Anschutz, P., and Jorissen, F. J.: Benthic and planktic foraminifera as indicators of late glacial to Holocene paleocli- matic changes in a marginal environment: An example from the southeastern Bay of Biscay, Acta Protozool., 52, 163–182, 2013.
Garcia-Soto, C. and Pingree, R. D.: Atlantic Multidecadal Oscilla- tion (AMO) and sea surface temperature in the Bay of Biscay and adjacent regions, J. Mar. Biol. Assoc. UK, 92, 213–234, 2012.
Garcia-Soto, C., Pingree, R. D., and Valdés, L.: Navidad develop- ment in the southern Bay of

Biscay: Climate change and swoddy structure from remote sensing and in situ measurements, J. Geo- phys. Res., 107, doi:10.1029/2001JC001012, 2002.

Gaudin, M., Mulder, T., Cirac, P., Berne, S., and Imbert, P.: Past and present sedimentation activity in the Capbreton Canyon, southern Bay of Biscay, Geo-Mar. Lett., 26, 331–345, 2006.

Giraudeau, J., Jennings, A. E., and Andrews, J. T.: Timing and mechanisms of surface and intermediate water circulation changes in the Nordic Seas over the last 10,000 cal years: a view from the North Iceland shelf, Quaternary Sci. Rev., 23, 2127– 2139, 2004.

Giraudeau, J., Grelaud, M., Solignac, S., Andrews, J. T., Moros, M., and Jansen, E.: Millennial-scale variability in Atlantic wa- ter advection to the Nordic Seas derived from Holocene coccol- ith concentration records, Quaternary Sci. Rev., 29, 1276–1287, doi:10.1016/j.quascirev.2010.02.014, 2010.

Guiot, J. and de Vernal, A.: Transfer functions: Methods for quan- titative paleoceanography based on microfossils, in: Proxies in Late Cenozoic Paleoceanography, edited by: Hillaire-Marcel, C. and de Vernal, A., Amsterdam: Elsevier, 523–563, 2007.

Guiot, J. and de Vernal, A.: Is spatial autocorrelation introducing bi- ases in the apparent accuracy of paleoclimatic reconstructions?, Quaternary Sci. Rev., 30, 1965–1972, 2011.

Hatun, H., Britt Sandø, A., Drange, H., Hansen, B., and Valdimarsson, H.: Influence of the Atlantic Subpolar Gyre on the Thermohaline Circulation, Science, 309, 1841–1844, 2005. Hayes, A., Kucera, M., Kallel, N., Sbaffi, L., and Rohling, E. J.: Glacial Mediterranean sea surface temperatures based on plank- tonic foraminiferal assemblages, Quaternary Sci. Rev., 24, 999– 1016, 2005.

Jackson, L. C., Kahana, R., Graham, T., Ringer, M. A., Woollings, T., Mecking, J. V., and Wood, R. A.: Global and European cli- mate impacts of a slowdown of the AMOC in a high resolution GCM, Clim. Dynam., 45, 3299–3316, doi:10.1007/s00382-015- 2540-2, 2015.

Kennedy, J. J.: A review of uncertainty in in situ measurements and data sets of sea surface temperature, Rev. Geophys., 52, 1–32, doi:10.1002/2013RG000434, 2014.

Koutsikopoulos, C., Beillois, P., Leroy, C., and Taillefer, F.: Tempo- ral trends and spatial structures of the sea surface temperature in the Bay of Biscay, Oceanol. Acta, 21, 335–344, 1998.

Kucera, M., Weinelt, M., Kiefer, T., Pflaumann, U., Hayes, A., Weinelt, M., Chen, M.-T., Mix, A.-C., Barrows, T. T., Cortijo, E., Duprat, J., Juggins, S., and Waelbroeck, C.: Reconstruc- tion of sea-surface temperatures from assemblages of planktonic foraminifera: multi-technique approach based on geographically constrained calibration data sets and its application to glacial At- lantic and Pacific Oceans, Quaternary Sci. Rev., 24, 951–998, doi:10.1016/j.quascirev.2004.07.014, 2005.

Landsea, C. W., Vecchi, G. A., Bengtsson, L., and Knutson, T. R.: Impact of Duration Thresholds on Atlantic Tropical Cyclone Counts*, J. Climate, 23, 2508–2519, 2010.

Le Cann, B. and Serpette, A.: Intense warm and saline upper ocean inflow in the southern Bay of Biscay in autumn–winter 2006–2007, Cont. Shelf Res., 29, 1014–1025, doi:10.1016/j.csr.2008.11.015, 2009.

Lherminier, P. and Thierry, V.: The Reykjanes Ridge Experiment, http://wwz.ifremer.fr (last access: 22 November 2016), 2015. Lozier, M. S.: Overturning in the North Atlantic,

Annual Review of
Marine Science, 4, 291–315, 2012. Lozier, M. S. and Stewart, N. M.: On the Temporally Varying Northward Penetration of Mediterranean Overflow Water and East- ward Penetration of Labrador Sea Water, J. Phys. Oceanogr., 38, 2097–2103, 2008.

Lozier, M. S., Roussenov, V., Reed, M. S. C., and Williams, R. G.: Opposing decadal changes for the North Atlantic meridional overturning circulation, Nat. Geosci., 3, 728–734, 2010.

Magny, M., Bégeot, C., Guiot, J., and Peyron, O.: Contrasting pat- terns of hydrological changes in Europe in response to Holocene climate cooling phases, Quaternary Sci. Rev., 22, 1589–1596, 2003.

Mann, M. E., Zhang, Z., Rutherford, S., Bradley, R. S., Hughes, M. K., Shindell, D., Ammann, C. Faluvegi, G., and Ni, F.: Global signatures and dynamical origins of the Little Ice Age and Medieval Climate Anomaly, Science, 326, 1256–1260, 2009 (data available at: http://www.meteo.psu.edu/holocene/public_ html/supplements/MultiproxySpatial09/, last access: July 2016).

Marchal, O., Cacho, I., Stocker, T. F., Grimalt, J. O., Calvo, E., Martrat, B., Shackleton, N., Vautravers, M., Cortijo, E., and van Kreveld S.: Apparent long-term cooling of the sea surface in the northeast Atlantic and Mediterranean during the Holocene, Qua- ternary Sci. Rev., 21, 455–483, 2002.

Martín-Chivelet, J., Muñoz-García, M. B., Edwards, R. L., Turrero, M. J., and Ortega, A. I.: Land surface temperature changes in Northern Iberia since 4000 yr BP, based on $\delta^{13}C$ of speleothems, Global Planet. Change, 77, 1–12, 2011.

Martrat, B., Grimalt, J. O., Shackleton, N. J., de Abreu, L., Hutterli, M. A., and Stocker, T. F.: Four Climate Cycles of Recurring Deep and Surface Water Destabilizations on the Iberian Margin, Science, 317, 502–507, 2007 (data available at: doi:10.1594/PANGAEA.771894).

Mary, Y., Eynaud, F., Zaragosi, S., Malaizé, B., Cremer, M., and Schmidt, S.: High frequency environmental changes and depo- sition processes in a 2kyr-long sedimentological record from the Cap-Breton canyon (Bay of Biscay), Holocene, 25, 348–365, doi:10.1177/0959683614558647, 2015.

Mary, Y., Eynaud, F., Colin, C., Rossignol, L., Brocheray, S., Moj- tahid, M., Garcia, J., Peral, M., Howa, H., Zaragosi, S., and Cre- mer, M.: Interactive comment on "Changes in Holocene merid- ional circulation and poleward Atlantic flow: the Bay of Biscay as a nodal point" by Yannick Mary et al., Clim. Past. Discuss., doi:10.5194/cp-2016-32-AC2, 2016.

McCartney, M. S. and Mauritzen, C.: On the origin of the warm inflow to the Nordic Seas, Prog. Oceanogr., 51, 125–214, 2001.

McGregor, H. V., Evans, M. N., Goosse, H., Leduc, G., Martrat, B., Addison, J. A., Mortyn, P. G., Oppo, D. W., Seidenkrantz, M.-S., Sicre, M.-A., Phipps, S. J., Selvaraj, K., Thirumalai, K., Filipsson, H. L., and Ersek, V.: Robust global ocean cooling trend for the pre-industrial Common Era, Nat. Geosci., 8, 671–677, doi:10.1038/ngeo2510, 2015.

Mojtahid, M., Jorissen, F. J., Garcia, J., Schiebel, R., Michel, E., Ey- naud, F., Gillet, H., Cremer, M., Diz Ferreiro, P., Siccha, M., and Howa, H.: High resolution Holocene record in the southeastern Bay of Biscay: Global versus regional climate signals, Palaeo- geogr. Palaeocl., 377, 28–44, doi:10.1016/j.palaeo.2013.03.004, 2013.

Morley, A., Rosenthal, Y., and deMenocal, P.: Ocean-atmosphere climate shift during the mid-

to-late Holocene transition, Earth Planet. Sc. Lett., 388, 18–26, doi:10.1016/j.epsl.2013.11.039, 2014.

Moros, M., Jansen, E., Oppo, D. W., Giraudeau, J., and Kuijpers, A.: Reconstruction of the late-Holocene changes in the Sub-Arctic Front position at the Reykjanes Ridge, north Atlantic, Holocene, 22, 877–868, 2012.

Naughton, F., Bourillet, J. F., Sanchez Goni, M.-F., Turon J.-L., and Jouanneau J.-M.: Long-term and millennial-scale climate variability in northwestern France during the last 8850 years, Holocene, 17, 939–953, 2007a.

Naughton, F., Sanchez Goñi, M. F., Desprat, S., Turon, J.-L., Duprat, J., Malaizé, B., Joli, C., Cortijo, E., Drago, T., and Freitas, M. C.: Present-day and past (last 25000 years) marine pollen signal off western Iberia, Mar. Micropaleontol., 62, 91– 114, doi:10.1016/j.marmicro.2006.07.006, 2007b.

Ollitrault, M. and Colin de Verdière, A.: The ocean general circula- tion near 1000 m depth, J. Phys. Oceanogr., 44, 384–409, 2014.

Oppo, D. W., McManus, J. F., and Cullen, J. L.: Deepwater variabil- ity in the Holocene epoch, Nature, 422, 277–278, 2003.

Peliz, Á., Dubert, J., Santos, A. M. P., Oliveira, P. B., and Le Cann, B.: Winter upper ocean circulation in the Western Iberian Basin – Fronts, Eddies and Poleward Flows: an overview, Deep-Sea Res. Pt. I, 52, 621–646, doi:10.1016/j.dsr.2004.11.005, 2005.

Pena, L. D., Francés, G., Diz, P., Esparza, M., Grimalt, J. O., Nombela, M. A., and Alejo, I.: Climate fluctuations during the Holocene in NW Iberia: High and low latitude linkages, Cont. Shelf Res., 30, 1487–1496, doi:10.1016/j.csr.2010.05.009, 2010.

Penaud, A., Eynaud, F., Sánchez-Goñi, M. F., Malaizé, B., Turon, J. L., and Rossignol, L.: Contrasting sea-surface responses between the western Mediterranean Sea and eastern subtropical latitudes of the North Atlantic during abrupt climatic events of MIS 3, Mar. Micropaleontol., 80, 1–17, 2011.

Pérez-Brunius, P., Rossby, T., and Watts, D. R.: Absolute transports of mass and temperature for the North Atlantic Current-Subpolar Front system, J. Phys. Oceanogr., 34, 1870–1883, 2004.

Pflaumann, U., Duprat, J., Pujol, C., and Labeyrie, L. D.: SIMMAX: A modern analog technique to deduce Atlantic sea surface tem- peratures from planktonic foraminifera is deep-sea sediments, Paleoceanography, 11, 15–35, 1996.

Pingree, R.: North Atlantic and North Sea climate change: curl up, shut down, NAO and ocean colour, J. Mar. Biol. Assoc. UK, 85, 1301–1315, 2005.

Pingree, R. D. and Garcia-Soto, C.: Plankton blooms, ocean circu- lation and the European slope current: Response to weather and climate in the Bay of Biscay and W English Channel (NE At- lantic), Deep-Sea Res. Pt. II, 106, 5–22, 2014.

Pingree, R. D. and Le Cann, B.: Structure, strength and seasonality of the slope currents in the Bay of Biscay region, J. Mar. Biol. Assoc. UK, 70, 857–885, 1990.

Planque, B., Beillois, P., Jégou, A.-M., Lazure, P., Petitgas, P., and Puillat, I.: Large-scale hydroclimatic variability in the Bay of Biscay: the 1990s in the context of interdecadal changes, in: ICES Marine Science Symposia, 219, 61–70, 2003.

Reimer, P. J., Bard, E., Bayliss, A., Beck, J. W., Blackwell, P. G., Ramsey, C. B., Buck, C. E., Cheng, H., Edwards, R. L., Friedrich, M., Grootes, P. M., Guilderson, T. P., Haflidason, H., Hajdas, I., Hatté, C., Heaton, T. J., Hoffmann, D. L., Hogg, A. G., Hughen, K. A., Kaiser, K. F.,

Kromer, B., Manning, S. W., Niu, M., Reimer, R. W., Richards, D. A., Scott, E. M., Southon, J. R., Staff, R. A., Turney, C. S. M., and van der Plicht, J.: IntCal13 and Marine13 Radiocarbon Age Calibration Curves 0–50,000 Years cal BP, Radiocarbon, 55, 1869–1887, doi:10.2458/azu_js_rc.55.16947, 2013.

Retailleau, S., Howa, H., Schiebel, R., Lombard, F., Eynaud, F., Schmidt, S., Jorissen, F., and Labeyrie, L.: Planktic foraminiferal production along an offshore-onshore transect in the south- eastern Bay of Biscay, Cont. Shelf Res., 29, 1123–1135, 2009.

Retailleau, S., Eynaud, F., Mary, Y., Schiebel, R., and Howa, H.: An Ocean – Canyon head and river plume: how they may influ- ence neritic planktonic foraminifera communities in the SE Bay of Biscay?, J. Foramin. Res., 42, 257–269, 2012.

Risebrobakken, B., Dokken, T., Smedsrud, L. H., Andersson, C., Jansen, E., Moros, M., and Ivanova, E. V.: Early Holocene tem- perature variability in the Nordic Seas: The role of oceanic heat advection versus changes in orbital forcing, Paleoceanography, 26, PA4206, doi:10.1029/2011PA002117, 2011.

Rodrigues, T., Grimalt, J. O., Abrantes, F. G., Flores, J. A., and Lebreiro, S. M.: Holocene interdependences of changes in sea surface temperature, productivity, and fluvial inputs in the Iberian continental shelf (Tagus mud patch), Geochem. Geophy. Geosys., 10, Q07U06, doi:10.1029/2008GC002367, 2009 (data available at: doi:10.1594/PANGAEA.761812).

Roth, R. and Joos, F.: A reconstruction of radiocarbon produc- tion and total solar irradiance from the Holocene ^{14}C and CO_2 records: implications of data and model uncertainties, Clim. Past, 9, 1879–1909, doi:10.5194/cp-9-1879-2013, 2013.

Salgueiro, E., Voelker, A., Abrantes, F., Meggers, H., Pflau- mann, U., Loncaric, N., Gonzalez-Ãlvarez, R., Oliveira, P., Bartels-Jónsdóttir, H. B., Moreno, J., and Wefer, G.: Planktonic foraminifera from modern sediments reflect upwelling patterns off Iberia: Insights from a regional transfer function, Mar. Mi- cropaleontol., 66, 135–164, 2008.

Salgueiro, E., Voelker, A. H. L., de Abreu, L., Abrantes, F., Meg- gers, H., and Wefer, G.: Temperature and productivity changes off the western Iberian margin during the last 150 Â ky, Quater- nary Sci. Rev., 29, 680–695, 2010.

Sánchez Goñi, M. F., Bakker, P., Desprat, S., Carlson, A. E., Van Meerbeeck, C. J., Peyron, O., Naughton, F., Fletcher, W. J., Ey- naud, F., Rossignol, L., and Renssen, H.: European climate opti- mum and enhanced Greenland melt during the Last Interglacial, Geology, 40, 627–630, 2012.

Sánchez Goñi, M. F., Bard, E., Landais, A., Rossignol, L., and d'Errico, F.: Air–sea temperature decoupling in western Europe during the last interglacial–glacial transition, Nat. Geosci., 6, 837–841, doi:10.1038/ngeo1924, 2013.

Sarnthein, M., Van Kreveld, S., Erlenkeuser, H., Grootes, P. M., Kucera, M., Pflaumann, U., and Schulz, M.: Centennial-to- millennial-scale periodicities of Holocene climate and sediment injections off the western Barents shelf, 75° N, Boreas, 32, 447– 461, 2003.

Schäfer-Neth, C. and Manschke, A.: WOA-Sample tool, http: //www.geo.uni-bremen.de/geomod/staff/csn/woasample.html (last access: January 2016), 2002.

Solignac, S., Grelaud, M., de Vernal, A., Giraudeau, J., Moros, M., McCave, N., and Hoogakker, B.: Reorganization of the upper ocean circulation in the mid-Holocene in the Northeastern At- lantic, Can. J. Earth Sci., 45, 1417–1433, 2008.

Sorrel, P., Tessier, B., Demory, F., Delsinne, N., and Mouazé, D.: Evidence for millennial-scale climatic events in the sedimentary infilling of a macrotidal estuarine system, Quaternary Sci. Rev., 28, 499–516, 2009.

Sorrel, P., Debret, M., Billeaud, I., Jaccard, S. L., McManus, J. F., and Tessier, B.: Persistent non-solar forcing of Holocene storm dynamics in coastal sedimentary archives, Nat. Geosci., 12, 892– 896, doi:10.1038/ngeo1619, 2012.

Staines-Urías, F., Kuijpers, A., and Korte, C.: Evolution of subpo- lar North Atlantic surface circulation since the early Holocene inferred from planktic foraminifera faunal and stable isotope records, Quaternary Sci. Rev., 76, 66–81, 2013.

Tanner, B. R., Lane, C. S., Martin, E. M., Young, R., and Collins, B.: Sedimentary proxy evidence of a mid-Holocene hypsithermal event in the location of a current warming hole, North Carolina, USA, Quaternary Res., 83, 315–323, doi:10.1016/j.yqres.2014.11.004, 2015.

Telford, R. J. and Birks, H. J. B.: Effect of uneven sampling along an environmental gradient on transfer-function performance, J. Paleolimnol., 46, 99–106, 2011.

Telford, R. J., Li, C., and Kucera, M.: Mismatch between the depth habitat of planktonic foraminifera and the calibration depth of SST transfer functions may bias reconstructions, Clim. Past, 9, 859–870, doi:10.5194/cp-9-859-2013, 2013.

Thornalley, D. J. R., Elderfield, H., and McCave, I. N.: Holocene oscillations in temperature and salinity of the surface subpolar North Atlantic, Nature, 457, 711–714, 2009.

Trouet, V., Scourse, J. D., and Raible, C. C.: North Atlantic stormi- ness and Atlantic Meridional Overturning Circulation during the last Millennium: Reconciling contradictory proxy records of NAO variability, Global Planet. Change, 84–85, 48–55, 2012.

Valencia, V., Borja, Å., Fontán, A., Pérez, F. F., and Rios, A. F.: Temperature and salinity fluctuations along the Basque Coast (southeastern Bay of Biscay), from 1986 to 2000, related to cli- matic factors, ICES J. Mar. Sci., 219, 340–342, 2003.

Van Vliet-Lanoe, B., Goslin, J., Hallegouet, B., Henaff, A., Delacourt, C., Fernane, A., Franzetti, M., Le Cornec, E., Le Roy, P., and Penaud, A.: Middle- to late-Holocene storminess in Brittany (NW France): Part I – morphologi- cal impact and stratigraphical record, Holocene, 24, 413–433, doi:10.1177/0959683613519687, 2014a.

Van Vliet-Lanoe, B., Penaud, A., Henaff, A., Delacourt, C., Fer- nane, A., Goslin, J., Hallegouet, B., and Le Cornec, E.: Middle- to late-Holocene storminess in Brittany (NW France): Part II – The chronology of events and climate forcing, Holocene, 24, 434–453, doi:10.1177/0959683613519688, 2014b.

Voelker, A. H. L. and de Abreu, L.: A Review of Abrupt Climate Change Events in the Northeastern Atlantic Ocean (Iberian Mar- gin): Latitudinal, Longitudinal, and Vertical Gradients, in: Geo- physical Monograph Series, edited by: Rashid, H., Polyak, L., and Mosley-Thompson, E., American Geophysical Union, Wash- ington, D.C., 15–37, 2011.

Walker, M. J. C., Berkelhammer, M., Björck, S., Cwynar, L. C., Fisher, D. A., Long, A. J., Lowe, J. J., Newnham, R. M., Ras- mussen S. O., and Weiss, H.: Formal subdivision of the Holocene Series/Epoch: a Discussion Paper by a Working Group of INTI- MATE (Integration of ice-core, marine and terrestrial records) and the Subcommission on Quaternary Stratigraphy (Interna- tional Commission on Stratigraphy), J. Quaternary Sci., 27, 649– 659, 2012.

Wanner, H., Beer, J., Bütikofer, J., Crowley, T. J., Cubasch, U., Flückiger, J., Goosse, H., Grosjean, M., Joos, F., Kaplan, J. O., Küttel, M., Müller, S. A., Prentice, I. C., Solomina, O., Stocker, T. F., Tarasov, P., Wagner, M., and Widmann, M.: Mid- to Late Holocene climate change: an overview, Quaternary Sci. Rev., 27, 1791–1828, doi:10.1016/j.quascirev.2008.06.013, 2008.

Werner, K., Spielhagen, R. F., Bauch, D., Hass, H. C., and Kandi- ano, E. S.: Atlantic Water advection versus sea-ice advances in the eastern Fram Strait during the last 9 ka: Multiproxy evidence for a two-phase Holocene, Paleoceanography, 28, 283–295, 2013 (data available at: doi:10.1594/PANGAEA.810415).

Most Earth-surface Calcites Precipitate Out of Isotopic Equilibrium

M. Daëron* (1), R. N. Drysdale (2,3), **M. Peral** (1), D. Huyghe (4,5), D. Blamart (1), T. B. Coplen (6), F. Lartaud (4), G. Zanchetta (7)

(1) Laboratoire des Sciences du Climat et de l'Environnement, LSCE / IPSL, CEA-CNRS-UVSQ, Université Paris-Saclay, France
(2) University of Melbourne, Australia
(3) EDYTEM UMR CNRS 5204, Université Savoie Mont Blanc, France
(4) Sorbonne Université, Laboratoire d'Ecogéochimie des Environnements Benthiques, UMR CNRS 8222, F-66650 Banyuls-sur-mer, France
(5) Géosciences Environnement Toulouse, Université Paul Sabatier Toulouse 3, France
(6) U.S. Geological Survey, Reston, Virginia, USA
(7) University of Pisa, Italy

Correspondence to:
daeron@lsce.ipsl.fr

Submitted in: *Nature Communication*

Oxygen-isotope thermometry played a critical role in the rise of modern geochemistry and is now extensively used in (bio-)geoscience. Its theoretical foundations rest on the assumption that $^{18}O/^{16}O$ partitioning among water and oxygen-bearing minerals, such as carbonates, primarily reflects thermodynamic equilibrium constants. However, after seven decades of research, there is still no consensus on the true equilibrium $^{18}O/^{16}O$ fractionation factor ($^{18}\alpha_{C/W}$) between calcite ($CaCO_3$) and water. Here, we constrain the equilibrium relationships linking crystallization temperature, $^{18}\alpha_{C/W}$, and clumped isotopes (Δ_{47}) between 8 °C and 34 °C based on the composition of extremely slow-growing calcites from Devils Hole (Nevada, USA) and Laghetto Basso (Corchia Cave, Italy). Equilibrium values of $^{18}\alpha_{C/W}$ are found to be 1–2 ‰ greater, regardless of temperature, than those observed in biogenic and synthetic calcite traditionally considered to approach oxygen-isotope equilibrium. We further demonstrate that subtle, but resolvable, disequilibrium effects also influence the relationship between Δ_{47} and calcification temperatures in biogenic calcite. Together, these observations provide robust evidence that most Earth-surface calcites never achieve isotopic equilibrium, highlighting the need to improve our quantitative understanding of non-equilibrium isotope fractionation effects instead of relying on phenomenological calibrations of both oxygen-isotope and Δ_{47} thermometry.

Harold Urey's prediction [1], based on fundamental thermodynamic principles, that the isotopic composition of carbonate minerals must be strongly influenced by their crystallization temperature is the cornerstone of both stable-isotope geochemistry and paleoclimatology. $^{18}O/^{16}O$ abundance ratios in carbonates primarily reflect the temperature and oxygen-isotope composition of the water from which they precipitated, both of which vary in complex but generally understood ways under the influence of important environmental parameters, such as altitude, latitude, atmospheric circulation, greenhouse gas concentrations, global ice volume, and rainfall distribution. For seven

decades, this relationship has been extensively applied to study past climates [2], sedimentary and diagenetic processes in the Earth's crust [3], the global carbon cycle [4], biological mechanisms of calcification [5], ore deposits and petroleum geology [6], the petrogenesis of carbonatites [7], the ecology of marine and terrestrial species [8], and the early Solar System [9]. This versatility stems from the ubiquity of carbonate minerals in the geologic record and the biosphere, and from the ease with which dissolved inorganic carbon (DIC) species exchange oxygen isotopes with water, reaching chemical and isotopic equilibrium on short time scales [10].

Despite the historical and contemporary importance of oxygen-isotope geochemistry, there is still no consensus on the true equilibrium $^{18}O/^{16}O$ fractionation factors between carbonates and water [11–16]. Different groups of inorganic and biogenic carbonates appear to follow different fractionation laws, prompting the use of phenomenological calibrations believed to describe the behaviour of various specific types of natural carbonates [e.g., 17, 18]. Although many of these calibrations display similar temperature sensitivities, with $\delta^{18}O$ values decreasing by 0.21 ‰/K around 20 °C, certain types of carbonates, such as speleothems [19, 20], corals [5, 21] or coccoliths [22], are clearly influenced by additional parameters beyond precipitation temperature. These discrepancies most likely reflect isotopic disequilibrium related to poorly constrained kinetic/metabolic processes, consistent with the fact that Earth-surface carbonates generally precipitate rapidly from supersaturated solutions [23]. Our understanding of such non-equilibrium processes, however, is far from complete. The main unanswered questions concern which DIC species are directly involved in crystallization, the processes by which different reaction pathways may be favored or inhibited, and how to quantitatively describe nucleation effects, crystal-surface phases, or the role of amorphous calcite [24–26].

To isolate and understand these non-equilibrium processes, it is necessary to establish a baseline of $^{18}O/^{16}O$ equilibrium fractionation as a function of temperature. Both theory [23, 27] and empirical results [28] suggest that full attainment of oxygen-isotope equilibrium might not be achievable in laboratory experiments, so that one must instead turn to natural minerals precipitated very slowly from slightly supersaturated environments. Suitable natural carbonates, however, remain exceedingly rare.

Slow-growing Calcites from Devils Hole and Laghetto Basso

It has been argued, based on its extremely slow growth and the long-term stability of its geochemical environment, that the subaqueous mammillary calcite coating the walls of the Devils Hole cave system (Nevada, USA) offers optimal conditions for equilibrium crystallization [16]. Devils Hole calcite of Holocene age, precipitated at ~33.7 °C, is known to yield significantly higher $\delta^{18}O$ values than those predicted from laboratory experiments and from many biogenic calcite calibration studies, suggesting that most natural carbonates are affected by non-equilibrium oxygen-isotope fractionations with magnitudes on the order of 1-2 ‰. Several recent theoretical models of kinetic fractionation [23, 27, 29] have postulated equilibrium fractionation factors anchored to the Devils Hole data, but relying on a single observation remains problematic, particularly when extrapolating to cooler environments.

Here, we extend the isotopic equilibrium baseline to low temperatures based on another instance of extremely slow-growing calcite, originating from an unusual karstic environment. The subaqueous calcite coating found at the bottom of Laghetto Basso, a small lake in Corchia Cave (Italy), provides an apparently continuous paleoclimate record of the last 960 ka [30]. *In situ* observations, spanning 10 years, of pH and temperature, as well as isotopic and elemental analyses of water samples, demonstrate that modern pool water is thermally and chemically stable, with pH = 8.2 ± 0.1 and T = 7.9 ± 0.2 °C (1SD). In contrast to most karstic environments of paleoclimatic interest, dripwater must percolate through the Corchia Cave system for long durations on the order of years to decades before reaching Laghetto Basso. As a result, the subaqueous calcite precipitates from a solution, which is already very close to chemical and isotopic equilibrium with host rocks and the local cave atmosphere [30, 31]. Laghetto Basso calcite shares many other similarities with Devils Hole mammillary calcite, making it very likely that it was also precipitated in isotopic equilibrium. Both sites are characterized by low values of calcite saturation indices ($0.18 \leq \log(\Omega) \leq 0.30$), very slow growth rates (≤ 0.8 µm/y), similar crystalline structures, and comparable solution ratios of $[DIC]/[Ca^{2+}]$ and $[Mg^{2+}]/[Ca^{2+}]$ [31, 32].

Oxygen-18 equilibrium

We sampled calcite from the outer surface of coatings from both sites and measured their carbon and oxygen stable-isotope compositions (Table 1). Both samples yield calcite/water oxygen-18 fractionation factors ($^{18}\alpha_{C/W}$) which are 1.5 ‰ greater than predicted by the experimental calibration of *Kim & O'Neil* [15] (Figure 1), defining an equilibrium baseline (Equation 1, with crystallization temperature T in kelvins) whose slope is indistinguishable from that of the synthetic precipitates.

$$10^3 \ln(^{18}\alpha_{C/W}) = 17.57 \times 10^3 / T - 29.13 \quad (1)$$

The temperature sensitivity of Equation (1) is 0.20 ‰/K at 20 °C, which is very similar to that of equilibrium oxygen-18 fractionation between dissolved (bio)carbonate ions (CO_3^{2-}, HCO_3^-) and water (0.19 and 0.21 ‰/K, respectively [33]). Our findings are thus consistent with the hypothesis that the kinetic components of $^{18}\alpha_{C/W}$ vary primarily with pH, crystallization rates, and/or solution saturation, but remain relatively insensitive to temperature (at least within the range of typical Earth-surface conditions), as postulated in several theoretical models [23, 27, 29].

Clumped-isotope disequilibrium in biogenic calcites

As a complementary characterization of isotopic equilibrium, we also measured the clumped-isotope composition (Δ_{47}) of these two samples (Table 1). Clumped isotopes describe statistical anomalies in the abundance of isotopologues with multiple rare isotopes, such as $(^{13}C^{18}O^{16}O_2)^{2-}$ [34]. In the same way that carbonate $\delta^{18}O$ values potentially record equilibrium oxygen-isotope fractionation factors between the mineral and aqueous phases, Δ_{47} values of calcite are expected to reflect temperature-dependent isotopic equilibrium constants within the mineral phase [35], providing a complementary

but independent isotopic thermometer.

The Devils Hole – Laghetto Basso calibration for equilibrium values of Δ_{47} in calcite at Earth-surface temperatures (Figure 2A) is described by the following equation:

$$\Delta_{47} = 46.0 \times 10^3 / T^2 + 0.142 \qquad (2)$$

The slope of this regression is consistent with most of the latest Δ_{47} calibration studies [28, 36–38]. However, precise comparisons between clumped-isotope measurements performed in different laboratories remain challenging due to several methodological issues [39, 40]. For instance, earlier Δ_{47} measurements of Devils Hole calcite [41, 42] are not directly comparable to the values reported here because they are anchored to CO_2 standards instead of the carbonate standards used in our study. To circumvent this problem, we compare our equilibrium observations to the clumped-isotope compositions of planktonic and benthic foraminifera collected from marine sediment core-tops [43] and of modern calcitic bivalves from environments with minimal seasonal variability, all of which were analyzed in a single laboratory, following identical analytical procedures, using the same set of carbonate standards, within a limited time frame (10 months).

The compositions of biogenic samples formed at low temperatures (≤ 5 °C) are consistent with equilibrium Δ_{47} values extrapolated from Equation (2), but biogenic samples with warmer calcification temperatures display significantly higher Δ_{47} values than the equilibrium baseline (Figure 2A). In spite of statistically indistinguishable regression slopes (Figure 2B), an analysis of covariance based on conservative estimates of analytical errors and temperature uncertainties demonstrates that the observed differences between the slow-growing inorganic calcites and the biogenic samples are statistically significant ($p \leq 10^{-3}$). Contrary to the case of oxygen isotopes, these differences are not much larger than the current precision limits on Δ_{47} measurements, particularly when taking inter-laboratory discrepancies into account.

`

Broader implications

Our ability to jointly define equilibrium values for the two independent isotopic thermometers opens up interesting new possibilities. For instance, combining Δ_{47} and ${}^{18}\alpha_{c/w}$ observations clearly exposes large isotopic differences between our biogenic carbonates and the slow-growing calcites, without requiring any assumptions on their crystallization temperatures (Figure 3). We anticipate that this kind of combined observations will be particularly useful in studies such as those of diagenetic carbonates, where temperatures remain poorly constrained but where the oxygen-isotope composition of parent waters may be estimated from independent methods (e.g., fluid inclusions [44]).

It should be noted that "oxygen-18 equilibrium", referring to oxygen-isotope exchange between water and mineral phases, and "clumped-isotope equilibrium", referring to internal isotopic exchanges between isotopologues within the mineral phase, are logically independent, i.e. neither implies the other, because ultimately they reflect different processes. It is still an open question whether the clumped-isotope signature of calcite is inherited from that of one or more DIC species, or whether it reflects partial or complete isotopic exchanges occurring in transitional phases such as amorphous calcite or crystal-surface phases [25, 26, 28, 42]. By contrast, achieving oxygen-18 equilibrium between water and calcite requires establishing a series of intermediate equilibria: between water and DIC, then between DIC and calcite, either directly or through the intermediate phases mentioned above. Each of these exchange steps may fail to achieve equilibrium, which potentially manifests in very different ways. For example, rapid CO_2 degassing of DIC solutions is associated with kinetic isotope fractionation effects, which strongly affect both $\delta^{18}O$ and Δ_{47} [45], contrary to the disequilibrium observations reported here which only weakly affect the latter.

Our findings provide robust new evidence that the majority of calcites precipitated at the surface of the Earth achieve neither oxygen-18 nor clumped- isotope equilibrium, probably because most of them precipitate rapidly from supersaturated solutions. Potential

counterexamples are expected to be found in environments with very low supersaturation states, including for example carbonates associated with low-temperature hydrothermal alteration of young oceanic crust [46] or recrystallized carbonates from deep-sea sediments [47].

Another class of exceptions, depending on the definition of "Earth surface", is that of diagenetic or metamorphic carbonates formed deeper in the crust at significantly warmer temperatures, where isotope exchange reaction rates are much faster.

In most other cases, kinetic components of $^{18}\alpha_{c/w}$ (excluding those reflecting isotopic disequilibrium between DIC and water) typically decrease $\delta^{18}O$ values by 1-2 ‰ or more, even in "well-behaved" biogenic carbonates where $^{18}\alpha_{c/w}$ varies mostly with temperature. As noted by *Watkins et al.* [27], oxygen-isotope thermometry works reasonably well in spite of these strong kinetic effects because many types of natural carbonates precipitate under limited ranges of pH and growth rates. However, the observation that non-equilibrium oxygen-18 effects in coccolithophores have varied drastically at geologic time scales [22, 48] offers a cautionary tale regarding the long-term applicability of modern calibrations for biogenic carbonates. Moving beyond phenomenological characterizations of oxygen-isotope and Δ_{47} thermometry calls for substantial improvements in our ability to model isotopic fluxes and fractionations in the water/DIC/carbonate system. In our view, the use of non-classical isotopic tracers, such as clumped isotopes and oxygen-17 anomalies ($\Delta^{17}O$), offers appealing new opportunities to test and improve these models.

		Devils Hole	Laghetto Basso
Sample		DVH	LGB
Temperature	(°C ±1SD)	33.7 ± 0.2	7.9 ± 0.2
Water $\delta^{18}O_{VSMOW}$	(‰ ±1SE)	-13.54 ± 0.05	-7.39 ± 0.09
Calcite $\delta^{13}C_{VPDB}$	(‰ ±1SE)	-1.95 ± 0.01	0.02 ± 0.02
Calcite $\delta^{18}O_{VPDB}$	(‰ ±1SE)	-15.83 ± 0.04	-4.48 ± 0.03
1000 ln($^{18}\alpha_{c/w}$)	(±1SE)	28.13 ± 0.06	33.38 ± 0.10
Calcite Δ_{47}	(‰ ±1SE)	0.631 ± 0.004	0.725 ± 0.004

Table 1: Crystallization temperature and stable-isotope composition of water and calcite from Devils Hole and Laghetto Basso. Because of low supersaturation conditions and extremely slow growth rates, the composition of these two natural samples is very likely to record equilibrium values of $^{18}\alpha_{c/w}$ and Δ_{47}.

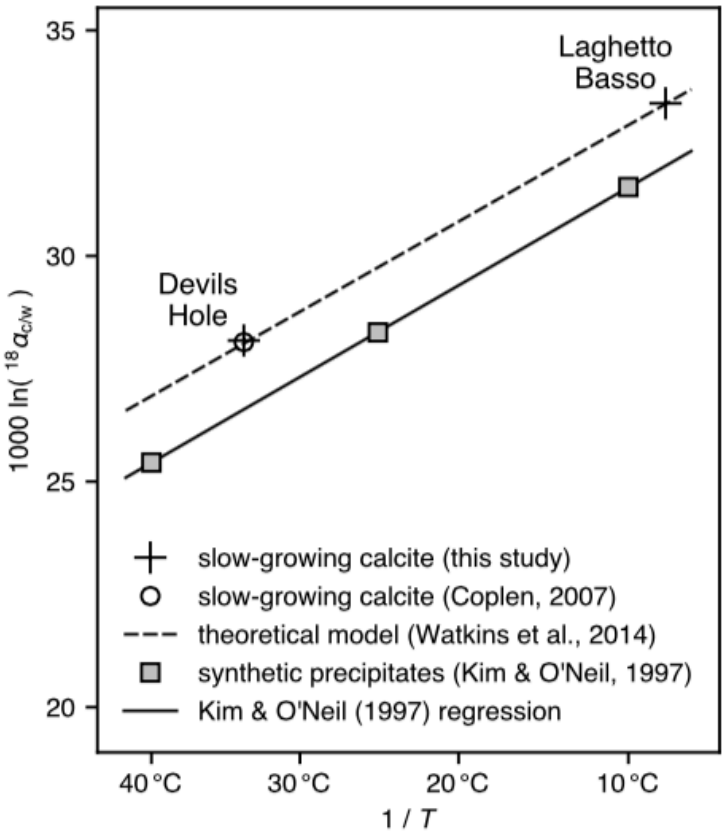

Figure 1: Equilibrium $^{18}O/^{16}O$ fractionation between calcite and water ($^{18}\alpha_{c/w}$) as a function of crystallization temperature (T). Our results support the hypothesis that equilibrium $^{18}\alpha_{c/w}$ values vary with T in a manner that mirrors equilibrium $^{18}O/^{16}O$ partitioning between DIC and water.

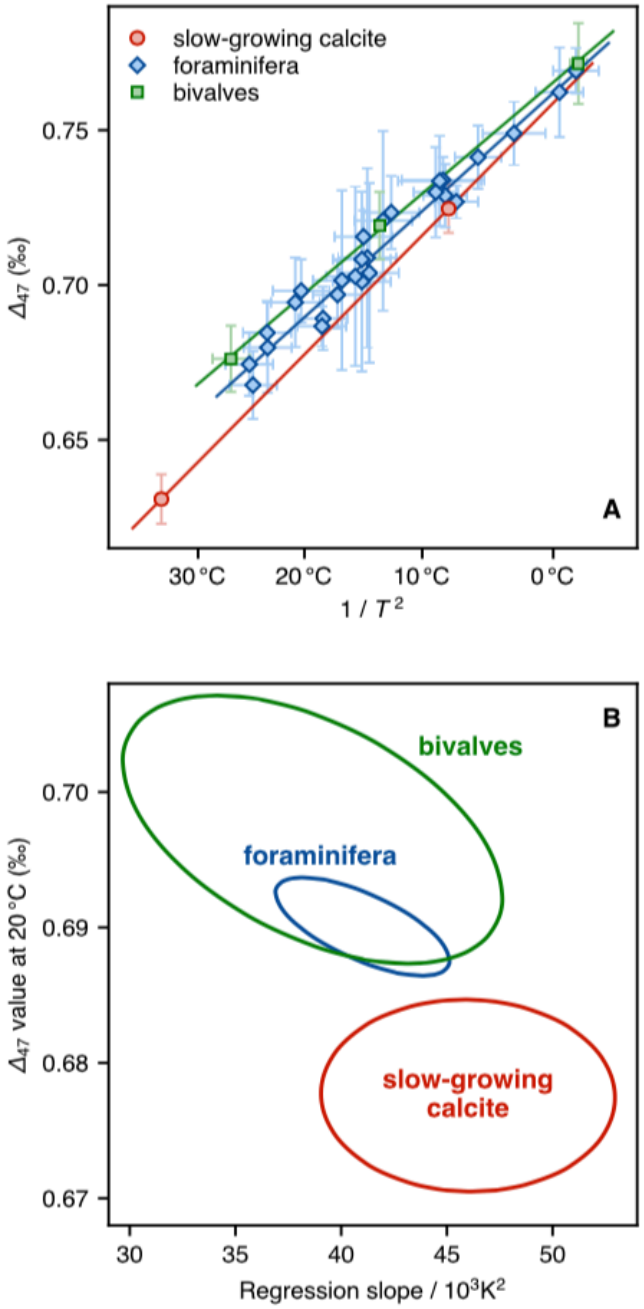

Figure 2: (A) Observed relationships between clumped isotopes (Δ_{47}) and crystallization temperature (T) in slow-growing calcite calcite from Devils Hole and Laghetto Basso (red circles), in modern calcitic bivalves (green squares), and in foraminifera from sedimentary core-tops (blue diamonds, data from *Peral et al.* [43]), all of which were analyzed in the same laboratory over a short period of time. Error bars represent 95 % confidence intervals. **(B)** Comparison of the 95 % confidence regions of regression slopes and 20 °C intercept values for slow-growing and biogenic calcite. Both of the biogenic regression lines differ significantly ($p \leq 10^{-3}$) from the equilibrium baseline defined by slow-growing calcites.

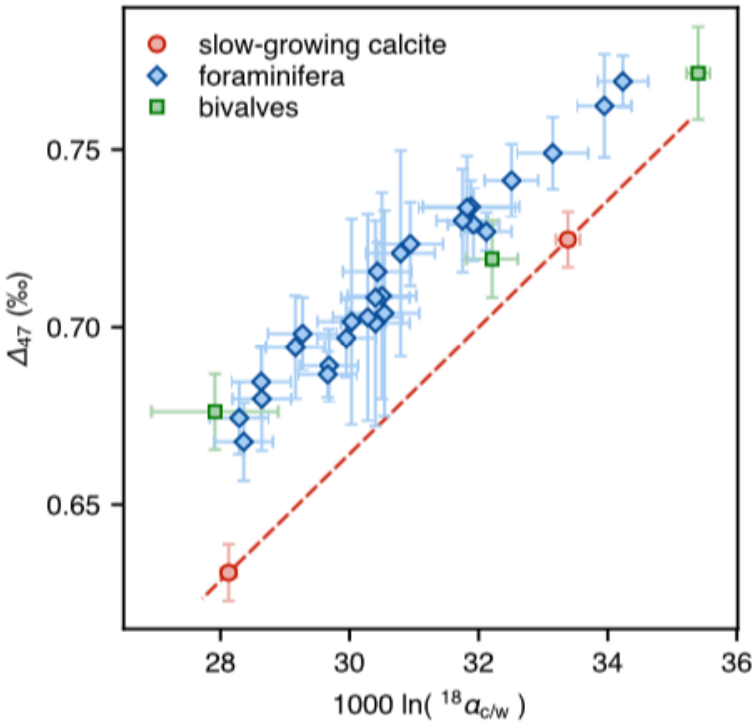

Figure 3: Combining the $^{18}O/^{16}O$ and Δ_{47} thermometers requires some constraints on water $\delta^{18}O$ values, but makes it possible to test whether carbonates precipitated in isotopic equilibrium even if crystallization temperature is unknown. Error bars represent 95 % confidence intervals. Bivalve species *S. cucullata* is not shown here because sufficient constraints on $\delta^{18}O$ of the local water are lacking.

Methods

Inorganic calcite samples

Holocene Devils Hole calcite (sample DVH) was collected from the outer surface of sample DHC2-8, which was previously described by *Winograd et al.* [49] and *Coplen* [16]. After a 15-min ultrasonic bath treatment with reagent-grade methanol, we abraded the surface of DHC2-8 to a maximum depth of 100 µm using a programmable micro-mill at its slowest setting. Laghetto Basso calcite (sample LGB) was collected from the top of core CD3-12, located a few centimeters away from core CD3, which was described by *Drysdale et al.* [30]. Each half of CD3-12 was ultrasonically cleaned in deionized water to remove loose particles from the active growth surface, then air-dried at ambient temperature. Calcite was abraded from fifteen discrete 1-cm^2 regions of its outer surface using a Dremel hand tool fitted with a diamond burr and a magnification lens. The depth of abrasion was estimated to be no more than 100 µm. Both DVH and LGB powders were then rinsed in methanol and dried at room temperature.

Bivalve samples

Three specimens of Antarctic scallop species *Adamussium colbecki* were collected at a water depth of 15 m near the Dumont d'Urville Antarctic station in January 2007 (66.658 °S, 140.008 °E). Seawater temperature remains stable annually (mean T = –1.8 °C) except for a summer warming peak around –0.5 °C between January and March [50]. Seawater $\delta^{18}O_{VSMOW}$ value, estimated from the Global Seawater Oxygen-18 Database of *Schmidt et al.* [51], is –0.26±0.06 ‰.

Five live specimens of the deep-sea oyster species *Neopycnodonte cochlear* were collected in March 2010 from the Lacaze-Duthiers canyon (42.533 °N, 3.453 °E, Mediterranean Sea) at a depth of 270 m, about 20 km east of the coast. Mean annual temperature remains constant at 13.5±0.1°C [52]. Local $\delta^{18}O_{VSMOW}$ values vary seasonally between 0.23 and 0.93 ‰, with an average value of 0.70 ‰ (M. Sebilo, pers. comm.).

Four live *Saccostrea cucullata* oysters from the warm shallow waters of the Kenyan

coast (Tiwi Beach, 4.239 °S, 39.604 °E) were collected in September 2005. Local seawater temperatures vary annually from 25.1 to 28.5 °C (T = 26.7±0.9 °C).

All bivalves were rinsed with deionized water and bathed in 5 % H_2O_2 to remove organic matter. Subsampling of *N. cochlear* and *S. cucullata* targeted the hinge area of each specimen, potentially offering a complete record of life-long calci□ication. Approximately 15 mg calcite powder was collected from each hinge area using a Dremel hand tool □itted with a 0.2-mm bit. For *A. colbecki*, we selected a small piece of the shell and ground it manually in an agate mortar.

Traditional stable-isotope analyses

Traditional stable-isotope analyses ($\delta^{13}C$, $\delta^{18}O$) of samples DVH and LGB were performed using a MultiCarb system coupled to an Isoprime 100 mass spectrometer in dual-inlet mode. International carbonate standards NBS 19 ($\delta^{13}C_{VPDB}$ = 1.95 ‰; $\delta^{18}O_{VPDB}$ = –2.20 ‰) and NBS 18 ($\delta^{13}C_{VPDB}$ = 5.01 ‰; $\delta^{18}O_{VPDB}$ = –23.01 ‰) were analyzed along with DVH and LGB. All samples and standards were analyzed six times, with each replicate analysis requiring about 150 µg of carbonate. Sample $\delta^{13}C$ and $\delta^{18}O$ values were computed directly from ion current ratios 45/44 and 46/44 using the IUPAC-recommended oxygen-17 correction parameters of *Brand et al.* [53]. As recommended by *Coplen* [54], final $\delta^{18}O_{VPDB}$ values are scaled to the nominal oxygen isotope compositions of NBS 19 and NBS 18.

Clumped-isotope analyses

Clumped isotope measurements were performed according to previously described protocols [39, 43]. Carbonate samples were converted to CO_2 by phosphoric acid reaction at 90 °C. After cryogenic removal of water, the evolved CO_2 was helium-flushed through a purification column packed with Porapak Q and held at –20 °C, then quantitatively recollected by cryogenic trapping and transferred into an Isoprime 100 dual-inlet mass spectrometer equipped with six Faraday collectors (m/z 44–49). Pressure-dependent background current corrections were measured independently for each sample.

Background-corrected ion current ratios were converted to $\delta^{13}C$, $\delta^{18}O$, and $\Delta^{raw}{}_{47}$ as described by *Daëron et al.* [39], using the IUPAC oxygen-17 correction parameters [53]. The $\Delta^{raw}{}_{47}$ values were converted to the "absolute" Δ_{47} reference frame defined by the "ETH" carbonate standards [40]. Average Δ_{47} values are based on 22 replicate analyses (each) for samples DVH and LGB, 20 replicates for *N. cochlear*, 17 for *S. cucullata*, and 12 for *A. colbecki*. Analytical errors are derived from the external reproducibility of carbonate standards (N = 151) and samples (N = 93) within each analytical session, and conservatively account for the uncertainties in $\Delta^{raw}{}_{47}$ measurements as well as those associated with the conversion to the "absolute" Δ_{47} reference frame.

Statistical methods

Relationships between Δ_{47} and crystallization temperature are modelled using weighted orthogonal distance regressions of the form $\Delta_{47} = A / T^2 + B$ in order to account for errors in both variables. In all three regressions, root mean square weighted deviation (RMSWD) values are smaller than one, implying that analytical and observational errors are sufficient to explain the scatter in the mean observations.

Analysis of covariance (ANCOVA) was performed by first computing the probability for the null hypothesis that two independent regression lines have identical slopes. If the two slopes are statistically indistinguishable (at a given confidence level), observations from both data sets are jointly fit to a new model with two parallel lines. If the distance between these two lines is statistically indistinguishable from zero, the null hypothesis that the two data sets follow the same relationship between Δ_{47} and T cannot be excluded.

Data and materials availability

The complete raw data and all associated code used in this study are available under a Creative Commons license at *https://doi.org/xxxx*.

Author contributions

MD initiated the project aiming to determine baseline equilibrium Δ_{47} values based on natural slow-growing calcite. He set up the clumped-isotope facility at LSCE and oversaw the quality of all clumped-isotope measurements; performed most of the clumped-isotope analyses of DVH and LGB; designed the statistical analysis and Figures presented here; wrote the present report with primary contributions from RND, DB, and TBC, and additional contributions from other co-authors. RND conducted preliminary work that originally recognized that Laghetto Basso calcite could be used to constrain oxygen-isotope equilibrium fractionation at low temperatures; helped conceive the research; compiled the water chemistry data from Laghetto Basso; prepared and subsampled the outer surface of CD3-12. MP selected sedimentary core-tops; picked, identified, and cleaned foraminifera; performed foraminiferal clumped-isotope analyses; compiled seawater composition estimates. DH selected and subsampled bivalve specimens; performed bivalve clumped-isotope analyses. DB helped develop the LSCE clumped-isotope facility and subsampled the outer surface of DHC2-8; performed some of the clumped-isotope analyses of DVH and LGB. TBC provided sample DHC2-8. FL helped select bivalve specimens; collected seawater samples from Lacaze-Duthiers canyon; compiled seawater composition estimates for *A. colbecki*. GZ oversaw the geochemical monitoring of Laghetto Basso and collected core CD3-12.

References

[1] H. C. Urey. The thermodynamic properties of isotopic substances. *Journal of the Chemical Society* (1947), pp. 562–581.

[2] N. Shackleton. Oxygen isotope analyses and Pleistocene temperatures re-assessed. *Nature* 215 (1967), pp. 15–17.

[3] U. Brand & J. Veizer. Chemical diagenesis of a multicomponent carbonate system - 2: stable isotopes. *Journal of Sedimentary Research* 51 (1981). doi: 10.1306/212f7df6-2b24-11d7-8648000102c1865d.

[4] K. M. Gillis & L. A. Coogan. Secular variation in carbon uptake into the ocean crust. *Earth and Planetary Science Letters* 302:3-4 (2011), pp. 385–392. doi: 10.1016/j.epsl.2010.12.030.

[5] T. McConnaughey. ^{13}C and ^{18}O isotopic disequilibrium in biological carbonates: I. Patterns. *Geochimica et Cosmochimica Acta* 53:1 (1989), pp. 151–162. doi: 10.1016/0016-7037(89)90282-2.

[6] S. M. F. Sheppard. Stable isotope geochemistry of fluids. *Physics and Chemistry of the Earth* 13-14 (1981), pp. 419–445. doi: 10.1016/0079-1946(81)90021-5.

[7] P. Deines. Stable isotope variations in carbonatites. *Carbonatites: Genesis and Evolution*. Ed. by K. Bell. Unwin & Hyman, London, 1989, pp. 301–359.

[8] J. S. Killingley. Migrations of California gray whales tracked by oxygen-18 variations in their epizoic barnacles. *Science* 207:4432 (1980), pp. 759–760. doi: 10.1126/science.207.4432.759.

[9] W. Guo & J. M. Eiler. Temperatures of aqueous alteration and evidence for methane generation on the parent bodies of the CM chondrites. *Geochimica et Cosmochimica Acta* 71:22 (2007), pp. 5565–5575. doi: 10.1016/j.gca.2007.07.029.

[10] J. Uchikawa & R. E. Zeebe. The effect of carbonic anhydrase on the kinetics and equilibrium of the oxygen isotope exchange in the CO_2–H_2O system: Implications for $\delta^{18}O$ vital effects in biogenic carbonates. *Geochimica et Cosmochimica Acta* 95 (2012), pp. 15–34. doi: 10.1016/j.gca.2012.07.022.

[11] J. M. McCrea. On the isotopic chemistry of carbonates and a paleotemperature scale. *The Journal of Chemical Physics* 18:6 (1950), pp. 849–857. doi: 10.1063/1.1747785.

[12] S. Epstein, R. Buchsbaum, A. Lowenstam & H. C. Urey. Revised carbonate-water isotopic temperature scale. *Bulletin of the Geological Society of America* 64 (1953), pp. 1315–1326.

[13] T. Tarutani, R. N Clayton & T. K Mayeda. The effect of polymorphism and magnesium substitution on oxygen isotope fractionation between calcium carbonate and water. *Geochimica et Cosmochimica Acta* 33:8 (1969), pp. 987–996. doi: 10.1016/0016-7037(69)90108-2.

[14] J. R. O'Neil, R. N. Clayton & T. K. Mayeda. Oxygen isotope fractionation in divalent metal carbonates. *The Journal of Chemical Physics* 51:12 (1969), pp. 5547–5558. doi: 10.1063/1.1671982.

[15] S.-T. Kim & J. R. O'Neil. Equilibrium and nonequilibrium oxygen isotope effects in synthetic carbonates. *Geochimica et Cosmochimica Acta* 61:16 (1997), pp. 3461–3475. doi: 10.1016/s0016-7037(97)00169-5.

[16] T. B. Coplen. Calibration of the calcite–water oxygen-isotope geothermometer at Devils Hole, Nevada, a natural laboratory. *Geochimica et Cosmochimica Acta* 71:16 (2007), pp. 3948–3957. doi: 10.1016/j.gca.2007.05.028.

[17] S. R. Thorrold, S. E. Campana, C. M. Jones & P. K. Swart. Factors determining $\delta^{13}C$ and $\delta^{18}O$ fractionation in aragonitic otoliths of marine fish. *Geochimica et Cosmochimica Acta* 61:14 (1997), pp. 2909–2919. doi: 10.1016/s0016-7037(97)00141-5.

[18] D. M. Tremaine, P. N. Froelich & Y. Wang. Speleothem calcite farmed *in situ*: Modern calibration of $\delta^{18}O$ and $\delta^{13}C$ paleoclimate proxies in a continuously-monitored natural cave system. *Geochimica et Cosmochimica Acta* 75:17 (2011), pp. 4929–4950. doi: 10.1016/j.gca.2011.06.005.

[19] P. J. Mickler, L. A. Stern & J. L. Banner. Large kinetic isotope effects in modern speleothems. *Geological Society of America Bulletin* 118:1-2 (2006), pp. 65–81. doi: 10.1130/b25698.1.

[20] M. Daëron, W. Guo, J. M. Eiler, D. Genty, D. Blamart, R. Boch, R. Drysdale, R. Maire, K. Wainer & G. Zanchetta. $^{13}C^{18}O$ clumping in speleothems: Observations from natural caves and precipitation experiments. *Geochimica et Cosmochimica Acta* 75:12 (2011), pp. 3303–3317. doi: 10.1016/j.gca.2010.10.032.

[21] C. Emiliani, J. H. Hudson, E. A. Shinn & R. Y. George. Oxygen and carbon isotopic growth record in a reef coral from the Florida Keys and a deep-sea coral from Blake Plateau. *Science* 202:4368 (1978), pp. 627–629. doi: 10.1126/science.202.4368.627.

[22] C. T. Bolton, H. M. Stoll & A. Mendez-Vicente. Vital effects in coccolith calcite: Cenozoic climate-pCO_2 drove the diversity of carbon acquisition strategies in coccolithophores? *Paleoceanography* 27:4 (2012). doi: 10.1029/2012pa002339.

[23] J. M. Watkins, L. C. Nielsen, F. J. Ryerson & D. J. DePaolo. The influence of kinetics on the oxygen isotope composition of calcium carbonate. *Earth and Planetary Science Letters* 375 (2013), pp. 349–360. doi: 10.1016/j.epsl.2013.05.054.

[24] R. I. Gabitov, E. B. Watson & A. Sadekov. Oxygen isotope fractionation between calcite and fluid as a function of growth rate and temperature: An in situ study. *Chemical Geology* 306-307 (2012), pp. 92–102. doi: 10.1016/j.chemgeo.2012.02.021.

[25] M. P. Andersson, J. D. Rodriguez-Blanco & S. L. S. Stipp. Is bicarbonate stable in and on the calcite surface? *Geochimica et Cosmochimica Acta* 176 (2016), pp. 198–205. doi: 10.1016/j.gca.2015.12.016.

[26] D. Gebauer, A. Völkel & H. Cölfen. Stable prenucleation calcium carbonate clusters. *Science* 322:5909 (2008), pp. 1819–1822. doi: 10.1126/science.1164271.

[27] J. M. Watkins, J. D. Hunt, F. J. Ryerson & D. J. DePaolo. The influence of temperature, pH, and growth rate on the $\delta^{18}O$ composition of inorganically precipitated calcite. *Earth and Planetary Science Letters* 404 (2014), pp. 332–343. doi: 10.1016/j.epsl.2014.07.036.

[28] N. P. Levitt, J. M. Eiler, C. S. Romanek, B. L. Beard, H. Xu & C. M. Johnson. Near equilibrium ^{13}C–^{18}O bonding during inorganic calcite precipitation under chemo-stat conditions. *Geochemistry, Geophysics, Geosystems* (2018). doi: 10.1002/2017gc007089.

[29] L. S. Devriendt, J. M. Watkins & H. V. McGregor. Oxygen isotope fractionation in the $CaCO_3$-DIC-H_2O system. *Geochimica et Cosmochimica Acta* 214 (2017), pp. 115–142. doi: 10.1016/j.gca.2017.06.022.

[30] R. N. Drysdale, B. T. Paul, J. C. Hellstrom, I. Couchoud, A. Greig, P. Bajo, G. Zanchetta, I.

Isola, C. Spötl, I. Baneschi, E. Regattieri & J. D. Woodhead. Precise microsampling of poorly laminated speleothems for U-series dating. *Quaternary Geochronology* 14 (2012), pp. 38–47. doi: 10.1016/j.quageo.2012.06.009.

[31] L. Piccini, G. Zanchetta, R. N. Drysdale, J. Hellstrom, I. Isola, A. E. Fallick, G. Leone, M. Doveri, M. Mussi, F. Mantelli, G. Molli, L. Lotti, A. Roncioni, E. Regattieri, M. Meccheri & L. Vaselli. The environmental features of the Monte Corchia cave system (Apuan Alps, central Italy) and their effects on speleothem growth. *International Journal of Speleology* 37:3 (2008), pp. 153–172. doi: 10.5038/1827-806x.37.3.2.

[32] L. N. Plummer, E. Busenberg & A. C. Riggs. In-situ Growth of Calcite at Devils Hole, Nevada: Comparison of Field and Laboratory Rates to a 500,000 Year Record of Near-Equilibrium Calcite Growth. *Aquatic Geochemistry* 6:2 (2000), pp. 257–274. doi: 10.1023/a:1009627710476.

[33] W. C. Beck, E. L. Grossman & J. W. Morse. Experimental studies of oxygen isotope fractionation in the carbonic acid system at 15°, 25°, and 40°C. *Geochimica et Cosmochimica Acta* 69:14 (2005), pp. 3493–3503. doi: 10.1016/j.gca.2005.02.003.

[34] J. M. Eiler. "Clumped-isotope" geochemistry—The study of naturally-occurring, multiply-substituted isotopologues. *Earth and Planetary Science Letters* 262 (2007), pp. 309–327. doi: 10.1016/j.epsl.2007.08.020.

[35] E. A. Schauble, P. Ghosh & J. M. Eiler. Preferential formation of ^{13}C–^{18}O bonds in carbonate minerals, estimated using first-principles lattice dynamics. *Geochimica et Cosmochimica Acta* 70 (2006), pp. 2510–2529. doi: 10.1016/j.gca.2006.02.011.

[36] M. Bonifacie, D. Calmels, J. M. Eiler, J. Horita, C. Chaduteau, C. Vasconcelos, P. Agrinier, A. Katz, B. H. Passey, J. M. Ferry & J.-J. Bourrand. Calibration of the dolomite clumped isotope thermometer from 25 to 350 °C, and implications for a universal calibration for all (Ca, Mg, Fe)CO_3 carbonates. *Geochimica et Cosmochimica Acta* 200 (2017), pp. 255–279. doi: 10.1016/j.gca.2016.11.028.

[37] J. R. Kelson, K. W. Huntington, A. J. Schauer, C. Saenger & A. R. Lechler. Toward a universal carbonate clumped isotope calibration: Diverse synthesis and preparatory methods suggest a single temperature relationship. *Geochimica et Cosmochimica Acta* 197 (2017), pp. 104–131. doi: 10.1016/j.gca.2016.10.010.

[38] S. F. M. Breitenbach, M. J. Mleneck-Vautravers, A.-L. Grauel, L. Lo, S. M. Bernasconi, Inigo A. Müller, James Rolfe, Fernando Gázquez, Mervyn Greaves & D. A. Hodell. Coupled Mg/Ca and clumped isotope analyses of foraminifera provide consistent water temperatures. *Geochimica et Cosmochimica Acta* (2018). doi: 10.1016/j.gca.2018.03.010.

[39] M. Daëron, D. Blamart, M. Peral & H. P. Affek. Absolute isotopic abundance ratios and the accuracy of Δ_{47} measurements. *Chemical Geology* 442 (2016), pp. 83–96. doi: 10.1016/j.chemgeo.2016.08.014.

[40] S. M. Bernasconi, I. A. Müller, K. D. Bergmann, S. F. M. Breitenbach, A. Fernandez, D. A. Hodell, A. N. Meckler, I. Millan & M. Ziegler. Reducing uncertainties in carbonate clumped isotope analysis through consistent carbonate-based standardization. *Geochemistry, Geophysics, Geosystems* (2018). In press.

[41] T. Kluge, H. P. Affek, Y. Dublyansky & C. Spötl. Devils Hole paleotemperatures and implications for oxygen isotope equilibrium fractionationole paleotemperatures and implications for oxygen isotope equilibrium fractionation. *Earth and Planetary Science Letters* 400 (2014), pp. 251–260. doi: 10.1016/j.epsl.2014.05.047.

[42] A. K. Tripati, P. S. Hill, R. A. Eagle, J. L. Mosenfelder, J. Tang, E. A. Schauble, J. M. Eiler, R. E. Zeebe, J. Uchikawa, T. B. Coplen, J. B. Ries & D. Henry. Beyond temperature: Clumped isotope signatures in dissolved inorganic carbon species and the in□luence of solution chemistry on carbonate mineral composition. *Geochimica et Cosmochimica Acta* 166 (2015), pp. 344–371. doi: 10.1016/j.gca.2015.06.021.

[43] M. Peral, M. Daëron, D. Blamart, F. Bassinot, F. Dewilde, N. Smialkowski, G. Isguder, J. Bonnin, F. Jorissen, C. Kissel, E. Michel, N. Vázquez Riveiros & C. Waelbroeck. Updated calibration of the clumped isotope thermometer in planktonic and benthic foraminifera. *Geochimica et Cosmochimica Acta* (2018). doi: 10.1016/j.gca.2018.07.016.

[44] E. P. Dassié, D. Genty, A. Noret, X. Mangenot, M. Massault, N. Lebas, M. Duhamel, M. Bonifacie, M. Gasparrini, B. Minster & J.-L. Michelot. A newly designed analytical line to examine fluid inclusion isotopic compositions in a variety of carbonate samples. *Geochemistry, Geophysics, Geosystems* 19 (2018). doi: 10.1002/2017gc007289.

[45] W. Guo. Carbonate clumped isotope thermometry: application to carbonaceous chondrites and effects of kinetic isotope fractionation. PhD dissertation. California Institute of Technology, 2009.

[46] L. Coogan, M. Daëron & K. Gillis. Oxygen isotope exchange between the ocean and the upper oceanic crust. *Geophysical Research Abstracts* 20 (2018), EGU2018–4994.

[47] M. S. Fantle & D. J. DePaolo. Ca isotopes in carbonate sediment and pore fluid from ODP Site 807A: The Ca^{2+}(aq)–calcite equilibrium fractionation factor and calcite recrystallization rates in Pleistocene sediments. *Geochimica et Cosmochimica Acta* 71:10 (2007), pp. 2524–2546. doi: 10.1016/j.gca.2007.03.006.

[48] H. M. Stoll. Limited range of interspecific vital effects in coccolith stable isotopic records during the Paleocene-Eocene thermal maximum. *Paleoceanography* 20:1 (2005). doi: 10.1029/2004pa001046.

[49] I. J. Winograd, J. M. Landwehr, T. B. Coplen, W. D. Sharp, A. C. Riggs, K. R. Ludwig & P. T. Kolesar. Devils Hole, Nevada, $\delta^{18}O$ record extended to the mid-Holocene. *Quaternary Research* 66:02 (2006), pp. 202–212. doi: 10.1016/j.yqres.2006.06.003.

[50] F. Lartaud, L. Chauvaud, J. Richard, A. Toulot, C. Bollinger, L. Testut & Y.-M. Paulet. Experimental growth pattern calibration of Antarctic scallop shells (Adamussium colbecki, Smith 1902) to provide a biogenic archive of high-resolution records of environmental and climatic changes. *Journal of Experimental Marine Biology and Ecology* 393:1-2 (2010), pp. 158–167. doi: 10.1016/j.jembe.2010.07.016.

[51] G. A. Schmidt, G. R. Bigg & E. J. Rohling. Global Seawater Oxygen-18 Database - v1.22. https://data.giss.nasa.gov/o18data. 1999.

[52] X. Durrieu de Madron, L. Houpert, P. Puig, A. Sanchez-Vidal, P. Testor, A. Bosse, C. Estournel, S. Somot, F. Bourrin, M. N. Bouin, M. Beauverger, L. Beguery, A. Calafat, M. Canals, C. Cassou, L. Coppola, D. Dausse, F. D'Ortenzio, J. Font, S. Heussner, S. Kunesch, D. Lefevre, H. Le Goff, J. Martín, L. Mortier, A. Palanques & P. Raimbault. Interaction of dense shelf water cascading and open-sea convection in the northwestern Mediterranean during winter 2012. *Geophysical Research Letters* 40:7 (2013), pp. 1379–1385. doi: 10.1002/grl.50331.

[53] W. A. Brand, S. S. Assonov & T. B. Coplen. Correction for the ^{17}O interference in $\delta(^{13}C)$ measurements when analyzing CO_2 with stable isotope mass spectrometry (IUPAC Technical Report). *Pure and Applied Chemistry* 82:8 (2010), pp. 1719–1733. doi:

10.1351/PAC-REP-09-01-05.

[54] T. B. Coplen. More uncertainty than necessary. *Paleoceanography* 11:4 (1996), pp. 369–370.

HIGH-RESOLUTION FORAMINIFER STABLE ISOTOPE RECORD OF MIS 19 AT MONTALBANO JONICO, SOUTHERN ITALY: A WINDOW INTO MEDITERRANEAN CLIMATIC VARIABILITY DURING A LOW-ECCENTRICITY INTERGLACIAL

S. Nomade[1]., F. Bassinot[1]., M. Marino[2]., Q. Simon[3]., F. Dewilde[1]., P. Maiorano[2]., G. Isguder[1]., D. Blamart[1]., A. Girone[2]., V. Scao[1]., A. Pereira[1,4,5,6]., F. Toti[7]., A. Bertini[7]., N. Combourieu-Nebout[6]., **M. Peral**[1]., D. L. Bourlès[3]., P. Petrosino[8]., S. Gallicchio and N. Ciaranfi[2].

1. Laboratoire des Sciences du Climat et de L'Environnement, UMR8212, LSCE/IPSL, CEA-CNRS-UVSQ and Université Paris-Saclay, Gif-Sur-Yvette, France.
2. Dipartimento di Scienze della Terra e Geoambientali, Università degli Studi di Bari Aldo Moro, via E. Orabona 4, 70125 Bari, Italy
3. CEREGE UM34, Aix Marseille Univ, CNRS, IRD, Coll France, Aix en Provence, France
4. Ecole française de Rome, Piazza Farnese 67, 00186 Roma, Italy.
5. Sezione di scienze preistoriche e antropologiche, Dipartimento di Studi Umanistici, Università degli Studi di Ferrara, Corso Ercole d'Este I, 32, Ferrara, Italy.
6. Département de Préhistoire du Museum national d'Histoire Naturelle, UMR 7194 du CNRS, 1 rue René Panhard, 75013 Paris, France.
7. Dipartimento di Scienze della Terra, Università degli Studi di Firenze, via G. La Pira 4, 50121 Firenze, Italy
8. Dipartimento di Scienze della Terra dell'Ambiente e delle Risorse, Università degli Studi di Napoli Federico II, Largo San Marcellino 10, 80138, Napoli, Italy

Submitted in: Quaternary Science Reviews

ABSTRACT

Understanding millennial and sub-millennial climate variability during past low eccentricity interglacials similar to the Holocene is fundamental if one wants to forecast properly the evolution of climate and better decipher human-induced perturbations on natural variability. The *Ideale section* (Montalbano Jonico, Southern Italy) provides one of the best sedimentary records of MIS 19c, the closest orbital analog to the Holocene. This exposed marine series covers Termination IX to the inception of MIS 18 with high sedimentation rates (> 97 cm/ka). This work presents 1) benthic $\delta^{18}O$ and $\delta^{13}C$ records at 90-200 year time-resolution, 2) a new $^{40}Ar/^{39}Ar$ age of 774.1 ± 0.9 ka for tephra layer V4 lying within the Matuyama-Brunhes transitional period and 3) new calcareous plankton, palynological and authigenic $^{10}Be/^{9}Be$ data. Our age model suggests a 11.3 ka duration for the climatic optimum. The $\delta^{18}O$ reveal millennial-scale oscillations (with sharp transitions < 200 years) between ~774.0 ka and MIS 18 onset (~ 757.0 ka) with a cyclicity of about 5.3 ka. Those climate oscillations existed throughout the entire MIS 19, but hampered during MIS 19c. Amplitude of those sub-orbital oscillations increased towards MIS18 as climate dried off and cooled. The oscillations take place in one single precession cycle. The *Ideale section* reveals with unprecedented details these millennial-scale climatic oscillations of MIS19b-a that have been observed worldwide. It highlights the extreme sensitivity of the central Mediterranean area to the North Atlantic climatic variations (i.e. oceanic circulation and atmospheric processes related to ice-sheet dynamics) during this low eccentricity interglacial.

Keywords

Interglacial; Paleoclimatology; Stable isotopes; Micropaleontology; Pollen; Cosmogenic isotopes; $^{40}Ar/^{39}Ar$ dating; Montalbano-Jonico; Italy.

1. INTRODUCTION

Forecasting climate changes at global to regional scales requires improved knowledge of natural climate variability. The study of millennial to centennial changes recorded in natural climatic archives (e.g. marine and/or lake sediments) has the potential to provide valuable information on rapid past climate variability with different orbital forcing configurations and greenhouse gas atmospheric contents. Over the last 1 Ma, from an orbital point of view, the current interglacial (Holocene) is comparable only to Marine Isotopic Stages (MIS) 11 and 19, sharing with them a low eccentricity and quasi similar precession parameters (Tzedakis et al., 2012; Yin and Berger, 2012). If MIS 11 was considered for a long time to be the closest analogue to the Holocene, several authors pointed out differences in the phase between precession and obliquity, likely accounting for differences in the deglaciation dynamics (i.e. Loutre and Berger, 2000, Masson-Delmotte et al., 2006, Ruddiman et al., 2007). In the recent years, many studies have focused on the orbital analogy between the Holocene and MIS 19 (e.g. Pol et al., 2010; Tzedakis et al., 2012; Giaccio et al., 2015; Maiorano et al., 2016). The values reached by obliquity are slightly different during MIS 19 and the Holocene, but the maximum obliquity is in phase with minimum precession at the onset of these two interglacials. Several records with sub-millennial resolution within MIS 19 document paleoclimatic similarities between this interglacial and the Holocene. These records come from high latitudes sites (Pol et al., 2010, Tzedakis et al., 2012), from the Iberian margin (Sanchez-Goñi et al., 2016), from the central Italy Sulmona paleolake (Giaccio et al., 2015), as well as from the marine onland Montalbano Jonico section (MJS hereafter) in southern Italy (Basilicata region) (i.e. Ideale section, IS hereafter; Maiorano et al., 2016; Simon et al., 2017). All these records suggest the existence of a relatively warm and wet climatic period with a duration ranging from 10 to 13 ka, which is equivalent, taking into account the uncertainties of each estimates, to the time elapsed since the onset of the Holocene (Pol et al., 2010; Tzedakis et al., 2012; Giaccio et al., 2015; Simon et al., 2017). It is observed that this relatively stable climatic period is followed by millennial scale climatic oscillations during MIS19b and –a, which deeply impact the transition to cold stage MIS 18 (e.g. Pol et al., 2010; Tzedakis et al., 2012; Giaccio et al., 2015; Sanchez-Goñi et al., 2016). Such millennial-scale climatic oscillations have been linked to the modification of

North Atlantic oceanic circulation and atmospheric processes related to ice-sheet dynamics (Tzedakis et al., 2012; Giaccio et al., 2015; Sanchez-Goñi et al., 2016). Sanchez-Goñi et al. (2016) further suggested that the entire MIS19 might have been characterized by ~ 5 ka millennial–scale oscillations visible in both the atmosphere and ocean, and interpreted as probably related to the fourth harmonic of precession. These authors hypothesized that such climatic oscillations may have been amplified during MIS19b and MIS 19a intervals in response to iceberg discharges in the subpolar gyre, which resulted in cyclic arrival of freshwater pulses at the Iberian margin.

In addition to its global implications, understanding natural millennial-scale climate variability during MIS 19 in the Mediterranean area is particularly important for improving the forecasting of climate changes over this densely populated area subjects to a complex interplay of tropical and polar influences. In this general context, the IS hereafter from the MJS looks as an ideal studying site given its i) easy accessibility (Fig. 1), ii) excellent exposure covering the transition between MIS 20 and 19 (i.e. deglaciation or Termination IX (T.IX hereafter)) to MIS 18 inception and, iii) extremely high sedimentation rates (i.e. > 97 cm/ka). The MIS 19 in the MJS area has undergone, multidisciplinary studies since 1994 (Ciaranfi et al., 1994), which generated top-quality reconstructions between MIS 20 up to the MIS 19/18 transition of (i) marine environment based on planktonic and benthonic taxa (e.g. D'Alessandro et al., 2003; Stefanelli, 2003; Aiello et al., 2015, Marino et al., 2015; Maiorano et al., 2016), (ii) terrestrial vegetation and climate (Bertini et al., 2015; Toti, 2015), (iii) paleohydrological and mineralogical changes (Maiorano et al., 2016) and (iv) chemical characterization and chronology of tephra layer V3 and V4 embedded in the IS (Petrosino et al., 2015). In this contribution we present new high-resolution $\delta^{18}O$ and $\delta^{13}C$ data (i.e. 90-200 years resolution) obtained on two species of benthic foraminifera: *Melonis barleeanum* and *Cassidulina carinata* covering MIS 20 to MIS 18. New higher resolution calcareous plankton and authigenic $^{10}Be/^{9}Be$ data obtained on the same samples used for isotope analyses are also provided to improve the pattern of climate change as recorded in marine and terrestrial realms. Pollen data-set is here slightly improved with respect to previous record as shown in Maiorano et al. (2016) thank to the additional data point around T.IX in particular. We modified the strategy to develop the age model from Simon et al. (2017) but the final chronology proves to be similar within uncertainties to the one

previously developed for the deglaciation (T.IX). The dating strategy rests upon the fine-tuning of these new $d^{18}O$ and $d^{13}C$ records to orbital oscillations combined with a new $^{40}Ar/^{39}Ar$ age for the tephra layer (V4) deposited within the Matuyama-Brunhes transition (MBT hereafter). This age model together with improved resolution of the calcareous plankton, palynological and authigenic $^{10}Be/^{9}Be$ records, allows discussing the timing of the T.IX, the duration of the climatic optimum as well as millennial climatic and environmental variations at the regional scale, with unprecedented details. The fact that continental signals (i.e. pollen and mineralogical content) and paleoceanographic proxies (stable oxygen and carbon isotopes, calcareous plankton, ostracods) are obtained in a single record allows for a direct comparison between ocean and terrestrial changes, bypassing chronological problems and correlation uncertainties.

2. GENERAL GEOLOGICAL CONTEXT

The MJS crops out in the southwestern margin of the Bradano Trough (Casnedi, 1988) at about 16 km inland from the Ionian Coast (Fig. 1b). The Bradano Trough is located between the Apennines Chain to the west and the Apulian foreland eastward (Fig. 1b). Its geological origin and history are linked to the eastward roll-back of the subduction hinge of the Apulia platform and evolution of the external Apennines thrust during the Plio-Pleistocene (e.g. Patacca and Scandone, 2007). Following subsidence until the Calabrian, the basin underwent a diachronous uplift starting from the Genzano-Banzi area during late Calabrian and proceeding southeastward to the current Ionian coast until the Holocene. In the late Calabrian, the central sector of the Bradano Trough emerged while the southern sector, where the MJS is located, was still subsiding. Simultaneously, on the western side of the trough, the uplift of Nocara ridge was taking place, isolating from the open basin a western piggy-back type depocenter known as the Sant'Arcangelo basin (e.g. Patacca and Scandone, 2007). The central foredeep sector reached its maximum deepening during the Early-Middle Pleistocene (Ciaranfi et al., 1996). From the Middle Pleistocene onward, the sedimentation underwent a shoaling-upward trend due to the uplift of the area (uplift rate of 0.1–0.5 mm/year; Doglioni et al., 1996) that led to the emersion of the area. The MJS clayey succession belongs to the argille subapennine

informal unit (Azzaroli, 1968), representing its middle-upper portion with an Early to Middle Pleistocene age (Ciaranfi et al., 2010).

2.1 The Montalbano Jonico succession

The MJS composite section is about 450 m thick and consists of coarsening upwards deposits ranging from silty clays to silty sands and includes nine tephra layers (labeled V1–V9) (Figs. 1, 2). V3 and V4 were chemically associated to the Vulture stratovolcano complex, and almost all the volcanic level correlated to other tephra layers from south-central Italy lacustrine and marine successions, within a Lower-Middle Pleistocene Mediterranean tephrostratigraphic frame (Petrosino et al., 2015). The V3, V4 and V5 tephra layers were dated by $^{40}Ar/^{39}Ar$ to 801.2 ± 19.5 ka (Maiorano et al., 2010), 773.9 ± 1.3 ka (Petrosino et al., 2015), 719.5 ± 12.6 ka (Ciaranfi et al., 2010), respectively. $^{40}Ar/^{39}Ar$ ages have been calculated following the total decay ^{40}K decay constant of Min et al. (2000) and recalculated according to Alder Creek sanidine (ACs hereafter) flux standard with an age of 1.186 Ma (Jicha et al., 2016). The MJS, in its lower part, records five dark horizons (Fig. 2) that evidence depleted oxygen conditions at the sea bottom (or less oxygenated sediments), testified by the micro- and macro-invertebrate benthic assemblage content of these layers (D'Alessandro et al., 2003; Stefanelli, 2004; Stefanelli et al., 2005; Maiorano et al., 2008). These horizons have been referred to sapropel layers and correlated, from oldest to youngest, to insolation cycles i-112, i-104, i-102, i-90, and i-86 according to the Mediterranean sapropel stratigraphy of Lourens (2004) (Fig. 2). The calcareous nannofossil biostratigraphy indicates that the succession belongs to the small *Gephyrocapsa* and *Pseudoemiliania lacunosa* zones, based on the biostratigraphic scheme of Rio et al. (1990) equivalent to the CNPL9 and CNPL10 biozones of Backmann et al. (2012) and Raffi et al. (2016) who reported the biohorizons of worldwide significance. Numerous calcareous plankton (nannofossils and foraminifera) additional bioevents have been recognized throughout the section based on quantitative analyses (Marino, 1996; Ciaranfi et al., 1997; Maiorano et al., 2004, 2010; Joannin et al., 2008; Girone et al., 2013). Stable oxygen isotope analyses performed throughout the entire succession on planktonic (*Globigerina bulloides*) (Brilli, 1998) and benthic (*Cassidulina carinata*) foraminifer tests, combined with calcareous plankton biostratigraphy, allowed the recognition of the time

interval from MIS 37 to 16 (Brilli et al., 2000; Maiorano et al., 2004; 2008; 2010; Ciaranfi et al., 2010).

Several deepening-shallowing cycles forming a regressive succession up to the ending infill of Lucania Basin have been recognized based on micro- and macro-invertebrate benthic assemblages. These observations mainly indicate changes in paleo-bathymetry from bathyal to circalittoral environments (Fig. 2) (D'Alessandro et al., 2003; Stefanelli, 2003; Ciaranfi and D'Alessandro, 2005; Girone, 2005; Aiello et al., 2015). The climate and paleoenvironmental changes are clearly evidenced by the Pollen Temperature Index (PTI), i.e., ratio between mesothermic arboreal taxa (e.g. *Quercus*, *Carpinus* and *Carya*) and steppe taxa (e.g. *Artemisia* and *Ephedra*). The index provides a direct identification of warm-temperate and cold fluctuations (Joannin et al., 2008; Bertini et al., 2015; Toti, 2015; Vannacci, 2016) matching the oscillations of $\delta^{18}O$ at the millennial-scale (Fig. 2). The $\delta^{18}O$ record combined with calcareous plankton biostratigraphy, radiometric data ($^{40}Ar/^{39}Ar$ ages of tephra V3, V4 and V5), and sapropel stratigraphy, allowed the astronomical calibration of the MJS that covers the time interval 1.240-0.645 Ma (Ciaranfi et al., 2010).

2.2. The MIS 19 in the Montalbano Jonico succession: the Ideale section

The IS from the interval B of the MJS (Fig. 2) provides a particularly expanded record (74.19 m thick; Figs. 2 and 3) covering the MIS 20 to MIS 18 time interval (Ciaranfi et al., 2010). A peak of authigenic $^{10}Be/^{9}Be$ ratio recorded between 3450 cm and 4100 cm which corresponds to the global ^{10}Be overproduction episode associated with the MBT (Simon et al., 2017, 2018a, 2018b) allows fixing the chronostratigraphic boundary between Lower and Middle Pleistocene (Head and Gibbard, 2015). Since the IS is one of the global scale reference sections for the Lower-Middle Pleistocene boundary, obtaining a high-resolution and continuous stable isotope record is crucial to better understand this transition period. Following the initial *Cassidulina carinata* and *Globigerina bulloides* $\delta^{18}O$ records (Brilli et al., 2000; Ciaranfi et al., 2010) (Fig. 2), the IS was re-sampled in 2014 and 2015 to increase the resolution (1 sample every 20 cm, ~90-200 years resolution). The *Melonis barleeanum* $\delta^{18}O$ record first presented in Simon et al. (2017) provided a

marine isotopic record of T.IX and of the beginning of MIS 19 structure at an unprecedented average 150-year resolution. The record showed millennial scale oscillations marked by extremely abrupt changes in benthic $\delta^{18}O$ after the interglacial (*sensu-stricto*). Unfortunately, the high-resolution record from Simon et al. (2017) did not cover the entire MIS 19 (i.e. the record stopped before the MIS 18 inception) and presented a gap of exposure starting at 4435 cm and estimated to be about 485 cm (Simon et al., 2017), preventing the complete recording of MIS 19. These elements precluded the establishment of a robust age model for the entire MIS 19 by limiting our ability to decipher paleoclimatic implications at a centennial scale and to compare this sequence with the few high-resolution records available worldwide. Our new set of data overcome these issues allowing us to propose a continuous high-resolution climatic and environmental records covering MIS 20 up to MIS 18 with centennial resolution.

3. MATERIAL AND METHOD

To obtain a complete coverage from the end of MIS 20 until the next glacial inception (i.e. MIS 19/18 transition), the upper part of the IS as well as a new section, the Ciaranfi Master (Hereafter CM), located 450 m to the Northeast (Fig. 1d; see details below) were sampled. The base of the CM section corresponds to the V4 tephra layer (3660 cm in IS, Fig. 3). This layer provides an unambiguous stratigraphic marker for correlating the IS and the CM section (Fig. 3). The dark and light grey bands easily identified in both sections from the onset of MIS 19 up to the MIS 18 inception reflect the local sedimentary response to the climate conditions in neighboring continental areas (e.g. Bertini et al. 2015; Maiorano et al. 2016) and permit to correlate both sections with the upmost confidence (Fig. 3).

3.1. Oxygen and Carbone Stable isotope

A total of 31 levels (every 40 cm, 300-400 years resolution) were sampled in 2016 in the upper part of the IS (Fig. 3). We sampled with a 1 m overlap between the 2015 and 2016 sampled intervals in order to insure the continuity between the two series. Overall,

a total of 353 levels are now sampled along the IS. Starting 49 cm above V4, we collected during the same field trip a total of 76 new levels in the CM section covering a total of 1392 cm (Fig. 3) which corresponds to the same temporal resolution (i.e. 90-200 years) than the ones taken in the lower part of the IS. In addition to the previously measured benthic foraminifera *M. barleeanum* (315–355 mm size fractions), O-C stable isotope compositions were obtained on another benthic foraminifer, *C. carinata*. This species lives at the sediment/water interface contrary to *M. barleeanum* that lives within the first centimetres of the sediment. Because the number of *M. barleeanum* tests used is reduced (i.e. 2-3 individuals), measurements are often made several times for this species (see supplementary material S1). All analyses presented hereafter were performed on an Isoprime 100 (Elementar) dual-inlet Isotope Ratio Mass Spectrometer (Elementar) at LSCE laboratory. The results are expressed as $\delta^{18}O$ and $\delta^{13}C$ vs V-PDB (in ‰). The external analytical reproducibility determined from replicate measurements of a carbonate standard is ± 0.05 ‰ (1s) and ± 0.03 ‰ (1s) for $\delta^{18}O$ and $\delta^{13}C$ respectively. Values obtained for the calcite international standard NBS-18 are -23.27 ‰ for $\delta^{18}O$ and -5.01 ‰ $\delta^{13}C$. Because measurements were done over a period exceeding one year and to insure the homogeneity of the final dataset, several levels presented in Simon et al. (2017) were re-measured together with the new samples, resulting into a correction of 0.03 ‰ to 0.06 ‰ applied to the $d^{18}O$ and $d^{13}C$ data measured in 2016 (Simon et al., 2017). All $\delta^{18}O$ and $\delta^{13}C$ results presented in this study are listed in supplementary material (Table S1) and plotted against depth and lithology for both studied sections in figure 3.

3.2. $^{40}Ar/^{39}Ar$ dating

About 4 kg of tephra V4 were collected at the IS. After crushing and sieving, clear and non-altered sanidine crystals ranging from 350 to 500 μm in size were concentrated using Lithium MetaTungstate (LMT) liquor adjusted at a density of 2.55 and handpicked under a binocular microscope. Sanidines were then leached for 5 minutes in a 7 % HF acid solution in order to remove the possibly attached groundmass and then repeatedly rinsed with distilled water in an ultrasonic bath. At least 30 crystals were then chosen for each sample and separately loaded in aluminium disks. V4 sanidines were irradiated for 90

min (IRR 110) in the b1 tube of the OSIRIS reactor (CEA Saclay, France). After irradiation, 15 crystals were individually loaded in a copper sample holder. The sample holder was then put into a double vacuum Cleartran window. Each crystal was then fused using a Synrad CO_2 laser at 10 to 15 % of nominal power (c.a. 25 Watts). The extracted gas was purified for 10 minutes by two hot GP 110 and two GP 10 getters (ZrAl). Argon's isotopes (^{36}Ar, ^{37}Ar, ^{38}Ar, ^{39}Ar and ^{40}Ar) were analysed by mass spectrometry using a VG5400 equipped with an electron multiplier Balzers 217 SEV SEN coupled to an ion counter. Neutron fluence J for each sample is calculated using co-irradiated Alder Creek Sanidine (ACs-2 hereafter) standard with an age of 1.186 Ma (Jicha et al., 2016) and the total decay constant of Min et al. (2000). J-values computed from standard grains is J = 0.00037970 ± 0.00000140. Mass discrimination was estimated by analysis of Air pipette throughout the analytical period, and was relative to a $^{40}Ar/^{36}Ar$ ratio of 298.56 (Lee et al., 2006). Procedural blank measurements are computed after every two or three unknown depending on the beam measured. For 10 minutes static blank, typical backgrounds are about 2.0-3.0 x 10^{-17} and 5.0 to 6.0 x 10^{-19} moles for ^{40}Ar and ^{36}Ar, respectively. The precision and accuracy of the mass discrimination correction was monitored by weekly measurements of air argon of various beam sizes. Aware of the various standards and decay constant values used in the literature (e.g. Kuiper et al., 2008, Renne et al., 2011, Phillips and Matchan, 2013, Rivera et al., 2013, Jicha et al., 2016; Niespolo et al., 2017) we choose to follow Jicha et al. (2016) because it is the one used by Petrosino et al. (2015) who first published the V4 age and because the standardisation used is based on astrochronological approach following Kuiper et al. (2008) (see details below).

3.3. Calcareous plankton and pollen

Calcareous plankton study has been performed on 166 samples from those used for isotope analysis on the IS. For planktonic foraminifera study, the washed residues > 150 mm were split until a representative aliquot containing about 300 specimens has been obtained. All specimens were counted in the aliquots and species abundances were quantified as percentages on the total number of planktonic foraminifers. Slides for coccolithophore analysis were prepared according to the method of Flores and Sierro (1997) to estimate the absolute coccolith abundances (coccolith/g of sediment).

Quantitative analyses were performed using a polarized light microscope at 1000X magnification and abundances were determined by counting at least 500 coccoliths of all sizes. Changes in the calcareous plankton have been considered in order to identify main surface water temperature variations, based on quantitative pattern of warm-water taxa. Among planktonic foraminifera *G. ruber* group (sensu Aurahs et al., 2011) and SPRUDTS group (sensu Rohling et al., 1993) were grouped as warm water taxa (wwt hereafter). For calcareous nannofossil assemblage warm-water taxa (wwt) lump together *Umbilicosphaera* spp., *Calciosolenia* spp., *Oolithotus* spp., *Rhabdosphaera clavigera*, and *Discosphaera tubifera* in agreement with their ecological preference (McIntyre and Bé, 1967; Saavedra-Pellitero et al., 2010; Palumbo et al., 2013; Maiorano et al., 2015).

Quantitative palynological analyses were carried out on a total of 57 samples. Samples were processed using standard chemical-physical procedures at the Department of Earth Sciences, University of Florence. Dry samples were first weighed and *Lycopodium* tablets were added to each sample to obtain palynomorph concentrations. The method included treatments with HCl (10%), HF (48%), sodium hexametaphosphate, KOH (10%) and $ZnCl_2$ separation (solution density ca. 2.0). Residues were sieved at 10 mm and mounted using glycerol. Transmitted light microscopy, using x750 and x1250 (oil immersion) magnifications, was used for identification and counting of pollen. Pollen relative abundances allow the description of the main floristic, vegetation and climate changes at both orbital and suborbital scale. Main results are summarized here by the curve of the mesothermic arboreal pollen group, which include as main components temperate broad-leaved deciduous forest taxa (e.g. *Quercus* and *Carpinus*). Its fluctuations indicate phases of forest expansion (vs reduction) in relation to climatic phases of amelioration (vs deterioration).

3.4. Authigenic ^{10}Be and ^{9}Be

A total of 90 new levels were measured in the upper IS and CM sections in order to improve and complete the authigenic $^{10}Be/^{9}Be$ ratio record of the IS presented in Simon et al. (2017). The analyses were carried out at the CEREGE National Cosmogenic Nuclides Laboratory (LN_2C, France) following the same method used in Simon et al. (2017). The ^{9}Be concentrations were measured using a graphite-furnace Atomic Absorption

Spectrophotometer (AAS) with a double beam correction (Thermo Scientific ICE 3400®). The ^{10}Be concentrations were calculated from the accelerator mass spectrometer (AMS) measurements of $^{10}Be/^{9}Be$ ratios normalized to the BeO STD-11 in-house standard (1.191 ± 0.013x10^{-11}) (Braucher et al., 2015) and decay-corrected using the ^{10}Be half-life ($T_{1/2}$) of 1.387 ± 0.012 Ma (Chmeleff et al., 2010; Korschinek et al., 2010). All data can be found as supplementary material (Table SM2).

4. RESULTS

4.1 Stable isotopic records

The almost perfect correlation between the $\delta^{18}O$ profiles of the two sections allows centimetric precision for establishing a composite curve and calculating the sampling gap situated in the early part of MIS 19a in the IS (grey band in Fig. 3; Simon et al., 2017). The thickness of the gap previously estimated to be about 485 cm (Simon et al., 2017) is now reduced to only 154 cm thanks to the continuous CM section data obtained (Fig. 3). All stable isotope compositions discussed below can be found as supplementary material (table SM1)

Benthic $d^{18}O$ records

In this contribution, we present an extended version of $\delta^{18}O_{M.\ barleeanum}$ record (extending to MIS 18), together with a new $\delta^{18}O_{C.\ carinata}$ record. These high-resolution benthic oxygen records span the stratigraphic interval from MIS 20 to MIS 18 (Fig. 3). *M. barleeanum* and *C. carinata* are two benthic foraminifer species characteristic of mesotrophic to eutrophic environments with moderate oxygen depletions in the bottom water and in pore-water (Stefanelli and Capotondi, 2008). Their $\delta^{18}O$ records in the IS are similar, except for an average offset of ~ 1.07 ‰ (*C. carinata* showing heavier $d^{18}O$ values than *M. barleeanum*) likely reflecting a vital effect on the isotopic composition (e.g. Duplessy et al., 1970; Shackleton and Hall, 974; De Abreu et al., 2005). Along the entire IS, $\delta^{18}O$ values range between 0.6 and 2.7 ‰ for *M. barleeanum* and 1.63 and 3.91 ‰ for *C. carinata*. These data reveal a highly detailed marine isotopic record of the T.IX, and

extends upward into MIS 18 (Fig. 3). Because *M. barleeanum* specimens are large and heavy, isotopic analyses were conducted on 2-3 specimens per level, whereas for *C. carinata* - a very small benthic species - isotopic analyses were conducted on ~ 30 specimens per level. Despite the fact that *M. barleeanum* $\delta^{18}O$ values were only obtained from a very limited set of shells, both *M. barleeanum* and *C. carinata* records show strikingly similar $\delta^{18}O$ curves, with little "noise" on both records (Fig. 3). The fact that the *M. barleeanum* record does not show a significantly higher noise/signal ratio suggests that temperature and $\delta^{18}O_{sw}$ of bottom water were stable, and that bioturbation had little impact on the vertical redistribution of foraminifers due to the very high sedimentation rates (e.g. Bard et al., 1987).

The deglaciation is 16 m-thick, taking place between 1240 and 2860 cm (Fig. 3). It corresponds to a decrease of ~ 2.00 ‰ of the $d^{18}O$ values, with values ranging from ~ 2.66 ‰, at the glacial maximum, to ~ 0.64 ‰ at the peak of MIS 19 for *M. barleeanum* record and from 3.70 ‰ to 1.63 ‰ for *C. carinata* record (Fig. 3). This range of deglacial variation is about twice that found in the LR04 global oxygen isotopic stack (~1.2 ‰) reconstructed by averaging out 57 benthic records worldwide (Lisiecki and Raymo, 2005). The higher amplitude change during T.IX in the IS likely suggests that the benthic oxygen records did not record only a global ice volume signal, due to the very shallow water depth of the site at the time of deposition (few hundred meters, Aiello et al., 2015). Despite the very shallow water that may have influenced our benthic oxygen records it is worth mentioning that the amplitude of $d^{18}O$ change across the deglaciation is of the same order of magnitude than in the Mediterranean benthic stack based on much deeper records (i.e. 2.4‰ in Konijnendijk et al., 2015). However, our benthic oxygen records were also likely affected by surface water variability, picking-up changes related to local/regional climatic processes (temperature, precipitation), which were transferred vertically through upper water mixing. Such hypothesis is strengthened by the fact that in the last part of MIS 19, both our benthic $\delta^{18}O$ records show several abrupt and large amplitude oscillations, that mimic climatic variability seen in the paleo-lacustrine record of Sulmona as well as in other marine sediments (e.g. Tzedakis et al., 2012; Giaccio et al., 2015; Sanchez-Goñi et al., 2016) but with greater amplitude than in all other records. Further studies are being conducted at LSCE to reconstruct sea-surface and bottom temperature changes from Mg/Ca-thermometry and clumped isotopes applied to benthic

and planktonic foraminifers (much rarer) in order to disentangle properly the local temperature and precipitation ($\delta^{18}O_{sw}$) contributions in the benthic $\delta^{18}O$ records. From the interglacial peak of MIS 19, at ~ 2860 cm, both benthic $\delta^{18}O$ records show a rather progressive increase upward with minor scale oscillations until about 3640 cm followed by a more rapid increase to 2.79 ‰. After a very brief period both $\delta^{18}O$ records show an extremely abrupt decrease, with values dropping by more than 0.7 ‰ (from 1.83 to 1.10 ‰ for *M. barleeanum* and from 2.69 to 1.97 ‰ for *C. carinata*) in only 40 cm, and by ~1 ‰ in one meter (Fig. 3). This abrupt shift marks the beginning of the upper part of the IS $d^{18}O$ record, which is characterized by relatively stable intervals with low $\delta^{18}O$ values (suggesting a return to warm and/or wetter conditions), limited by extremely abrupt $\delta^{18}O$ changes towards more positive values (cooler and/or drier conditions). Three main warmer/wetter episodes are clearly visible in the $\delta^{18}O$ record: between 3975–4656 cm, 5049–5718 cm, 6119-6639 cm, and a smaller one between 6812-7072cm. These phases are also well marked alongside the section by distinct darker silty clay intervals (Fig. 3). The second of these warm intervals, between 5049 and 5718 cm, shows the higher amplitude changes with values of *C. carinata* dropping abruptly at its onset by 1.23 ‰ over about 30 cm (corresponding to ~150 years if we convert depth to age using the average sedimentation rate over this interval; see below), and limited by an abrupt $d^{18}O$ increase of ~ 0.9 ‰ at its termination (Fig. 3). The last of these oscillations shows the lowest amplitude. We interpret the maximum $\delta^{18}O$ value at 7115 cm (2.3 ‰ for *M. barleeanum* and 3.47 ‰ for *C. carinata*) as corresponding to the beginning of MIS 18 glacial stage (Fig. 3). As evidenced by Figure 3, the very high-resolution $\delta^{18}O$ records of the IS provide one of the most detailed recording of the MIS 20-MIS 18 interval and of termination IX.

Stable oxygen isotopic stratigraphy labeling

The seminal works of Arrhenius (1952) and Emiliani (1955) set up the strategy used for Marine Isotope Stage labeling, with stage boundaries defined at the mid-point transition of major $\delta^{18}O$ changes. Later, Shackleton (1969) refined this labeling scheme by introducing letter-based designation for isotopic sub-stages of MIS 5. Such approach was extended by several authors on an *ad hoc* basis for sub-dividing older isotopic stages. Tzedakis et al. (2012) were the first to propose the subdivision of interglacial 19 in three

sub-stages (a,b,c), but these authors only provided a figure showing MIS 19c. Their MIS 19c appears to correspond to what we considered to be stage 19 climatic optimum hereafter but its onset does not correspond to the mid-point transition between MIS 20 and MIS 19, as a direct application of Emiliani 1955' and Shackleton 1969's labeling strategy would imply. In order to remain consistent with stage/sub-stage labeling strategy initiated in the 50-60s (Arrhenius, 1952; Emiliani, 1955; Shackleton, 1969) and followed by Railsback et al. (2015), and keeping only three sub-stages as suggested by Tzedakis et al. (2012), we subdivided the oxygen isotope record at IS as follows:

- Differently from Tzedakis et al. (2012) and Simon et al. (2017), we followed the traditional approach to define marine oxygen isotopic stage boundaries and selected the midpoint of the deglaciation to mark the transition between MIS 20 and interglacial MIS 19, and thus the beginning of MIS 19c (i.e. 2280 cm; Fig. 3); In order to compare our record with previous works we also indicate figure 3 the "climatic optimum" of MIS19 starting at 2600 cm with corresponds to the stable climate period within MIS19c. This climatic optimum is indeed equivalent to "MIS19c" as defined by Tzedakis et al., (2012) or Giaccio et al., (2015).
- We identified the end of MIS 19c – beginning of MIS 19b as the first clear climatic degradation (increase in $d^{18}O$) following MIS 19c (i.e. 3697cm, Fig. 3);
- We defined the beginning of MIS 19a at the mid-point of the first rapid drop in $\delta^{18}O$ immediately following the high $d^{18}O$ interval of MIS 19b (i.e. 3975cm; Fig. 3).
- Last, the end of MIS 19a corresponds evidently to the beginning of MIS 18 corresponding to return of the $\delta^{18}O$ close to glacial values (Fig. 3).

The three rapid oscillations of stage 19 are thus assigned to MIS 19a, while MIS19b corresponds to only one cooler/drier interval and has a significantly shorter duration than the two other sub-stages. Overall, the MIS 19c corresponds to the more climatically stable part of stage 19, MIS 19b to the first climatic degradation and MIS 19a to the most unstable part of stage 19, characterized by short but relatively stable intervals separated by abrupt "warming" or "cooling" episodes. For clarity, we subdivided MIS 19a and labeled the warmer/wetter, millennial-scale episodes: MIS 19a-1, MIS19a-2 and MIS 19a-3 (Fig. 3).

Benthic d^{13}C records

Contrary to similar benthic d^{18}O records, striking differences are observed between the $\delta^{13}C$ records from *M. barleeanum* and *C. carinata*. The *C. carinata* $\delta^{13}C$ record shows significantly larger and rapid variability in the upper of MIS 19 than *M. barleeanum* record, with $\delta^{13}C$ oscillations showing in-phase co-variance with the four abrupt oscillations described in both $\delta^{18}O$ records (see above, Fig. 3). This rapid variability is not significantly expressed in the *M. barleeanum* $\delta^{13}C$ record. Although additional work is necessary to fully understand the reason for such a discrepancy between the two carbon isotopic records, it is likely that ecological factors play an important role in explaining such differences. Although both *M. barleeanum* and *C. carinata* are known to be infaunal benthic foraminifers (i.e. living buried within the sediment, below the sediment/water interface), the former lives at intermediate depths (and may feed on refractory organic matter), whereas the latter is known as a shallow endo-benthic species, leaving closer to the sediment/water interface (Morigi et al., 2001; Fontanier et al., 2003; Abu-Zied et al., 2008). The difference between the $\delta^{13}C$ records of these two species could reflect a different contribution of bottom water $\delta^{13}C$ signal and interstitial water $\delta^{13}C$ signal (which reflects the oxidation of organic carbon). Another striking difference between the two records is the stronger noise/signal ratio in the *M. barleeanum* $\delta^{13}C$ record. We suggest that the variability in carbon supply to the seafloor (i.e. changes in productivity) at different timescales (seasonal, inter-annual or even decadal) likely resulted in a large variability of the $\delta^{13}C$ in interstitial waters, which is more readily observed in the poorly averaged *M. barleeanum* data (obtained on a couple of shells per sample) than on *C. carinata* (whose $\delta^{13}C$ is averaged out from the analysis of 30 specimens per sample). In the following paragraph, we will therefore describe in detail the *C. carinata* benthic $\delta^{13}C$ record as it is more relevant for the aim of present paper.

The $\delta^{13}C_{C\ carinata}$ record shows less change associated to deglaciation than during the rapid oscillations of the upper MIS 19. The onset of the MIS 20/MIS 19 deglaciation is marked by a short interval with higher $\delta^{13}C$ values. During the course of the deglaciation the $\delta^{13}C$ varies from ~ -0.45 ‰ to ~ -0.75 ‰, corresponding to a net decrease of 0.3 ‰, which is equivalent to the global $\delta^{13}C$ effect known for the last deglaciation (T.I, Köhler et al., 2005). Then, the final part of the deglaciation shows an abrupt decrease in $\delta^{13}C$, with values dropping by ~ 0.4 ‰ in less than 40 cm (~ 200 years) to reach ~ -1.15 ‰. This

abrupt drop in $d^{13}C$ is coeval with the final, rapid decrease in $\delta^{18}O$, which ends up the deglaciation interval. The interval characterized by low $\delta^{13}C$ values at the end of T.IX extends from ~ 2540 cm to 2960 cm (see discussion below). The rapid oscillations of *C. carinata* $\delta^{13}C$ occurring in the upper part of MIS 19 and mimicking the oscillations seen in $\delta^{18}O$ record, suggest a direct response of productivity/ventilation over the paleo-margin to rapid climatic changes. Further studies are needed to reveal the exact mechanisms explaining those rapid oscillations in the carbon isotopic record but such detail investigations are out of the scope of this article.

4.2. $^{40}Ar/^{39}Ar$ on sanidine single crystals

Full analytical details for individual crystal are given in the supplementary dataset (Table SM3). In figure 4 our new results are presented in comparison with the data produced by the University of Wisconsin Argon Laboratory in 2015 (Petrosino et al., 2015). In this figure individual crystal age uncertainties are given at 1s level but weighted mean age uncertainties are quoted at 2s level. A homogeneous population is considered relevant when the weighted mean of these crystals has a Probability fit ≥ 0.1. The weighted average ages are calculated using IsoPlot 3.0 (Ludwig, 2001) and given at 2s (95 % of probability, analytical uncertainty only). Excluding three xenocrysts with ages between 816 and 803 ka all other crystals we analyzed have equivalent ages within uncertainty (Fig. 4). A weighted mean age of 774.6 ± 1.5 ka (MSWD = 0.61, P = 0.52; Fig. 4) was calculated for this population. This age is undistinguishable within uncertainty with the one reported in Petrosino et al. (2015) (Fig. 4). As all crystals come from the same volcanic horizon and that all single crystal ages were obtained using the same standardization, i.e., "*astronomical calibration*" with ACs flux standard age at 1.186 Ma according to Jicha et al. (2016) and the total decay constant of Min et al. (2000), we decided to treat all crystals analyzed from both works as a single dataset. The weighted mean age of all crystals extracted from V4 (excluding xenocrystic contamination) is 774.1 ± 0.9 ka (MSWD = 0.92, P = 0.58; Fig. 4) and includes 26 crystals. Recently, Niespolo et al. (2017) proposed a slightly younger age for ACs (i.e. 1.1848 Ma) using the same total decay constant. However, the difference in the final age (i.e. 773.3 ka) is within the reported uncertainty and will not be considered further. In the same work, Niespolo et al.

(2017) also pointed-out that if the "*optimization calibration"* proposed by Renne et al. (2011) is considered the age of ACs become 1.1891 Ma. If we use this calibration, V4 become statistically older (i.e. 776.1 ka). It is not the scope of this article to discuss which calibration gives the more accurate age and because we used astronomical tuning approach to develop the age model (see below), we decided to stick to the $^{40}Ar/^{39}Ar$ age obtained using the astronomical derived calibration hereafter. As a consequence, the age of 774.1 ka for V4 is not totally independent as it relies on the astronomical calibration of FCs at 28.201 Ma proposed by Kuiper et al. (2008).

4.3. Calcareous plankton and pollen

The planktonic foraminifera and calcareous nannofossil wwt curves record variable values through the investigated interval, showing increases up to 70 % and 2.5 x 10^6 coccolith/g, respectively (Fig. 5). Very low abundances of wwt characterize MIS 20 and 18 due to unfavorable cold conditions in surface waters. During the interglacial MIS 19, besides a general increase of wwt in both the groups, shorter-term fluctuations are clearly visible and result in very good agreement with the high frequency variability (stadials and interstadials) recorded in $\delta^{18}O$ pattern (Fig. 5).

The curve of the mesothermic arboreal pollen group along with the PTI ratio (Fig. 5) allow to recognize different climate conditions expressed by several fluctuations corresponding to the isotopic ones. Interglacial climatic optimum and MIS 19a interstadials are expressed by the dominance of mesophilic vegetation typical of a (warm) temperate and relatively humid climate. Deciduous *Quercus* dominated fully temperate arboreal forest already devoid of subtropical taxa. Wooded steppes expanded during glacial MIS 20 and stadials when cold and dry conditions prevailed. The main expansion of temperate forest, dominated by broad-leaved trees, closely correlates to climatic optimum during MIS19c, whereas the expansion of steppe vegetation, during drier conditions, marks especially the main part of the deglaciation period but also MIS 19b (Fig. 5). A peculiar pattern, including successive stadial/interstadial fluctuations marks the MIS 19a and the transition to MIS 18. Millennial to sub-millennial-scale climate variability is also well expressed and evidenced by several short-term pollen events

usually characterized by the dominant increase of the cosmopolitan herbaceous component.

5. DISCUSSION

5.1. Paleoenvironmental and paleoclimatic records in the Ideale section

The high resolution stable isotopic data, calcareous plankton, pollen record and authigenic $^{10}Be/^{9}Be$ ratios newly acquired or previously published from the IS, provide numerous proxies from both marine and terrestrial realms as well as geochemical signals allowing comprehensive discussion of paleoenvironmental changes related to local and global climate evolution at the Lower-Middle Pleistocene transition (Fig. 5).

The section records a detailed pattern of shallowing-deepening cycles and changing environmental conditions through MIS 20-19 and towards MIS 18 as highlighted by data from marine micro- and macrobenthic assemblages (D'Alessandro et al., 2003; Stefanelli, 2003; Aiello et al., 2015; Marino et al., 2015, 2016; Maiorano et al., 2016), and terrestrial pollen, here summarized by the curves of the Pollen Temperature Index (Bertini et al., 2015) and the mesothermic arboreal pollen group (Figs. 2, 5). The relative paleodepth throughout the Ideale section varies from about 100 m (in MIS 20) to 180-200 m (MIS 19) based on ostracod assemblages (Aiello et al., 2015). An upper Lower Circalittoral Subzone (LCS, sensu Sgarrella and Moncharmont-Zei, 1993) ostracod association is also recorded in the upper MIS 20 (Fig. 5). Benthic foraminifera indicate two low sea-level minima at 1370 cm and 2150 cm during MIS 20, and a prominent deepening trend toward 2700 cm, matching the variations highlighted by the $\delta^{18}O$ pattern during deglaciation (Fig. 5). The paleodepth increase begins from 2700 cm (ostracofauna), nearly concurrent with the higher values in Pollen Distality Index (Bertini et al., 2015; Marino et al., 2015), in agreement with benthic foraminifera paleodepth reconstruction (Fig. 5). Such pattern is in line with a trend of deepening corresponding to the overall decrease in $\delta^{18}O$ (Fig. 5) that can be partly attributed to the waxing of

continental ice caps and overall seems to be more gradual that other proxies. Distinct deeper seawater condition marking the beginning of climatic optimum, at about 2750 cm, is recorded by the replacing of the upper LCS assemblages with the lower LCS ostracofauna (Fig. 5). The MIS 19 climatic optimum is indeed marked by a climate warming highlighted by calcareous plankton wwt curves, at about 2600 cm in wwt-foram, and at 2700 cm in wwt-nanno (Fig. 5), suggesting rapid increasing temperatures of sea surface waters. An almost synchronous climate warming occurred on land based on the pattern of mesothermic arboreal pollen taxa (Fig. 5) and persisted up to about 3850 cm. All these proxies characterized the climatic optimum within MIS 19c along with light values of $\delta^{18}O$. During this time interval characterized by stable warm conditions, a bathyal environment is established with a Maximum Flooding (MF) followed by a period of maximum depth (MD) (Fig. 5).

At the beginning of the MIS 19 climatic optimum, Maiorano et al. (2016) suggested the existence of sapropel-like event analogue to the "red interval" ("ghost sapropel", Emeis et al., 2000) or i-cycle 74 (Lourens, 2004), based on peculiar patterns of selected taxa during this interval such as the increases of *G. ruber* group, *F. profunda* and *Syracosphaera* spp. indicating warmer and well stratified surface waters, and deep nutricline. The co-occurrence of lower oxygen content at the sea-bottom attested by the increase of benthic foraminifera infauna/epifauna ratio (Stefanelli, 2003; diamond symbol in Fig. 5) and by the peak of dinocyst *Polysphaeridium zoharyi* (star symbol in Fig. 5) were considered consistent with the oceanographic condition during sapropel formation (Maiorano et al., 2016). Our new high-resolution $\delta^{13}C_{\textit{C. carinata}}$ record documents for the first time very low values at the beginning of MIS 19 climatic optimum between 2620 and 2840 cm (Figs. 3, 5). This period also coincides with a rapid increase in humidity and inputs of fresh water coming from land and strengthen monsoons, during the insolation maximum (Fig. 5), which in turn may have help stratifying the water column. The low values in the benthic $\delta^{13}C_{\textit{C. carinata}}$ suggest higher organic matter flux maybe linked to higher surface water primary productivity or to enhanced supply from on land, as expected during a sapropelic event. However, and because we are not in open, deep waters we cannot name this interval a "sapropel" *sensu-stricto*. Nevertheless, the clear identification of this peculiar "event" equivalent in time to the i-cycle 74 (Lourens et al., 2004) represents an additional key level of chronological and paleoceanographical

importance at the scale of central and eastern Mediterranean Basin. Decreasing paleodepth and climatic cooling, from 3850 cm to 3980 cm, are evidenced by the patterns of all biological proxies coeval with heavier $\delta^{18}O$ values during MIS 19b. Similarly, the shallowing/deepening trends and climate phases recorded upwards in the $\delta^{18}O$ records, are also documented by changes in calcareous plankton, pollen, benthic foraminifera and ostracod assemblages (Fig. 5), attesting a mostly genuine signal of sea level and climate fluctuations towards MIS 18 onset.

These multiproxy investigations support recognition of orbital-suborbital climate variability, which are reinforced by our new high-resolution isotopic records. In detail, three major "warmer/wetter" interstadial oscillations (MIS 19a-1, MIS 19a-2 and MIS 19a-3) are highlighted during MIS 19a. They are synchronous to stable isotopic variations from the benthic foraminifera (Fig. 5). The less negative $d^{13}C$ values are associated to heavier $\delta^{18}O$ suggesting that during "cold/dryer" phases the bottom waters were more oxygenated and/or received less land-derived carbon. During warmer/wetter conditions (MIS 19a-1, MIS 19a-2 and MIS 19a-3), $\delta^{13}C_{\textit{C. carinata}}$ values are low and $\delta^{18}O$ are much lighter suggesting enhanced stratification of the water column and less oxygenated condition and/or arrival of land-based carbon. Such conditions are associated with warmer temperature in surface waters and more humid and warmer conditions on land, as shown by the calcareous plankton assemblages as well as pollen data (Fig. 5). These cyclic variations documented by the presented new high-resolution data through MIS 19b-MIS 18 agree with those discussed in Maiorano et al. (2016). They are associated, although at lower sample resolution, to variations in the grain size and mineral content through the IS in relation to succeeding warmer/wetter-colder/arid climate phases on land. Within the MIS 19a interval, nearly perfect agreement of the authigenic $^{10}Be/^{9}Be$ ratio record with $\delta^{18}O$ and $\delta^{13}C$ series also support a primary imprint of this climatic succession on the Be-budget (Fig. 5). Namely, the two largest authigenic $^{10}Be/^{9}Be$ ratio increase intervals observed between 19a-2 and 19a-3 and at the transition toward MIS 18 (Fig. 5) correspond to two significant ^{9}Be-lows (not observed in the ^{10}Be signal) associated with periods of mineralogical changes and coarser grain size fraction supply (Maiorano et al., 2016). The influence of such grain size and mineralogical changes on Be-budget is averaged out when using the ratio between both Be isotopes, but the ^{9}Be load during these two stadial episodes is likely acting as the primary controlling parameter on

the authigenic $^{10}Be/^{9}Be$ ratio signature (Simon et al., 2016). This observation precludes any geomagnetic interpretations of the authigenic $^{10}Be/^{9}Be$ ratio at these levels, contrarily to the MIS 20 – 19b interval (see Simon et al., 2017 for details), but provides hint on the denudation rate and terrigenous input variations. Following the method introduced by von Blanckenburg et al. (2012), these can be grossly estimated at 20% decreases during those two cold/dryer intervals. It is worth noting that large variations of ^{9}Be concentration similar to those observed within these two MIS 19a stadials are not observed during the MIS 20 glacial, although they both express colder/dryer conditions. This is most likely induced by sea-level change which plays a crucial role on the homogenization and sensitive response of Be inputs to climatic variations in such shallow environment.

5.2 Age model and chronological constrains on MIS 19

The initial chronological framework of the IS has been drawn by Marino et al. (2015) using the $^{40}Ar/^{39}Ar$ ages of the V3 and V4 tephras (Maiorano et al., 2010; Petrosino et al., 2015) and tuning the low-resolution benthic $\delta^{18}O$ record to the LR04 benthic stack of Lisiecki and Raymo (2005). However, recent works had suggested that tuning benthic $\delta^{18}O$ records to a unique global reference curve such as the LR04 stack neglects potential regional diachronisms (Lisiecki and Raymo, 2009; Lisiecki and Stern, 2016). In the Mediterranean basin, such diachronisms can result in average 2-3 ka offsets between age assignment of major isotopic features at glacial terminations, reaching a maximum bias of ~ 9 ka during termination VII (Konijnendijk et al., 2015). To circumvent this issue, Simon et al. (2017) set up a regional strategy for developing an age model for the end of MIS 20 and the MIS 19c. This strategy rests upon the assumption that insolation forcing across MIS 20-MIS 19 transition (T.IX) having been similar to insolation forcing over the last termination (T.I hereafter, Tzedakis et al., 2012a; Giaccio et al., 2015; Yin and Berger, 2015), the combination of global/local features across T.IX may have set up a deglaciation signal in MJ section similar to that recorded across T.I in the Adriatic/Ionian area. Thus, Simon et al. (2017) used well-dated (AMS ^{14}C) $d^{18}O$ isotopic records from nearby Adriatic and Ionian seas covering the last deglaciation (cores MD90-917, MD90-918, Siani et al., 2004 and Caron et al., 2012 respectively; Fig. 1a) in order to

decipher precisely the phase relationship between climatic changes (as recorded by foraminifer $d^{18}O$) and insolation which served to phase-lock T.IX relative to the well dated T.I. The age-model was settled by linear interpolation adding the age of V4 at 773.9 ka available at that time.

The approach followed by Simon et al. (2017), strictly speaking, is nothing less than an astronomical tuning strategy that proposes to phase-lock past regional climatic changes to orbital forcing functions based on the best existing regional information available about lead/lag relative to insolation (i.e. based on ^{14}C dating of upper Quaternary series). Such a strategy was used, for instance, to infer the age of sapropels in the Mediterranean Sea (Lourens et al., 2004). Yet, the Mediterranean area is a complex area, and IS isotopic records likely convey a complex interplay of regional/global changes and a mix of surface/thermocline influences. In order to critically check the age model developed in Simon et al. (2017) and its potential flaws, we decided to explore different age-model strategies, taking advantage of the complete MIS 19, IS benthic record in our hands, and a refined $^{40}Ar/^{39}Ar$ age for V4.

We constructed three age models:

- The first age model (pure astronomical tuning) contains three robust tie-points: (i) the onset of deglaciation aged at 794 ka, based on LR04 (Lisiecki and Raymo, 2005) and/or the stacked Mediterranean benthic record (Konijnendijk et al., 2015), (ii) the onset of "sapropel-like event", that here correspond to the maximum of insolation at 785.4 ka (Laskar et al., 2004) equivalent to phase lag of about 3 ka relative to maximum northern insolation in June; Langereis et al. 1997; Lourens, 2004), and (iii) the MIS 18 astronomically dated at 757 ka (LR04; Lisiecki and Raymo, 2005) (Fig. 6, blue line);
- The second age model rests only on $^{40}Ar/^{39}Ar$ ages and uses three tephras: V3 (801.2 ± 18.5 ka); V4 (774.1 ± 0.9 ka); V5 (718.6 ± 2.4 ka; recalculated at 1.186 Ma for ACs from Giaccio et al., 2015) (Fig. 6, black line);
- And finally a hybrid age-model including both astronomical tie-points and the most precisely dated tephra layer present in the IS section (i.e. V4; Fig. 6, green line).

The two first age models, constructed with fully independent constraints, yield an almost similar deglaciation duration/path, within uncertainty limits (Fig. 6). After MIS 19c,

however, age models diverge.

Developing a purely $^{40}Ar/^{39}Ar$-bayesian age model, as achieved for the Sulmona lacustrine section, is unfortunately not as robust for IS due to the following reasons: (i) only three tephra layers dated by $^{40}Ar/^{39}Ar$ are available over an interval of > 80 ka; (ii) the age uncertainty on V3 corresponds to about one precession cycle (i.e. ± 18.5 ka) and (iii) V5 is about 60 ka younger than V4, making this tie-point interesting only for long term chronological framework but useless to constrain age model for addressing orbital and sub-orbital oscillations across MIS 19 (Figs. 2, 3, 5). The astronomically-tuned age model is unable to produce an age for V4 (Fig. 6) that is similar to any of the two $^{40}Ar/^{39}Ar$ standardizations currently considered as the most accurate (i.e. 774.1 ± 0.9 ka following Jicha et al., 2016 and Niespolo et al., 2017; and 776.1 ± 0.9 ka using the Renne et al. (2011) optimization (see Niespolo et al., 2107 for details)). This suggests that (an) important change(s) in sedimentation rates exist(s) between the two astronomical tie-points at 785.4 and 757 ka.

Based on these observations and the fact that the astronomically-tuned framework makes the duration of climatic optimum MIS 19c much shorter than any other available record from the same time period including the most robust estimates based on the independently dated of the Sulmona lacustrine record (Giaccio et al., 2015), we are currently inclined to favor our hybrid age model to better resolve the duration of MIS 19c and the millennial-scale variability particularly well expressed in MIS 19a and therefore used in the following discussion. Thus, we conclude that our best estimate for the MIS 19c is 13.6 ka, and it is 11.3 ka for climatic optimum of MIS19. These durations are only marginally different from the ones suggested by Simon et al., 2017 age model.

We performed spectral analysis of the $d^{18}O$ records using SSA-MTM Toolkit package (Ghil et al., 2000) based on the three age models discussed above ($^{40}Ar/^{39}Ar$ model, Fig. 7a; the astronomically-tuned age model, Fig. 7b; and the hybrid age model, Fig. 7c). In all three cases we were able to extract different, statistically significant millennial cyclicity at 3.3, 7.1 and 5.3 ka, respectively. We performed a similar spectral analysis on the $d^{18}O_{carbonate}$ record from the Sulmona paleolake dated by $^{40}Ar/^{39}Ar$ (Giaccio et al., 2015) and covering the same time interval (see supplementary material). This record reflects the hydrological variations over the central Apennines region. The spectral analysis enables us to extract a significant main cyclicity at 5.9 ka (see supplementary

material), in good agreement (within uncertainty limits) with the cyclicity extracted from the $d^{18}O$ record of IS using our hybrid age-model. The average duration of interstadial oscillations, which are well expressed in MIS 19a, is therefore of 5.3 ka in duration using our preferred age model, in good accordance with the results found by Sanchez-Goñi et al. (2016). We would like to stress out, however, that even our hybrid age model is unable to properly resolve all the changes in the sedimentation rates that probably occurred during MIS 19 as suggested by lithological changes as well as environmental variations. This comment is, of course, valid for any age model that is constrained by a limited number of tie-points, absolute or not. As a consequence, the precise duration of the rapid interstadials we defined during MIS 19a (i.e. MIS 19a-1 to -3) can be improved.

5.3 The Mediterranean paleoenvironmental sensibility to the global climatic variability during MIS 19 low eccentricity period.

All records presented in Figures 8 and 9 show a generally good concordance regarding patterns of climatic variability, without taking into account the associated chronological uncertainties. Regional and global scale patterns clearly emerge from this comparison (Figs. 8, 9) illustrating striking similarities between proxy records over the time interval 800-755 ka. It includes records from Alpine and Apennines paleolakes i.e. Piànico-Sèllere (Moscariello et al., 2000; Rossi et al., 2003) and Sulmona (Giaccio et al., 2015) (see Fig.1a for locations); Iberian margin (Sanchez-Goñi et al., 2016); North Atlantic marine sediments (Kleiven et al., 2011), as well as Antarctica (Pol et al., 2010; Bazin et al., 2013) together with the $\delta^{18}O$ and $\delta^{13}C$ profiles we obtained in the IS and CM.

Figure 8a compares the Ideale $\delta^{18}O$ and $\delta^{13}C$ profiles with the $\delta^{18}O_{\textit{U. peregrina}}$ profile recently obtained in the Valle di Manche (VdM) section (Capraro et al., 2017). We compare the stable isotope profiles of IS with the $d^{18}O$ profile from VdM, based on the age model developed using the benthic stack of Konijnendijk et al. (2015) (green line in Fig. 7a) as well as with the alternate age model based on the planktonic stack of Wang et al. (2010) (i.e. orange dashed line in Fig. 8a) (see Capraro et al., 2017 for details). Despite the lower-resolution of the $\delta^{18}O_{\textit{U. peregrina}}$ record from this exposed section located about 130 km south of Montalbano Jonico (Fig. 1) the two records show a generally good concordance (Fig. 8a). Because VdM and IS are very close to each other we expect both

records to be synchronous. The inferred durations of MIS 19c are similar if we considered only the benthic stack-based age model of VdM (i.e. 10.0 ka and 13.3 ka for VdM and IS; Fig. 8a). However, when we look at the three warm/wetter interstadials during MIS 19a there are clear discrepancies whatever the age model considered for VdM (Fig. 8a). Nevertheless, during each cold/drier phases, the $\delta^{18}O$ of foraminifera is becoming heavier towards typical glacial values in both records suggesting an overall cooling trend leading to the onset of MIS 18, which is only interrupted by periodical warmer and wetter periods. The ~ 2 ka offset observed among millennial oscillations between IS and VdM during MIS 19a is within the uncertainty of both age models. However, we suggest that this systematic offset could be due to the fact that the VdM age model lacks of an independent tie-point such as V4. We therefore argue that the IS age model is more robust between the end of MIS 19c and the beginning of MIS 19b. As a result, it seems that the duration of MIS 19b is largely overestimated in VdM. As already mentioned the durations of interstadials following MIS 19c are extremely difficult to access given chronological limitations (see above). In order to further test our age model we compare in figure 8b the $\delta^{18}O$ and $\delta^{13}C$ profiles at IS with the pollen record of paleolake Piànico-Sèllere (Moscariello et al., 2000; Rossi et al., 2003; Mangili et al., 2007) that was recognized to cover the entire MIS 19 interglacial (Scardia and Muttoni, 2009; Roulleau et al., 2009). This paleolake succession is located in the southern edge of the Alpine massif north of lake Iseo (North Italy) and has a floating varve-based chronology of 15500 ± 620 varve years (Brauer et al., 2007), which corresponds to the main part of the Banco Varvato Carbonatico (BVC) section covering the equivalent time from MIS 19c to MIS 19a (Fig. 8b). We did not attempt to synchronize the oceanic proxy records with the climatic oscillations observed in the Piànico-Sèllere pollen record because oceanic and land proxies were not obtained on the same sediments and are located 800 km from each other. As a result we cannot fully exclude leads and lags between the two records. However, concordance between climatic patterns of these two records is striking (Fig. 8b). The duration of MIS 19b equivalent to the "Lovere event" and "PIO III" is estimated to range from 800 to 1080 years (Rossi, 2003; Mangilli et al., 2007), which is shorter -but within uncertainty- equivalent to the duration of MIS 19b in the IS (i.e. 1.5 ka Fig. 7b). The 19a-1 interstadial (first warm/wetter oscillation known as the Piànico-Sèllere interstadial) is estimated to last about 4.9 ka (Rossi, 2003; Mangilli et al., 2007)

whereas we found only 3.3 ka in the IS (Fig. 8b). The differences in duration could be due to several causes among them the fact that the age model between the tie points V4 and 757 ka cannot fully reproduce changes in sedimentation rate or accurate duration of these millennial climatic events. It is worth mentioning that the top of the Piànico-Sèllere pollen records could be correlated to the Sulmona record using tephra layer t32 that is equivalent to tephra SUL2-11 (755 ± 4 ka Giaccio et al., 2015; Sottili et al., 2018) (Fig. 8b). Both age and climatostratigraphic position of t32 agreed with the fourth and minor climatic warming that is recorded in the IS just before the onset of MIS 18 (Fig. 8b) reinforcing the similar climatic patterns and trajectory between the north and southern Italian peninsula between 775 and 757 ka (i.e. toward the onset of the glacial MIS 18). Another important information that could be drawn from this comparison between oceanic and in land record is that both climatic compartments display extremely rapid transition periods (i.e << 200 years; Fig. 8b) between two main climatic states (i.e. warm/wet and cold/dry) during MIS 19a suggesting a highly non-linear response of the regional climate to orbital forcing during this period.

Figure 9 offers the opportunity to enlarge the discussion by comparing the IS stable isotope profiles between 800 and 755 ka with high latitude climatic records (North Atlantic ODP 983, Kleiven et al., 2011), Antarctica (Pol et al., 2010) as well as with the MIS 19 isotope record of paleolake Sulmona (Central Apennines, Italy, Giaccio et al., 2015) and the record from U1385 from the southern Iberian margin recently obtained by Sanchez-Goñi et al. (2016). The IS isotopic record resembles and reproduces with great details the variability observed in the records of the European Project for Ice Coring in Antarctica (EPICA) Dome C Antarctic ice (Pol et al., 2010; Extier et al., 2018) and of planktonic $\delta^{18}O$ from the subpolar North Atlantic ODP Site 983 (Kleiven et al., 2011), including the series of three warm main oscillations. These observations provide new evidence for a great sensitivity of the Mediterranean climatic and oceanic conditions to global changes as well as highlights the highly interconnected North Atlantic and Mediterranean climatic regimes following the climatic optimum (i.e. 19c) as already shown by Giaccio et al. (2015). The pattern of climatic variability during MIS 19a in the IS and Sulmona are almost synchronous despite being based on two different age models (Fig. 9). Sulmona succession has the advantage of yielding the only chronological framework truly independent of any orbital assumptions for this time period. Its good

synchronism of the millennial scale oscillations with the IS record is another strong argument supporting the reliability of our hybrid chronology similarly to the comparison with the Piànico-Sèllere sequence. The duration of climatic optimum in Sulmona is 10.8 ± 3.7 ka is identical within uncertainty to the duration estimated in the IS (i.e. 11.3 ka; Fig. 9), which in turn is within uncertainty equivalent to the duration reported for this interglacial worldwide (Fig. 9). In the IS, the climatic optimum during MIS 19c (interglacial *sensus stricto)* is marked by increasing $\delta^{18}O_{benthic}$ values toward MIS 19b (Fig. 5). It is known that the $\delta^{18}O_{benthic}$ variations depend on changes in continental ice volume, local deep-water temperatures and hydrographic conditions (Skinner and Shackleton, 2009). Despite being in shallow depth environment (180-200 m depth maximum), therefore reflecting local conditions, it seems that the $\delta^{18}O_{benthic}$ obtained during MIS 19c in IS is also carrying a global signal (i.e. global ice volume). A cooling trend observed on the EPICA dome C record over MIS 19c (Pol et al., 2010) agrees with a global climatic cooling starting very early during MIS 19c. The $\delta^{13}C$ benthic signal suggests a good ventilation of the lower part of the water column of this shallow basin since the end of the sapropel-like event (i-cycle 74). Following MIS 19c, starting ~773.9 ka ago, a short period displayed colder sea surface and inland temperatures (MIS 19b) that we interpreted as the first bipolar seesaw oscillation. It is worth mentioning that even if each record is plotted on its own chronological framework (Fig. 9), this short period is restricted in time between 775.0 and 772.5 ka worldwide. This event occurred after the minimum of insolation and displays an asymmetric shape in all records that contrasts with the "box shape" observed for the following millennial scale oscillations toward the onset of MIS 18. One final observation is that the transition between circalittoral and bathyal environment in the IS occurred at about 784 ka (Fig. 9) and the maximum depth between 778 and 773.5 ka, as reconstructed by benthic foraminifera (Stefanelli, 2003; Fig. 5). The maximum depth period is in agreement with the global sea level timing reconstructed by Elderfield et al. (2012) at around 776 ka (Fig. 9F) whereas it is conflicting with the one proposed by Rohling et al. (2014, Fig. 9F) that suggests a much earlier sea level maximum at 794 ka. However, it could be said with confidence that locally the sea level started to decrease shortly after 774.1 ± 0.9 ka ($^{40}Ar/^{39}Ar$ age of V4, Figs. 5, 9). However, it is interesting to notice that all records - despite having age model based on very different approaches, including the fully independent Sulmona one -

suggest that the beginning of the climatic optimum is at least 4 ka younger than the age proposed by Rohling et al. (2014) for the sea level maximum. Furthermore, the fact that the maximum sea level is at least 6 ka younger than the maximum of insolation (65 North 21st June, Fig. 9) as suggested by Rohling et al., 2014 is most unlikely.

If the distinction between glacial and interglacial is related to ice volume and sea level, the definition of interstadials is more difficult to decipher since both regional and local expression of these climatic events may differ from one oceanic basin to another, but also have contrasting inland effects. For recent periods (i.e. MIS 3, 5) or at the end of MIS 19, authors have suggested that these millennial scale oscillations in the Mediterranean region are linked directly or indirectly to North Atlantic ice sheet dynamics (i.e. Brauer, 2007; Tzedakis et al., 2012; Martrat et al., 2014; Giaccio et al., 2015; Regattieri et al., 2015). An indirect indication of the growth of the ice sheets is provided by millennial-scale records of ice rafted debris (IRD) produced by iceberg discharges to the North Atlantic (Kleiven et al., 2011, Fig. 9F) likely associated with the triggering mechanism of Northern Hemisphere cold events and bipolar seesaw oscillations (Tzedakis et al., 2012). The first IRD highlighted by ODP 983 (Kleiven et al., 2011) is climatostratigraphically identified in marine sediment at the end of MIS 19b (Fig. 9G). Cold events that could be directly linked to ice shelf dynamics during glacial inception (MIS 19a) can also be traced in Iberian margin as well as Mediterranean marine and terrestrial records by sea-surface cooling (e.g. Sanchez-Goñi et al., 2016) or decreasing precipitations (e.g. Bertini et al., 2015; Giaccio et al., 2015; Sanchez-Goñi et al., 2016). All these features are well expressed in the IS (Figs. 5, 9), in particular: 1) the sudden arrival of more ventilated/oxygenated bottom water as suggested by our new $\delta^{13}C$ data, associated with colder surface waters (Fig. 9M), 2) reduced precipitation and lower temperatures inland during MIS 19a (Fig. 5), and 3) decrease of terrigenous inputs associated with lower denudation rates (Figs. 5 and 9L). Superimposed on the long-term drying and cooling trend at least three major warm and wetter periods are now well established during MIS 19a at both high and low latitude as well as in marine and inland records (Fig. 9). The phase relationship between proxies in ODP 983, U1385 and the IS are identical with the second warm oscillations (19a-2) centered at the maximum of insolation (i.e. minimum of precession but minimum of obliquity) in all records (Fig. 9). Our new $d^{18}O$ data strengthen the existence of a 5.0 to 6.0 ka millennial-scale oscillations

during the entire MIS 19 in the Mediterranean Sea $\delta^{18}O$ signal and in the atmosphere as suggested by the $\delta^{18}O_{carbonate}$ record of Sulmona similarly to the observations made by Sanchez-Goni et al. (2016) in the Iberian margin or by Ferretti et al. (2015) in North Atlantic. The amplification of these oscillations during MIS19b and especially MIS19a was likely associated with the iceberg discharges in the subpolar gyre as well as arrival of fresh water to the Iberian Margin (Sanchez-Goni et al, 2016). It remains difficult to directly transfer this mechanism to explain the large amplitude of these millennial oscillations in our record without adding a local effect such as discharged of fresh water into the Montalbano basin coming from nearby continent combined with the influence of the amount and composition of surface water flowing into the Mediterranean basin at Gibraltar (Grant et al., 2016). Additional independent information such as salinity variations or sea surface temperatures are still needed to untangle the main forcing parameters and propose a robust interpretative hypothesis.

Even if the exact origin of the high amplitude $\delta^{18}O$ oscillations during MIS19a is not fully understood, it is known for more recent periods that wetter conditions of the Mediterranean climate are driven by orbital forcing, particularly coinciding with precession minima (e.g. Magri and Tzedakis, 2000; Tzedakis, 2007; Sanchez-Goñi et al., 2008; Milner et al., 2012). These recent wettest periods are recorded when the precession index is minimum and the insolation reaches its maximum over central Mediterranean (e.g. Regattieri et al., 2015, 2016). Similar orbital configuration prevails during MIS19a (Fig. 9), suggesting similar mechanisms to could explain these changes. Many studies invoke a northward penetration of the Intertropical Convergence Zone (ITCZ) during precession minima that would have strengthened and shifted northwards the summer high-pressure system of the Mediterranean, amplifying summer aridity in the region but in turn leading to enhanced winter precipitation (e.g. Tzedakis, 2007; Milner et al., 2012; Regattieri et al., 2015). Other studies propose a zonal interconnection with the Asian summer monsoon and the Mediterranean climate leading to dry summers during minima in precession (Sanchez-Goñi et al., 2008).

Atmospheric methane records from Antarctic ice cores (Fig. 9N) also provide additional constraints concerning the link between precession and these millennial wet events, with CH_4 records mainly reflecting the global strength of tropical monsoons (e.g. Fischer et al., 2008; Loulergue et al., 2008). The good coherence, despite being build in

totally different age models, of our $\delta^{18}O$ records with the three major methane peaks observed during MIS 19a at EDC (Fig. 9) suggests that the wet/warm oscillations highlighted in our record are not only restricted to the Mediterranean area, but correspond to worldwide climatic phenomena, even if the exact amplitude of these climatic oscillations as recorded by $\delta^{18}O$ in the Ionian Sea may have been amplified by local phenomena.

6. CONCLUSION

We provide new centennial isotopic records based on two benthic foraminifera species *(Melonis barleeanum* and *Cassidulina carinata*) collected from two sections of the Montalbano Jonico succession (southern Italy) covering Termination IX up to the MIS 18 onset. Improved temporal resolution of the Ideale section is also attained by new calcareous plankton, pollen data and authigenic $^{10}Be/^{9}Be$ ratio results. Moreover, new $^{40}Ar/^{39}Ar$ measurements performed on 15 sanidine single crystals from the tephra layer V agree with those obtained previously allowing to establish a robust radiometric age of 774.1 ± 0.9 ka (2s analytical uncertainty). The new stable isotope stratigraphy is combined to this independent radio-isotopic age. We estimate a duration of 13.6 ka for the MIS 19c and of 11.3 ka for the climatic optimum of MIS19. The clear identification of sapropel like-event at the beginning of the climatic optimum during MIS 19c where the "red interval" or i-cycle 74 equivalent was suggested to exist, allows to propose the first local estimate for the duration of this event of ~ 2.5 ka (785.0-782.5 ka). Between 773.9 and 757.0 ka (i.e. MIS 19a), superimposed to the long-term drying and cooling trend, our $d^{18}O$ records show millennial oscillations towards the MIS 18 onset, highlighting a climatic regime characterized by two main climatic modes (i.e. wet/warm and dry/cold) limited by abrupt transitions (i.e. << 200 years). At least three main interstadials (19a-1, 19a-2 and 19a-3), restricted in time within one precession cycle, are individualized and they are mostly expression of warm and wetter climate phases as suggested by increases of calcareous plankton warm water taxa and of Mesothermic arboreal pollen taxa. This oscillatory climatic regime could be fuelled by cyclic northward shifts of the Intertropical Convergence Zone (ITCZ) over the Mediterranean region or zonal teleconnection between

the Asian summer Monsoon and the Mediterranean climate. The Montalbano Jonico centennial isotopic record from the Ideale section reproduces with unprecedented details the variability observed worldwide. It also highlights the interconnection between the North Atlantic (i.e. oceanic circulation and atmospheric processes related to ice-sheet dynamics) and the Mediterranean climatic regime at the end of the MIS 19 low eccentricity interglacial.

Acknowledgments

This study is supported by the INSU LEFE 2014-2016 “INTERMED” project assigned to S. Nomade and the Fondi di Ateneo 2014 (University of Bari Aldo Moro, Italy) assigned to M. Marino, Fondi di Ateneo 2014 (University of Firenze, Italy) assigned to A. Bertini. Authors would like to specially acknowledge the support of the municipality of Montalbano Jonico in 2014 and 2015. Special thanks to Dr. L. Bazin and the colleagues from the PALEOCEAN team for the fruitful discussions. Authors extend their thanks to the two reviewers and editor that helped improving the manuscript. QS and DB would like to thank Sandrine Choy, Georges Aumaître and Karim Keddadouche for Be samples preparation and AMS measurements. The ASTER AMS national facility (CEREGE, Aix en Provence) is supported by the INSU/CNRS, the ANR through the "Projets thématiques d’excellence" program for the "Equipements d’excellence" ASTER-CEREGE action and IRD. This is LSCE contribution N°XXXX.

Supplementary material

Table SM1, supplementary material: Authigenic $^{10}Be/^{9}Be$ data

Table SM2, supplementary material: Stable isotopes data

Table SM3, supplementary material: Full $^{40}Ar/^{39}Ar$ data

Figure SM1, supplementary material: spectral analysis of the Sulmona record (Giaccio et al., 2015)

Figures captions

Figure 1: a) General view of the Italian peninsula with the location of Montalbano Jonico succession (MJS) as well as of other sites discussed in the text: MD90-917 and MD90-918 cores, Valle di Manche (VdM), and Piànico-Sèllere (PS) successions; b) General geological context of the Montalbano Jonico succession; c) Map showing the location of the regional reserve of the badlands; d) Geological map showing the two sections studied (IS for Ideale Section and CM for Ciaranfi Master section)

Figure 2: Lithological and stratigraphical features of the composite Montalbano Jonico section (Intervals A and B). Biostratigraphical and paleonvironmental details are traced according to Ciaranfi et al. (2001, 2010), Stefanelli (2003, 2004), D'Alessandro et al. (2003), Maiorano et al. (2004, 2010), Girone et al. (2013). $\delta^{18}O_{planktonic}$ *and* $\delta^{18}O_{benthic}$ *are from Brilli (1998), Brilli et al. (2000) and Ciaranfi et al. (2010). Pollen Temperature Index (PTI) record (in logarithmic scale) derives from Mesothermic/Steppic taxa ratio and is from Joannin et al. (2008) for Interval A, Vannacci (2016) for MIS 22, Bertini et al. (2015) and Toti (2015) for MIS 21-17 interval. LO: Lowest Occurrence; HO: Highest Occurrence; LCO: Lowest Common Occurrence; HCO: Highest Common Occurrence; reap: reappearance. The correlations to sapropel stratigraphy are according to Lourens (2004) and Konijnendijk et al. (2014). Summer insolation is from Laskar et al. (2004) and* $^{40}Ar/^{39}Ar$ *ages of V3-V5 from Ciaranfi et al. (2010); Maiorano et al. (2010) and Petrosino et al. (2015).*

Figure 3: $\delta^{18}O_{C.\ carinata}$, $\delta^{18}O_{M.\ barleeanum}$, $\delta^{13}C_{C.\ carinata}$ *and* $\delta^{13}C_{M.\ barleeanum}$ *records (vs depth) at the Ideale and Ciaranfi Master sections. This figure illustrates the matching between the stable isotope data and specific lithological changes in each section.*

Figure 4: $^{40}Ar/^{39}Ar$ *single crystal age obtained for V4 in this study (LSCE laboratory, France) compared to the one obtained in the UW Laboratory (USA; Petrosino et al., 2015). The reported ages are all at 2s level (analytical uncertainty). The black boxes correspond to crystals not included on the weighted mean age(s) calculation(s).*

Figure 5: Stratigraphic log of the Ideale section showing the new high-resolution stable isotopes results in correlation with the main stratigraphic, chronological, and

paleoenvironmental constraints from new or published data. I-cycle 74 corresponds to the "ghost sapropel" (see text for explanation). MBT is for Matuyama-Brunhes transition; T.IX stands for Termination IX. The climatic optimum within MIS19c and MIS 19 interstadials (19a-1, 19a-2, 19a-3) are also indicated and discussed in detail in the text. The "end temp. disap. G. omega" is the end of temporary disappearance of nannofossil Gephyrocapsa omega. MD (maximum depth) and MF (maximum flooding) according to D'Alessandro et al. (2003). Star and diamond symbols indicate the acme of dinocyst Polysphaeridium zoharyi (Maiorano et al., 2016) and the peak of benthic foraminifera infauna/epifauna ratio (Stefanelli, 2003).

Figure 6: Chronological framework of the Ideale Section. Benthic $\delta^{18}O_{M.\ barleeanum}$ *records the Ideale section with three alternate chronological approaches. Mean summer (JAS) and 21*St *June insolation curves are from Laskar et al. (2004). The purple stripe corresponds to the* $\delta^{13}C_{C.\ carinata}$ *anomaly duration (sapropel like-event close to the i-74 ghost sapropel position) in the Ideale section taking into account all three age models. TP1, TP2 and TP3 are orbital tuning tie-points.*

Figure 7: Spectral analysis based on $\delta^{18}O_{C.carinata.}$ *a) for the* $^{40}Ar/^{39}Ar$ *age model; b) for the astronomically derived age model; c) for the hybrid age model (see text for details).*

Figure 8: a) $\delta^{18}O_{M.\ barleeanum}$ *,* $\delta^{18}O_{C.\ carinata}$ *and* $\delta^{13}C_{C.\ carinata}$ *profiles at the Ideale section with the* $\delta^{18}O_{U.\ perigrina}$ *profiles from Valle di Manche section corresponding to two distinct age models, i.e. green-line and orange dashed line corresponding to the Mediterranean benthic and planktonic stack age model option, respectively (Capraro et al., 2017). The two different targets used by Capraro et al. (2017) are from Konijnendijk et al. (2014) and Wang et al. (2010) for the benthic and planktonic stack respectively (see bottom of the Fig. 8a). Yellow circles, green and orange lozenges correspond to the tuning tie-points used for the Ideale and Valle di Manche age models, respectively. b) Ideale section* $d^{18}O$ *profiles compared with the pollen record from the Piànico-Sèllere MIS 19 interglacial (Moscariello et al., 2000; Rossi et al., 2003). The floating varve-based chronology is from Moscariello et al. (2000) and Mangili et al. (2007).*

Figure 9: High temporal resolution paleoclimatic and environmental records during the MIS 20–MIS 18 period. The vertical dash line corresponds to the $^{40}Ar/^{39}Ar$ age and climatostratigraphic position of V4 in the IS. The grey shaded is V4 age uncertainty (2s analytical uncertainty). A) MIS limits are according to Lisieki and Raymo (2005). B) Mean July-August-September insolation at 65°N (JAS), dashed line, C) 21th June insolation at 65°N and D) Obliquity from Laskar et al. (2004). E) Benthic stack, Lisiecki and Raymo (2005). F) Sea level reconstructions (blue for Elderfield et al., 2012; red for Rohling, et al., 2014). G) Ice rafted debris (IRD) records from North Atlantic Ocean Drilling Program Site 983 (Kleiven et al., 2011). H) Planktonic foraminifera $\delta^{18}O$ (PDB) from North Atlantic Ocean Drilling Program Site 983 (Kleiven et al., 2011). I) $\delta^{18}O_{G.\ bulloïdes}$ (PDB) from the Iberian margin Ocean Drilling Program site U1385 (Sanchez-Goñi et al., 2016). J) Log Ca/Ti ratio from the Iberian margin Ocean Drilling Program site U1385 (Hodell et al., 2015). K) $\delta^{18}O_{carbonates}$ from the Sulmona paleolake (Central Italy, Giaccio et al., 2015). L) $\delta^{18}O_{C.\ carinata}$ and $\delta^{18}O_{M.\ barleeanum}$ in blue, and red respectively (PDB) obtained at the Ideale section (this study). M) $\delta^{13}C_{C.\ carinata,}$ from the Ideale section (this study). N) dDeuterium from EPICA Dome C, Antarctica (Pol et al., 2010; Extier et al., 2018). O) CH_4 from EPICA dome C, Antarctica (Pol et al., 2010) with the new chronology of Extier et al. (2018).

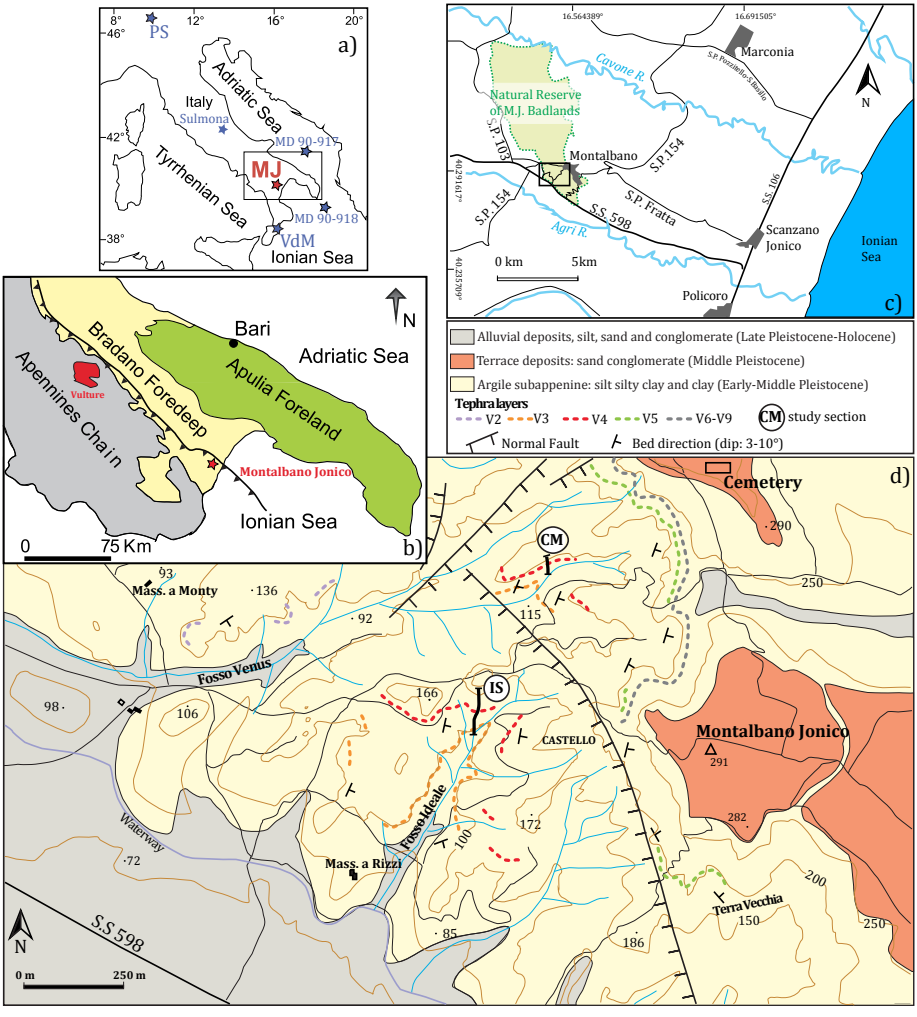
a)
PS
MJ
VdM
MD 90-917
MD 90-918
Adriatic Sea
Tyrrhenian Sea
Italy
Sulmona
Ionian Sea
b)
Bari
Adriatic Sea
Bradano Foredeep
Apulia Foreland
Apennines Chain
Vulture
Montalbano Jonico
Ionian Sea
0
75 Km
N
c)
Marconia
Natural Reserve of M.J. Badlands
Cavone R.
Montalbano
S.P. 154
S.P. Fratta
S.S. 598
S.S. 106
Agri R.
Scanzano Jonico
Ionian Sea
Policoro
0 km
5km
Alluvial deposits, silt, sand and conglomerate (Late Pleistocene-Holocene)
Terrace deposits: sand conglomerate (Middle Pleistocene)
Argile subappenine: silt silty clay and clay (Early-Middle Pleistocene)
Tephra layers
V2
V3
V4
V5
V6-V9
CM study section
Normal Fault
Bed direction (dip: 3-10°)
d)
Cemetery
CM
IS
Mass. a Monty
Fosso Venus
Waterway
CASTELLO
Montalbano Jonico
Fosso Ideale
Mass. a Rizzi
Terra Vecchia
S.S 598
0 m
250 m

Figure 1

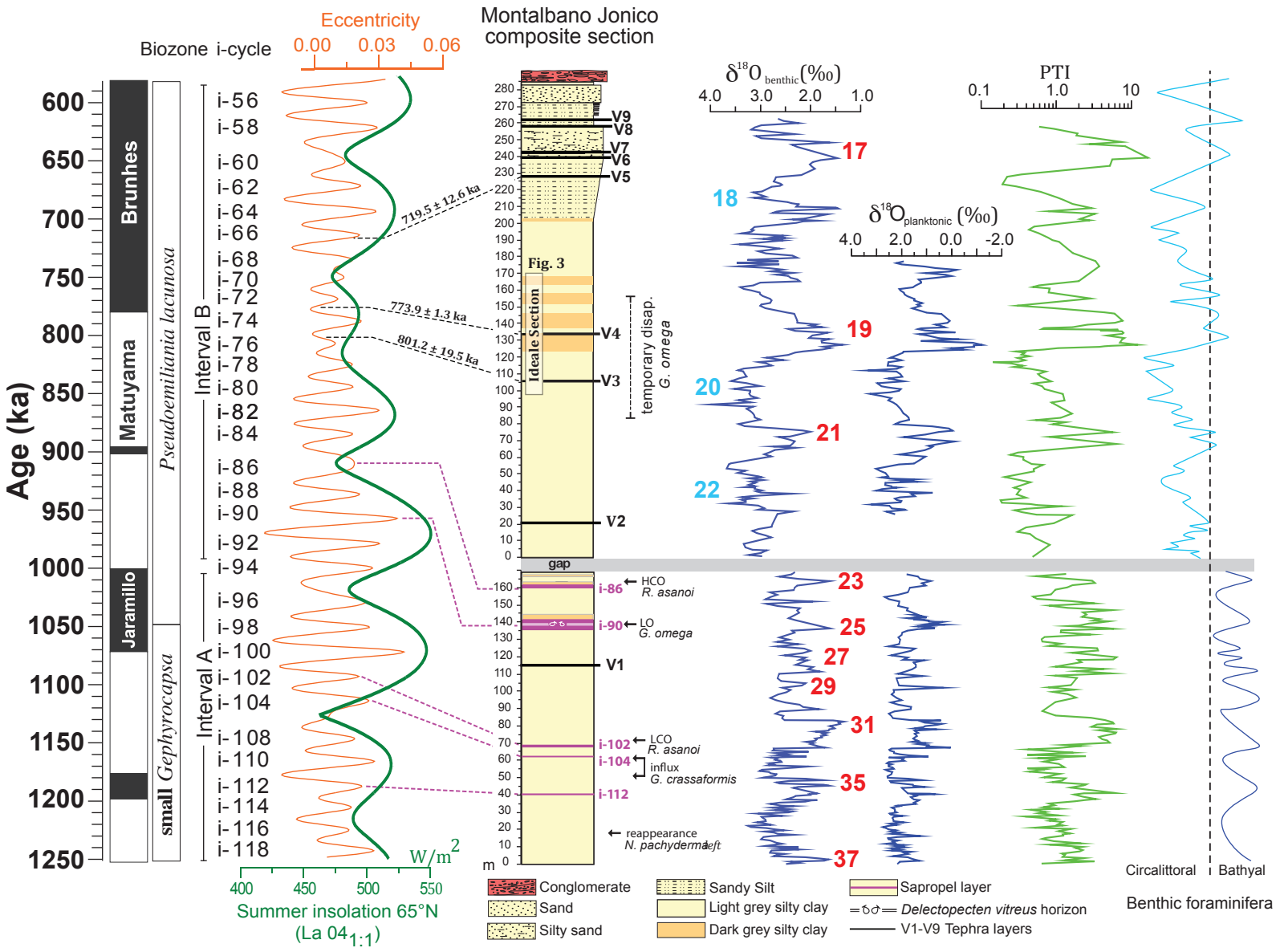
Eccentricity
0.00 0.03 0.06
Biozone i-cycle
Montalbano Jonico composite section
Age (ka)
Brunhes
Matuyama
Jaramillo
Pseudoemiliania lacunosa
small Gephyrocapsa
Interval B
Interval A
719.5 ± 12.6 ka
773.9 ± 1.3 ka
801.2 ± 19.5 ka
Fig. 3
Ideale Section
temporary disap. G. omega
V9
V8
V7
V6
V5
V4
V3
V2
V1
gap
i-86 HCO R. asanoi
i-90 LO G. omega
i-102 LCO R. asanoi
i-104 influx G. crassaformis
i-112
reappearance N. pachyderma left
δ18O benthic (‰)
δ18O planktonic (‰)
PTI
Circalittoral
Bathyal
Benthic foraminifera
W/m2
Summer insolation 65°N
(La 04 1:1)
Conglomerate
Sand
Silty sand
Sandy Silt
Light grey silty clay
Dark grey silty clay
Sapropel layer
Delectopecten vitreus horizon
V1-V9 Tephra layers

Figure 2

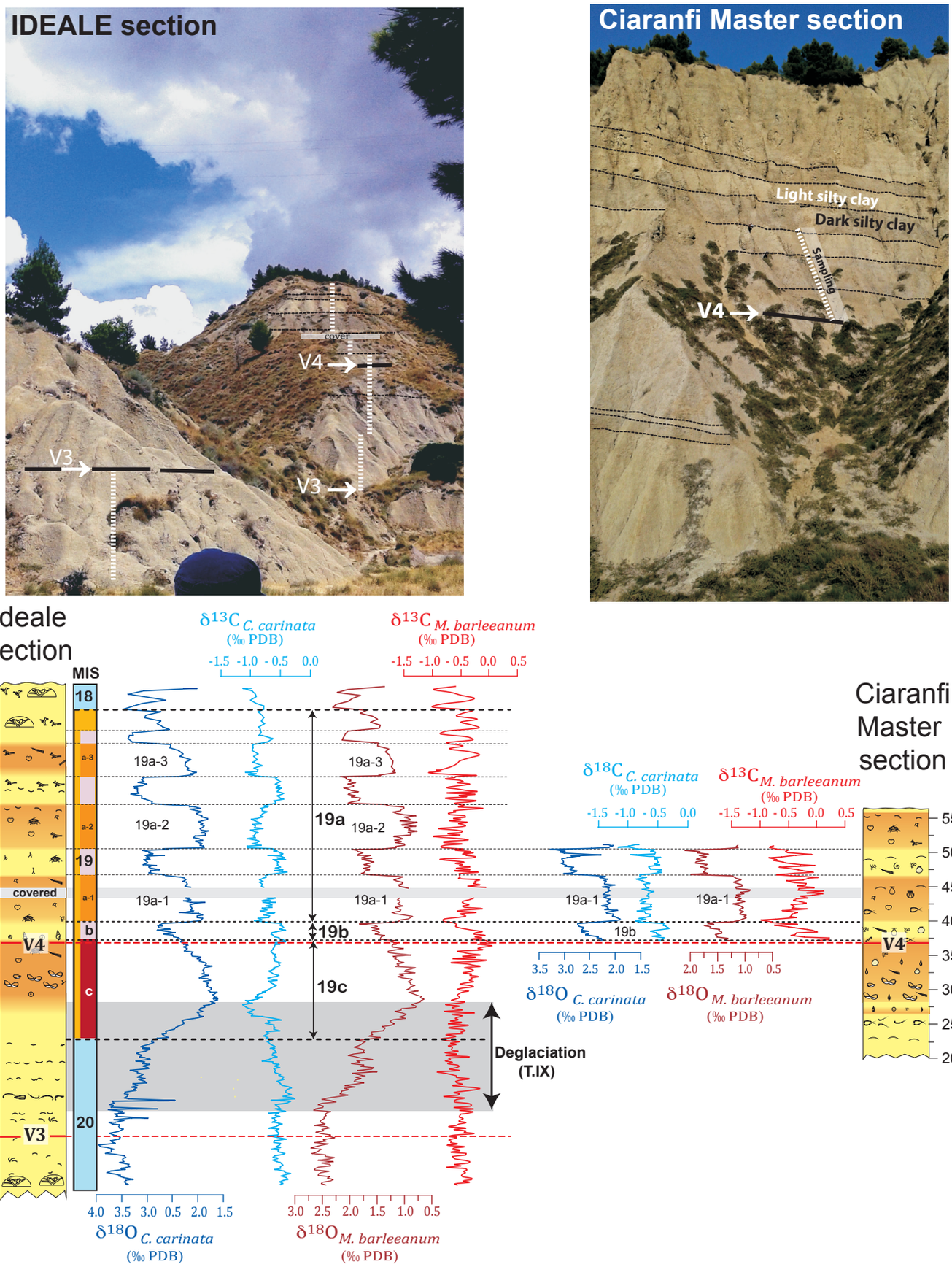
IDEALE section
cover
V4
V3
V3
Ciaranfi Master section
Light silty clay
Dark silty clay
Sampling
V4
Ideale section
MIS
18
a-3
19a-3
a-2
19a-2
19
a-1
19a-1
b
19a
19b
c
19c
20
covered
V4
V3
Deglaciation
(T.IX)
7500
7000
6500
6000
5500
5000
4500
4000
3500
3000
2500
2000
1500
1000
500
0
cm
δ13C C. carinata
(‰ PDB)
-1.5 -1.0 - 0.5 0.0
δ13C M. barleeanum
(‰ PDB)
-1.5 -1.0 - 0.5 0.0 0.5
δ18O C. carinata
(‰ PDB)
4.0 3.5 3.0 0.5 2.0 1.5
δ18O M. barleeanum
(‰ PDB)
3.0 2.5 2.0 1.5 1.0 0.5
Ciaranfi Master section
δ18C C. carinata
(‰ PDB)
-1.5 -1.0 - 0.5 0.0
δ13C M. barleeanum
(‰ PDB)
-1.5 -1.0 - 0.5 0.0 0.5
19a-1
19b
V4
3.5 3.0 2.5 2.0 1.5
δ18O C. carinata
(‰ PDB)
2.0 1.5 1.0 0.5
δ18O M. barleeanum
(‰ PDB)
5500
5000
4500
4000
3500
3000
2500
2000
cm

Figure 3

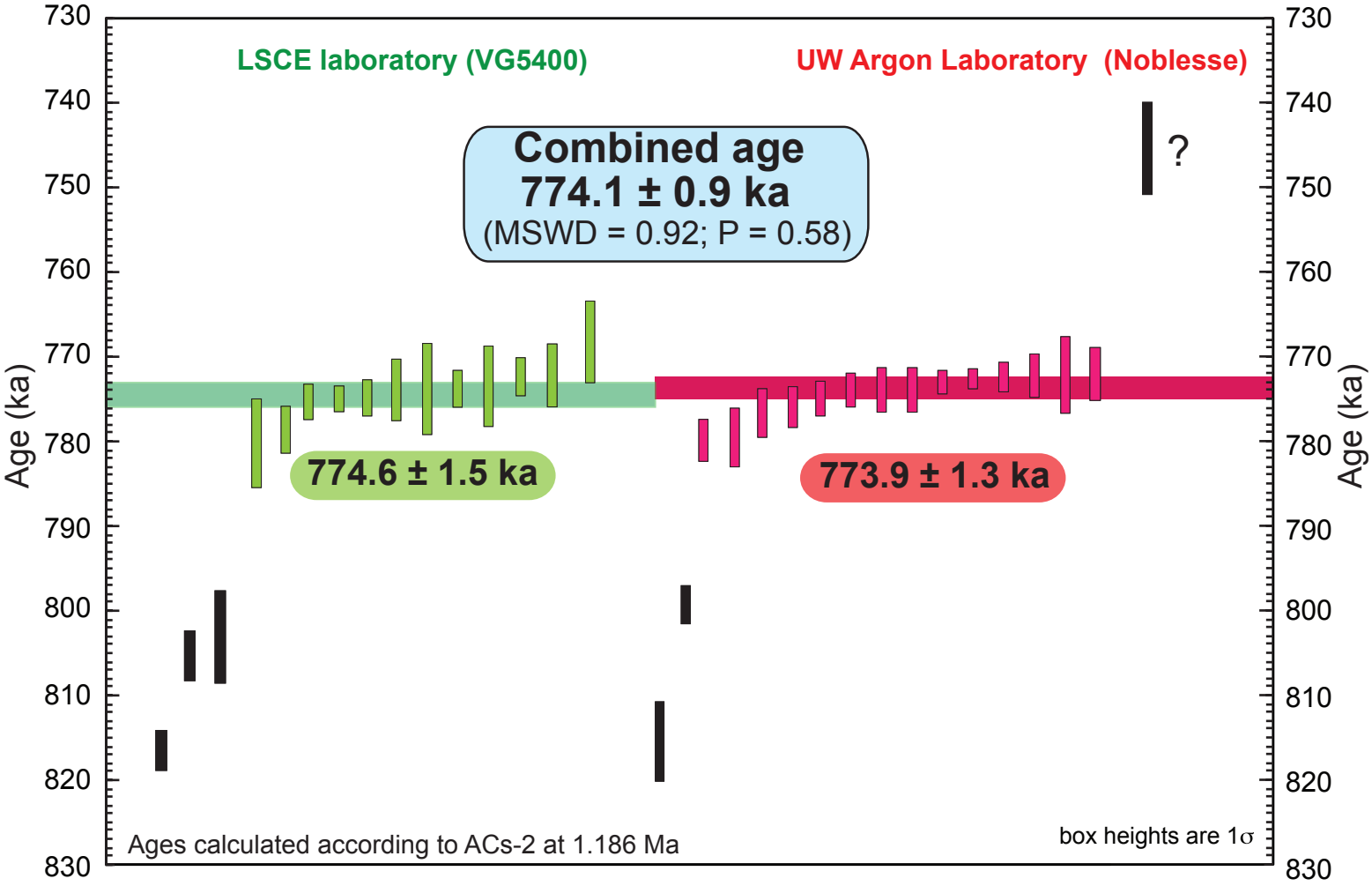
LSCE laboratory (VG5400)
UW Argon Laboratory (Noblesse)
Combined age
774.1 ± 0.9 ka
(MSWD = 0.92; P = 0.58)
?
774.6 ± 1.5 ka
773.9 ± 1.3 ka
Age (ka)
730
740
750
760
770
780
790
800
810
820
830
Ages calculated according to ACs-2 at 1.186 Ma
box heights are 1σ

Figure 4

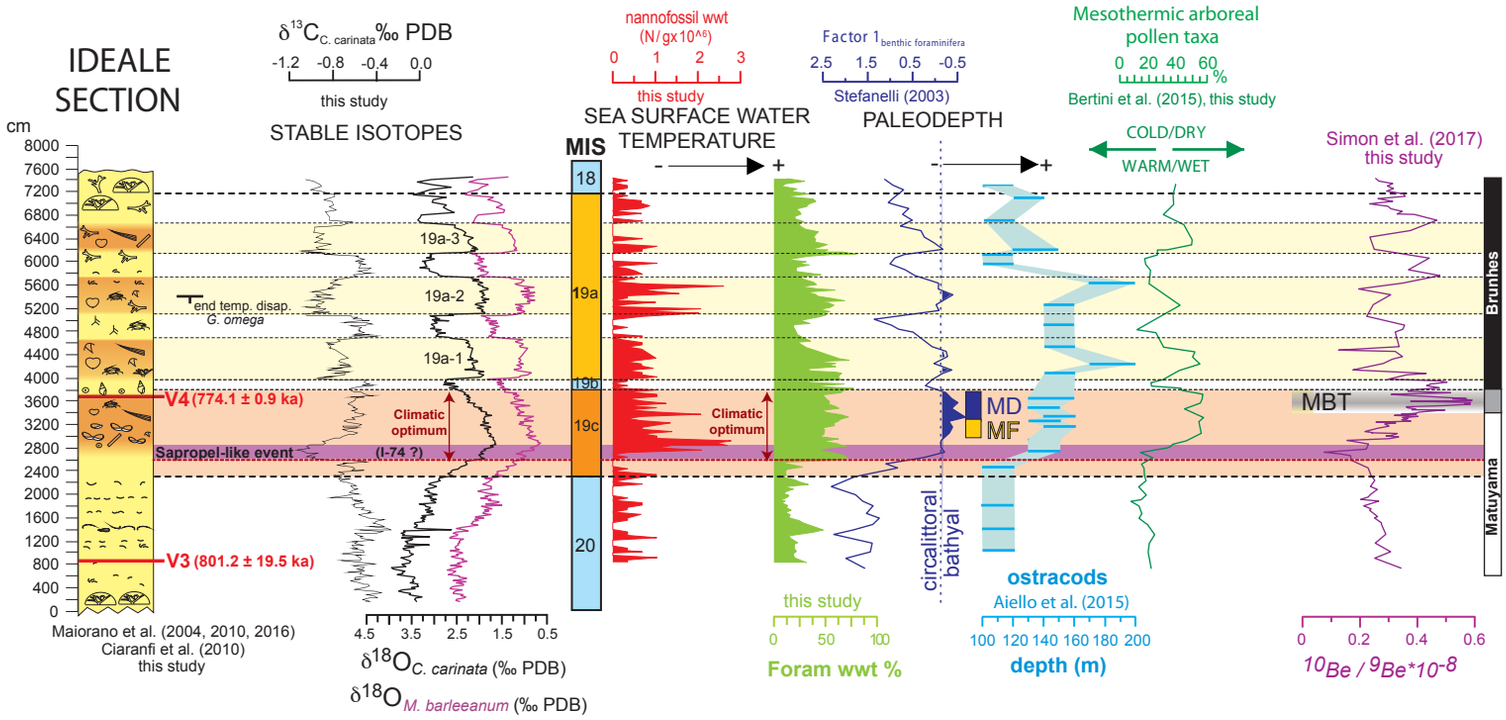

Light grey silty clay
Dark grey silty clay
V3-V4 tephra layers

Bryozoans
Fissidentalium rectum
Echinoids
Chondrites
Crab shell
Ditrupa
Pteropods
Octocorallia
Neopycnodonte cochlear
Discospirina
Nassarius
Pseudamussium
Disarticulated bivalves
Articulated bivalves
Delectopecten
Aequipecten

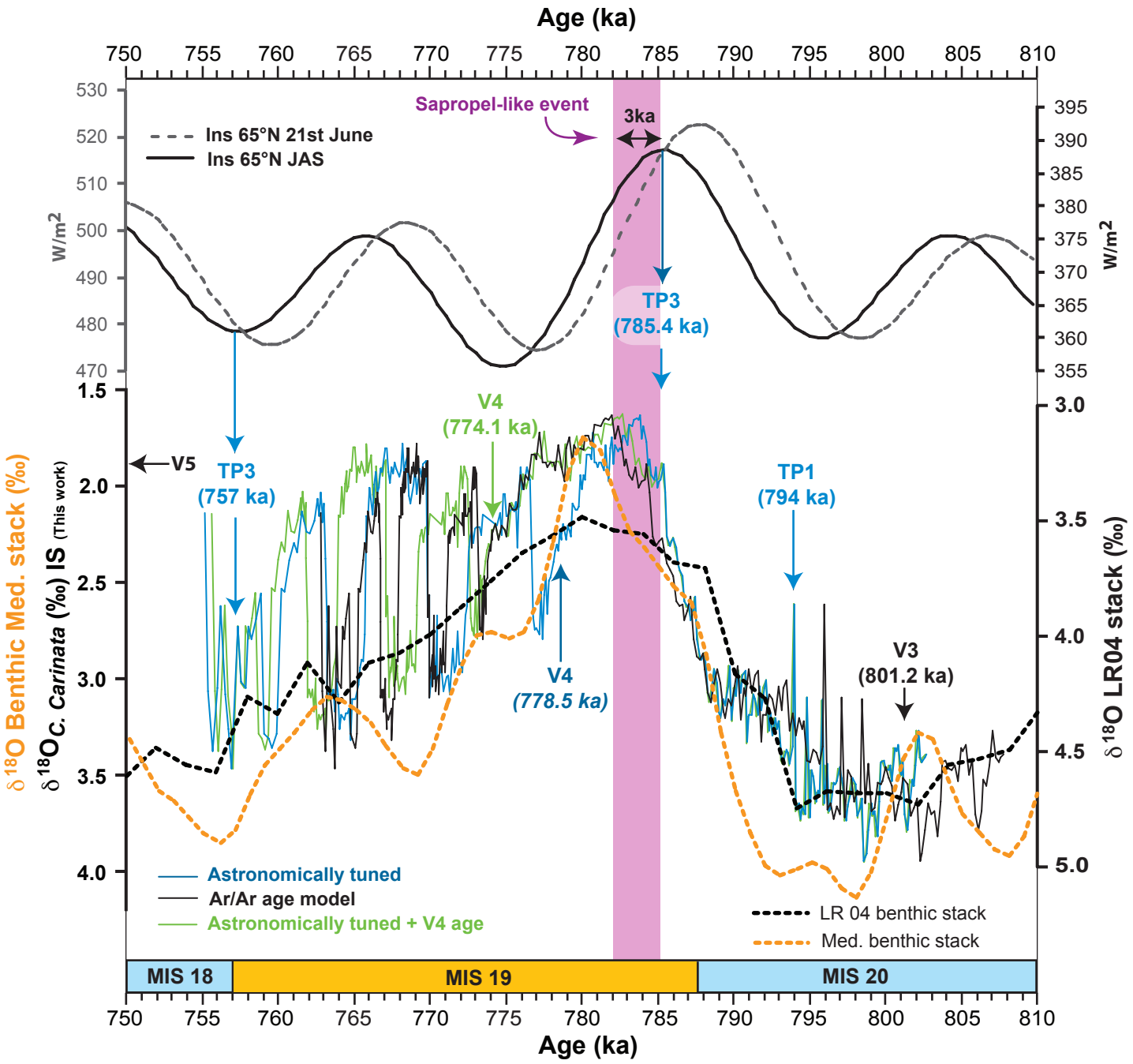
Age (ka)
Sapropel-like event
3ka
Ins 65°N 21st June
Ins 65°N JAS
W/m2
TP3
(785.4 ka)
V4
(774.1 ka)
V5
TP3
(757 ka)
TP1
(794 ka)
V4
(778.5 ka)
V3
(801.2 ka)
δ18O Benthic Med. stack (‰)
δ18O C. Carinata (‰) IS (This work)
δ18O LR04 stack (‰)
Astronomically tuned
Ar/Ar age model
Astronomically tuned + V4 age
LR 04 benthic stack
Med. benthic stack
MIS 18
MIS 19
MIS 20

Figure 6

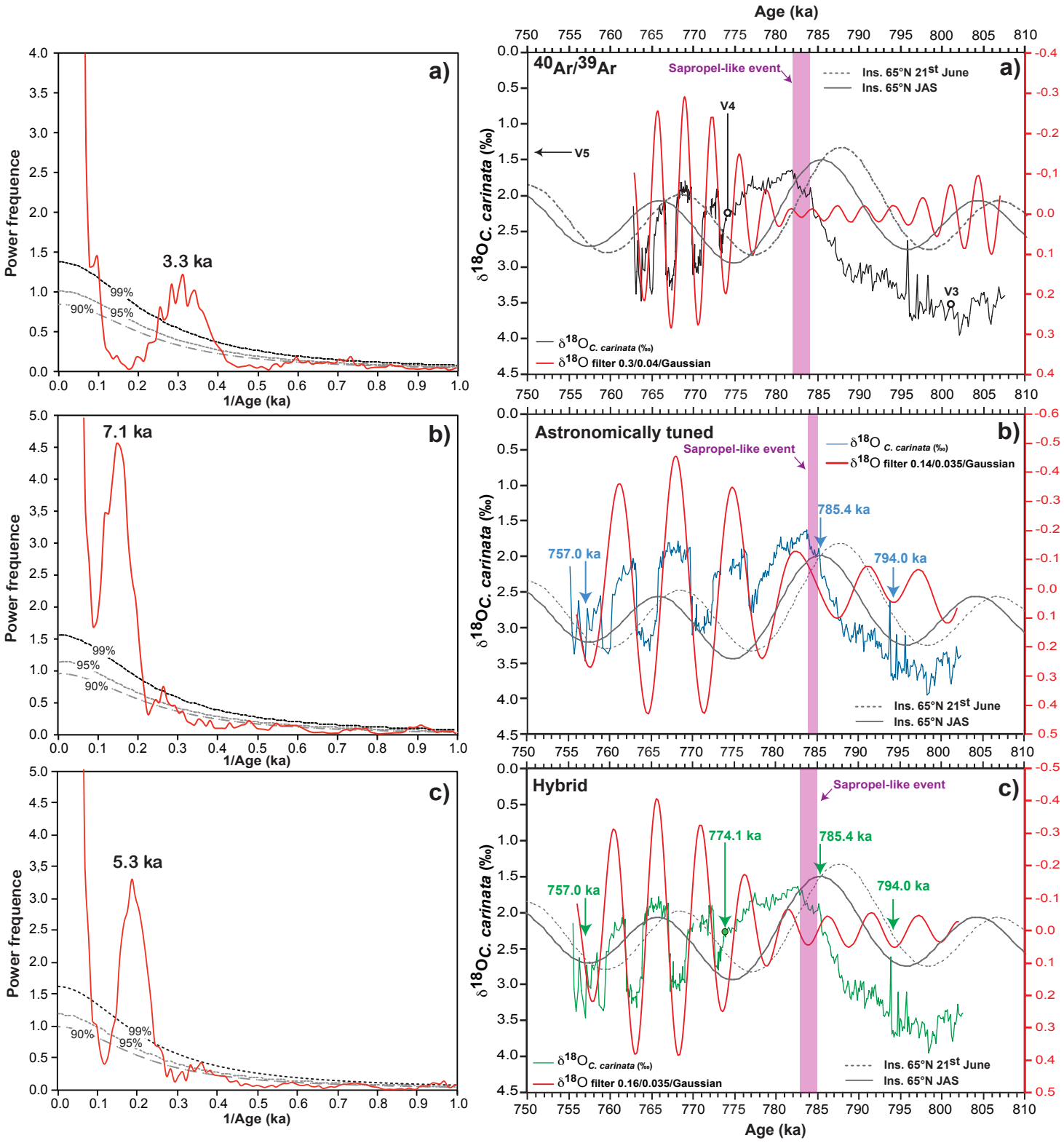
a)
Power frequence
3.3 ka
99%
95%
90%
1/Age (ka)
b)
7.1 ka
99%
95%
90%
1/Age (ka)
c)
5.3 ka
99%
95%
90%
1/Age (ka)
Age (ka)
40Ar/39Ar
Sapropel-like event
Ins. 65°N 21st June
Ins. 65°N JAS
V4
V5
V3
δ18O C. carinata (‰)
δ18O filter 0.3/0.04/Gaussian
Astronomically tuned
δ18O filter 0.14/0.035/Gaussian
757.0 ka
785.4 ka
794.0 ka
Hybrid
δ18O filter 0.16/0.035/Gaussian
774.1 ka

Figure 7

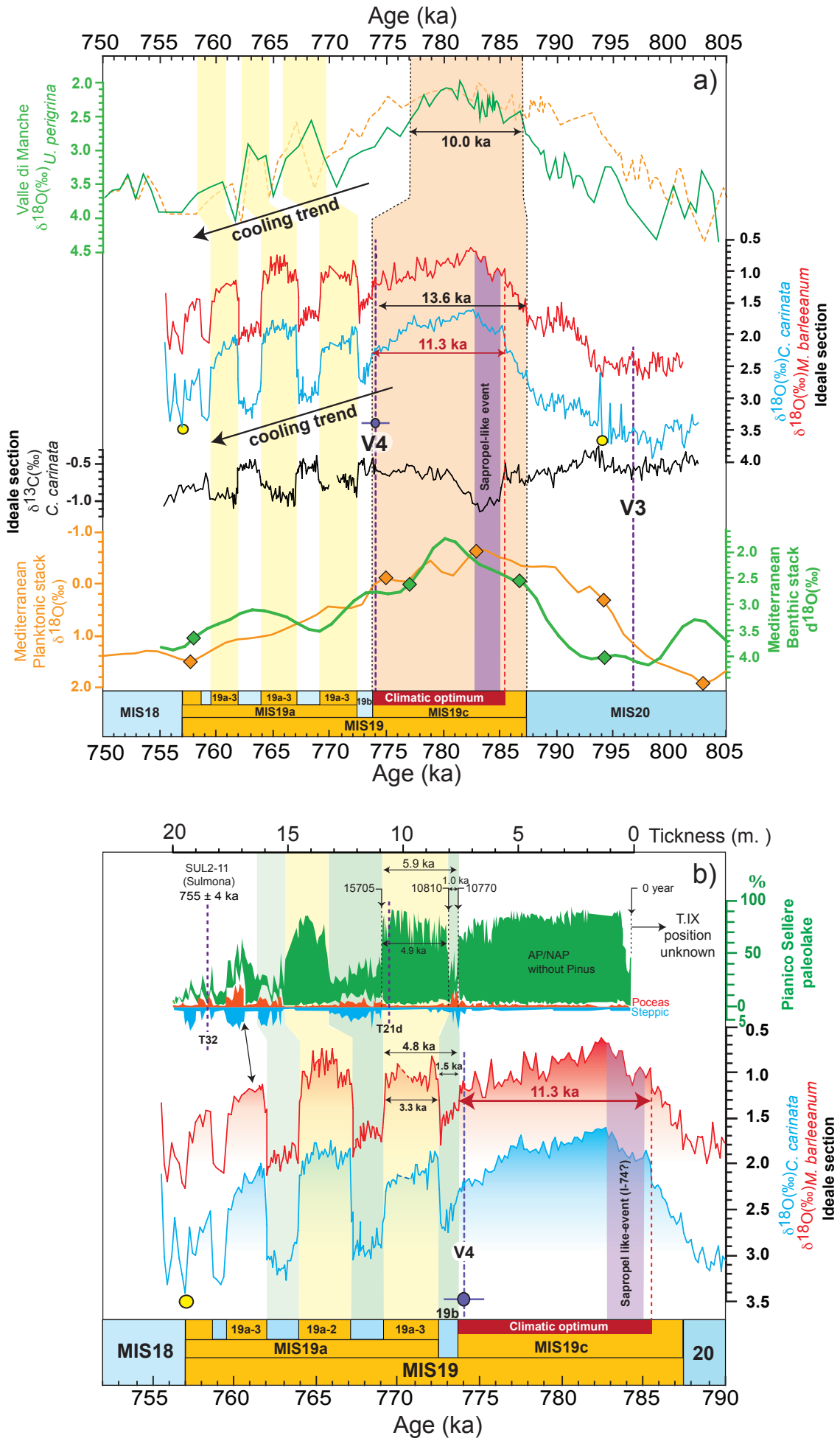
a)
Age (ka)
750 755 760 765 770 775 780 785 790 795 800 805
Valle di Manche
δ18O(‰) U. perigrina
10.0 ka
cooling trend
13.6 ka
11.3 ka
cooling trend
V4
Sapropel-like event
V3
Ideale section
δ13C(‰)
C. carinata
δ18O(‰)C. carinata
δ18O(‰)M. barleeanum
Ideale section
Mediterranean
Planktonic stack
δ18O(‰)
Mediterranean
Benthic stack
d18O(‰)
MIS18
19a-3
19a-3
19a-3
19b
Climatic optimum
MIS19a
MIS19c
MIS19
MIS20
Age (ka)
b)
Tickness (m.)
SUL2-11
(Sulmona)
755 ± 4 ka
5.9 ka
15705
10810
1.0 ka
10770
0 year
T.IX
position
unknown
4.9 ka
AP/NAP
without Pinus
Poceas
Steppic
Pianico Sellère
paleolake
T32
T21d
4.8 ka
1.5 ka
3.3 ka
11.3 ka
V4
Sapropel like-event (I-74?)
19b
δ18O(‰)C. carinata
δ18O(‰)M. barleeanum
Ideale section
MIS18
19a-3
19a-2
19a-3
Climatic optimum
MIS19a
MIS19c
MIS19
20
Age (ka)

Figure 8

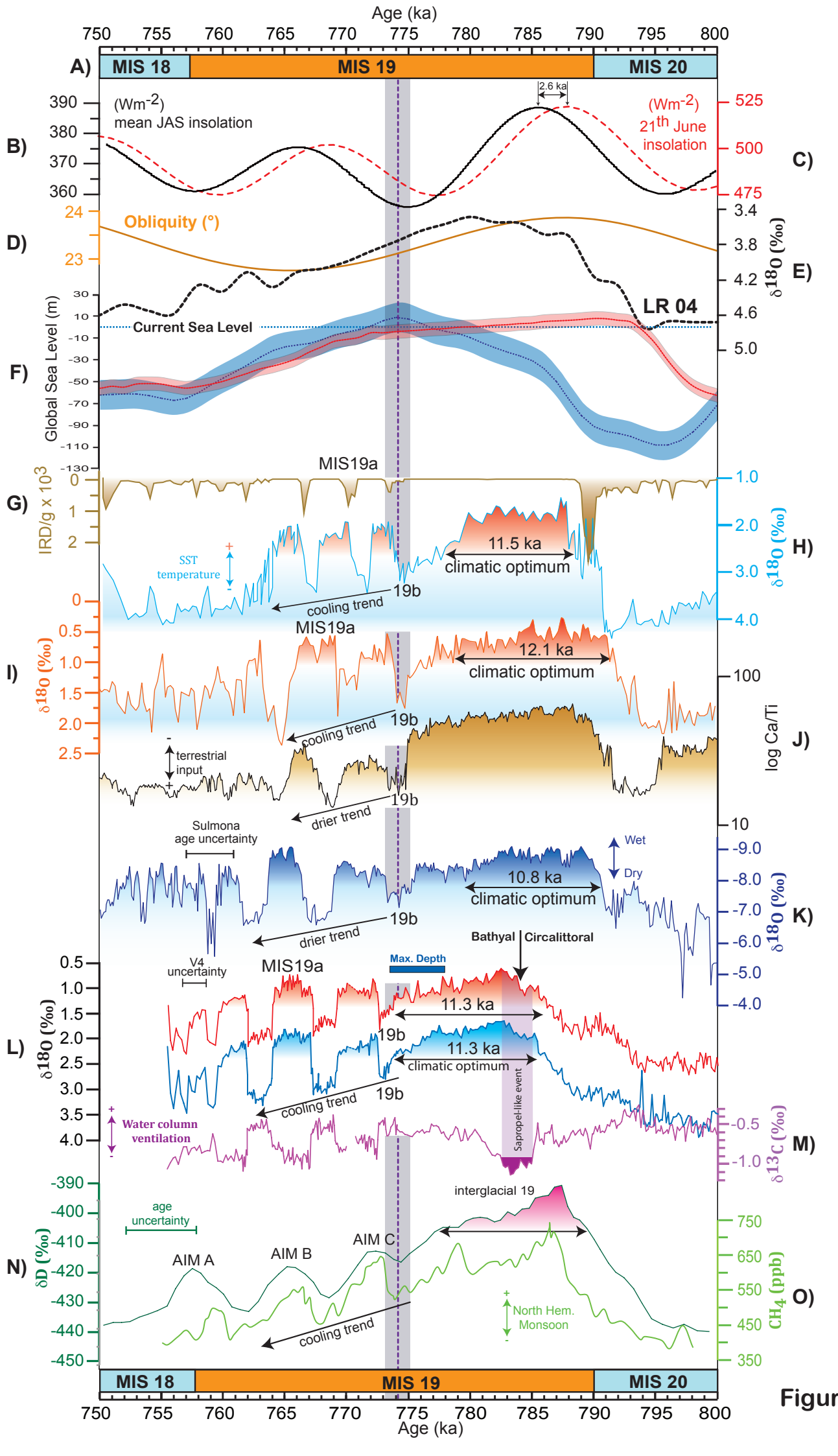
Age (ka)
750 755 760 765 770 775 780 785 790 795 800
A)
MIS 18
MIS 19
MIS 20
B)
(Wm-2)
mean JAS insolation
390 380 370 360
2.6 ka
(Wm-2)
21th June
insolation
525 500 475
C)
D)
Obliquity (°)
24 23
E)
δ18O (‰)
3.4 3.8 4.2 4.6 5.0
LR 04
F)
Global Sea Level (m)
30 10 -10 -30 -50 -70 -90 -110 -130
Current Sea Level
MIS19a
G)
IRD/g x 10-3
0 1 2
H)
δ18O (‰)
1.0 2.0 3.0 4.0
SST
temperature
11.5 ka
climatic optimum
cooling trend
19b
I)
δ18O (‰)
0 0.5 1.0 1.5 2.0 2.5
MIS19a
12.1 ka
climatic optimum
cooling trend
19b
J)
log Ca/Ti
100 10
terrestrial
input
drier trend
19b
Sulmona
age uncertainty
Wet
Dry
10.8 ka
climatic optimum
drier trend
19b
K)
δ18O (‰)
-9.0 -8.0 -7.0 -6.0 -5.0 -4.0
Bathyal
Circalittoral
Max. Depth
V4
uncertainty
MIS19a
11.3 ka
19b
11.3 ka
climatic optimum
cooling trend
19b
Sapropel-like event
L)
δ18O (‰)
0.5 1.0 1.5 2.0 2.5 3.0 3.5 4.0
Water column
ventilation
M)
δ13C (‰)
-0.5 -1.0
N)
δD (‰)
-390 -400 -410 -420 -430 -440 -450
age
uncertainty
AIM A
AIM B
AIM C
interglacial 19
cooling trend
North Hem.
Monsoon
O)
CH4 (ppb)
750 650 550 450 350
MIS 18
MIS 19
MIS 20
750 755 760 765 770 775 780 785 790 795 800
Age (ka)

Figure 9

References

Abu-Zied, R.H., Rohling, E.J., Jorissen, F.J., Fontanier, C., Casford, J.S.L., Cooke, S., 2008 Benthic foraminiferal response to changes in bottom-water oxygenation an organic flux in the eastern Mediterranean during LGM to recent times. Mar. Micropal., 67, 46–68.

Aiello, G., Barra, D., Parisi, R., 2015. Lower-Middle Pleistocene ostracod assemblages from the Montalbano Jonico section (Basilicata, southern Italy). Quat. Int. 383, 47–73.

Arrhenius, G., 1952. Sediment cores from the East Pacific. Reports of the Swedish Deep-Sea Expedition 1947–1948 5, Fasc. 1, 227 p.

Aurahs, R., Treis, Y., Darling, K., Kucera, M., 2011. A revised taxonomic and phylogenetic concept for the planktonic foraminifer species *Globigerinoides ruber* based on molecular and morphometric evidence. Mar. Micropaleontol. 79, 1–14.

Azzaroli, A., Perno, U., Radina, B., 1968. Note illustrative della Carta Geologica d'Italia alla scala 1:100.000, Foglio 188 Gravina di Puglia. Serv. Geol. Ital. 57 pp

Backman, J., Raffi, I., Rio, D., Fornaciari, E., Pälike, H., 2012. Biozonation and biochronology of Miocene through Pleistocene calcareous nannofossils from low and middle latitudes. Newsletters on Stratigraphy, 45(3), 221–244.

Bard, E., Arnold M., Duprat J., Moyes J., Duplessy J.-C., 1987. Reconstruction of the last deglaciation: deconvolved records of d^{18}O profiles, micropaleontological variations and accelerator mass spectrometric ^{14}C dating. Clim. Dynamics 1, 101-112.

Bazin, L., Landais, A., Lemieux-Dudon, B., Toyé M.K., Veres, D., Parennin, F., Martinerie, P., Ritz, C., Capron, E., Lipenkov, V.Y., Loutre, M.F., Raynaud, D., Vinther, Bo M., Svensson, A.M., Rasmussen, S.O., Severi, M., Blunier T., Leuenberger, M., Fischer, H., Masson-Delmotte, V., Chappellaz, J., Wolff E.W., 2013. The Antarctic ice core chronology (AICC2012): 120-800 ka. Climate of the Past 9, 1715–1731.

Bertini, A., Toti, F., Marino, M., Ciaranfi, N., 2015. Vegetation and climate across the Early-Middle Pleistocene transition at the Montalbano Jonico section (southern Italy). Quat. Int. 383, 74–88.

Braucher, R., Guillou, V., Bourlès, D.L., Arnold, M., Aumaître, G., Keddadouche, K., Nottoli, E., 2015. Preparation of ASTER in-house ^{10}Be/^{9}Be standard solutions. Nuclear Instruments and Methods in Physics Research Section B: Beam Interactions with Materials and Atoms 361, 335-340

Brauer, A., Wulf, S., Mangili, C., Moscariello, A., 2007. Tephrochronological dating of varved interglacial lake deposits from Piànico-Sèllere (Southern Alps, Italy) to around 400 ka. J. Quat. Sci. 22, 85–96.

Brilli, M., 1998. Stratigrafia isotopica del carbonio e dell'ossigeno della successione infra e mesopliocenica di Montalbano Jonico (Basilicata, Italia meridionale). Tesi di Dottorato di Ricerca in Scienze della Terra XI ciclo. Universit. degli Studi di Roma "La Sapienza", 112 pp.

Brilli, M., Lerche, J., Ciaranfi, N., Turi, B., 2000. Evidence of precession and obliquity orbital forcing in Oxygen 18 isotope composition of Montalbano Jonico section (Basilicata, southern Italy). Applied Radiation and Isotope, 52, 957–964.

Caron, B., Siani, G., Sulpizio, R., Zanchetta, G., Paterne, M., Santacroce, R., Terna, E., Zanella, E., 2012. Late Pleistocene to Holocene tephrostratigraphic record from the Northern Ionian Sea. Mar. 698 Geol. 311, 41–51.

Ceregato, A., Raffi, S., Scarponi, D., 2007. The circalittoral/bathyal in the Middle Pliocene

of Northern Italy: the case of the *Korobkovia oblonga–Jupiteria concave* paleocommunity type. Geobios 40, 555–572.

Chmeleff, J., von Blanckenburg, F., Kossert, K., Jakob, D., 2010. Determination of the ^{10}Be half-life by multicollector ICP-MS and liquid scintillation counting. Nuclear instruments and methods in physics research B. 268, 192-199.

Ciaranfi, N., D'Alessandro, A., Marino, M., Sabato, L., 1994. The Montalbano Jonico Section in the Bradanic Foredeep (southern Italy): a potential early-middle Pleistocene Boundary Stratotype. Contribution in Cita, M.B. and Castradori, D. (1994) "Workshop on marine sections from the Gulf of Taranto (Southern Italy) usable as potential stratotypes for the GSSP of the Lower, Middle and Upper Pleistocene (Bari, Italy, Sept. 29-Oct. 4, 1994). Il Quaternario, 7, pp. 677–692.

Ciaranfi, N., Marino, M., Sabato, L., D'Alessandro, A., De Rosa, R., 1996. Studio geologico-stratigrafico di una successione infra e mesopleistocenica nella parte sud-occidentale della Fossa bradanica (Montalbano Jonico, Basilicata). Bolletino Società Geologica Italiana 115, 379–391.

Ciaranfi N., D'Alessandro A., Marino M., 1997. A candidate section for the lower-middle Pleistocene boundary (Apennine foredeep, South Italy). In: Naiwen W., Remane J. (Eds.), Proceedings 30th International Geological Congress. Vol. 11, 201–211.

Ciaranfi, N., D'Alessandro, A., 2005. Overview of the Montalbano Jonico area and section: aproposal for a boundary stratotype for the lower-middle Pleistocene, southern Italy Foredeep. Quat. Int. 131, 5–10.

Ciaranfi, N., Lirer, F., Lirer, L., Lourens, L.J., Maiorano, P., Marino, M., Petrosino, P., Sprovieri, M., Stefanelli, S., Brilli, M., Girone, A., Joannin, S., Pelosi, N., Vallefuoco, M., 2010. Integrated stratigraphy and astronomical tuning of the Lower-Middle Pleistocene Montalbano Jonico land section (southern Italy). Quat. Int. 210, 109–120.

Capraro, L., Ferretti, P., Macrì, P., Scarponi, D., Tateo, F., Fornaciari, E., Bellini, G., Dalan, G., 2017. The Valle di Manche section (Calabria, Southern Italy): A high resolution record of the Early-Middle Pleistocene transition (MIS 21-MIS 19) in the Central Mediterranean. Quat. Sci. Rev. 165, 31–48.

D'Alessandro, A., La Perna, R., Ciaranfi, N., 2003. Response of macrobenthos to changes in paleoenvironment in the Lower-Middle Pleistocene (Lucania Basin, southern Italy). Il Quaternario, 16, 167–182.

De Abreu, L., Abrantes, F., Shackleton, N.J., Tzedakis, P., McManus, J.F., Oppo, D.W., Hall, M.A., 2005. Ocean climate variability in the eastern North Atlantic during interglacial marine isotope stage 11: A partial analogue to the Holocene? Paleoceanography, 20 (3), DOI: 10.1029/2004PA001091.

Doglioni, C., Tropeano, M., Mongelli, F., Pieri, P., 1996. Middle-Late Pleistocene uplift of Puglia: an "anomaly" in the Apenninic foreland. Mem. Soc. Geol. Ital. 51, 101–117.

Duplessy, J.C, Lalou, C., Vinot, A.C. 1970. Differential isotopic fractionation in benthic foraminifera and paleotemperatures reassessed. Science 168, 250–251.

Elderfield, H., Ferretti, P., Greaves, M., Crowhurst, S., McCave, I.N., Hodell, D., Piotrowski, A. M., 2012. Evolution of ocean temperature and ice volume through the mid-Pleistocene climate transition. Science 337, 704-709.

Emeis, K., Sakamoto, T., Wehausen, R., Brumsack, H.J., 2000. The sapropel record 763 of the eastern Mediterranean Sea - results of Ocean Drilling Program Leg 160. Palaeogeogr. Palaeoclimatol. Palaeoecol. 158, 371–395.

Emiliani, C., 1955. Pleistocene temperatures. J. Geol. 63, 538–578.

Ferretti, P., Crowhurst, S.J., Naafs, D.A., Barbante, C., 2015. The Marine Isotope Stage 19

in the mid-latitude North Atlantic Ocean: astronomical signature and intra-interglacial variability. Quat. Sci. Rev. 108, 95–110.

Fischer, H., Behrens, M., Bock, M., Richter, U., Schmitt, J., Loulergue, L., Chappellaz, J., Spahni, R., Blunier, T., Leuenberger, M., Stocker, T.F., 2008. Changing boreal methane sources and constant biomass burning during the last termination. Nature 452, 864–867.

Flores, J.A., Sierro, F.J., 1997. Revised technique for calculation of calcareous nannofossil accumulation rates. Micropaleontology 43, 321–324.

Fontanier, C., Jorissen, F.J., Chaillou, G., David, C., Anschutz, P., Lafon, V., 2003. Seasonal and inter-annual variability of benthic foraminiferal faunas at 550 m depth in the Bay of Biscay. Deep-Sea Res., part 1: Oceanographic Res. Papers, 50, 457–494.

Giaccio, B., Regattieri, E., Zanchetta, G., Nomade, S., Renne, P.R., Sprain, C.J, Drysdale, R.N., Tzedakis, P.C., Messina, P., Scardia, G., Sposato, A., Bassinot, F., 2015. Duration and dynamics of the best orbital analogue to the present interglacial. Geology 43, 603-606.

Ghil, M., Allen, R.M., Dettinger, M.D., Ide, K., Kondrashov, D., Mann, M.E., Robertson, A., Saunders, A., Tian Y., Varadi, F., Yiou, P., 2002. Advanced spectral methods for climatic time series," Rev. Geophys., 40, p. 3.1-3.41, 10.1029/2000RG000092.

Girone, A., 2005. Response of otolith assemblages to sea-level fluctuations at the Lower Pleistocene Montalbano Jonico section (southern Italy). Bollettino della Società Paleontologica Italiana, 44 (1), 35–45;

Girone, A., Capotondi, L., Ciaranfi, N., Di Leo, P., Lirer, F., Maiorano, P., Marino, M., Pelosi, N., Pulice, I., 2013. Paleoenvironmental change at the lower Pleistocene Montalbano Jonico section (southern Italy): global versus regional signals. Palaeogeogr. Palaeoclimat. Palaeoec. 371, 62–79.

Grant, K.M., Grimm, R., Mikolajewicz, U., Marino G., Ziegler M., Rohling E.J., 2016. The timing of Mediterranean sapropel deposition relative to insolation, sea-level and African monsoon changes. Quaternary Science Reviews 140, 125-141.

Head, M.J., Gibbard, P.L., 2015. Formal subdivision of the Quaternary System/Period: Past, present, and future. Quat. Int. 383, 4–35.

Hodell, D., Lourens, L. Crowhurst, S., Konijnendijk, T., Tjallingii, R., Jiménez-Espejo, F., Skinner, L., Tzedakis, P.C., Shackleton Site Project Members., 2015. A reference time scale for Site U1385 (Shackleton Site) on the SW Iberian Margin. Global and Planet. Change 133, 48–64.

Jicha, B.R., Singer, B.S., Sobol, P., 2016. Re-evaluation of the ages of $^{40}Ar/^{39}Ar$ sanidine standards and supereruptions in the western U.S. using a Noblesse multi-collector mass spectrometer. Chem. Geol. 431, 54–66.

Joannin, S., Ciaranfi N., Stefanelli, S., 2008. Vegetation changes during the late Early Pleistocene at Montalbano Jonico (Province of Matera, southern Italy) based on pollen analysis. Palaeogeogr. Palaeoclimat. Palaeoec. 270, 92–101.

Kleiven, H., Hall, I.R., McCave, I.N., Knorr, G., Jansen, E., 2011. North Atlantic coupled deep water flow and climate variability in the middle Pleistocene. Geology 39, 343–346.

Köhler, P., Fischer, H., Munhoven, G., Zeebe, R.E., 2005. Quantitative interpretation of atmospheric carbon records over the last glacial termination. Global Biogeochem. Cycles, 19. GB4020, doi:10.1029/2004GB002345.

Konijnendijk, T.Y.M., Ziegler, M., Lourens, L.J., 2014. Chronological constraints on Pleistocene sapropel depositions from high-resolution geochemical records of ODP Sites 967 and 968. Newsl. Stratigr. 47, 263–282.

Korschinek, G., Bergmaier, A., Faestermann, T., Gerstmann, U.C., Knie, K., Rugel, G., Wallner, A., Dillmann, I., Dollinger, G., Lierse von Gostomski, Ch., Kossert, K., Maiti, M., Poutivtsev, M., Remmert, A., 2010. A new value for the half-life of ^{10}Be by Heavy-Ion Elastic Recoil Detection and liquid scintillation counting. Nuclear Instruments and Methods in Physics Research B. 268, 187-191.

Kuiper, K.F., Deino, A., Hilgen, F.J., Krijgsman, W., Renne, P.R., Wijbrans, J.R., 2008. Synchronizing rock clocks of Earth history. Science 320, 500–504.

Langereis, C.G., Dekkers, M.J., de Lange., G.J., Paterne, M., van Santvoort, P.J.M., 1997. Magnetostratigraphy and astronomical calibration of the last 1.1 Myr from an eastern Mediterranean piston core and dating of short events in the Brunhes. Geophys. J. Int. 129, 75–94.

Laskar, J., Robutel, P., Joutel, F., Gastineau, M., Correia, A.C.M., Levrard, B., 2004. A long Term numerical solution for the insolation quantities of the Earth. Astron. Astrophys. 428, 261–285.

Lee, J.Y., Marti, K., Severinghaus, J.P., Kawamura, K., Yoo, H.S., Lee, J.B., Kim, J.S., 2006. A redetermination of the isotopic abundance of atmospheric Ar. Geochim. Cosmochim. Acta 70, 4507–4512.

Lisiecki, L.E., Raymo, M.E., 2005. A Pliocene-Pleistocene stack of 57 globally distributed benthic d18O records. Paleoceanography, 20, PA1003.

Lisiecki, L.E., Stern, J.V. 2016. Regional and global benthic d^{18}O stacks for the last glacial cycle. Paleoceanography 31, 1–27.

Loutre, M.F., Berger, A., 2000. Future Climatic Changes: Are We Entering an exceptionally Long Interglacial? Climatic Change 46, 61–90.

Loulergue, L., Schilt, A., Spahni, R., Masson-Delmotte, V., Blunier, T., Lemieux, B., Barnola, J.-M., Raynaud, D., Stocker, T.F., Chappellaz, J., 2008. Orbital and millennial-scale features of atmospheric CH_4 over the past 800,000 years. Nature 453, 383–386.

Lourens, L.J., 2004. Revised tuning of Ocean Drilling Program Site 964 and KC01B (Mediterranean) and implications for the δ^{18}O, tephra, calcareous nannofossil, and geomagnetic reversal chronologies of the past 1.1 Myr. Paleoceanography 19, PA3010.

Maiorano, P., Marino, M., Di Stefano, E., Ciaranfi, N., 2004. Calcareous nannofossil events in the lower-middle Pleistocene transition at the Montalbano Jonico section and ODP Site 964: calibration with isotope and sapropel stratigraphy. Rivista Italiana di Paleontologia e Stratigrafia, 110, 547–557.

Maiorano, P., Aiello, G., Barra, D., Di Leo, P., Joannin, S., Lirer, F., Marino, M., Pappalardo, A., Capotondi, L., Ciaranfi, N., Stefanelli, S,. 2008. Paleoenvironmental changes during sapropel 19 (i-cycle 90) deposition: evidences from geochemical, mineralogical and microplaoentological proxies in the mid Pleistocene Montalbano Jonico land section (southern Italy). Palaeogeogr. Palaeoclimat. Palaeoecol. 257, 308–334.

Maiorano, P., Capotondi, L., Ciaranfi, N., Girone, A., Lirer, F., Marino, M., Pelosi, N., Petrosino, P., Piscitelli, A., 2010. Vrica-Crotone and Montalbano Jonico sections: a potential unit-stratotype of the Calabrian Stage. Episodes, 33, 218–233.

Maiorano, P., Marino, M., Balestra, B., Flores, J.A., Hodell, D.A., Rodrigues, T., 2015. Coccolithophore variability from the Shackleton Site (IODP Site U1385) through MIS 16–10. Glob. Planet. Change 133, 35–48.

Maiorano, P., Bertini, A., Capolongo, D., Eramo, G., Gallicchio, S., Girone, A., Pinto, D., Toti, F., Ventruti, G., Marino, M., 2016. Climate signatures through the Marine Isotope Stage

19 in the Montalbano Jonico section (Southern Italy): a land-sea perspective. Palaeogeoge. Palaeoclimat. Palaeoecol. 461, 341–361.
Magri, D., Tzedakis P.C., 2000. Orbital signatures and long-term vegetation patterns in the Mediterranean. Quat. Int. 74, 69–78.
Mangili, C., Brauer, A., Plessen, B., Moscariello, A,. 2007. Centennial-scale oscillations in oxygen and carbon isotopes of endogenic calcite from a 15,500 varve year record of the Piànico interglacial. Quat. Sci. Rev. 26, 1725–1735.
Marino, M., 1996. Quantitative nannofossil biostratigraphy of the lower-middle Pleistocene Montalbano Jonico section, southern Italy. Paleopelagos, 6, 347–360.
Marino, M., Bertini, A., Ciaranfi, N., Aiello, G., Barra, D., Gallicchio, S., Girone, A., La Perna, R., Lirer, F., Maiorano, P., Petrosino, P., Toti, F., 2015. Paleoenvironmental and climatostratigraphic insights for Marine Isotope Stage 19 (Pleistocene) at the Montalbano Jonico section, South Italy. Quat. Int. 383, 104–115.
Marino, M., Aiello, G., Barra, D., Bertini, A., Gallicchio, S., Girone, A., La Perna, R., Lirer, F., Maiorano, P., Petrosino, P., Quivelli, O., Toti, F., Ciaranfi, N., 2016. The Montalbano Jonico section (South Italy) as a reference for the Early/Middle Pleistocene boundary. Alp. Mediterranean Quat. 29 (1), 45–57.
Martrat, B., Jimenez-Amat, P., Zahn, R., Grimalt, J.O., 2014. Similarities and dissimilarities between the last two deglaciations and interglaciations in the North Atlantic region: Quater. Sci. Rev. 99, 122–134.
McIntyre, A., Bé, A.H.W., 1967. Modern coccolithophores of the Atlantic Ocean - I. Placolith and cyrtoliths. Deep Sea Res. 14, 561–597.
Massari, F., Rio, D., Sgavetti, M., Prosser, G., D'Alessandro, A., Asioli, A., Capraro, L., Fornaciari, E., Tateo, F., 2002. Interplay between tectonics and glacioeustasy, Pleistocene of the Crotone Basin, Calabria (southern Italy). Geol. Soc. Am. Bull. 114, 1183–1209
Masson-Delmotte, V., Dreyfus, G., Braconnot, P., Johnsen, S., Jouzel, J., Kageyama, M., Landais, A., Loutre, M.F., Nouet, J., Parrenin, F., Raynaud, D., Stenni, B., Tuenter, E., 2006. Past temperature reconstructions from deep ice cores: relevance for future climate change. Climate of the Past 2, 145–165.
Niespolo, E.M., Rutte, D., Deino, A.L., Renne, P.R., 2017. Intercalibration and age of the Alder Creek sanidine $^{40}Ar/^{39}Ar$ standard. Quat. Geochronol. 39, 205–213.
Milner, A.M, Collier R.E.L, Roucoux, K.H, Müller, U.C., Pross, J., Kalaitzidis, S., Christanis, K., Tzedakis, P.C., 2012. Enhanced seasonality of precipitation in the Mediterranean during the early part of the Last Interglacial. Geology 40, 919–922.
Min, K., Mundil, R., Renne, P.R., Ludwig, K.R., 2000. A test for systematic errors in $^{40}Ar/^{39}Ar$ geochronology through comparison with U/Pb analysis of a 1.1-Ga rhyolite. Geochim. Cosmochim. Acta 64, 73–98.
Morigi, C., Jorissen, F.J., Gervais, A., Guichard, S., Borsetti, A.M., 2001. Benthic foraminiferal faunas in surface sediments off NW Africa: relationship with organic flux to the ocean floor. J. Foraminiferal Res., 31, 350–368.
Moscariello, A., Ravazzi, C., Brauer, A., Mangili, C., Chiesa, S., Rossi, S., de Beaulieu, J.L., Reille, M., 2000. A long lacustrine record from the Piànico-Sèllere Basin (Middle-Late Pleistocene, Nothern Italy). Quat. Int. 73-74, 47–68.
Palumbo, E., Flores, J.A., Perugia, C., Petrillo, Z., Voelker, A.H.L., Amore, F.O., 2013. Millennial scale coccolithophore paleoproductivity and surface water changes between 445 and 360 ka (Marine Isotope Stages 12/11) in the Northeast Atlantic. Palaeogeogr. Palaeoclimatol. Palaeoecol. 383–384, 27–41.

Patacca, E., Scandone, P. 2007. Geology of the Southern Apennines. Boll. Soc. Geol. Ital., Spec. Issue 7, 75–119.

Petrosino, P., Jicha, B.R., Mazzeo, F.C., Ciaranfi, N., Girone, A., Maiorano, P., Marino, M., 2015. The Montalbano Jonico marine succession: An archive for distal tephra layers at the Early-Middle Pleistocene boundary in southern Italy. Quat. Int., 383, 89–103.

Phillips, D., Matchan, E.L., 2013. Ultra-high precision $^{40}Ar/^{39}Ar$ ages for Fish Canyon Tuff and Alder Creek Rhyolite sanidine: New dating standards required? Geochimica et Cosmochimica Acta 121, 229–239

Pol, K., Masson-Delmotte, V., Johnsen, S., Bigler, M., Cattani, O., Durand, G., Falourd, S., Jouzel J., Minster B., Parrenin, F., Ritz, C., Steen-Larsen, H.C., Stenni, B., 2010. New MIS 19 EPICA Dome C high-resolution deuterium data: hints for a problematic preservation of climate variability in the "oldest ice". Earth Planet. Sci. Lett. 298, 95–103.

Raffi, I., Agnini, C., Backman, J., Catanzariti, R., 2016. A Cenozoic calcareous nannofossil biozonation from low and middle latitudes: A synthesis. J. Nannoplankton Res. 36, 121–132.

Railsback, L.C., Gibbard, P.L., Heas, M.J., Voarintsoa N.R.G., Tucanne S., 2015. An optimized scheme of lettered marine isotope substages for the last 1.0 million years, and the climatostratigraphic nature of isotope stages and substages. Quat. Sci. Rev. 111, 94-106.

Regattieri, E., Giaccio, B., Zanchetta, G., Drysdale, R.N., Galli, P., Peronace, E., Nomade, S., Wulf, S., 2015. Hydrological variability over Apennine during the Early Late Glacial precession minimum, as revealed by a stable isotope record from Sulmona basin, central Italy. J. Quat. Sci. 30, 19–31.

Regattieri, E., Giaccio, B., Galli, P., Nomade, S., Peronace, E., Messina, P., Sposato, A., Boschi, C., Gemelli, M., 2016. A multi-proxy record of MIS 11-12 deglaciation and glacial MIS 12 instability from the Sulmona Basin (central Italy). Quat. Sci. Rev. 132, 12–145.

Rio, D., Raffi, I., Villa, G., 1990. Pliocene-Pleistocene calcareous nannofossil distribution patterns in the western Mediterranean. In: Kastens, K.A., Mascle, J., et al. (Eds.), Proceedings of the ODP. Scientific Results, 107. Ocean Drilling Program, College Station, TX, pp. 513–533.

Rivera, T.A., Storey,M., Schmitz, M.D., Crowley, J.L., 2013. Age intercalibration of $^{40}Ar/^{39}Ar$ sanidine and chemically distinct U/Pb zircon populations from the Alder Creek rhyolite Quaternary geochronology standard. Chem. Geol. 345, 87–98.

Renne, P.R., Balco, G., Ludwig, K.R., Mundil, R., Min, K., 2011. Response to the comment by W.H. Schwarz et al. on "Joint determination of ^{40}K decay constants and $^{40}Ar^*/^{40}K$ for the Fish Canyon sanidine standard, and improved accuracy for $^{40}Ar/^{39}Ar$ geochronology" by P.R. Renne et al. (2010). Geochim. Cosmochim. Acta 75, 5097–5100.

Rohling, E.J., Jorissen, F.J., Vergnaud Grazzini, C., Zachariasse, W.J., 1993. Northern Levantine and Adriatic Quaternary planktic foraminifera; reconstruction of paleoenvironmental gradients. Mar. Micropaleontogy 21, 191–218.

Rohling, E.J., 1999. Environmental control on Mediterranean salinity and $d^{18}O$. Paleoceanography 14, 706-715.

Rohling, E.J., Foster, G.L., Grant, K.M., Marino, G., Roberts, A.P., Tamisiea, M.E., Williams, F., 2014. Sea-level and deep-sea-temperature variability over the past 5.3 million years. Nature 508, 477-482.

Rossi, S., 2003. Etude pollinique de la séquence lacustre Pléistocène de Piànico-Sèllere (Italie). Ph.D. Thesis, Université de Droit d'Economie et des Sciences d'Aix Marseille III.

Roulleau, E., Pinti, D.L., Rouchon, V., Quidelleur, X., Gillot, P.Y., 2009. Tephro-chronostratigraphy of the lacustrine interglacial record of Piànico, Italian Southern Alps: Identifying the volcanic sources using radiogenic isotopes and trace elements. Quat. Int 204, 31–43.

Ruddiman, W.F., 2007. The early anthropogenic hypothesis: Challenges and responses. Rev. Geophys. 45, RG4001.

Saavedra-Pellitero, M., Flores, J.A., Baumann, K-H., Sierro, F.J., 2010. Coccolith distribution patterns in surface sediments of Equatorial and Southeastern Pacific Ocean. Geobios 43, 131–149.

Sanchez-Goñi, M.F., Landais, A., Fletcher, W.J., Naughton, F.N., Desprat. S., Duprat, J., 2008. Contrasting impacts of Dansgaard–Oeschger events over a western European latitudinal transect modulated by orbital parameters. Quater. Sci. Rev. 27, 1136–1151.

Sanchez-Goñi, M.F., Rodrigues, T., Hodell, D.A., Polanco-Martinez, J.M., Alonso-Garcia, M. Hernandez-Almeida, I., Desprat, S., Ferretti, P., 2016. Tropically-driven climate shifts in southwestern Europe during MIS 19, a low eccentricity interglacial. Earth Planet. Sci. Lett. 448, 81–93.

Scardia, G., Muttoni G., 2009. Paleomagnetic investigations on Pleistocene lacustrine sequence of Piànico-Sèllere (northern Italy). Quat. Int. 204, 44–53.

Shackleton, N.J., 1969. The last interglacial in the marine and terrestrial record. P. Roy. Soc. Lond., B. 174, 135–154.

Shackleton, N.J., Hall, M.A., 1974. Oxygen and carbon isotope data from leg 74 foraminifers. In Moore T.C, Rabinowitz, P.D. et al. Init. Rpts. DSDP 74, Washington (US Govt Printing Office), 599–612.

Siani, G., Sulpizio, R., Paterne, M., Sbrana, A., 2004. Tephrostratigraphy study for the last 18,000 ^{14}C years in a deep-sea sediment sequence for the South Adriatic. Quat. Sci. Rev., 23, 2485–2500.

Simon, Q., Thouveny, N., Bourlès, D.L., Nuttin, L., Hillaire-Marcel, C., St-Onge, G., 2016. Authigenic $^{10}Be/^{9}Be$ ratios and ^{10}Be-fluxes ($^{230}Th_{xs}$-normalized) in central Baffin Bay sediments during the last glacial cycle: Paleoenvironmental implications. Quaternary Science Reviews 140, 142-162.

Simon, Q., Bourlès, L.D., Bassinot, F., Nomade S., Marino, M., Ciaranfi, N., Girone, A., Maiorano, P., Thouveny, N., Choya, S., Dewil, F., Scao, V., Isguder, G., Blamart, D., ASTER Team., 2017. Authigenic $^{10}Be/^{9}Be$ ratio signature of the Matuyama–Brunhes boundary in the Montalbano Jonico marine succession. Earth Planet. Sci. Lett. 460, 255–267.

Simon, Q., Bourlès, D.L., Thouveny, N., Horng, C.-H., Valet, J.P., Bassinot, F., Choy, S., 2018a. Cosmogenic signature of geomagnetic reversals and excursions from the Reunion event to the Matuyama-Brunhes transition (0.7 - 2.14 Ma interval). Earth Planet. Sci. Lett., 482, 510-524.

Simon, Q., Thouveny, N., Bourlès, D.L., Bassinot, F., Savranskai, T., Valet., J.P., ASTER Team, 2018b. Increased production of cosmogenic ^{10}Be recorded in oceanic sediment sequences : Information on the age, duration and amplitude of the geomagnetic dipole moment minimum over the Matuyama-Brunhes transition. Earth Planet. Sci. Lett., 489, 191-202.

Skinner, L.C., Shackleton, N.J., 2006. Deconstructing Terminations I and II: revisiting the glacioeustatic paradigm based on deep-water temperature estimates. Quat. Sci. Rev. 25, 3312–3321.

Stefanelli, S., 2003. Benthic foraminiferal assemblages as tools for paleoenvironmental reconstruction of the early-middle Pleistocene Montalbano Jonico composite section. Bollettino della Società Paleontologica Italiana 42, 281–299.

Stefanelli, S., 2004. Cyclic stages in oxygenation based on foraminiferal microhabitats: early-middle Pleistocene, Lucania basin, southern Italy. Journal of Micropaleontology, 23, 81–95.

Stefanelli, S., Capotondi, L., Ciaranfi, N., 2005. Foraminiferal record and environmental changes during the deposition of early-middle Pleistocene sapropels in southern Italy. Palaeogeogr., Palaeoclimat. Palaeoecol. 216, 27–52.

Stefanelli, S., Capotondi, L., 2008. Foraminiferal response to the deposition of insolation cycle 90 sapropel in different Mediterranean areas. J. of Micropalaeontology 27, 45–61. Sottili G., Arienzo I., , Castorina F., Gaeta M., Giaccio B., Marra F., Palladino D-M. 2018. Sr and Nd isotope signatures during the evolution of the ultrapotassic Sabatini Volcanic District (Roman Province, central Italy). Accepted to Quat. Sci. Rev.

Toti, F., 2015. Interglacial vegetation patterns at the Early-Middle Pleistocene transition: a point of view from Montalbano Jonico section (southern Italy). Alpine and Mediterranean Quaternary 28, 131–143.

Tzedakis, P.C., 2007. Seven ambiguities in the Mediterranean palaeoenvironmental narrative. Quat. Sci. Rev. 26, 2042– 2066.

Tzedakis, P.C., Channell, J.E.T., Hodell, D.A., Kleiven, H.F., Skinner, L.C., 2012. Determining the natural length of the current interglacial. Nature Geoscience 5. http://dx.doi.org/10.1038/NGEO1358.

Vannacci, M., 2016. Cambiamenti climatici durante lo stadio isotopico 22 come registrato nella successione marina di Montalbano Jonico (Italia meridionale) tramite indagine palinologica. Tesi di Laurea Magistrale. Università di Firenze, AA 2014-2015, 70 pp.

von Blanckenburg, F., Bouchez, J., Wittmann, H., 2012. Earth surface erosion and weathering from the ^{10}Be (meteoric)/^{9}Be ratio. Earth Planet. Sci. Lett. 351–352, 295–305.

Wang, P., Tian, J., Lourens, L., 2010. Obscuring of long eccentricity cyclicity in Pleistocene oceanic carbon isotopic records. Earth Planet. Sci. Lett. 290, 319–330.

Wisshak, M., Lopez Correa, M., Gofas, S., Salas C., Taviani, M., Jakobsen, J., Freiwald, A. 2009. Shell architecture, element composition, and stable isotope signature of the giant deep-sea oyster *Neopycnodonte zibrowii sp.* n. from the NE Atlantic. Deep-Sea Research I 56, 374–407.

Yin, Q.Z., Berger, A., 2012. Individual contribution of insolation and $C0_2$ to the interglacial climates of the past 800,000 years, Clim. Dyn. 38(3-4), 709–724.

Yin, Q., Berger, A., 2015. Interglacial analogues of the Holocene and its natural near future. Quat. Sci. Rev. 120, 28–46.

Ziegler, M., Tuenter, E., Lourens L.J., 2010. The precession phase of the boreal summer Monsoon as viewed from the eastern Mediterranean (ODP Site 968). Quat. Sci. Rev. 29, 1481–1490.

ÉCOLE DOCTORALE
Sciences mécaniques et énergétiques, matériaux et géosciences (SMEMAG)

Mots clés : Clumping isotopique, températures, foraminifères, calibration, transition du Pléistocène moyen, glaciaires-interglaciaires, Méditerranée, MIS 31, MIS 19

Quantifier les variations de température océanique du passé est nécessaire pour comprendre les mécanismes qui régissent l'évolution climatique. Les méthodes de paléo-thermométrie classiques peuvent souffrir de limitation inhérents à l'écologie des organismes et/ou à cause de l'influence d'effets physico-chimiques (salinité, acidité de l'eau de mer…). Ce travail se focalise sur la technique de paléothermométrie Δ_{47}, qui repose sur la mesure du « clumping isotopique » dans les carbonates. Il vise d'abord à établir une calibration appliquée aux foraminifères et ensuite à mettre en œuvre cette calibration pour l'étude des variations climatiques au cours de la transition du Pléistocène moyen (MPT). Notre calibration Δ_{47}-température des foraminifères planctoniques et benthiques, prélevés dans des sédiments modernes, couvre une gamme de température de -2 à 25 °C. Les valeurs de Δ_{47} sur 9 espèces de foraminifères présentent une excellente corrélation avec la température de calcification des organismes, estimée à partir des mesures isotopiques de l'oxygène. Les résultats obtenus confirment l'absence d'effets liés à l'écologie des foraminifères (effets vitaux et de taille des organismes) et démontrent que la salinité n'affecte pas les mesures de Δ_{47}. Cette étude constitue une avancée méthodologique importante pour les futures études paléocéanographiques sur les foraminifères.
La MPT correspond à une transition climatique marquée par un changement de fréquence des cycles glaciaires-interglaciaires (de 41 000 à 100 000 ans). La compréhension de cette période est un enjeu scientifique majeur pour appréhender la mise en place du climat actuel. Notre calibration Δ_{47}-température a permis de quantifier les variations de températures au cours de la MPT en mer méditerranée (Section de Montalbano Jonico, sud de l'Italie) et particulièrement des stades isotopiques marins 31 et 19, considérés comme des analogues à l'Holocène. Les résultats indiquent que (i) les températures (Δ_{47}) obtenues sont en adéquation avec les températures obtenues par d'autres paléothermomètres, (2) les températures permettent de retracer les changements de régime océanographique et hydrologique, et (3) la mesure du Δ_{47} est complément prometteur pour les études multi-méthodes en paléocéanographie.

Keywords : Clumped isotopes, temperatures, foraminifera, Mid-Pleistocene transition, glacial-interglacial, Mediterranea Sea, MIS 31, MIS 19.

The quantification of past oceanic temperature changes is a critical requirement for understanding the mechanisms which regulate climate variations. Classical methods of paleothermometry could suffer from well-known limitations related to ecology and/or to physico-chemical biases (sea water salinity, acidity…). This work focuses on clumped-isotope carbonate thermometry (Δ_{47}). It aims to establish a calibration of Δ_{47} foraminifera and use it to study past climatic variations through the Mid-Pleistocene Transition (MPT). Our Δ_{47} calibration in planktonic and benthic foraminifera collected from modern marine sediment covers a temperature range of -2 to 25 °C. The clumped-isotope compositions of 9 species of foraminifera show a robust correlation with the calcification temperature, estimated from the measurements of oxygen-18. These results confirm the absence of bias linked to foraminifer ecology (species-specific and foraminifer size effects) and provide evidence that salinity does not affect the Δ_{47} thermometer.
This study constitutes significant methodological progress for future paleoceanographic applications in foraminifera. The MPT is a climatic transition characterized by a shift in the frequencies of glacial-interglacial cycles (from 41 000 to 100 000 years). Understanding the MPT is a major scientific objective, which underlies our effort to study the establishment of our present climate. Our Δ_{47} calibration was used to quantify temperature changes through the MPT in the Mediterranea Sea (Montalbano Jonico section, south of Italy), and in particular the marine isotopic stages 31 and 19, which may be described as Holocene analogues. We find that (1) Δ_{47} temperatures are in good agreement with temperatures reconstructed from other paleothermometers, (2) these results allow reconstructing changes in past oceanographic and hydrologic regime, and (3) Δ_{47} measurement are a promising component of multi-proxy paleoceanographic studies.

Université Paris-Saclay
Espace Technologique / Immeuble Discovery
Route de l'Orme aux Merisiers RD 128 / 91190 Saint-Aubin, France